

Proceedings of the 18th annual symposium of the IEEE Photonics Society Benelux Chapter, November 25-26, 2013, Eindhoven, The Netherlands

Citation for published version (APA):

Leijtens, X., & Pustakhod, D. (Eds.) (2013). *Proceedings of the 18th annual symposium of the IEEE Photonics Society Benelux Chapter, November 25-26, 2013, Eindhoven, The Netherlands*. (IEEE/LEOS Benelux Chapter : annual symposium; Vol. 18). Technische Universiteit Eindhoven.

Document status and date:

Published: 01/01/2013

Document Version:

Publisher's PDF, also known as Version of Record (includes final page, issue and volume numbers)

Please check the document version of this publication:

- A submitted manuscript is the version of the article upon submission and before peer-review. There can be important differences between the submitted version and the official published version of record. People interested in the research are advised to contact the author for the final version of the publication, or visit the DOI to the publisher's website.
- The final author version and the galley proof are versions of the publication after peer review.
- The final published version features the final layout of the paper including the volume, issue and page numbers.

[Link to publication](#)

General rights

Copyright and moral rights for the publications made accessible in the public portal are retained by the authors and/or other copyright owners and it is a condition of accessing publications that users recognise and abide by the legal requirements associated with these rights.

- Users may download and print one copy of any publication from the public portal for the purpose of private study or research.
- You may not further distribute the material or use it for any profit-making activity or commercial gain
- You may freely distribute the URL identifying the publication in the public portal.

If the publication is distributed under the terms of Article 25fa of the Dutch Copyright Act, indicated by the "Taverne" license above, please follow below link for the End User Agreement:

www.tue.nl/taverne

Take down policy

If you believe that this document breaches copyright please contact us at:

openaccess@tue.nl

providing details and we will investigate your claim.

**Proceedings of the
18th Annual Symposium
of the
IEEE Photonics Society Benelux Chapter**

Proceedings of the 18th Annual Symposium of the IEEE Photonics Society Benelux Chapter



**Monday-Tuesday, November 25-26, 2013
Auditorium TU Eindhoven
Eindhoven, the Netherlands**

Editors

Xaveer Leijtens & Dzmitry Pustakhod

Organized by

**Photonic Integration Group, Eindhoven University of Technology,
the Netherlands
in association with the IEEE Photonics Society Benelux Chapter**

Supported by

Phoenix Software B.V.

Ocean Optics

Lionix B.V.

TNO

STW

Genexis B.V.

Bright Photonics B.V.

Proceedings of the 18th Annual Symposium of the IEEE Photonics Society Benelux Chapter

A catalogue record is available from the Eindhoven University of Technology Library

ISBN 978-90-386-3512-5

NUR 950

Published by Department of Electrical Engineering
Eindhoven University of Technology
Eindhoven, the Netherlands

Copyright © 2013, all rights reserved. No parts of this book may be reproduced or transmitted in any form or by any means, electronic, mechanical, photocopying, recording, or otherwise, without the prior written permission of the editor.

Abstracting is permitted with credit to the source. Individual readers and libraries acting for them are permitted to make fair use of the material in these proceedings, such as to copy an article for use in teaching or research, provided that such copies are not sold. Authors are permitted to copy or reprint their own papers.

The papers in this book comprise the digest of the meeting mentioned on the cover and title page. They reflect the authors opinions and are published as presented and without change, in the interest of timely dissemination. Their conclusion in this publication does not necessarily constitute endorsement by the publisher or the editors.

Preface

Dear participant,

We are very pleased to welcome you to Eindhoven for the 18th annual Benelux symposium of the IEEE Photonics Society. This should be a great opportunity for all of you to meet and interact with people with an interest in photonics.

First a little bit of background information. The IEEE Photonics Society is a world-wide society of the IEEE with the following fields of interest: lasers, optical devices, optical fibers, and associated lightwave technology and their applications in systems and subsystems, in which the quantum electronic devices are key elements. Our society was not always called the “Photonics Society”. The foundation was made already in 1965 with the establishment of the Quantum Electronics Council (QEC). The council became the Quantum Electronics and Applications Society (QEAS) in 1977. This society was renamed in 1985 to become the Lasers and Electro-Optics Society (LEOS). The Benelux chapter of the Lasers and Electro-Optics Society was formed in 1996 with the goal of promoting the development of photonics, as it is now called, in the Benelux area: Belgium, Netherlands and Luxemburg. One of the main activities of the Benelux chapter is the organization of this annual symposium. At the symposium we are bringing together scientists and engineers working in universities, industries and other research institutes. The very first Benelux symposium was organized in 1996 at the University of Twente. This was a big success and since then the symposium has been organized every year, by different universities and organizations in Belgium and the Netherlands. In 2009, LEOS changed its name to become the Photonics Society.

This year’s symposium, the 18th in the series, is organized again as a two-day event, starting on Monday with an invited talk by prof Ursula Keller from ETH Zürich, followed by a dinner and then an invited talk by prof Liam Barry from Dublin City University. After this we have two contributed presentations and the remainder of the evening is for a poster session where all posters are displayed and the odd-numbered posters are presented. This will allow for an informal meeting and exchange of ideas, with drinks and some snacks.

The next day starts with two invited talks presented by prof Wood-Hi Cheng from the National Sun Yat-sen University and by Pim Kat from Technobis. Following a coffee break there will be a parallel sessions with twelve (2×6) presentations. After the first session there is a 2½ hour break for lunch and for the second poster session, where the even-numbered posters are presented. The poster session is followed by a second parallel session with twelve (2×6) presentations. In the closing session we will announce the location of next year’s symposium and will hand out the best poster award.

The organizing committee of the symposium would like to thank the invited speakers and the presenters of oral and poster contributions for their presentations. We thank the scientific committee for their work in selecting the papers and their feedback on the symposium program. Finally, we are grateful for the support from various organizations that made this symposium possible: TU Eindhoven, the COBRA research institute, Phoenix software, LioniX, Ocean Optics, TNO, Genexis, STW, Bright Photonics, the ECOC foundation and the Photonics Society.

We welcome you to the 18th symposium and wish you a good time with valuable interactions with your fellow photonics colleagues.

On behalf of the organizing committee,

Xaveer Leijtens

October 2013

Scientific and Organizing Committees

Scientific Committee

Dr. Xaveer Leijtens
Dr. Mirvais Yousefi
Dr. Kerstin Wörhoff
Ir. Henrie van den Boom
Prof. Geert Morthier
Dr. Guy Verschaffelt
Prof. Pascal Kockaert
Prof. Marc Wuilpart
Dr. Michael Peeters
Dr. Jose Pozo
Dr. Douwe Geuzebroek

Technische Universiteit Eindhoven
Photonic Sensing Solutions
Universiteit Twente
Technische Universiteit Eindhoven
Universiteit Gent
Vrije Universiteit Brussel
Université Libre de Bruxelles
Université de Mons
Alcatel-Lucent
TNO
Xio Photonics

Organizing Committee

Xaveer Leijtens, chairman
Sylwester Latkowski
Longfei Shen
Dima Pustakhod
Valentina Moskalenko
Aura Higuera Rodriguez
Jolanda Levering, secretary

Technische Universiteit Eindhoven

Contents

Preface	v
Scientific and organizing committees	vii
I Invited papers	1
High power ultrafast VECSELs and MIXSELs	
B.W. Tilma, C.A. Zaugg, M. Mangold, S.M. Link, A. Klenner, M. Golling, U. Keller	3
Characterisation of wavelength tuneable lasers for use in coherent burst/packet switched networks employing spectrally efficient modulation formats	
L.P. Barry, A.J. Walsh, T. Huynh, K. Shi, J. Mountjoy, A. Fagan, A.D. Ellis	11
The Art and Science of Packaging High-Coupling Photonics Devices and Modules	
W.-H. Cheng	13
ASPIC and Packaging solutions for demanding industrial applications, an overview	
R. Evenblij, P. Kat	15
II Oral contributions	19
Germanium-on-Silicon Mid-infrared Photonic Integrated Circuits	
A. Malik, M. Muneeb, S. Pathak, Y. Shimura, J. Van Campenhout, R. Loo, G. Roelkens	21
Delivering 10 Gb/s optical data with picosecond timing accuracy over 75 km distance	
N. Sotiropoulos, C.M. Okonkwo, R. Nuijts, H. de Waardt, J.C.J. Koelemeij	25
Improving single mode transmission performance using few-mode fibers and space-time coding	
R.G.H. van Uden, C.M. Okonkwo, H. Chen, H. de Waardt, A.M.J. Koonen	29
Graphene plasmonics: Tunable coupling with nano-cavities	
G. Rosolen, B. Maes	33
Characterization of silicon micro-ring resonators	
W.J. Westerveld, J.M. Pozo, S.M. Leinders, M. Yousefi, H.P. Urbach	37

Colloidal PbS Quantum Dot Photodetectors for Short-wave Infrared applications	
C. Hu, A. Gassenq, E.M.P. Ryckeboer, Y. Justo, Z. Hens, G. Roelkens	41
Monolithically Integrated InGaAsP/InP Active-Passive 8×8 Cross-Connect	
R. Stabile, A. Rohit, K.A. Williams	45
Raman Spectroscopy using photonic waveguides	
A. Dhakal, P. Wuytens, F. Peyskens, A.Z. Subramanian, N. Le Thomas, R. Baets	49
Full Rate-equation Description of Multi-mode Semiconductor Lasers	
D. Lenstra, M. Yousefi	53
Monolithic Integration of a InP Nano-laser on (001) Si Substrate	
Z. Wang, B. Tian, M. Paladugu, M. Pantouvaki, C. Merckling, W. Guo, J. Dekoster, J. Van Campenhout, D. Van Thourhout	57
Progress report on on-wafer testing of Photonic Integrated Circuits (PICs)	
E. Bitincka, M.K. Smit	61
Board-level single-mode polymer optical waveguides	
A. Elmogi, E. Bosman, S. Kalathimekkad, N. Teigell Beneitez, R. Guindi, J. Missinne, G. Van Steenberge	65
SOI and InP based on-chip 3×3 interferometers for wavelength interrogation	
S.M.C. Abdulla, B.M. de Boer, J.M. Pozo, D.M.R. Lo Cascio, P.J. Harmsma	69
Localization and quantification of reflective events along an optical fiber using a Two-Wavelength Transmission-Reflection-Analysis (TRA)	
M. Cen, P. Mégret, J. Chen, V. Moeyart, M. Wuilpart	73
Reduction of bend losses in polymer waveguides by thin metallic layers	
M.A. Sefünç, A. Pace, M. Dijkstra, G. Sengo, S.M. García-Blanco	77
Long wavelength generic components in COBRA platform	
H. Rabbani Haghighi, D. D'Agostino, P.J. van Veldhoven, P. Thijs, H.P.M.M. Ambrosius, M.K. Smit	81
Novel pure-optical test-on-wafer technique based on a Point Reflector Optical Waveguide	
D. Melati, F. Morichetti, F.M. Soares, N. Grote, A. Melloni	85
Measurements of integrated mode-locked laser for laser library development	
V. Moskalenko, M.K. Smit, E.A.J.M. Bente	89
Tunable two color emission in a compact semiconductor ring laser with filtered feedback	
M. Khoder, R.M. Nguimdo, J. Danckaert, X.J.M. Leijtens, J. Bolk, G. Verschaffelt	93

A Monolithically Integrated Tunable Single Longitudinal Mode Extended Cavity Ring Laser using Intracavity Mach-Zehnder Interferometers	
S. Latkowski, T. De Vries, L. Augustin, M.K. Smit, E.A.J.M. Bente	97
DMT based Multi-Gbit/s Communication in Indoor Optical Networks using R-SOA	
N. Mehta, E. Tangdionga, A.M.J. Koonen	101
Optomechanically actuated slot cantilever for mass sensing	
J. Håkansson, D. Van Thourhout	105
Experimental refutation of a class of quantum epistemic models	
L. Olislager, F. Duport, J. Safioui, M.K. Patra, S. Pironio, S. Massar	109
Dual polarization biosensing with SOI microring	
J.-W. Hoste, S. Werquin, P. Bienstman	113
Study of etched polymer optical fiber Bragg gratings for ethanol vapor sensing	
X. Hu, Chao Zhang, D. Kinet, M. Debligny, P. Mégret, C. Caucheteur	117
Simultaneous 1.5 Gbps Multilink Indoor Optical Wireless System Using Diffractive Optics	
C.W. Oh, E. Tangdionga, A.M.J. Koonen	121
III Poster contributions	125
Integrated dual-wavelength AWG lasers for sub-terahertz wave generation	
A. Corradi, G. Carpintero, M.K. Smit, E.A.J.M. Bente	127
Nanoplasmonic enhancement of Raman signals by a bowtie antenna on a silicon nitride waveguide	
F. Peyskens, A.Z. Subramanian, A. Dhakal, N. Le Thomas, R. Baets	131
Parallel Optical Delay Detector for Angle-of-arrival Measurement of a Microwave Signal with Accuracy Monitoring	
Z. Cao, H.P.A. van den Boom, E. Tangdionga, A.M.J. Koonen	135
Fast Phase Shifted asymmetrical DFB laser for ultrafast all-optical flip-flop operation	
A. Abbasi, S. Keyvaninia, G. Roelkens, G. Morthier	139
Shaping sub-wavelength plasmonic funnels	
N. Rivolta, B. Maes	143
Modeling of a phosphor plate in a white phosphor-converted remote-phosphor LED	
P. Acuña, S. Leyre, J. Audenaert, G. Deconinck, Y. Meuret, P. Hanselaer	147

Microwave Modeling and Analysis of an InP based Phase Shifter from a Generic Foundry Process	
W. Yao, G. Gilardi, M.K. Smit, M.J. Wale	151
Thermal Crosstalk reduction in InP based Photonic Integrated Circuits	
G. Gilardi, W. Yao, X.J.M. Leijtens, M.K. Smit, M.J. Wale	155
Design of MEMS tunable mid-infrared VCSEL integrated on the SOI platform	
R. Wang, D. Sanchez, S. Kumari, R. Baets, G. Roelkens	159
Investigation of Carbon Doped Amorphous Silicon, an Alternative Material for All-Optical Signal Processing for On-Chip SOI PICs	
P.K. Pal, G. Morthier	163
C₆₀-assisted electron-beam lithography for loss reduction in InP membrane waveguides	
Y. Jiao, J. Pello, E. Smalbrugge, E.J. Geluk, M.K. Smit, J.J.G.M. van der Tol	167
Reflective Arrayed Waveguide Grating with flattened response	
E. Kleijn, M.K. Smit, X.J.M. Leijtens	171
Colloidal Quantum Dot Silicon Nitride Platform	
Y. Zhu, W. Xie, S. Verstuyft, T. Aubert, Z. Hens, D. Van Thourhout	175
Fabrication and characterization of a wet-etched InP-based vertical coupling mirror	
R. Santos, D. D'Agostino, F.M. Soares, H. Rabbani Haghighi, M.K. Smit, X.J.M. Leijtens	179
Ferrule-top optical fibre sensor for the measurement of magnetic fields	
M. Aerssens, G. Gruca, A. Gusarov, V. Massaut, P. Mégret, D. Iannuzzi, M. Wuijpart	183
Test structures for SOA gain and absorption measurement	
D. Pustakhod, M.K. Smit, X.J.M. Leijtens	187
Manipulating optical qubits in the frequency domain	
L. Olislager, E. Woodhead, K. Phan Huy, J.-M. Merolla, P. Emplit, S. Massar	191
Design and simulation of a high bandwidth optical modulator for IMOS technology based on slot-waveguide with electro-optical polymer	
A. Millán-Mejía, J.J.G.M. van der Tol, M.K. Smit	195
A new zero-level package approach for receiver modules	
P. Duan, O. Raz, E. Smalbrugge, H.J.S. Dorren	199
Towards densely integrated lasers for optical data communication	
A. Higuera-Rodriguez, D. Heiss, A. Fiore, M.K. Smit	203
Spatial polarization domain-wall in colloidal semiconductor nanocrystals	
M. Swaelens, S.-P. Gorza, P. Kockaert, S. Coen, M. Haelterman	207

Design of a Uni-Traveling-Carrier (UTC) photodetector in InP Membrane on Silicon (IMOS)	
L. Shen, J.J.G.M. van der Tol, G. Roelkens, M.K. Smit	211
Optimization of fiber Bragg grating physical parameters for polarization-assisted transverse strain measurements	
F. Descamps, S. Bette, C. Caucheteur	215
Uniform planarization technique for the realization of a twin-guide membrane laser	
S.P. Bhat, L. Fernandez, J.J.G.M. van der Tol, G. Roelkens, H.P.M.M. Ambrosius, M.K. Smit	219
SOI lattice filters design framework: from functional parameters to layout	
A. Ruocco, D. Van Thourhout, W. Bogaerts	223
Improving organic photovoltaic cell efficiency with enhanced exciton dissociation by incorporating local field enhancement of sub-bandgap infrared light	
T.A. Hendriks, M.A. Sefünç, L.J.A. Koster, S.M. García-Blanco	227
Silicon Nitride based high contrast grating for heterogeneously integrated tunable VCSELs	
S. Kumari, R. Wang, D. Sanchez, J. Gustavsson, R. Safaisini, A. Haglund, J. Bengtsson, A. Larsson, G. Roelkens, R. Baets	231
Optical radiative cross-talk in photonic integrated circuits	
D. Melati, F. Morichetti, G.G. Gentili, M. Achouche, D. Lanteri, H. Debregeas, F.M. Soares, N. Grote, A. Melloni	235
Guided waves in hyperbolic media	
N.J. Schilder, H.P. Urbach	239
Fabrication technology of metal-cavity nanolasers in III-V membranes on silicon	
V. Dolores-Calzadilla, E.J. Geluk, T. de Vries, E. Smalbrugge, P.J. van Veldhoven, H.P.M.M. Ambrosius, D. Heiss, A. Fiore, M.K. Smit	243
Towards High-Density Space Division Multiplexed Transmission Systems	
C.M. Okonkwo, R.G.H. van Uden, H. de Waardt, A.M.J. Koonen	247
Dynamic routing in a resonant switch matrix	
P. DasMahapatra, R. Stabile, A. Rohit, K.A. Williams	251
WDM Modulator circuit for High Energy Physics Applications	
D. Gajanana, M.G. van Beuzekom, M.K. Smit, X.J.M. Leijtens	255
An InP based generic photonic integration platform for Photonic Integrated Circuits operating up to 2 μm wavelength	
D. D'Agostino, S. Latkowski, H. Rabbani Haghighi, E. Kleijn, E.A.J.M. Bente, H.P.M.M. Ambrosius, M.K. Smit	259

Robust Optimization of 2×2 Multimode Interference Coupler Affected by Parametric Uncertainties	
S.U. Rehman, M. Langelaar, F. van Keulen	263
Optical memory operation of two semiconductor ring lasers coupled by a single waveguide	
G. Van der Sande, W. Coomans, L. Gelens	267
Nonmagnetic transformation optics for two-dimensional photonic devices	
S. Viaene, V. Ginis, P. Tassin, J. Danckaert	271
Single contact double-waveguide SOAs in AWG-based lasers fabricated on InP generic photonic integration platform	
K. Ławniczuk, M.J. Wale, P. Szczepański, R. Piramidowicz, M.K. Smit, X.J.M. Leijtens	275
Wavelength-driven positioning of a trapped particle on a photonic crystal waveguide	
M.M. van Leest, J. Caro	279
On-chip Raman spectroscopy with a Triplex dual-waveguide trap	
M.J. Boerkamp, J.T. Heldens, T. van Leest, A. Leinse, M. Hoekman, R. Heide- man, J. Caro	283
Design and performance of a packaged InP wavelength meter	
R.G. Broeke, D. Melati, F. Morichetti	287
Scalable Optical Switch System with Optical Flow Control for Flat Datacenter Architecture	
W. Miao, S. Di Lucente, J. Luo, H.J.S. Dorren, N. Calabretta	291

Part I

Invited papers

High power ultrafast VECSELs and MIXSELs

B. W. Tilma, C. A. Zaugg, M. Mangold, S. M. Link, A. Klenner, M. Golling and U. Keller

Institute for Quantum Electronics, Department of Physics, ETH Zürich, Wolfgang-Pauli-Strasse 16, 8093 Zürich, Switzerland.

We present an overview of the latest results in high power ultrafast semiconductor laser sources based on vertical-external-cavity surface-emitting lasers (VECSELs) and modelocked integrated external-cavity surface-emitting lasers (MIXSELs). The on-going power scaling and reduction in pulse duration, in combination with the excellent noise performance makes these laser sources highly attractive for many applications in tele and data communications, optical clocking, and multi-photon imaging for example and in addition for new technological fields such as frequency comb metrology.

Introduction

The development of picosecond and femtosecond lasers has made a large impact in both fundamental science and industrial applications [1, 2]. Examples of successful implementation of these ultrafast lasers are the use in optical data transmission [3], photonic signal processing [4] and frequency combs [5, 6]. So far, these lasers mainly rely on modelocked diode-pumped solid-state lasers (DPSSL), which are often relative complex, bulky and expensive systems. Semiconductor lasers have already proven to be very reliable for continuous wave (cw) operation and are nowadays used in many applications ranging from the compact disc player up to complex integrated laser sources in optical networks [7]. Semiconductor based modelocked laser so far haven't had a large impact in industrial applications, mainly due to their complexity or lack in device performance.

Optically pumped vertical-external-cavity surface-emitting lasers (VECSELs [8]) modelocked with a semiconductor saturable absorber mirror (SESAM [9]) (a typical laser setup is shown in Fig. 1a) are very attractive ultrafast laser sources, which have the potential to replace modelocked DPSSL for a widespread field of applications. High output power levels, very good noise performance and excellent beam qualities clearly set them apart other semiconductor based modelocked lasers.

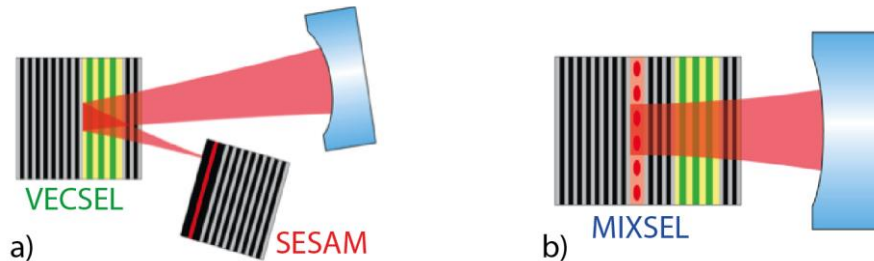


Fig. 1. Schematic diagram of: a) A conventional SESAM modelocked VECSEL consisting of a separate VECSEL gain chip and SESAM chip in a V-shaped cavity with an external output coupler. b) A MIXSEL where the saturable absorber is integrated in the gain chip, which forms a straight cavity with the output coupler.

After we demonstrated the first SESAM modelocked VECSEL in 2000 [10], we then demonstrated for the first time femtosecond pulses with >1 W of average output power

in 2011 [11]. This important milestone has been improved the last year to a record high average output power of 5.1 W in 682-fs-pulses [12] and 3.3 W in 400-fs-pulses [13]. To date, the shortest pulses achieved from a fundamentally SESAM modelocked VECSEL are 107-fs pulses with 3 mW of average output power [14]. Even shorter pulses of only 60 fs were achieved with bursts of pulses [15]. However, the combination of a sub-200-fs pulses with average output power levels above 1 W is still challenging. In order to improve our gain chips towards such high powers with short pulses, we recently developed a numerical model based on measurable macroscopic parameters. The calculations revealed, that 200-fs pulses and an average output power of 1 W should be feasible with a properly designed and fabricated VECSEL-SESAM combination [16].

The demonstration of the modelocked integrated external-cavity surface emitting laser (MIXSEL) [17], which combines the gain of the VECSEL with the saturable absorber of a SESAM in one single semiconductor layerstack (Fig. 1b), brought the technology to a higher integration level. Stable self-starting passive modelocking can be achieved in a simple straight cavity. A record high average output power of 6.4 W was achieved in 28-ps pulses at a repetition rate of 2.5 GHz [18]. Most recently we have been able to demonstrate the first femtosecond operation of a MIXSEL, generating 620-fs pulses at a repetition rate of 4.8 GHz and 101 mW of average output power [19]. In Fig. 2a an overview of the reported average output power levels versus pulse duration is given for both the SESAM modelocked VECSELs as well as for MIXSELs.

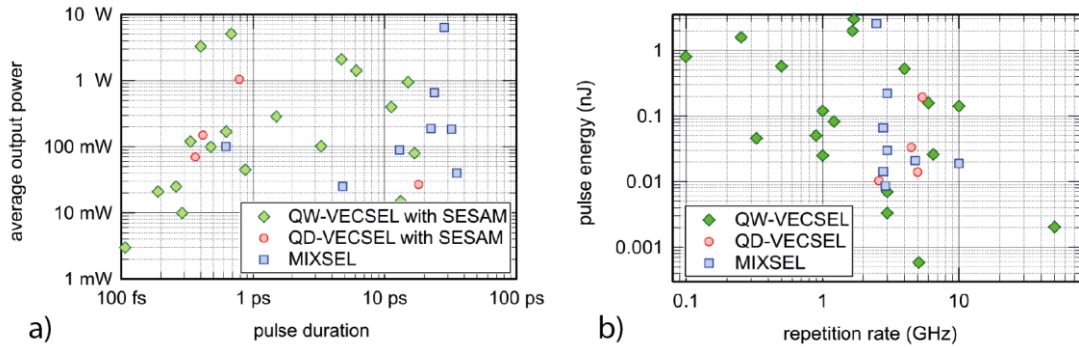


Fig. 2. Overview of published results achieved with QW-VECSELs (green), QD-VECSELs (red) and MIXSELs (blue): a) Recorded average output power versus pulse duration. b) Recorded pulse energy versus repetition rate.

Repetition rate scaling

Besides the optimization in terms of shorter pulses and higher output power, there is also a demand for stable pulse trains at certain repetition rates. Low repetition rates in the MHz-range in combination with high pulse energies are very attractive for numerous applications such as biomedical multi-photon imaging [20] where tissue heating has to be avoided by reducing the average output power, maintaining the high pulse energy. In other applications, such as optical sampling by laser cavity tuning (OSCAT) [21] and on-chip optical clocking [22], a very high repetition rate of 10 GHz or higher is required. Due to the very flexible cavity configuration, the VECSEL and MIXSEL technology can operate over this large operation range of almost three orders of magnitude (Fig. 2b). A 253 MHz fundamentally modelocked VECSEL was demonstrated producing 400 mW of average output power in 11.3-ps-pulses leading to

1.6 nJ pulse energy and 124 W peak power [23]. An even lower repetition rate of 100 MHz has been demonstrated with 30 mW of average output power in 20-ps-pulses and 0.3 nJ pulse energy [24]. The major challenge in low repetition rate fundamentally modelocked VECSELs and MIXSELs is the suppression of multiple pulses in the laser cavity, which decreases the pulse energy and destabilizes the repetition rate.

On the other side, ultrafast VECSELs with repetition rates as high as 50 GHz in the fundamentally modelocked regime [25] and up to 175 GHz in harmonically modelocked operation [26] were demonstrated. The repetition rate of fundamentally modelocked VECSELs is limited by the nature of the cavity design and the pulse duration. The MIXSEL approach on the other hand benefits from the simple straight cavity in which the output coupler can be moved closer to the semiconductor chip. Preliminary results show that in this way the repetition rate of a fundamentally modelocked MIXSEL can reach 100 GHz. Repetition rate tuning, required for example for OSCAT, has been demonstrated with a SESAM modelocked VECSEL from 6.5 GHz up to 11.3 GHz [27] with a nearly constant pulse duration of 625 fs and 169 mW average output power.

Noise performance and frequency stabilization

The high power levels achieved with the VECSEL and MIXSEL technology in combination with the short pulses in the fs-regime, makes them highly attractive sources for applications that rely on stable frequency combs [5]. So far these technologies benefit from the excellent low-noise performance of DPSSLs. For bringing the technology from scientific labs into industrial applications or even households, more compact, robust and cheaper sources are required. For a long time it was assumed that semiconductor lasers could not compete with the excellent noise figures of DPSSLs, mainly due to their low-Q cavities and the long gain sections which introduce complex dispersion, waveguiding effects and nonlinear dynamics. However, SESAM modelocked VECSELs and MIXSELs operate in high-Q cavities with low intracavity losses (including output coupling) in the range of 1%-5%. In addition, the interaction length with the quantum well or quantum dot based gain is very short due to the vertical propagation of the laser mode in the structure. One would expect low-noise performance from SESAM modelocked VECSELs and MIXSELs to compete with the excellent performance of modelocked DPSSL.

We therefore performed timing jitter measurements on a free-running [28] and a stabilized [29] SESAM modelocked VECSEL with a 2-GHz repetition rate at a center wavelength of 953 nm. The stabilized laser was actively stabilized to an electronic reference source with a cavity length control loop using a piezo-electric actuator. After detection of the output pulse train with a highly linear photodiode, the single-sideband timing phase noise power spectral density (PSD) was measured with a Signal Source Analyzer (SSA) (Fig. 3). Integration over an offset frequency range of 100 Hz – 100 MHz resulted in an rms timing jitter of 201 fs for the free-running laser and only 47 fs for the stabilized laser (34 ps and 58 fs in the range from 1 Hz – 100 MHz, respectively). These results are comparable to state-of-the-art timing jitter measurements on modelocked DPSSL [30] where values of 190 fs were measured in free-running operation (100 Hz – 1.56 MHz) and 26 fs for a stabilized cavity length (6 Hz - 1.56 MHz).

These results clearly demonstrate that SESAM modelocked VECSELs and MIXSELs can compete with modelocked DPSSLs in terms of low-noise performance and could therefore be used for applications such as frequency comb metrology in the near future.

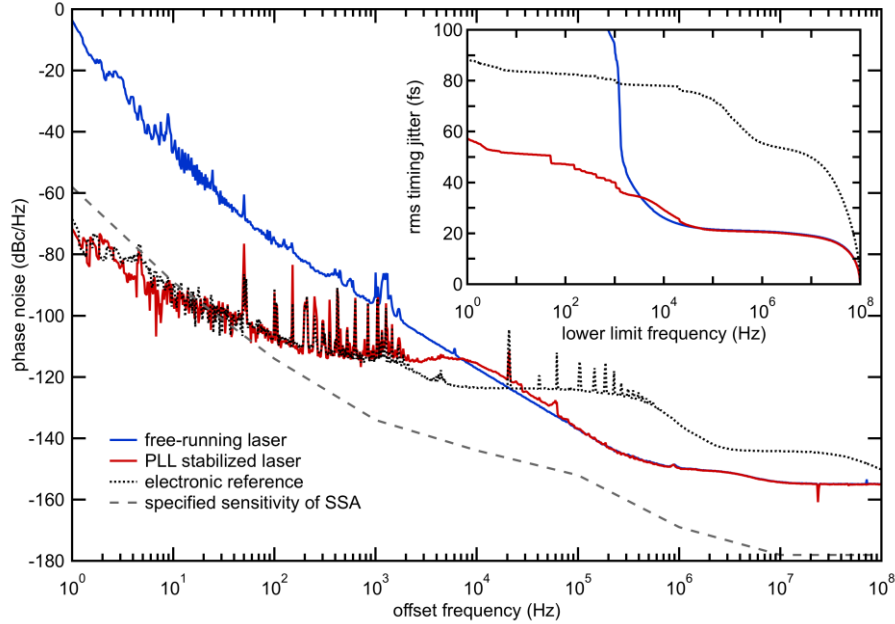


Fig. 3. Measured timing phase noise PSD (SSB) of the free-running laser (blue), the PLL stabilized laser (red) and the reference source (dotted black). The specified sensitivity level of the SSA is given as well (dashed grey). Inset: RMS timing jitter integrated from the lower limit frequency to 100 MHz.

Electrically pumped VECSELs

Another obvious step in the continuous improvement of the technology is to go from optically pumped VECSELs to electrically pumped VECSELs (EP-VECSELs) [31, 32]. Discarding the external pump diode reduces setup complexity and makes these lasers highly attractive for system integration. So far, there were only a few successful attempts of modelocked EP-VECSELs [33-35] since the step from optical pumping to electrical pumping is challenging. The main difference to optical pumping is the fundamental trade-off between optical and electrical losses due to required doping in the semiconductor layerstack to conduct the electrical current. The additional optical losses can be compensated with an intracavity DBR mirror to enhance the electrical field in the active region for more gain. Unfortunately, this step limits the available gain bandwidth and large values of group delay dispersion inhibit femtosecond pulse durations [35]. Besides that, mode-size power scaling is limited by non-uniform current injection in the active region at larger devices [32]. Despite these major challenges we recently demonstrated 6.3 ps pulses in 6.2 mW of average output power [36]. To our knowledge these are the shortest pulses from a modelocked EP-VECSEL producing several milliwatts of average output power.

Conclusion and outlook

SESAM modelocked VECSELs and MIXSELs are attractive semiconductor laser sources that deliver ultrashort laser pulses with picosecond and femtosecond pulse durations in combination with watt-level average output power levels in the gigahertz

repetition rate range. The excellent beam quality and low-noise performance makes them highly attractive for several applications where they can replace conventional complex ion-doped DPSSLs. With the ongoing development we expect the first fully stabilized frequency comb from a modelocked VECSEL or MIXSEL within the near future.

Acknowledgments

This work was supported by ETH Zurich with the FIRST cleanroom facility and was financed by the Swiss Confederation Program Nano-Tera.ch, which was scientifically evaluated by the Swiss National Science Foundation (SNSF).

References

- [1] U. Keller, "Recent developments in compact ultrafast lasers," *Nature*, vol. 424, pp. 831-838, 14.08. 2003.
- [2] U. Keller, "Ultrafast solid-state laser oscillators: a success story for the last 20 years with no end in sight," *Appl. Phys. B*, vol. 100, pp. 15-28, 2010.
- [3] D. Hillerkuss, R. Schmogrow, T. Schellinger, M. Jordan, M. Winter, G. Huber, T. Vallaitis, R. Bonk, P. Kleinow, F. Frey, M. Roeger, S. Koenig, A. Ludwig, A. Marculescu, J. Li, M. Hoh, M. Dreschmann, J. Meyer, S. Ben Ezra, N. Narkiss, B. Nebendahl, F. Parmigiani, P. Petropoulos, B. Resan, A. Oehler, K. Weingarten, T. Ellermeyer, J. Lutz, M. Moeller, M. Huebner, J. Becker, C. Koos, W. Freude, and J. Leuthold, "26 Tbit s⁻¹ line-rate super-channel transmission utilizing all-optical fast Fourier transform processing," *Nat. Photon.*, vol. 5, pp. 364-371, 2011.
- [4] P. J. Delfyett, S. Gee, C. Myoung-Taek, H. Izadpanah, L. Wangkuen, S. Ozharar, F. Quinlan, and T. Yilmaz, "Optical frequency combs from semiconductor lasers and applications in ultrawideband signal processing and communications," *Lightwave Technology, Journal of*, vol. 24, pp. 2701-2719, 2006.
- [5] I. Coddington, W. C. Swann, and N. R. Newbury, "Coherent Multiheterodyne Spectroscopy Using Stabilized Optical Frequency Combs," *Physical Review Letters*, vol. 100, p. 013902, 2008.
- [6] H. R. Telle, G. Steinmeyer, A. E. Dunlop, J. Stenger, D. H. Sutter, and U. Keller, "Carrier-envelope offset phase control: A novel concept for absolute optical frequency measurement and ultrashort pulse generation," *Appl. Phys. B*, vol. 69, pp. 327-332, 1999.
- [7] R. Nagarajan, M. Kato, J. Pleumeekers, P. Evans, D. Lambert, A. Chen, V. Dominic, A. Mathur, P. Chavarkar, M. Missey, A. Dentai, S. Hurtt, J. Bäck, R. Muthiah, S. Murthy, R. Salvatore, C. Joyner, J. Rossi, R. Schneider, M. Ziari, H.-S. Tsai, J. Bostak, M. Kauffman, S. Pennypacker, T. Butrie, M. Reffle, D. Mehuys, M. Mitchell, A. Nilsson, S. Grubb, F. Kish, and D. Welch, "Large-scale photonic integrated circuits for long-haul transmission and switching," *Journal of Optical Networking*, vol. 6, pp. 102-111, 2007/02/01 2007.
- [8] M. Kuznetsov, F. Hakimi, R. Sprague, and A. Mooradian, "High-power (>0.5-W CW) diode-pumped vertical-external-cavity surface-emitting semiconductor lasers with circular TEM₀₀ beams," *IEEE Photon. Technol. Lett.*, vol. 9, pp. 1063-65, 1997.
- [9] U. Keller, K. J. Weingarten, F. X. Kärtner, D. Kopf, B. Braun, I. D. Jung, R. Fluck, C. Hönninger, N. Matuschek, and J. Aus der Au, "Semiconductor saturable absorber mirrors (SESAMs) for femtosecond to nanosecond pulse generation in solid-state lasers," *IEEE J. Sel. Top. Quantum Electron.*, vol. 2, pp. 435-453, 1996.
- [10] S. Hoogland, S. Dhanjal, A. C. Tropper, S. J. Roberts, R. Häring, R. Paschotta, and U. Keller, "Passively mode-locked diode-pumped surface-emitting semiconductor laser," *IEEE Photon. Technol. Lett.*, vol. 12, pp. 1135-1138, 2000.
- [11] M. Hoffmann, O. D. Sieber, V. J. Wittwer, I. L. Krestnikov, D. A. Livshits, Y. Barbarin, T. Südmeier, and U. Keller, "Femtosecond high-power quantum dot vertical external cavity surface emitting laser," *Optics Express*, vol. 19, pp. 8108-8116, 2011.
- [12] M. Scheller, T. L. Wang, B. Kunert, W. Stolz, S. W. Koch, and J. V. Moloney, "Passively modelocked VECSEL emitting 682 fs pulses with 5.1W of average output power," *Electronics Letters*, vol. 48, pp. 588-589, 2012.

- [13] K. G. Wilcox, A. C. Tropper, H. E. Beere, D. A. Ritchie, B. Kunert, B. Heinen, and W. Stolz, "4.35 kW peak power femtosecond pulse mode-locked VECSEL for supercontinuum generation," *Opt. Express*, vol. 21, pp. 1599-1605, 2013.
- [14] P. Klopp, U. Griebner, M. Zorn, and M. Weyers, "Pulse repetition rate up to 92 GHz or pulse duration shorter than 110 fs from a mode-locked semiconductor disk laser," *Applied Physics Letters*, vol. 98, pp. 071103-3, 2011.
- [15] A. H. Quarterman, K. G. Wilcox, V. Apostolopoulos, Z. Mihoubi, S. P. Elsmere, I. Farrer, D. A. Ritchie, and A. Tropper, "A passively mode-locked external-cavity semiconductor laser emitting 60-fs pulses," *Nat. Photonics*, vol. 3, pp. 729-731, Dec 2009.
- [16] O. Sieber, M. Hoffmann, V. Wittwer, M. Mangold, M. Golling, B. Tilma, T. Sudmeyer, and U. Keller, "Experimentally verified pulse formation model for high-power femtosecond VECSELs," *Applied Physics B*, 2013/04/27 2013.
- [17] D. J. H. C. Maas, A.-R. Bellancourt, B. Rudin, M. Golling, H. J. Unold, T. Südmeier, and U. Keller, "Vertical integration of ultrafast semiconductor lasers," *Appl. Phys. B*, vol. 88, pp. 493-497, 2007.
- [18] B. Rudin, V. J. Wittwer, D. J. H. C. Maas, M. Hoffmann, O. D. Sieber, Y. Barbarin, M. Golling, T. Südmeier, and U. Keller, "High-power MIXSEL: an integrated ultrafast semiconductor laser with 6.4 W average power," *Opt. Express*, vol. 18, pp. 27582-27588, 2010.
- [19] M. Mangold, V. J. Wittwer, C. A. Zaugg, S. M. Link, M. Golling, B. W. Tilma, and U. Keller, "Femtosecond pulses from a modelocked integrated external-cavity surface emitting laser (MIXSEL)," *accepted for publication in Opt. Exp.*, 2013.
- [20] R. Aviles-Espinosa, G. Filippidis, C. Hamilton, G. Malcolm, K. J. Weingarten, T. Südmeier, Y. Barbarin, U. Keller, S. I. C. O. Santos, D. Artigas, and P. Loza-Alvarez, "Compact ultrafast semiconductor disk laser: targeting GFP based nonlinear applications in living organisms," *Biomed. Opt. Express*, vol. 2, pp. 739-747, 2011.
- [21] T. Hochrein, R. Wilk, M. Mei, R. Holzwarth, N. Krumbholz, and M. Koch, "Optical sampling by laser cavity tuning," *Optics Express*, vol. 18, pp. 1613-1617, 2010/01/18 2010.
- [22] A. Bhatnagar, C. Debaes, R. Chen, N. C. Helman, G. A. Keeler, D. Agarwal, H. Thienpont, and D. A. B. Miller, "Receiver-less clocking of a CMOS digital circuit using short optical pulses," in *2002 IEEE/LEOS Annual Meeting; Conference Proceedings, 15th Annual Meeting of the IEEE Lasers & Electro-Optics Society*, Glasgow, Scotland, 2002, pp. 127-8.
- [23] C. A. Zaugg, M. Hoffmann, W. P. Pallmann, V. J. Wittwer, O. D. Sieber, M. Mangold, M. Golling, K. J. Weingarten, B. W. Tilma, T. Sdmeyer, and U. Keller, "Low repetition rate SESAM modelocked VECSEL using an extendable active multipass-cavity approach," *Opt. Express*, vol. 20, pp. 27915-27921, 2012.
- [24] C. A. Zaugg, A. Klenner, O. D. Sieber, M. Golling, B. W. Tilma, and U. Keller, "Sub-100 MHz Passively Modelocked VECSEL," in *CLEO: 2013*, San Jose, California, 2013, p. CW1G.6.
- [25] D. Lorensen, D. J. H. C. Maas, H. J. Unold, A.-R. Bellancourt, B. Rudin, E. Gini, D. Ebling, and U. Keller, "50-GHz passively mode-locked surface-emitting semiconductor laser with 100 mW average output power," *IEEE J. Quantum Electron.*, vol. 42, pp. 838-847, Aug. 2006.
- [26] K. G. Wilcox, A. H. Quarterman, V. Apostolopoulos, H. E. Beere, I. Farrer, D. A. Ritchie, and A. C. Tropper, "175 GHz, 400-fs-pulse harmonically mode-locked surface emitting semiconductor laser," *Opt. Express*, vol. 20, pp. 7040-7045, 2012.
- [27] O. D. Sieber, V. J. Wittwer, M. Mangold, M. Hoffmann, M. Golling, T. Sdmeyer, and U. Keller, "Femtosecond VECSEL with tunable multi-gigahertz repetition rate," *Opt. Express*, vol. 19, pp. 23538-23543, 2011.
- [28] V. J. Wittwer, C. A. Zaugg, W. P. Pallmann, A. E. H. Oehler, B. Rudin, M. Hoffmann, M. Golling, Y. Barbarin, T. Sudmeyer, and U. Keller, "Timing Jitter Characterization of a Free-Running SESAM Mode-locked VECSEL," *Photonics Journal, IEEE*, vol. 3, pp. 658-664, 2011.
- [29] V. J. Wittwer, R. van der Linden, B. W. Tilma, B. Resan, K. J. Weingarten, T. Sudmeyer, and U. Keller, "Sub-60-fs Timing Jitter of a SESAM Modelocked VECSEL," *IEEE Photonics Journal*, vol. 5, pp. 1400107-1400107, 2013.
- [30] A. Schlatter, B. Rudin, S. C. Zeller, R. Paschotta, G. J. Spühler, L. Krainer, N. Haverkamp, H. R. Telle, and U. Keller, "Nearly quantum-noise-limited timing jitter from miniature Er:Yb:glass lasers," *Opt. Lett.*, vol. 30, pp. 1536-1538, June 15, 2005.
- [31] P. Kreuter, B. Witzigmann, D. J. H. C. Maas, Y. Barbarin, T. Südmeier, and U. Keller, "On the Design of Electrically-Pumped Vertical-External-Cavity Surface-Emitting Lasers," *Appl. Phys. B*, vol. 91, pp. 257-264, 2008.

- [32] Y. Barbarin, M. Hoffmann, W. P. Pallmann, I. Dahhan, P. Kreuter, M. Miller, J. Baier, H. Moench, M. Golling, T. Südmeyer, B. Witzigmann, and U. Keller, "Electrically pumped vertical external cavity surface emitting lasers suitable for passive modelocking," *IEEE J. Selected Topics in Quantum Electronics*, vol. 17, pp. 1779-1786, 2011.
- [33] K. Jasim, Q. Zhang, A. V. Nurmikko, A. Mooradian, G. Carey, W. Ha, and E. Ippen, "Passively modelocked vertical extended cavity surface emitting diode laser," *Electron. Lett.*, vol. 39, pp. 373-375, 2003.
- [34] K. Jasim, Q. Zhang, A. V. Nurmikko, E. Ippen, A. Mooradian, G. Carey, and W. Ha, "Picosecond pulse generation from passively modelocked vertical cavity diode laser at up to 15 GHz pulse repetition rate," *Electron. Lett.*, vol. 40, pp. 34-35, 2004.
- [35] W. P. Pallmann, C. A. Zaugg, M. Mangold, V. J. Wittwer, H. Moench, S. Gronenborn, M. Miller, B. W. Tilma, T. Südmeyer, and U. Keller, "Gain characterization and passive modelocking of electrically pumped VECSELs," *Opt. Express*, vol. 20, pp. 24791-24802, 2012.
- [36] W. P. Pallmann, C. A. Zaugg, M. Mangold, I. Dahhan, M. Golling, B. W. Tilma, B. Witzigmann, and U. Keller, "Ultrafast Electrically Pumped VECSELs," *Photonics Journal, IEEE*, vol. 5, pp. 1501207-1501207, 2013.

Characterisation of wavelength tuneable lasers for use in coherent burst/packet switched networks employing spectrally efficient modulation formats

Liam P. Barry¹, Anthony J. Walsh^{1,2}, Tam Huynh¹, Kai Shi¹, James Mountjoy³, Anthony Fagan³, Andrew D. Ellis^{1,4}

¹The Rince Institute, Dublin City University, Glasnevin, Dublin 9, Ireland.

²Tyndall National Institute, University College Cork, Lee Maltings, Dyke Parade, Cork, Ireland

³School of Electronic and Communications Engineering, University College Dublin, Dublin, Ireland.

⁴Aston Institute of Photonic Technologies, Aston University, Birmingham B4 7ET, England.

Future networks will need to be capable of offering Triple Play, IPTV, Video-on-Demand, Voice-over-IP and High-Speed Internet Access, combined with guaranteed Quality of Service. These networks will employ WDM technology and advanced modulation formats to achieve the high capacities required. In addition, given the bursty nature of this data it is expected that dynamic bandwidth allocation will be implemented to efficiently use network capacity. The key component in these networks will be the tuneable laser transmitters that generate the different wavelength packets, and the phase noise of these lasers will determine their coherent system performance. It is thus vital to characterise the phase noise of these devices to understand their performance in coherent systems, and to develop technologies to overcome limitations posed by using tuneable lasers in coherent packet switched networks.

Introduction

To address the capacity crunch in optical networks, high spectral efficiency transmission schemes employing high order quadrature amplitude modulation (QAM) formats with coherent detection, cooperating polarization multiplexing (PM), and spatial division multiplexing techniques [1] are being explored. In addition, rapid reconfiguration of the optical network with optical packet/burst switching technology allows the amplification bandwidth of the fibre to be used more efficiently [2-4]. Combining coherent transmission techniques with optical packet/burst switching can enable optical networks which are highly efficient both temporally and spectrally. One of the key elements in these systems will be the laser transmitter, and the phase noise of laser sources has been identified as a crucial characteristic that affects the performance of the coherent detection schemes [5]. In this paper we will present the detailed characterisation of the phase noise of a tuneable laser using an optical quadrature front end [6]. As the instantaneous phase of the laser is recorded in the time domain, the transient variation of the linewidth during switching can be derived by dividing the captured time domain signal into short gating windows at different times during the switching interval. We will then go on to present the performance of these tuneable lasers in various coherent optical communication systems using DQPSK and 16-QAM modulation formats, in both static and switching conditions [5, 7, 8], and identify some of the limitations of using these devices in coherent packet switched networks. Finally we will propose a number of techniques that can be used to overcome these limitations [9, 10].

References

- [1] R. J. Essiambre, R.W. Tkack, "Capacity trends and limits of optical communication networks," *Proceedings of the IEEE*, vol. 100, pp. 1035-1055, 2012.
- [2] J.E. Simsarian, J. Gripp, A.H. Gnauck, G. Raybon, P.J. Winzer, "Fast-tuning 224-Gb/s Intradyne receiver for optical packet networks," in *OFC 2010*, paper PDPB5.
- [3] S. Shinada, H. Furukawa, N. Wada, "Huge capacity optical packet switching and buffering," *Optics Express*, vol. 19 (26), B406–B414, 2011.
- [4] T.N. Huynh, K. Shi, F. Smyth, L.P. Barry, "DQPSK optical packet switching using an SGDBR laser," in *CLEO Europe 2011*, paper C11.
- [5] T.N. Huynh, F. Smyth, L. Nguyen, L.P. Barry, "Effects of phase noise of monolithic tunable laser on coherent communication systems," *Optics Express*, vol. 20, pp. B244–B249, 2012.
- [6] Kai Shi, Regan Watts, Doug Reid, Tam N. Huynh, Colm Browning, Prince M. Anandarajah, Frank Smyth, and Liam P. Barry, "Dynamic Linewidth Measurement Method via an Optical Quadrature Front End", *IEEE Photonics Technology Letters*, Vol. 23, pp. 1591 – 1594, 2011.
- [7] A. Mishra, L.P. Barry, and A.D. Ellis, 'Time-resolved Q-factor Measurement and its Application in Performance Analysis of 42.6 Gbit/s Packets Generated by SGDBR Lasers', *IEEE Journal of Lightwave Technology*, Vol. 28, pp. 1144-1151, 2010
- [8] John O' Dowd, Anthony Walsh, Kai Shi, Frank Smyth, Liam P. Barry, and Andrew Ellis, 'Time resolved bit error rate analysis of a fast switching tunable laser for use in optically switched networks', *IEEE/OSA Journal of Optical Communications and Networking*, Vol. 4, pp. A77- A81, 2012.
- [9] A. J. Walsh, T. Huynh, J. Mountjoy, A. Fagan, A. D. Ellis and L. P. Barry, "Employing DDBPSK in Optical Burst Switched Systems to Enhance Throughput", in *ECOC (Institution of Engineering and Technology, London 2013)*, paper P.3.17.
- [10] Tam N. Huynh, Lim Nguyen, V. Vujicic and Liam P. Barry, "Pilot-Tone Aided Transmission of High-Order QAM for Optical Packet Switched Networks" accepted for publication in *IEEE/OSA Journal of Optical Communications and Networks*.

The art and science of packaging high-coupling photonics devices and modules

Wood-Hi Cheng

Department of Photonics, National Sun Yat-sen
University, Kaohsiung, 804 Taiwan

Abstract

A new scheme of hyperboloid microlens (HM) employing automatic grinding and precise fusing techniques to achieve high-average and high-yield coupling efficiency from high-power 980-nm lasers into single mode fibers is proposed and demonstrated. The fiber endface of the HM exhibited a double-variable curvature in the major and minor axes which was characterized as a hyperboloid. By selecting half transverse length of the hyperbola and using fusing process to precise and quantitative controlling the required minor radius of curvature within 2.4–2.8 μm and offset within 0.8 μm , the HMs exhibited a high-average coupling efficiency of 83%. This study demonstrates that the proposed HMs through both automatic grinding and precise fusing techniques can achieve high-average and high-yield coupling efficiency better than any other grinding techniques to form asymmetric microlenses for utilizing in many low-cost interconnection applications. From art (or engineering) point of view, we are able to fabricate any kinds of perfect fiber microlenses.

Mode (spot size and phasefront) mismatch between the laser diodes and single-mode fibers (SMFs) can lead to a significant insertion loss. A direct near-field phase and intensity measurements in diode lasers, cleaved SMFs, and HMs is demonstrated by employing a SMF interferometer. From science point of view, detailed understanding of the near-field phase and intensity distributions of light sources and optical components may broadly benefit to provide practical micro-optic designs with better mode matching for interconnect applications.

ASPIC and Packaging solutions for demanding industrial applications, an overview

R. Evenblij, P. Kat

Technobis Fibre Technologies

In the last few decades there is a broad oriented rising awareness with regard to photonics as an enabling technology. The applications of photonics as an enabling technology are extremely broad and will keep on growing rapidly. Photonics is being regarded not only as supplemental but also as a base technology platform similar to what electronics has become nowadays. Integrated electronics is already globally used in billions of applications and its functionality is still increasing according to Moore's law. With similarity Integrated Photonics has emerged as the generic photonic development platform for many future applications. Certainly not to replace electronics but to provide an enormous surplus in capabilities for an extremely wide range of applications.

Application Specific Photonic Integrated Circuits

An Application Specific Photonic Integrated Circuit (ASPIC) is an optical chip designed for a rather dedicated purpose. As similar to electronics ASPICs allows a variety of solutions all based on a small set of components. And unlike integrated electronics where silicon is the dominant material, APICS have been fabricated on different material platforms having each of them providing advantages and limitations depending on the functions to be integrated. For instance, Silica has desirable properties for passive components like Arrayed Waveguide Gratings (AWGs) while GaAs or InP allow direct integration of active components, i.e. lights sources, detectors, etc.

Although the fabrication process is similar to integrated electronics, there is no dominant device like the transistor. The range of photonic functions include low loss interconnect waveguides, power splitters, optical amplifiers, optical modulators, filters, lasers, detectors, etc.

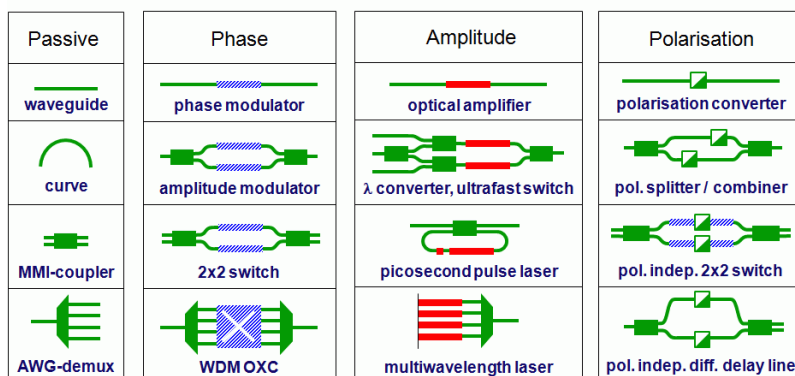


Figure 1 : Example of the functionalities that can be realized in a generic integration technology that supports four basic building blocks: Passive Waveguide Devices (PWD), (Optical) Phase Modulators (PHM), Semiconductor Optical Amplifiers (SOA) and Polarization Converters. (Courtesy of PARADIGM)

The versatile ability to replace traditional assemblies of multiple discrete optical or micro-optical components by a single small sized chip, makes ASPICs highly favorable for next generation optical systems for benefits like cost reduction, functionality

aggregation and standardization of specifications and processes. And certainly, this broad applicable versatility requires this standardization need to preserve compatibility between the development platforms allowing to integrate the best of worlds to provide the best possible solution available. In that respect valuable lessons in platform material selection for ASPICs are repeatedly discussed which ultimately will determine the success of the ASPICs industry. For instance several successes have been achieved in both InP-based and silicon-based systems. As cost and performance may currently prove silicon-based devices preferable, it is certainly the capability of having both passive and active functions combined that proves InP more worthwhile depending on the required system functionality. Moreover, the integration of both electronic circuits with photonics circuits, i.e. hybrid systems, will most likely lead to more applicable development platforms yet to be invented.

ASPIC technology may just as well be moving towards a paradigm shift once it establish a state where the complexity of optical systems will no longer be a major determining factor in optical system development. And this shift may very well cause an unpredictably large growth of applications and their markets in the next decades.

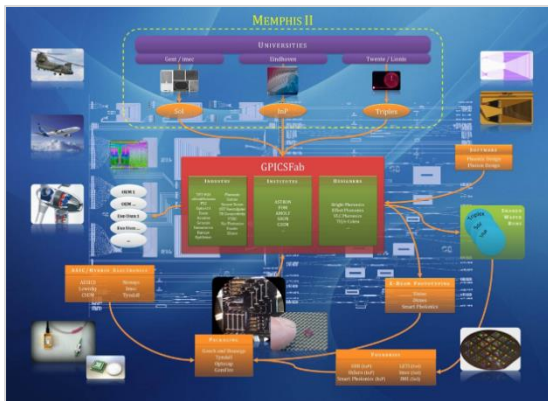
As data- and telecommunication needs have been the major driver for some time, other applications fields appear to gain increasing necessity for smaller sized, more affordable and repeatable and reliable performance devices just as well. An example of another rapidly growing application area is for instance optical sensing. Sensing is and shall always be an integral part of a large variety applications in its most wide perspective and remains expressing the need for an increasing improvement of sensing devices. Photonic Integrated Circuit technology will play a major role in this transition of current conventional systems into next generation optics based systems throughout major technology market segments like Aerospace, Automotive, Medical and Robotics, Civil, etc.

For many small and medium enterprises the rising awareness for these needs not only revealed the current ASPIC value chain and its promising capabilities but just as important its shortcomings. Bringing ASPICs to the market requires extensive development steps and associated logistics. Starting from an product idea to having a series production of ASPIC based devices involves sufficient product and technology knowledge, value assessment, sophisticated photonics integrated system design, chip manufacturing in the foundries, chip testing and prototyping, chip packaging, device integration and interfacing, series production development, and finally implementation. As the ASPIC technology is in the process of coming loose from its academic roots, some important aspects of the value chain need to be improved or developed in order to get to a valuable supply chain transition.

Generic Photonics Integrated Circuits Fabrication (GPICSFab)

The need for SME's to improve time to market for ASPIC based system is imperative. The current availability of resources like foundries, designers, packagers, still needs maturing for several reasons. Although the first complex PIC's started to be published in the late 80's and despite the similarities in chip development complexity, there still remains a significant difference in research and development methodology. The development of ASPICs is obviously very dedicated and focused to its application. As a result there are almost as many technology customizations as applications, often quite similar but different enough to prevent sufficient standardization and subsequently easy transfer from one design to the other. Although a growing trend in the market is tangible, due to this fragmentation current markets are still too small to justify extensive development into a low cost industrial volume manufacturing process, making chip fabrication practically out of reach for many SME's.

It is precisely this fundamental technology versatility which allows an enormous spread of possibilities that needs the required standardization in order to supply a lateral supported ASPIC technology. Subsequently, the ASPIC value chain appears to illustrate a certain reluctance when it comes to the development of not only follow up processes like packaging and integration but also in the design and prototyping processes of ASPICs.



As a result of this imminent need the consortium GPICSFab – initiated from the industry – was founded that facilitates a Lean and Asset-Light manufacturing and logistics infrastructure to accelerate the introduction of integrated photonic functionalities.

Its mission is to accelerate the introduction of ASPIC functionalities for Integrated Device Manufacturers (IDM) and Original Equipment Manufacturers (OEM) by means of facilitating production and logistics infrastructure using minimal in-house resources and optimizing outsourcing possibilities.

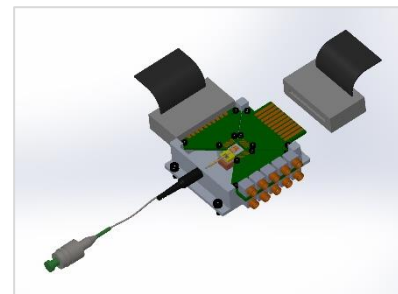
GPICSFab is convinced that the generic fabrication approach will cause a revolution in micro and nano-photonics, just like it did in microelectronics thirty years ago. In Europe, three integration technology platforms are actively introducing the generic foundry concept for the major integration technologies in photonics: JePPIX for InP-based monolithic integration, ePIXfab for silicon photonics and TriPLEX for low-loss dielectric waveguide technology. GPICSFab concerns itself by selecting and offering those parts of these development platforms which are ready for product development today and offers them to the marketplace.

Given the tremendous impact of photonics as enabling technology for further expansion of high-performance telecom networks, the availability of dedicated PICs will enable the development and efficient implementation of advanced systems and instrumentation for a multitude of applications. To maximize its reach GPICSFab aims

to collaborate with national and international partners and programs like Memphis II, IOP Photonic Devices and IPC HTSM Photonics, to secure state-of-the-art and world leading photonics integration competences.

GPICSFab provides access to a suite of quality manufacturing and logistics solutions. Instead of having a general ability to subscribe to a Multi Project Wafer run once a year, the initiative of GPICSFab now offers SME's accessible and even hybrid options to subscribe to Shared Wafer Runs multiples times a year. This increase in availability of best-in-class methods for volume production will boost speed and reduce costs for the development of ASPIC based systems considerably. With regard to that, one of the important achievements of GPICSFab so far is establishing an agenda for Shared Wafer Runs with an interval period of 3 to 4 months which significantly exceeds current affordable availability of MPWs.

Another important achievement by GPICSFab in the process of standardization, is the development of a generic package for ASPICs. Packaging is one of the most important steps in bringing ASPICs to the market for which no generic volume process has been established yet. Although photonic packaging researchers have been working on a range of technologies for application across a number of key industry sectors, including telecommunications, medical devices, biotechnology and consumer electronics, many of these research activities are still being performed through industry collaborations with the expectance of growth as photonics becomes the technology of choice for an increasing range of applications.



Conclusion

Photonic Integrated Circuits represent a disruptive technology break-through that promises the delivery of immediate benefits and significant future development opportunities. To accomplish this important steps need to be taken with regard to standardization and further value chain development. GPICSFab is a good example of an industrial initiative to close a gap between technology and markets and to increase Time to Market.

References

1. D. Liang and J.E. Bowers, "Photonic integration: Si or InP substrates?", Electronic Letters 4th June 2009.
2. PARADIGM, "How Generic Integration Technology works".
3. L.Augustin, M.Smit, N.Grote, M.Wale, R.Visser, "Standardized Process Could Revolutionize Photonic Integration", photonics.com September 2013.
4. P. O'Brien, "Photonic Packaging", The Tyndall National Institute.
5. Infinera, "Photonic Integrated Circuits, A Technology and Application Primer"

Part II

Oral contributions

Germanium-on-Silicon Mid-Infrared Photonic Integrated Circuits

A. Malik,^{1,2} M. Muneeb,^{1,2,3} S. Pathak,^{1,2} Y. Shimura,^{4,5} J. Van Campenhout,⁴ R. Loo⁴
and G. Roelkens^{1,2,3}

¹ Photonics Research Group, Ghent University-imec, Sint-Pietersnieuwstraat 41, 9000 Ghent, Belgium

² Center for Nano- and Biophotonics, Ghent University, 9000 Ghent, Belgium

³ COBRA Research Institute, Eindhoven University of Technology, P.O. Box 513, Eindhoven 5600 MB, The Netherlands

⁴ imec, Kapeldreef 75, Leuven, 3001, Belgium

⁵ Instituut voor Kern- en Stralingsfysica, KU Leuven, 3001 Leuven, Belgium

Photonic integrated circuits based on the Germanium on Silicon platform are presented for operation in the 5 μm wavelength range. Waveguide losses in the range of 2.5 - 4 dB/cm for TE/TM polarization and Mach-Zehnder interferometers with an extinction of 20 dB for TE polarization are reported. Wavelength multiplexers based on Arrayed Waveguide Gratings are reported with an insertion loss and cross talk of -2.5/-3.1 dB and 20/16 dB for TE/TM polarized light while those based on Planar Concave Gratings are shown to have an insertion loss/cross talk of -4.9/-4.2 dB and 22/23 dB for TE/TM polarization.

Introduction

Photonic integrated circuits (PICs) have allowed the realization of various on-chip optical functionalities such as wavelength filters, (de)multiplexers, routers and switches. This has led to the development of compact and robust systems operating in the telecommunication wavelength range. Silicon on Insulator (SOI) is now the first choice material platform for this wavelength range because of (a) compatibility with the CMOS pilot lines which makes mass manufacturing possible and (b) higher index contrast which allows to make circuits with small footprint. For spectroscopic sensing applications, the wavelength regime which is of interest is the mid-infrared (3 - 12 μm). Most of the atmospheric gases and biological liquids have a strong absorption feature in this wavelength regime and therefore the development of PICs for longer wavelengths promises to provide compact hand held components which could be utilized to tap the full potential of this wavelength range. Silicon itself has a large transparency window from 1.2 μm to 8 μm however the underlying oxide starts absorbing beyond 4 μm [1]. Various alternative waveguide platforms have been proposed in recent literature such as free standing Si[2], Silicon on Sapphire[3], Silicon on Silicon Nitride[4] and Germanium on Silicon[5]. The key requirements for a waveguide platform are (a) transparency in the wide mid-IR, (b) straightforward fabrication scheme and (c) CMOS compatibility which will allow mass manufacturing.

Free standing Si has a very wide transparency window but suffers from the fact that the

waveguide structures are fragile and prone to collapsing. Silicon-on-Sapphire has a transparency limited to $5.5 \mu\text{m}$ because of the sapphire absorption and Silicon-on-Silicon Nitride has a complicated fabrication scheme which requires wafer bonding. Germanium-on-Silicon fits all the above mentioned requirements and thus seems the ideal candidate for the mid-IR.

In the past decade, advancements in Quantum cascade lasers (QCLs) and Interband cascade lasers (ICLs) have enabled efficient on chip mid-IR light generation[6]. The integration of these light sources with a passive PIC can help in the realization of interesting functionalities. Two possible applications based on this integration are described in Fig 1. In a first case, a broad band fabry-perot QCL is integrated with a wavelength selective feedback circuit present on the passive PIC. This can enable the realization of a compact and hand held mid-IR light source and can replace existing bulky devices. In second case, an array of DFB lasers can be integrated with a wavelength multiplexer present on the PIC. This arrangement promises to allow efficient on -chip beam combining which has been realized using free space optics till now.

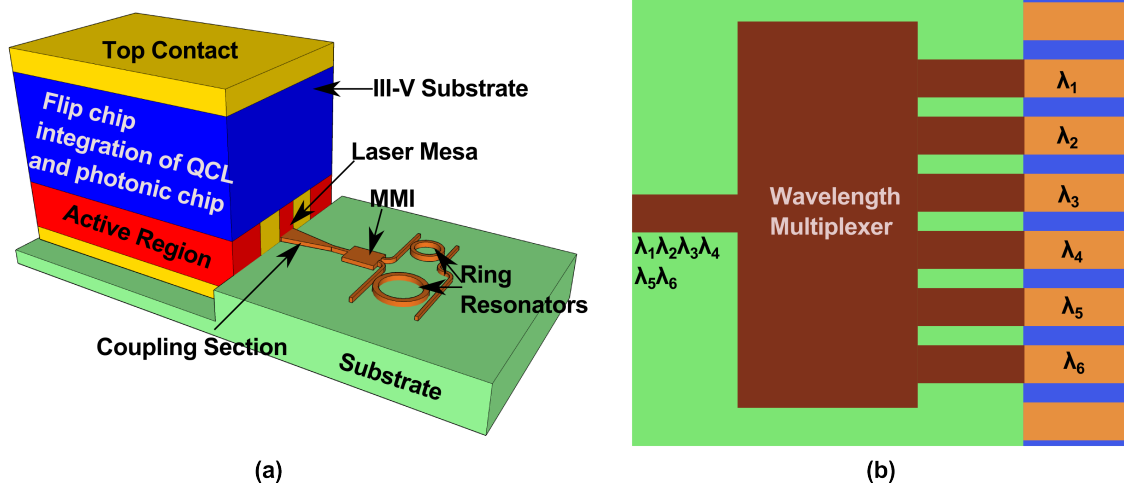


Figure 1: Schematic diagram of (a) a broadband QCL integrated with a photonic chip via flip chip integration and (b) an array of DFB QCL lasers integrated with a wavelength multiplexer.

Waveguide Loss

Fully etched waveguides (etching through the $2 \mu\text{m}$ thick Ge waveguide layer) of width $2.2 \mu\text{m}$ and lengths 0.5 cm, 1 cm, 2 cm and 3 cm were characterized for transverse electric (TE) and transverse magnetic (TM) polarizations[7]. The fabrication details of these waveguides and the measurement setup required to characterize these waveguides is described in [7]. Fig. 2 (a) and (b) respectively show the cutback measurements at $5.3 \mu\text{m}$ and the waveguide losses for the $5.15 - 5.45 \mu\text{m}$ wavelength range are presented in Fig. 2 (c) for both polarizations.

Mach Zehnder Interferometers

1×1 and 1×2 Mach Zehnder interferometers (MZIs) were designed using 1×2 and 2×2 Multimode interferometers (MMIs) with a delay length of $260 \mu\text{m}$ for TE polarized

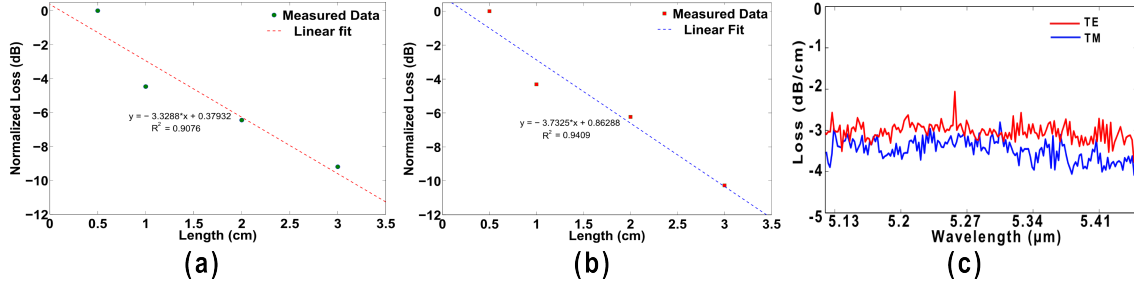


Figure 2: Cutback measurements at $5.3 \mu\text{m}$ for (a) TE polarized light, (b) TM polarized light and (c) loss measurements in the $5.1 - 5.45 \mu\text{m}$ wavelength range for TE and TM polarizations.

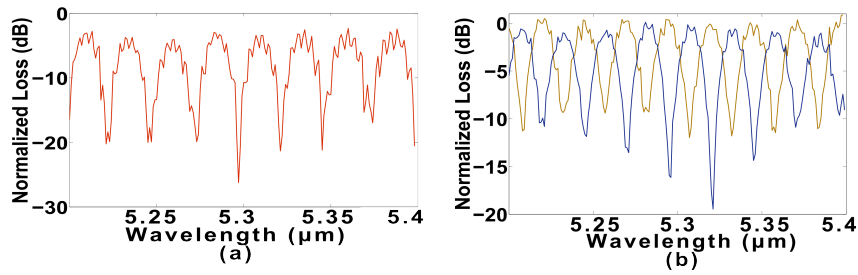


Figure 3: Normalized spectrum of (a) 1×1 MZI and (b) 1×2 MZI.

light[8]. This resulted in a free spectral range (FSR) of 25 nm and an extinction of 23 dB for a 1×1 MZI at $5.3 \mu\text{m}$ and 20 dB for a 1×2 MZI at $5.32 \mu\text{m}$ as seen in Fig. 3 (a) and (b) respectively. An array of such MZIs can be used as wavelength multiplexer to enable mid-ir beam combining.

Arrayed Waveguide Gratings

A 5×200 GHz arrayed waveguide grating (AWG) was designed and found to have an insertion loss of -2.5/-3.1 dB while the cross talk was found to be 20/16 dB for TE/TM polarization[7]. Normalized spectra for TE and TM polarizations are shown in Fig 4 (a) and (b) respectively. Since the AWG has a lower insertion loss and cross talk, it can be deployed both to separate broadband light in different channels and to combine light from individual DFB lasers in a single beam.

Planar Concave Gratings

A six channel planar concave grating (PCG) having DBR gratings with 25 nm channel spacing was designed and found to have an insertion loss of -4.9/-4.2 dB and cross talk of 22/23 dB for TE/TM polarizations[9]. Normalized spectra for TE and TM polarizations are shown in Fig 5 (a) and (b) respectively. The insertion loss of the PCG is higher than the AWG however this is mainly due to the fact that because of the limits of i-line contact lithography, the minimum feature is $1 \mu\text{m}$. This results in a third order DBR with 66% reflection. With the access to standard CMOS tools, first order DBRs can be fabricated which will reduce the insertion loss enabling the use of this PCG as wavelength (de)multiplexer.

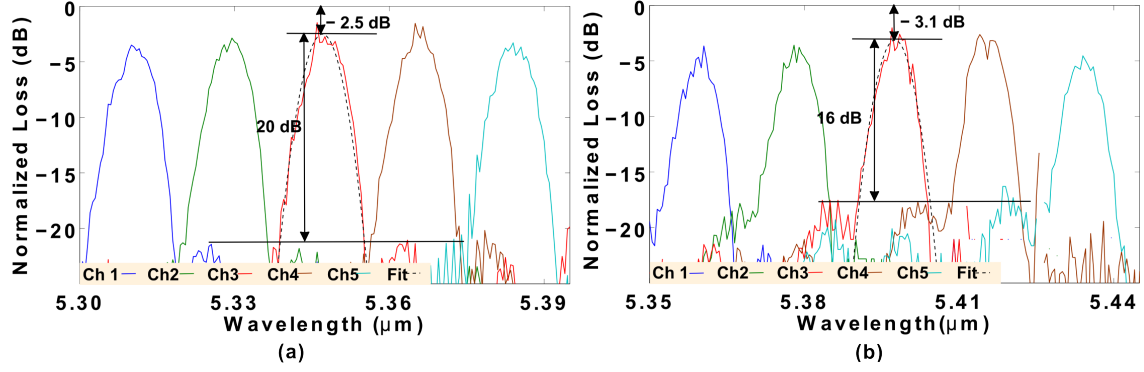


Figure 4: Normalized spectrum for a 5×200 GHz AWG for (a) TE polarized light and (b) TM polarized light.

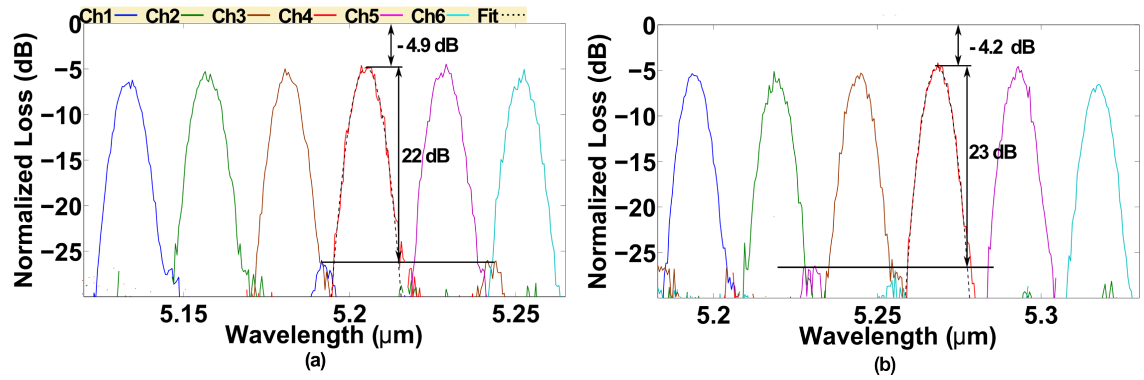


Figure 5: Normalized spectrum for a 6 channel PCG with 25 nm channel spacing for (a) TE polarized light and (b) TM polarized light.

References

- [1] R. Soref, *Mid-infrared photonics in silicon and germanium*, Nat. Phot., Vol. **4**, pp. 495 - 497 (2010).
- [2] Y. Xia, C. Qiu, X. Zhang, W. Gao, J. Shu, Q. Xu, *Suspended Si Ring Resonator for Mid-IR Application*, Opt. Lett., Vol. **38**, pp. 1122 - 1124 (2013).
- [3] T.B. Jones, A. Spott, R. Ilic, A. Spott, B. Penkov, W. Asher and M. Hochberg *Silicon-on-sapphire integrated waveguides for the mid-infrared*, Opt. Exp., Vol. **18**, pp. 12127 - 12135 (2010).
- [4] S. Khan, J. Chiles, J. Ma and S. Fathpour, *Silicon-on-nitride waveguides for mid- and near-infrared integrated photonics*, App. Phys. Lett., Vol. **102**, pp. 121104 - 121104-3 (2013).
- [5] Y.C. Chang, V. Paeder, L. Hvozdar, J.M. Hartmann, H.P. Herzig, *Low loss germanium strip waveguides on silicon for the mid-infrared*, Opt. Lett., vol. **37**, no. 14, pp. 2883-2885, (2012).
- [6] R.F. Curl, F. Capasso, C. Gmachl, A.A. Kosterev, B. McManus, R. Lewicki, M. Pusharsky, G. Wysocki, F.K. Tittel, *Chem. Phys. Lett., Quantum cascade lasers in chemical physics*, Vol. **487**, pp. 1 - 18 (2010).
- [7] A. Malik, M. Muneeb, S. Pathak, Y. Shimura, J. Van Campenhout, R. Loo and G. Roelkens, *Germanium-on-Silicon Mid-Infrared Arrayed Waveguide Grating Multiplexers*, IEEE Phot. Tech. Lett. Vol. **25**, No. 18, pp. 1805 - 1808 (2013).
- [8] A. Malik, M. Muneeb, Y. Shimura, J. Van Campenhout, R. Loo and G. Roelkens *Germanium-on-silicon mid-infrared waveguides and Mach-Zehnder interferometers* in IEEE Photonics Conference 2013.
- [9] A. Malik, M. Muneeb, Y. Shimura, J. Van Campenhout, R. Loo and G. Roelkens, *Germanium-on-Silicon Planar Concave Grating Wavelength (de)multiplexers in the Mid-Infrared* App. Phys. Lett. Vol. **103**, pp. 161119 (2013).

Delivering 10 Gb/s optical data with picosecond timing accuracy over 75 km distance

N. Sotiropoulos¹, C. M. Okonkwo², R. Nuijts^{3,4}, H. de Waardt²,
and J. C. J. Koelemeij¹

¹ Vrije Universiteit Amsterdam, Dept. of Physics and Astronomy,
De Boelelaan 1081, 1081 HV Amsterdam, The Netherlands

² Eindhoven University of Technology, Dept. of Electrical Engineering,
Den Dolech 2, P.O. Box 513, NL 5600 MB Eindhoven, The Netherlands

³ Network Services, SURFnet, Radboudkwartier 273, P.O. Box 19035, 3501 DA Utrecht, The Netherlands

⁴ Currently with Ciena Corporation, Ferring Building,
Polaris Avenue 140A, 2132 JX Hoofddorp, The Netherlands

The transfer of very accurate time information over long distances has numerous applications in modern society. Satellite-based links have typically been used so far, but fiber-optical signals can transfer time with increased precision. In this paper, a novel method suited for time transfer employing conventional optical data signals is demonstrated; specifically, transmission of 10 Gb/s signals for up to 75 km over an amplified bidirectional link enabling time transfer with 4 ps accuracy is shown. The very high accuracy achieved and compatibility with existing optical links may allow reliable synchronization of vital infrastructure, and positioning systems with mm-level precision.

Introduction

The dissemination of precise time information and clock synchronization is of fundamental value in modern society. Navigation systems for vehicles and ships, telecommunication networks, systems that handle financial transactions, they all depend on the availability of an accurate timing signal, with more applications being developed [1]. Global Navigation Satellite Systems (GNSS) are arguably the most successful example of a time-dissemination network, providing positioning and timing services across the globe. However, due to its satellite-based nature, GNSS has a number of vulnerabilities (*e.g.* susceptibility to jamming or disruptions due to space weather) that may necessitate a back-up system for critical applications [1]. Moreover, the accuracy achieved by satellite systems is limited to around 1 ns if bidirectional transmission is used [2] and can be as low as tens of ns for commercial receivers.

Fiber-based timing dissemination systems can provide a back-up solution for GNSS that is virtually free from interference (natural or man-made), and at the same time considerably increase the timing accuracy. Optical frequency transfer over 1840 km of fiber [3] and time transfer with offsets as low as 35 ps over 480 km [4] has been demonstrated. However, such methods use either ‘dark’ fiber (a dedicated fiber link for time/frequency transfer) or a ‘dark’ channel (a dedicated wavelength), which means that significant capacity is being lost for data transfer. It would be preferable and more cost-effective to implement simultaneous data and time transfer. The most sophisticated approach in this respect is the White Rabbit Ethernet project, which combines 1 Gb/s data transfer with a precision below 1 ns for links up to 10 km [5].

In this paper, a novel method of determining delay times in optical links (the key step to implementing time transfer between clocks) using typical optical data signals that is

scalable in both bit rate and link length is proposed and demonstrated for 10 Gb/s signals and 25, 50 and 75 km links, achieving 4 ps accuracy over only 1 ms of data.

Proposed Method and Experimental Approach

In order to synchronize two clocks that are situated at different locations, typically electromagnetic signals are exchanged between the clocks, the process being known as Two-Way Time Transfer (TWTT). To ensure accurate synchronization, the signal delay between the two locations needs to be known with high precision. A powerful method for estimating time delays between signals is cross-correlation; similar to the technique used in GNSS, we estimate the signal delay in the link by cross-correlating Pseudo-Random Binary Sequences (PRBSs) transmitted using optical signals.

To validate the concept of such a delay-determination method, an experimental set-up was designed and built, shown in Fig. 1. A rubidium (Rb) atomic clock serves as the reference time base. A Bit Pattern Generator (BPG) creates a 10 Gb/s bit stream, a PRBS of $2^{23}-1$, which is amplified and used to modulate an optical carrier at 1550.52 nm through on-off keying modulation. Part of the signal at point A (Fig. 1) is fed into a Digital Phosphor Oscilloscope (DPO), which samples the reference, non-delayed electrical signal. The optical data signal is then launched into a fiber spool (25 km long) through an ITU grid wavelength multiplexer. An optical amplification stage is located after the fiber spool; two Semiconductor Optical Amplifiers (SOAs) amplify the downstream and upstream channels, which are separated by demultiplexers. Optical isolators ensure that no back-reflected light enters the amplifiers. After the amplification stage, a short patchcord, a 25 km or a 50 km fiber spool is inserted, enabling measurements over 25, 50 or 75 km links. In the remote end, a receiver consisting of photodiode, a transimpedance amplifier and a limiting amplifier convert the optical signal to the electrical domain. The signal of one of the two outputs of the receiver is sampled by the DPO (point B in Fig. 1), while the second output signal is amplified and modulates an optical carrier at a different wavelength than the downstream channel. The return channel is then launched into the link and is received at point C, where it is also sampled by the DPO.

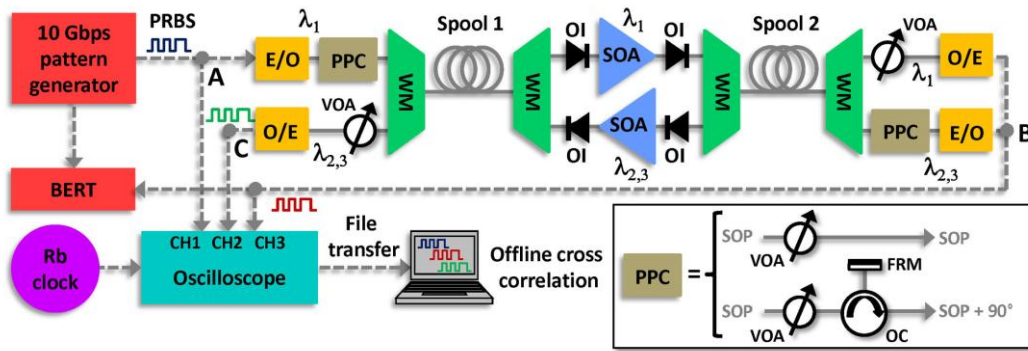


Fig. 1 Experimental set-up

In order to synchronize two clocks located at each end of the optical link, the One-Way Delay (OWD) delay t_{AB} needs to be determined. Since the clock at point B would not be initially synchronized, the OWD has to be estimated using the Round-Trip Delay (RTD) t_{AC} , which can be directly measured. Ideally, the OWD would be the half of the RTD: $t_{AB} = t_{AC}/2$. However, a number of asymmetries are present in the link, which will

introduce a delay asymmetry Δ so that $t_{AB}=(t_{AC}-\Delta)/2$. The delay asymmetry can be further subdivided into the instrument asymmetry, Δ_I , and the link asymmetry, Δ_L . The instrument asymmetry arises from unequal path lengths, electrical or optical, for the downstream and upstream signals in the transceivers and the optical amplification stage. The link asymmetry is a result of the difference in propagation time between the downstream and upstream signals over the common fiber link; the two signals are transmitted over different wavelengths, which results into different propagation speeds due to Chromatic and Polarization-Mode Dispersion (CD and PMD, respectively).

The combined effect of Δ_I and Δ_L can amount to several ns, which means that in order to achieve ps-level precision, the delay asymmetries need to be carefully accounted for. To estimate Δ_I , the fiber spools are removed and the instrument delays, denoted t'_{AB} , t'_{AC} are directly measured. Then, the instrument asymmetry is calculated as $\Delta_I = t'_{AC} - 2t'_{AB}$. The link delay asymmetry, on the other hand, is not so straightforward to calculate. The asymmetry due to CD can be estimated by measuring the dispersion parameters of the fiber. However, the uncertainty in the measurement of the dispersion parameters translates to a total delay uncertainty higher than 10 ps. Moreover, as these parameters change over time due to environmental conditions, the measurements should be repeated periodically. A more accurate method of estimating the delay asymmetry due to CD is to use two different wavelengths for the upstream channel. By combining the delay measurements performed with the two possible wavelength pairs, a very accurate estimate of Δ_L is obtained. The details of the method and the dispersion model used here will be presented in a longer manuscript. The asymmetry caused by PMD, which is statistical in nature, is estimated by performing a second set of measurements where the input State Of Polarization (SOP) of the optical signals is rotated by 90° . This is accomplished by inserting a circulator and a Faraday mirror in the set-up, as is shown in Fig. 1. The full PMD analysis is also to be expanded on in a longer manuscript.

Results and Discussion

By propagating the uncertainty introduced by all the parameters involved in the estimate of the OWD of the link, with the most important ones being the uncertainty in Δ_I , the time base stability of the DPO, the error in determining the peak of the correlation spectrum and the estimation of PMD, the total time uncertainty of the system can be calculated. The error propagation described above yields a system-level uncertainty of 4 ps. To assess the performance of the delay estimation method, the estimated OWD, θ_{AB} , is compared with the directly measured t_{AB} for different link lengths, with the results (including the uncertainty) shown in Fig. 2b-d. It is observed that all 24 estimates are within ± 5 ps of the measured delay, while 20 of them are within ± 4 ps, confirming the very high precision allowed by the method. Moreover, there is no sign of increasing errors as the link becomes longer, indicating scalability of the method to link lengths longer than 75 km. In addition, the Bit Error Rate (BER) of the downstream data signal is measured and is shown in Fig. 2a. It can be seen that error-free transmission ($BER < 10^{-9}$) is possible for the 25 and 50 km links. For the 75 km link, a BER of 10^{-9} can be achieved if slightly higher signal powers are used, or if compensation for the accumulated dispersion is implemented (or a better receiver is used).

The very high precision in the estimation of delay, in combination with the compatibility of the proposed system with existing optical networks and the fast acquisition time (only 1 ms of data are captured to produce each measurement) indicate the potential of the

method to provide a fiber-optical back-up for GNSS timing, to supply a time reference for cutting-edge scientific research, and to enable novel applications. For example, the positioning accuracy of a system with 4 ps resolution would be $c \times 4 \text{ ps} \times \sqrt{4} = 2.4 \text{ mm}$. Other potential applications could take advantage of the availability of very precise timestamps to offer more secure transactions over communication networks and synchronize wireless base stations to achieve faster mobile communication links.

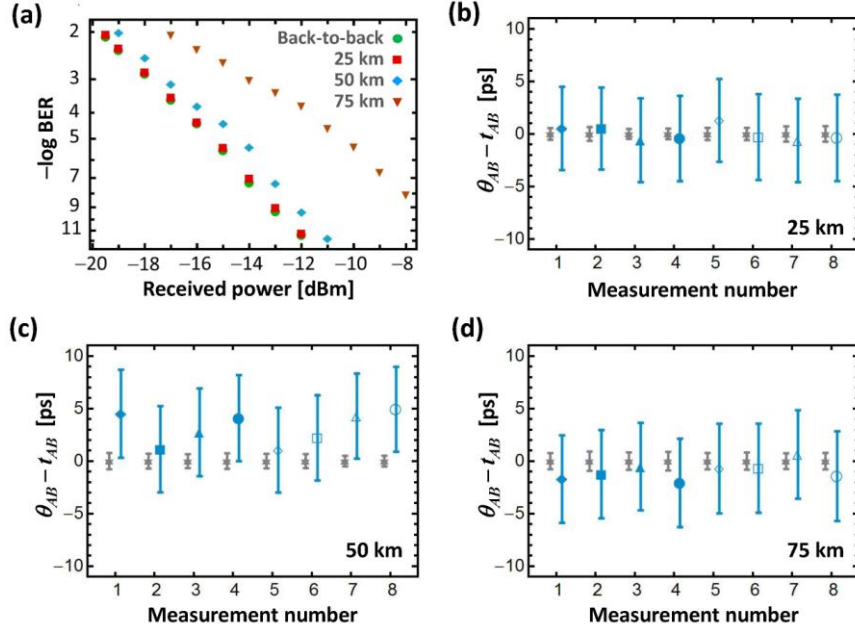


Fig. 2 Experimental results: BER curves (a) Delay errors (b) 25 km (c) 50 km (d) 75 km

Conclusion

A novel method of estimating the propagation delay of optical data transmitted through fiber-optical links with unprecedented accuracy is described and its key functionality is demonstrated over 75 km employing 10 Gb/s signals. The proposed system can enable ubiquitous availability of ps-range timing signals, providing GNSS back-up for critical infrastructure and supporting novel applications such as mm-level positioning and new techniques for fast and secure communications.

References

- [1] "Global Navigation Space Systems: Reliance and Vulnerabilities," The Royal Academy of Engineering, London, UK, 2011.
- [2] T. E. Parker and V. Zhang, "Sources of instabilities in two-way satellite time transfer," in Proceedings of the IEEE Int. Frequency Control Symp. and Exp., pp. 745-751, 2005.
- [3] S. Droste, F. Ozimek, Th. Udem, K. Predehl, T. W. Hänsch, H. Schnatz, G. Grosche, and R. Holzwarth, "Optical-Frequency Transfer over a Single-Span 1840 km Fiber Link," Phys. Rev. Lett. vol. 111, 110801, 2013.
- [4] L. Sliwczynski, P. Krehlik, A. Czubla, L. Buczek, and M. Lipinski, "Dissemination of time and RF frequency via a stabilized fibre optic link over a distance of 420 km," Metrologia, vol. 50, no. 2, p.p. 133-145, 2013.
- [5] J. Serrano, P. Alvarez, M. Cattin, E. G. Cota, P. M. J. H. Lewis, T. Włostowski, G. Gaderer, P. Loschmidt, J. Dedič, R. Bär, T. Fleck, M. Kreider, C. Prados, and S. Rauch "The White Rabbit Project," in Proceedings of ICALEPCS, paper TUC004, 2009.

Improving Single Mode Transmission Performance using Few-Mode Fibers and Space-Time Coding

R.G.H. van Uden*, C.M. Okonkwo, H. Chen, H. de Waardt, and A.M.J Koonen

COBRA Research Institute, Eindhoven University of Technology, The Netherlands

* r.g.h.v.uden@tue.nl

Space-time block codes can extend the optical signal to noise ratio tolerance in multiple-input multiple-output optical coherent spatial division multiplexing transmission systems with respect to single-mode transmission performance. The OSNR tolerance gain is achieved through exploiting the spatial diversity few-mode-fibers offer. An OSNR gain of 3.2, 4.1, 4.9, and 6.8 dB at the hard-decision forward error correcting limit with respect to single mode fiber back-to-back performance is shown for DP-QPSK, 8,16, and 32 DP-QAM, respectively.

Introduction

Enabled by multiple-input multiple-output (MIMO) digital signal processing (DSP), coherent transmission (Tx), and the development of key optical components, spatial division multiplexing (SDM) continues to be proposed as the solution to extend the capacity of a single optical fiber. Also known as Bell Laboratories Layered Space-Time (BLAST) in wireless communications [1], spatial multiplexing remains a key area of interest for increasing capacity. In optical transmission systems, SDM can be achieved by multi-core and multi-mode transmission [2-4]. Focusing on a specific case of the latter, namely few-mode fiber (FMF) transmission, 3 linearly polarized (LP) modes, the LP_{01} , LP_{11a} , and the LP_{11b} mode are excited and propagated [5]. Hence in this case, the capacity of a single fiber can be increased threefold with respect to single-mode fiber (SMF) transmission. Each LP mode contains two polarizations, which can be employed as transmission channels. Therefore, the total number of transmittable channels in FMFs is $3 \times 2 = 6$. Note that in SMFs, 2 polarization channels can be employed simultaneously.

Clearly, FMFs can offer an increased capacity with respect to SMF transmission. However, the FMF transmission systems can also be used to improve the transmission quality of single mode transmission through space-time coding (STC). The transmission quality improvement is investigated through optical-signal-to-noise ratio (OSNR) performance with respective bit error rates (BERs). For STC, there are three main contenders: space-time trellis codes (STTCs) [6], orthogonal STCs [7], and delay diversity. The latter two are linear space-time block codes (STBCs) and have a lower complexity than trellis codes. Although the STTCs offer better performance than the

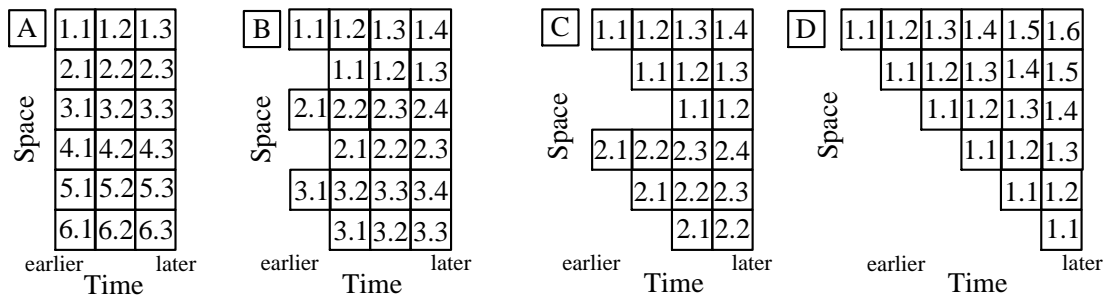


Fig. 1 Space and time allocation for FMF transmission blocks showing (A) 6, (B) 3, (C) 2, and (D) 1 transmitted channel. The first and second number denote the channel and block number, respectively.

linear variants, for high throughput optical transmission systems complexity is a key factor [8]. Therefore, we focus on the linear STBCs. The orthogonal STBCs are linear codes where the data is formed as unitary matrices. The most common orthogonal STBCs are Alamouti and Tarokh codes [7,8]. However, these only exist for certain numbers of transmitters. To this end, we use the simplest STBCs, purely exploiting the space and delay diversity. Fig. 1 shows the 4 cases of delay-diversity STBCs investigated in this work, where (A) 6, (B) 3, (C) 2 (SMF capacity), or (D) 1 polarization channel are received.

This work shows that either the capacity of a single fiber can be increased by transmitting an increased number of spatial channels, or that the transmission quality can be improved by employing STC with the existing spatial channels. In this work the resulting tradeoff is studied. The quality improvement is demonstrated through OSNR characterization of 28GBaud quadrature phase shift keying (QPSK), 8, 16, and 32 quadrature amplitude modulation (QAM) constellation sequence transmission over 41.7km FMF using a 6×6 MIMO frequency domain equalizer (FDE).

Experimental Setup

The experimental setup is depicted in Fig. 2. At the transmitter, a 1555.75 nm external cavity laser (ECL) is used. The output is guided through an IQ-modulator, where the laser light is modulated by a 28GBaud signal. The IQ-modulator is driven by two digital-to-analog converters (DACs), which represent the in-phase (real) and quadrature (imaginary) components of the transmitted constellations. The transmitted constellations under investigation are QPSK, 8, 16, and 32QAM.

The transmitted sequences are formed in the digital domain by a number of fully uncorrelated pseudo random bit sequences (PRBSs), each of length 2^{15} , which avoids correlation within the 2^{15} symbol sequence. The output of the IQ-modulator is split, and one arm is delayed by 1233 symbols for polarization decorrelation. After recombining the two arms, the uncorrelated dual polarization (DP) signal is noise loaded to characterize the optical OSNR system performance. To achieve 3 DP multiplexed mode channels, the noise loaded signal is split into three equal tributaries. Two arms are delayed for mode decorrelation by 3714 and 8233 symbols, respectively. Each arm is separately amplified before going into the mode multiplexer (MMUX). As a MMUX, a single prism spot launcher is used [9], resulting in equal excitation of the three LP

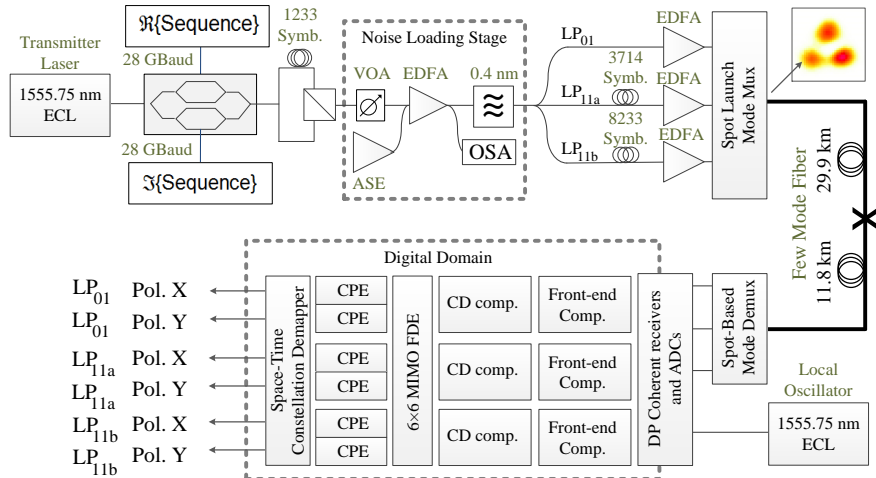


Fig. 2 Experimental setup (inset: measured alignment from spot launcher).

modes, guaranteeing full mixing. For all inputs, the losses are approximately 4.5 dB. The transmission link consists of two spans of few-mode fiber with lengths of 29.9 km and 11.8 km, respectively [5]. At the receiver side, a reciprocal setup of the MMUX comprising a single prism splits the FMF output into 3 separate outputs. Each output contains a mix of the 3 transmitted modes. The loss in the mode demultiplexer is approximately 4.5 dB for each output. After transmission, the three outputs from the mode demultiplexer are received using DP coherent receivers, where a second laser acts as the local oscillator (LO) and mixes with the signal. Real-time oscilloscopes act as 12 (3 modes \times 2 polarizations \times 2 real-valued axes of a complex symbol) analog to digital converters (ADCs). The captured data is post-processed offline.

In the digital domain, first the optical front-end impairments are compensated. Then, the chromatic dispersion (CD) is removed. To invert the channel mixing effects, a 6×6 MIMO FDE with adaptive step size is used [10]. The weight matrix of the FDE is heuristically updated using the least mean squares (LMS) algorithm during convergence and decision-directed least mean squares (DD-LMS) during data transmission. To compensate the frequency offset between the transmitter laser and LO, one carrier phase estimation (CPE) block per output channel in the form of a digital phase locked loop is used [11]. After this stage, the received constellations are demapped using a space-time demapper. The output of the space-time demapper can be 6, 3, 2, or a single output, depending on the STBC setup used. Note that single-mode transmission performance has 2 output channels, as each of the polarizations is employed.

Results

Fig. 3 shows the performance results of the space-time coded FMF transmission experiment for (A) QPSK, (B) 8, (C) 16, and (D) 32QAM. As the primary benchmark indicator, the 7% overhead hard-decision forward error correcting (HD-FEC) limit is used. If the BER is below this threshold, after error correction, theoretically the data transmission can be seen as error free ($<10^{-9}$). As there are 3 LP modes transmitted, and hence 6 polarization channels, the system capacity versus performance can be subdivided into 3 categories; 3, 1.5, 1, and $0.5 \times$ SMF capacity using no STBC, STBC over 2, 3, and all 6 transmitted channels, respectively.

For QPSK transmission, as shown in Fig. 3a, for threefold capacity increase there is a 0.6 dB OSNR penalty at the HD-FEC limit with respect to SMF back-to-back (BTB) performance. When applying STBC on 2 polarizations for a single channel, the performance is already better than the theoretical SMF performance. However, the FMF transmission capacity is reduced to $1.5 \times$ the SMF capacity. When using a 3 channel STBC, the FMF capacity equals the SMF capacity. The OSNR gain between STBC transmission and SMF BTB is approximately 3.2 dB.

As for QPSK, the same STBCs can be applied to 8QAM transmission. Fig. 3b depicts the 8QAM transmission performance. For threefold capacity increase there is a 0.5 dB OSNR penalty with respect to SMF BTB performance. A performance increase of 2.7 dB and 4.1 dB is seen when comparing the FMF capacity of $1.5 \times$ and $1 \times$ the SMF capacity to SMF BTB, respectively.

16QAM transmission is the next constellation when further increasing the number of constellation points. 16QAM performance is shown in Fig. 3c. The $3 \times$ SMF capacity OSNR penalty with respect to SMF BTB is 1.5 dB. However, when applying STBCs, and reducing the FMF transmission system capacity to SMF capacity, an OSNR gain of

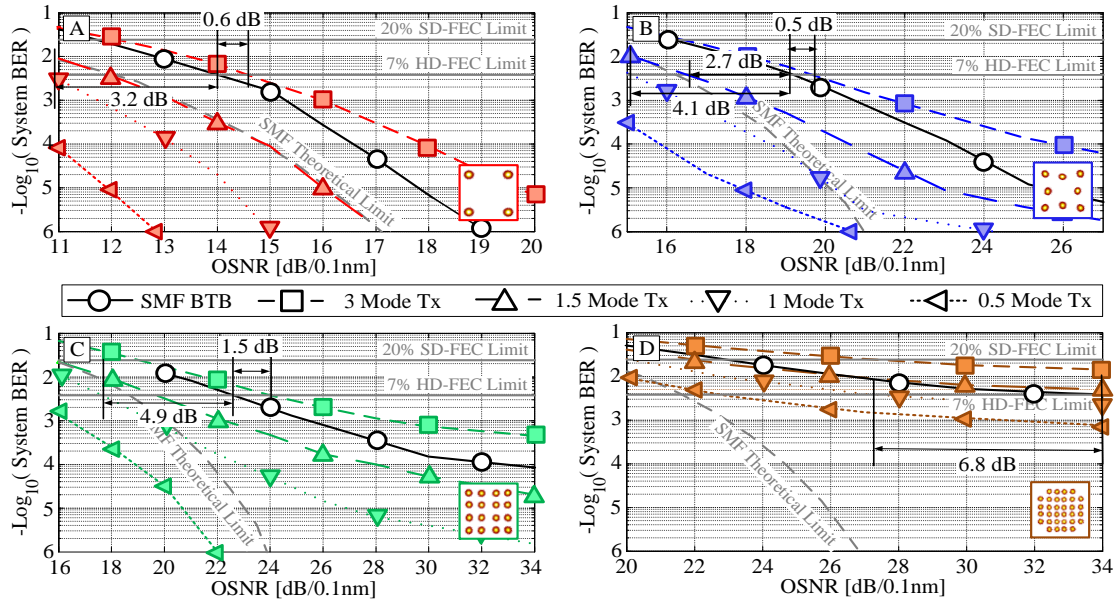


Fig. 3 (A) QPSK, (B) 8QAM, (C) 16QAM, and (D) 32QAM transmission performance for 6,3,2, and 1 channel using STC over a 41.7km FMF with respect to single mode BTB performance.

4.9 dB OSNR is observed. For 32QAM transmission, as depicted in Fig. 3d, the 20% overhead soft-decision FEC (SD-FEC) is required for successful transmission for 3-fold capacity increase with respect to SMF. However, after applying STBCs, a 6.8 dB OSNR performance gain is observed at the HD-FEC limit.

Conclusions

The successful transmission of 3×28GBaud DP-QPSK, 8, 16, and 32 DP-QAM over 41.7 km FMF has been demonstrated. Space-time coding was applied to improve the FMF transmission quality to outperform single mode fiber back-to-back performance. An OSNR gain of 3.2, 4.1, 4.9, and 6.8 dB at the hard-decision forward error correcting limit with respect to single mode fiber back-to-back performance is shown for DP-QPSK, 8,16, and 32 DP-QAM, respectively. Through STC, an additional dimensionality for potential FMF flex (flexible)-grid/flex-rate applications was demonstrated.

We acknowledge the EU FP7-ICT MODE-GAP project (grant agreement 258033), the IT R&D Program of MKE/KIAT (2010-TD-200408-001) of the Republic of Korea, the EU FP7-ICT IDEALIST project (grant agreement 317999). We want to thank Lars Grüner-Nielsen and Yi Sun from OFS Denmark and OFS USA, respectively, for the few-mode fibers.

References

- [1] G.J. Foschini, Bell Labs Technical Journal, 41-59 (1996).
- [2] V.A.J.M. Sleiffer et al., Optics Express **20**(26), B428-B438 (2012).
- [3] R.G.H. van Uden et al., *Proc. OFC* (2014), Submitted.
- [4] K. Igarashi et al., *Proc. ECOC*, paper PD3.E.3 (2013).
- [5] L. Grüner-Nielsen et al., Journ. Lightw. Techn. **30**(23), 3693-3698 (2012).
- [6] V. Tarokh et al., Trans. on Inf. Theory **44**(2), 744-765 (1998).
- [7] S.M. Alamouti, Journ. on Select Areas in Comm. **16**(8), 1451-1458 (1998).
- [8] V. Tarokh et al., Trans. on Inf. Theory **45**(5), 1456-1467 (1999).
- [9] H. Chen et al., *Proc. OECC*, PD3-6 (2013).
- [10] R.G.H. van Uden et al., *Proc. ECOC*, paper Th.2.C.2 (2013).
- [11] R.G.H. van Uden et al., Phot. Techn. Lett. **25**(14), 1381-1384 (2013).

Graphene plasmonics: Tunable coupling with nano-cavities

G. Rosolen,¹ B. Maes,¹

¹ Micro- and Nanophotonic Materials Group, Faculty of Science, University of Mons, 20, place du Parc, B-7000 Mons, Belgium

Since graphene supports low loss surface plasmon polaritons (SPPs) in the infrared range, we theoretically investigate the coupling of the SPPs in patterned sheets with nano-cavities. By using the finite-element method, we illustrate SPP propagation in filter-type circuits. Resonant frequencies are observed as a dip in the reflection spectrum, and fully described by the coupled mode theory. The shift of frequency is easily obtained by tuning the doping of graphene (e.g. via voltage tuning). We can reach quality factors up to 42 for cavities of 20nm length around 5 μ m wavelength. This may pave the way towards ultra-compact optoelectronic devices.

Introduction

Graphene has a lot of interesting properties in various domains, but we will focus here on its optical properties in the near-infrared range of frequencies. The plasmonic modes of graphene has already been theoretically and experimentally studied, and some applications were pointed out [1]. For example, propagating plasmons in nano-ribbons were investigated in [2] and directional couplers were designed in [3].

Here we present a filter-type circuit based on graphene nano-cavities. By means of the finite-element method (COMSOL), we compute the reflection of a surface plasmon polariton (SPP) along a 2D ribbon. We observe deep dips in the reflection spectrum and an easy tuning of the resonant frequency. This remarkable circuit application comes from the specific properties of graphene.

Materials and method

The two dimensional system is composed of a semi-infinite nano-ribbon of graphene (waveguide) and a small ribbon (cavity) of length W_c at distance d from the first one (Figure 1). The background medium is air with $n_{air} = 1$. Graphene is modelled as a thin layer of $t = 0.5\text{nm}$ thickness with the edges rounded by semicircular profiles to avoid large field in the corners. The material is characterized by a dielectric function $\epsilon(\omega) = 1 + 4\pi i\sigma/\omega t$. We use the surface conductivity $\sigma(\omega, E_F)$ obtained via the Kubo-Greenwood formulation [4] where ω is the light angular frequency and E_F is the Fermi energy relative to the Dirac points, which can be chemically or electrostatically tuned. The relaxation time of scatterers in graphene is fixed to 10^{-12}s .

The plasmonic mode is excited along the first ribbon and the reflection is measured. On the right part of Figure 1, the normalized H_z field is plotted at a resonant frequency and we observe high concentration of the field in the cavity.

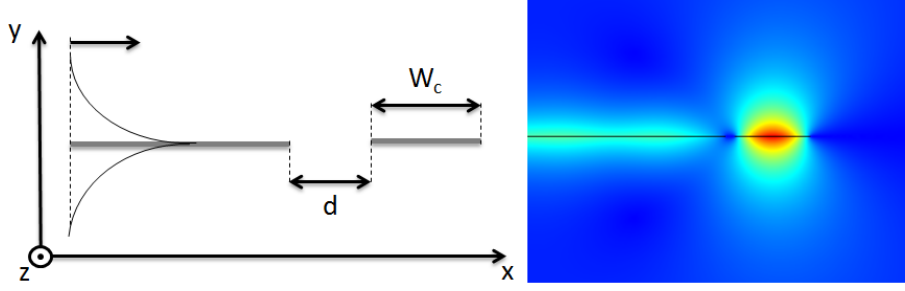


Figure 1: 2D structure studied, the plasmonic mode is excited on the graphene ribbon along the x-direction (left). $|H_z|$ field of a resonance for $E_F = 0.3\text{eV}$ and $\lambda = 7.95\mu\text{m}$ (right).

Coupled Mode Theory (CMT)

The resonances in the reflection spectrum can easily be described by the Coupled Mode Theory (CMT) [5]. This is based on a development of the solution in eigenmodes. The cavity mode is characterized by a waveguide coupling lifetime τ_c , an absorption lifetime τ_a and a radiation lifetime τ_r . We find for the reflection

$$R(\omega) = R_{wg} \frac{(\omega - \omega_0)^2 + \left(\frac{1}{\tau_a} - \frac{1}{\tau_c} + \frac{1}{\tau_r}\right)^2}{(\omega - \omega_0)^2 + \left(\frac{1}{\tau_a} + \frac{1}{\tau_c} + \frac{1}{\tau_r}\right)^2} \quad (1)$$

where ω_0 is the resonant frequency and R_{wg} is the reflection without the cavity. Since lifetimes are supposedly independent, one writes $1/\tau = 1/\tau_a + 1/\tau_c + 1/\tau_r$. It turns out we can neglect τ_r in regard to $\tau_c \approx \tau_a \approx 10^{-13}\text{s}$. Indeed, integrating the energy escaping the system, we find that radiation losses are less than 0.01%. In this report, the reflections are normalized and we plot R/R_{wg} .

We can analytically model the absorption lifetime via $\tau_a = 1/v_g \Im(\beta)$ where v_g is the group velocity and β is the propagation constant of the plasmonic mode. $\Im(\beta)$ indicates the imaginary part.

Tuning graphene for tunable resonances

The results are plotted in Figure 2. The cavity has a size of $W_c = 75\text{nm}$ and it is separated of $d = 10\text{nm}$ from the waveguide. The doping of graphene is shifted from $E_F = 0.2\text{eV}$ to $E_F = 0.5\text{eV}$ and we show a shift of the resonant wavelength from $\lambda = 10$ to $6\mu\text{m}$. This can be realized by introducing a gate voltage on the graphene ribbon. Table 1 shows different fitted parameters from these spectra using Equation 1.

First of all, we observe that the theoretical absorption lifetime matches the fitted value, increasing with the doping of graphene. It can be understood considering the interband transitions in graphene. They occur above a threshold related to the Fermi energy ($2E_F$) which can be shifted to higher frequencies by larger doping [6]. That has an impact on the imaginary part of the propagation constant : doping graphene decreases its value, leading to less losses.

On the contrary, τ_c decreases when increasing doping level. Note that the coupling lifetime is tunable: it increases with the distance d (not shown) since it depends on an overlap integral of the fields.

For this configuration, a point $R = 0$ is reached only for $E_F = 0.3\text{eV}$ where $\tau_a = \tau_c$, leading to a critical coupling (see Equation 1).

The resonances can be described more analytically by the phase condition $2\Re[\beta(\omega)]W_c + 2\phi_r = 2m\pi$ with ϕ_r the phase induced by the reflection at the edge of the ribbon, and m an integer. Since ϕ_r is relatively constant in our range of frequencies, the (first order) resonance always occurs at the same value of the propagation constant $\beta = 30.2\mu\text{m}^{-1}$. This is a consequence of the special properties of graphene : just applying a gate voltage shifts the optical properties to another range of frequencies, so this value of β is reached for a wavelength depending on doping.

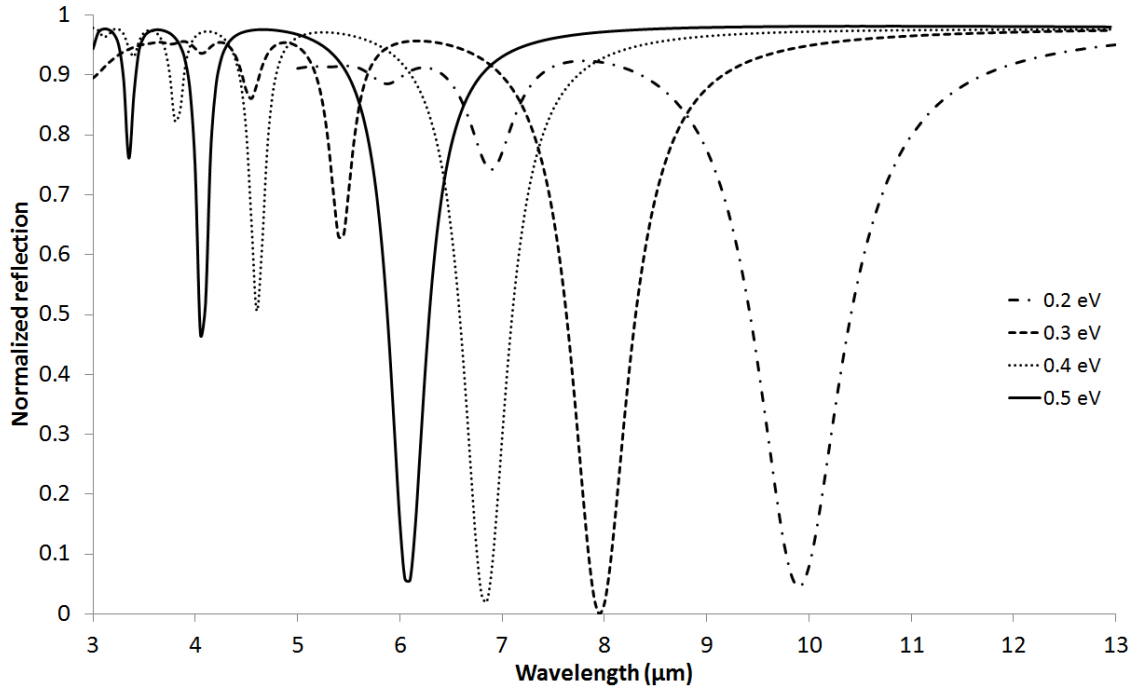


Figure 2: Normalized reflection spectrum R/R_{wg} for different doping of graphene (E_F). Three orders of resonances are shown for each E_F and a shift in the resonant wavelength is observed.

The second order dip is less deep than the first order one. Indeed, the coupling is less efficient, so τ_c is bigger. If we examine equation 1, in order to deepen the dip, we would have to increase τ_a , and thus decrease the losses in graphene. In the case of 0.4eV doping, the second order dip has a quality factor $Q = 15$. The value is higher than the one obtained for the first order dip (where $Q = 13$), but it is mainly due to the resonant frequency ω_0 .

In order to improve the quality factor, one needs smaller cavities i.e. bigger resonant frequencies. However, going in this direction increases losses, interband transitions occurring when $\omega > 2E_F$. Thus, in order to avoid huge losses, we need to increase this threshold, doping graphene. When $E_F = 1\text{eV}$, one reaches a quality factor of $Q = 42$

Doping (eV)	Fitted			Q	Theoretical τ_a (10^{-13} s)
	τ_c (10^{-13} s)	τ_a (10^{-13} s)	ω_0 (10^{14} rad/s)		
0.2	2.6	1.7	1.9	9.2	1.7
0.3	2.0	2.0	2.4	12	2.0
0.4	1.7	2.2	2.8	13	2.3
0.5	1.5	2.3	3.1	13	2.4

Table 1: Result table of the fitted lifetimes and resonant frequency ω_0 for the first order mode. Theoretical absorption lifetime is also shown. The quality factors are also computed from the fitted parameters as $Q = \omega_0 / \Delta\omega_{FWHM}$.

with a cavity of $W_c = 10$ nm. This occurs for $\lambda = 2.8\mu\text{m}$. It has the same order of magnitude than the quality factor of localized surface plasmon resonance of metals like silver ($Q \approx 30$) or gold ($Q \approx 10$) [7].

Conclusion

From our simulations based on the optical conductivity of graphene, we demonstrated a filter-type circuit, excited with SPPs. The resonances are fully described with CMT and tuning the resonance frequency can easily be performed by tuning the applied gate voltage on the graphene nano-ribbon. We computed a cavity of 10nm width with a quality factor of $Q = 42$ at a wavelength $2.8\mu\text{m}$.

Acknowledgement

This work is supported by the Belgian Science Policy Office under the project "Photon@be" (P7-35) and by the Fonds National de Recherche Scientifique (FNRS) in Belgium.

References

- [1] A. N. Grigorenko, M. Polini, and K. Novoselov. Graphene plasmonics. *Nature photonics*, 6:749–758, 2012.
- [2] J. Christensen, A. Manjavacas, S. Thongrattanasiri, F. Frank H. L. Koppens, and F. J. G. de Abajo. Graphene plasmon waveguiding and hybridization in individual and paired nanoribbons. *ACS Nano*, 6:431–440, 2012.
- [3] B. Wang, X. Zhang, X. Yuan, and J. Teng. Optical coupling of surface plasmons between graphene sheets. *Applied Physics Letters*, 100:131111, 2012.
- [4] L.A. Falkovsky. Optical properties of graphene. *Conference series*, 129:1–7, 2008.
- [5] Hermann A. Haus. *Waves and Fields in Optoelectronics*. Prentice-Hall, INC., 1984.
- [6] Z. Q. Li, E. A. Henriksen, Z. Jiang, Z. Hao, M. C. Martin, P. Kim, H.L. Stormer, and D. N. Basov. Dirac charge dynamics in graphene by infrared spectroscopy. *Nature physics*, 4:532–535, 2008.
- [7] P.R. West, S. Ishii, G.V. Naik, N.K. Emani, V.M. Shalaev, and A. Boltasseva. Searching for better plasmonic materials. *Laser Photonics Review*, 4:795–808, 2010.

Characterization of silicon micro-ring resonators

W.J. Westerveld,^{1,2} J. Pozo,² S.M. Leinders,¹ M. Yousefi,³ and H.P. Urbach¹

¹ Delft University of Technology, Van der Waalsweg 8, 2628CH Delft, The Netherlands

² TNO, Stieltjesweg 1, 2628CK Delft, The Netherlands

³ Photonic Sensing Solutions, Haarlemmerstraat 141, 1013EN Amsterdam, The Netherlands

Silicon micro-ring resonators are now widely used and studied as filters in the field of optical communication and as sensitive elements in the field of sensing. This work aims to provide silicon photonic designers with a set of results and reasoning to assist them with the design of micro-rings. We fully and detailedly characterized waveguide, waveguide bends, and directional couplers including their dispersion. The chip was fabricated via the ePIXfab platform. To the best of our knowledge, we are the first to report on the exceptional phase shift of directional couplers in the situation when they are used as cross-coupler.

Introduction, devices, and setup

Silicon photonic micro-ring resonators receive large interest [1]. In this work, we present a methodology to characterize the components of such resonators and the obtained set of figures.

We characterized integrated optical devices in silicon-on-insulator technology, having 220 nm thick rectangular waveguides. The devices were fabricated via the EU-funded ePIXfab consortium at IMEC (Leuven) in their IMEC8 multi-project-wafer shuttle. IMEC fabricated the devices in their semi-industrial CMOS line with deep-UV lithography. We measured the dimensions of the waveguides with a helium-ion-microscope (Carl Zeiss SMT), providing 15 nm accuracy. We deposited a 2 μm thick SiO_2 cladding using plasma-enhanced chemical vapor deposition (PECVD). However, the disagreement between the measured coupling of directional couplers and the simulated coupling suggests that the PECVD may be imperfect. The main concern is the deposition of SiO_2 in the small gap between the waveguides.

The photonic chips have out-of-plane grating couplers [2] and are measured in an automated setup to provide high alignment repeatability that is necessary for loss measurements [3]. The fibers are manually positioned above the chip for a set of consecutive measurements. Fine in-plane alignment is achieved by sequentially scanning the 4 in-plane axis of the two piezo-actuated stages to maximize the transmitted power. We used amplified spontaneous emission (ASE) light-source and recorded the transmittance spectra around $\lambda_c = 1550$ nm free-space wavelength with an optical spectrum analyzer (OSA).

Loss characterization

The devices in Fig. 1a only differ in the length l' of the straight waveguides, with a total length difference of 5 cm. Transmission spectra of these devices were recorded and averaged over 5 nm wavelength spans to remove the “noise” originating from spurious reflections. The loss per length was found by linear fitting of the transmitted power versus

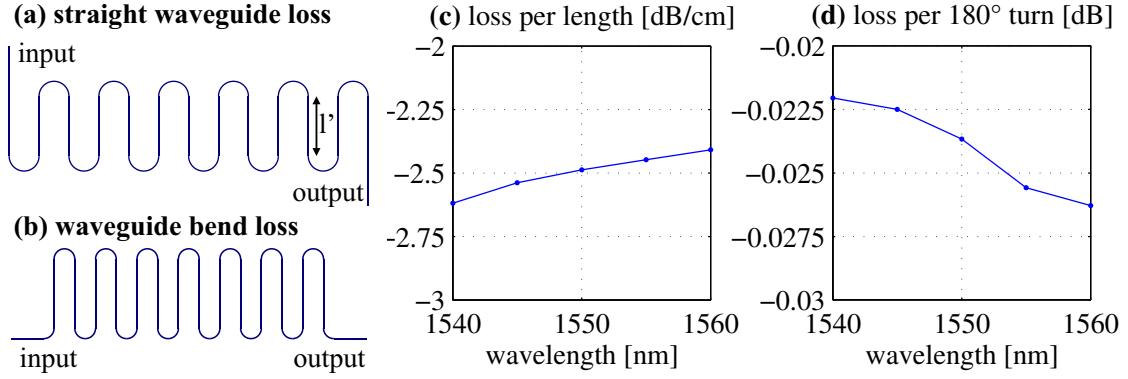


Figure 1: Sketch of devices for measuring loss of straight (a) and bend (b) waveguides with 397 nm. Measured loss in straight (c) and bend (d) waveguides (radius 5 μm).

the length of the straight waveguides. The average loss over the 25 nm wavelength span is -2.50 dB/cm and there is only a weak wavelength dependence (Fig. 1c). This loss is slightly higher than the values reported in literature [4], possibly because our waveguides are 60 nm smaller and our SiO_2 cladding deposition is not optimized. Loss in waveguide bends are characterized by comparing the transmission through waveguides with a different number of bends (Fig. 1b, with upto 359 bends). The transmission is compensated for the loss in the straight waveguides and the loss per 180° turn is found by linear fitting. The averaged loss is -0.024 dB/turn with low wavelength dependency (Fig. 1c).

Directional coupler characterization

A directional coupler consists of two parallel waveguides so close that power couples from one waveguide to the other via the evanescent fields of the modes (Fig. 2a). Using coupled mode theory, the total electric field is approximated by a superposition of the two modes of the isolated waveguides. Lossless couplers have straight-through power $|t|^2$, coupled power $(1 - |t|^2)$, and a straight-through amplitude transmission t given by [5]

$$t = e^{-i(\beta_b + \kappa_{bb} - \delta)\tilde{L}} (\cos s\tilde{L} - i\delta/s \cdot \sin s\tilde{L}), \quad (1)$$

with β_b the propagation constant of the lower waveguide, κ_{bb} a correction on β_b due to the vicinity of the other waveguide, 2δ the difference between the corrected propagation constants of the two waveguides, s the coupling coefficient, $\tilde{L} = L + \Delta L$ the effective length of the coupler, where L is the length of the parallel waveguides, and ΔL is a correction for the coupling occurring in the bends. The correction κ_{bb} is smaller than the fabrication-induced uncertainty in β_b , hence we neglect $\kappa_{bb} \ll \beta_b$. Dispersion in waveguide propagation constant β_b is taken into account by assuming linear dispersion of the effective index $n_e(\lambda)$, hence $\beta_b(\lambda, n_e, n_g) = 2\pi((n_e - n_g)/\lambda_c + n_g/\lambda)$, with n_e and $n_g \equiv n_e - \lambda(\partial n_e / \partial \lambda)$ evaluated at λ_c . Dispersion in the coupling $s(\lambda) = s + s'(\lambda - \lambda_c)$ is assumed linear. We neglect dispersion in ΔL , which is validated by the fact that the obtained relations accurately describe the measured spectra. We measured directional couplers in ring resonators (Fig. 2b) having power transmission T given by [5]

$$T = (\alpha^2 + 1 - 2\alpha \cos \theta) |t|^2 / (1 + \alpha^2 |t|^4 - 2\alpha |t|^2 \cos \theta) \cdot P_0, \quad (2)$$

with α the round-trip amplitude transmission of the ring ($\alpha = 1$ means no loss), $|t|$ the amplitude transmission through the coupler, θ the round-trip phase delay of the ring in-

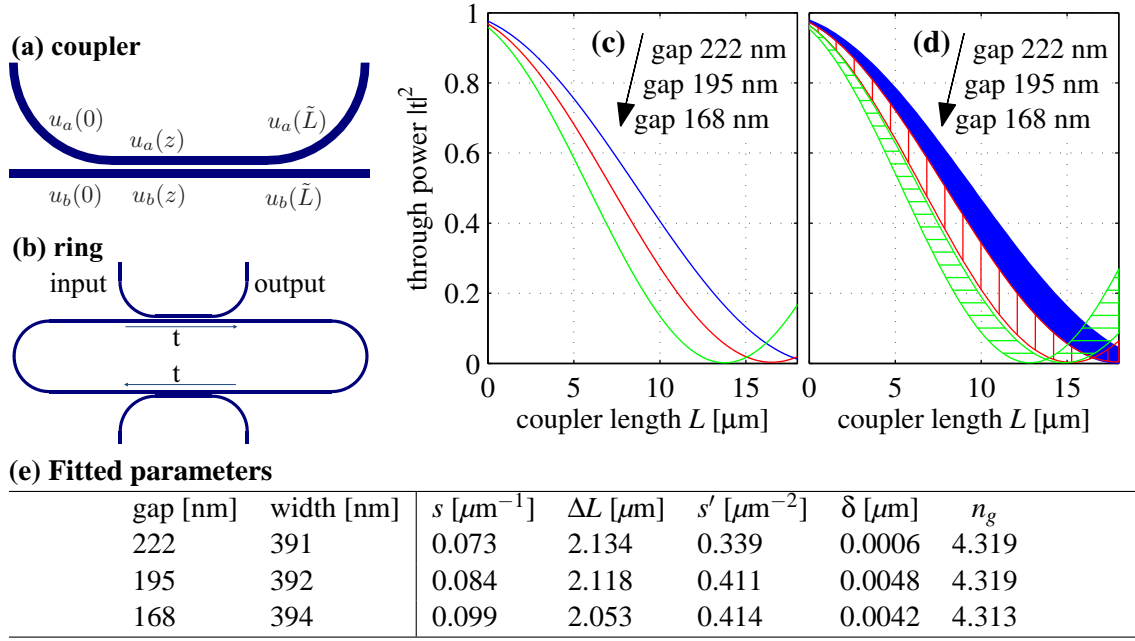


Figure 2: Directional coupler characterization. **(a)** Sketch of coupler. Waveguide width ~ 400 nm and bending radius $5 \mu\text{m}$. **(b)** Sketch of ring with two couplers. $40 \mu\text{m}$ straight waveguides and $5 \mu\text{m}$ bending radius. **(c)** and **(d)** Straight-through transmission power $|t|^2$ of the directional coupler for $\lambda_c = 1550$ nm and $\lambda_c \pm 15$ nm, respectively. **(e)** Table of fitted parameters.

cluding the two couplers, and P_0 the power in the input waveguide. For a ring with two directional couplers, the phase delay θ is, using Eq. (1),

$$\theta = -\beta_b l + 2\delta\tilde{L} + 2 \arg \left\{ \cos s\tilde{L} - i\delta/s \cdot \sin s\tilde{L} \right\}. \quad (3)$$

We measured three sets of couplers with different gaps and similar waveguides. Each set consists of eleven devices with coupler length L varying from $0 \mu\text{m}$ to $18 \mu\text{m}$. Equation (2 with 3 and 1) was fitted to the set of spectra. Transmittance α was calculated using Fig. 1, leaving unknowns s , ΔL , s' , δ , n_g , $\{n_e\}$ and $\{P_0\}$. The effective index n_e and input power P_0 vary from device to device due to variations in fabrication [1] and in fiber-chip alignment, respectively, while the other unknowns share single values for all spectra. Levenberg-Marquardt optimization is used to minimize the squared difference between the measured and computed spectra $T(\lambda)$. To weight all spectra approximately equally, we weighted each datapoint (wavelength) with $1/I$, with I the average intensity in a 5 nm span around this wavelength. An accurate initial guess is necessary, which we obtained using less complete analysis neglecting dispersion and asymmetry in the coupler ($\delta = 0$, $s' = 0$), and by choosing $\{n_e\}$ and n_g to match the wavelengths of the resonance dips in the recorded spectra.

Fig. 3 shows that the fitted spectra agree very well with the measured spectra, indicating that the theory indeed contains all important effects. Length $L = 8 \mu\text{m}$ shows a typical spectrum with a FSR of 5.0 nm, but $L = 14 \mu\text{m}$ is in the particular cross-coupling regime with nearly all light coupled to/from the ring ($|t|^2 \approx 0$). The change in FSR is due to the additional phase delay of the directional couplers (Fig. 3c). We define the third term on the right-hand-side of Eq. (3) as this additional phase delay, which only occurs for couplers with asymmetry between its waveguides ($\delta \neq 0$). We designed the two waveguides

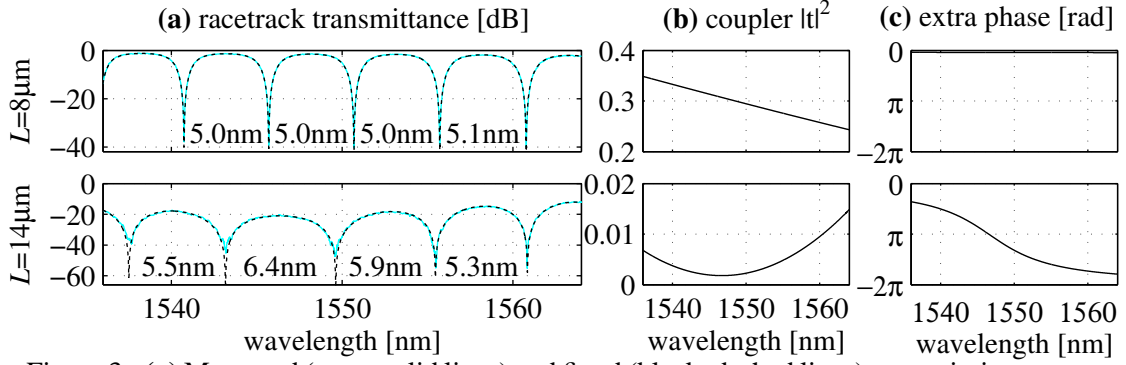


Figure 3: **(a)** Measured (cyan, solid lines) and fitted (black, dashed lines) transmission spectra of the ring resonators (two different coupler lengths L). Normalized to the transmission of a single-mode waveguide. **(b)** and **(c)** Quantities obtained from the fitted curve.

to be identical ($\delta = 0$) but observed small asymmetry δ . This additional phase delay is usually negligible as the real part inside this argument is much smaller than the imaginary part ($\delta \ll s$), but around $|t| \approx 0$, we have $\cos s\tilde{L} = 0$ so that the real part vanishes and the phase delay rapidly increases. In one spectrum, \tilde{L} is fixed but s varies slightly due to linear dispersion s' . The straight-through power of the coupler $|t|^2$ is plotted in Fig. 3b, and the wavelength of minimal transmission agrees with the rapid variation in additional phase delay (Fig. 3c) and with the corresponding change in the FSR (Fig. 3a). This significant change is explained by a small difference between the corrected propagation constants of the waveguides, $2\delta/\beta$, of 0.1%. To get a feeling for δ , we numerically compute the difference in the widths of the waveguides Δw that would give such an asymmetry, giving $\Delta w \approx \partial w / \partial \beta \cdot 2\delta = 1 \text{ nm}$.

Fig. 2e shows the fitted unknowns and Fig. 2c shows the corresponding behavior of the couplers. Fig. 2d presents their wavelength dependency, showing a variation in the coupled power ($1 - |t|^2$) up to 0.18 within the wavelength span of 30 nm.

Conclusion

We measured propagation loss of straight and bent waveguides and observed a weak wavelength dependency. We characterized directional couplers using an analysis based on coupled-mode-theory and found excellent agreement between the measured spectra and the theoretical shape, indicating that all relevant physics is included. The couplers showed significant wavelength dependency. We demonstrated that a tiny (nanoscale) asymmetry in the two waveguides of a coupler causes a significant additional phase delay in the cross-coupling regime where most light is coupled from one waveguide to the other.

We acknowledge the ePIXfab consortium for the fabrication of the devices, with special thanks to dr. Pieter Dumon and dr. Amit Khanna of IMEC (Leuven). At TNO (Delft), we thank ing. Hans van den Berg, dr. Emile van Veldhoven, dr. Peter Harmsma, and ir. Remco Nieuwland.

- [1] W. Bogaerts *et al.*, “Silicon microring resonators,” *Laser & Photonics Reviews*, vol. 6, p. 47, 2012.
- [2] D. Taillaert, P. Bienstman, and R. Baets, “Compact efficient broadband grating coupler for silicon-on-insulator waveguides,” *Optics Letters*, vol. 29, p. 2749, 2004.
- [3] W. J. Westerveld, “Silicon integrated optomechanical sensors,” Presented at the European Conference on Optical Communication (ECOC), workshop WS07, Amsterdam, Sep. 2012, (*invited*).
- [4] W. Bogaerts and S. Selvaraja, “Compact single-mode silicon hybrid rib/strip waveguide with adiabatic bends,” *Photonics Journal, IEEE*, vol. 3, p. 422, 2011.
- [5] A. Yariv and P. Yeh, *Photonics*. Oxford University Press, 2007.

Colloidal PbS Quantum Dot Photodetectors for Short-wave Infrared applications

Chen Hu,^{1,2,3} Alban Gassenq,^{1,2} Eva M.P. Ryckeboer,^{1,2} Yolanda Justo,^{2,3} Zeger Hens,^{2,3} and Gunther Roelkens^{1,2}

¹ Photonics Research Group, INTEC Department, Ghent University-IMEC, Sint-Pietersnieuwstraat 41, 9000 Ghent, Belgium

² Center for Nano- and Biophotonics (NB-Photonics), Ghent University, Belgium

³ Physics and Chemistry of Nanostructures, Ghent University, Krijgslaan 281-S3, 9000 Gent, Belgium

In this study, the use of PbS colloidal quantum dots for short-wave infrared photodetector applications is explored. To achieve effective carrier transport between the dots in a film, a layer-by-layer approach is used to deposit uniform, ultra-smooth and crack-free QD films, where each deposition cycle involves the replacement of the native organic ligands by inorganic moieties (OH^- and S^{2-}) followed by a thorough cleaning procedure. The photodetector shows clear photoconductive gain. The cut-off wavelength of these devices is $\sim 2.2 \mu\text{m}$. Integration of these photodetectors on silicon photonic circuits is demonstrated.

Introduction

Nowadays the short-wave infrared (SWIR) region gets more and more attention for applications. Traditional spectroscopic systems are nowadays mainly based on discrete components based on epitaxial materials¹. However, the cost of these components hampers large scale deployment of such systems and the size of the system makes their use difficult in the field. Low cost colloidal quantum dots (QDs) offer an alternative way to implement SWIR photodetectors and can be integrated on silicon-based waveguide circuits, resulting in very small and cheap spectroscopic sensing systems². Colloidal QDs are new optoelectronic materials that raise a lot of interest for photonic applications. They are prepared by simple hot injection chemical synthesis, which offers a significant cost reduction³. Another advantage of colloidal QDs is the spectral tunability due to the quantum size effect⁴. The suspension of colloidal QDs in solution provides an easy way to realize large-area heterogeneous integration by solution based processing⁵.

In this study we use PbS colloidal QDs for short-wave infrared photodetector applications. A layer-by-layer (LBL) approach is demonstrated to realize homogeneous and crack-free QD films. In this approach, each cycle involves a QD layer deposition by dip coating, followed by inorganic ligand exchange, and then a thorough cleaning procedure is used to remove impurities. Metal-free inorganic ligands, such as OH^- and S^{2-} , are used to enhance carrier transport in QD films⁶. The QD films are realized on prefabricated interdigitated electrodes (for surface illuminated devices) and also on silicon photonics planar concave grating spectrometers (PCG). Afterwards a selective wet etching approach is used to achieve a micropatterned QD film.

Experimental details

1. Fabrication of QD films

The QD films were formed by a layer-by-layer (LBL) approach. Each cycle contains a dip coating of the substrates into a 1 μM PbS QD suspension in toluene with an 80 mm/min dipping speed. After completely drying, the QD films were re-immersed into a solution of either $\text{Na}_2\text{S}\cdot 9\text{H}_2\text{O}$ (10 mg/mL) or KOH (0.01 mg/mL) in formamide to exchange the original oleate ligands by S^{2-} and OH^- . At the end of each cycle, the sample was thoroughly cleaned by immersing it twice in formamide, twice in acetone and once in isopropanol. Afterwards the sample was dried under nitrogen.

2. Micropatterning of QD films

Micropatterned QD films were realized by optical lithography and wet etching. The photoresist was spun on top of the QD layer and post baked. After exposure and development, the pattern was transferred from the mask to the photoresist layer. After this a mixture of HCl and H_3PO_4 was used to remove the uncovered QD film. The volume ratio between HCl and H_3PO_4 is $\sim 1:10$. After the desired etching time, the photoresist was stripped by acetone, resulting in a well defined micropatterned QD film.

3. Photodetector Fabrication

PbS photodetectors are fabricated similar to the PbS thin films. For the surface illuminated PbS photodetectors, an isolating SiO_2 layer was deposited by plasma enhanced chemical vapor deposition (PECVD) on a silicon substrate. A pair of interdigitated finger shape electrodes was formed by optical lithography through a lift-off process consisting of 10 nm Ti and 100 nm Au. The fingers are designed with 2 μm wide fingers with 2 μm separation and are attached to two independent contact pads (shown in Figure 1). For integrated photodetectors on planar concave gratings, an array of electrodes was defined by photolithography and lift-off. After the QD films were deposited with a layer-by-layer (LBL) approach, selective wet etching was used to obtain micropatterned QD detectors for surface illumination on silicon substrate and on photonic integrated circuits.

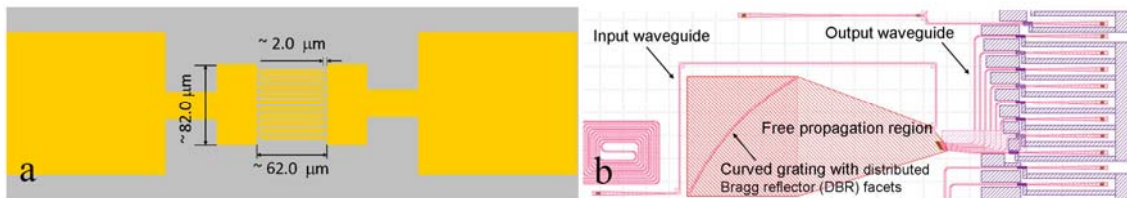


Figure 1. (a) Illustration of the PbS detector electrodes design (top view) (b) schematic of integrated photodetector electrodes design on a planar concave grating

Results and Discussion

1. Layer-by-layer assembly of QD films

After synthesis, the electrically isolating organic oleate ligands need to be replaced by inorganic ligands to facilitate carrier transport in QD films and implement photoconductive devices. Thus a solid state ligand exchange process is proposed to remove the original organic capping of the QDs. Transmission electron microscopy (TEM) is used to examine the ligand exchange of QDs on a small scale. As shown in Figure 2, the distances between QDs are clearly decreased after ligand exchange, which indicates that the oleate ligands were removed after chemical treatment. The corresponding surface morphology of the QD films obtained by the LBL approach is

measured by scanning electron microscopy (SEM), which confirms that crack-free, homogeneous QD films can be obtained.

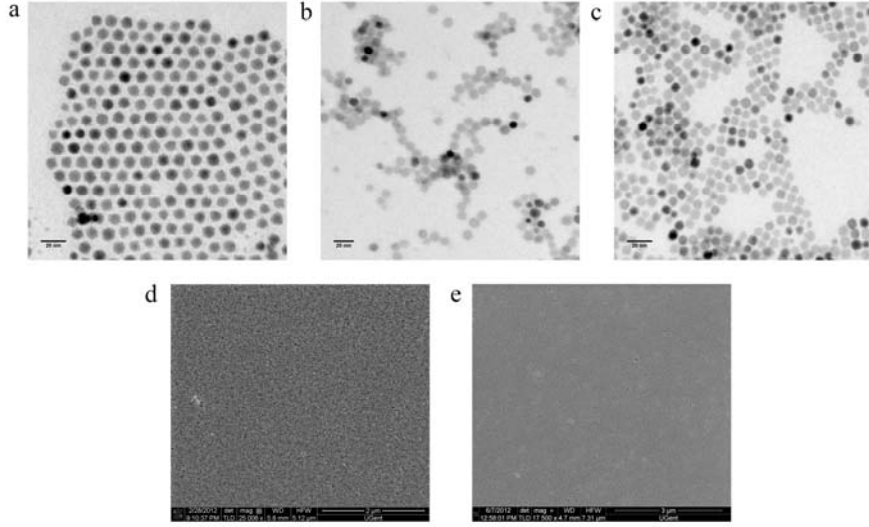


Figure 2. (a) TEM images of OIAc (a), S^{2-} (b) and OH^- (c) -terminated colloidal PbS QDs. SEM images of S^{2-} (d) and OH^- (d) -terminated PbS films.

2. Characterization of PbS photodetectors

The current-voltage characterization of S^{2-} -terminated PbS photodetectors was done under surface illumination with a fiber coupled near infrared SLED ($\lambda \sim 1.55 \mu m$). As shown in Figure 3(b), under illumination, the PbS photodetector shows photoconductive behavior and a linear I-V characteristic is observed, which indicates that the carrier transport is facilitated by the inorganic ligand exchange. The responsivity of S^{2-} -terminated PbS photodetectors as a function of illumination power level is represented in Figure 3(c), which shows an increase of responsivity with decreasing illumination. The photodetector shows internal photoconductive gain, which indicates that the carrier lifetime (related to the trapping of carriers in the dots) is longer than the carrier transit time. Probably, the long-lived trap states are filled with increasing incident power, such that a lower responsivity is obtained for increased input power.

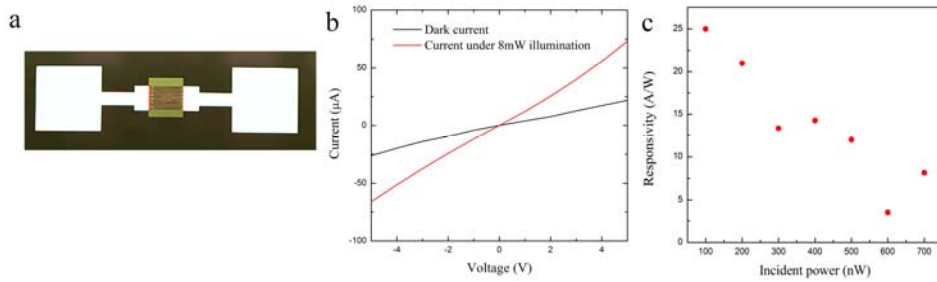


Figure 3. (a) microscope picture of a S^{2-} -terminated PbS colloidal QD photodetector. (b) Current-voltage characteristics of processed S^{2-} -terminated PbS colloidal QD photoconductors. (c) Responsivity dependence as a function of optical power at $1.55 \mu m$ and a bias voltage of 10 V for an S^{2-} -terminated PbS colloidal QD photodetector.

Integrated QD photodetectors are obtained by the deposition of OH^- -terminated PbS QD on a PCG. This is shown in Figure 4. Measurements are currently being carried out to assess the performance of such a spectrometer.

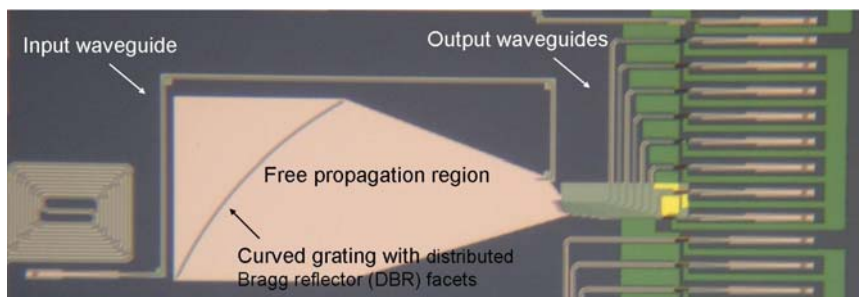


Figure 4. microscope picture of a OH^- -terminated PbS colloidal QD photodetector array integrated on a planar concave grating spectrometer.

Conclusions

In this paper, PbS QDs are explored for SWIR photodetector applications. We have demonstrated a uniform, ultra-smooth colloidal QD film without cracks by the LBL assembly method. Metal-free inorganic ligands, such as OH^- and S^{2-} are investigated to facilitate the charge carrier transport between the dots. PbS photoconductors show clear photoconductive gain. The integration of PbS QD photodetectors on photonic integrated circuits has also been realized.

Acknowledgements

This work is supported by the FWO-NanoMIR project and the FP7-ERC-MIRACLE project. We acknowledge the assistance from Steven Verstuyft during the device fabrication. We also acknowledge the assistance from Liesbet Van Landschoot and Kasia Komorowska during SEM measurement.

References

- [1] Baile Chen, W. Y. Jiang, Jinrong Yuan, Archie L. Holmes, Jr, and Bora. M. Onat, "Demonstration of a room-temperature InP-based photodetector operating beyond $3\ \mu\text{m}$ ", *Photonics Technology Letters*, Volume 23, Issue 4, 218–220 (2011).
- [2] Gerasimos Konstantatos, Ian Howard, Armin Fischer, Sjoerd Hoogland, Jason Clifford, Ethan Klem, Larissa Levina & Edward H. Sargent, "Ultrasensitive solution-cast quantum dot photodetectors", *Nature* 442, 180-183 (2006).
- [3] Iwan Moreels, Yolanda Justo, Bram De Geyter, Katrien Hastraete, José C. Martins, and Zeger Hens, "Size-Tunable, Bright, and Stable PbS Quantum Dots: A Surface Chemistry Study", *ACS Nano*, 5 (3), pp 2004–2012 (2011).
- [4] Iwan Moreels, Karel Lambert, Dries Smeets, David De Muynck, Tom Nollet, José C. Martins, Frank Vanhaecke, Andre' Vantomme, Christophe Delerue, Guy Allan and Zeger Hens, "Size-Dependent Optical Properties of Colloidal PbS Quantum Dots", *ACS Nano* Vol. 3(10), 3023–3030 (2009).
- [5] Michaela Böberl, Maksym V. Kovalenko, Stefan Gamerith, Emil J. W. List, and Wolfgang Heiss, "Inkjet-Printed Nanocrystal Photodetectors Operating up to $3\ \mu\text{m}$ Wavelengths", *Adv. Mater.* 19, 3574–3578 (2007).
- [6] Angshuman Nag, Maksym V. Kovalenko, Jong-Soo Lee, Wenyong Liu, Boris Spokoyny, and Dmitri V. Talapin, "Metal-free Inorganic Ligands for Colloidal Nanocrystals: S^{2-} , HS^- , Se^{2-} , HSe^- , Te^{2-} , HTe^- , TeS_3^{2-} , OH^- , and NH_2^- as Surface Ligands", *J. Am. Chem. Soc.* 133, 10612–10620 (2011).

Monolithically Integrated InGaAsP/InP Active-Passive 8×8 Cross-Connect

R. Stabile,¹ A. Rohit,¹ and K. A. Williams¹

¹ COBRA Research Institute, Eindhoven University of Technology, Den Dolech 2, 5600 MB, Eindhoven, The Netherlands

The increasing bandwidth and connectivity requirements in data- and tele-communications have led to a considerable interest in space and wavelength switching. Optoelectronic switching has been proposed for scalable optical switching systems but these approaches so far have used hundreds of discrete components. We present the first monolithically integrated InP active-passive 8×8 cross-connect which provides $8 \times 8 \times 8\lambda$ capacity within a $14.6 \times 6.7 \text{ mm}^2$ area. 432 unique optical connected paths are characterized. Data routing studies are performed for a representative range of paths to show optical signal-to-noise ratios of greater than 30dB/0.1nm. Switch rise and fall times are measured to be 3.8 and 3.2ns respectively.

Introduction

Increasingly sophisticated optical signal routing offers the possibility to define connectivity in terms of the product of physical inputs and wavelength channel numbers per port, allowing order of magnitude scaling with respect to space switches and wavelength routed switches only. This has motivated large scale experimental switch fabric demonstrations for tele- and computer-communications [1,2]. The largest fully implemented fabric has used multiplexes of eight wavelengths on each of eight input ports to enable 64×64 connectivity [3]. The use of discrete photonic components in these proof of principle implementations is however restrictive in terms of scalability and power consumption.

Extensive photonic integration can provide synchronized switch states, allowing considerable reductions in control complexity, calibration, and an improved control of optical losses, as well as decreased footprint and power consumption. Recently we have reported the first 8×8 space- and wavelength-selective cross-connect [4,5]. Arrayed waveguide grating (AWG) based architectures are chosen to offer a high scalability route to rich functionality optical cross-connect circuits. The combination of wavelength selective switches with semiconductor optical amplifier (SOA) switches is implemented to offer flexible control and re-configurability with fast switching speeds.

In this work we present the first monolithically integrated 8×8 WDM cross-connect. The combination of both space- and wavelength-selective routing is exploited on a single monolithic InP circuit. Dynamic multi-path provisioning is performed in time and wavelength. Data integrity for received channel is evaluated in term of measured power penalty.

8×8 Integrated Cross-Connect

The monolithically integrated 8×8 space and wavelength selection switch consists of a broadcast port selection or photonic switch stage (PSS) and a color selection or wavelength selective stage (WSS), as shown in the architecture in Fig. 1a. In the first

stage, eight colorless inputs are broadcast to 64 broadband SOA gates for input port select through a shuffle network. Eight parallel 8 input-8 output cyclic AWGs map each of the input ports to a second stage of 64 SOAs gates which perform the color selection. The selected wavelength channels are combined and sent to the eight colorless outputs. The grey-scale layers in Fig. 1a are the seven identical layers implemented in the integrated circuit for both stages.

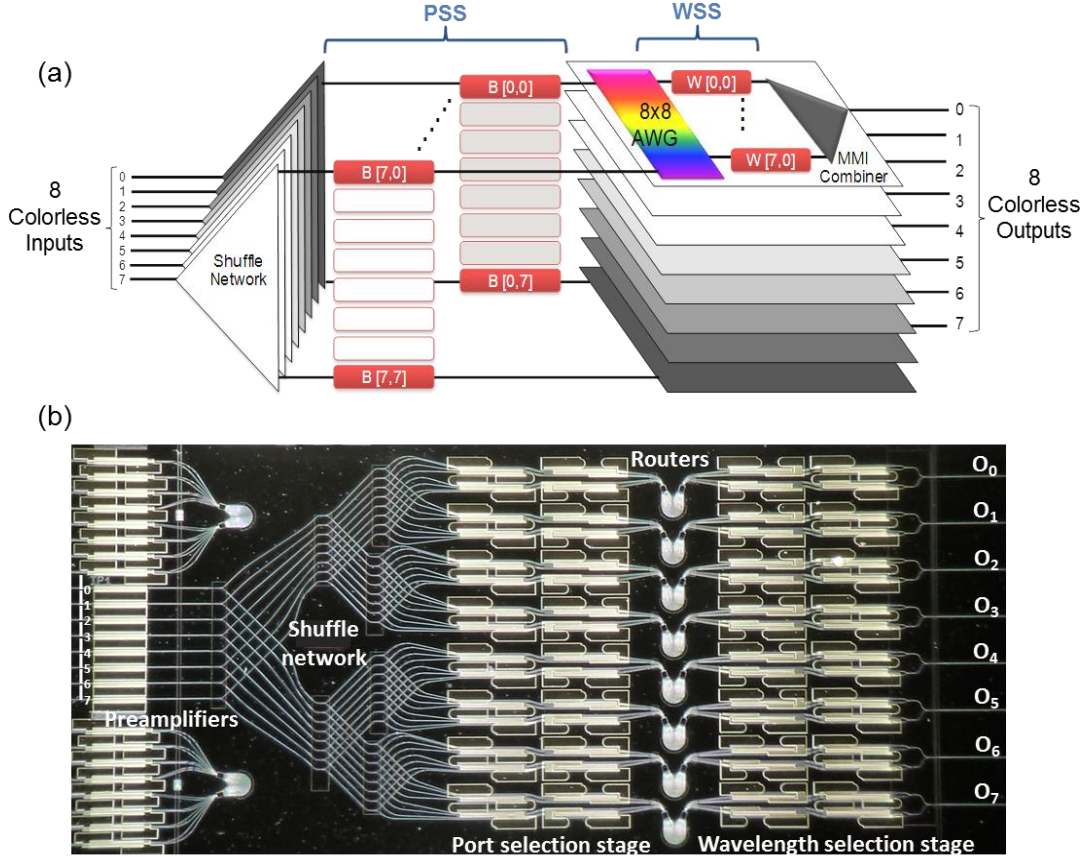


Fig. 1 – Architecture (a) and microscope image (b) of the $16.4 \times 6.7 \text{ mm}^2$ 8×8 cross-connect.

The device is realized on a re-grown active-passive InGaAsP/InP epitaxy. An optical image of the chip is shown in Fig. 1b. The eight pre-amplified colorless inputs are broadcast through a shuffle network made of cascaded 1×2 multimode interferometer (MMI) splitters. After port and color selection, the selected channels are combined with broadcast cascaded 2×1 MMI couplers. The active islands in the InP wafer are used for SOAs gates and preamplifiers, while the passive regions are used for waveguide wiring, splitters and cyclic routers. Shallow waveguides allow low leakage amplifiers and low divergence 90° waveguide crossings. Deep etch waveguides are used for splitters and low-radius micro-bends for a more compact chip size. To reduce further the total circuit area, pairs of 1mm long BSS and WSS SOAs share one active island. The cyclic AWG used in the WSS is designed with a channel spacing of 3.2 nm (400GHz) and a free spectral range of 25.6 nm. All inputs and output waveguides are positioned on a $250 \mu\text{m}$ pitch to enable simultaneous access to all the ports using a commercially sourced lensed fibre array. The 136 SOA contacts are wire-bonded to an electronic printed circuit board (not shown). The chip is attached with conductive epoxy to a water-cooled block. The total footprint of the switch is $16.4 \times 6.7 \text{ mm}^2$.

WDM and Multi-Path Dynamic Routing Assessment

The chip connectivity is evaluated by using the SOA amplified spontaneous emission as a source and measuring AWG transfer functions at both chip sides. The SOAs on the selected path are biased with 40 mA current. Sixty paths out of sixty-four connections are verified from the wavelength selection SOAs to the input side. From the photonic switching stage to the output side, 432 paths out of 512 paths connections are verified. In total 84% of the paths from the input to the output side of the chip are electrically and optically connected.

Data integrity for multiple simultaneously routed 10 Gb/s wavelength channels is evaluated by optical spectra and bit error rate assessment. The experimental control plane to demonstrate multi-path WDM data routing is schematically shown in Fig. 2.

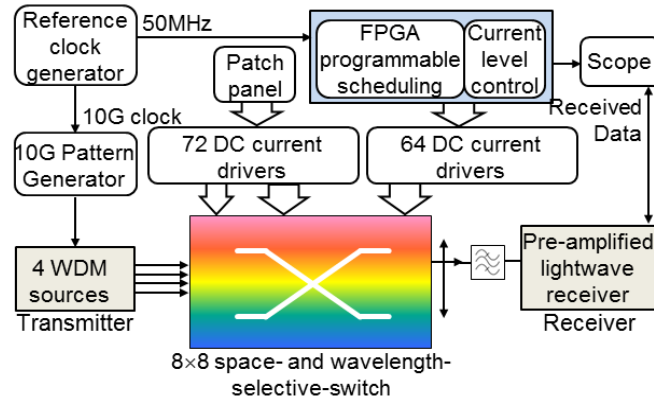


Fig. 2 – Setup for WDM single and multi-port simultaneous routing.

An Altera Stratix III FPGA provides control signals to the high speed current drivers for optical path selection using a round-robin schedule. A common reference clock generator for the FPGA and the bit error rate test equipment allows synchronization between the routed data and the switch controller. Four different wavelength channels, $\lambda_0=1543.1$ nm, $\lambda_1=1546.3$ nm, $\lambda_2=1549.8$ nm and $\lambda_3=1552.7$ nm, with a nominal channel separation of 400GHz are multiplexed and modulated using a single Mach-Zehnder modulator with a pseudo random bit sequence (PRBS) of $2^{13}-1$ bit length. The WDM signal is then amplified, de-multiplexed, de-correlated and used as input to the device. The chip output is connected to a pre-amplified optical receiver after a 0.95 nm bandwidth filter for broadband noise rejection.

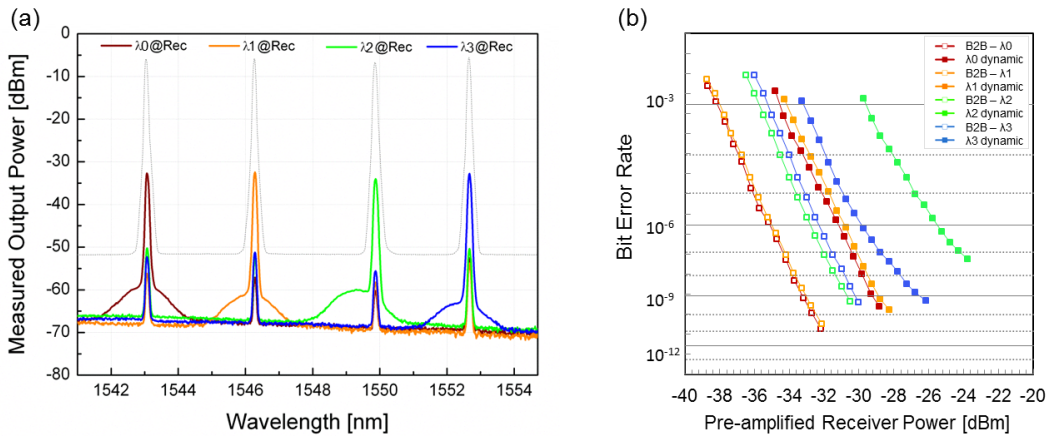


Fig. 3 – Optical spectra (a) and bit error rate measurements (b) for WDM routing through path 0 to 0.

Each path include three SOAs. An average total current per path in the range from 120 to 160 mA is used. The optical spectra of multiplexed channel at input 0 are evaluated at output 0. Optical signal to noise ratios greater than 27.0 dB for 0.1 nm resolution bandwidth are measured for each of the channels in Fig. 3a. A mean chip to fibre-array coupling loss is estimated to be 13.5 dB when all waveguides are simultaneously aligned indicating a mean 13.3 dB on-chip loss. Moderate power penalties in the range from 3.6 to 4 dB for three of the four filtered output wavelength data signals are measured (Fig. 3b). The third channel is compromised by the pass-band misalignment imposed by the WDM source multiplexer.

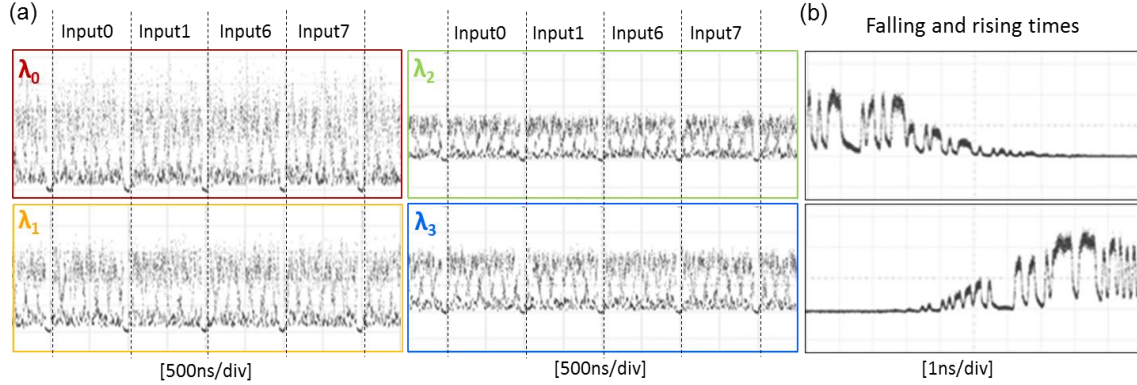


Fig. 4 – Time traces (a), rise and fall time (b) for dynamic multi-port WDM routing at output 0.

To demonstrated simultaneous WDM multi-path data routing the wavelength multiplexed data is split into four copies using broadband splitters and launched into four input ports: 0, 1, 6 and 7 of the chip. Sixteen channels are routed within the 8×8 cross-connect to output port 0. All four input paths are sequentially enabled with a round-robin scheduling and loaded with WDM input signals for dynamic multi-path WDM reconfigurability studies. The color-select SOAs are enabled with fixed current levels of order of 35 mA. The correspondent SOAs are biased with order of 60 mA current and are driven by periodic 1μs pulses with 60 ns guard-bands programmed via the FPGA. Fig. 4a shows the time traces of the output WDM signals. Along the x-axis the selected input port changes at each time slot as for the round-robin scheduling. The four sets of wavelengths are selected using external optical filters and are displayed as four separate graphs. Fig. 4b also shows fall and rise time for the output signal taken for λ_0 when moving from one time slot to the next one: The switching occurs within 5 ns.

Conclusions

Simultaneous colourless multipath routing for sixteen 10Gb/s data channels is demonstrated through the first integrated 8×8 broadcast and select WDM cross-connect, with low excess power penalties and OSNR values higher than 27 dB/0.01nm.

References

- [1] S. Araki et al., *J. Opt. Netw.*, 2, 213–228, 2003.
- [2] R. Hemenway et al., *J. Opt. Netw.*, 3, 9000-913, 2004.
- [3] R.Luijten et al., *Proc. OFC'09*, OTuF3, 2009.
- [4] A. Rohit et al., *Proc. OFC'13*, OW1C.4, 2013.
- [5] R. Stabile, et al., *Proc. ECOC'13*, We.4.B.2, 2013.

Raman spectroscopy using photonic waveguides

A. Dhakal^{1,3}, P. Wuytens^{1,2,3}, F. Peyskens^{1,3}, A. Z. Subramanian^{1,3},
N. Le Thomas^{1,3}, and Roel Baets^{1,3}

¹Photonics Research Group, INTEC Department, Ghent University- imec, Ghent, Belgium

²Department of Molecular Biotechnology, Ghent University, Ghent, Belgium

³Center of Nano- and Biophotonics, Ghent, Belgium

Email: ashim.dhakal@intec.ugent.be

We propose to use silicon nitride (Si_3N_4) based photonic waveguides in a lab-on-a-chip context for Raman spectroscopy. The evanescent tail of the guided modes can efficiently excite Raman active molecules located in the cladding of a waveguide. Similarly, a significant fraction of the total emitted Stokes power is evanescently coupled to the same mode. We calculate the spontaneous Raman scattering efficiency as a function of Si_3N_4 strip waveguide dimensions and show that under typical conditions, the efficiency is in the order of 10^{-8} . Preliminary experimental results are reported, as the first demonstration of waveguide assisted Raman spectroscopy (to the best of our knowledge).

Introduction

Sensors based on integrated photonics have evolved as a very promising route for lab-on-a-chip sensing applications [1]. One class of sensors is aimed at waveguide assisted spectroscopic techniques, such as absorption spectroscopy, fluorescence spectroscopy and Raman spectroscopy. These spectroscopic sensors are based on light-matter interaction of the evanescent field of the waveguide and allow a direct measurement of the specific spectrum of the molecules rather than other indirect methods using evanescent fields, such as refractive index sensing. Further, compared to free-space spectroscopy, the enhancement effects inherent to the waveguide, alongside with the long interaction length, lead to an increased light-matter interaction, resulting in a higher sensitivity as required by spectroscopic applications, especially in the context of Raman spectroscopy. In this paper, we summarize the theoretical and experimental results to realize Raman sensors based on Si_3N_4 photonic waveguides.

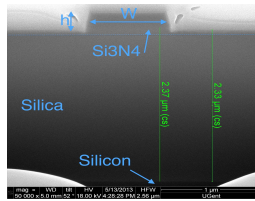


Fig. 1: SEM picture of the complete Si_3N_4 waveguide cross-section discussed in this paper including underlying SiO_2 and silicon substrate.

Recently, we investigated the scattering efficiency of a particle located in the vicinity of a channel waveguide for several geometries [2]. We theoretically determined the overall efficiency (η) of (Raman) scattering from a guided mode and subsequent emission coupled back to the fundamental mode (both TE and TM) of a rectangular channel waveguide by uniformly distributed particles in its surrounding. We define η as the ratio between the emitted power collected by the waveguide and the incident pump power in the mode. It was shown that η is highly dependent on the mode area that further depends on the waveguide index and geometry. The same methodology can be applied to more

popular strip waveguide geometry (Fig. 1) for silicon nitride (Si_3N_4) waveguides [5]. In this paper, we numerically evaluate η as a function of the waveguide width (w) for several thickness (h) values for Si_3N_4 ($n=2$) waveguides in water ($n=1.33$) cladding. The preliminary result of the on-going experimental investigation to verify the aforementioned theoretical results is also reported.

Theoretical investigations for collection of Raman signal for silicon nitride waveguides

Assuming that the Raman scattering mechanism can be modelled as the radiation of an oscillating dipole, and neglecting the Stokes shift, in the weak coupling regime, it can be shown that the efficiency of spontaneous Raman collection from molecules of scattering cross section σ and density ρ lying in the surrounding of a waveguide into a mode of a channel waveguide of length l is given by [2]:

$$\eta = \frac{\pi^2 \lambda_0^2}{(\epsilon_0 \epsilon)^2 n} (\kappa n_g^2 \Gamma^2 l) \sigma \rho \quad (1)$$

Where, n_g is the group index of the mode, $n=\sqrt{\epsilon}$ is the refractive index of the surrounding medium, and ϵ_0 is the permittivity of the vacuum, κ is a constant relating the polarizability and the cross-section of the molecule, Γ is a parameter dependent on the overlap of the mode area and the sensing area, given by:

$$\Gamma^2 = \int_{\text{sens}} ds \left(\frac{\epsilon_0 \epsilon |\vec{E}(\vec{r}_0)|^2}{\iint \epsilon_0 \epsilon(\vec{r}) |\vec{E}(\vec{r})|^2 d\vec{r}} \right)^2 \quad (2)$$

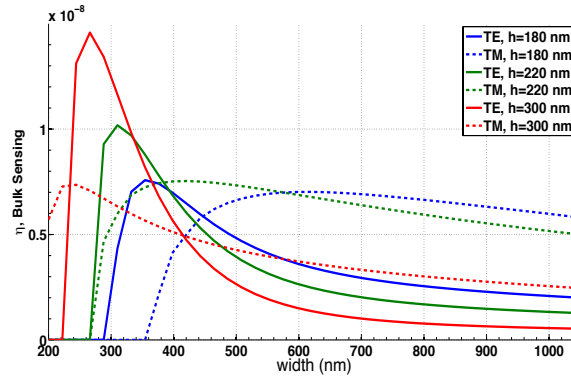


Fig. 2: Efficiency of Raman signal collection for the fundamental TE and TM mode of Si_3N_4 strip waveguides [5] as a function of waveguide widths for several heights (h) of the strip.

We use the COMSOL finite element eigenmode solver to determine the field of the waveguide modes for several waveguide geometries and solve Eq. (1). For simplicity, we neglect material dispersion, pump depletion, and assume $n_g \approx n_{\text{eff}}$ as this will have negligible impact. As an example, we take $\sigma=3 \times 10^{-30} \text{ m}^2 \text{Sr}^{-1} \text{molecule}^{-1}$, as a typical cross-section of the dyes, $\rho=1 \text{ mole/liter}$ and calculate η for a 1 cm long waveguide. It is emphasized that the parameter values we have chosen do not affect the generality of our results because η scales in a simple way with these parameters as per Eq. (1).

Fig. 2 shows the calculated η as a function of the waveguide width (w) and height (h) for Si_3N_4 waveguides for bulk sensing for fundamental TE and TM polarized mode. The maximal efficiency, η_{max} is approximately 1.5×10^{-8} , implying that under ideal conditions, for 1 mW of pump power in the waveguide, 15 pW of scattered signal can be collected by the guided mode. It is to be noted that the equivalent efficiency in a free-space confocal microscope system using diffraction-limited beams would be in the order of 10^{-10} . The efficiency is maximal near the cutoff widths and decreases sharply before becoming almost constant for wider widths.

Experimental observation of Raman peaks of Rhodamine 6G dye

The experimental setup is illustrated in Fig. 3. The setup is designed to measure the spontaneous Raman signal in a back-reflection configuration to reduce the collection of direct pump light by the spectrometer. A tuneable Ti-Sapphire CW laser ($\lambda=720\text{-}975$ nm) was used as the pump source. For the experiments, a wavelength of 785 nm is coupled to the waveguide by end-fire coupling using an aspheric lens of effective focal length 2.75 mm (NA=0.64). In order to avoid collecting the pump light, it passes via a dichroic beam splitter reflecting 785 nm and transmitting wavelengths longer than 790 nm. The counter-propagating Raman signal (Stokes) collected by the waveguide is then collimated via the same lens towards the dichroic filter. The collimated light is filtered using an edge filter, with the edge wavelength at 790 nm so as to block any stray pump light leaking into the spectrometer. The Raman signal is then focused to a multimode optical fibre of 50-microns core diameter using an aspheric lens of 11 mm effective focal length (NA=0.2) and measured using a commercial spectrometer (Avantes SensLine).

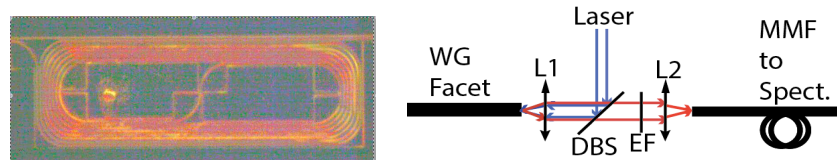


Fig. 3: (Right) The schematic of experimental setup. The pump laser at 785 nm is focused at the waveguide (WG) facet using an aspheric lens (L1). The counter propagating spontaneous Raman signal from the waveguide is coupled to the multimode fibre (MMF) using another aspheric lens (L2) via a dichroic beam splitter (DBS) and long pass edge filter (EF). (Left) The spiral used for measurement tinted with R6G dye used as Raman active molecules.

We take a silicon nitride waveguide ($w=500$ nm, $h=220$ nm) on top of a $2.4\text{ }\mu\text{m}$ silica cladding on a silicon substrate (Fig. 1). A spiral waveguide (1 cm in length) is used as the sensing region for the experiment (Fig. 3). The laser power is set to 150 mW, but it was sub-optimally coupled (coupling loss: ~ 15 dB) to the waveguide so as to avoid pump hitting the substrate and under-cladding that would otherwise generate a background that saturates the detector. A drop of 0.41 mM Rhodamine 6G (R4127, Sigma Aldrich) dissolved in ethanol was dried on top of the waveguide spiral (Fig. 3). During this procedure, special attention was taken not to stain the facet with the solution that would make coupling of pump and signal difficult. The measured spectrum (60 s integration time) before and after the application of the dye is shown in Fig. 4. A noticeable feature of both spectra is that they have the strongest peak at 520 cm^{-1} corresponding to the silicon substrate and a broad fluorescence background due to the undercladding or the substrate of the waveguide. The small peaks due to the dye are

clearly visible, but are embedded in a broad background. In order to extract the spectrum, we take the spectrum in the range 1000-1700 cm^{-1} and apply the I-polyfit algorithm [3] to remove the background and compare the result (Fig. 4) with the Raman spectra of the dye provided by the manufacturer [4]. An excellent match between the spectra can clearly be seen after removing the fluorescence background.

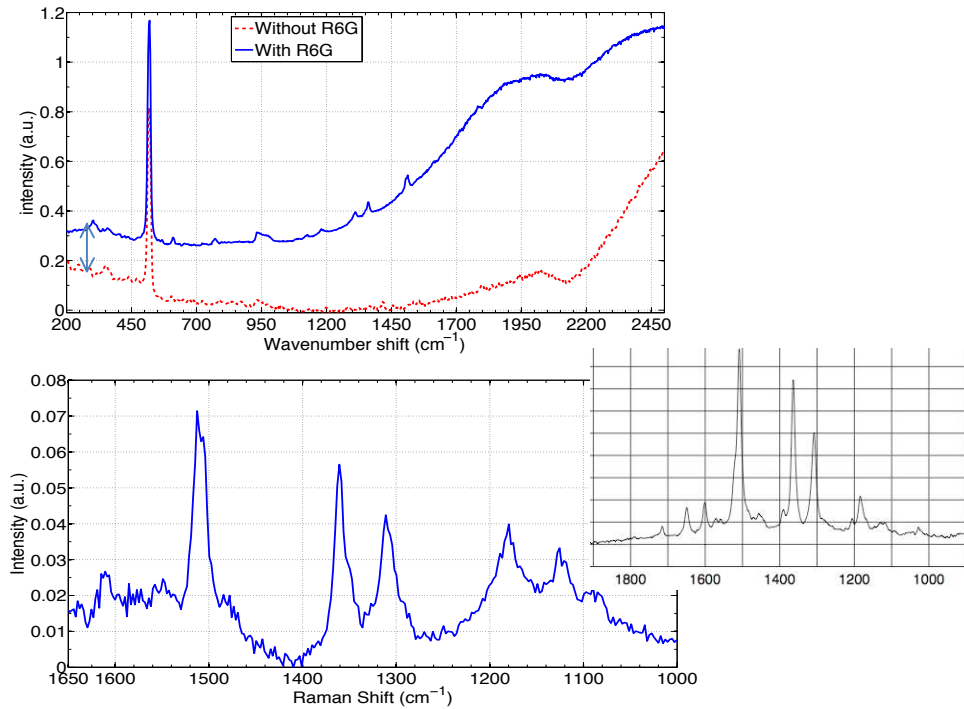


Fig. 4: (Top) Spectra measured before (red-dashed line) and after (blue-solid line) application of the dye. The spectrum with dye is shifted up by 0.2 units, for clear visualization. The peak at 520 cm^{-1} corresponds to Raman emission of silicon. The broad fluorescence from the under cladding forms the background for the emission from the dye, which are visible as small peaks. (Bottom) The spectra of dye extracted using I-polyfit algorithm [3]. In the inset, the section of spectrum provided by the manufacturer is also presented for comparison.

Conclusion

The theory predicts Raman signals of 10 pW per cm of waveguide per molar concentration of dyes for 1 mW pump. Initial experimental results suggest that photonic waveguides provide a very promising route for miniature Raman spectroscopy. More experiments are needed to confirm the numerical prediction of the theory.

The authors acknowledge ERC advanced grant InSpectra for the funding and imec, Leuven for processing of the waveguide.

References

- [1] X. Fan, I. M. White et.al., "Sensitive optical biosensors for unlabeled targets: A review," *Anal. Chem. Acta*, vol. 620, pp. 8-26, 2008
- [2] A. Dhakal et. al, "Enhancement of light emission, scattering, and emission in high index contrast waveguides" OSA Advanced Photonics Congress, Sensors , PuertoRico, ST2B.5, 2013
- [3] J. Zhao et. al, "Automated Autofluorescence background subtraction algorithm for biomedical Raman spectroscopy", *Appl. Spec*, 61 (11), 1225-1232, 2007
- [4] www.sigmaaldrich.com/spectra/rair/RAIR003657.PDF
- [5] A. Subramanian et. al., "Low-loss singlemode PECVD silicon nitride photonic wire waveguides for 532-900 nm wavelength window fabricated within a CMOS pilot line", *IEEE Photonics Journal* (submitted), 2013

Full Rate-equation Description for Multi-mode Semiconductor Lasers

Daan Lenstra^{1,*}, Mirvais Yousefi²

¹Photonic Integration Group, Department of Electrical Engineering, Eindhoven University of Technology, Eindhoven, The Netherlands

²Photonic Sensing Solutions, Amsterdam, The Netherlands
*d.lenstra@tue.nl

A set of rate equations is presented describing the deterministic multi-mode dynamics of a semiconductor laser. Mutual interactions among the lasing modes, induced by high frequency modulations of the carrier distribution, are described by carrier-inversion moments and lead to special spectral content of each spatial mode. The Bogatov effect of asymmetric gain suppression in semiconductor lasers will be derived. We will explicitly discuss the nontrivial relationship between the modes of the nonlinear cavity and the optical spectrum of the laser output and illustrate this for a two and three-mode laser.

Introduction

Many phenomena in multi-mode semiconductor diode lasers have their origin in the nonlinear dynamical evolution of the lasing modes and certain hole-burning (grating) effects in the population inversion. The numerical analysis of the resulting, often complicated, dynamics would benefit greatly from a set of coupled rate equations capable of describing the full deterministic dynamics of the lasing modes as well as their mutual interactions. Such description in terms of first-order ordinary differential equations (ODEs) is thus perfectly suited for an efficient bifurcation analysis using existing standard tools. Moreover, the inclusion of spontaneous-emission noise in the modes and recombination noise in the carriers in such formalism is straightforward and could easily be carried through.

In this paper we report on the derivation of multi-mode rate equations for a semiconductor laser in terms of ODE's for the complex modal field amplitudes, the overall population inversion and the various lasing-induced population-inversion gratings (spatial hole burning). This is a big advantage over existing theories, which are based on complicated partial-differential and/or integral equations [1-3]. We take into account two mode-mode interaction mechanisms: (i) carrier sharing and (ii) mutual coherent optical injection. Different modes are identified by their spatial profiles in the laser cavity and described by their complex amplitudes. The full electron-hole density in the active medium is expanded in a complete set of base functions, which allow the introduction of inversion moments describing not only the formation of gratings burned by the modal fields, but also the mutual injection of modal fields. Thus, we reproduce the Bogatov-effect on asymmetric side-mode suppression [4] as well as the peculiar periodic multi-mode switching scenario reported and explained in [5] and [6]. The full derivation of the multi-mode rate equations will be published elsewhere.

Multi-mode rate equations

The rate equations for a semiconductor laser operating in M longitudinal modes are given by

$$\frac{d}{dt} E_k(t) = -\frac{1}{2}(\Gamma_k - g_k)E_k(t) + \frac{1}{2} \sum_{j=1, \dots, M} \sum_n f_{kj;n} \xi_j (1 + i\alpha_j) N_n E_j(t) e^{i\omega_{jk}t}; \quad (1)$$

$$\frac{dN_n}{dt} = \Delta J_n - \frac{N_n}{T_n} - \text{Re} \left\{ \sum_{jk} g_j f_{jk;n} E_j^* E_k e^{i\omega_{jk}t} \right\} - \text{Re} \left\{ \sum_{jkm} \xi_j (1 + i\alpha_j) f_{jk;nm} N_m E_j^* E_k e^{i\omega_{jk}t} \right\}, \quad (2)$$

for $j, k=1, \dots, M$ and $m, n=0, 1, 2, \dots$ and where the meaning of the symbols is summarized in Table 1. Using sine functions as the spatial profiles the longitudinal modes and expanding the population inversion in cosine functions, the f-coefficients are given by:

$$f_{jk;0} = \delta_{jk}; \quad f_{jk;0m} = f_{jk;m0} = f_{jk;m}, \quad (\forall m); \quad f_{jk;m} = \frac{1}{\sqrt{2}} [\delta_{m,|k-j|} - \delta_{m,k+j}], \quad (m \geq 1);$$

$$f_{jk;nm} = \frac{1}{2} [\delta_{|j-k|,|n-m|} + \delta_{|j-k|,n+m} - \delta_{j+k,n+m} - \delta_{j+k,|n-m|}], \quad (n, m \geq 1).$$

The formation of inversion gratings (described by the moments N_m) is regulated by the spatial diffusion of carriers in the semiconductor medium. For this reason, the diffusion of carriers has to be considered in the dynamics of multimode semiconductor lasers. The grating formation is responsible for such effects as the gain asymmetry which favours longer wavelengths over shorter ones (in case of a positive alpha parameter and the other way around for negative alpha).

Table. 1 Explanation and meaning of the various symbols in (1) and (2)

	Unit	Name	Value in Figs.1 and 2
E_k	1	Field amplitude (complex) for mode k	
N_0	1	Overall population inversion w.r.t. lasing threshold	
N_m	1	m-th population inversion moment	
k, j	1	Mode number	1, 2, 3
m, n	1	Inversion-moment number	0, 1, 2
α_k	1	Linewidth parameter for mode k	3
Γ_k	1/s	Cavity loss rate for mode k	1 ps^{-1}
g_k	1/s	Linear gain for mode k	$g_1 = 0.9996 \text{ ps}^{-1}, g_2 = 0.9999 \text{ ps}^{-1}, g_3 = 1.0 \text{ ps}^{-1}$
ξ_k	1/s	Differential gain coefficient for mode k	5000 s^{-1}
$f_{kj;n}$	1	Coupling coefficient of modes k and j via n-th moment	see (3)
$f_{kj;nm}$	1	Coupling coefficient of moments n and m via modes j and k	see (3)
$\omega_{jk} \equiv \omega_j - \omega_k$	Rad/s	Angular mode-frequency difference	$\Delta\omega = 2\pi * 12 \text{ GHz}$
ω_k	Rad/s	Optical angular frequency of mode k	$\omega_3 > \omega_2 > \omega_1$
ΔJ_k	1/s	k-th injection-current moment w.r.t. threshold current	$\Delta J_0 = 1.0 \cdot 10^{17} \text{ s}^{-1}$
T_m	s	lifetime for moment m	1 ns

Numerical Results

An interesting consequence of mode-mode interaction through grating formation is illustrated in Fig.1. Two modes are considered with mode spacing 80 GHz and equal losses. In the absence of hole-burning, i.e. no induced carrier grating ($N_1=0$), the system would be indifferent as to which mode will be excited: the total laser power will be distributed over the two modes

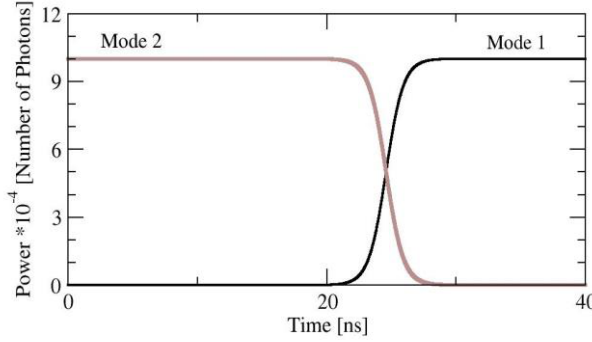


FIG. 1: Transition of lasing mode due to modal interaction: the frequency spacing between the two modes is taken as 80GHz. The system is prepared in the short wavelength mode and gradually evolves to the long-wavelength mode, because of the Bogatov effect (see text below). The time is measured in nanoseconds and the power is given in number of photons. Parameters are as in Table 1. The laser is pumped twice above threshold.

determined by initial conditions. When the carrier grating is taken into account ($N_1=0$), the system becomes bi-stable, meaning that either one of the modes can be lasing, the other being off. However, only one of the modes is stable and for positive α this will be the long-wavelength mode. This effect, named Bogatov effect [4], is also responsible for the asymmetric side-mode suppression observed in multi-mode semiconductor lasers. It is also sometimes referred to as a four-wave mixing process. The qualitative explanation for this phenomenon is that if two modes are lasing simultaneously, their fields create an oscillating grating in the inversion (N_1). This grating causes the waves in each mode to be scattered into the other mode thus creating additional gain or loss in that other mode.

Fig.2 shows the simulation result for a 3-mode laser with mode spacing 12 GHz. The modes have slightly different linear gains as indicated in Table 1. Once there is power in mode 3 (dashed line in Fig. 2), it automatically feeds the other modes through the effective dynamical (Bogatov) gain effect (see the above-given discussion). The reddest mode (1) takes the most advantage of this gain as it is most favored by the dynamical gain and starts building up power. This decreases the amount of gain available for operation in mode 3. While the power builds up in mode 1, mode 2 experiences two effects, i.e. suppression by mode 1 and enhancement by mode 3. Apparently, mode 2 survives only during the short time interval, where mode 1 is decreasing under influence of its higher loss and mode 3 is recovering. As soon mode 1 starts to grow, it effectively suppresses mode 2. This cycle then repeats itself. We note in Fig.2 that the relaxation oscillation (~ 3.8 GHz) plays an important intermingling role in the above-described scenario and that the slow dynamics-induced oscillation corresponds to ~ 760 MHz, which seems to define a period-5 limit cycle.

Another interesting aspect of these dynamics becomes evident once we look at the optical spectra in Fig.3 for the same case as Fig.2. Each mode contains spectral components of itself and other modes. Interestingly, dynamics at the frequency of the middle mode (mode 2) have been fully suppressed as can be concluded from the absence of any substantial spectral content at ~ 12 GHz. Clearly, mode 2 is only driven by the injection fields of the side modes and generates no frequency content at its “own” frequency. Mode 2 is used rather as ‘stepping stone’ while the energy bounces between mode 1 and mode 3. Although there are three active (spatial) modes inside the laser, a diffraction-grating-resolved spectrum taken from the laser output would show only two dominant frequencies separated by ~ 24 GHz (and higher harmonics).

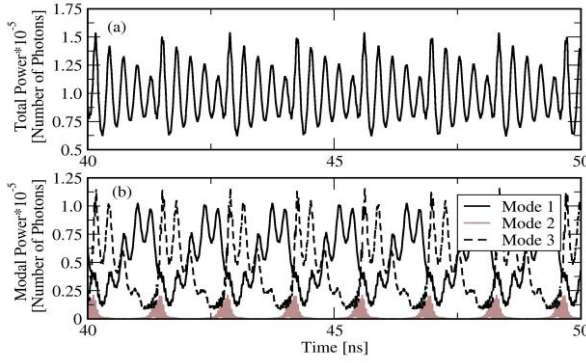


Fig.2 Sequential on-off switching of modes in the mode-resolved time series. (a) shows the total photon number and (b) the power of the individual modes. The parameters are as in the table. The mode spacing is $\Delta\omega = 2\pi * 12$ GHz. Note the period-5 dynamics.

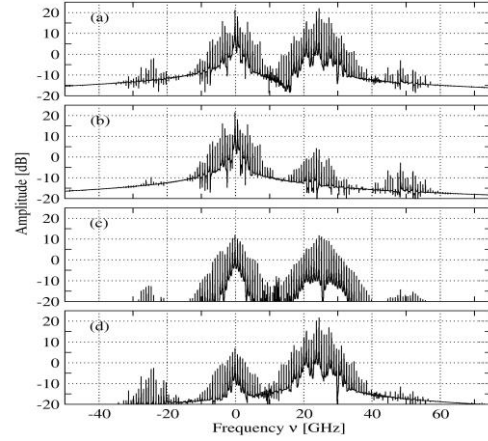


Fig.3 Optical spectra of the dynamics depicted in Fig.2. Plot (a) shows the spectrum of the total field $\Sigma E_j(t)e^{i\omega_j t}$, plots (b), (c) and (d) show modes 1, 2 and 3, respectively. The relaxation oscillation is ~ 3.6 GHz and the ~ 720 MHz peak fine structure corresponds to the period-5 oscillation in Fig.2 and is caused by the system dynamics and mode competition. Note that each mode contains spectral components of itself and other modes.

Conclusion

A new rate-equation model for a multi-mode semiconductor laser has been developed and shown to be applicable to two and three-mode lasers. For a positive value of the α -parameter, side modes with longer wavelengths compared to the dominant mode will be amplified, whereas side modes with shorter wavelengths will be suppressed (Bogotov effect).

The simulated spectrum shows that a straight correspondence between modes and externally observed spectral peaks is not possible due to the parametric interactions. The spectral contents belonging to one mode shows aspects of other modes as well. An observation of the output field will not provide full information on each modal amplitude inside the laser. This is clearly visible in the spectrum shown in Fig. 3.

References

- [1] M. Homar, S. Balle and M. San Miguel, Opt. Commun. 131, 380 (1996);
- [2] C. Serrat and C. Masoller, Phys.Rev.A73, 043812 (2006);
- [3] M. Yamada, J. Appl. Phys. 66(1), 81-89 (1989)
- [4] A. P. Bogatov, P. G. Eliseev, and B. N. Sverdlov, IEEE Journal of Quantum Electronics, QE-11, pp 510–515 (1975)
- [5] A.M. Yacomotti, L. Furfaro, X. Hachair, F. Pedaci, M. Giudici, J. Javaloyes, S. Balle, E. A. Viktorov and P. Mandel, Phys. Rev. A 69, pp. 053816 (2004);
- [6] M. Ahmed and M. Yamada, IEEE J. Quantum Electron. QE-38, pp.682-693(2002)

Monolithic Integration of a InP Nano-laser on (001) Si Substrate

Z. Wang,¹ B. Tian,¹ M. Paladugu,² M. Pantouvaki,² C. Merckling,² W. Guo,² J. Dekoster,² J. Van Campenhout,² and D. Van Thourhout¹

¹ Ghent University, INTEC, Sint-Pietersnieuwstraat 41, 9000 Gent, Belgium

² IMEC, Kapeldreef 75, 3001 Heverlee, Belgium

A unique epitaxy process has been developed to grow high quality InP nanowires on (001) Si substrates. By optical pumping, room temperature lasing has been successfully achieved and a large spontaneous emission factor is obtained, indicating strong confinement of the optical mode in the cavity.

Introduction

As the microelectronics manufacturers keep shrinking transistor sizes and manage to integrate more and more devices on a single chip, the bottleneck that limits the overall system performance becomes the conventional copper based interconnects. In the meantime, optical interconnect is attracting more and more attention, and the evolution of the underlying technology strongly supports the anticipation that optical interconnects will become a competitive solution for overcoming the intra- and inter chip communication bottleneck [1, 2]. As the key component for an optical communication system, however, a high performance on-chip laser source is still missing. Different approaches are being actively explored across the world. For instance, extensive work is being carried out nowadays to engineer silicon or germanium for optical gain generation [3, 4]. Nevertheless, III-V materials are still the best option, considering their superior performance and the technology that has been developed for decades. Wafer bonding based integration techniques were proposed for III-V on silicon integration and resulted in considerable success over the last decade [5, 6]. On the other hand, although the more appealing monolithic approach is challenging for implementation, considerable progress has recently been made.

Among various solutions, localized epitaxial approaches, e.g. the growth of III-V nanowires on silicon, have shown remarkable progress [7, 8]. However, most of the demonstrated growth processes were carried out on a (111) silicon surface, making it not compatible with the advanced complementary metal-oxide-semiconductor (CMOS) infrastructure. In addition, due to the limited dislocation-free lateral dimensions of the III-V nanowires grown on silicon, the integration approach normally utilized is to grow relatively wide III-V nanowires on a III-V wafer as the first step, and then a complex cleavage and transfer process is employed to integrate the Fabry-Perot nanowire cavity on a silicon wafer [9, 10]. A more controllable growth scheme is needed to increase the low yield and high cost associated with the approach mentioned above. In this work, a new approach is proposed for growing relatively thick InP nanowires on a pre-defined (001) silicon substrate. Without any complex post-processing, InP nano-lasers are successfully integrated on silicon by using a metal-organic chemical vapor deposition process (MOCVD). Under pulsed optical pumping, low threshold room-temperature laser operation is successfully achieved.

Experimental

Different from the recently demonstrated InGaAs laser on silicon, whereby the growth was preceded by a surface roughening process [11], we start the epitaxy selectively within 100 nm diameter sized circular openings that were defined in a 350 nm thick SiO₂ mask on a (001) silicon substrate. The definition of these SiO₂ patterns was carried out in a standard CMOS fab, using a modified shallow trench isolation process (STI) [12]. A schematic of the process flow of the epitaxial growth can be found in Fig. 1(a).

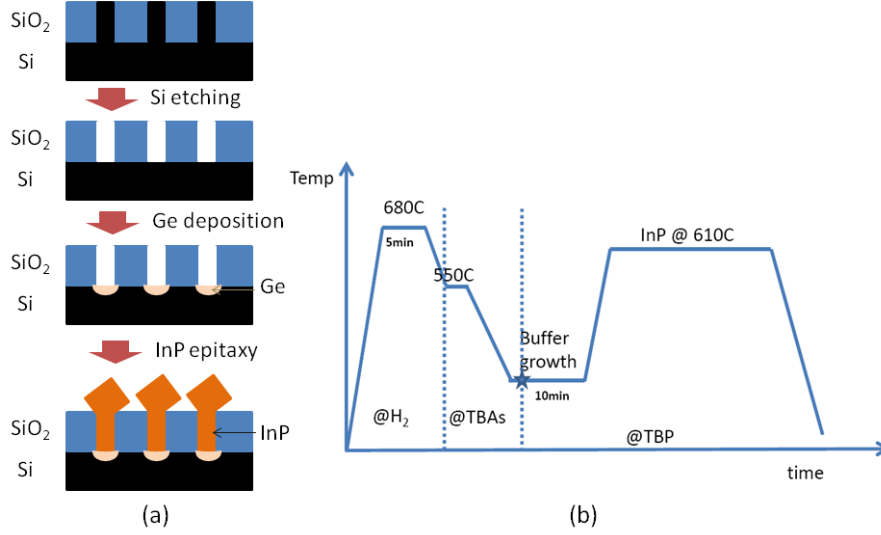


Figure 1. (a) Process flow for the InP MOCVD growth on the STI templates and (b) the growth thermal cycle for InP growth.

After etching the silicon channels by HCl at high temperature (600°C) in a CVD reactor, a thin Ge seed layer is deposited. The Ge layer is used to reduce the lattice mismatch between silicon and InP, while after a subsequent high temperature (680 °C) annealing in a H₂ flow, the Ge surface will form appropriate steps for better InP nucleation, reducing the generation of anti phase boundaries (APBs)[13]. As presented in Fig. 1(b), in the next step, the MOCVD reactor temperature is reduced to 380 °C and low flow rates Tertiarybutyl phosphine (TBP) and Trimethylindium (TMI) are introduced for the InP nucleation. After 10 minutes of InP growth, the reactant flow rates are increased while the temperature is increased to 610 °C, and the main part of the InP growth starts. By making the STI trenches narrow (aspect ratio > 2), all the dislocations that propagate from the lattice mismatched interface will be annihilated at the trench sidewalls, because dislocations normally glide along certain angles respect to the (001) surface [13].

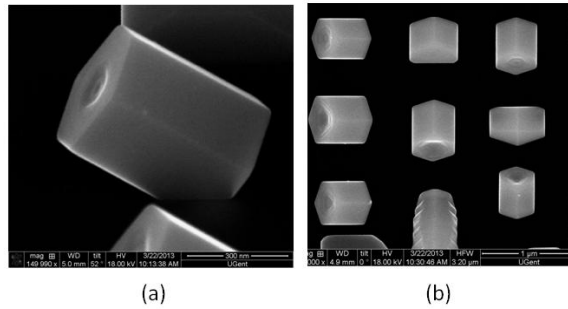


Figure 2. (a) A tilted scanning electron microscopy (SEM) view of a typical nano-laser cavity and (b) a top view of the nanowire array grown on (001) silicon substrate

In such a way, dislocation-free InP is obtained at the top part of the STI trenches, and the subsequent growth is carried out on this virtual lattice matched substrate. In the later epitaxial growth above the SiO₂ mask surface, nanowires with a diameter of about 400 nm are formed. A typical scanning electron microscopy (SEM) image of an InP nanowire on silicon can be found in Fig. 2(a). Similar to most of the works reported in literature, the obtained nanowire is oriented along the $\langle 111 \rangle$ axis, with a hexagonal cross-section. In Fig. 2(b), we also present a SEM image of the sample surface in a larger scale to show the yield of the epitaxial growth. Nanowires are found to be oriented along four equivalent $\langle 111 \rangle$ directions. Due to the close distance between the pre-defined SiO₂ holes, failure to grow a certain nanowire affects the surrounding nanowires, resulting in different growth dimensions. This is mainly due to the loading effect of the epitaxial growth and it provides a way to control the wavelength of the nanowire laser, i.e. by controlling the nanowire dimensions through the careful design of the surrounding mask.

Characterization Results

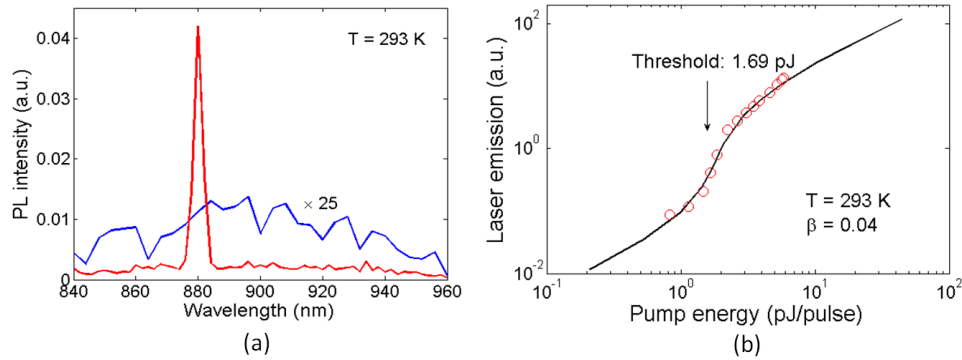


Figure 3. (a) PL emission spectrums recorded below (blue) and above (red) the threshold. (b) Light in – Light out curve of a nano-laser (open circles are measured results, and solid curve is the rate equation fitting)

Using a micro-PL setup, room-temperature lasing behavior has been achieved from these InP/Si nanowire cavities. A Nd:YAG nanosecond pulsed laser (Ekspla, 532 nm, repetition rate 321 Hz) was used as the pump source, and the collected PL signal was detected through a ¼ m monochromator (MS257, Newport) by a TE-cooled silicon detector. The signal-to-noise ratio was improved by using a lock-in amplifier.

A typical laser emission spectrum from a signal nanowire cavity can be found in Fig. 3(a). The PL spectrum below threshold (magnified by a factor of 25) is also plot as a reference. As one can see, by increasing the pump intensity, a laser peak located around 880 nm can be clearly identified (see the red curve). The relatively wide linewidth, which is routinely found in literature for micro-cavity based lasers, is mainly due to the large spontaneous emission factor β . The spontaneous emission and stimulated emission rates are increased considerably so that the carrier distribution is largely distorted and extra noise is introduced [14, 15]. In Fig. 3(b), the collected PL emission of the lasing peak as a function of the input pump energy is presented on a logarithmic scale (red open circles). The clear transition proves the laser exhibits threshold behavior. A low threshold of 1.69 pJ is derived. By performing a standard rate equation fitting, a large β

of around 0.04 is extracted, which indicates that a large portion of the spontaneous emission is coupled into the lasing mode. It supports the hypothesis for the large linewidth discussed above.

Conclusion

In summary, a unique epitaxial scheme was developed and relatively thick InP nanowires with good material quality were successfully integrated on pre-defined (001) silicon substrates without any complex post-processing. Pulsed lasing from these nanowires has been obtained at room temperature with a low threshold. The demonstrated laser may find a role in the application field of on-chip optical interconnects.

References

- [1] G. Chen, H. Chen, M. Haurylau, N. A. Nelson, D. H. Albonese, P. M. Fauchet, and E. G. Friedman, "Predictions of CMOS compatible on-chip optical interconnect," *Integration, the VLSI Journal*, vol. 40, pp. 434-446, 2007.
- [2] D. A. B. Miller, "Device Requirements for Optical Interconnects to Silicon Chips," *Proceedings of the IEEE*, vol. 97, pp. 1166-1185, 2009.
- [3] L. Pavesi, L. Dal Negro, C. Mazzoleni, G. Franzo, and F. Priolo, "Optical gain in silicon nanocrystals," *Nature*, vol. 408, pp. 440-444, 2000.
- [4] H. Rong, R. Jones, A. Liu, O. Cohen, D. Hak, A. Fang, and M. Paniccia, "A continuous-wave Raman silicon laser," *Nature*, vol. 433, pp. 725-728, 2005.
- [5] A. W. Fang, H. Park, O. Cohen, R. Jones, M. J. Paniccia, and J. E. Bowers, "Electrically pumped hybrid AlGaInAs-silicon evanescent laser," *Opt. Express*, vol. 14, pp. 9203-9210, 2006.
- [6] J. Van Campenhout, P. Rojo Romeo, P. Regreny, C. Seassal, D. Van Thourhout, S. Verstuyft, L. Di Cioccio, J. M. Fedeli, C. Lagahe, and R. Baets, "Electrically pumped InP-based microdisk lasers integrated with a nanophotonic silicon-on-insulator waveguide circuit," *Opt. Express*, vol. 15, pp. 6744-6749, 2007.
- [7] W. Guo, M. Zhang, A. Banerjee, and P. Bhattacharya, "Catalyst-Free InGaIn/GaN Nanowire Light Emitting Diodes Grown on (001) Silicon by Molecular Beam Epitaxy," *Nano Letters*, vol. 10, pp. 3355-3359, 2010/09/08 2010.
- [8] K. Tomioka, T. Tanaka, S. Hara, K. Hiruma, and T. Fukui, "III-V Nanowires on Si Substrate: Selective-Area Growth and Device Applications," *Selected Topics in Quantum Electronics, IEEE Journal of*, vol. 17, pp. 1112-1129, 2011.
- [9] X. Duan, Y. Huang, R. Agarwal, and C. M. Lieber, "Single-nanowire electrically driven lasers," *Nature*, vol. 421, pp. 241-245, 2003.
- [10] S. Gradecak, F. Qian, Y. Li, H.-G. Park, and C. M. Lieber, "GaN nanowire lasers with low lasing thresholds," *Applied Physics Letters*, vol. 87, pp. 173111-3, 2005.
- [11] R. Chen, T.-T. D. Tran, K. W. Ng, W. S. Ko, L. C. Chuang, F. G. Sedgwick, and C. Chang-Hasnain, "Nanolasers grown on silicon," *Nat Photon*, vol. 5, pp. 170-175, 2011.
- [12] G. Wang, M. R. Leys, N. D. Nguyen, R. Loo, G. Brammertz, O. Richard, H. Bender, J. Dekoster, M. Meuris, M. M. Heyns, and M. Caymax, "Selective Area Growth of InP in Shallow-Trench-Isolated Structures on Off-Axis Si(001) Substrates," *Journal of The Electrochemical Society*, vol. 157, pp. H1023-H1028, November 1, 2010 2010.
- [13] G. Wang, M. R. Leys, R. Loo, O. Richard, H. Bender, N. Waldron, G. Brammertz, J. Dekoster, W. Wang, M. Seefeldt, M. Caymax, and M. M. Heyns, "Selective area growth of high quality InP on Si (001) substrates," *Applied Physics Letters*, vol. 97, pp. 121913-3, 2010.
- [14] U. Mohideen, R. E. Slusher, F. Jahnke, and S. W. Koch, "Semiconductor Microlaser Linewidths," *Physical Review Letters*, vol. 73, pp. 1785-1788, 1994.
- [15] S. Ates, C. Gies, S. M. Ulrich, J. Wiersig, S. Reitzenstein, A. Löffler, A. Forchel, F. Jahnke, and P. Michler, "Influence of the spontaneous optical emission factor β on the first-order coherence of a semiconductor microcavity laser," *Physical Review B*, vol. 78, p. 155319, 2008.

Progress report on on-wafer testing of Photonic Integrated Circuits (PICs)

E. Bitincka,¹ R. G. Broeke,² and M. K. Smit¹

¹COBRA Research Institute, Technische Universiteit Eindhoven, 5600MB Eindhoven, Netherlands

²Bright Photonics BV, Netherlands, ronald.broeke@brightphotonics.eu, www.brightphotonics.eu

The accurate characterization of photonic integrated circuits is time consuming and is influenced by the alignment tolerance. To overcome these problems we decided to characterize optical properties of the most important Basic Building Blocks (BBB) by means of electrical signals.

Introduction

Important progress has been made in developing a generic foundry approach [1]. With this approach a broad range of functionalities can be realized starting from a small set of Basic Building Blocks (BBBs). A BBB is a photonic component that implements a basic functionality like: optical amplification, modulation, power detection etc.

The foundry process is validated by measuring a few test cells containing the BBBs. If they perform according to specs the wafer is approved. To speed up the wafer validation we propose on-wafer probing of the BBBs by means of electrical signals. The use of electrical signals, to probe the integrated sources and detectors, eases the aligning requirements compared to the classical optical measurement. The most important BBBs selected for on-wafer characterization are: Straight Waveguides (SW), Phase Modulators (PM) and Semiconductor Optical Amplifiers (SOA).

Basic Building Block characterization

On-wafer characterization of the BBBs is applied to validate the Multi Project Wafer runs (MPW) [1]. Test structures presented in this paper were first introduced in [2].

- *Straight Waveguides (SW)*

Propagation loss is the main parameter that describes the SW performance. To measure it several test structures are proposed. Here we report on the Ring Resonator (RR) based test structure with a small footprint and promising in terms of accuracy as shown in Figure 1.

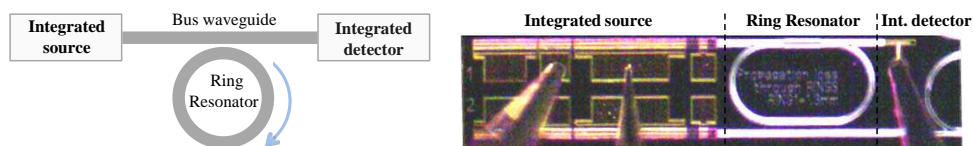


Figure 1 Schematic of the test structure for on-wafer characterization of propagation loss, composed of an integrated tunable Distributed Bragg Reflector (DBR) laser at the input, a ring resonator and an integrated full absorbing detector at the output (left) and a microscope objective picture of the fabricated device is shown (right).

The RR is very sensitive to waveguide loss therefore suitable for this purpose. As coupling element between the ring and the bus waveguide we have chosen the Multimode Interference (MMI) coupler for its tolerance to the fabrication process.

The power transmission at the output waveguide is obtained by a generalization of the RR equations in [3] that take into account the MMI coupling loss [4]:

$$|T|^2 = \alpha_{MMI}^2 \left[\frac{\tau^2 + t^2 - 2\tau t \cos \theta}{1 + \tau^2 t^2 - 2\tau t \cos \theta} \right]$$

Where t^2 is the power coupler coefficient which in the MMI we assume equal to $1/2$, τ^2 is the total loss factor that includes the MMI imaging loss (α_{MMI}^2) and the total ring propagation loss which includes also the MMI propagation loss (α^2), $\tau^2 = \alpha_{MMI}^2 \alpha^2$ as in [4] and θ is the round trip phase. The ratio between the maximum power transmission ($|T|_{\max}^2$) and the minimum power transmission ($|T|_{\min}^2$), obtained for $\cos \theta = 1$ and $\cos \theta = -1$ respectively, is called the Power Transmission Ratio (PTR)

$$PTR = \frac{|T|_{\max}^2}{|T|_{\min}^2} = \frac{(\tau - t)^2 (\tau t + 1)^2}{(\tau + t)^2 (\tau t - 1)^2}$$

The typical RR transmission measured at the integrated detector as a function of the tuning current is shown in Figure 2.

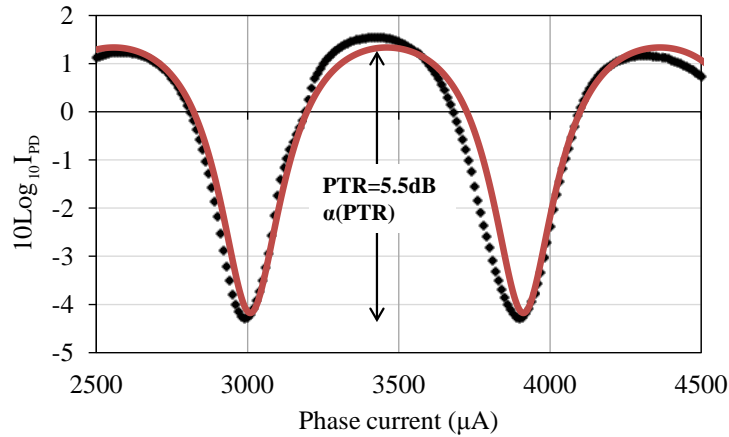


Figure 2 Measured (dotted black) and simulated (solid red) transmission of a 5.2mm long ring resonator. From the measured PTR the propagation loss is estimated. The phase current, applied at the phase section of the DBR laser, is used to fine tune its wavelength.

As MMI imaging loss the measured value of 0.7dB is used in the simulation. The propagation loss, estimated from the PTR of the transmission curve and the MMI imaging loss, is $\sim 15.0\text{dB/cm}$. We tested the structure on a waveguide with high losses and found from comparison between different structures an accuracy in the order of 10% of the propagation loss. Based on simulations we expect an absolute measurement accuracy of about 0.5dB/cm for low loss values.

-Phase Modulator (PM)

Phase modulation efficiency is the main parameter that describes the PM performance. To measure phase modulation on-wafer the test structure shown in Figure 3 has been tested.

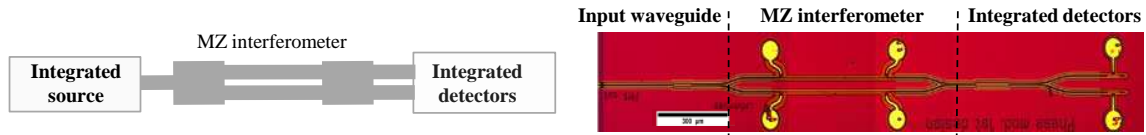


Figure 3 Schematic of the test structure for on-wafer characterization of phase modulation efficiency, composed of an integrated laser source at the input, a Mach-Zehnder interferometer and 2 integrated full absorbing detectors at the output (left) and a microscope objective picture of the fabricated device is shown (right).

The power splitter and combiner are a 1x2 and a 2x2 MMI coupler respectively. The device uses an external laser source. In the future run an integrated source will be present. The PM in the Mach-Zehnder (MZ) interferometer is 500μm long. The typical switching curves of a MZ interferometer when in one of the arms is injected current or applied a reverse bias are shown in the Figure 4 and agree well with measurement on non-integrated structures.

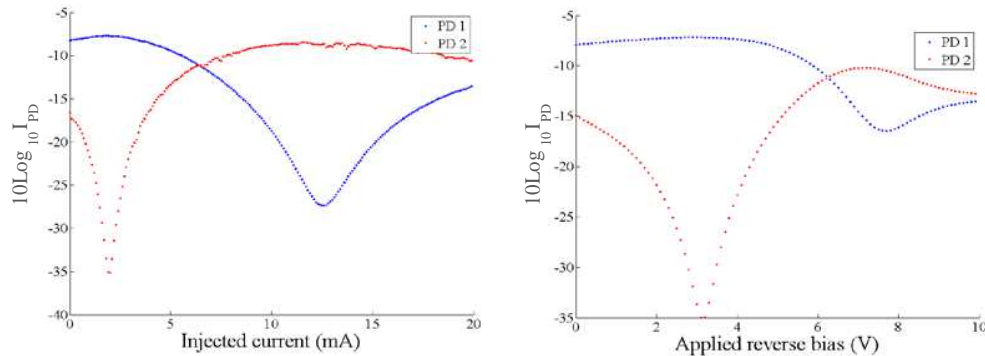


Figure 4 Mach-Zehnder interferometer switching curves when in one of the arms is applied a current (left) and a reverse bias (right). Due to the use of the 1x2MMI splitter at the input the switching curves maxima and minima do not start at 0 applied current or voltage.

-Semiconductor Optical Amplifier (SOA):

Modal gain is a major parameter that describes the SOA performance. To measure the SOA modal gain on-wafer the integrated test structure in Figure 5 is proposed.

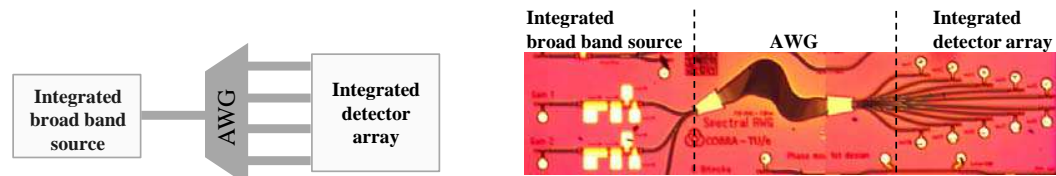


Figure 5 Schematic of the test structure for on-wafer characterization of SOA gain curves composed of a multisection SOA as a broad band source at the input, a large free spectral range arrayed waveguide grating and an array of integrated detectors at the output (left) and a microscope objective picture of the fabricated device is shown (right).

The integrated broad band source consists of SOAs of different length (50-50-100-200 μm). The large FSR AWG (120nm) is used to spectrally resolve the emission of the SOAs into the output PDs. The FSR is chosen large enough to cover most of the power emitted by the SOAs. By pumping a combination of these SOAs the Amplified Spontaneous Emission (ASE) spectra of 50-100-200-400 μm long SOA is measured, according to the Thomson measurement method [5].

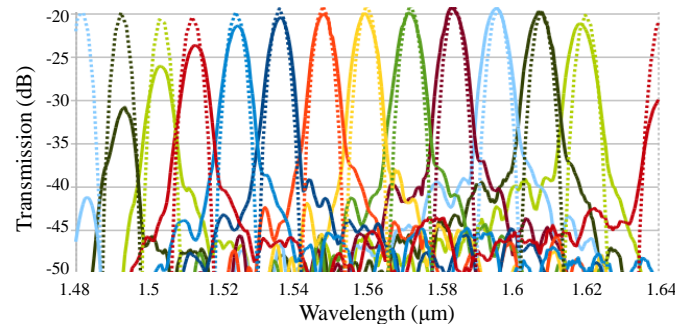


Figure 6 Simulated (dotted) vs. measured (solid) TE transmission spectra of the AWG used for on-wafer gain curves characterization. The output power is collected at the integrated detector array whereas at the input an external tunable source is used temporary.

The measured transmission of the large FSR AWG matches very well the simulated one. There is ongoing work to determine the SOA modal gain curves on-wafer.

Conclusions

In this paper an electrical on-wafer characterization approach is applied to characterize the fundamental BBBs as alternative to the classical optical method. It permits a faster and more accurate characterization of the BBBs thanks to the integration of light sources and detectors.

Acknowledgement

The research leading to these results has received funding from the European Community's Seventh Framework Program FP7/2007-2013 under grant agreement ICT 257210 PARADIGM. The authors acknowledge as well Bright Photonics for AWG design and simulation.

References

- [1] M. Smit, *et. al.*, "'Generic foundry model for InP based photonics'," *IET Optoe.*, pp. 187-194, 2011.
- [2] E. Bitincka, *et. al.*, "On-wafer testing of of Basic Building Blocks in Photonic Integrated Circuits (PICs)", *17th Annual Symposium of the IEEE Photonics Benelux Chapter*, 2012.
- [3] Yariv, A., "Universal relations for coupling of optical power between microresonators and dielectric waveguides", *Elec. Lett.*, 2000.
- [4] D.-X. Xu, S. Janz and P. Cheben, "Design of Polarization-Insensitive Ring Resonators in SOI Using Cladding stress Engineering and MMI Couplers", *Phot. Technol. Lett.*, 2006.
- [5] Thomson, *et. al.*, "Determination of single-pass optical gain and internal loss using a multisection device", *Appl. Phys. Lett.*, 1999.

Board-Level Single-mode Polymer Optical Waveguides

Ahmed Elmogi^{1,2,3}, Erwin Bosman¹, Sandeep Kalathimekkad¹, Nuria Teigell Beneitez¹, Rafik Guindi³, Jeroen Missinne¹, Geert Van Steenberge¹

¹Centre for Microsystems Technology (CMST), imec and Ghent University, Gent, Belgium

²KACST-Intel Consortium Center of Excellence in Nano-manufacturing Applications (CENA), Riyadh, Saudi Arabia

³Nano-electronics Integrated Systems Center (NISC), Nile University, Cairo, Egypt

In optical interconnects, there is an increasing discrepancy between current proposals for optical backplanes, which strongly focus on multimodal waveguides, and those for very high capacity transmitter and receiver modules being realized in silicon photonics, which focus on single mode transmission systems. In this paper we present a board-level single mode polymer optical waveguide technology which may merge these two worlds. First, the refractive indices of selected commercially available polymers have been measured, and used as an input for the design of the single-mode waveguides. Simulations are performed using an FDTD (finite-difference time domain) method (Lumerical). Depending on the core/cladding material combination, point-to-point square waveguide structures, with typical dimensions between $1 \times 1 \mu\text{m}^2$ and $5 \times 5 \mu\text{m}^2$, have been fabricated by laser direct imaging (LDI).

Introduction

Optical interconnects are being used for shorter and shorter distances, and the first (near) commercial demonstrations of optical transmission over the back plane of computing systems are starting to appear. However, there is an increasing discrepancy between current proposals for optical backplanes, which strongly focus on multimodal waveguides [1-2], and those for very high capacity transmitter and receiver modules being realized in silicon photonics, which focus on single mode transmission systems. Fabrication of single mode polymer waveguides on standard printed circuit boards (PCBs) is extremely challenging, as the waveguide patterning technology has to be compatible with large panels, being mechanically instable. Amongst all reported single mode waveguide technologies, laser direct imaging was selected as the most promising approach. This technique is mask-less which allows faster prototyping in contrast to conventional mask-based photolithographic approaches in which a mask first has to be designed and fabricated before waveguides can be produced. Hence, the waveguide core can be directly patterned according to the desired pattern. Moreover, this technique is capable of patterning high resolution features with long and linear dimensions over comparatively large planar areas.

The waveguide models were simulated based on a finite difference time domain (FDTD) method (Lumerical) to ensure the single mode operation at the telecom wavelengths. The graph in Figure 1 gives the relation between the maximum core size and the relative index difference between the core and cladding materials for single mode operation at a 1550 nm wavelength. For this simulation, the index of the cladding material was assumed to be 1.553, in agreement with the typical polymer cladding

materials being used. It is clear that for a certain index contrast there is a corresponding maximum core size for single mode operation and the higher this index contrast, the smaller the single-mode core size. In this work, LightLink™ (core) and DWL-Epo were used as the waveguide core materials, in combination with respectively LightLink™ (cladding) and ormocer as cladding materials. The refractive indices of the LightLink core and cladding at 1550 nm are 1.506 and 1.481 respectively. But, the refractive index of the DWL-Epo material is estimated to be 1.556 at 1550 nm and the refractive index of ormocer material is 1.5375 at the same wavelength. Therefore, the maximum single-mode core sizes for the DWL-Epo and LightLink waveguides are about 4 μm and 3.8 μm respectively. The LDI design is developed based on the simulations results.

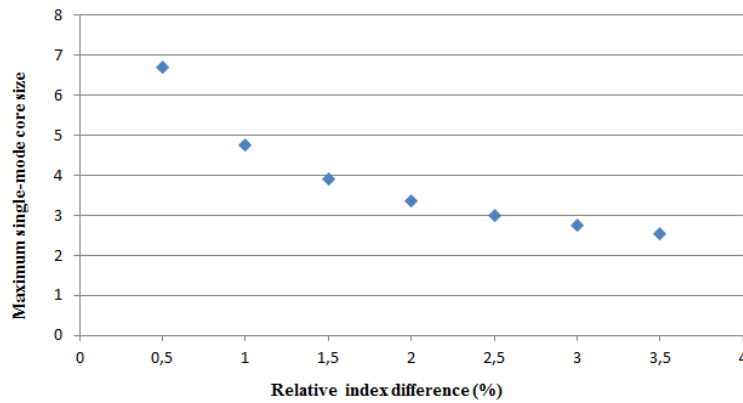


Figure 1: The maximum single-mode core size vs. the relative index difference

Waveguide Fabrication

The waveguide process flow is illustrated in Figure 2. Before depositing the waveguide layers, the FR4 substrate is cleaned by rinsing in acetone, then in a mix of acetone & IPA and then in DI water (2 minutes in each bath) and dried for 20 minutes on a hotplate at 120 °C. The optical materials are then deposited by means of spin coating and subsequently soft baked on a hotplate. Table 1 gives a detailed overview of the waveguide processing parameters for the two different core materials.

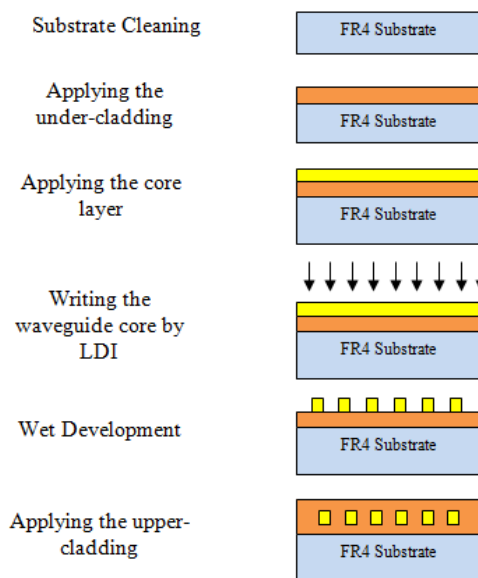


Figure 2: The process flow of the waveguide fabrication using Laser direct Imaging (LDI)

Table 1: The waveguide processing parameters

Process Step	LightLink cladding	LightLink core	DWL-Epo core	Ormocer (ormocore)
Soft bake	15 minutes @ 90 °C	30 minutes @ 90 °C	2 minutes @ 50 °C then 4 minutes @ 90 °C	4 minutes @ 80 °C
UV exposure	2 minutes (flood exposure) at 10 mwatt/cm ² lamp intensity	LDI processing	LDI processing	2 minutes (flood exposure)) at 10 mwatt/cm ² lamp intensity
Post exposure bake (PEB)	10 minutes @ 90 °C	10 minutes @ 90 °C	3 minutes @ 50 °C then 5 minutes @ 90 °C	2 minutes @ 80 °C
Development		20 seconds in LightLink XP-3636 developer then DI rinse	1 minute in mr-Dev 600 then 1 minute in IPA	
Hard bake	90 minutes @ 150 °C	90 minutes @ 150 °C	15 minutes @ 120 °C	90 minutes @ 150 °C

The laser imaging process was optimized by writing waveguides at different intensities and defocusing values so that the parameters, at which the waveguide width matches the design itself, can be determined. Figure 3 shows the effect of the laser intensity on the waveguide width for the two different materials. When the nominally 5 μm -wide waveguide in the design was taken as a reference and the laser power equals 150 mW, it was found that the points, at which the intensity equals 239 mJ/cm² and 537 mJ/cm² are the optimum doses that match the 5 μm width for the LightLink and the DWL-Epo materials respectively.

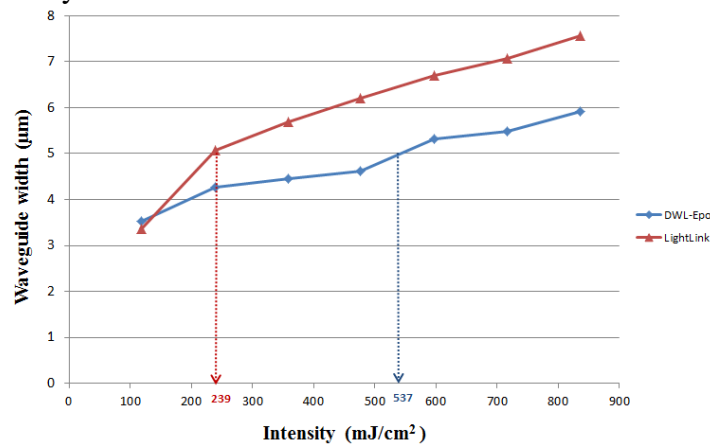


Figure 3: The relation between the laser intensity and the waveguide width

Scanning electron microscope (SEM) images of DWL-Epo patterned core of 3 μm thickness and width ranging from 1 to 5 μm are shown in Figure 4. Furthermore, cross section views of other waveguides arrays of the LightLink and the DWL-Epo on an FR4 substrate are shown in Figure 5. These waveguides are written using the laser parameters determined in Figure 3 in order to precisely match the waveguide dimensions. Optical profiler measurements (using Wyko NT3300) show the surface corrugation of the fabricated waveguides as introduced in Figure 6. Cut-back measurements are currently on-going in order to determine the propagation losses.

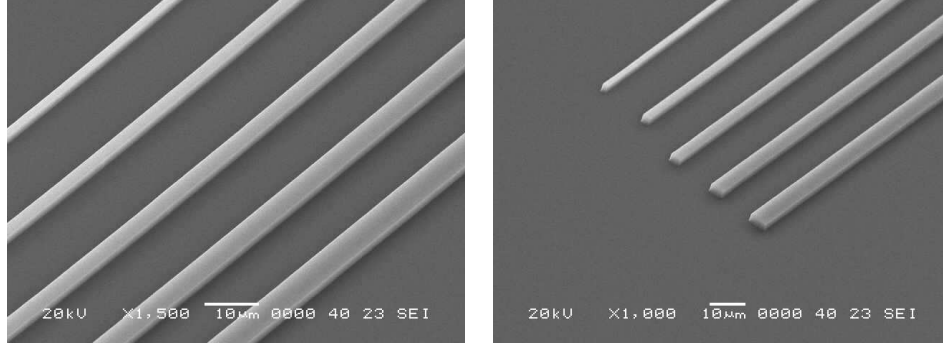


Figure 4: SEM images of the patterned DWL-Epo core layer

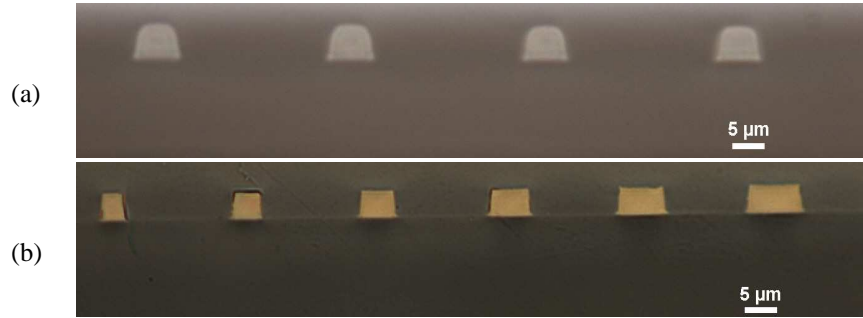


Figure 5: Cross section view of waveguides array (a) LightLink waveguides (b) DWL-Epo waveguides

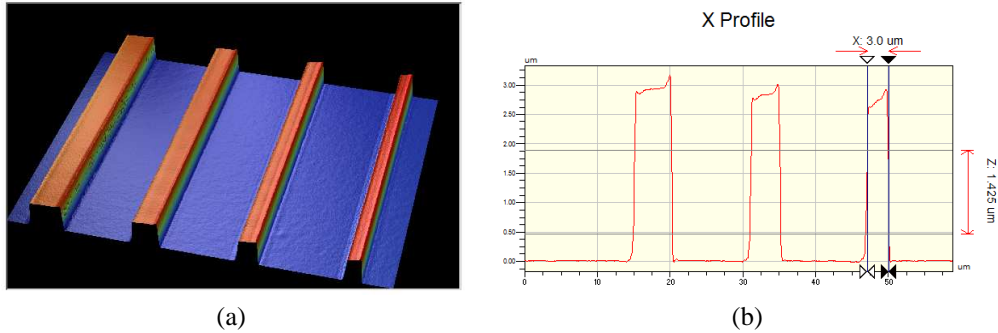


Figure 6: Surface corrugation of waveguides array (a) 3D view of the fabricated waveguides (b) the 2D view of waveguides array of 3 µm thickness and width ranging from 3 to 5 µm

Conclusion

In this paper, we have presented board level single-mode polymer waveguides fabricated by the laser direct imaging (LDI) technique. This technique is cost-effective and provides faster prototyping and fabrication of high resolution structures. The waveguides have been first simulated using an FDTD method. Then, square waveguides with dimensions of about 1 to 5 µm have been fabricated using LDI.

References

- [1] G. Van Steenberge, P. Geerinck, S. Van Put, J. Van Koetsem, H. Ottevaere, D. Morlion, H. Thienpont, P. Van Daele, "MT-compatible laser-ablated interconnections for optical printed circuit boards", *Journal of Lightwave Technology* (special issue on optical interconnects), Vol. 22, No. 9, pp. 2083-2090, SEP (2004).
- [2] B. Swatoski, C. Amb, S. Breed, D. Deshazer, W. Ken Weidner, R. Dangel, N. Meier, and B. Offrein, "Flexible, stable, and easily processable optical silicones for low loss polymer waveguides," *Proc. SPIE* 8622, 8622–8624 (2013).

SOI and InP based on-chip 3x3 interferometers for wavelength interrogation

S. M. C. Abdulla, B. M. de Boer, J. M. Pozo, D. M. R. Lo Cascio, P. J. Harmsma

TNO, Stieltjesweg 1, 2628 CK Delft, The Netherlands

We have successfully designed and characterized compact three-port interferometers on chip for accurate wavelength tracking. These interferometers are ideal candidates for on-chip read-out of photonic sensors such as ring resonators. On-chip implementation offers the advantage of low cost, high mechanical stability and accurate optical path length difference. We have realized devices in both Silicon-On-Insulator (SOI) and Indium Phosphide (InP) technology.

Keywords: On-chip interrogator, photonic sensor, ring resonator, 3x3 interferometer, ePIXfab, PARADIGM, multi-parameter sensing.

Introduction

Photonic multi-parameter sensing has attracted increased attention in recent years [1][2][3]. In particular, ring resonator (RR) based sensors are promising for gas sensing and bio sensing due to their high sensitivity to refractive index variations and their potential for multiplexing. In these applications, RRs are coated with a gas-selective coating or a layer of antibodies. The presence of the target gas or the bio-counterpart, respectively, causes a detectable shift of the resonance wavelengths. For bio sensing applications, the sensor is a single-use device which is read out by means of a stand-alone unit. For gas sensing, we propose to integrate the read-out unit with the sensor itself to obtain a small, robust, low-cost and accurate stand-alone system [1].

Sensor read-out concept

The concept is as shown in Figure 1. The wavelength of a narrow-band source is swept in time. The optical signal passes through an interferometer to enable time-to-wavelength calibration for each wavelength sweep. Using this calibration data, the transmission of the sensor vs. time is then translated to the wavelength response, from which the sensor read-out is obtained by means of a microprocessor. This concept enables the use of a low-cost laser, such as a Vertical Cavity Surface Emitting Laser (VCSEL), the wavelength of which is swept by sweeping the drive current [4]. The sweep-specific wavelength calibration provides a high-accuracy sensor read-out.

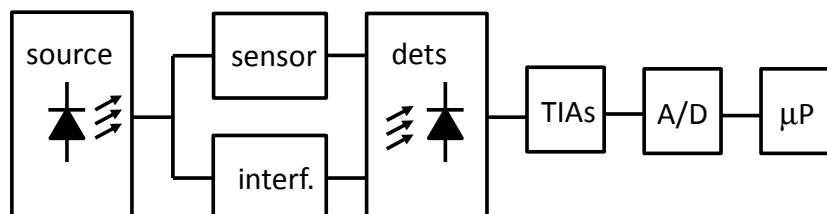


Figure 1. Sensor and read-out unit. Sensor, interferometer and detectors can be integrated on a single SOI chip, in InP technology also the source can be integrated.

3-Port interferometer

We propose to use a 3-port interferometer (Figure 2) which has three outputs at a 120° mutual phase difference, for the following reasons:

1. At any input wavelength, at least one output has considerable amplitude and derivative with respect to wavelength.
2. The combined outputs enable unambiguous tracking over wavelength spans larger than the Free Spectral Range (FSR). In comparison, a 2-port interferometer has two 180° out-of-phase outputs, and the sign of change is unknown at the boundaries of one FSR range, where the output derivatives to wavelength are zero.
3. It is insensitive to the modulation depth of the interference.

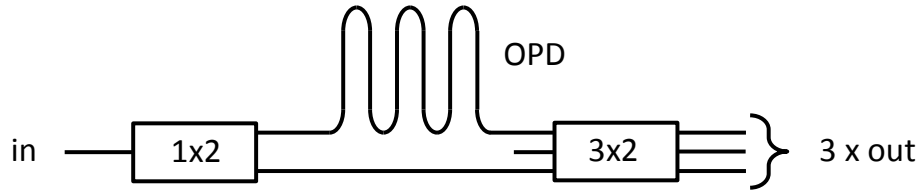


Figure 2. 3-port interferometer consisting of two splitters/combiners and an Optical Path length Difference (OPD). Note that one input of the 3x3 splitter/combiner is not used.

Interferometer in Silicon On Insulator

We realized the test circuit shown in Figure 3. It was fabricated at IMEC using the multi-project wafer run service of the Silicon Photonics platform ePIXfab [5]. The laser input (connected either from the top coupler, or from the left port on the bottom) is distributed over 6 ring resonators and a 3-port interferometer. The tested device has a $2\mu\text{m}$ oxide cladding.

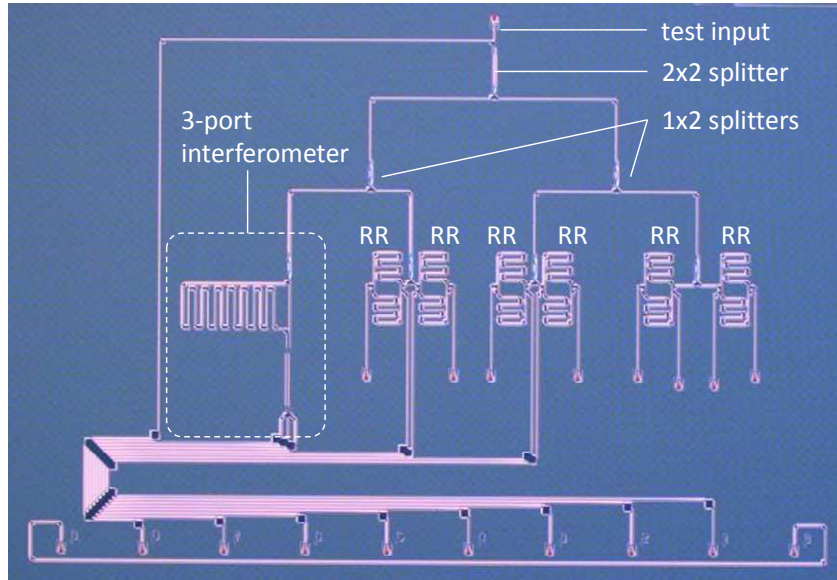


Figure 3. Microscope image of a test circuit consisting of a 3-port interferometer and 6 ring resonators. The grating couplers are arranged at a $250\mu\text{m}$ pitch to enable standardized fiber array coupling. The 8 inputs connect to (from left to right) the circuit input, three interferometer outputs, and 4 ring ‘through’ ports.

The top left graph of Figure 4 shows the normalized response of all three interferometer ports. The expected 120° shift between the channels can be observed. We notice some amplitude variations which are not the same for each channel, possibly caused by inter-interferometer reflections. To correct for this we applied the following procedure for each channel individually:

1. Locate the local minima and maxima
2. Obtain the lower and higher amplitude envelopes by linear interpolation between all minima and maxima, respectively.
3. Correct the data by these envelopes (subtraction and division) to obtain signals between zero and unity.

From this corrected data (Figure 4, top right) we calculate the phase using [3]:

$$\tan(2\pi n \frac{\Delta L}{\lambda}) = -\sqrt{3} \frac{I_3 - I_1}{2I_2 - I_3 - I_1}$$

where I_k is the output of channel k , $n\Delta L$ is the optical path length difference, and λ is the wavelength. The result is nearly a straight line (Figure 4, lower left) with deviations less than 1% of the interferometer FSR (Figure 4, lower right).

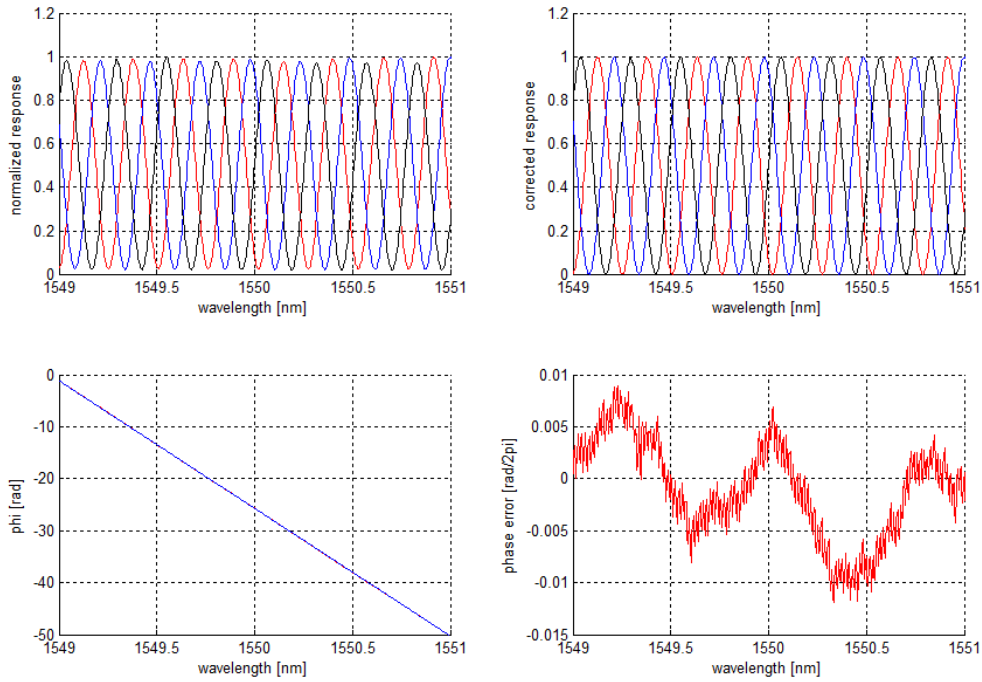


Figure 4. Response of the SOI interferometer. Upper left: normalized data; upper right: corrected data (see text); lower left: phase vs. wavelength and lower right: phase error.

It should be mentioned that for large wavelength spans the quadratic wavelength dependence of the interferometer FSR must be taken into account.

Interferometer in Indium Phosphide

We have also realized similar interferometers in InP active passive technology. Devices were fabricated at Oclaro in the framework of the PARADIGM program [8] (Figure 5). In spite of the high waveguide losses of this particular fabrication run, we obtained again the characteristic 3-port interferometer responses (Figure 6).

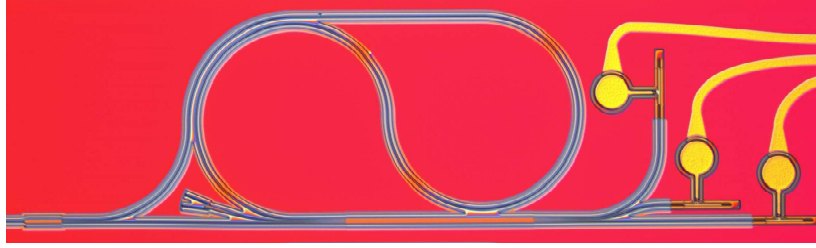


Figure 5. Microscope photograph of 3-port interferometer in InP, having integrated photo diodes.

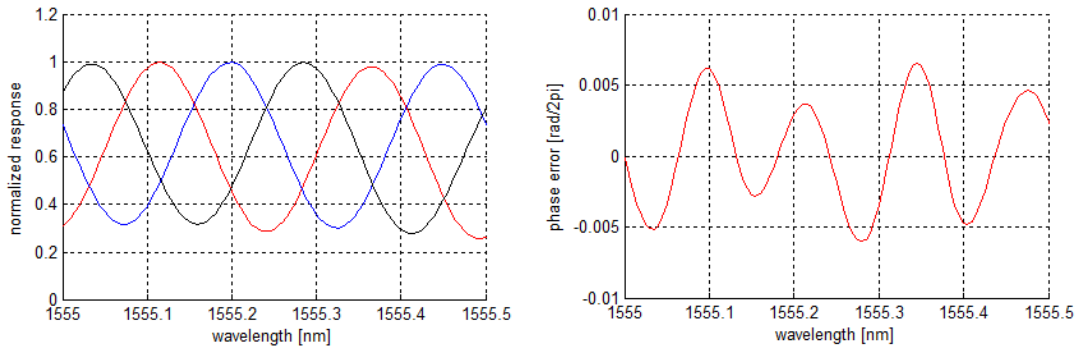


Figure 6. Response of the InP interferometer. Left: normalized data; right: phase error.

Conclusions

We have demonstrated on-chip 3-port interferometers for wavelength tracking, realized both in SOI and InP multi-project wafer services. These interferometers are key building blocks for low-cost on-chip read-out units, in particular for ring resonator based multi-parameter environmental sensors and for biosensors. The concept is robust, yielding 120° phase difference in the three output ports of the 3x3 splitter for both concepts, in spite of high fabrication-induced losses of the InP devices. The measured phase error was less than 1% of the free spectral range, which can be improved by suppressing unwanted reflections.

References

- [1] T. Claes, W. Bogaerts, P. Bienstman, “Vernier-cascade label-free biosensor with integrated arrayed waveguide grating for wavelength interrogation with low-cost broadband source”, *Optics Letters*, Vol. 36, No. 17, 2011, pp. 3320-3322.
- [2] P. Harmsma, J. Staats, D. Lo Cascio, L. Cheng, “Three-port interferometer in silicon-on-insulator for wavelength monitoring and displacement measurement”, *Lasers and Electro-Optics Europe (CLEO EUROPE/EQEC)*, 12th European Quantum Electronics Conference, Munich, May 2011.
- [3] J. Pozo, W. Westerveld, P. J. Harmsma, S. Yang, “Silicon on insulator photonic integrated sensors: On-chip sensing and interrogation”, 13th International Conference on Transparent Optical Networks (ICTON), pp. 1-4, Stockholm, June 2011.
- [4] R. Heideman, M. Hoekman, E. Schreuder, “TriPlex-Based Integrated Optical Ring Resonators for Lab-on-a-Chip Environmental Detection”, *IEEE JSTQE*, Vol. 18, No. 5, pp. 1583 – 1596, 2012.
- [5] <http://www.epixfab.eu/>
- [6] X. Leijtens, “JePPIX: the platform for Indium Phosphide-based photonics,” *IET Optoelectron*, Vol 5, No 5, pp. 202-206, 2011.
- [7] P. Dumon, W. Bogaerts, R. Baets, J. M. Fedeli, and L. Fulbert, “Towards foundry approach for silicon photonics: silicon photonics platform ePIXfab,” *Electron. Lett*, Vol 45(12), 581-582, 2009.
- [8] <http://paradigm.jeppix.eu/>

Localization and Quantification of Reflective Events along An Optical Fiber Using A Two-Wavelength TRA

Min Cen¹, Patrice M  gret¹, Jiajia Chen², V  ronique Moeyart¹ and Marc Wuilpart¹

¹ Universit   de Mons, Service d'Electromagn  tisme et de T  l  communications, Boulevard Dolez 31, 7000 Mons, Belgium

² KTH Royal Institute of Technology, Optical Networks Lab, Isafjordsgatan 22, 16440 Kista, Sweden

We propose a novel transmission-reflection analysis (TRA) method for detection and localization of any type of single event occurring along an optical fiber. By analysing the transmitted and reflected/backscattered power of continuous signals, it is possible to monitor the event and to simultaneously quantify its induced insertion and return losses. The proposed scheme utilizes two interrogating wavelengths, which allows the supervision of both reflective and non-reflective events. Our analytical studies have shown that for a 20 km-long single mode fiber, the accuracy of event localization is kept in the range of $\pm 1.0\text{m}$ by applying the proposed approach.

Introduction

Nowadays, optical time domain reflectometry (OTDR) and optical frequency domain reflectometry (OFDR) are widely used schemes for fiber monitoring. However, OTDR and OFDR require either time- or frequency-modulated light sources, which makes the methods not very cost-effective. Moreover, some breakthroughs are still required to address certain limitations, e.g., to address limitations on long measurement time (several minutes are normally needed for monitoring a fiber with a length in tens of kilometers with OTDR [1]) and short measurement range (only a few hundred meters for OFDR [2]). In [3], a transmission-reflection analysis (TRA) method is reported, which is based on the measurement of transmitted and backscattered powers and using an un-modulated light source. This method was proposed for the detection and localization of a non-reflective optical event such as bending. However, most optical events in a fiber are reflective such as discontinuities, misalignments, and breaks that can be present in telecommunication networks. In sensing applications, some transducing processes also results in the presence of a reflective event along the sensing fiber [4].

In order to address the aforementioned problems, a novel solution is proposed to localize both non-reflective and reflective optical events by using a two-wavelength TRA (i.e., 2λ -TRA) technique in a single mode fiber.

Operation Principle

The schematic diagram of the proposed 2λ -TRA is shown in Figure 1. Continuous-wave light emitted by a light emitting diode (LED around λ_1) is launched into a single mode fiber through an optical circulator. An optical isolator is implemented to minimize the back reflections from the fiber end. The transmitted signal (P_{TI}) is measured by the powermeter located after the isolator. The integrated Rayleigh-backscattered/reflected power (P_{BI}) is measured by the second powermeter connected to the third end of the circulator. The same measurement is repeated a second time after changing the wavelength of the LED source (λ_2) in order to get the corresponding transmission and

backscattered powers (P_{B2} and P_{T2} respectively). The localization process of a reflective event is based on the unique relationship between the powers backscattered (P_{B1} and P_{B2}) and transmitted (P_{T1} and P_{T2}) for a given event location (see Figure 1).

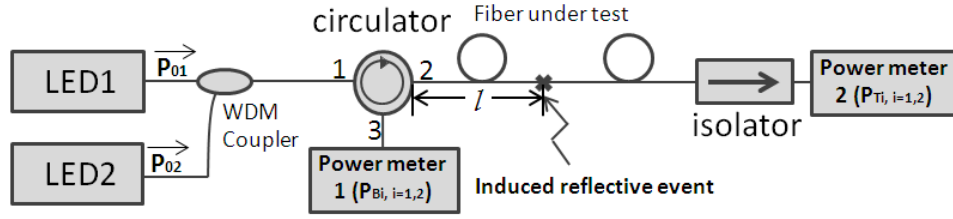


Figure 1: Schematic of the proposed 2λ -TRA technique

Let us consider a fiber with a total length L and an initial transmitted power of the reference undisturbed system:

$$\begin{aligned} P_{T01} &= P_{01} \cdot T_1(L) \\ P_{T02} &= P_{02} \cdot T_2(L) \end{aligned} \quad (1)$$

in which $P_{0i(2)}$ is the input power and $T(L)$ is the transmission coefficient associated with the attenuation coefficient α of the fiber, which can be expressed as: $T(\Delta L) = e^{-\alpha \Delta L}$. Since α changes with the wavelength, different interrogating wavelengths will lead to different $T(L)$. Taking into account the directivity of the circulator R_{DIR} and the reflection from the isolator R_{ISO} , the total backscattered/reflected power of the reference undisturbed system can be expressed as:

$$\begin{aligned} P_{B01} &= P_{01} \cdot [R_{DIR} + R_{ray1}(L) + T_1^2(L) \cdot R_{ISO}] \\ P_{B02} &= P_{02} \cdot [R_{DIR} + R_{ray2}(L) + T_2^2(L) \cdot R_{ISO}] \end{aligned} \quad (2)$$

in which $R_{ray1(2)}(L)$ is the Rayleigh backscattered power coefficient that can be expressed as: $R_{ray}(\Delta L) = S \left(\frac{\alpha_s}{2\alpha} \right) (1 - e^{-2\alpha \Delta L})$ [5]. α_s is the scattering coefficient of the Rayleigh scattering and is proportional to $1/\lambda^4$ [5], ΔL is the length of the fiber segment and S is a capture coefficient [5], which changes with the wavelength.

Let us consider that a reflective event with a return loss RL and insertion loss IL is introduced into the fiber at a distance of l ($l \leq L$), and here we suppose RL is not changed with wavelength (referring non-reflective event, RL is usually higher than 75dB, e.g. bending). The transmitted power P_{Tl} and the reflected power P_{Bl} with interrogating wavelength λ_1 can be expressed as:

$$P_{T1} = P_{T01} \cdot 10^{\left(-\frac{IL_1}{10}\right)} \quad (3)$$

$$P_{B1} = P_0 \cdot [R_{DIR} + R_{ray1}(l) + T_1^2(l) \cdot RL + [R_{ray1}(L) - R_{ray1}(l)] \cdot t_{n1}^2 + T_1^2(L) \cdot t_{n1}^2 \cdot R_{ISO}] \quad (4)$$

With the second interrogating wavelength λ_2 , P_{T2} and P_{B2} can be expressed as:

$$P_{T2} = P_{T02} \cdot 10^{\left(-\frac{IL_2}{10}\right)} \quad (5)$$

$$P_{B2} = P_0 \cdot [R_{DIR} + R_{ray2}(l) + T_2^2(l) \cdot RL + [R_{ray2}(L) - R_{ray2}(l)] \cdot t_{n2}^2 + T_2^2(L) \cdot t_{n2}^2 \cdot R_{ISO}] \quad (6)$$

With equation (1), (2) and (3), the normalized power reflection coefficient R_{n1} and R_{n2} can be written as:

$$R_{n1} = \frac{P_{B1}}{P_{B0}} = \frac{R_{DIR} + R_{ray1}(l) + T_1^2(l) \cdot RL + [R_{ray1}(L) - R_{ray1}(l)] \cdot t_{n1}^2 + T_1^2(L) \cdot t_{n1}^2 \cdot R_{ISO}}{R_{DIR} + R_{ray1}(L) + T_1^2(L) \cdot R_{ISO}} \quad (7)$$

$$R_{n2} = \frac{P_{B2}}{P_{B0}} = \frac{R_{DIR} + R_{ray2}(l) + T_2^2(l) \cdot RL + [R_{ray2}(L) - R_{ray2}(l)] \cdot t_{n2}^2 + T_2^2(L) \cdot t_{n2}^2 \cdot R_{ISO}}{R_{DIR} + R_{ray2}(L) + T_2^2(L) \cdot R_{ISO}} \quad (8)$$

where $t_{n1(2)}$ is the normalized power transmission coefficient, $P_{T1(2)}/P_{T01(2)}$, which is only dependent on the insertion loss of the event.

Since R_{DIR} , α , α_s , R_{ISO} , and L are known parameters, and P_{B1} , P_{B2} and P_{T1} , P_{T2} can be obtained by the measurements, the problem finally becomes solving a set of two equations with only two unknown variables (i.e., l and RL).

Localization Accuracy of the 2 λ -TRA Technique

In this section, analytical studies about the measurement accuracy of the proposed solution with different wavelength combinations are carried on. We take four commonly used wavelengths in our study, and made six different wavelength combinations. Parameters related to the calculation model are listed in Table 1[5].

Table 1: Parameters of four interrogating wavelengths

Interrogating wavelength λ (nm)	capture coefficient S	attenuation coefficient α (dB/km)	scattering coefficient α_s (dB/km)
λ_1 : 850	0.0013	2	1.9157
λ_2 : 1310	0.001	0.35	0.33
λ_3 : 1550	0.0012	0.2	0.1723
λ_4 : 1650	0.0012	0.23	0.135

The powermeter output uncertainty mainly affects the localization accuracy of the proposed 2 λ -TRA technique. Consequently, we introduce two measurement uncertainty coefficients ζ_1 and ζ_2 , which are maximum measurement errors of the two powermeters, respectively. According to our previous experiments, both ζ_1 and ζ_2 are equal to 0.001 (0.1 %, repeatability test). The measurements can be therefore positioned inside the ranges $P_B \pm P_B \zeta_1$ and $P_T \pm P_T \zeta_2$ (here P_T and P_B are the exact power values). Simulations taking into account a uniform distribution of the measured powers within the above-mentioned ranges were undertaken (1000 samples). The length of the fiber (L) in our simulation is varied from 0 to 100 km to cover different applications (e.g. for sensing applications L is usually less than a few hundreds of meters, while referring to the field of telecommunication, such as the next generation PON system, a 100-km fiber length is normally employed). Here we consider a reflective event with a 20 dB return loss, and an event location l equal to $L/4$. We will discuss about the standard deviation below.

In Figure 2, the relationship between the localization error and the length of the fiber link with different wavelength combinations are presented. According to this figure, when the fiber length is less than 25km, three combinations (i.e. $\lambda_1 + \lambda_2$, $\lambda_1 + \lambda_3$ and $\lambda_1 + \lambda_4$) give very good localization accuracies (less than 1m, while for OTDR measurement is usually around a few meters for a 10km-long fiber [1]). However, as the fiber length approaches over 35km, their localization errors show a rapid increase. Regarding the other three wavelength combinations (i.e. $\lambda_2 + \lambda_3$, $\lambda_2 + \lambda_4$ and $\lambda_3 + \lambda_4$), the localization error remains almost constant (e.g. around 15m for $\lambda_2 + \lambda_3$; more than 50 meters for OTDR measurement in a 100 km-long fiber [1]) as the fiber length increase, which

could be an acceptable performance in long reach applications (i.e. the fiber length is longer than 20km). Figure 3 shows the relationship between the measured return loss error and the fiber length. Compared with Figure 3, the return loss error shows a similar trend. When the fiber length is less than 25 km, the return loss measurement error is around 0.0005dB for the three wavelength combinations $\lambda_1 + \lambda_2$, $\lambda_1 + \lambda_3$ and $\lambda_1 + \lambda_4$. For the long reach cases, by using the wavelength combination of $\lambda_2 + \lambda_3$, a 0.01 dB error can be reached. From the discussion above, one can expect that by choosing different interrogating wavelengths, high measurement accuracy can be achieved for both short range and long reach applications (i.e. for short range applications, one can use $\lambda_1 + \lambda_2$ as the combination of interrogating wavelengths, while for the long reach cases, $\lambda_2 + \lambda_3$ can be utilized).

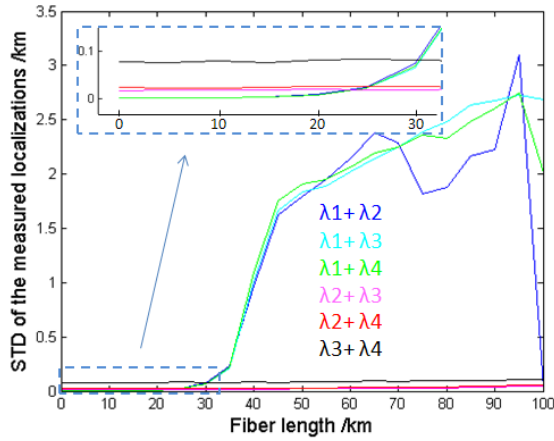


Figure 2: Analytical localization error with different interrogating wavelengths

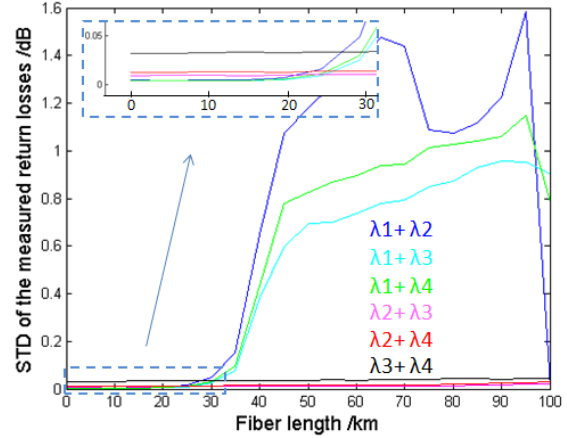


Figure 3: Analytical RL measurement error with different interrogating wavelengths

Conclusion

2 λ -TRA scheme is proposed to localize and quantify a single reflective event on a fiber link. Analytical results show that by appropriately selecting two interrogating wavelengths, the proposed solution is able to detect the location and value of the return loss with sufficient measurement accuracy (i.e. 1m, 5×10^{-3} dB for a 20km-long fiber and 0.01dB, 15m for a 100-km long fiber). The whole system is characterized by a simple structure and low cost, the monitoring of both short range (less than 1km) and long range (100 km) systems can also be processed in a fast manner (a few seconds) thanks to its simple measurement of power variations. Consequently, the proposed 2 λ -TRA solution provides a novel and simple solution for future distributed monitoring.

References

- [1] D. Derickson, Fiber Optic Test and Measurement, New Jersey: Prentice Hall PTR, ch. 11, pp. 444-445, 1997.
- [2] K. Yüksel, M. Wuilpart, and P. Mégret, "Analysis and suppression of nonlinear frequency modulation in an OFDR," Optics Express, vol. 17, no. 7, pp. 5845–5851, 2009.
- [3] V.V Spirin, M.G. Shlyagin, S.V. Miridonov and P.L. Swart, "Transmission/reflection analysis for distributed optical fiber loss sensor interrogation," Electronics Letters, vol. 38, 117-118, 2002.
- [4] A. Girard, "FTTx PON technology and testing", EXFO Electro-Optical Engineering Inc., 2005.
- [5] M.Wuilpart. Rayleigh scattering in optical fibers and applications to distributed measurements. EPFL Press / CRC, Ch. 8, pp. 1-2, 2011

Reduction of bend losses in polymer waveguides by thin metallic layers

M. A. Sefunc, A. Pace, M. Dijkstra, G. Sengo, S.M. García-Blanco, Member IEEE

Optical Sciences Group, MESA+ Institute for Nanotechnology, University of Twente
P.O. Box 217, 7500 AE Enschede, The Netherlands

Polymeric materials have attracted much attention in photonics due to low material costs and fabrication complexity. However, the low refractive index contrast in polymer waveguides leads to high propagation losses in sharp bends. In large-scale photonic integration, sharp bent waveguides-with radii of a few micrometers are essential to decreasing the footprint of photonic circuitry. In this work, embodying a thin metallic layer underneath the core of a sharp bent polymer waveguide is shown to considerably reduce bend losses both in TE and TM polarizations. The physical model that permits understanding these effects as well as early fabrication/characterization results will be discussed.

Introduction

In the last years, significant amount of effort has been devoted to polymeric materials for integrated optical devices due to several advantages including low cost, flexibility, ease of fabrication and processability[1][2]. However, one of the drawbacks of polymer based waveguides is the low refractive index contrast between core and cladding. This is the reason why a large radius of curvature of typically tens of micrometers is required for low-loss propagation in such waveguides. In this work, the introduction of a thin metallic layer underneath the core of a polymer bent waveguide is shown to reduce the calculated total losses (dB/90°) with respect to the equivalent pure dielectric counterpart (i.e., the architecture in which the metal layer is omitted) for a large range of bend radii. The amount of reduction is dependent on the polarization of the light in the waveguide structure. For the quasi-transverse-electric (TE) mode, the loss reduction is significant for radii below 35 μm . For this polarization, losses as low as ~ 0.02 dB/90° have been calculated for a wide range of radii that can be tuned by properly optimizing the structural parameters. In the case of the quasi-TM mode, the total losses of the metallic structure are smaller than those of the dielectric structure for radii ranging from 3 to 10 μm [3].

Investigated Structure

The schematic configurations of the waveguide geometries studied in this work are shown in Fig. 1. The proposed structure corresponds to a dielectric-loaded hybrid plasmonic waveguide consisting of a polymer ridge separated from the metal underneath by a thin dielectric layer. The wavelength of interest in this study is 1.55 μm . The material selected for the ridge is the negative tone epoxy resist, SU-8 ($n_{\text{SU-8}} = 1.57 + i \cdot 4.93 \times 10^{-6}$), although similar results apply to a wide range of architectures exhibiting low refractive index contrast between substrate and core. The material of the thin buffer layer is SiO_2 ($n_{\text{SiO}_2} = 1.444$). Gold ($n_{\text{Au}} = 0.55 + i \cdot 11.5$ [4]) was selected for the metallic layer. The substrate consists of silicon with a sufficiently thick layer of thermal SiO_2 . Figure 1(b) shows the cross-section of the entirely dielectric structure used as a benchmark. The dielectric-loaded hybrid plasmonic waveguide [Fig. 1(a)] will be referred to as “metallic” in the subsequent sections, whereas the dielectric polymer

waveguide [Fig. 1(b)] will be called “non-metallic”. The distance between the center of curvature and the outer rim of the waveguide defines the bend radius, R , as depicted in Fig. 1. Two-dimensional finite-difference (FD) calculations were carried out using the FieldDesigner module of Phoenix B.V. for bend mode analysis [5]. The fields were calculated in a sufficiently large calculation window ($10\ \mu\text{m} \times 10\ \mu\text{m}$) with extra mesh grids for mitigating numerical errors in the calculations. The total bend loss in a 90 degree bend of radius R can be calculated from the imaginary part of the effective refractive index of the mode as $\text{Total Loss (dB/90}^\circ) = 10 \log_{10}[\text{Im}(n_{\text{eff}})k_0 R \pi]$, where n_{eff} is the calculated complex effective refractive index of the mode of the bent waveguide, k_0 is the wavenumber in vacuum ($k_0 = 2\pi/\lambda$) and R is the bend radius. The calculated total loss includes both the propagation loss due to scattering and absorption in the metal and SU-8 material and the radiation loss due to the waveguide curvature (i.e., bend losses).

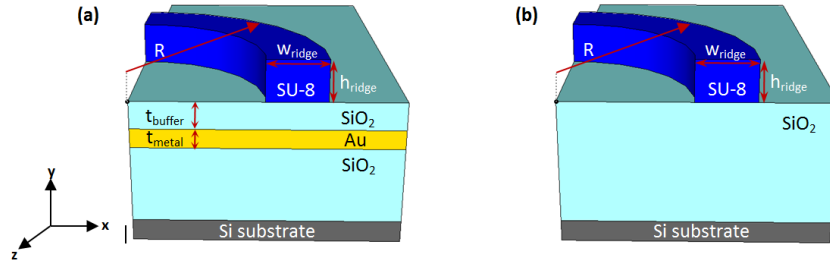


Fig. 1. Considered waveguide architectures in this study: (a) dielectric-loaded hybrid plasmonic waveguide (“metallic” structure) and (b) dielectric reference structure (“non-metallic” structure). Parameters of the structure: $h_{\text{ridge}} = w_{\text{ridge}} = 2\ \mu\text{m}$, $t_{\text{buffer}} = 100\ \text{nm}$, $t_{\text{metal}} = 100\ \text{nm}$. The silicon substrate was not taken into account in the simulations, as the thickness of the SiO_2 undercladding was considered sufficiently thick for the mode not to be influenced by the presence of the silicon substrate.

Simulation Results

Figure 2 depicts the real part of the dominant electric field component for the quasi-TE (E_x) and quasi-TM (E_y) modes supported by non-metallic [Fig. 2 (a) and (b)] and metallic [Fig. 2 (c) and (d)] waveguide structures.

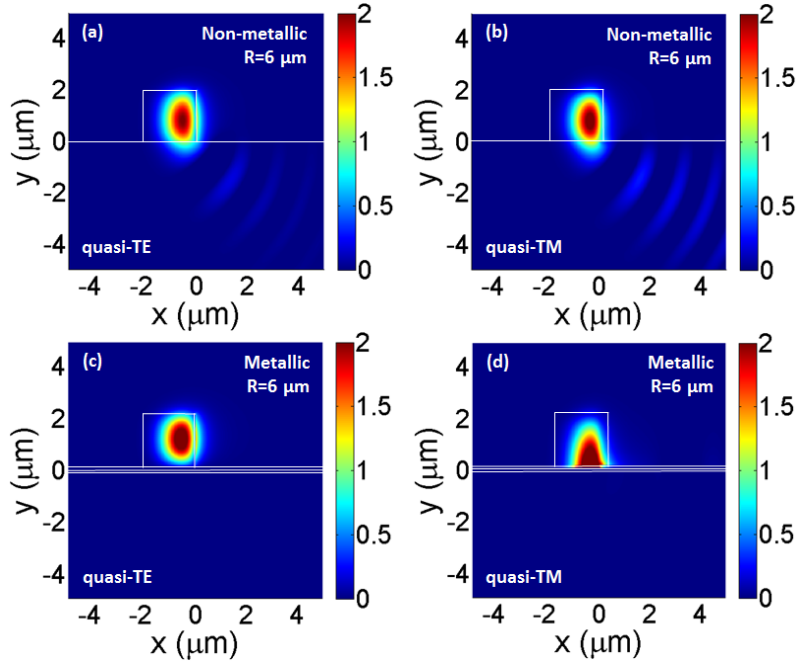


Fig. 2. Calculated 2-D mode profiles (showing the real part of the dominant electrical field component, E_x for TE and E_y for TM) at $\lambda = 1.55 \mu\text{m}$, $R = 6 \mu\text{m}$ for the non-metallic structures (top) with the parameters of $w_{\text{ridge}} = 2 \mu\text{m}$, $h_{\text{ridge}} = 2 \mu\text{m}$ for the (a) quasi-TE and (b) quasi-TM modes and for the metallic structures (bottom) with the parameters of $w_{\text{ridge}} = 2 \mu\text{m}$, $h_{\text{ridge}} = 2 \mu\text{m}$, $t_{\text{buffer}} = 100 \text{ nm}$ and $t_{\text{metal}} = 100 \text{ nm}$ for the (c) quasi-TE and (d) quasi-TM modes.

The guided mode binds to the outer rim of the ridge, since the turning is in the direction of the negative x-axis. In the non-metallic structure, the generated leaky waves can be clearly observed and are due to the sharp bending of the waveguide. As the radius of curvature is further decreased, leakage into the substrate increases with the consequent increase in bend losses. Introduction of a thin metallic layer underneath the polymer ridge blocks the radiation modes and pushes the quasi-TE mode towards the ridge in the positive y-axis direction [Fig. 2 (c) and Fig. 3(a)].

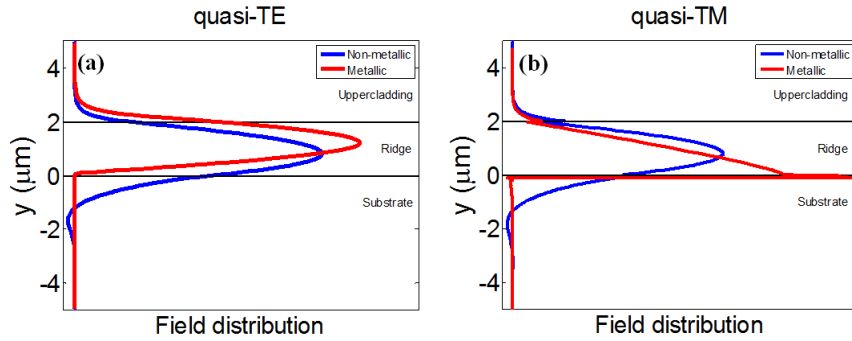


Fig. 3. Cross-sectional field distributions for both non-metallic and metallic waveguide architectures for (a) quasi-TE and (b) quasi-TM mode profile. The cross-section profiles are given at the points in x-axis where the field intensity maximized (at $x = -0.55 \mu\text{m}$ for quasi-TE and $x = -0.35 \mu\text{m}$ for quasi-TM). As introduced in Table 1, uppercladding and ridge correspond to air and SU-8 respectively for both metallic and non-metallic. Substrate refers to buffer/metal/undercladding layers stack for metallic and only undercladding for non-metallic.

Figure 4 (a) shows the total losses per 90 degree bend for the metallic quasi-TE mode in comparison with those of the quasi-TE mode of the non-metallic structure. For large radii of curvature, the total losses per 90 degree bend of the metallic structure rise linearly with increasing radius. In this radius range, the total losses are dominated by the propagation losses and thus, they augment as the length of the 90 degree waveguide segment increases. When the radius decreases below a critical radius, the total losses rise again, this time due to the radiative losses introduced by the bend. It can be clearly seen in Fig. 4 (a) that the introduction of the thin metal layer shifts the critical radius to a much lower value (i.e., $\sim 7 \mu\text{m}$) than in the non-metallic waveguide.

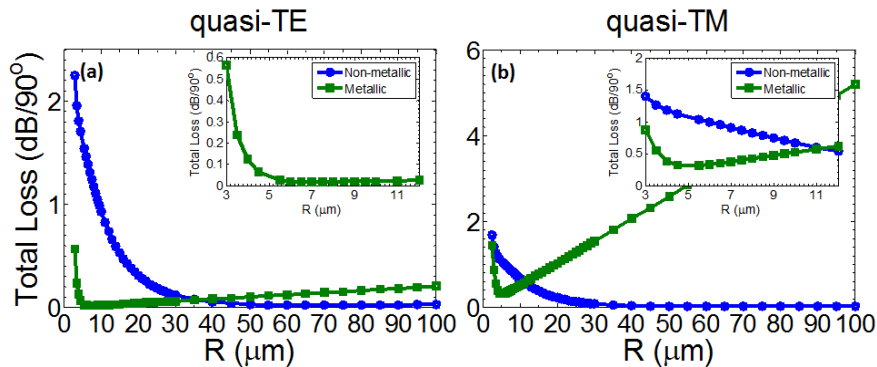


Fig. 4. Total loss ($\text{dB}/90^\circ$) versus bend radius (R) for metallic and non-metallic structures for (a) quasi-TE and (b) quasi-TM modes with the parameters of $w_{\text{ridge}} = 2 \mu\text{m}$, $h_{\text{ridge}} = 2 \mu\text{m}$, $t_{\text{buffer}} = 100 \text{ nm}$, and $t_{\text{metal}} = 100 \text{ nm}$ (only for metallic structure). The insets are a zoom of the corresponding loss plots in the region of interest.

The thin metallic layer underneath the polymer ridge transforms the quasi-TM mode of the non-metallic structure [Fig. 2 (b)] into a hybrid plasmonic-photonic mode. Such a

mode is strongly coupled to the metal, thereby reducing leakage to the substrate and, therefore, the bend losses for small radii of curvature [Fig. 2 (d) and Fig. 3]. However, since the metal is highly absorptive at the wavelength of interest, high propagation losses are expected. High propagation losses are dominant for increasing radii [Fig. 4 (b)]. A shift of the critical radius, below which the bend losses become dominant, to a smaller value than in the non-metallic structure still occurs despite the large propagation losses. For a narrow range of bend radii from 3 μm to 10 μm , the metallic structure exhibits lower total losses compared to the non-metallic counterpart [inset of Fig. 4 (b)].

Fabrication

A two-step microfabrication process was followed to realize the proposed structures. Due to the elevated propagation losses of the metallic structures, a lift-off process was utilized to define the gold layer underneath the bends. The SU-8 bent waveguides are patterned in the second fabrication step. Sets of bent waveguides with increasing number of bends were fabricated in order to characterize the total losses per 90 degree bend. The results of the fabrication process for a set of non-metallic structures are depicted in Fig. 5. On the left side, Fig. 5 (a), a top view of set of SU-8 dielectric waveguides is shown. In Fig. 5 (b), a Scanning Electron Microscope of one of such bent waveguides is illustrated.

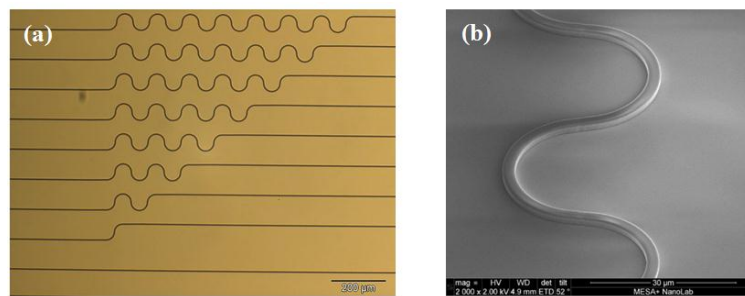


Fig. 5. Fabrication process results: (a) a set of SU-8 waveguides on SiO_2 substrate.; (b) SEM picture of a SU-8 bent waveguide.

Conclusion

In this work, we proposed and demonstrated numerically that introducing a thin metal layer underneath the core of a polymer waveguide permits the realization of sharp bends with calculated total losses (dB/90°) smaller than those of the equivalent dielectric waveguide without the metallic layer, both for quasi-TE and quasi-TM modes. The optical characterization for fabricated structures is still under way.

The authors acknowledge support from the FP7 Marie Curie Career Integration Grant PCIG09-GA-2011-29389 and the University of Twente Aspasia fund.

References

- [1] L. Eldada and L. W. Shacklette, "Advances in polymer integrated optics," IEEE J. Sel. Top. Quantum Electron. vol. 6, 54-68, 2000.
- [2] H. Ma, A. K. Y. Jen, and L. R. Dalton, "Polymer-based optical waveguides: materials, processing and devices," Adv. Mater. 14, 1339-1365 (2002).
- [3] M. A. Sefunc, M. Pollnau, and S. M. Garcia-Blanco, "Low-loss sharp bends in polymer waveguides enabled by the introduction of a thin metal layer," submitted.
- [4] E. D. Palik, "Handbook of Optical Constants of Solids," Academic, Orlando, Fla., 1985.
- [5] Phoenix B.V., Enschede, The Netherlands (www.phoenixbv.com).

Long-wavelength Generic Components in COBRA Platform

H. Rabbani-Haghighi,¹ D. D'Agostino,¹ R. van Veldhoven,² P. Thijs,² H.P.P.M. Ambrosius,¹ and M.K. Smit¹

¹ Technical University of Eindhoven (TU/e), Dept. of Electrical Engineering, Photonic Integration group, COBRA, PO Box 513 - 5600 MB, Eindhoven, the Netherlands

² Technical University of Eindhoven (TU/e), PSN group, 5600 MB Eindhoven, the Netherlands

The importance of Photonic Integrated Circuits (PICs) operating at wavelengths around 2 μm is rapidly increasing. Applications are in the bio/chemo sensing domain, e.g. gas detection in breath analysis. The COBRA research group at the University of Eindhoven is developing a generic integration platform functioning at wavelengths up to 2.1 μm . The research in this platform covers integration of a number of active and passive building blocks. Integration of active and passive waveguides is achieved with excellent butt-joint quality, leading to the first COBRA laser emitting at 2 μm . Research on a library for passive components is underway.

Introduction

Generic photonic integration technology is an approach which offers monolithic fabrication of miniaturized photonic devices with diverse functionalities at a reduced price. This goal is achievable through development of a library of fully-characterized basic building blocks including passive components, detectors, modulators, lasers and optical amplifiers (SOAs). In this context, integrated circuits on Indium-phosphide (InP) substrate are of particular interest since both active and passive components are supported [1]. Since the launch of InP-based generic integration concept in 2007 by the European Network of Excellence (ePIXnet), the COBRA research group together with some other leading partners have successfully demonstrated a number of milestones for devices operating at 1.55 μm . A next step is to extend the platform operation to wavelengths around 2 μm . The wavelength range around 2 μm is of great interest since strong absorption lines of various gas species (carbon dioxide (2.05 μm), nitrous oxide (2.13 μm) and carbon monoxide (2.33 μm)) are located in this region and the absorption of water is very low. This provides excellent opportunities for trace-gas monitoring applications in environmental and medical diagnostics.

Since the existing platform for PICs at 1.55 μm has become mature the targeted long-wavelength platform will be based on the same principles but with some minor adaptations. This comprises changes in the active and passive building blocks. The latter is easily achievable since the fabrication technology is already in place for PICs at 1.55 μm . Some redesigning is required to adjust the dimensions of the existing building blocks at 1.55 μm for operation at 2 μm wavelength. In this paper, the focus of our study is on the long wavelength active material and its integration with the passive waveguides which resulted in the first COBRA laser emission at ~ 2 μm . Moreover, some simulations results on an important, but still missing building block in the COBRA platform, i.e. a Spot-Size Convertors (SSCs) for adapting the small size of an InP-based waveguide mode to that of a (lensed) fibre, will be discussed.

Long-wavelength active material

The long wavelength active material is a multi-quantum well (MQW) structure consisting of 4 periods of compressively-strained (2.12%), 5.5-nm-thick InGaAs(Sb) wells, placed between the 22.5-nm-thick InGaAs barriers, lattice matched to InP. This layer stack is sandwiched between InGaAsP separate confinement heterostructure (SCH) layers (band gap=1.25 μm), thus forming a ~ 500 -nm-thick active core waveguide. The peak photoluminescence (PL) of this material was measured to be at 2.06 μm . The antimony (Sb) plays the role of a surfactant in the active material growth. It enables suppressing the very high compressive lattice strain originating from high concentrations of Indium (In), which is required to achieve long-wavelength emission [2]. The gain of this material was determined by the variable-stripe-length (VSL) method. Through this technique, a modal peak gain of 7 cm^{-1} was measured at a current density of 3.5 kA/cm^2 [3].

Active-passive integration

Having the active material characterized, the next step is to integrate it with the passive core material (InGaAsP, band gap of 1.25 μm). The procedure includes definition of the active regions via a lithography step followed by etching of the surrounding (unmasked) material and do a passive regrowth followed by the top cladding layer growth. In the last step, the contact layer will be grown on the top. Figure 1 shows a SEM image of the realized active/passive butt-joint. Following this process, a very smooth transition between the active and passive core was achieved.

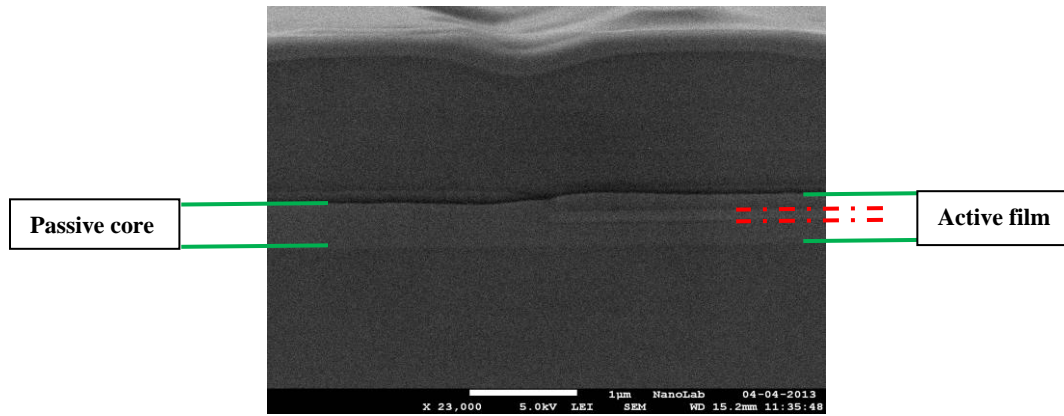


Figure 1 - SEM image of the realized active/passive butt-joint. The dash/dot lines show the active region sandwiched between the top and bottom InGaAsP layers (solid line). The perturbation in the middle is the point where the passive core starts.

In order to have a qualitative evaluation of the butt-joint, shallowly-etched straight waveguides were fabricated through the active regions. The chip was cleaved through the passive waveguides at both ends to form Fabry-Pérot laser architecture. The active region was pumped under continuous wave (CW) regime and the device temperature was actively controlled using a thermo-electric cooler. The single-side edge emission was collected by a lensed fibre and sent to an optical spectrum analyzer (YOKOGAWA AQ6375). The results of the measurements for a typical device with active region length of 750 μm over a total device length of 4.6 mm are shown in the following graphs (figure 2).

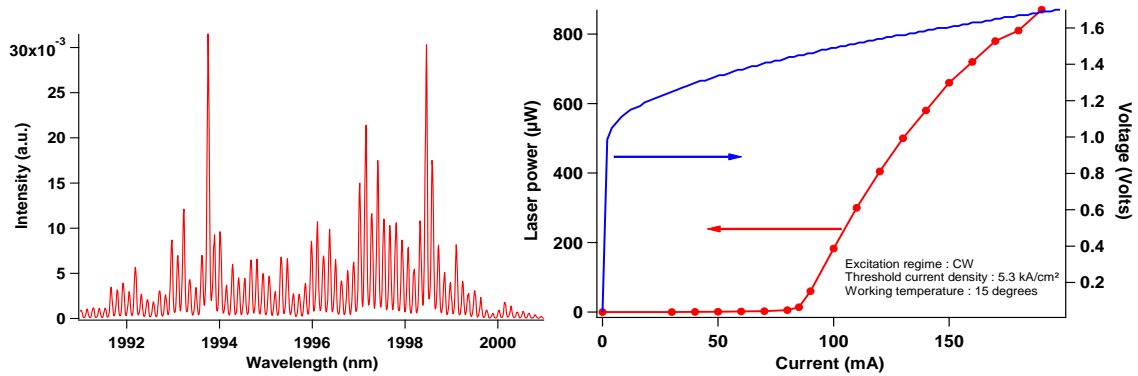


Figure 2 - (left) typical lasing emission spectrum above threshold. (right) L-I-V curve of the device under test. The filled circles are the power values measured by the optical spectrum analyzer.

For the device under test, a maximum output power close to 1 mW and a threshold current density of 5.3 kA/cm² were measured. The lasing threshold is a few times higher than the threshold current density of a similar structure at 1.55 μ m, fabricated in COBRA runs. This may be due to lower available gain of the active material at longer wavelengths. Moreover, in the passive region, there are significant absorption losses at 2 μ m wavelength caused by the p-dopants. Based on simulations, these losses increase by a factor of 3 from 3dB/cm at 1.55 μ m to around 10dB/cm at 2 μ m wavelength [4]. This source of loss can be eliminated if the p-dopants can be restricted to the active regions. For this purpose, some tests will be done to examine local Zn (p-dopant) diffusion limited to the surface area above the active regions.

Passive building block investigation: Spot-Size convertor

A component which is still missing from the list of available passive building blocks in COBRA at 1.55 μ m wavelength is the SSC. An investigation has been carried out on this module. In our approach, the design of SSCs is based on adiabatic lateral tapering. The FIMMPROP simulation tool from Photon Design was used to model the behaviour of the SSC. The simulated structure consists of a linear waveguide section with a length of 5 μ m which is connected through a junction to a linearly tapered waveguide. The taper width varies linearly from 2 μ m (optimized waveguide width for light propagation at 2 μ m wavelength range) to 0.3 μ m (the minimum width which we can be fabricated with optical contact lithography in combination with underetching) over the taper length. The taper length was varied from 0 to 2 mm. The fibre-matched waveguide width was set to be 5 μ m with an etch depth of 6 μ m (200 nm below the core layer). The simulation was carried out by using the FDM solver. The fundamental TE mode was launched at the input and the power of the first five excited TE modes at the output was monitored.

Based on the depicted graph in figure 3, it is predicted that for a taper length of 1000 μ m, 94% of the input TE power is coupled into the fundamental TE mode at the output, and for a taper length of 1500 μ m more than 99%. In practice, taking into account the propagation losses, we expect that more than 90 % of the power will be coupled to the fundamental TE mode at the output. A further reduction of the taper length to 800 μ m can be achieved through etching of the top cladding down to 200 nm above the passive core.

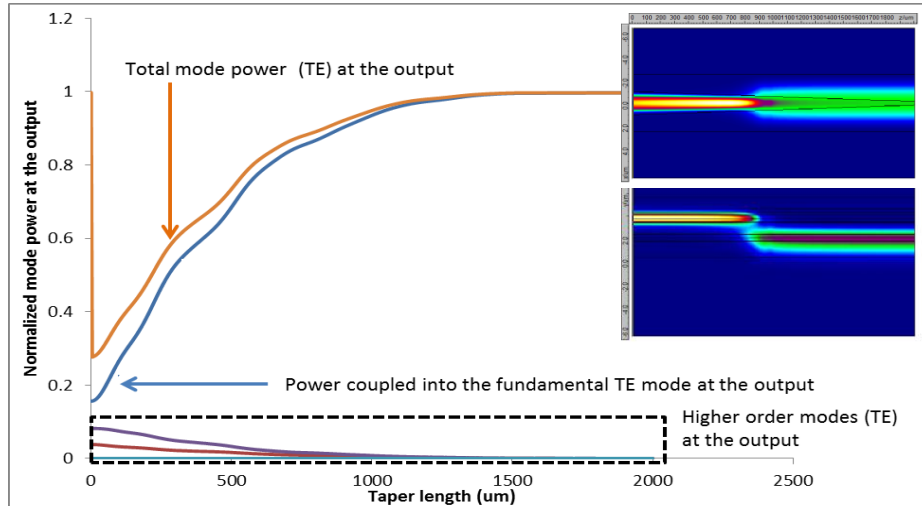


Figure 3 - Power evolution over the taper length for the first five TE modes. (inset) top and side view of the simulated structure showing the mode transition from the upper waveguide to lower fiber-matched waveguide.

Summary

We have successfully demonstrated Fabry-Pérot laser emission at 2 μm wavelength in an active-passive integrated structure. A maximum output power close to 1 mW and a threshold current density of 5.3 kA/cm² were measured. Design results for an integrated laterally-tapered SSC were presented. This has made the platform ready for a trial multi-project wafer run which is currently underway.

Acknowledgments

The authors would like to gratefully acknowledge support of the EU FP7 through the PARADIGM project (ICT 257210).

References

- [1] M. Smit, X. Leijtens, E. Bente, J. Van der Tol, H. Ambrosius, D. Robbins, M. Wale, N. Grote, M. Schell, "Generic foundry model for InP-based photonics", IET Optoelectronics, Volume 5, Issue 5, p.187–194, 2011.
- [2] T. Sato, M. Mitsuhashi, T. Watanabe, and Y. Kondo, "Surfactant-mediated growth of InGaAs multiple-quantum-well lasers emitting at 2.1 μm by metalorganic vapor phase epitaxy," Appl. Phys. Lett., vol. 87, no. 21, pp. 211903–211903–3, Nov. 2005.
- [3] S. Latkowski, P. Thijs, P.J. van Veldhoven, H. Rabbani-Haghighi, M.K. Smit, E.A.J.M. Bente, "Small signal modal gain measurement of ridge waveguide semiconductor optical amplifiers operating at 2 μm suitable for active-passive integration", IEEE photonic conference (IPC), 2013.
- [4] H. Rabbani-Haghighi, D. d'Agostino, P. Thijs, H.P.M.M. Ambrosius and M.K. Smit, "Generic components for long-wavelength applications", Proceedings of the 2012 annual symposium of the IEEE Photonics society BENELUX chapter, 143-146, 2012.

Novel pure-optical test-on-wafer technique based on a Point Reflector Optical Waveguide

D. Melati¹, F. Morichetti¹, F.M. Soares², N. Grote² and A. Melloni¹

¹ Politecnico di Milano, Dip. di Elettronica, Informazione e Bioingegneria, 20133 Milano, Italy

² Fraunhofer Heinrich Hertz Institute, 10587 Berlin, Germany

Wafer-level test approaches enabling a fast and low-cost quality assessment of the fabrication process, in terms of uniformity and repeatability, are of fundamental importance to any photonic integration foundries. In this work, we present a novel test-on-wafer technique based on a suitably engineered Point Reflector Optical Waveguide (PROW) spanning across the entire photonic wafer. The proposed technique exploits coherent optical frequency domain interferometry (OFDR) for the optical read-out of the PROW, allowing the estimation of key optical parameters of the waveguides on several points of the wafer from a single frequency domain measurement.

Introduction

It is widely recognized that in the near future the market breakthrough for integrated optical circuits (PICs) will be closely related to the increasing of the complexity of the circuits, with new applications and business opportunities [1]. The challenge of new markets require the possibilities of high volume productions at lower costs to ensure the necessary competitiveness. The yield of the production processes will therefore be one of the key aspects for the photonic companies in the near future, as it happens in the electronics market. In this framework, the measurement of the quality at the end of a production process in term of compliance with the guaranteed specifications is a valuable instrument for the foundries. These measurements have to be done directly on wafer, before the dicing of the single cells, with a quick and cheap technique that allows evaluate few parameters descriptive of the quality of the completed process, its uniformity and repeatability. The proposed solution is based on a Point Reflector Optical Waveguide (PROW). It is a full-optical technique that allows the measurement of the optical parameters of the waveguides directly at a wafer level. With a single test, it is possible to retrieve information from several measuring points distributed across the wafer, allowing a quick sampling of the whole area. In the next sections the concept of the test technique is described and the design of the probe element is discussed.

Design and concept of optical probing

Figure 1(a) shows the proposed approach for the measurements of optical parameters throughout the wafer. As already mentioned, it is based on a Point Reflector Optical Waveguide (PROW) which consists of a long waveguide with several probe elements exploited to measure the required parameters along the waveguide. In this scheme the light is coupled in the structure via butt-coupling and the wafer has to be prepared with two cleaving (see figure 1(a)) in order to have straight facets and a good coupling coefficient on both side of the PROW. Other solutions may rely on grating-assisted vertical coupling.

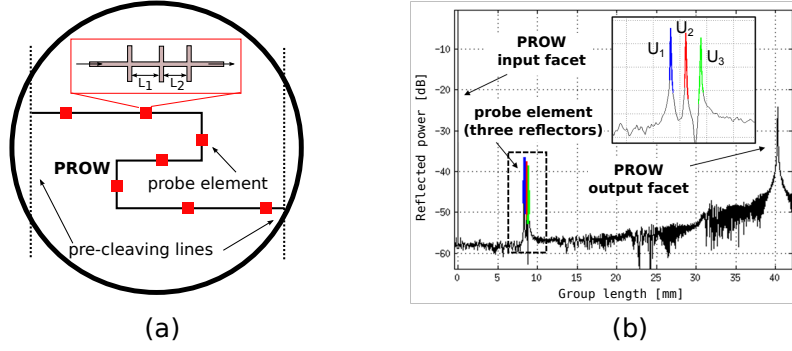


Figure 1: (a) Sketch of a single PROW with several probe points distributed along the waveguide. In the inset, a scheme of a single probe point. (b) An example of (simulated) data collected from a PROW with a single probe element.

An arbitrary number of PROWs can be placed on the wafer to measure the parameter in any required point but each structure has to be measured independently. Several parameters can be used to monitor the compliance of a waveguide to the specifications, including phase and group effective indices, losses, and the average backscatter generated by the sidewall roughness [2]. The technique proposed in this work focuses on group effective index and propagation losses whose values are strongly tied to the waveguide geometry. The probe element is composed by three lumped reflective sections which form a single sensing unit. A fundamental assumption for the application of this technique is that the perturbation the reflectors produce on the parameters of propagating mode is negligible with respect to the sensitivity required to the measurement. The measurement of the PROW is done by exploiting an Optical Frequency Domain Reflectometry (OFDR) technique [2], which allows an interferometric analysis of the light reflected along a waveguide. Reflected power spectrum is collected in the spectral domain and then Fourier transformed to retrieve the data in the spatial domain. Each reflective section contributing to the total power reflected by the PROW is then identified and measured.

The main constraints to the design of a PROW are related to the total number of reflectors placed on the waveguide. Larger amount of reflectors implies also larger losses along the whole waveguide and then a reduced sensitivity for the farther elements. Depending on the involved technology, good compromise between density of the probes and total losses must be found to ensure reliably results.

An example of this kind of analysis is shown in figure 1(b), where a simulation of a 11.5mm-long PROW with a single probe element is reported. Propagation losses of 2dB/cm have been assumed. Each reflector generates a lumped loss of 0.5dB and a reflection coefficient of $-40dB$. The physical lengths of the waveguides between the three reflectors are respectively $L_1 = 80\mu m$ and $L_2 = 79\mu m$. The graph shows the power reflected at each section of the long waveguide: the input/output facets are clearly visible as well as the three reflectors which form the sensing element (in the inset the area close to the probe). The distance of each section from the input facet is reported as group length.

Parameters extraction

In this section the extraction the group index and the propagation loss through the data collected from the PROW is shown. This processing is applied to each probe element,

resulting in a mapping of the values in the chosen points of the PROW.

The group effective index is directly calculated from the phase of each reflection measured with the OFDR technique described in the previous section. The basic assumption is that the value of the index is constant on the entire waveguide section occupied by the probe. The three reflections U_i (with $i = 1, 2, 3$) generated inside a single probe element posses a phase that can be defined as

$$\angle U_i = \theta_i + \varphi_i = \theta_i + \beta_0 2z_i + \beta_1 (\omega - \omega_0) 2z_i \quad (1)$$

where θ_i is the phase of the reflector and φ_i the propagation contribution for a section placed at distance z_i inside the structure. A linear expansion of the propagation constant around the central frequency ω_0 in the form $\beta(\omega) = \omega_0 n_{eff}/c + (\partial\beta/\partial\omega)|_{\omega_0}$ has been used. The physical lengths z_i must be doubled because of the double passage inside the structure required by the measurement. We can then compute the phase difference between two adjacent reflectors inside a single triplet, which is only dependent on the two physical lengths L_1 and L_2 of the waveguide sections inside the probe unit, assuming the two reflectors add the same contribution θ_i . With a linear interpolation of the two differences we can finally estimate the linear term β_1 , which is related to the group index in the section on the sensing unit by the relation $\beta_1 = \partial\beta/\partial\omega = n_g/c$.

The reflections generated by the crossings inside each probe elements can be used also to measure the distribution of the attenuation coefficient along the waveguide. The amplitude of each reflection $|U_i|$ can be extracted from the temporal trace generated by the OFDR measurement. We can now reasonably assume that all the crossings placed in a PROW produce the same reflection and attenuation coefficients and hence we can extract the propagation losses comparing two couples of adjacent reflections $|U_i|$ and $|U_{i-1}|$. Amplitudes in the same couple differ only for the extra losses experienced by the light reflected farther from the input facet (e.g. red peak in figure 1(b)) induced by the first crossing (the blue peak) and longer propagation distance inside the probe element. Their ratio results

$$\frac{|U_i|}{|U_{i-1}|} = IL_c^2 e^{2\alpha L_j} \quad (2)$$

where IL_c is the insertion loss of a single crossing and α the attenuation coefficient. If the two considered couples of reflections have a different distance L_j between the reflectors than we can extract α with a simple linear interpolation (because IL_c is constant), effectively exploiting a cutt-back technique. This linear regression can be particularly critical if the involved lengths L_j are too small. On the other hand larger distances mean a degradation of the spatial resolution.

Experimental results

Temporal distribution of the reflections in a 6-cm long PROW are shown in Fig.2(a) while results of the extraction of the propagation losses and group index for both TE and TM polarized light from these data can be seen in Fig.2(b) and (c). The waveguide exploited for the characterization is the InP-based deeply-etched rib structure described in [3]. For the group index (Fig.2(a)) the behaviour is similar for both polarization, with a slight increasing of its value moving from the external area towards the centre of the wafer, in the order of $5 \cdot 10^{-3}$. A simulation of the expected waveguide group index variation as function

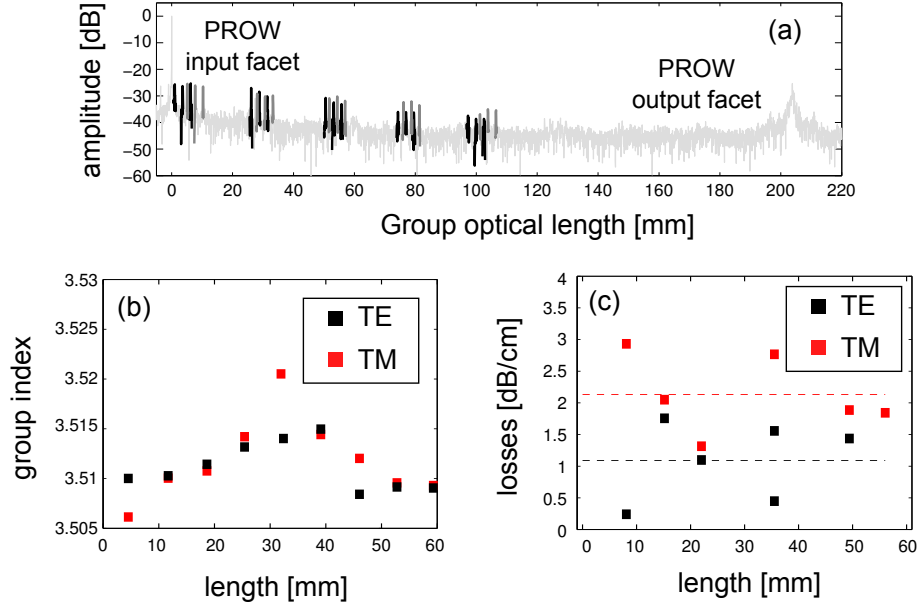


Figure 2: (a) Measured space distribution of the reflections in a PROW. Based on these data, measurements of (b) group index and (c) losses distribution are performed.

of an uncertainty in the thickness of the core layer (supposed to have the nominal value of the refractive index) reveals that this number is compatible with a variation comprised between 50 nm and 100 nm, in accordance with the specifications of the foundry.

Measurements of the propagation losses are shown in Fig.2(b). In this case a clear trend along the PROW cannot be easily recognized which suggests that the dispersion of the measured data is higher than the possible variations of α . The standard deviation of the data is about 0.5 dB for both TE and TM results, which is a good results related to the fact that the length of the involved waveguides is smaller than 0.5 cm (and hence the total insertion losses that has to be estimated are rather small and noise-affected). The average value of α for the TM mode is about 1 dB/cm higher than the TE polarized light, which is in accordance with previous measurements conducted on the same type of waveguides.

Acknowledgement

The research leading to these results has received funding from the European Community's Seventh Framework Program FP7/2007-2013 under grant agreement ICT 257210 PARADIGM.

References

- [1] M.K. Smit, R. Baets, M. Wale, "InP-based Photonic Integration: Learning from CMOS", 35th European Conference on Optical Communication (ECOC), 2009.
- [2] F. Morichetti, A. Canciamilla, C. Ferrari, M. Torregiani, A. Melloni, M. Martinelli, "Roughness Induced Backscattering in Optical Silicon Waveguides", Phys. Rev. Lett., vol. 104, no. 3, p.033902, 2010.
- [3] D. Melati, F. Morichetti, A. Canciamilla, D. Roncelli, F. M. Soares, A. Bakker, A. Melloni "Validation of the Building-Block-Based Approach for the Design of Photonic Integrated Circuits", Journal of Lightwave Technology, vol.30, no.23, 2012.

Measurements of integrated mode-locked laser for laser library development

V. Moskalenko, M. K. Smit, E. A. J. M. Bente

Technical University of Eindhoven, Eindhoven, Netherlands

In this paper results of measurements on monolithic extended cavity ring passively mode-locked semiconductor lasers (PMMLs) are presented. We have designed PMMLs in various geometries in order to use them for theoretical model verification and subsequent development of a library of short-pulsed lasers within an active-passive integration platform. The different dynamic regimes depending on the voltage applied to the saturable absorber and current injected into the amplifier are characterized in both time and frequency domains. At the mode-locking operational conditions the output signal features an optical comb centered at 1.55 μm and a 3dB bandwidth of 8.5 nm.

Introduction

A large number of applications in areas as high-speed communications [1], optical recovery [2], and high-speed gas spectroscopy [3] require short stable optical pulses or coherent optical frequencies which can be generated by mode-locked lasers (MMLs). However, such systems can be quite bulky, complex and vulnerable. In order to overcome these issues a photonic integration approach is used. In this technology passive MLLs (PMLs) can be realized as a photonic integrated circuit (PIC) on which these lasers can be combined with other optical devices on the single monolithic chip. The aim of this work is to study PMLs in the framework of active-passive integration technology, which enables the combination of passive and active waveguide devices. Through the use of the active-passive integration, the performance of a semiconductor mode-locked laser can be significantly improved due to several reasons. First, active-passive integration allows for a decoupling of amplifier lengths and the resonator length which determines the repetition rate. This helps to reduce the issue of amplitude modulations [4] and self-phase modulation as observed in all-active two-section devices. Another advantage of this technology is that the relative position of the SA and SOA and output coupler in cavity can be optimized. But also other optical devices can be included which can be freely located.

In integrated photonics, as in micro-electronics, the broad range of complex circuits can be realized using a set of small standard components, so called building blocks. Building blocks (BB) are organized in libraries. This approach enables one to design a large variety of complex optical devices relatively fast by combining building blocks from various libraries. Since there is large variety of complex optical devices which require short-pulsed laser as an optical source the library approach can be also applied to the PMLs.

In this work we investigate PMLs performance for various designs and operating conditions in order to use them in short-pulsed laser development in active-passive integration platform. The paper is organized as follow: in the first section we will introduce the concept of the library of short-pulsed lasers and main steps that have to be

made. In the next two sections we present the PMLLs geometry and main experimental results that have been achieved. The conclusions are given in the last section.

The idea of library of short-pulsed lasers

Depending on the circuit functionality and application the requirements on a PMML can vary over a wide range. For example, for high speed gas-spectroscopy applications the pulses repetition rate should not exceed 3 GHz and for a wavelength division multiplexing source it has to be in the order of tens of GHz. Thus, the BBs have to be developed in a way that designer in principle could change the characteristics of output signal without spending additional time on the BBs properties simulation. However, in order to link the characteristics of output signal and BB layout the performance of mode-locked lasers needs to be properly investigated using both experimental and simulation approaches. In spite of the fact that semiconductor mode-locked lasers have been studied for more than two decades theoretical prediction of their properties still remains challenging. A systematic study of theoretical predictions and experimental results under a range of operating conditions of a series of different devices is required to a) achieve high level of understanding of the non-linear processes taking place in the laser cavity and b) to determine which theoretical model is the most suitable to be used in laser library development. For this purpose several ring PMLLs of different geometry were fabricated. In the next section we will detail the device design used in this work.

Symmetrical ring mode-locked laser

Passive mode-locking can be achieved by combining two elements a semiconductor optical amplifier (SOA) which provides gain that saturates at high intensities and a saturable absorber (SA) which introduces losses that are relatively large for low intensities but which become significantly smaller due to the saturation of absorption for a pulse with high intensity. In this work we present the ring symmetrical design of PMLL which includes not only SOA and SA sections but also passive waveguides (shallow and deep) and a 50% multi-interference coupler (MMI) output coupler. A schematic sketch of the laser cavity is presented on Fig. 1.

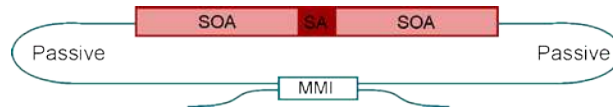


Fig. 1. Sketch of symmetrical ring PMML.

The use of passive waveguides in a PMLL allows to overcome or reduce issues in standard two-sections all active PMLLs, in particular self-phase modulations effects [4]. The symmetrical ring cavity enables operating in a self-colliding regime which provides more stable mode-locking and a more deeply saturated absorber. Due to the fact that in the ring cavity there is no need of cleaved facets the repetition rate can be controlled more accurately than that of a Fabry-Perot type structure with cleaved facets.

In order to minimize back reflections into the device the output waveguides are tilted under an angle of 7 degrees. The SOA and SA section contain a layer structure with four InGaAs quantum wells. The SOA and SA sections were electrically independent by

introducing electrical isolation sections. The device results presented here are on a PIC fabricated within a multiproject wafer run available through an Oclaro foundry service. Three 16 GHz ring mode-locked lasers with different lengths of SOAs (1300 μm , 1500 μm and 1700 μm) and 50 μm long SAs were fabricated. In the next section the experimental results of the laser with a 1700 μm SOA are presented.

Measurements results

The device was mounted on a copper chuck and the temperature was stabilized at 12° C. The output light was collected using lensed fibers with antireflection coating. Optical isolators were used to prevent back reflections into the cavity. The PMLL laser was operated with a total injection current (I_{soa}) to the SOA sections and a reverse voltage (V_{sa}) applied to the SA. The mode-locking was confirmed by observation of RF spectra, optical spectra and autocorrelation trace. The RF spectra were recorded using a 50 GHz electrical spectrum analyser connected to the fast photodiode. The optical spectra were characterized using an optical spectrum analyser (OSA) with a resolution of 0.16 pm. In order to obtain autocorrelation traces the optical signal from PMML went through the polarization controller and was amplified by the erbium doped fiber amplifier (EDFA) with a 10 m long fiber.

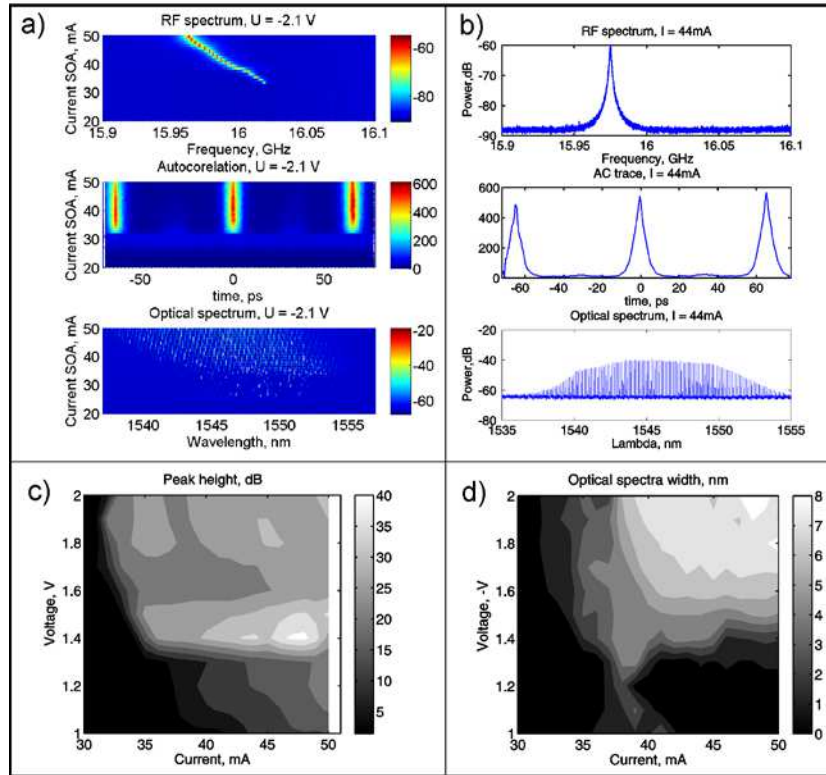


Fig. 2. a) Evolution of RF spectra, autocorrelation trace and optical spectra with injected current at $U_{\text{sa}} = -2.1 \text{ V}$. b) RF spectrum, autocorrelation trace and optical spectrum at $U_{\text{sa}} = -2.1 \text{ V}$ and $I_{\text{soa}} = 44 \text{ mA}$, c) A map of the RF peak height as a function biasing conditions applied to the SOA and SA d) A map of the spectral bandwidth (FWHM) measured at the same set of operating conditions as in (c)

The device has been measured under various operating conditions. The Fig. 2 (a) shows RF spectra, AC traces and optical spectra at the range of injected currents ($I_{\text{soa}} = 10\text{--}50 \text{ mA}$). The maximum injected current was determined by the maximal power of the

optical signal which can be absorbed by the SA without causing damage. The lasing threshold of the PMLL at 2.1V applied reverse voltage was $I_{\text{soa}} = 27$ mA. The signal recorded by the OSA shows continuous wave lasing at the currents above threshold until $I_{\text{soa}} = 33$ mA. At the injected currents above $I_{\text{soa}} = 33$ mA the device operates in a mode-locking regime. At these conditions the electrical spectrum shows a clear peak at 16.02 GHz which corresponds to the roundtrip time. Analysis of autocorrelation shows pulse duration of 3.8 ps.

By further increasing the injected current, the beat tone between modes shifts to lower values. As described in [5] the repetition frequency is led by a change of detuning due to the gain/absorber saturation effects. In our case we operate at low injection currents, where most of the gain section isn't saturated. According to [5] at unsaturated gain conditions the repetition frequency decreases with increasing pulse energy.

Increasing of the current leads to the optical spectrum shift to shorter wavelengths, this is caused by the blue shift of the gain spectra at higher carrier densities. Examples of the RF spectrum, AC trace and optical spectrum at the fixed injected current ($I_{\text{soa}} = 44$ mA) are presented on Fig. 2 (b). Fig. 2 (c) shows a map of height of RF peak (in dB) at the fundamental frequency over the low frequency noise as a function of I_{soa} and V_{sa} . The main gray area indicates the presence of RF peak. Since the injected currents were relatively low the signal to noise ratio of the RF analyzer plays a role and therefore RF peak heights don't exceed 40 dB. The maximum observed RF height over the noise floor is 41 dB. Fig. 2(d) shows a map of the full width at half maximum (FWHM) of the optical spectral width. The maximum observed FWHM is 8.5 nm.

Summary

The ring geometry passively mode-locked laser realized as a PIC fabricated within the Oclaro InP generic technology has been demonstrated. The mode-locking regime over range of the operating conditions was observed. The output signal features a FWHM of 8.5 nm and a minimum pulse width of 3.8 ps.

Acknowledgement.

The research leading to these results has received funding from European Community's Seventh Framework Program FP7/2007-2013 under grant agreement 257210 PARADIGM

References

- [1] H. Takara, "High speed optical time-division multiplexed signal generation," *Optical and Quantum Electronics*, vol. 32, 795-810, 2001.
- [2] T. Ohno, K. Sato, R. Iga, Y. Kondo, T. Ito, T. Furuta, K. Yoshino, and H. Ito, "Recovery of 160 GHz optical clock from 160 gbit-s data stream using modelocked laser diode," *Electronics letters*, vol. 40, no. 4, 1-2, 2004.
- [3] J.Mandon, "Spectroscopy: Frequency comb benefits", *Nature Photonics*, vol. 3, p. 82, 2009.
- [4] Y. Barbarin, E.A.J.M. Bente, M.J.R. Heck, J. Pozo, J.M. Rorison, Y.S. Oei, R. Nötzel and M.K. Smit, "18GHz Fabry-Pérot integrated extended cavity passively modelocked lasers," *European Conference on Integrated Optics*, April 25-27, 2007, Copenhagen, Denmark: Conference Proceedings ThG07
- [5] S. Arahira and Y. Ogawa, "Repetition-frequency Tuning of monolithic passively mode-locked semiconductor lasers with integrated extended cavities," *IEEE Journal of Quantum Electronics*, vol. 33, no. 2, 1997

Tunable two color emission in a compact semiconductor ring laser with filtered optical feedback

M. A. Khoder,¹ R. M. Nguimdo,¹ J. Danckaert,¹ X. J. M. Leijts,² J. Bolk,² G. Verschaffel¹

¹ Vrije University Brussels, Applied Physics research group (APHY),
Pleinlaan 2, B-1050 Brussels, Belgium

² Eindhoven University of Technology, COBRA Research Institute,
5600 MB Eindhoven, The Netherlands

We report on an integrated approach to obtain two color emission from a semiconductor ring laser with filtered optical feedback. This feedback is realized on-chip by employing two arrayed waveguide gratings to split/recombine light into different wavelength channels. Semiconductor optical amplifiers are used in the feedback loop to control the feedback strength of each wavelength channel independently. Results show that the effective gain of the different modes is the key parameter which has to be balanced to obtain two color emission. This can be achieved by tuning the injection current in each amplifier.

Introduction and Device description

For numerous scientific and industrial applications, it is of interest to have tunable, two color emission (TCE) lasers. Such applications include wavelength-division multiplexing in optical communications systems, optical sensing and THz generation [1]. Several approaches have been proposed to achieve TCE using different laser systems, such as fiber lasers, solid-state lasers and external cavity laser diodes. Although these systems show a good performance, they tend to be bulky and expensive. Therefore, there is a profound interest in achieving TCE in single-chip laser diodes, with devices being potentially small in size, low-cost and integrable with other photonic components.

In this paper we propose an approach to achieve TCE in a monolithic laser diode structure. Semiconductor ring lasers (SRLs) with on-chip filtered optical feedback have been proposed in [2] to obtain tunable single color emission (SCE). Here, we will show that the same scheme can also support the simultaneous emission of two longitudinal modes (LMs) by balancing the effective gain of selected LMs. This scheme has several advantages: Firstly, the SRL does not require distributed feedback or DBR mirrors, it is easily integrable with other photonic components. Secondly, The competition between

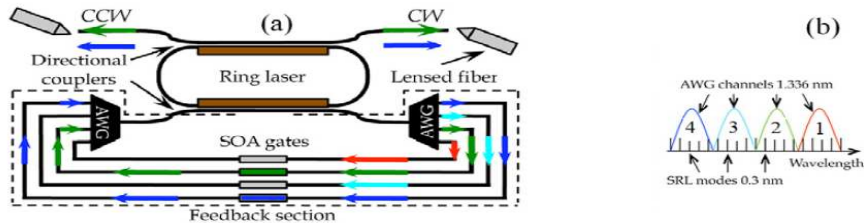


Figure 1: (a) Layout of the integrated ring laser with on-chip filtered optical feedback. (b) The alignment of the AWG channels .

the clockwise/counterclockwise propagating modes of a SRL cavity leads to interesting dynamical regimes. Thirdly, we can select different pairs of wavelengths under TCE in a non-thermal fashion by changing the current injected in the different SOA gates. Finally, we can easily switch between TCE and single-mode operation by changing one of the gate currents.

The device consists of a SRL, two arrayed waveguide gratings (AWG) which are used to split/recombine light into 4 different wavelength channels, four semiconductor optical amplifier (SOAs) gates and passive and active waveguides to connect these components. The AWG channel spacing is 1.336 nm and the AWG free spectral range is 5.65 nm, whereas the mode spacing is 0.305 nm. Therefore, each AWG channel supports 4 modes. The scheme of the device is shown in Fig. 1(a). The channels alignment of the AWGs is shown in figure 1(b). Each SOA gate can be independently pumped electrically. When a gate is biased, the feedback strength and phase of the LMs in the corresponding AWG channel will change. When a gate is not biased, or when it is reverse biased, light is absorbed and therefore there is no feedback effect.

Experimental study

We use electrical probes to pump the SRL and the gates which are chosen to provide feedback. We measure the output in the clockwise (CW) and counter clockwise (CCW) directions using lensed optical fibers. The threshold current of this device is 64.5 mA. We pump the SRL well above the threshold at 85 mA. Without filtered feedback, the laser emits multiple longitudinal modes. By pumping one gate with sufficient current we obtain a SCE in agreement with [2]. Next when two gates are pumped simultaneously, (for example we choose to bias gates 2 and gate 3), TCE can be observed in the CCW direction for a gate 3 current of 8.63 mA and a gate 2 current of 20.6 mA as shown in figure 2(a). The two dominant peaks are located at $\lambda_3=1582.296$ nm , and $\lambda_2=1583.210$ nm (which corresponds to the wavelength channels of gate 3 and gate 2, respectively). Similar TCE is noticed in the CW direction. We can also tune the emission wavelengths under TCE operation electrically by changing the gates that are forwardly biased. Although we cannot tune the wavelengths continuously, a discrete set of simultaneously emitted wavelengths can be selected.

To investigate the influence of the gate currents on the TCE, we fix the laser current at 85 mA and the gate 3 current at 8.63 mA. We gradually increase the gate 2 current from 0

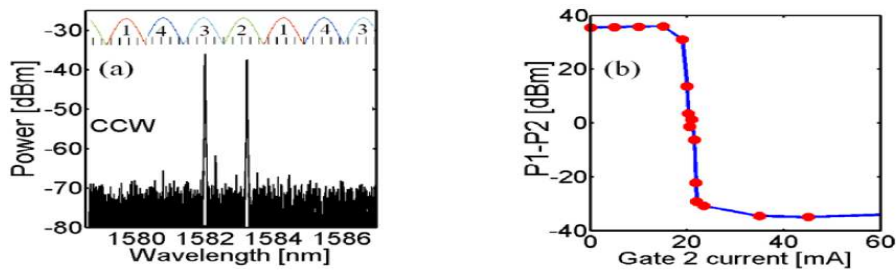


Figure 2: (a) Optical spectrum in CCW direction for a SRL current of 85 mA, a gate 3 current of 8.63 mA, and a gate 2 current of 20.6 mA. (b) Optical power difference between the two peak wavelengths in the spectrum as a function of gate 2 current. SRL current fixed to 85 mA, gate 3 current fixed to 8,63 mA. Solid line is to guide the eye

mA to 60 mA. For each value of the gate 2 current, we measure the optical spectrum and we extract the optical power at the peak wavelengths shown in figure2(a). The difference between the power P1 at the wavelength λ_3 and the power P2 at the wavelength λ_2 is plotted in figure2(b) as a function of the current applied to gate 2. When this difference is equal to 0, both wavelength modes are emitted with the same power and we achieve TCE. When the power difference is larger than 30 dBm, the laser emits only the LM at λ_3 . Likewise, when the power difference is smaller than -30 dBm, the laser emits only the LM at λ_2 . From figure2(b) it can be seen that there is TCE in a relatively narrow range of gate 2 currents (from 19 mA to 21 mA). If the gate 2 current is tuned away from this value, there is a continuous transition region where the power in one of the LMs decreases (accompanied by a similar increase in the other LM). A similar transition region can be observed when gate 2 is fixed at 20.6 mA and the gate 3 current is changed. Performing the measurement shown in figure 2 both for increasing and decreasing the current injected in gate 2, yields the same results. This shows that there is no hysteresis in the transition from SCE behavior to TCE. More details about this work can be found in [3]

Numerical study

We use a two-directional mode rate-equation model of the SRL extended with Lang-Kobayashi terms to take into account the effect of optical feedback. In terms of the mean-field slowly varying complex amplitudes of the electric field associated with the two propagating modes E_m^{cw} and E_m^{ccw} , and the carrier number N , these equations are

$$\dot{E}_m^{cw} = \kappa(1 + i\alpha)[N\mathcal{G}_m^{cw} - 1]E_m^{cw} - (k_d + ik_c^{ccw})E_m^{ccw} + \eta_m E_m^{cw}(t - \tau)e^{i\theta_m} \quad (1)$$

$$\dot{E}_m^{ccw} = \kappa(1 + i\alpha)[N\mathcal{G}_m^{ccw} - 1]E_m^{ccw} - (k_d + ik_c^{cw})E_m^{cw} + \eta_m E_m^{ccw}(t - \tau)e^{i\theta_m} \quad (2)$$

$$\dot{N} = \gamma \left[\mu - N - N \sum_{m=1}^n (\mathcal{G}_m^{cw}|E_m^{cw}|^2 + \mathcal{G}_m^{ccw}|E_m^{ccw}|^2) \right] \quad (3)$$

where "m" refers to different longitudinal modes. In these equations $\alpha=3.5$ is the linewidth enhancement factor, $\kappa=200 \text{ ns}^{-1}$ is the field decay rate, $\gamma = 0.4 \text{ ns}^{-1}$ is the carrier inversion decay rate, $\mu=1.2$ is the normalized injection current, η_m and θ_m represent the feedback strength and phase, respectively, $\tau = 76 \text{ ps}$ is the delay time which corresponds to the propagation time in the filtered feedback section, $k_d = 0.2 \text{ ns}^{-1}$ represents the dissipative backscattering and is taken equal for the two directional modes. A small asymmetry between the two directional modes is introduced via the conservative backscattering coefficients: $k_c^{cw}=0.88 \text{ ns}^{-1}$ whereas $k_c^{ccw}=1.144 \text{ ns}^{-1}$. This asymmetry is needed in order to reproduce the experimentally observed asymmetry in the power output when the gates in the filtered-feedback section are unpumped [8]. The differential gain functions are given by $\mathcal{G}_m^{cw}=(1 - s|E_m^{cw}|^2 - c|E_m^{ccw}|^2)$, $\mathcal{G}_m^{ccw}=(1 - s|E_m^{ccw}|^2 - c|E_m^{cw}|^2)$, where $s=0.005$ is the self saturation and $c = 0.01$ is the cross-saturation between the two directions of the same LM. We have limited the number of LMs to two ($n=2$) as it corresponds to the minimum number of equations needed to describe TCE.

We consider the case for which LM₁ is initially selected by introducing a finite amount of feedback $\eta_1=15 \text{ ns}^{-1}$ in the corresponding filter channel. We then change the feedback strength η_2 experienced by LM₂ while the feedback phases are fixed to $\theta_1 = \theta_2 = 0.5\pi$. As long as η_2 is much smaller than η_1 , LM₁ will be lasing while LM₂ remains switched off. When the feedback strength η_2 becomes comparable to η_1 , the intensity in LM₂

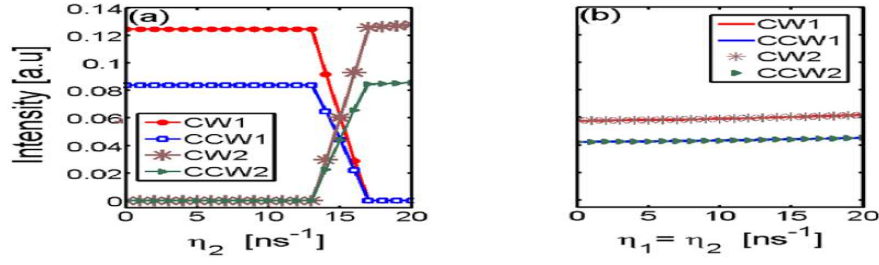


Figure 3: (a) Intensities of both modes when the feedback strength η_2 was increased while η_1 was fixed to 15 ns^{-1} and $\theta_1 = \theta_1 = 0.5\pi$. (b) Intensities of both modes when feedback strengths η_1, η_2 are equal and increased equally at the same time.

gradually grows and it becomes equal to the intensity in LM_1 when η_2 is equal to η_1 . For still higher values of η_2 , LM_1 will gradually be switched off, as can be seen in figure 3(a). This indicates that the TCE is actually due to a precise balancing of the total gain (i.e. including gain, losses and feedback) in the SRL. We also checked in the simulations that there is no hysteresis in the transition between LM_1 and LM_2 plotted in figure 3(a). We obtain the same results by increasing or decreasing η_2 , similarly as in the experiments. The simulations shown in figure 3(a) indicate that TCE is obtained when the feedback strengths in the two selected wavelength channels are equal. This is further elaborated on in figure 3(b) where we plot the simulated intensities when keeping η_1 equal to η_2 and changing both feedback strengths simultaneously. In that case we obtain TCE for all values of the feedback strength. This clarifies why TCE can be observed experimentally for several different values of the gate currents.

Conclusions

In this contribution, we have experimentally and numerically demonstrated that TCE can be achieved in a SRL with filtered optical feedback. The wavelengths can be tuned discretely by selecting different wavelength channels. This can be done by changing the currents injected in the SOA gates to balance the effective gains of the two modes. We have supported these experimental results by numerical simulations which have shown qualitative agreement with the experimental observations.

Acknowledgment

The authors acknowledge the Research Foundation Flanders (FWO) and the Interuniversity Attraction Poles IAP P7-35 photonics@be. This research was also supported by the Hercules Foundation. M. K acknowledges Damascus University for financial support.

References

- [1] J. Buus and E. J. Murphy, "Tunable lasers in optical networks", *IEEE Journ. of Lightw. Techn.*, vol. 24, pp. 5-11, 2006.
- [2] I. V. Ermakov, S. Beri, M. Ashour, J. Danckaert, B. Docter, J. Bolk, X. J. M. Leijtens, and G. Verschaffelt, "Semiconductor ring laser with on-chip filtered optical feedback for discrete wavelength tuning", *IEEE J. Quantum Electron.*, vol. 48, pp. 129-136, 2012.
- [3] M. Khoder, G. Verschaffelt, R. M. Nguimdo, J. Bolk, X. J. M. Leijtens, and J. Danckaert, "Digitally tunable dual wavelength emission from semiconductor ring lasers with filtered optical feedback", *Laser Phys. Lett.*, vol. 10, 075804, 2013.

A Monolithically Integrated Tunable Single Longitudinal Mode Extended Cavity Ring Laser Using Intracavity Mach-Zehnder Interferometers

S. Latkowski¹, T. De Vries¹, L. Augustin¹, M. Smit¹, E.A.J.M. Bente¹

¹ COBRA Research Institute, Department of Electrical Engineering, Technische Universiteit Eindhoven
PO Box 513, 5600 MB Eindhoven, The Netherlands

A ring geometry laser with a wavelength tunable intracavity filter is demonstrated. The device is realized as a photonic integrated circuit and fabricated within COBRA InP active-passive multi project wafer run. The device under test features a three stage asymmetric Mach-Zehnder interferometer filtering scheme allowing for a single mode operation with the side mode suppression and contrast ratios of 43 dB and 60 dB respectively when the laser is DC biased at 2.5 times of the threshold current.

Introduction

An extended ring laser with an intracavity wavelength filter for gas sensing applications is proposed. The wavelength discrimination mechanism is based on a sequence of asymmetric Mach-Zehnder interferometers (AMZI) and has potential for a wide wavelength tuning range. The device is designed and fabricated as a Photonic Integrated Circuit (PIC) which is realized in a multi project wafer (MPW) run within the COBRA active-passive integration platform. Preliminary characterizations of the fabricated device reveal a single-mode (longitudinal) operation, showing a good agreement with initial simulations and design objectives [1].

Laser geometry

The laser under investigation has a geometry as schematically depicted in Fig. 1. It consists of semiconductor optical amplifier (SOA) providing optical gain, the AMZI based wavelength selective filter and a multimode interference coupler (MMI) for coupling out the optical signal. All elements are connected with straight and curved passive waveguides forming an extended ring cavity.

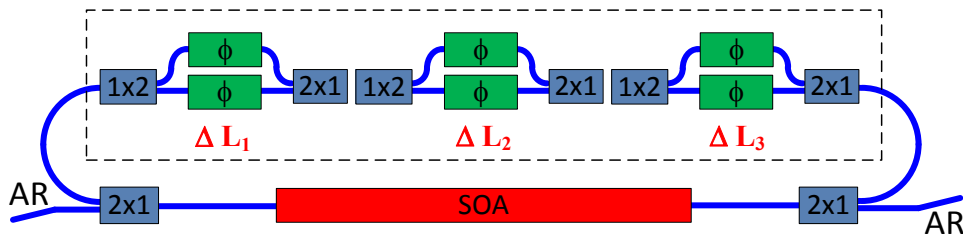


Fig. 1. Schematic diagram of extended cavity ring laser with AMZI based intracavity wavelength selection filter. The ring cavity consists of a three stage wavelength filter (dashed box), semiconductor optical amplifier (SOA), and two 2x1 MMI couplers used for coupling out the optical signal. All components are connected with passive waveguides (in blue).

In the presented configuration, the wavelength filter consists of three AMZIs in series. A transmission of an individual AMZI is periodic with respect to the frequency (wavelength) with a free spectral range $FSR=c/\Delta L_x$ with c being the speed of light in

vacuum and ΔL_x an optical path length unbalance. The unbalanced interferometric configuration enables a tuning mechanism in which a change of the respective optical phase by 2π between the arms tunes the filter over one full FSR regardless of its value. Provided that the length of optical waveguides can be defined on a micrometer scale and efficient phase shifters are available within the integration platform used, AMZI based filters with a tuning range in the order of tens of nanometers (a few terahertz) can be realized [2], [3]. A single AMZI features a finesse of 2 (sinusoidal profile) which in many cases does not suffice when combined with the fundamental mode structure of the laser cavity and a gain profile of semiconductor material to achieve a single mode operation. The mode selection principle of a single AZMI filter combined with resulting longitudinal cavity mode selection is depicted in Fig. 2(a).

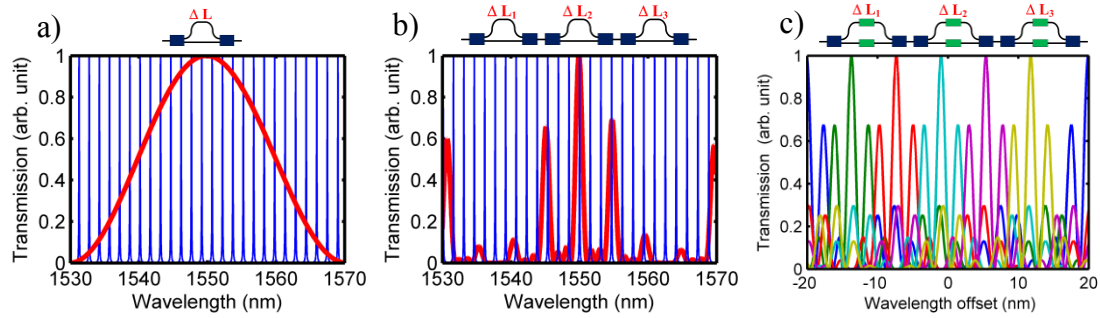


Fig. 2. The transmission profiles of a filter (shown in red color) consisting of (a) a single AMZI and (b) a series of three unbalanced interferometers; longitudinal cavity modes are indicated in blue with the separation frequency scaled up for clarity (c) Examples of filter's transmission envelope for several phase shifter settings, with the control signals S_ϕ applied within $S_{2\pi}$.

A combination of several AMZI in series can improve the finesse of the filter, or using a sequence of AMZIs with e.g. decreasing optical unbalances ($\Delta L_1 < \Delta L_2 < \Delta L_3$) allows one to select the required longitudinal mode of the ring laser cavity. A transmission profile of a three stage serial filter is shown in Fig. 2(b). A relatively simple and predictable tuning scheme can be used when phase shifters ϕ ($\phi=1,2,3$) of equal lengths are used in the AMZIs, as shown in Fig. 1. The equal lengths means the phase shifters require the same control signal $S_{2\pi}$ for a phase delay of 2π . Furthermore, as the unbalances $\Delta L_{1,2,3}$ are fixed, a simple linear relationship between the change in control signals $\Delta S_{1,2,3}$ and the frequency detuning Δf of the series of three AMZIs exists. The required control signals can be calculated from the required detuning Δf as follows:

$$\Delta S_\phi = \frac{\Delta f}{v_g} S_{2\pi} \Delta L_\phi \quad \text{Eq. 1}$$

with v_g being a group velocity. With the relationship given by Eq. 1 a set of S_ϕ control signals within $S_{2\pi}$ can be calculated to allow for continues frequency tuning of the filter over its full FSR, as depicted in Fig. 2(c).

Photonic Integrated Circuit

In the COBRA active-passive integration platform a set of basic building blocks (BB) which can be combined in the form of complex photonic integrated circuits is available. All of these BB are allocated on either active or passive layers stacks grown on InP substrate. The extended cavity ring laser as depicted in Fig. 1. was designed and

fabricated within this technology. The ring cavity consists of a three stage wavelength filter (dashed box in the Fig. 1.), a 1 mm long semiconductor optical amplifier, and two 2x1 MMI couplers used for coupling out the optical signal, all components are connected with passive waveguides. The ring cavity features an overall average length of $L_R=18$ mm with corresponding fundamental free spectral range of 5 GHz (~ 5 nm). The three individual AMZIs are formed by 2x1 MMIs, passive waveguides, and a 1.8 mm phase shifter (ϕ) in each branch to allow for wavelength tuning and calibration. The optical unbalances ΔL_1 , ΔL_2 and ΔL_3 , were selected to be 15 μm , 200 μm , 1529 μm respectively. Such a combination of the AMZIs allows for tuning range of ~ 40 nm while maintaining a single-mode operation. The optical output is angled with respect to the cleaved edge of the chip and antireflection coated in order to reduce impact of potential back-reflections.

Modeling of this ring laser with the PICwaveTM circuit simulator shows that side-mode suppression ratios in the excess of 30 dB can be achieved at any operation point within the 3 dB bandwidth of the SOA as depicted in Fig. 3(a).

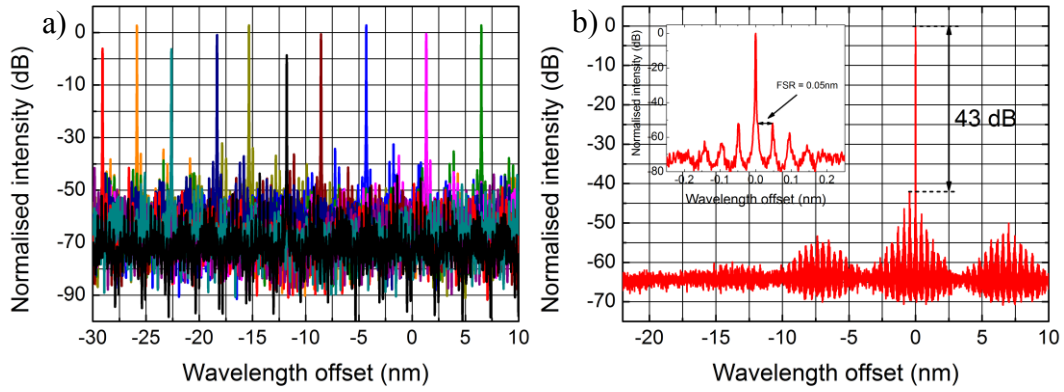


Fig. 3. Spectral output provided by a photonic circuit simulator from a designed PIC based ring laser, for various sets of biasing signals applied to three phase shifters, showing a tunability potential across whole bandwidth of an amplifier (a). Spectral features of a selected operation point showing a single mode operation with SMSR of ~ 43 dB. Inset: Close scale view of the lasing mode and neighboring cavity modes at FSR = 0.05 nm (5 GHz) (b).

Experimental results

The fabricated PIC chip is mounted on aluminum block and electrical contacts of phase shifters and SOA are wire bonded to electrical signal distribution PCBs for an ease of control and characterization. The aluminum sub-mount is temperature stabilized with a passive water cooling system. Optical signal is collected with an antireflection coated lensed fiber and fed with a standard single mode fiber to the measurement equipment being an optical power meter and high resolution (20 MHz) optical spectrum analyzer. At the temperature of 15.5 $^{\circ}\text{C}$, the threshold current has been measured at $I_{th}=48\text{mA}$ as shown in Fig. 4(a). The slope resistance is $R_{sl}=5.5\ \Omega$. A single-mode operation with the SMSR of 43 dB at the bias current $I_{SOA}=134\text{ mA}$ has been achieved as depicted in Fig. 4(b). Spectral properties are in good agreement with the values targeted during the design process.

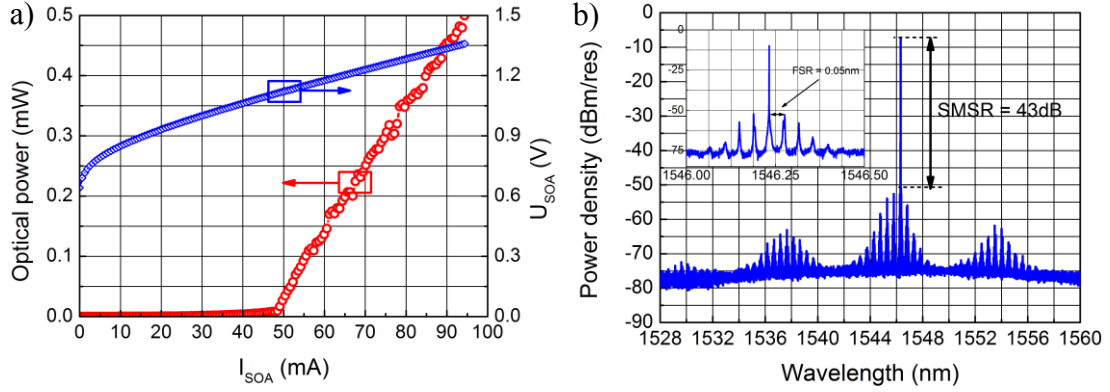


Fig. 4. Characteristics of the device fabricated in COBRA MPW run: optical power and SOA voltage versus bias current characteristics of tested device indicate threshold current $I_{th}=48\text{mA}$ and a slope resistance $R_{sl}=5.5\ \Omega$; (a) a high resolution optical spectrum recorded with SOA section DC biased at $I_{SOA}=134\text{ mA}$ (~ 2.5 of I_{th}) and temperature set at $15.5\ ^\circ\text{C}$. Inset: Detailed view of the lasing mode with neighboring cavity side modes, $\text{FSR}=0.05\text{ nm}$ (5 GHz). (b)

Summary

A tunable ring geometry laser with an intracavity wavelength filters based on AMZI was designed and fabricated on the COBRA photonic integration platform at $1.5\ \mu\text{m}$. The measurement results obtained show a good performance in terms of single mode operation and an optical power of several mW assuming 5 dB coupling efficiency to the fiber, which is also in good agreement with the simulations.

Acknowledgement

Presented research is supported by the Technology Foundation STW under the project 11360 LWAVE-TECH and the NRC Photonics program.

References

- [1] S. Latkowski, M. Smit, and E. A. J. M. Bente, "Integrated tunable semiconductor laser geometry based on asymmetric Mach-Zehnder interferometers for gas sensing applications," in *Proceedings of the 17th Annual Symposium of the IEEE Photonics Society Benelux Chapter*, Mons, Belgium, 2012.
- [2] M. Kuznetsov, P. Verlangieri, A. G. Dentai, C. H. Joyner, and C. A. Burrus, "Asymmetric Y-branch tunable semiconductor laser with 1.0 THz tuning range," *IEEE Photonics Technology Letters*, vol. 4, no. 10, pp. 1093–1095, Oct. 1992.
- [3] S. Calvez, X. Rejeaunier, P. Mollier, J.-P. Goedgebuer, and W. T. Rhodes, "Erbium-Doped Fiber Laser Tuning Using Two Cascaded Unbalanced Mach-Zehnder Interferometers as Intracavity Filter: Numerical Analysis and Experimental Confirmation," *J. Lightwave Technol.*, vol. 19, no. 6, p. 893, Jun. 2001.

DMT based Multi-Gbit/s Communication in Indoor Optical Networks using R-SOA

N.Mehta, E. Tangdiongga, and A.M.J. Koonen

COBRA Research Institute, Dept. of Electrical Engineering, Eindhoven University of Technology, Den Dolech 2, PT 11.06, P.O. Box 513, NL 5600MB, Eindhoven, The Netherlands

After 'fiber to the home', fiber has reached in the room. To make such fiber based indoor networks cost and energy efficient, reflective modulators (like R-SOA and R-EAM) are core components which are also wavelength agile. They remove the need of laser sources at antenna access points for upstream signal. The baseband version of OFDM (i.e. DMT) along with bit-and power-loading algorithm can overcome the bandwidth limitation of R-SOA. In this paper, we have shown experimental results of multi-gb/s communication for upstream signal in indoor optical networks. DMT modulation scheme has been used to obtain throughput of 9 Gb/s with a 750MHz R-SOA.

Introduction

Recent years have seen growing demand for multi-media services such as high definition video streaming in hospitals, sharing of large data files in office building etc. To fulfill this ever increasing bandwidth demand from the users, fiber-to-the-home networks is not sufficient [1]; the fiber needs to be extended till the room. The indoor network architecture we propose is outlined in Fig. 1. For downstream path, we use pencil beams to connect mobile devices in a room. For upstream path, 60GHz radio connection is used for high speed wireless connection [2]. Within each room, there are antenna access points (AAP) which consist of 1) pencil-beam radiating antennas (PRAs): to direct pencil beams 2) receiving antenna and mixer: to capture 60 GHz upstream signal and down-convert it 3) reflective modulators: to re-modulate upstream signal on CW light at a room specific wavelength and send back to central communication controller (CCC). The solution for directive beam steering through PRA is ongoing topic of research. The CCC hosts all the intelligence for routing of wavelengths channels in each room. The CCC hosts all the intelligence for routing of wavelengths channels in each room.

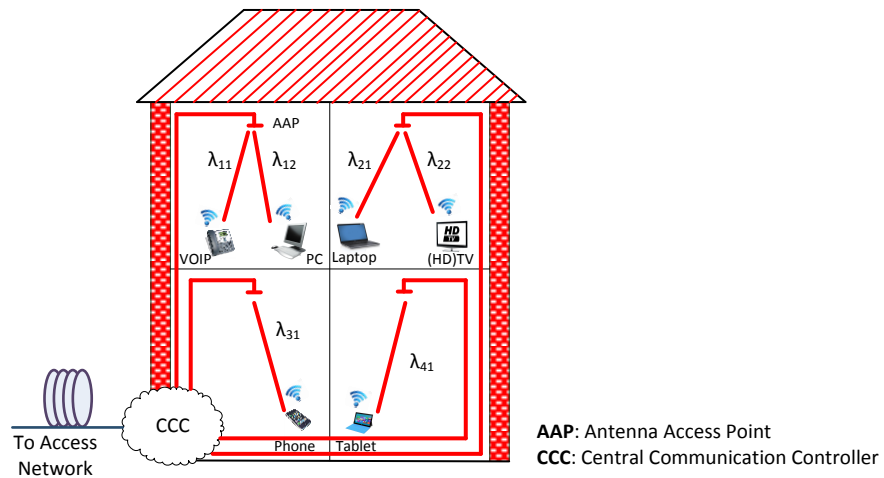


Fig.1. Indoor network infrastructure

The implementation of centrally controlled dynamic wavelength management in CCC allows the reflected upstream signal transmission from the AAP in a wavelength agnostic manner.

Numerous attempts have been made to use colorless reflective modulators at remote end such as reflective-semiconductor optical amplifiers (R-SOA), ASE injected febr-y-perot laser diodes (FP-LDs) and reflective-electro absorption modulator (R-EAM) etc [3,4,5]. R-SOA seems to be very attractive because of its dual properties of modulation and amplification for broad range of wavelengths (~ 40 nm). However the bandwidth limitation of R-SOA is not suitable for next generation optical networks. To overcome the bandwidth limitation we use discrete multi-tone (DMT) modulation scheme. DMT is the base band version of orthogonal frequency division multiplexing (OFDM) which is a multi-carrier transmission technique, where a high data rate stream is split into many lower rate sub-streams and allowing low cost implementation.

In this paper, we experimentally demonstrate the use of DMT for remote modulation of upstream signal by using low bandwidth R-SOA at AAP in indoor optical networks.

Experimental Set-up

Fig 2 presents the experimental set-up. For downstream, we use simple NRZ. For upstream path, DMT is being used to fully exploit the narrow bandwidth of R-SOA. In the experiment, we multiplex NRZ signal (directly modulated at $\lambda_1=1550.16$ nm) and CW signal (at $\lambda_2=1555.84$ nm) and send through 200 m SMF fiber. At AAP, both signals are de-multiplexed. Modulated signal for downstream is sent to PRA for correct directing of a beam to mobile unit and CW light signal is sent to R-SOA (operated at 25°) for re-modulating upstream signal. After re-modulation signal is sent back to CCC through the same fiber. For short distance, Rayleigh scattering is not significant and hence not considered. In this paper, we discuss only upstream performance.

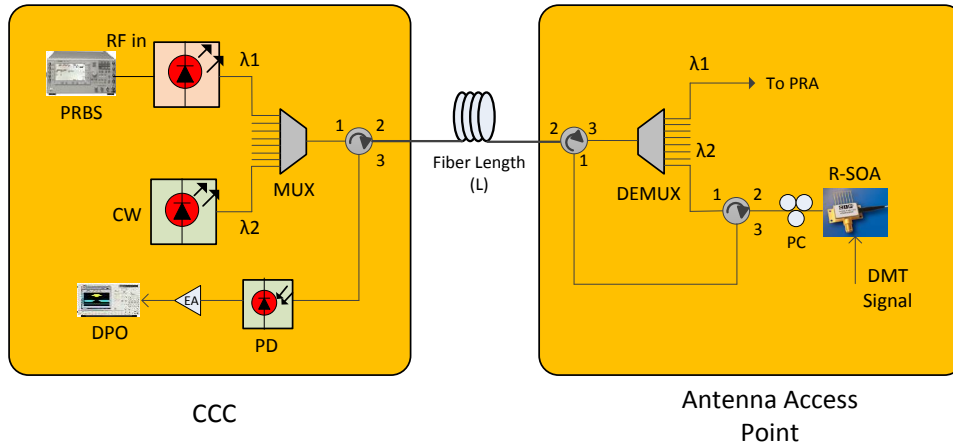


Fig.2. Experimental Set-up

In the experiment, the baseband electrical DMT signal is generated by Tektronix AWG using offline signal processing. Offline signal processing at transmitter side consist of serial to parallel conversion of data, QAM symbol mapping, inverse fast fourier transform, parallel to serial conversion, cyclic prefix (CP) insertion and digital to analog conversion (DAC). For receiving optical signal, we use a photo detector with 7 GHz bandwidth. The received DMT signal is captured with Tektronix 50GHz real time

oscilloscope for demodulation. The demodulation process consists of synchronization, de-mapping of QAM signal, FFT, CP removal, and analog to digital conversion. After demodulation, offline signal processing is done in Matlab for obtaining net throughput.

Experimental Results and Discussion

Fig 3 shows static characterization of R-SOA. Fig. 3 (a) shows the frequency response of R-SOA and fig. 3 (b) shows the throughput versus bias current for different input powers. Higher input power increases the relaxation oscillation frequency and hence the modulation speed of R-SOA [6]. The further analysis is done at 30mA bias (highest throughput point).

Fig 4(a) shows bits allocated to different subcarrier indices after bit loading algorithm. For 2 GHz transmitted bandwidth, 64-QAM is used for subcarriers having higher signal to noise ratio (SNR) whereas for 5 GHz, 16-QAM is used. Corresponding constellation diagram @ $BER < 10^{-3}$ is shown in fig 4(b).

Fig 5 shows throughput versus transmitted bandwidth for two different subcarrier indices. The highest throughput obtained is ~ 9 Gbit/s.

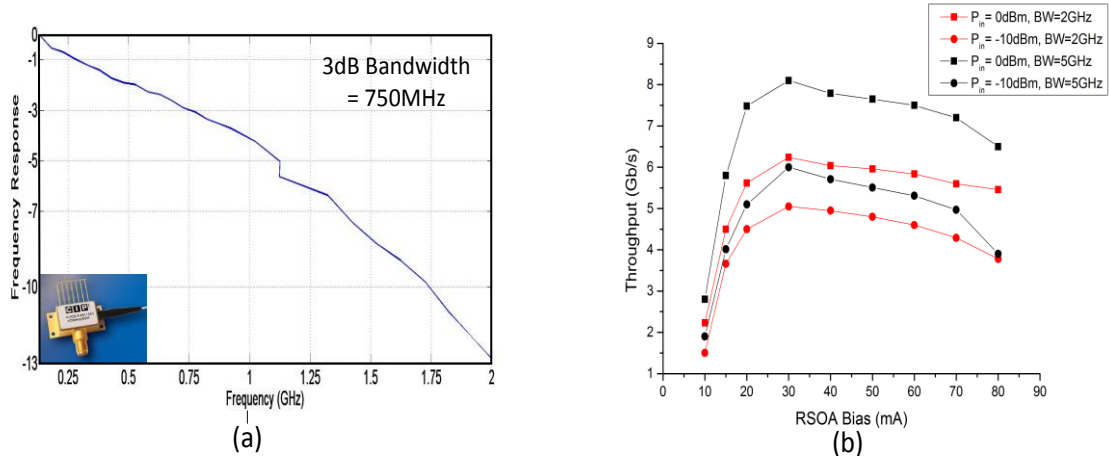


Fig.3. (a) Frequency response of R-SOA; (b) Throughput versus bias current for different input power

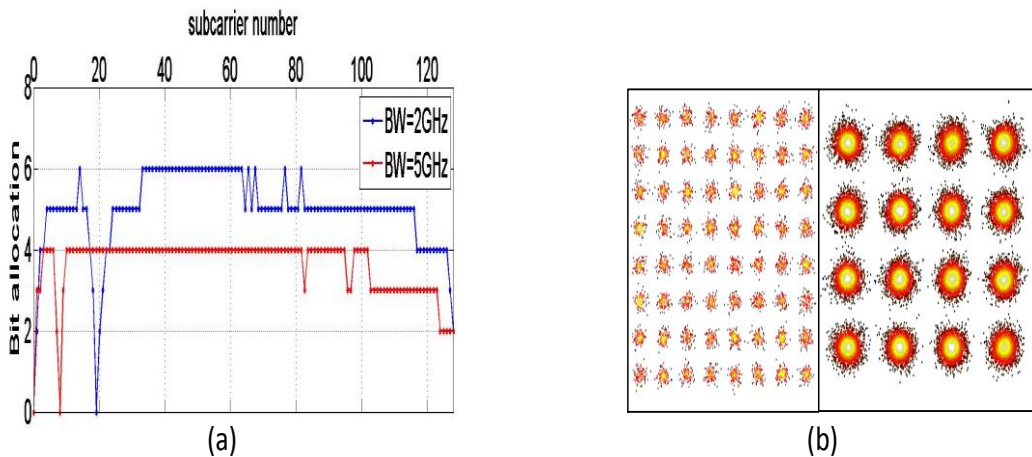


Fig.4. (a) Bit-loading per subcarrier @ $BER < 10^{-3}$; (b) Constellation for BW=2GHz (64-QAM) and BW=5GHz (16-QAM)

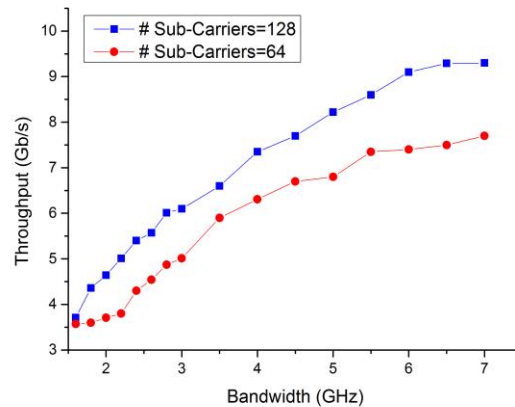


Fig.5. Throughput versus transmitted bandwidth

Conclusion

We have demonstrated the feasibility of operating an R-SOA based indoor optical network architecture by using DMT. Although R-SOA is bandwidth limited by 750MHz, maximum throughput of 9Gbit/s is achieved at $BER < 10^{-3}$ by using 7GHz DMT with 128 sub-carriers. The maximum throughput can further be improved by using reflective-electro absorption modulator (R-EAM) as a reflective modulator.

Acknowledgement

This work is part of the Beam-Steered Reconfigurable Optical-Wireless System for Energy-efficient Communication (BROWSE) project, funded by the European Research Council within the FP7 program.

References

- [1] M. Popov, "The convergence of wired and wireless services delivery in access and home networks," Proc. OFC 2010, San Diego, Mar. 2010, paper OWQ6.
- [2] Su-Khiong Yong, Pengfei Xia and Alberto Valdes-Garcia, "60 GHz technology for Gbps WLAN and WPAN: From theory to practice," John Wiley & Sons Ltd, 2011
- [3] Hong M-K, Tran N.C., Shi Y., Tangdionga E., Han S-K, Koonen A. M J, "10Gb/s transmission over 20km single fiber link using 1GHz RSOA by discrete multi-tone with multiple access," Proc. Optical Communication (ECOC), Sep 2011
- [4] Nguyen Q.T., Vaudel G., Vaudel O., Bramerie L., Besnard P., Garreau A., Kazmierski C., Shen A., Duan G-H, Chanclou P., Simon J.-C., "Multi-functional R-EAM-SOA for 10-Gb/s WDM access," Proc. OFC 2011
- [5] Hanlin Feng, Shilin Xiao, Pei Yang, Zhao Zhou, Jie Shi, "A re-modulation scheme in WDM-PON based on FP-LD and RSOA cascaded structure," *Communications and Photonics Conference (ACP), 2012 Asia*, Nov. 2012
- [6] Chien-Hung Yeh, Chi-Wai Chow, Ming-Feng Chiang, Ci-Ling Pan and Fu-Yuan Shih, "Compensation of power drops in reflective semiconductor optical amplifier-based passive optical network with upstream data rate adjustment," *Opt. Eng.* 50, 095004(2011)

Optomechanically actuated slot cantilever for mass sensing.

Jesper Håkansson¹ and Dries van Thourhout¹

¹ Photonic Research Group(INTEC), Ghent University

NEMS cantilever systems have been pushing the sensitivity of mass, force and pressure sensing over the last decades. However conventional electrical designs for transduction and readout are lacking in bandwidth and free space optical methods are difficult to integrate because of diffraction limits. We demonstrate a broadband, all optically transduced cantilever for mass sensing using end coupled slot waveguides in the silicon platform. Simulations show a displacement responsivity of 1.4 um^{-1} and many times greater forces at lower effective mass for similar designs.

Introduction

NEMS cantilevers are rapidly becoming more attractive as mass sensors in biological and chemical sensing. They are compatible with CMOS fabrication methods allowing dense arrays to be fabricated with small footprint and at low cost. For mass sensing applications the sensitivity of the resonance frequency to changes in mass is utilized as a sensor. Most electrical transduction methods have a limited bandwidth, a problem not found for optical methods. We suggest using end-coupled cantilevers. These have been successfully investigated before [2] [1] and to expand upon this work we suggest utilizing optomechanically transduced slot waveguides. They are an attractive choice because the sharp contrast at the air-silicon boundary enhances both optomechanical forces as well as sensitivity to displacement. Unlike cantilevers which must be bent in post processing to optimize the displacement sensitivity, slot waveguides vibrate in the plane of the substrate can be aligned for optimal sensitivity lithographically. This improves yield and repeatability. By relying on near field effects for transduction and detection we bypass diffraction limits and by not relying on interferometric schemes of detection we get a broadband device that does not need a coherent light source. Another benefit of integrated photonics is that difficulties in alignment are avoided.

Results

Three ways to improve the mass sensitivity of the cantilever has been suggested [3] [4] ; reducing the resting mass of the cantilever, reducing the modal effective mass fraction and increasing the mechanical quality factor. Reducing the dimensions of the cantilever reduces the resting mass but how far this can be taken is limited by practical factors such as retaining a guided optical mode, fabrication limits and the sensitivity of the detection setup. For cantilevers the mass is reduced quite significantly with higher order modes, sadly the force that excites the vibrations is homogenous along the cantilever and thus only the fundamental mode will be efficiently pumped. The quality factor can be increased foremost by reducing the effects of air damping either through increasing the

resonance frequency to the GHz range or through operating the device in vacuum, secondly through reducing clamping losses.

A first order approximation of the frequency response to added mass can be written as [3],

$$\frac{\Delta f}{\Delta m} = -\frac{1}{2}f_n \frac{1}{m_{eff,n}} \quad (1)$$

where f_n is the resonance frequency of the mechanical mode n and $m_{eff,n}$ is the effective mass of the same mode n .

The mechanical actuation of the slot beams is achieved through the optical gradient force. The attractive force generated between the two beams in the slot by the optical field can be calculated using the response theory for optical forces [5].

$$F_q(\omega, q) = \frac{LP_{op}}{c} \frac{\partial N_{eff}}{\partial q} \quad (2)$$

where F_q is the force for a given slot width, q , and optical frequency, ω . L is the interaction length, P_{op} the optical power, c the speed of light and N_{eff} the effective refractive index. The force increases inversely with the slot width so a slot as small as possible would be desirable but we are limited by fabrication to a slot width of 110 nm. From this and the shape of the first vibrational mode it is possible to write down the expected displacement noise at resonance,

$$D_{disp} = \frac{2\pi \cdot P_{pump} \cdot \epsilon_{mode,n} \cdot F_q \cdot Q_{mech} \cdot L^3 \cdot \sqrt{m_{rest}}}{\beta_n^4 \cdot E \cdot I} \quad (3)$$

where $\epsilon_{mode,n}$ is the mean normalized displacement of the vibrational mode n , P_{pump} the amplitude of the modulated optical power, m_{rest} is the resting mass of the cantilever, β_n the eigenvalue corresponding to the vibrational mode, E the Young's modulus and I the area moment of inertia. The displacement is then transduced to optical power as the slot misaligns. The displacement sensitivity,

$$S_{disp} = \frac{\partial T}{\partial q} \quad (4)$$

is calculated using FDTD simulations. The results, shown in Fig. 2b, show that the sensitivity grows with the width of the opposite slot. Because a slot on oxide, when compared to a suspended slot, have a significantly smaller cut off width for the optical mode the slot must be tapered down to a width that can support the mode, see Fig. 3b. We fabricated the cantilevers using the IMEC's standard passives line. It uses DUV-lithography on SOI, the result can be seen in Fig. 3a. The effective mass of the fundamental mechanical mode for a 3μm long cantilever is 263 fg resulting in a frequency shift of 56 Hz/ag. The setup used for detection is shown in Fig. 4. By letting the pump and the probe laser propagate in different directions beat noise is avoided. Ultimately the phase of the signal relative to the pump must be measured and compared to the expected phase difference for forced oscillations to exclude other potential signal sources.

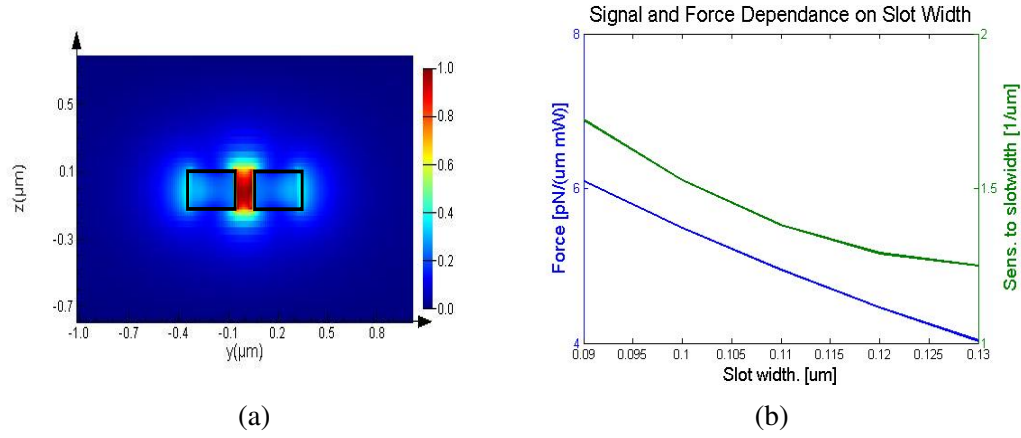


Figure 1: (a) The mode of the electric field in an under etched slot waveguide. The outline of the waveguide is drawn in black. (b) The graph shows how force and responsivity depends on slot width.

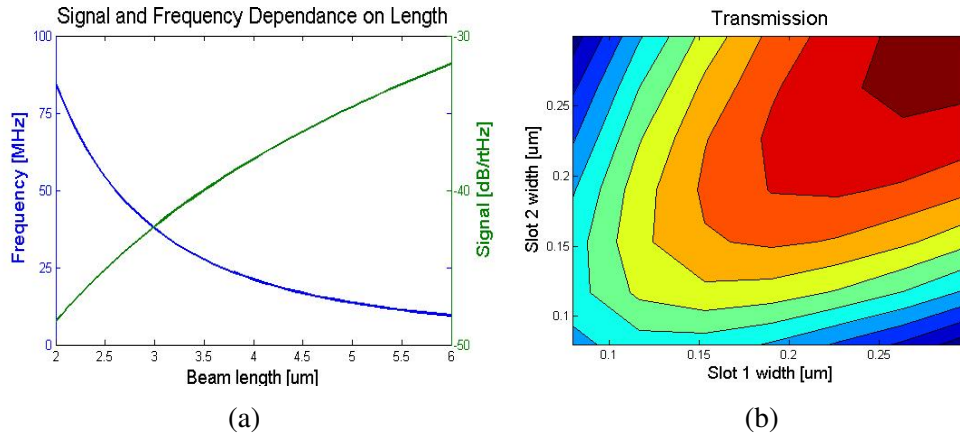


Figure 2: (a) How eigenfrequency and signal strength of the 1st mechanical mode depends on length of the suspended slot. The beams of the slot are 280nm wide and the slot 110nm. Q_m is assumed to be 4000 and P_{pump} is 1 mW. (b) FDTD simulations of the transmission of end-coupled slot waveguides as dependent on the width of the two slots.

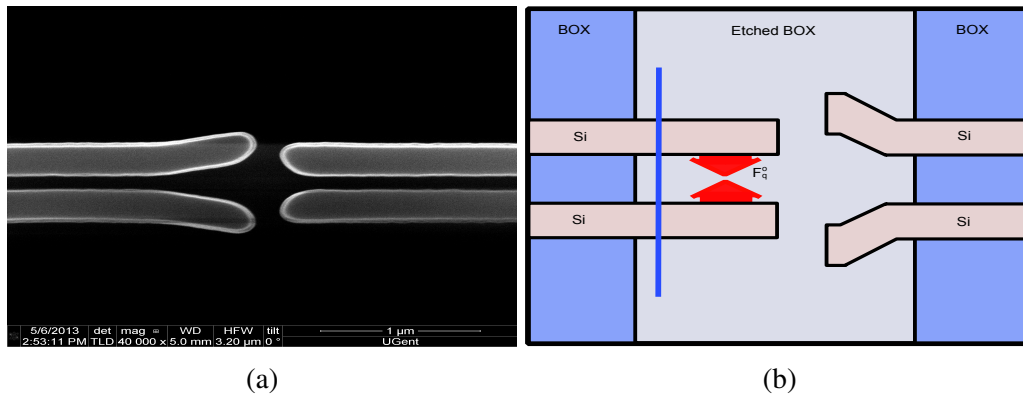


Figure 3: (a) SEM image of the fabricated cantilevers before underetching. (b) An illustrative sketch of the cantilever design as seen with a top view. The red arrow marks the direction of the optomechanical force.

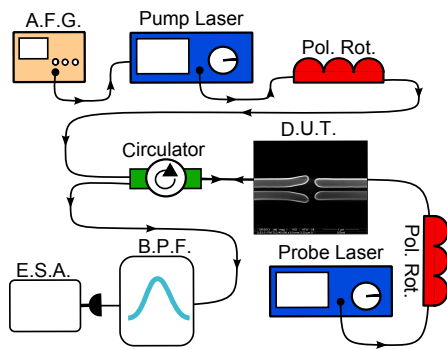


Figure 4: The pump laser is modulated through direct current modulation and excites the vibrations of the cantilever. The probe laser, passing through the cantilever in the opposite direction, is then detected by a photo diode and analyzed by the electric spectrum analyzer. To filter out any reflections of the pump beam a band pass filter is introduced between the circulator and the photodiode.

Conclusion

We have demonstrated a broadband, all optically transduced cantilever for mass sensing using end coupled slot waveguides in the silicon platform. Simulations show a displacement responsivity of $1.4 \text{ } \mu\text{m}^{-1}$ and many times greater forces at lower effective mass compared to previously reported optically transduced devices [2]. As for further improvements the displacement responsivity can be effectively doubled by introducing a broadband bragg reflector after the cantilevers. Simulations show a displacement sensitivity of 40 fm/rtHz . Measurements are to follow.

References

- [1] K. Zinoviev, C. Dominguez, J. A. Plaza, V. J. Cadarso Busto, and L. M. Lechuga, "A Novel Optical Waveguide Microcantilever Sensor for the Detection of Nanomechanical Forces" *Journal of lightwave technology*, vol. 24, no. 5, may 2006
- [2] Mo Li, W. Pernice, H. Tang, "Broadband all-photonic transduction of nanocantilevers", *Nature Nanotechnology* 4, 377 (2009)
- [3] M. Narducci, E. Figueras, M. J. Lopez, I. Gracia, J. Santander, P. Ivanov, L. Fonseca, C. Cane, "Sensitivity improvement of a microcantilever based mass sensor", *Microelectronic Engineering* 01/2009; 86(4):1187-1189.
- [4] Y. T. Yang, C. Callegari, X. L. Feng, K. L. Ekinici, and M. L. Roukes, "Zeptogram-scale Nanomechanical Mass Sensing", *Nano Lett.* 2006, 6 (4), pp 583-586
- [5] Peter T. Rakich, Zheng Wang, Milos A. Popovic, Engineering optical forces in waveguides and cavities based on optical response. *Laser Resonators and Beam Control XII*, 75790C (February 17, 2010)
- [6] J. Chaste, A. Eichler, J. Moser, G. Ceballos, R. Rurali and A. Bachold, "A nanomechanical mass sensor with yoctogram resolution", *Nature Nanotechnology*, 7, 301-304(2012).
- [7] Patrick A. Truitt, Jared B. Hertzberg, C. C. Huang, Kamil L. Ekinici, and Keith C. Schwab, "Efficient and Sensitive Capacitive Readout of Nanomechanical Resonator Arrays", *Nano Letters* 2007 Vol. 7, No. 1 120-126
- [8] Gabrielson, T.B., "Mechanical-thermal noise in micromachined acoustic and vibration sensors" *Electron Devices*, IEEE Transactions on, vol.40, no.5, pp.903,909, May 1993

Experimental refutation of a class of quantum epistemic models

L. Olislager,^{1,*} F. Duport,¹ J. Safioui,¹ M. K. Patra,² S. Pironio,² and S. Massar²

¹ Service OPERA-Photonique, Université libre de Bruxelles, Brussels, Belgium

² Laboratoire d'Information Quantique, Université libre de Bruxelles, Brussels, Belgium

* lolislag@ulb.ac.be

What is the fundamental nature of the quantum state? Is it ontic or epistemic? Or, in other words: does it correspond to a real property of the physical system or does it represent our knowledge about the system? These long-asked questions have seen recent theoretical breakthroughs: no-go theorems show that epistemic models reproducing the results of quantum theory are highly contrived – e.g., discontinuous. We present a simple optical experiment – based on modulated weak coherent states – allowing the experimental verification of one of these no-go theorems, therefore refuting a large class of quantum epistemic models.

Introduction

Quantum theory assigns to every physical system a given *quantum state* $|\psi\rangle$. Such a procedure has been well known for decades. However, there is still no definite answer to the following question: what is the fundamental nature of the quantum state? Let us indeed suppose that our present description of Nature is incomplete: the *real state* λ of a physical system is not known. Then, we have two alternatives.

First, the *ontic* (from Greek "ontos", real) alternative: the quantum state is a real property of the system. In this case, there is a one-to-one correspondence between λ and $|\psi\rangle$: reality corresponds to the quantum state $|\psi\rangle$ possibly complemented by some "hidden variables" that are still not known. Different quantum states $|\psi_1\rangle \neq |\psi_2\rangle$ correspond to different real states $\lambda_1 \neq \lambda_2$.

Second, the *epistemic* (from Greek "episteme", knowledge) alternative: the quantum state is *not* a real property of the system and reflects only our incomplete knowledge of the system – like statistical distributions in classical physics. There are indeed some reasons to doubt of the reality of the quantum state: this mathematical object cannot be measured directly and exhibits counter-intuitive phenomena, such as the measurement postulate and wave-function collapse, which would find a convincing explanation in such a model. With this hypothesis, different quantum states $|\psi_1\rangle \neq |\psi_2\rangle$ can correspond to the same underlying reality $\lambda_1 = \lambda_2$.

The above alternatives, illustrated in figure 1, have been formulated with precision in [1]. In [2], Pusey, Barrett, and Rudolph (PBR) have theoretically shown that these alternatives can be tested experimentally: epistemic models cannot reproduce all the predictions of quantum theory if they satisfy the property, termed *preparation independence*, that independently prepared pure quantum states correspond to product distributions over ontic states. An experiment based on the PBR theorem has been carried on with trapped ions and reported in [3].

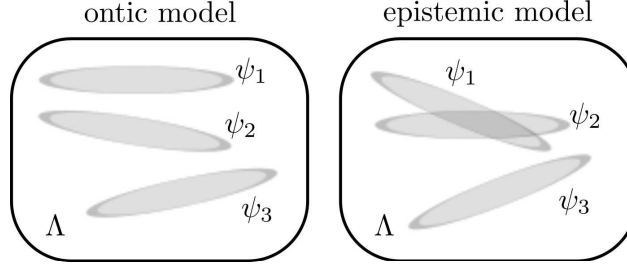


Figure 1: Illustrative distinction between ontic and epistemic models. Depicted are the support of probability distribution $P(\lambda|Q_k)$ for preparation Q_k of a physical system associated with distinct pure quantum states ψ_k , $k = 1, 2, 3$, in the space Λ of real states λ of the system. In an ontic model (left) distinct quantum states give rise to probability distributions with no overlap, while in an epistemic model (right) distinct quantum states may correspond to the same reality, as ψ_1 and ψ_2 in the figure.

The PBR paper has generated a certain "buzz": several studies inspired by this result have flourished, and we will not list them here. We will focus on the result demonstrated by Patra, Pironio, and Massar (PPM) in [4]. They have shown that epistemic models cannot reproduce all the predictions of quantum theory if they satisfy another constraint, a natural property of continuity. The advantage of this no-go theorem is that it allows an experimental test already at the level of a single system, contrary to the PBR argument. We have carried on such an experimental test, reported in [5], by using modulated weak coherent states of light.

In the following, we first present the PPM no-go theorem and outline its demonstration, since it is used for the experimental test. Then, we describe the quantum optics experiment allowing to test the predictions of quantum mechanics. Finally, we summarize the experimental results we have obtained, and conclude on the reality of the quantum state.

Theorem

We start with the definition of what we call δ -continuous epistemic models. Let $\delta > 0$ and let B_ψ^δ be the ball of radius δ centered on $|\psi\rangle$, i.e., B_ψ^δ is the set of states $|\phi\rangle$ such that $|\langle\phi|\psi\rangle| \geq 1 - \delta$. We consider the preparation procedure Q of a physical system, associated with the probability distribution $P(\lambda|Q)$ over real states λ . We say that a model is δ continuous if for any preparation Q , there exists a state λ such that for all preparations Q' corresponding to quantum states $\phi_{Q'}$ in the ball $B_{\psi_Q}^\delta$ centered on the state $|\psi_Q\rangle$, we have $P(\lambda|Q') > 0$.

The PPM no-go theorem states that if an epistemic model were to reproduce the predictions of quantum mechanics, then there is a fundamental constraint on its δ continuity. The theorem is as follows: δ -continuous epistemic models with $\delta \geq 1 - \sqrt{(d-1)/d}$ cannot reproduce all the measurement statistics of quantum states in a Hilbert space of dimension d .

To prove the theorem, we consider d preparations Q_k , $k = 1, \dots, d$, corresponding to distinct quantum states $|\psi_k\rangle$ all contained in a ball of radius δ , and a measurement M that yields one of d possible outcomes $r = 1, \dots, d$. If preparation Q_k is followed by measurement M , we denote by $P(r|M, Q_k)$ the probability of outcome r .

By definition of a δ -continuous epistemic model, it makes the prediction

$$\sum_k P(k|M, Q_k) = \sum_k \sum_\lambda P(k|M, \lambda) P(\lambda|Q_k) \geq \sum_\lambda \min_k P(\lambda|Q_k) \equiv \varepsilon > 0. \quad (1)$$

However, this is in contradiction with quantum theory. Indeed, let $\{|j\rangle : j = 1, \dots, d\}$ be a basis of the Hilbert space. The d distinct states $|\psi_k\rangle = \frac{1}{\sqrt{d-1}} \sum_{j \neq k} |j\rangle$ are all at mutual distance $\delta = 1 - |\langle \psi_k | \psi \rangle| = 1 - \sqrt{(d-1)/d}$ from the state $|\psi\rangle = \frac{1}{\sqrt{d}} \sum_j |j\rangle$. If M is the measurement in the basis $\{|j\rangle\}$, then $P(k|M, Q_k) = 0$ for all k , in contradiction with (1).

Experiment

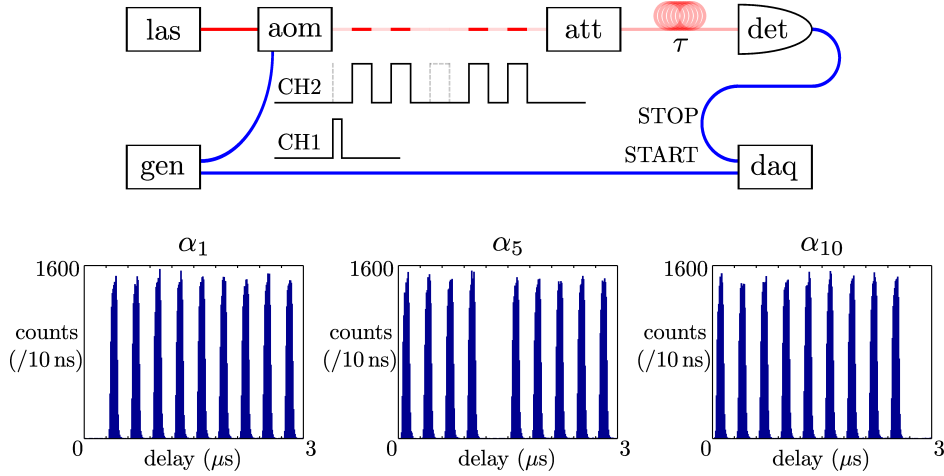


Figure 2: Quantum optics experiment allowing to test the distinct predictions of quantum theory and δ -continuous epistemic models. The light of a long-coherence-time continuous laser (las) in the telecommunication C-band is cut into $d = 3, 10, 30, 50$ or 80 pulses of 100 ns width, with one missing, by an acousto-optic modulator (aom) driven by a pattern generator (gen). The produced coherent states $|\alpha_k\rangle$, with mean photon number $\alpha^2 = 0.2$ after a strong attenuation (att) brings them to the single-photon level, are good approximations of the states $|\psi_k\rangle = \frac{1}{\sqrt{d-1}} \sum_{j \neq k} |j\rangle$, where $\{|j\rangle\}$ denotes a time basis. These states are stored during a time τ in a fiber loop before detection by a superconducting single-photon detector (det). A data acquisition system (daq) registers each detection time relative to the time at which the state preparation began. It thus allows the experimental evaluation of $\varepsilon = \sum_k P(k|M, Q_k)$. In the bottom of the figure are shown the measurement results in the case $d = 10$ for $k = 1, 5, 10$.

Our experimental setup is depicted and commented in figure 2. The proof of the PPM no-go theorem is at the heart of the experiment, which aims to product states $|\psi_k\rangle = \frac{1}{\sqrt{d-1}} \sum_{j \neq k} |j\rangle$, $j, k = 1, \dots, d$, in a Hilbert space of dimension d , measure them in the basis $\{|j\rangle\}$, and evaluate the quantity $\varepsilon = \sum_k P(k|M, Q_k)$. This is realized with modulated weak coherent states of light cut into time bins.

Results

Our experimental results are summarized in table 1.

d	3	10	30	50	80
δ	0.184	0.051	0.017	0.010	0.006
$\epsilon_m \times 10^3$	0.26	0.45	1.27	1.62	1.66
$\Delta\epsilon_m \times 10^3$	± 0.05	± 0.07	± 0.18	± 0.23	± 0.28
$\epsilon_p \times 10^3$	0.24	0.41	0.99	1.58	2.46
$\Delta\epsilon_p \times 10^3$	± 0.09	± 0.15	± 0.37	± 0.58	± 0.88

Table 1: Experimental results. Parameters d are the investigated dimensions of the quantum state space, with the corresponding values of $\delta = 1 - \sqrt{(d-1)/d}$. Measured values ϵ_m are given with their statistical uncertainty $\Delta\epsilon_m$. Values ϵ_p correspond to quantum theory predictions when taking into account experimental imperfections, with approximate uncertainty $\Delta\epsilon_p$ arising from uncertainty on instrument parameters.

Experimentally, the measured values of ϵ are non-zero and seem therefore in conflict with quantum theory prediction $\epsilon = 0$. Nevertheless, our experiment suffers from known imperfections, namely loss, limited detection efficiency, detector dark counts and finite extinction ratio of the modulator. When taking into account these imperfections, our measurements are in agreement with quantum theory predictions, see table 1.

Though because of experimental imperfections all continuous epistemic models cannot be ruled out by our experiment, we can refute a large class of epistemic models, the ones for which $\epsilon > \epsilon_m(\delta)$, with ϵ describing how epistemic the model is, and δ how continuous it is. It shows that, in order to reproduce the predictions of quantum theory, an epistemic model has to be highly discontinuous.

Finally, we note that such a claim can be made only by drawing careful assumptions on the experiment and its interpretation. A more complete discussion and a somewhat tempered conclusion are realized in [5].

Conclusion

In summary, building on recent theoretical breakthroughs, we have experimentally tested the fundamental nature of the quantum state. Our results are in agreement with the predictions of quantum mechanics, and therefore demonstrate – under certain assumptions – the reality of the quantum state.

This research was supported by the European Union under Project QCS, by the FRS-FNRS under Project DIQIP, and by the Brussels-Capital Region through a BB2B Grant.

References

- [1] N. Harrigan and R. W. Spekkens, "Einstein, Incompleteness, and the Epistemic View of Quantum States", *Foundations of Physics* **40**, 125 (2010).
- [2] M. F. Pusey, J. Barrett, and T. Rudolph, "On the reality of the quantum state", *Nature Physics* **8**, 475 (2012).
- [3] D. Nigg, T. Monz, P. Schindler, E. A. Martinez, M. Chwalla, M. Hennrich, R. Blatt, M. F. Pusey, T. Rudolph, and J. Barrett, "Can different quantum state vectors correspond to the same physical state? An experimental test", <http://arxiv.org/abs/1211.0942> (2012).
- [4] M. K. Patra, S. Pironio, and S. Massar, "No-Go Theorems for ψ -Epistemic Models Based on a Continuity Assumption", *Physical Review Letters* **111**, 090402 (2013).
- [5] M. K. Patra, L. Olislager, F. Duport, J. Safioui, S. Pironio, and S. Massar, "Experimental refutation of a class of ψ -epistemic models", *Physical Review A* **88**, 032112 (2013).

Dual polarisation biosensing with an SOI microring

J.W. Hoste,^{1,2} S. Werquin,^{1,2} and P. Bienstman^{1,2}

¹ Photonics Research Group (INTEC), Ghent University - imec

² Center for Nano- and Biophotonics (NB-Photonics), Ghent University,
Sint-Pietersnieuwstraat 41, B-9000 Ghent, Belgium

Optical microresonator biosensors have proven to be a valid tool for binding and affinity analysis of a biological binding event. However, when these microresonators are excited with a single optical mode they can not distinguish between a thin dense layer of biomolecules or a thick sparse layer. We succeeded in exciting a Silicon-on-Insulator (SOI) microring with both TE and TM polarisations simultaneously by using an asymmetrical directional coupler. A theoretical model is provided to solve the shifts of these modes to the thickness and refractive index of the biolayer. During a Bovine Serum Albumin (BSA) adsorption experiment, both shifts were tracked, showing the potential of the sensor for conformational analysis.

Introduction

The current crisis in the drug development industry can be hardly overlooked, with an increase in failure rate and a 50 % drop from 1996 to 2010 in number of applications to the U.S. Food and Drug Administration (FDA) as the main results. Connelly stated in a 2011 *Nature Chemistry Insight* [1] that the reason for this decline can be found in the lack of appropriate high-throughput tools to study molecular behaviour at an analytical and biophysical level of the drug candidates we produce.

To accommodate this, we propose an optical sensor system that can detect conformational changes of proteins. The preferred technology for this is based on microring resonators, designed for the Silicon-on-Insulator (SOI) platform. In a microring, specific optical modes can resonate at specific resonant wavelengths. Current microring resonators exploit this mainly by tracking the resonance wavelength of one optical mode and as such, they are able to measure the surface-bound mass as a function of time. In the past, biosensor arrays with each microring selective to a certain molecule have been reported [2]. Detection limits of this platform are ranging from 0.3 pg/mm^2 - 3 pg/mm^2 , comparable to surface plasmon resonance sensors [3].

However, single-mode optical sensors can't detect a conformational change of bound proteins, since this will not induce a direct change in the amount of bound mass. By simultaneously determining the thickness(t) and the refractive index(n) (which is linked to the

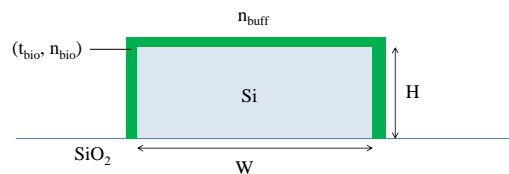


Figure 1: Cross section of the waveguide of which the microring consists.

density) of a biolayer, we can obtain information on the size and shape of biomolecules during binding with ligands. To track both t and n , we propose to excite the microring sensor with two optical modes simultaneously.

Methods & design of sensor

Working principle

The cross section of the microring consists of a 220 nm high silicon rectangle with air cladding, on top of a silicondioxide box. This vertical asymmetry causes the microring to be highly birefringent. The two optical modes that are used for the dual polarisation sensing technique are the fundamental quasi-TE and fundamental quasi-TM modes. In the remainder of this text, we shall call these modes TE and TM modes for ease of notation. The resonance wavelength of these two modes in the microring cavity is determined by:

$$\lambda_{res} = \frac{L n_{eff}}{m} \quad (1)$$

When biomolecules are streamed over the sensor, they can adsorb to the microring surface and form a biolayer with a certain thickness and refractive index, as illustrated in figure 1. The two optical modes interrogate the biolayer at the surface by means of their evanescent tail, that penetrates into the cladding of the waveguide. The capturing of biomolecules on the microring surface is reflected by a perturbation in n_{eff} and thus implies a shift in the resonance wavelength, which is governed by the following equation:

$$\Delta\lambda_{res}(n,t) = \frac{\Delta n_{eff}(n,t) \cdot \lambda_{res}}{n_g} \quad (2)$$

Extraction of (t,n) of the biolayer

The measurement setup tracks $\lambda_{res,TE}$ and $\lambda_{res,TM}$ during the experiment. In order to extract (t,n) of the biolayer, we propose a set of 2 equations linking the resonance wavelength shifts with (t,n) . The shifts are relative to the resonance wavelength when the cladding of the microring is the buffer solution. To find these equations, simulations have been done with the eigenmode solver *Fimmwave*. For a wire waveguide as depicted on Fig. 1, with dimensions W and H , the n_{eff} and n_g of the TE and TM modes are simulated. Using equation 2, $\lambda_{res,TE}$ and $\lambda_{res,TM}$ can be calculated from these indices. We propose a model with two different constants of decay per mode, due to a non-identical effective cladding index at the top and at the side of the waveguide:

$$\Delta\lambda_{TE}(n,t) = \left(\frac{1}{1 + \exp(-a_{TE}t) + \exp(-b_{TE}t)} - \frac{1}{3} \right) [c_{TE}(n - n_{buff}) + d_{TE}(n - n_{buff}^2)] \quad (3)$$

$$\Delta\lambda_{TM}(n,t) = \left(\frac{1}{1 + \exp(-a_{TM}t) + \exp(-b_{TM}t)} - \frac{1}{3} \right) [c_{TM}(n - n_{buff}) + d_{TM}(n - n_{buff}^2)] \quad (4)$$

By using a nonlinear regression algorithm, we can fit the 8 parameters (with the proper constraints) of these equations using a least-square metric, obtaining a R^2 goodness-of-fit of 0.9998 over a range of 200 nm for t and of 0.2 R.I.U for Δn , confirming the validity of this model.

Sensor design

In order to excite both polarisations simultaneously we use an asymmetrical directional coupler, which can couple the TE mode to the TM mode in an adjacent waveguide by using two waveguides with different widths, such that $n_{eff,TE} \approx n_{eff,TM}$. A microring with an asymmetrical coupling section has been examined in [4], where it is shown that a TE mode in the access waveguide can successfully excite a TM mode in the ring waveguide. However, if the gap in the coupling section is sufficiently small, the TE mode in the access waveguide can also excite the TE mode in the ring waveguide even though they have a substantial phase mismatch Δn_{eff} . Due to the proximity of the waveguides, the modal overlap can be large enough as to compensate for the phase mismatch.

The waveguide of the microring was designed to have a width of 480 nm, such that with an access waveguide of 280 nm, a small phase mismatch was achieved between the TE mode of the access waveguide and the TM mode of the ring waveguide of $\Delta n = 0.0516$. On Fig. 2(a), this phase matching is illustrated. Once the sensor was fabricated by imec, fiber to fiber measurements were performed with water as air cladding. The measured spectrum is shown in Fig. 2(b), where we can clearly see two sets of polarisations with a different free spectral range (FSR).

BSA experiment

To show the potential of this sensor, the wavelength shifts of the TE and TM mode were recorded during an adsorption experiment with BSA molecules. A 2mM phosphate buffer saline (PBS) solution was prepared with pH 3 and 5, to which BSA molecules were added until a concentration of 0.1 mg/ml was attained. Some PBS with pH 3 was left as running buffer. The fluids were cycled from BSA in PBS at pH 3 to BSA in PBS at pH 5 and back to BSA in PBS at pH 3, before returning to the running buffer and eventually back to water. The recorded wavelength shifts for both TE and TM mode are shown on fig. 3. There is an increase in wavelength shift for both modes when the fluid is switched from pH 3 to pH 5. This suggests that the adsorbed mass is increased, which is confirmed in [5]. Throughout the experiment, the different behaviour of the TE mode with respect to the TM mode is clearly visible. The TM mode is less confined to the waveguide core and

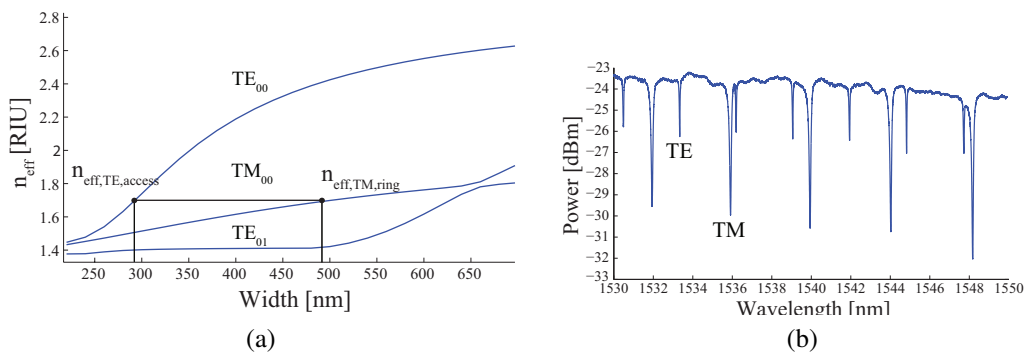


Figure 2: (a) Effective index of the first three guided modes for a rectangular waveguide with a height of 220 nm and water cladding. The black lines show how to phase match the fundamental TE mode with the TM mode. (b) Measured fiber to fiber spectrum of the microring with water cladding. Both the TE and the TM modes are visible

thus more sensitive to variations in the cladding. It is crucial that the TE mode and TM mode behave non-equally in order to make the solving to (t, n) feasible. This first test is a good indication that this biosensor can be used to measure the thickness and the refractive index of a bound biolayer.

Conclusion

We have succeeded in designing a microring which can excite both the fundamental quasi-TE mode and the fundamental quasi-TM mode simultaneously. By means of a BSA adsorption experiment we have shown that we can track the shift of both modes at the same time. A theoretical model has been presented which makes it possible to solve the obtained shifts to the thickness and the refractive index of a bound biolayer, confirming the potential of this sensor for conformational analysis.

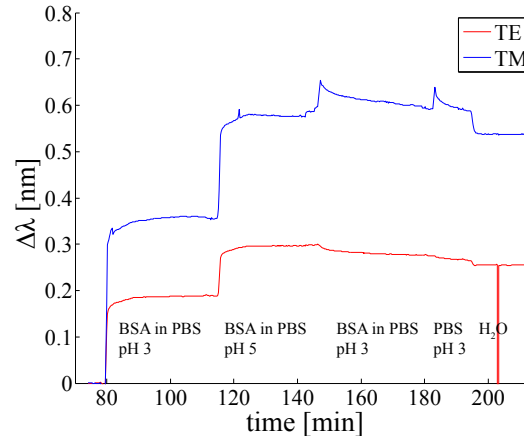


Figure 3: Resonance wavelength shift of the fundamental TE mode and the fundamental TM mode for a BSA adsorption experiment, when cycling through different pH values of the buffer .

References

- [1] P.R. Connelly, T.M. Vuong, M. Murcko, "Getting physical to fix pharma," *Nature Chemistry Insight*, vol. 3, pp. 692-695, 2011.
- [2] K. De Vos, J. Girones, T. Claes et al., "Multiplexed antibody detection with an array of silicon-on-insulator microring resonators," *IEEE Photonics J.*, vol. 1, pp. 225-235, 2009.
- [3] W. Bogaerts, P. De Heyn, T. Van Vaerenbergh, K. De Vos, S. Kumar, T. Claes, P. Dumon, P. Bienstman, D. Van Thourhout, and R. Baets, "Silicon Microring Resonators," *Laser & Photonics Reviews*, vol. 0, pp. 1-28, 2011.
- [4] P. De Heyn, D. Vermeulen, D. Van Thourhout, and G. Roelkens, "Silicon-on-Insulator All-Pass Microring Resonators Using a Polarization Rotating Coupling Section," *IEEE Photonics Technology Letters*, vol. 24, pp. 1176-1178, 2012.
- [5] N.J. Freeman, L. L. Peel, M. J. Swann, G. H. Cross, A. Reeves, S. Brand and J. R. Lu, "Real time, high resolution studies of protein adsorption and structure at the solid-liquid interface using dual polarization interferometry," *J. Phys.: Condensed Matter*, vol. 16, pp. 2493-2496, 2004.

Study of etched polymer optical fiber Bragg gratings for ethanol vapor sensing

X. Hu¹ C. Zhang,² D. Kinet,¹ M. Debligny,² P. Mégret,¹ and C. Caucheteur,¹

¹Electromagnetism and Telecommunication Department, University of Mons,
Bld Dolez 31, 7000 Mons, Belgium

²Material Science Department, University of Mons, Rue de l'Epargne 56, 7000 Mons, Belgium

For the first time to the best of our knowledge, we report an ethanol vapor sensor based on etched fiber Bragg gratings (FBGs) written into step-index polymer optical fibers (POFs). The end of POF with grating was etched by immersion in a mixture of acetone and methanol (ratio 2:1). The etching rate was computed equal to 3.44 $\mu\text{m}/\text{minute}$. Then, the etched FBG was exposed to ethanol vapors mixed with dry air in different concentrations at room temperature. The sensitivity of this sensor was tested with different grating lengths and diameters.

Introduction

Fiber Bragg gratings (FBGs) written in polymer optical fibers (POFs) present several attractive features, especially for sensing purposes. In comparison to FBGs written in silica fibers, they are more sensitive to temperature and pressure, because of the larger thermo-optic coefficient and smaller Young's modulus of polymer materials [1-3]. Although different polymer materials can be used to manufacture POF, the most often encountered one is poly (methyl methacrylate) (PMMA). Unlike silica, PMMA demonstrates absorption of moisture up to 2 w.t. %, so that PMMA FBGs can be used as humidity sensor [4], biochemical concentration sensor [5] and water detection sensor [6]. Besides water, PMMA can swell and vary its refractive index with low molecular weight alcohols [7]. Ethanol sensing has been tested in silica fiber Bragg grating coated with PMMA [8].

In this paper we demonstrate etched PMMA fiber Bragg gratings ethanol vapor sensor in the telecommunication window around 1550 nm. The fiber contains trans-4-stilbenemethanol in the core, as a photosensitive material, which makes inscription available with laser wavelength ranging around 310 nm [9,10]. FBGs were produced through the use of a phase mask and a Helium-Cadmium laser emitting at 325 nm. Using cylindrical lenses, the beam width was adjusted to the core of the desired grating in a single exposition. POF with grating was etched in a mixture solution then, it was exposed to ethanol vapors mixed with dry air in different concentrations.

Experimental setup for FBGs fabrication

Figure 1 depicts a sketch of the experimental set-up that was used to manufacture FBGs in POFs. Figure 2 shows the real devices in the experiment. The fiber was supplied by *The Hong Kong Polytechnic University*. It has a core diameter of 8.2 μm and a cladding diameter of 150 μm . The core is made of PMMA doped with Diphenyl sulfide (5 mol%) and Trans-4-stilbenemethanol (1 w.t. %) while the cladding is in pure PMMA. The refractive indices are computed equal to 1.5086 and 1.4904 for the core and the cladding, respectively, at the wavelength of 589 nm. The laser used in this work is a He-

Cd laser (Kimmon IK5751I-G) with an output power of 30 mW at 325 nm. The output beam diameter of the laser is 1.2 mm. The inscription was made from the top, and a uniform phase mask (Coherent) with a period of 1044 nm was placed above the fiber as closely as possible. Two plano-convex cylindrical lenses were incorporated in the inscription setup. One of the cylindrical lenses with 10 cm focus length was just in front of the phase mask, which was used to increase the power density on the core. The other lens was used to expand the laser beam diameter in the cross direction. Here, 10 mm long FBGs were photo-inscribed in the set-up. The inscription time was 45 minutes.

The grating was located at the end of a short section of POF (typically 5 cm) that was glued (using Norland optical adhesive 78) to a standard silica optical fiber pigtail.

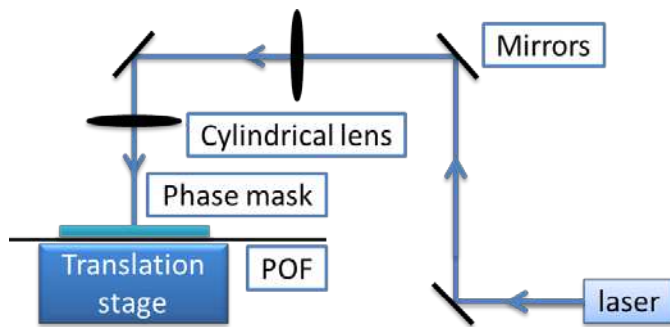


Figure 1: Sketch of the experimental set-up used for grating inscription in POF.

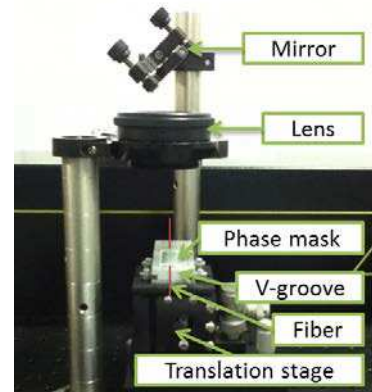


Figure 2: Real opto-mechanical devices in the experiment.

Etching process

The POF was etched by immersion in a mixture of acetone and methanol (ratio 2:1). Figure 3 shows the evolution of POF diameter when being etched. The etching rate was computed equal to 3.44 $\mu\text{m}/\text{minute}$, so that, after 30 minutes, the remaining fiber diameter was estimated to 47 μm . Figure 4 shows the evolution of the FBG reflected spectrum. A blue shift occurs during the etching process, which is attributed to the release of water molecules. At the end of etching process, the fiber was broken in the center of FBG. So the remaining length of FBG is estimated around 1 mm. Figure 5 shows the final FBG spectrum, which was used after drying in air during 2.5 hours.

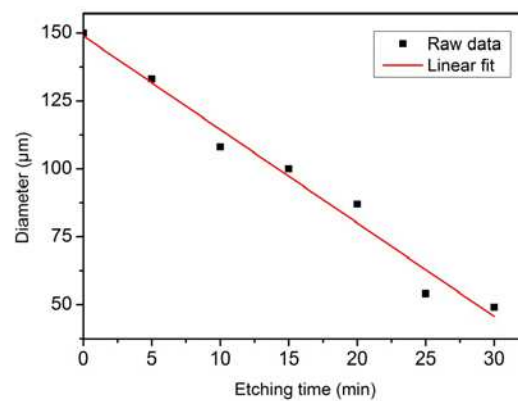


Figure 3: Evolution of the POF diameter during etching process.

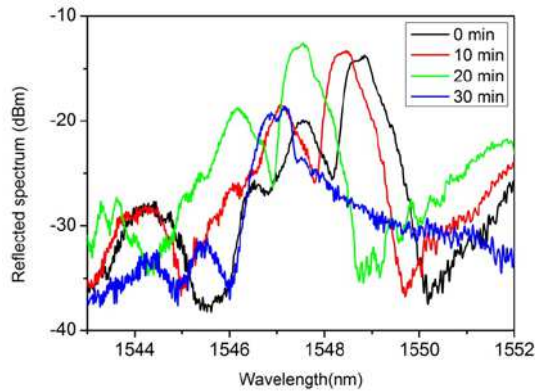


Figure 4: Evolution of the FBG reflected spectrum during etching process

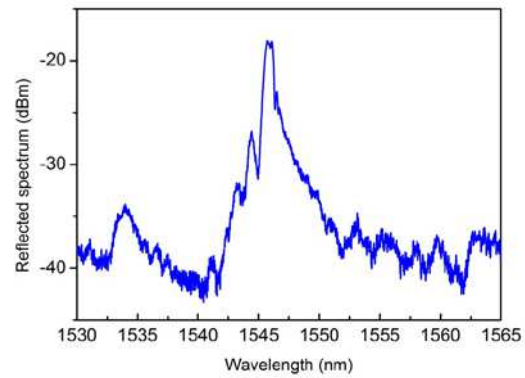


Figure 5: FBG reflected spectrum after 2.5h drying

Experimental setup for ethanol vapor test

The performances of the sensors were measured in a glass chamber which is connected with dry air and ethanol vapors at room temperature. The ethanol vapors were generated in bubbler when dry air was going through. The ethanol vapor concentration was controlled by adjusting two volume flow rates. Figure 6 shows that the total Bragg wavelength shift for the peak around 1546 nm occurred within 2 minutes of exposure while the recovery in dry air lasts for ~15 minutes. Finally, Figure 7 shows that the sensitivity of this sensor is equal to 56 pm/% of ethanol vapor concentration. Similar experiments were conducted on non-etched FBG and no response was obtained.

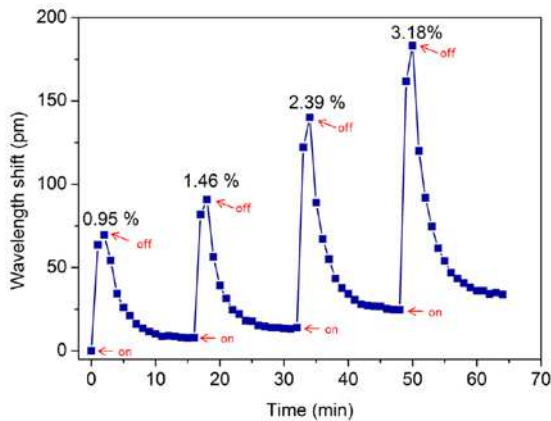


Figure 6: Wavelength shift of the etched FBG for different ethanol concentrations as a function of time.

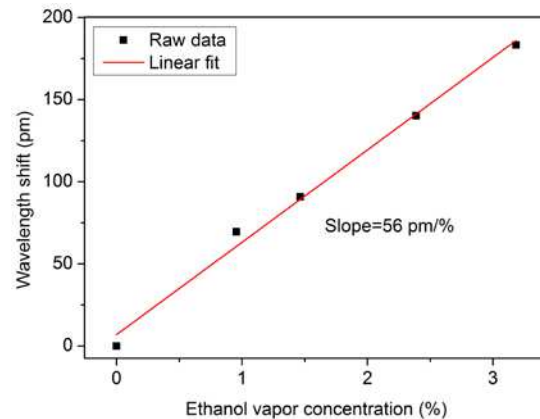


Figure 7: Sensitivity of ethanol vapor sensor.

Discussions

We have tested different fiber thicknesses ranging from 40 to 80 μm and different grating lengths varying between 1 mm and 4 mm. The results presented in Figure 6 are the best obtained until now. We are currently investigating the combined effect of fiber thickness and grating length on the sensitivity of the device. Although a full control is difficult to achieve, our observations are the following: in order to get a higher

sensitivity and faster response, thinner fiber with FBG is needed. Short length of FBG can dramatically decrease the drift during sensing test.

Conclusions

In this paper, we have reported an ethanol vapor sensor based on etched fiber Bragg gratings (FBGs) written into step-index POFs. The end of POF with grating was etched by immersion in a mixture of acetone and methanol (ratio 2:1). The etching rate was computed equal to 3.44 $\mu\text{m}/\text{minute}$. Then, the etched FBG was exposed to ethanol vapors mixed with dry air in different concentrations at room temperature. The sensitivity of this sensor is equal to 56 pm/% of ethanol vapor concentration.

Acknowledgements

Authors gratefully thank Professor Tam from *the Hong Kong Polytechnic Institute* for providing the optical fiber used in this work. This research has been conducted in the frame of the *ERC (European Research Council) Starting Independent Researcher Grant PROSPER* (grant agreement N° 280161 – <http://www.umons.ac.be/erc-prosper>) and the *Actions de la Recherche Concertées* research programme (PREDICTION project) supported by the *Ministère de la Communauté française de Belgique—Direction générale de l'Enseignement non obligatoire et de la Recherche scientifique*. C. Caucheteur is supported by the F.R.S.-FNRS.

References

- [1] W. Yuan, A. Stefani, “Tunable Polymer Fiber Bragg Grating (FBG) Inscription: Fabrication of Dual-FBG Temperature Compensated Polymer Optical Fiber Strain Sensors”, *IEEE Photonics Technology Letters*, 24, 5, 401-403, 2012.
- [2] X. Chen, C. Zhang, D.J. Webb, G.D. Peng, K. Kalli, “Bragg Grating in a Polymer Optical Fibre for Strain, Bend and Temperature Sensing”, *Measurement Science and Technology*, 21, 9, 094005, 2010.
- [3] X. Hu, D. Kinet, K. Chah, P. Mégret, C. Caucheteur, “Bragg Gratings Inscription at 1550 nm in Photosensitive Step-Index Polymer Optical Fiber”, in *Proceedings of SPIE 8794*, 87942Q, 2013.
- [4] Z.F. Zhang, X.M. Tao, “Synergetic Effects of Humidity and Temperature on PMMA Based Fiber Bragg Gratings”, *Journal of Lightwave Technology*, 30, 6, 841-845, 2012.
- [5] W. Zhang, D. Webb, G. Peng, “Polymer Optical Fiber Bragg Grating Acting as an Intrinsic Biochemical Concentration Sensor”, *Optics Letters*, 37, 8, 1370-1372, 2012.
- [6] C. Zhang, X. Chen, D.J. Webb, G.D. Peng “Water Detection in Jet Fuel Using a Polymer Optical Fibre Bragg Grating”, in *Proceedings of SPIE 7503*, 750380, 2009.
- [7] J.S. Papanu, D.W. Hess, D.S. Soane (Soong), A.T. Bell, “Swelling of Poly(methyl methacrylate) Thin Films in Low Molecular Weight Alcohols”, *Journal of Applied Polymer Science*, 39, 4, 803-823, 1990.
- [8] M. Latino, R. Montanini, N. Donato, G. Neri, “Ethanol Sensing Properties of PMMA-Coated Fiber Bragg Grating”, *Procedia Engineering*, 47, 1263–1266, 2012.
- [9] J.M. Yu, X.M. Tao, H.Y. Tam, “Trans-4-stilbenemethanol-doped Photosensitive Polymer Fibers and Gratings”, *Optics Letters*, 29, 2, 156–158, 2004.
- [10] J.M. Yu, X.M. Tao, H.Y. Tam, D.X. Yang, M.S. Demokan, “Photosensitivity and Grating Development in Trans-4-stilbenemethanol-doped Poly(methyl methacrylate) Materials”, *Optics Communications*, 265, 1, 132–139, 2006.

Simultaneous 1.5 Gbps Multilink Indoor Optical Wireless System Using Diffractive Optics

C. W. Oh, E. Tangdionga and A. M. J. Koonen

COBRA Research Institute, Eindhoven Univ. of Technology, P.O. Box 513, 5600MB Eindhoven, The Netherlands.

The shortage of available radio spectrum, catering to the ever increasing bandwidth demand, has impelled many initiatives to look for alternative measures. In the advent of optical wireless systems, high speed networks with vast amount of bandwidth can be realized. Multiple links can be provided to one or more users simultaneously by using efficient beam steering methods. An investigation for indoor optical communication system using diffractive optics has been carried out. This paper demonstrates that up to at least five simultaneous 1.5 Gbps NRZ-OOK links, with BER less than 10^{-9} , can be deployed.

1. Introduction

Many might still recall the arrival of portable devices, especially cell phones and personal digital assistants (PDAs), with embedded Infrared Data Association (IrDA) transceivers in the 90's, for one-to-one short range communication. Then, the first cell phone with Bluetooth arrived in the year 2000, which featured a better coverage of approximately 10m[1]. At about the same time, GPRS was introduced[2]. GPRS is an extension of the GSM network, where users can have access to the internet. This is followed by other technologies that offer better data rates. The Wireless Fidelity (WiFi) technology, which also uses radio signals, is similar to Bluetooth, but constitutes a much greater area. WiFi is by far the fastest and most stable mobile protocol at this point of time[3]. One thing all these technologies have in common is the reliance on radio waves, but is there enough room in the radio spectrum for all? Consider also that Cisco's Internet Business Solutions Group predicts some 50 billion devices that will be connected by 2020. Since year 2008, already more devices are connecting to the internet than people[4]. The radio spectrum is getting congested and devices are interfering with each other. With the explosion of wireless traffic over the next few years, solutions to enable support for the forecasted booming communication traffic are necessary[5][6].

Foreseeing the broad and unregulated bandwidth in the THz frequency, the optical spectrum has much to offer. A considerable amount of research on the visible light spectrum has been carried out. The visible light communication systems (VLC) have a basic system limitation on the bandwidth, i.e. a few 100s of mbps[7][8][9], up to the state of art of 3.22 Gbps, where wavelength division multiplexing (WDM), carrier-less amplitude and phase (CAP) modulation, and RGB light emitting diodes (LEDs) are employed[10]. The infrared communication systems, on the other hand, employ laser diodes, where high bandwidth is achievable due to narrow spectral linewidth. Data rates can go up to terabits per second. Furthermore, ambient light, which is the dominant noise in VLC systems, is eliminated. Since the emergence of fiber-to-the-home (FTTH) technology in 2004, infrared wireless communication is seen as a promising solution to bridge wirelessly the gap to the end user[11].

In this paper, we propose an infrared-based indoor optical wireless solution, employing passive diffractive optics for beam steering. We demonstrate the feasibility of using a passive grating as the beam steering medium for short-range indoor optical wireless communication. Therefore, we have compared the performance of the diffracted beams to the performance of a free space beam, and to the performance of a back-to-back (BtB) measurement with a 2m long single mode fiber(SMF). Subsequently, a multilink free space transmission of 1.5 Gbps, steered over 35cm, with bit error rate (BER) less than 10^{-9} , is demonstrated.

2. Indoor Optical Wireless System

Indoor optical wireless systems can be implemented as line-of-sight (LOS) or non-line-of-sight (NLOS) systems[12][13]. LOS systems are typically suited for point-to-point communication via highly directional power efficient beams, and therefore, require precise alignment. NLOS systems, on the other hand, are appropriate for point-to-multipoint systems via wide angle transmission, and thus, require less critical alignment. In addition, the implementation of a wireless network could be a hybrid of optical and radio links. As uplinks typically do not require as much bandwidth, radio wireless systems could be an option. Intelligence can be added to these systems to enable user

localization, and to have a power efficient system, for example, transmission can be turned off when there are no users and only transmits to a particular user when necessary. Fig. 1 shows a typical wireless- equipped building with fibers, such as SMF fiber, multimode fiber or plastic optical fiber[14], as the in-building backbone network. The building is equipped with a central communication controller (CCC), where it will receive traffic from the access network and route it to all the access nodes; in our case, beam steering modules (BSM) in different rooms.

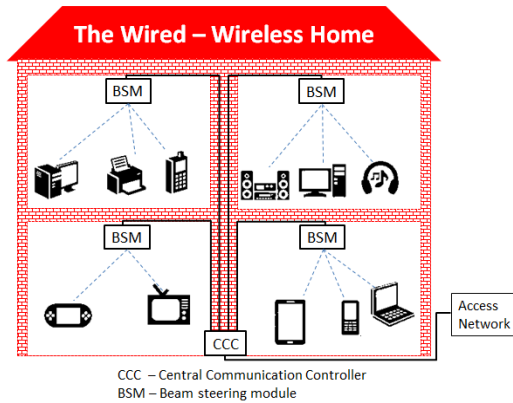


Fig. 1 Wired-Wireless-equipped home with beam steering modules

3. 1D Diffraction for Beam Steering

The novelty of our method for beam steering leads from the principle of diffraction. Diffraction stems from the ability of waves to bend, leading to a divergent profile as it propagates away from its source. At the same time, waves coincide constructively and destructively with neighbouring waves to give rise to interference. This phenomenon results in an array of bright and dark intensity patterns on the screen. These bright patterns are the spots where light beams are formed, as seen in Fig. 2c, which we can use as the medium of transmission in the optical wireless domain. The obvious advantage is that we gain from having multiple spots. These spots translate meaningfully into instantaneous multiple links with the capability of each link to carry the same amount of capacity. This is a win-win power-capacity sharing system, with a gradual power loss as the light intensity falls off towards higher angle diffracted beams. Yet, the same amount of data capacity can be transmitted in each link. As such, this solution is scalable depending on the available power budget of the system.

4. Experiment Setup and Results

The experiments were carried out with a non-return-to-zero on-off-keying direct-modulated 1558.98nm laser diode, with pseudorandom binary sequence of $2^{31}-1$ elements. The first experiment is carried out as shown in Fig. 2a. A beam of 3.3mm in diameter is launched through an SMF pigtailed coupler with a lens of 18mm in focal length, for a distance of 25cm, towards a near Littrow-mounted echelle grating. The free space transmission is received by another SMF pigtailed fiber placed at a horizontal distance of 35cm from the grating, attenuated, and finally, evaluated with a BER tester and eye-diagram. In the second experiment, the grating is replaced with a silver coated mirror mounted at 45° from the incident beam, while maintaining the rest of the setup, as shown in Fig. 2b. For the BtB measurement, the Tx and Rx couplers are replaced with a 2m long SMF fiber.

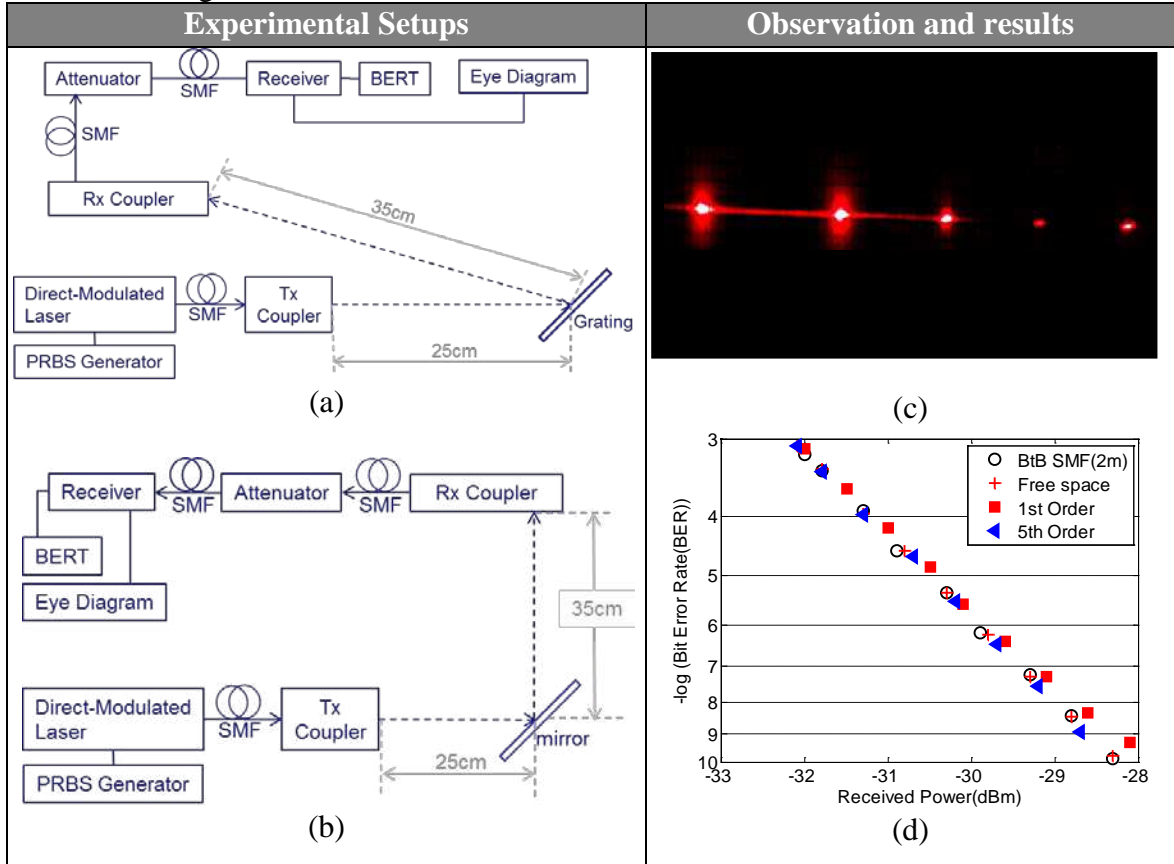


Fig. 2a) Experimental setup for free space transmission with grating b) Experimental setup for free space transmission with mirror c) Bright spots formed after diffraction grating with 657nm laser d) Resultant BER plot for BtB SMF with length of 2m, free space transmission with mirror and transmission of 1st and 5th diffracted orders of an echelle grating.

Clean open-eye diagrams are observed indicating negligible dispersion. The BER performance of the transmitted links, against the received power in dBm, is presented in Fig. 2d. The good overlap of the plot for BtB, free space, 1st order and 5th order links show that the grating induced negligible power penalty. We observe ≤ 1 dB, for up to the 5th order diffraction, compared to BtB. The distance of measurement and the number of links are scalable depending on the available power budget; therefore, measurements for a longer distance as well as more links can be measured if there is enough space on the testbed.

5. Conclusion

We have demonstrated, for the first time, a simultaneous multilink carrying 1.5 Gbps each, with a free space transmission of over 60 cm, by which 35 cm between grating and receiver plane are diffracted links. Additionally, a BER of $<10^{-9}$ has been achieved. In short, these results are promising for the deployment of gratings as the beam steering medium for indoor optical wireless system. The system complies with the eye-safety regulations) formulated in the ANZI Z-136 in the US and the international IEC 60825 specifications.

This work is part of the Beam-steered Reconfigurable Optical-Wireless System for Energy-efficient communication (BROWSE) project, funded by the European Research Council within the FP7 program.

7. References

- [1] "History of Bluetooth Special Interest Group," Bluetooth® [Online]. Available: <http://www.bluetooth.com/Pages/History-of-Bluetooth.aspx>, 2013 [Oct. 14, 2013].
- [2] R. Keller, "General Packet Radio Service (GPRS)" [Online]. Available: <http://misnt.indstate.edu/harper/Students/GPRS/GPRS.html> [Oct. 14, 2013].
- [3] "Mobile Marketing 101: Chapter 4: Mobile Technologies: SMS, MMS, USSD & Bluetooth/Wireless/Infrared," Quirk eMarketing [Online]. Available: http://www.quirk.biz/cms/3188.quirk_emarketing_mobile_marketing101_ch4.pdf [Oct. 14, 2013].
- [4] "The internet of things," Cisco [Online]. Available: <http://share.cisco.com/internet-of-things.html>, 2011 [Oct. 14, 2013].
- [5] G. Parodi, "Radio spectrum shortage prompts a growing number of initiatives," L'Atelier [Online]. Available: http://www.atelier.net/en/trends/articles/radio-spectrum-shortage-prompts-growing-number-initiatives_422770, July 15, 2013 [Oct. 14, 2013].
- [6] E. Savitz, "The solution to the wireless spectrum shortage: more wires," Forbes [Online]. Available: <http://www.forbes.com/sites/ciocentral/2012/03/23/the-solution-to-the-wireless-spectrum-shortage-more-wires/>, March 23, 2012 [Oct. 14, 2013].
- [7] Y. Wang, Y. Shao, H. Shang, X. Lu, Y. Wang, J. Yu, and N. Chi, "875-Mb / s Asynchronous Bi-directional 64QAM-OFDM SCM-WDM Transmission over RGB-LED-based Visible Light Communication System," Proceedings of the Optical Fiber Communication Conference and Exposition (OFC) National fiber optic engineers conference (NFOEC), 18–20, 2013.
- [8] G. Cossu, A. M. Khalid, R. Corsini, and E. Ciaramella, "Non-Directed Line-of-Sight Visible Light System providing High-Speed and Robustness to Ambient Light," Proceedings of the Optical Fiber Communication Conference and Exposition (OFC) National fiber optic engineers conference (NFOEC), 2–4, 2013.
- [9] W. Joachim and C. Technology, "Light LEOs OSC Colour Filter LED lamp," vol. 1, no. 1, 3–4.
- [10] F. Wu, C. Lin, C. Wei, C. Chen, Z. Chen, and H. Huang, "3.22-Gb / s WDM Visible Light Communication of a Single RGB LED Employing Carrier-Less Amplitude and Phase Modulation," Proceedings of the Optical Fiber Communication Conference and Exposition (OFC) National fiber optic engineers conference (NFOEC), 22–24, 2013.
- [11] T. Koonen, "Fiber to the home/fiber to the premises: What, where, and when?," Proceedings of the IEEE, vol. 94, No. 5, 911–934, 2006.
- [12] J. M. Kahn and J. R. Barry, "Wireless Infrared Communications," Proceedings of the IEEE, vol. 85, No. 2, 265–298, 1997.
- [13] H. Elgala, R. Mesleh, and H. Haas, "Indoor optical wireless communication: potential and state-of-the-art," IEEE Communications Magazine, vol. 49, no. 9, 56–62, 2011.
- [14] A. M. J. Koonen, H. P. a van den Boom, E. Ortego Martinez, a Pizzinat, P. Guignard, B. Lannoo, C. M. Okonkwo, and E. Tangdionga, "Cost optimization of optical in-building networks.," Optics express, vol. 19, no. 26, 399–405, 2011.

Part III

Poster contributions

Integrated dual-wavelength AWG laser for sub-terahertz wave generation

A. Corradi¹, G. Carpintero², M. K. Smit¹ and E.A.J.M. Bente¹

¹ COBRA Research Institute, Eindhoven University of Technology, PhI Group, Eindhoven, The Netherlands

² UC3M, Universidad Carlos III de Madrid, Spain

We present a monolithically integrated ring dual-wavelength semiconductor laser in which both wavelengths (λ_1 and λ_2) are generated and amplified by the same semiconductor optical amplifier (SOA). An arrayed waveguide grating (AWG) is used as intra-cavity filter to combine the two wavelengths. The use of a Mach-Zehnder construction allows equalizing actively the power of λ_1 and λ_2 and tuning their frequencies. An analytical model is exploited to investigate the influence of crosstalk on the functioning of the device and to identify a calibration strategy. The device has been fabricated using active/passive integration technology on a standardized photonic integration platform.

Introduction

The development of new applications of millimeter waves (mmWs) and terahertz (THz) radiation faces a lack of sources: this frequency range is known in literature as the “terahertz gap” [1]. In this paper we report on research into the development of an integrated dual wavelength laser that can be part of a millimeter wave transmitter. The design and fabrication of the device are done using existing standardized optical semiconductor device design platform and fabrication process based on InP [2].

Photonic-based millimeter wave generation

Several techniques based on photonics to generate millimeter waves have been reported in literature [3]. These methods are all based on generating an optical carrier wave with an amplitude modulation at the required millimeter wave frequency. In most systems this light is then modulated with the data to be transmitted and directed towards a high speed photodiode (Fig. 1). The photodiode rectifies the optical signal and the resulting millimeter wave signal can then be amplified electronically and coupled to a transmitting antenna [1].

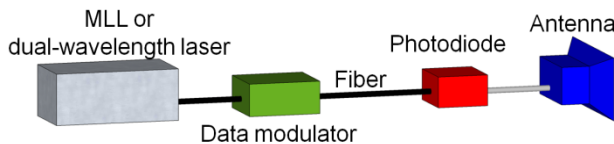


Fig. 1. Block scheme of an optical millimeter wave generator.

The main techniques for generating the modulated optical carrier are based on mode-locked lasers or optical mixing of two single frequency laser sources. The basic idea behind the work presented here is to

investigate photonic integrated dual-wavelength lasers based on optical mixing in which the frequency fluctuations of the two wavelengths λ_1 and λ_2 are correlated. This can be obtained using a dual-wavelength laser in which both wavelengths are generated and amplified by one common semiconductor optical amplifier (SOA). Being amplified by the same SOA, λ_1 and λ_2 share the same variations caused by changes in refractive

index due to changes in temperature and variations in carrier concentration. As a consequence, the instantaneous deviations in frequency of λ_1 and λ_2 can be close to identical if the laser cavity length for both laser modes is similar.

Ring dual-wavelength AWG-based laser

The schematic of the presented ring dual-wavelength laser is depicted in Fig. 2. In order to achieve lasing action simultaneously on two different wavelengths supported by a single SOA, accurate control of the roundtrip loss in the cavity is required to balance the power of λ_1 and λ_2 . As a consequence, part of the cavity of λ_1 must be separated from the cavity of λ_2 . A control system must be added to the parts of the cavities which are not shared in order to be able to control independently the losses. The requirement on the power ratio between the two wavelengths is not particularly strict though. A power ratio of 2 for $P_{\lambda_1} / P_{\lambda_2}$ leads to a reduction in difference frequency modulation depth to 0.94 compared the ideal power ratio of 1. Balanced Mach-Zehnder interferometers (MZIs) provided with voltage controlled electro-optic phase modulators (PHMs) are used to adjust the losses in each individual channel.

An AWG is used as intra-cavity filter to combine the two channels and consequently λ_1 and λ_2 . The advantages of using an AWG for this purpose and more details about the design parameters are presented in [4].

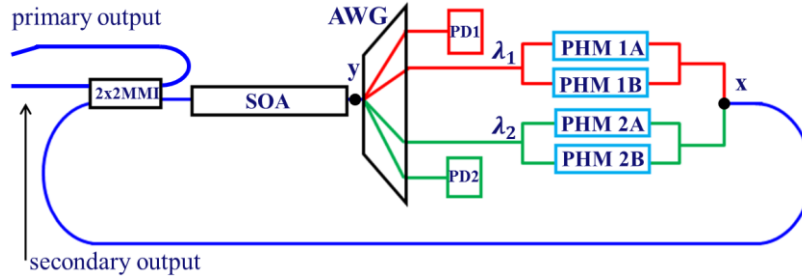


Fig. 2. Schematic of the ring dual-wavelength laser. An SOA provides gain for both wavelengths. An AWG is used as intracavity filter to combine λ_1 and λ_2 . MZIs are used to compensate losses in the individual channels. A 2x2 multimode interferometer (MMI) couples the light out of the ring cavity.

In order to monitor the power balance between λ_1 and λ_2 , photodiodes (PDs) are integrated and connected to the higher order outputs of the AWG. A 2x2 multi-mode interferometer (MMI) couples the light out from the ring cavity. The first output waveguides reaches the edge of the chip with a 7-degree angle in order to reduce back-reflections inside the cavity. The second output of the 2x2 MMI, instead, is connected through a straight waveguide to the edge of the chip in order to provide a considerable feedback inside the cavity and force the laser to work in clockwise direction. The reason for this design choice is to increase the signal power received by the PDs.

Calibration method and influence of crosstalk

In the ideal situation in which the AWG has no crosstalk between adjacent channels, the MZI are perfectly balanced and the PHMs have exactly the same length (and as a consequence the same voltage-to-phase relation), the control of the different signals applied to the device would be rather simple. The MZI configuration would simply allow setting a transmission loss for each channel. Furthermore an offset applied to both PHMs of the same channel would simply shift the cavity modes.

In reality, there is an optical length difference between the different PHMs and as a consequence they have different efficiency. Furthermore, a small imbalance between the two arms of the same MZI makes it necessary to apply a difference between the two PHMs in order to achieve the maximum in the transmission function of the MZI.

The crosstalk between the two adjacent channels of the AWG also plays an important role in the functioning of the device. The crosstalk complicates the control of the laser because the two channels are not independent from each other. While adjusting losses and tuning of λ_1 , also the transmission of λ_2 is affected.

Fig. 3 shows simulations of the transmission function of the filter composed of the AWG and the MZI construction (power transmission from point x to point y in Fig. 2). Two corner cases are compared. The red line refers to the following settings: $V_{1A}=V_{1B}=V_{2A}=V_{2B}=0$ V. The blue line corresponds to $V_{1A}=V_{1B}=0$ V, $V_{2A}=V_{2B}=V_\pi$.

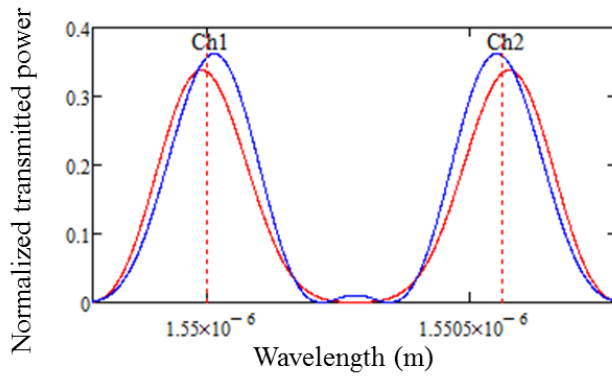


Fig. 3. Transmission function of the filter composed of the AWG and the MZI construction. The two lines represent two different voltage settings applied to PHMs.

GHz while $V_{1A}=V_{1B}=V_{2A}=V_{2B}=0$ V. If $V_{1A}=V_{1B}=0$ V, $V_{2A}=V_{2B}=V_\pi$, the difference in frequency becomes 67 GHz. Above threshold, the wavelength selection of the lasing modes results from the combination between the transmission of the filter and the cavity modes.

In order to calibrate the different components of the device and be able to control the laser, the following strategy is proposed. The idea is to maximize the transmission of the two channels, one at a time, and record the settings of the PHMs. Operating sub-threshold, while three PHMs are grounded, the voltage applied to V_{1A} , for example, is scanned. Once that a maximum in the transmission of channel 1 has been found, V_{1A} is kept fixed and V_{1B} is scanned. Afterwards, also the settings of PHM 2A and 2B are controlled and the transmission through channel 1 is optimized. The same procedure has to be applied to channel 2.

This method allows finding possible imbalances in the MZIs, differences in the efficiency of the PHMs and the value of V_π for each PHM.

Preliminary results

All the results reported in this section have been obtained at a temperature of 14°C of the actively cooled aluminum chuck on which the chip is mounted. The SOA, the PHMs and the PDs on the chip are wire bonded to a simple circuit board from which connections to the current and voltage suppliers are made. The threshold current of the

The dash lines indicate the center of the channels of the AWG. The simulation does not take into account any imbalance among PHMs and between MZI arms.

Fig. 3 demonstrates that the settings applied to PHMs affect the transmission of the filter and in particular change the difference in frequency between the maxima of the two channels. Being the channel spacing of the AWG equal to 70 GHz, the difference in frequency between the maxima of the transmission function is 73

laser is 130 mA. As expected, while biasing the common SOA without balancing the losses in the different channels using the MZIs, the device lases in a single mode; the modes in the other channel are suppressed. The mode spacing matches the expected value of 6.0 GHz being the cavity length 14 mm long.

The output power collected from the actual output waveguides is considerably higher than the output power collected from the secondary output (power difference higher than 30dB while biasing at 180 mA), demonstrating that the asymmetric output configuration successfully forces the laser to work in clockwise direction.

Fig. 4a shows that, adjusting the voltage values applied to the PHMs, the losses in the two channels can be balanced and dual-mode operation can be achieved. However, a power difference of 5 dB is still present between λ_1 and λ_2 meaning that the settings are not optimized. The frequency difference between the two lasing wavelengths is 61.8 GHz, considerably smaller than the designed channel spacing of the AWG. This is due to the influence of the crosstalk as explained in the previous paragraph but also to the fact that the actual channel spacing of the AWG is smaller than the designed value (65 GHz instead of 70 GHz).

Fig. 4b shows the power at a specific wavelength (1532.9 nm) as a function of the V_{IA} when the device is biased sub-threshold at $I = 125$ mA. This explains how the voltage applied to the PHM influences the transmission through the channels. A value of V_π equal to 3.9 V is measured.

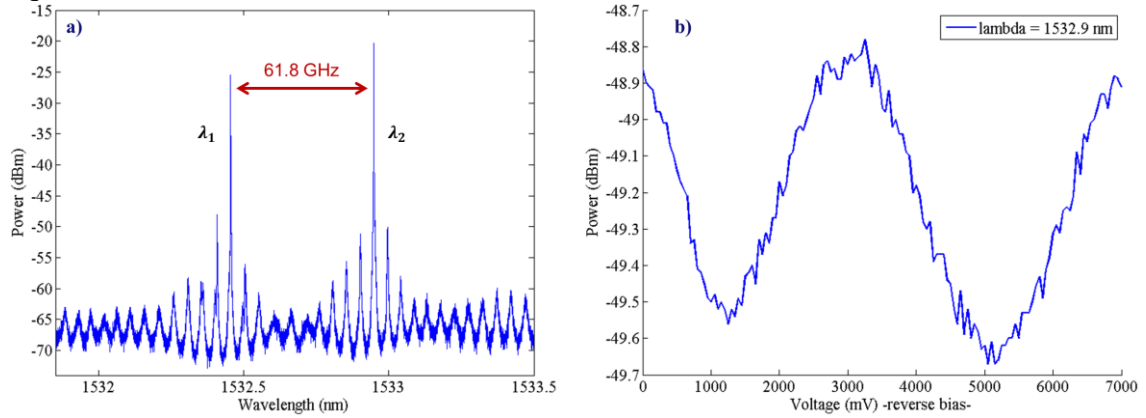


Fig. 4. a) Output spectra of the ring laser while operating in dual-mode. b) Power at $\lambda = 1532.9$ nm as a function of V_{IA} while biasing at $I = 125$ mA.

Acknowledgements

This work is supported by the European Commission (EC) under FP7 ICT European project iPHOS (www.iphos-project.eu).

References

- [1] T. Nagatsuma *et al.* "High-power RF photodiodes and their applications", Laser & Photon. Rev. 3, No. 1-2, 123-137, 2009.
- [2] M. Smit *et al.* "Generic foundry model for InP-based photonics", IET Optoelectron., vol. 5, issue 5, pp. 187-194, 2011.
- [3] T. Nagatsuma *et al.* "Photonic Generation of Millimeter and Terahertz Waves and Its Applications", 19th Int. Conf. on Applied Electromagnetics and Communications (ICECom), 2007.
- [4] A. Corradi *et al.* "Integrated dual-wavelength AWG-lasers for millimeter wave generation", Proc. of the 16th ECIO, 2012.

Nanoplasmonic enhancement of Raman signals by a bowtie antenna on a silicon nitride waveguide

F. Peyskens,^{1,2} A. Z. Subramanian,^{1,2} A. Dhakal,^{1,2} N. Le Thomas,^{1,2} and R. Baets^{1,2}

¹ Photonics Research Group, Ghent University-imec

² Center for Nano- and Biophotonics, Ghent University

In this paper we numerically investigate the coupling of dipole radiation into an integrated silicon nitride strip waveguide functionalized with a nanoplasmonic bowtie antenna. We show that the antenna can enhance Raman signals by a factor of 10^{10} and enables efficient coupling of these signals into the fundamental TE-mode of the waveguide. Furthermore the impact of several antenna parameters on the enhancement factor is investigated. Finally we discuss the potential advantages of these structures for on-chip biosensing applications.

Introduction

Lab-on-a-chip devices, enabling parallel study of multiple analytes, provide an alternative to the existing bulky technologies for spectroscopy and sensing. However, these technologies rely on labeling methods that are intrusive in nature. Either the particles are labeled by means of e.g. fluorescent dyes or the detection surface is functionalized to provide an increased affinity with the particles under study [1, 2]. In this regard, an integrated spectroscopic Raman sensor would enable label-free, high specificity and low-cost sensing platforms. However, Raman signals are inherently very weak and therefore require an additional enhancement mechanism for efficient detection. Surface Enhanced Raman Spectroscopy (SERS) is one such method and is based on the resonant plasmonic behavior of metallic nanoparticles or rough metallic surfaces to enhance Raman signals. Photonic integrated circuits offer the additional advantage of using single mode waveguides for both excitation and collection of Raman signals in a more controlled way. CMOS-compatible photonic integration technologies are particularly relevant in this context since they hold the promise of low cost lab-on-a-chip devices. One can choose between silicon and silicon nitride (Si_3N_4) waveguides depending on the targeted spectral range. It is known that an emission enhancement of dipole radiation can be achieved by means of high-index-contrast (HIC) waveguides and free-space nanoplasmonic antennas [3, 4]. Here we propose a combined approach where a HIC Si_3N_4 strip waveguide is patterned with a nanoplasmonic antenna to achieve enhanced Raman sensing. We consider a dipole located in the vicinity of the nano-antenna, which lies on top of the waveguide, and is excited by the fundamental TE-mode. We restrict ourselves to the TE-case since the TM polarization cannot efficiently excite the configuration under study. It is shown that our combined platform enables a transmission enhancement up to 10^{10} compared to Si_3N_4 waveguides with no nano-antenna on top. The high transmission enhancement combined with the simple excitation and collection approach makes this platform a valuable candidate for single to few molecule SERS.

Numerical Investigation of the Emission Enhancement

In this study we consider a single mode HIC Si_3N_4 strip waveguide ($n = 2.02$, width=600 nm, height=220 nm and $\lambda_0=900$ nm) on a SiO_2 substrate ($n = 1.45$) and water cladding ($n = 1.33$) with a gold bowtie antenna on top (Fig. 1(a)). We use the commercial finite element solver COMSOL to study the interaction between the guided mode of the waveguide and a dipole emitter for two cases: a dipole in the gap of the bowtie antenna and a dipole on the same waveguide but without the antenna (Fig. 1(a)). The dipole power coupled to the waveguide mode is denoted by P_{enh} and P_0 for the cases with and without the gold, respectively. The enhancement factor EF is defined as P_{enh}/P_0 . In order to test the meshing quality and the different numerical parameters, the total radiated power for a dipole parallel and perpendicular to the core region of a slab waveguide is calculated. An excellent correspondence (average error $\approx 2\%$) was found between our numerical results and the exact analytical results [5]. The EF s discussed hereafter are therefore expected to have a high accuracy. Since the fundamental TE-mode (polarized along \mathbf{e}_x) is used as the excitation field, the dominant and relevant part of the Raman dipole moment is given by $\mathbf{p}_x(\mathbf{r}_0) = \alpha_{xx}\mathbf{E}_x(\mathbf{r}_0)$; α_{xx} is the (1,1) component of the polarizability tensor given by the Kramers-Heisenberg-Dirac formula [6]. Since the highest EF s are expected in the gap of the antenna we only consider dipole positions in this region. Contributions from dipoles that are located outside of the gap region will be much smaller since the EF decays rapidly (the field enhancement region extends only over a few tens of nanometers). In Fig. 1(b) we plot the ratio P_{enh}/P_0 as a function of the ratio $\beta = |\mathbf{E}_{enh}(\mathbf{r}_0)| / |\mathbf{E}_0(\mathbf{r}_0)|$ (each dot corresponds to a different position \mathbf{r}_0 of the dipole); $\mathbf{E}_{enh}(\mathbf{r}_0)$ is the enhanced excitation field due to the plasmon resonance and $\mathbf{E}_0(\mathbf{r}_0)$ is the evanescent field of the regular waveguide. The simulation results (red dots) match the fitted β^4 curve (fit based on the β^4 rule of SERS [7]). Since the excitation enhancement scales with β^2 (because the respective dipole moments scale with β), it follows from this figure that the transmitted power by the dipole also scales with β^2 . This result shows that there is an efficient coupling of the enhanced emitted power into the fundamental TE-mode of the waveguide (which can be confirmed by a modematching of the TE-mode with the emitted dipole radiation).

The above observations allow us to extract three distinct advantages of using integrated waveguides with a nanoplasmonic structure. Firstly, the plasmons are always excited with the proper polarization to ensure optimal excitation enhancement (a plasmon resonance strongly depends on the orientation of the excitation polarization). Secondly, the nanoplasmonic structure has no detrimental impact on the output power but enables a significant emission enhancement compared to a regular HIC Si_3N_4 waveguide (see Fig. 1(b)). Finally, the emitted signal is coupled efficiently to the fundamental mode of the waveguide. This creates an ideal condition for on-chip spectral analysis of the signal. It is important to note that an absolute value of P_{enh} depends on both the excitation and emission wavelength. For small Stokes shifts, the excitation and emission enhancement factors will be practically equal as the resonance of the combined waveguide-plasmonics system is quite broadband, but for larger shifts the emission enhancement of P_{enh} (and thus the actual output power) will decrease.

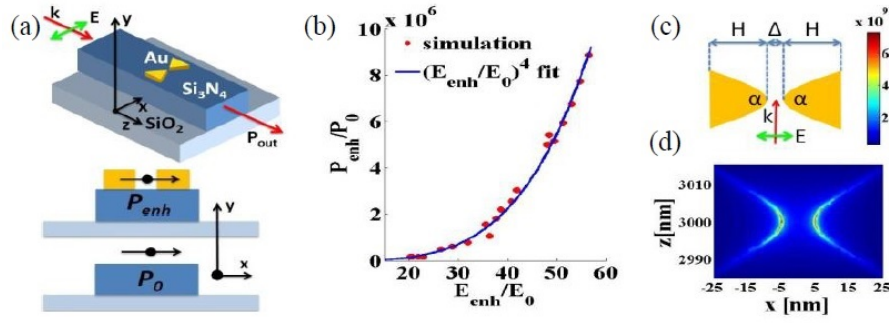


Figure 1: (a) HIC Si₃N₄ strip waveguide with a bowtie antenna; the polarization (green double arrow) and propagation (red arrow) direction of the modal field and the orientation of the radiating dipole are also marked. (b) EF of the Raman power coupled into the guided mode as a function of the field enhancement. (c) Bowtie antenna with dimensions (H, Δ, α). (d) Electric field distribution at the top surface of the gold for $\alpha = 60^\circ$ and $\Delta = 10$ nm.

Analysis of the on-chip bowtie antenna

In this section we investigate the impact of the parameters (H, Δ, α) of the bowtie antenna (defined in Fig. 1(c)) to study how we can optimize the excitation and emission of a dipole. The EF s for different geometry parameters are calculated via β^4 since Fig. 1(b) shows that EF scales with β^4 . Figure 2(a) gives an example of the field distribution in the gap of the antenna. The strong enhancement at the tips and the steep decay of the EF away from the tips is clearly visible.

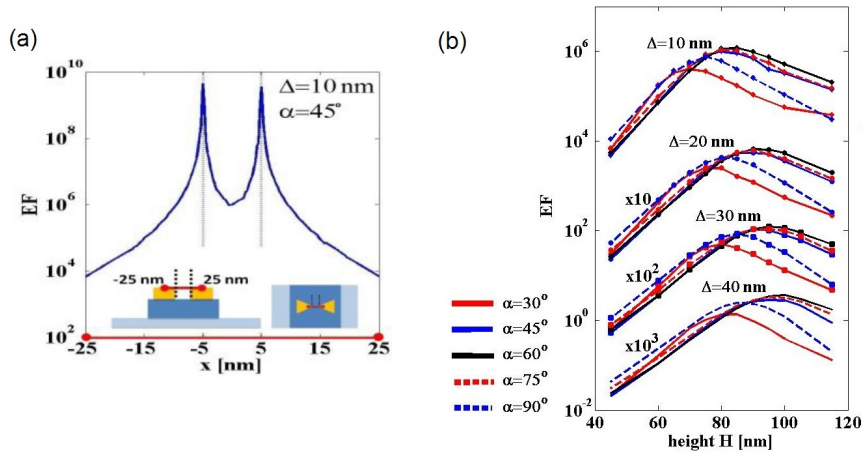


Figure 2: (a) EF at the top surface of the gold; the two inset figures mark the (y, z)-position where the slice (red line) is taken. (b) EF at the center of the bowtie for different (H, Δ, α) parameter combinations.

The simulation results are summarized in Fig. 2(b) where we plot the EF in the center of the gap for different parameter combinations (H, Δ, α). Generally, the optimal height for a given angle is dependent on the gap and for a given gap the optimal height depends on the angle. In the center of the gap, there is a 10^3 order difference for $\Delta = 10$ nm and $\Delta = 40$ nm and changing H by only 20 nm from the optimal H reduces the EF by 10.

Furthermore, we found that depending on the position of the dipole the EF is maximized for specific values of the (H, Δ, α) triplet. Our study shows that for $\alpha = 30^\circ$ and $\Delta = 10$ nm it is possible to obtain transmission enhancements EF up to 10^{10} in a 1 nm region near the tip (the mesh-size near the tip is 1 nm). As such it is clear that adding a properly designed nanoplasmonic structure gives an additional gain up to 10^{10} . This controllable high EF opens the possibility of doing single molecule SERS with our investigated structure. Furthermore our structure can also serve for nanoparticle detection but will be less efficient in the study of larger particles since the EF is large only in a tightly confined (nanosize) region around the metallic nano-antenna. To fabricate these nano-antennas we have explored the Focused Ion Beam (FIB) method but found that the process is not uniform and reproducible for the optimal dimensions from our simulation (see Fig. 2(b)). Therefore an e-beam lithography is currently being explored to produce these structures. The first results show great uniformity and the ability to produce bowties with the desired gap and angle.

Conclusion

In this paper, it is shown that the radiation originating from TE-excited dipoles is efficiently coupled into the fundamental TE-mode of a Si_3N_4 strip waveguide. We also showed that adding a single, well-designed, nanoplasmonic structure has no negative impact on the transmission of the coupled dipole radiation, but is capable of producing Raman scattering enhancements of 10^{10} compared to a simple Si_3N_4 strip waveguide. Furthermore, we investigated the impact of several antenna parameters on the overall performance of the structure and thereby showed that the obtained enhancement can be optimized by tuning the antenna.

Acknowledgements

This research is funded by the ERC grant InSpectra. FP also acknowledges support from the special research fund of Ghent University (BOF). We also acknowledge P. Neutens and P. Van Dorpe from imec for the fabrication of the bowties by means of e-beam lithography.

References

- [1] U. Resch-Genger, et al., "Quantum dots versus organic dyes as fluorescent labels", *Nature Methods*, vol. 5(9), pp. 763-775, 2008.
- [2] W.J. Rieter, K.M.L. Taylor and Wenbin Lin, "Surface Modification and Functionalization of Nanoscale Metal-Organic Frameworks for Controlled Release and Luminescence Sensing", *J.Am.Chem.Soc.*, vol. 129, pp. 9852-9853, 2007.
- [3] Y.C. Jun, et al., "Broadband enhancement of light emission in silicon slot waveguides", *Optics Express*, vol. 17(9), pp. 7479-7490, 2009.
- [4] K.C. Y. Huang, et al., "Power flow from a dipole emitter near an optical antenna", *Optics Express*, vol. 19(20), pp. 19084-19092, 2011.
- [5] L. Novotny and B. Hecht, "Dipole emission near planar interfaces", in *Principles of Nano-Optics*, Cambridge University Press, 2006, pp.335-362.
- [6] J.R. Lombardi and R.L. Birke, "A Unified Approach to Surface-Enhanced Raman Spectroscopy", *J.Phys.Chem. C*, vol. 112, pp. 5605-5617, 2008.
- [7] E.C. Le Ru and P.G. Etchegoin, "Rigorous justification of the $|E|^4$ enhancement factor in Surface Enhanced Raman Spectroscopy", *Chemical Physics Letters*, vol. 423, pp. 63-66, 2006.

Parallel Optical Delay Detector for Angle-of-arrival Measurement of a Microwave Signal with Accuracy Monitoring

Z. Cao, H.P.A. van den Boom, E. Tangdiongga, and A.M.J.Koonen

COBRA Institute, Eindhoven University of Technology, NL 5600 MB Eindhoven, The Netherlands

z.cao@tue.nl

A novel parallel optical delay detector for angle-of-arrival measurement is proposed and the measurement errors are experimentally studied and analyzed. Moreover, the measurement accuracy monitoring is investigated.

I Introduction

Determining location of a microwave signal is of great importance for retrieving the position of objects. The parameter angle-of-arrival (AOA) or equivalently the time difference of arrival (TDOA) is required to accurately identify the position. An optical approach to measure AOA can offer many benefits due to its intrinsic features like ultra-low loss and huge bandwidth, which allows high accuracy, and immunity to electromagnetic interference. Moreover, with the rapid development of ultra-low drive voltage electro-optical modulators (EOMs) [1] and high speed photo-diodes [2], barriers between electrical domain and optical domain are gradually eliminated. Recently some photonic approaches are proposed to measure AOAs of microwave signals [3-5]. In Ref.[5], a scheme with two electro-optical modulators (EOMs) and one optical delay line is proposed for AOA measurement. It is in principle an optical delay detector for microwave signals with serial configuration. In this paper, a novel parallel configuration optical delay detector (PODD) with accuracy monitored is proposed based on a dual parallel Mach-Zehnder modulator (P-MZM). Using one P-MZM, the parallel structure can reduce the perturbations. Moreover, the DC-drift induced measurement accuracy degradation can be monitored.

Thereafter, on the same page, follows the paper. The paper should consist of 4 pages. Please do not number the pages. The section headings should be 14 point Times (New) Roman Bold and the body text 12 point Times (New) Roman. Lettering in tables and figures should be 10 point Times (New) Roman. In order to conserve space, references should be given in 10 point. It is recommended that references conform to the IEEE conventions as shown in the example below.

II Operation Principle

The principle of AOA (or TDOA) measurement is schematically depicted in Fig.1. The distance between two antennas (Ante-1 and Ante-2) is denoted as d . The AOA is denoted as ψ and the corresponding TDOA can be expressed by $\tau = d \times \cos(\psi) / c$, where c is the light velocity in air. MZ-a and MZ-b are the sub-MZMs inside P-MZM, MZ-c is the tunable phase shift combining MZ-a and MZ-b. The electrical paths (including connections and necessary components like amplifiers) between Ante-1 and MZ-a, Ante-2 and MZ-b will introduce phase differences for different frequencies. Such phase difference can be easily compensated using a look-up table. The delay τ will introduce the phase shift ϕ between Ante-1 and Ante-2 with the expression $\phi = \tau \times 2\pi f_{mw}$, where f_{mw} is the frequency of the microwave signal. Therefore the task of proposed PODD scheme

is to measure the phase shift ϕ in optical domain. The PODD includes a CW laser, a P-MZM, an optical notch filter, and two power meters. MZ-a and MZ-b are connected to Ante-1 and Ante-2 and the phase shift ϕ caused by spatial delay τ will be translated to the phase difference of optical sidebands. The following task is to measure the phase difference of optical sidebands by using optical power meters. Both MZ-a and MZ-b are biased to suppress the optical carrier while MZ-c is biased at the maximum point to fully combine optical power from MZ-a and MZ-b. The lightwave from the CW laser is modulated by two replicas of microwave signal at MZ-a and MZ-b with spectrum shown in Fig.1 (a) and (b), respectively. The output optical signals from both MZ-a and MZ-b with phase shift ϕ are then combined at MZ-c without any additional phase shift. We assumed that the optical carriers are well rejected. The total output power is related to the phase shift ϕ with expression $P=(E_0 J_{+1}(m))^2(1+\cos(\phi))$, where E_0 is the amplitude of the optical carrier. $J_{+1}(m)$ is the Bessel function of first kind with regard to modulation index (m). It indicates that amplitudes of sidebands relate to the modulation index. The high order sidebands are negligible for low driving power, which is the case of AOA measurement. The value required for AOA estimation is the normalized power, thus the value of E_0 and $J_{+1}(m)$ are less relevant. We can obtain the expression for AOA and TODA as:

$$\phi = \arccos(P_n - 1), \tau = \arccos(P_n - 1)(2\pi f_{mw})^{-1}, \psi = \arccos(\tau c / d), P_n = P_m / P_0 \quad (1)$$

According to Eq.1, to get the values of τ and ψ , the required parameters are P_n and f_{mw} . The P_n can be obtained by measuring P_m and P_0 . P_0 is measured with zero phase shift but P_m is measured with unknown phase shift. If f_{mw} is unknown, an additional photonic scheme can be utilized to perform frequency measurement before AOA measurement. Thus the measurement of AOA (or TODA) is then translated into measurement of P_m . In the above discussion, we assume that the optical carriers are well suppressed, and thus the power and phase shift can be fully modeled according to Eq.1. However, both limited extinction ratio (LER) and DC-drift will introduce imperfect suppression (IS) of optical carriers. As shown in Fig.1(I), the DC-drift will introduce the phase shift to the optical carrier and thus to the sidebands. The phase shift in optical carrier leads to IS and the phase shift in sidebands will disturb the final measurement results. Both DC-drifts in MZ-a and MZ-b will introduce similar effect. For the IS induced by LER, since no additional phase shift in sidebands is added, it can be removed via an optical notch filter (ONF). Thus it is of interest to monitor the DC-drift during the measurement. Since the DC-drift is related to the IS, the power measurement of optical carrier can be used to monitor DC-drift. As shown in Fig.1, an ONF (ONF-1 shown in Fig.1) is employed to deeply separate the optical carrier and sidebands. The DC-drift during the measurement can be well monitored. Moreover the IS induced by LER can be eliminated after this process.

III Experimental Setup and Results

Fig. 2 shows the proof-of-concept experimental setup of AOA measurement based on PODD. The optical carrier is generated from a DFB laser at 1550.016nm with 1dBm optical output power. It is fed into a P-MZM after a polarization controller (PC). MZ-a and MZ-b are both biased at their minimum points of power transfer curves. Two commercial microwave sources (LO-1 and LO-2) are synchronized and are employed to

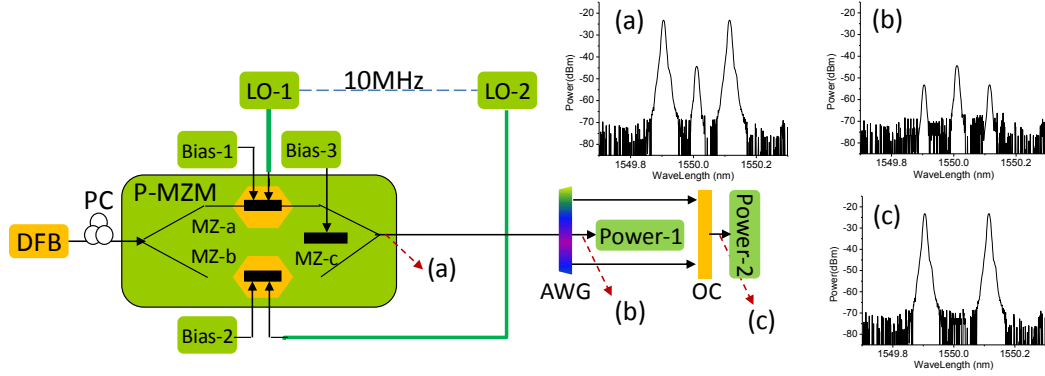
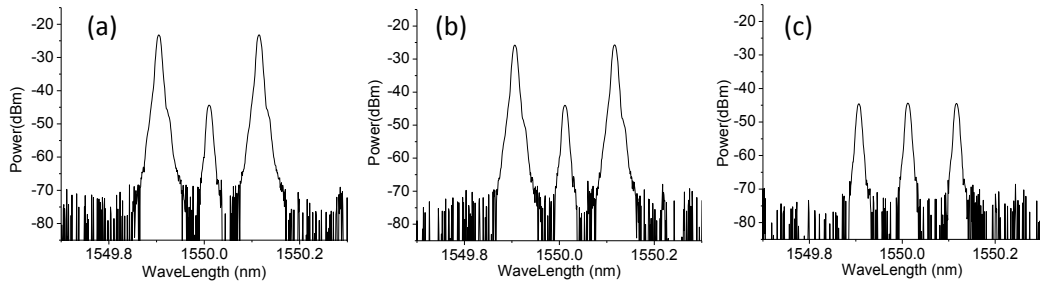
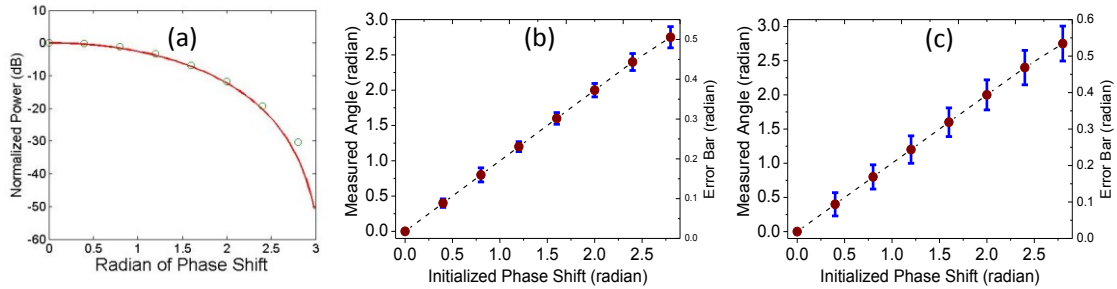


Fig. 2 The experimental setup of AOA measurement based on parallel optical delay detector


 Fig. 3 The measured spectrum for (a) 0° phase shift, (b) 90° phase shift, and (c) 180° phase shift

 Fig. 4. (a) Measured optical power (circles) and theoretical trend (curve); (b) Measured phase shift (dots) and their measurement errors (vertical bars), $P_{mo} = -47.6\text{dBm}$; (c) Measured phase shift (dots) and their measurement errors (vertical bars), $P_{mo} = -41.7\text{dBm}$;

drive MZ-a and MZ-b at frequency of 12.5GHz. A 10MHz sine signal generated from LO-1 is sent to LO-2 for synchronization. MZ-c is biased at the maximum point of its power transfer curve and the optical spectrum of combined signal is shown in Fig.2 (a). The phase difference between LO-1 and LO-2 induced by different electrical paths is calibrated by a commercial sampling oscilloscope (digital communication analyzer). The output optical signal is then separated by an array waveguide grating (AWG) which acts as an optical notch filter. The channel space of the AWG is 12.5GHz and the signal is then separated into three channels. The optical carrier is in the middle channel (noted as CH-2) and two sidebands are in two neighbor channels (noted as CH-1,3). The signal from CH-2 is used for DC-drift monitoring (measured at Power-1) and its spectrum is shown in Fig.2 (b). Optical signals from CH-1,3 are then coupled again via a 3-dB coupler (OC) for power measurement (at Power-2). Its spectrum is shown in Fig.2 (c). The measured spectra from CH-1,3 with different phase shifts are shown in Fig.3. We can clearly observe that the power of sidebands degrades when the phase shift increases. In Fig.3 (a) - (c), the optical carrier is not completely suppressed mainly due

to LER, because the DC-drift is mostly eliminated by optimizing biases at the initial stage. The power of filtered optical carrier (Pm0) is -47.6dBm at the beginning with biases optimized. And then we measure the phase shift ϕ and corresponding measurement errors. After a few tens of minutes, the Pm0 increased to -41.7dBm, the measurement errors are evaluated again for comparison. The measured powers versus different phase shifts (circles) are shown in Fig. 4(a). The theoretical power distribution (red curve) versus phase shift is also shown in Fig. 4(a). An accepted agreement is obtained. The measured phase shifts with their measurement errors are shown in Fig. 4(b) and (c). The measurement errors are less than 0.2 radian within the range from 0 to 2.8 (0° to 160°) when the filtered power is -47.6dBm. It is clear that the measurement errors increase when the phase shift goes to π (the measured power decreases). This is partially because of imperfect destruction of sidebands induced by LER. Comparing Fig.4 (b) and (c), it is obvious that the measurement errors increase when Pm0 drifts to -41.7dBm. It shows that the measurement accuracy caused by DC-drift can be well monitored in this scheme. Note that the zero phase shift is used for normalization and thus its measurement error is not applicable.

IV Conclusion

We have proposed a parallel optical delay detector for angle-of-arrival measurement with accuracy monitored. The spatial delay measurement is translated into the phase shift between two replicas of a microwave signal. The phase shifts from 0 radian to 2.8 radian are measured with 0.2 radian measurement error. Moreover, the measurement accuracy monitoring is investigated.

Acknowledge

The authors would like to thank Sesilia Kriswandhi and Arjen Bakker from Phoenix Software (<http://www.phoenixbv.com/>), and Ronald Broeke from Bright Photonics (<http://www.brightphotonics.eu/>) for their valuable discussions. This work is supported by The Netherlands Organization for Scientific Research NWO under the project grant Smart Optical-Wireless In-Home Communication Infrastructure (SOWICI).

References

- [1] M. Jarrahi, *et al.*, "Wideband, Low Driving Voltage Traveling-Wave Mach-Zehnder Modulator for RF Photonics," *Photonics Technology Letters, IEEE*, vol. 20, pp. 517-519, 2008.
- [2] L. Yu-Tai, *et al.*, "Characterization and Comparison of GaAs/AlGaAs Uni-Traveling Carrier and Separated-Transport-Recombination Photodiode Based High-Power Sub-THz Photonic Transmitters," *Quantum Electronics, IEEE Journal of*, vol. 46, pp. 19-27, 2010.
- [3] S. Pan, *et al.*, "Photonic approach to the simultaneous measurement of the frequency, amplitude, pulse width, and time of arrival of a microwave signal," *Opt. Lett.*, vol. 37, pp. 7-9, 2012.
- [4] X. Zou, *et al.*, "Photonic approach to the measurement of time-difference-of-arrival and angle-of-arrival of a microwave signal," *Opt. Lett.*, vol. 37, pp. 755-757, 2012.
- [5] R. K. Mohan, *et al.*, "Frequency resolved angle and time difference of arrival estimation with spatial spectral holography" OFC2010, p.OWF3

Fast Phase Shifted asymmetrical DFB laser for all-optical flip-flop operation

A. Abbasi, S. Keyvaninia, G. Roelkens, G. Morthier

Department of Information Technology, Ghent University - IMEC,

Sint-Pietersnieuwstraat 41, B-9000 Ghent, Belgium

A DFB laser with an asymmetric coupling coefficient is proposed for flip-flop operation. It has been demonstrated in simulation that a high confinement factor of the active region and use of an asymmetric configuration result in very short rise and fall times. In our simulation, nearly 10ps fall time and 5ps rise time have been observed.

1. Introduction

All-optical signal-processing devices are playing an essential role in the future of optical-data networks [1]. In order to increase the network efficiency and raise the bandwidth, all optical switching networks are desirable, because they can reduce the switching energy as well as increase speed by avoiding optical-to-electrical or electrical-to-optical signal conversion. Bistable optical devices can be used as the basis of all-optical flip-flops, in which switching happens by set and reset optical short pulses [2-4]. Our approach for the all optical flip flop switching is based on a $\lambda/4$ -shifted DFB laser, which becomes bistable by injecting a master laser light, with a wavelength is outside the DFB laser stop-band. This bistability is observed in the lasing light as well as in the amplification of the external light and is due to non-linear effects having their origins in the carrier distribution (i.e. longitudinal spatial hole burning).

2. Flip flop operation

When a cw light is injected inside the DFB laser, it will result in the bistable condition for certain input power levels, (i.e. for the same input power, two different output states are recognizable). Both states are stable and the way to reach each of them can be explained by introducing the carrier density profile. When the DFB laser is on, because of the gain clamping effect, the injected signal will not amplify efficiently, so the carrier density is almost uniform, the threshold gain is low for lasing and the laser will remain in the on state.

On the contrary, the DFB laser is off for the second state, so the carrier inversion is large, the high amplification of the injected light makes the carrier density non-uniform as can be seen in Figure 1. While the system is off, the threshold gain is high and the DFB laser could not reach the lasing threshold, so the state is stable.

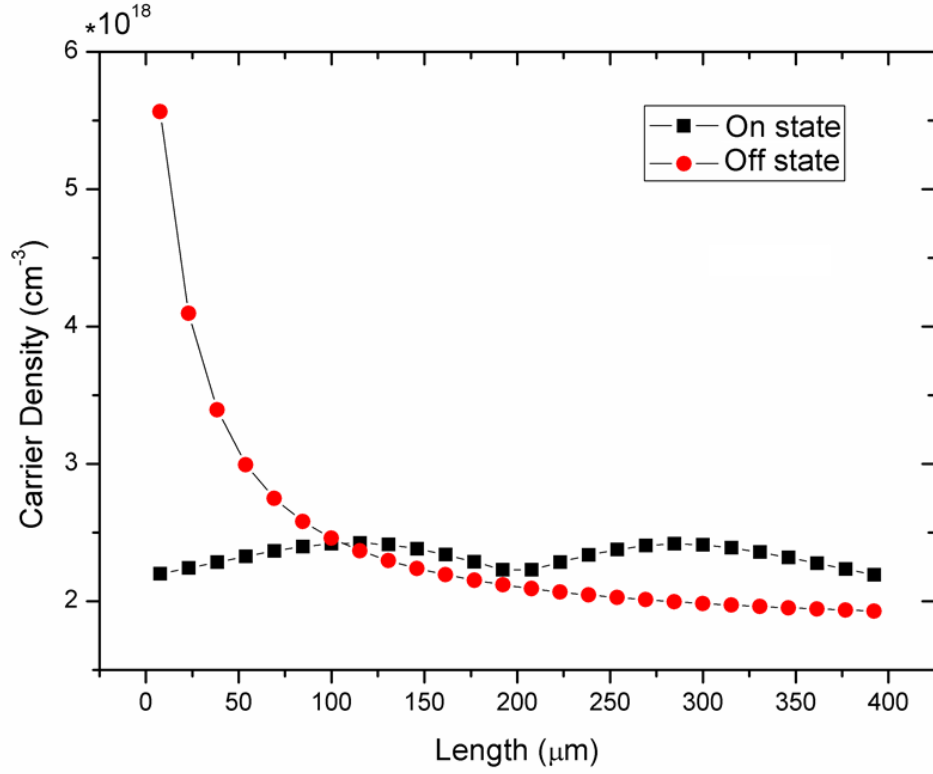


Figure 1: Longitudinal distribution profile of the carrier density in the DFB-laser.

Flip flop operation can be demonstrated by introducing the set and the reset pulses. The role of these pulses is to provide the temporary carrier density redistribution. If the reset pulse is injected from the same side as the cw light, it can pass through the laser cavity and make the longitudinal carrier density non-uniform, thus the laser is switched off. The set pulses can be injected from the other side to restore the uniformity and switch the laser on. The Optical spectra for the on and off states are shown in Figure 2. The laser is lasing at a wavelength of 1.57 μm and cw light is injected with a wavelength of 1.557 μm to simulate the hysteresis curve.

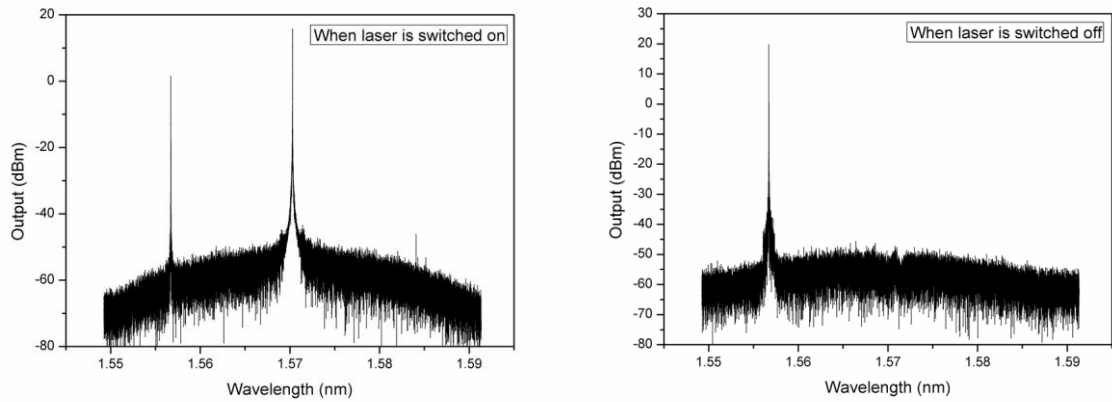


Figure 2: The output spectrum of the flip flop system (a) when the DFB laser is switched on and (b) when it is switched off.

3. Asymmetric design and Results

A fast performance for the processing application is desirable. Here we will discuss the influence of the grating structure and of the confinement factor of the active region on the flip flop operation speed.

We use a commercial software package, [5] based on a transmission line laser model (TLLM).

Our proposed structure has been depicted schematically in Figure 3. This is the two section DFB laser with two different coupling coefficients. For our simulation, the κ_1 is 3000 m^{-1} , κ_2 is 2550 m^{-1} and the length of the laser cavity is $400 \text{ }\mu\text{m}$. For the uniform laser $\kappa=3000 \text{ m}^{-1}$.

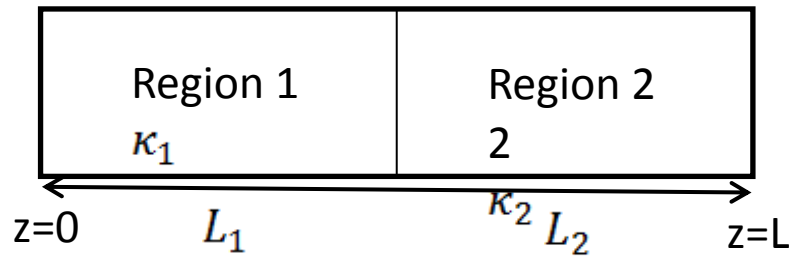


Figure 3: Schematic diagram of the phased-shifted DFB laser with two non-identical regions. $\kappa_{1(2)}$, $L_{1(2)}$ are coupling coefficients and $L_{1(2)}$ is the cavity length for each region, respectively.

The influence of the asymmetric design and the confinement factor is shown in Figure 4, where it is clear that the asymmetric configuration is faster than the symmetric one. Another fact that can be extracted from results is that the high confinement factor will result in faster devices.

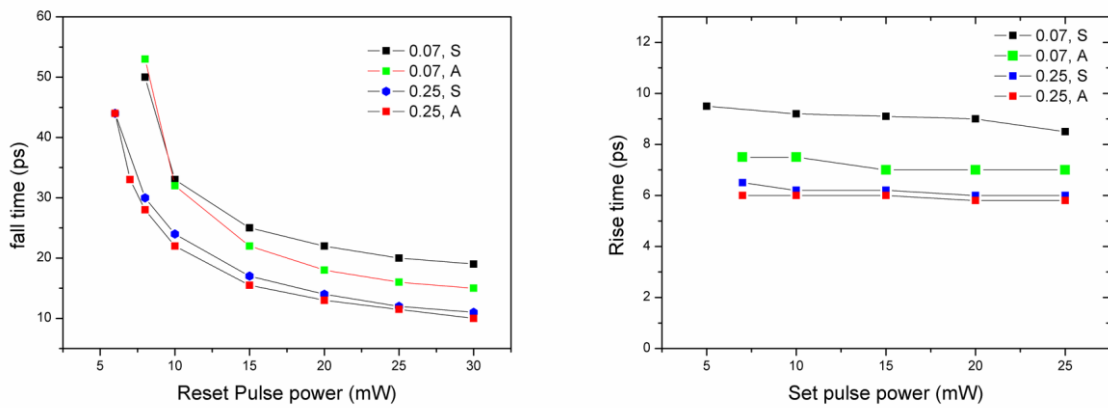


Figure 4: The simulated switching times for a DFB laser with length $L=400\mu\text{m}$ and $\Gamma_{\text{low}}=0.07$ and $\Gamma_{\text{high}}=0.25$. Rectangular pulses have durations of 100 ps. (S: symmetric cavity, A: asymmetric cavity)

4. Conclusion

It was shown that under injection of a holding beam, we can obtain a hysteresis in the output of a distributed feedback (DFB) laser diode. The asymmetric structure can reduce the switching time dramatically. From the fabrication point of view, making a DFB laser with a high confinement factor is challenging, while the design and fabrication of a DFB laser with asymmetric coupling coefficients are rather easy. In this work, switching times as low as 10 ps have been achieved by set and reset pulses with the duration of 100 ps. The broadband operation and fast switching makes the DFB flip-flop an ideal candidate to apply in all-optical packet switched networks.

References

- [1] Agrawal, G.P., "Lightwave technology: components and devices", Wiley, 2004.
- [2] K. Huybrechts, G. Morthier, and R. Baets, "Fast all-optical flip-flop based on a single distributed feedback laser diode," *Opt. Express* 16(15), 11405–11410, 2008.
- [3] M. Takenaka and Y. Nakano. "Multimode interference bistable laser diode". *IEEE Photonics Technology Letters*, 15(8):1035–1037, 2003.
- [4] R. Clavero, F. Ramos, J.M. Martinez, and J. Marti. "All-optical flip-flop based on a single SOA-MZI", *IEEE Photonics Technology Letters*, 17(4):843–845, 2005.
- [5] VPItransmissionmaker. Available: <http://www.vpisystems.com>

Shaping sub-wavelength plasmonic funnels

N. Rivolta,¹ B. Maes¹

¹ Micro- and Nanophotonic Materials Group, Faculty of Science, University of Mons, 20, place du Parc, B-7000 Mons, Belgium

We numerically study transmission through a silver grating with structured sub-wavelength slits. We examine a wide range of rectangular-type geometries, expanding upon previous results which considered basic triangular geometries. We identify the relevant parameters of the structure to get a narrow resonance or a broad transmission plateau in the visible or IR range. On the one hand, allowing resonances improves the maximal transmission through the grating, reminiscent of extraordinary transmission. On the other hand, when resonances are avoided very broadband, quasi-static behavior is observed in the mid-IR, which is governed by a limited number of parameters.

Introduction

Metallic gratings and apertures at the nanoscale have already been theoretically [1] and experimentally studied. Extraordinary transmission through rectangular holes or slits for example allows for very interesting transmission spectra. However, shaping of the slits gives us new features to explore. A funnel shape amongst others can improve the transmission in the visible or infrared range [2, 3]. Controlling the transmission in this way can be very useful for filters or transparent electrodes. Moreover this kind of structures can squeeze light in a very small space, which is often a desirable feature.

To understand the main phenomena in these shaped slits, we study simple rectangular geometries in order to find the relevant parameters that play a role in the transmission. We can often distinguish between resonant or quasi-static, broadband behavior. Our work is numerical in nature (finite element method, COMSOL), however some shapes should be attainable for experiments.

Infrared range

In the infrared range, we are in a quasi-static regime. There are no Fabry-Perot type resonances, so the transmission behavior is relatively easy to understand. Obviously, for straight slits, larger slits lead to higher transmission, and vice versa for the total film thickness. However, for more specific geometries (Fig. 1), there are new parameters that play a role.

For the geometries with ‘teeth’ we find that the number of teeth decreases the transmission, even when the total teeth thickness remains the same. Consequently for Fig. 1 the right structure has a lower transmission than the left one.

Shaping sub-wavelength plasmonic funnels

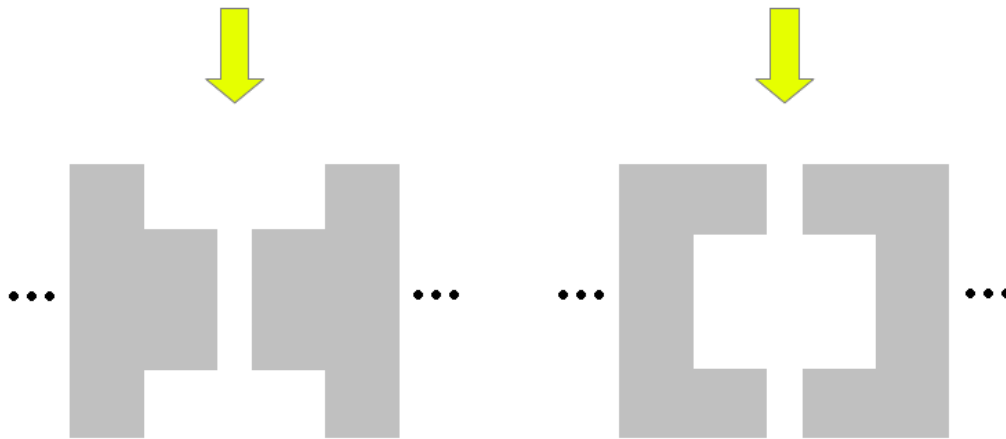


Figure 1: One period of gratings with ‘teeth’: one tooth on the left, two on the right. The yellow arrow represents the incident light.

Increasing the total thickness of all teeth also decreases the transmission (Figure 2). This behavior is valid for a wide range of wavelengths (3.5 - 10 μm) so we have a weak evolution in function of the wavelength.

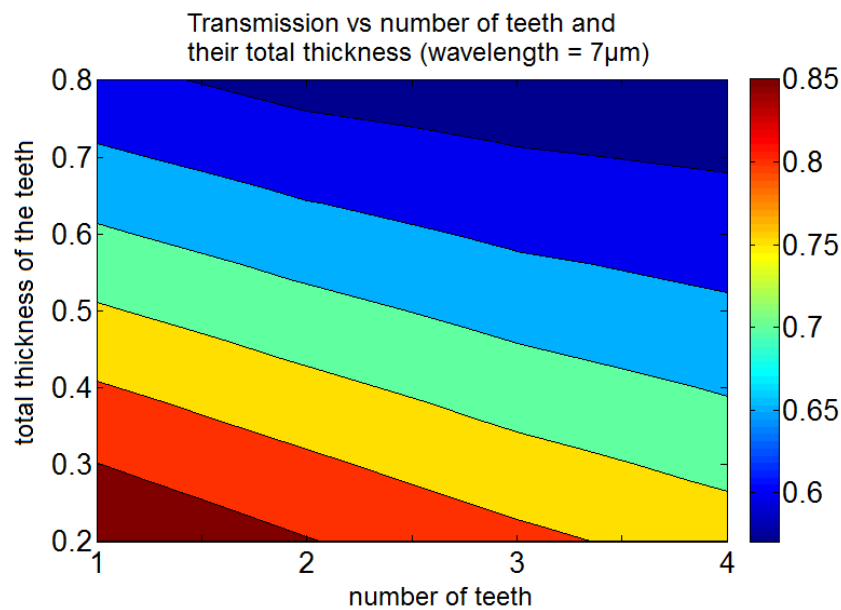


Figure 2: Transmission versus the number and total thickness of the teeth. The total thickness is the ratio of the sum of the teeth thicknesses over the total grating thickness.

Visible or near-infrared range

In the visible or near-infrared range, some resonances will occur if the structure has the necessary parameters, such as size.

Due to the different geometries, the one tooth structure has a qualitatively different behavior compared to two or more teeth. For one tooth, a resonance appears if the tooth thickness reaches a certain value. Thus, by increasing this quantity we can switch from a broadband (small) transmission to a resonance which allows higher transmission, but around a specific wavelength. This evolution is shown in Fig. 3.

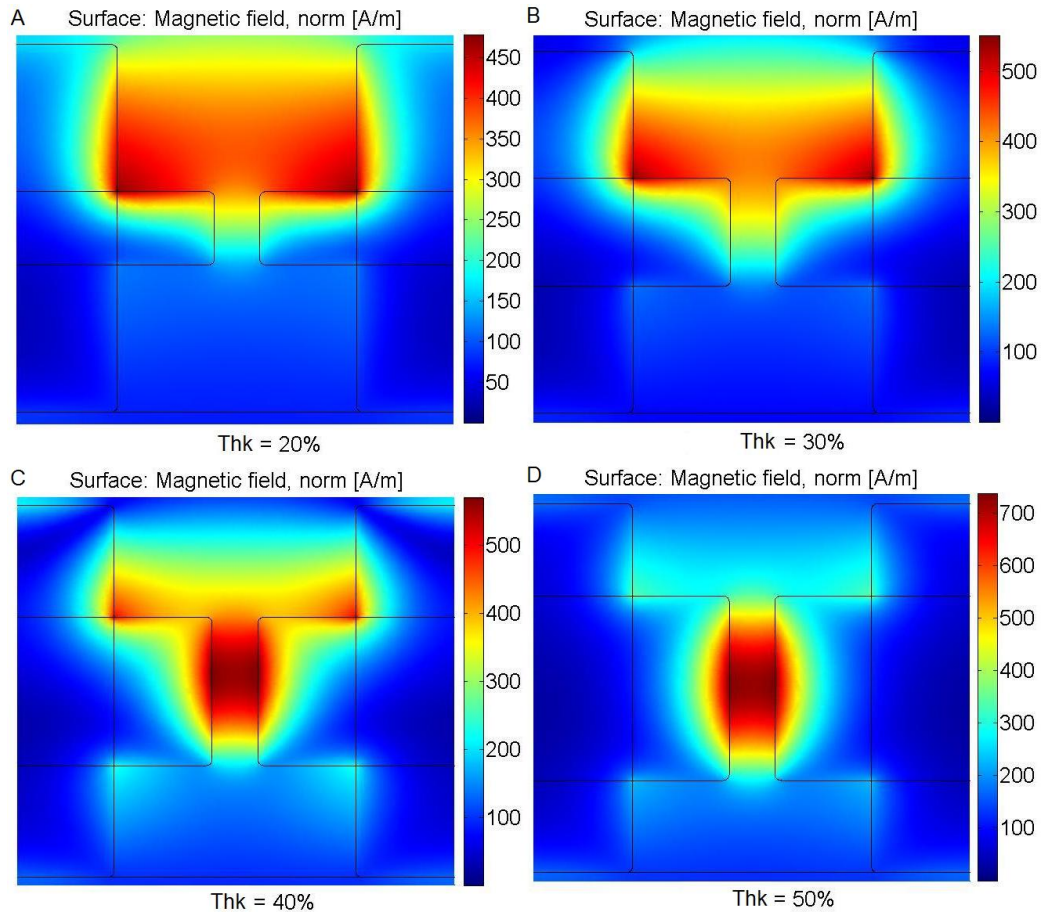


Figure 3: Magnetic field for the one tooth structure with different tooth thickness. A small thickness does not allow a resonance (A), but a bigger one can accommodate one (D). Thk is the ratio of the tooth thickness over the total thickness.

For the multiple teeth structure there is always a resonance that appear in the cavities formed by the teeth. The sum of the teeth thicknesses does not affect the resonance shape, see Fig. 4. The mode is just squeezed in a smaller space when the teeth thickness increases. The wavelength is not affected either. An origin of this phenomenon is found via the effective index. If we have more metal, the effective index of the guided slit mode increases, so the effective wavelength decreases. As a consequence, the cavity mode needs less space and can be squeezed.

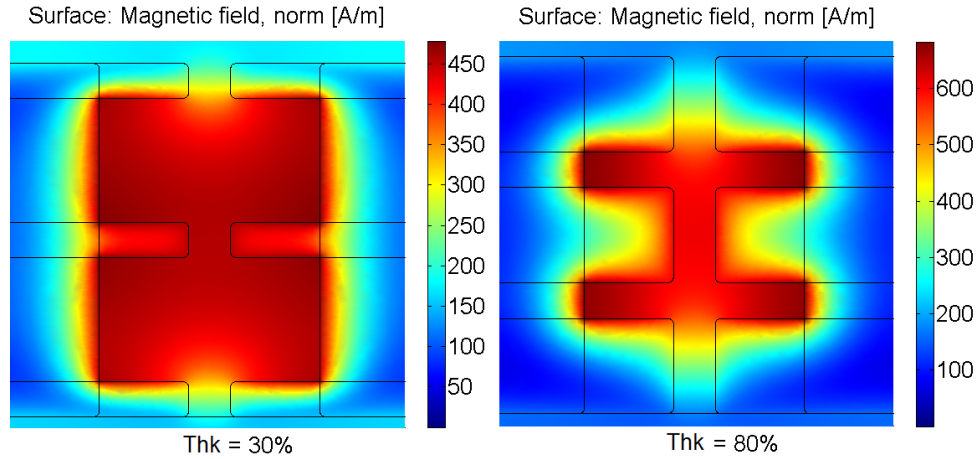


Figure 4: Magnetic field for the triple tooth structure with different total teeth thickness. This parameter does not affect the apparition of a resonance, but only squeezes the mode in a smaller space and thus increases the magnetic field.

In addition, a second order mode is allowed by the three and four teeth structures. This mode is understood via the middle teeth which make a boundary between the two maxima of the second order mode. This is not possible for a two teeth structure.

Conclusion

With rigorous simulations we have analyzed the behavior of metallic gratings with shaped slits.

In the infrared range, the properties are quasi-static and we identify the limited number of main parameters. These are mainly the parameters that characterize the aperture size(s). In the visible range, the resonances induce a more complicated behavior. We find that some sizes need to be big enough to allow for a resonance to develop, and to create a larger, but narrow-band, transmission.

References

- [1] A. Alu, G. D'Aguanno, N. Mattiucci and M.J. Bloemer, "Plasmonic Brewster Angle: Broadband Extraordinary Transmission through Optical Gratings", *Physical Review Letters*, vol. 29, pp. 123902, 2011.
- [2] T. Sondergaard, S.I. Bozhevolnyi, S.M. Novikov, J. Beermann, E. Devaux and T.W. Ebbesen, "Extraordinary Optical Transmission Enhanced by Nanofocusing", *Nano Letters*, vol. 10, pp. 3123-3128, 2010.
- [3] H. Shen and B. Maes, "Enhanced optical transmission through tapered metallic gratings", *Appl. Phys. Lett.*, vol. 100, pp. 241104, 2012.

Modelling of a phosphor plate of a white phosphor-converted remote phosphor LED

Acuña, P.¹, Leyre, S.¹, Audenaert, J.¹, Deconinck, G.², Meuret, Y.¹, Hanselaer, P.¹

¹ESAT/Light & Lighting Laboratory, KU Leuven – Technology Campus, Gebroeders De Smetstraat 1, 9000 Gent, Belgium

²ESAT/ELECTA, KU Leuven, Kasteelpark Arenberg 10, bus 2445, 3001 Heverlee, Belgium

[*paula.acuna@kuleuven.be](mailto:paula.acuna@kuleuven.be)

Light extraction efficiency in SSL with conformal phosphor-converted LEDs can be enhanced with remote phosphor LED technology which allows the extraction of backscattered light and lowers the thermal operation point of the phosphor. In this study, a remote phosphor module was simulated using ray tracing software. The BRDF of the reflective material in the cavity was determined, a ray file was obtained for the blue pump LEDs, and the remote phosphor component was modeled with experimentally obtained bi-spectral BSDF data. Simulation and experimental results match in the near and far field behaviour.

1. Introduction

In order to optimize a phosphor converted white LED (pcLED) system, different simulation models have been proposed for the phosphor element. In [1] and [2] a YAG phosphor is simulated within a pcLED by defining the reflected and transmitted flux of blue and yellow light measured with two integrating spheres. In [3] a model based on Mie theory using the microscopic parameters of the phosphor and the embedding matrix was defined. These models either do not consider the angular dependence in the scattering process, or they require plenty of microscopic parameters to be set in the simulation, whose acquisition is rather difficult. In [4], the interaction of the light with the phosphor is characterized by measuring the bi-directional scattering distribution function (BSDF) of a phosphor on a PET substrate and simulating the forward mode for a conformal pc LED.

A simulation model for a remote phosphor plate is proposed in this work, based on the bi-spectral BSDF, for both: backwards and forwards emission. The remote phosphor plate manufactured by Intematix consists of a diffuse polycarbonate plate coated on one side with a silicate phosphor doped with Eu. The proposed simulation model allows to analyse the influence of the incident angle on the phosphor extraction efficiency, that in turn can be used in the analysis of the recycling process due to the presence of the mixing chamber.

2. BSDF of the phosphor plate

The phosphor plate will be modelled based on the macroscopic scattering behaviour. The scattering of radiation can be described by the BSDF $q_e(\theta_i, \phi_i, \theta_s, \phi_s)$, according to [5], defined as:

$$q_e(\theta_i, \phi_i, \theta_s, \phi_s) = \frac{L_{e,\lambda,s}(\theta_i, \phi_i, \theta_s, \phi_s)}{E_{e,\lambda,i}(\theta_i, \phi_i)} \left[\frac{1}{sr} \right] \quad \text{Eq. 1}$$

With $L_{e,\lambda,s}(\theta_i, \phi_i, \theta_s, \phi_s)$ de radiance of the sample at a particular viewing angle (θ_s, ϕ_s) , and $E_{e,\lambda,i}$ the irradiance on the sample from a particular incident solid angle (θ_i, ϕ_i) .

When elastic scattering occurs, i.e. there is no wavelength conversion, this expression quantifies properly the impulse response of the material to the incident light at different angles. For inelastic scattering, i.e. when wavelength conversion takes place, this

expression is not valid anymore. To extend the Nicodemus' derivation to the cross-wavelength energy transfer, the contribution of each discrete incident wavelength within the excitation range to each scattered wavelength by the fluorescent material at a certain direction (θ_s, ϕ_s) has to be considered [6]. This is called the bi-spectral BSDF, expressing the fact that scattering at one wavelength is caused by several incident wavelengths. Mathematically expressed the bi-spectral BSDF $q_{e,\lambda}(\theta_i, \phi_i, \theta_s, \phi_s, \lambda_i, \lambda_s)$ can be defined as the derivative of the BSDF $q_e(\theta_i, \phi_i, \theta_s, \phi_s)$ with respect to the incident wavelength $d\lambda_i$:

$$q_{e,\lambda}(\theta_i, \phi_i, \theta_s, \phi_s, \lambda_i, \lambda_s) = \frac{dq_e}{d\lambda_i} = \frac{dL_{e,\lambda,s}(\theta_i, \phi_i, \theta_s, \phi_s, \lambda_s)}{E_{e,\lambda,i}(\theta_i, \phi_i, \lambda_i) \cdot d\lambda_i} \left[\frac{1}{sr \cdot nm} \right] \quad \text{Eq. 2}$$

In order to know the contribution of an incident wavelength range Λ_i to the spectral scattered flux at the scattered wavelength λ_s , it is necessary to integrate Eq. 2 with respect to $d\lambda_i$ over a particular range. The integration range is between 450 and 470 nm for incident blue light, mimicking the emission of blue LEDs. From this result an average value $\langle q_{e,\Lambda_i} \rangle$ can be calculated for any scattered wavelength λ_s as a function of the scattered angle (θ_s)

$$\langle q_{e,\Lambda_i}(\theta_i, \phi_i, \theta_s, \phi_s, \lambda_s) \rangle = \frac{L_{e,\lambda,s}(\theta_i, \phi_i, \theta_s, \phi_s, \lambda_s)}{\int_{\lambda_i=450}^{\lambda_i=470} E_{e,\lambda,i}(\theta_i, \phi_i, \lambda_i) \cdot d\lambda_i} \left[\frac{1}{sr \cdot nm} \right] \quad \text{Eq. 3}$$

Simulation of the detailed bi-spectral BSDF is extremely cumbersome, therefore it is simplified by simulating only two wavelengths, yet properly reproducing the conversion and scattering behaviour of the phosphor plate. Each wavelength takes an average value resulting from the integration of $\langle q_{e,\Lambda_i} \rangle$ over the scattered wavelengths, for both the BRDF and the BTDF.

3. Experiments and Simulation

This plate is meant to be excited by pump-LEDs whose emission peak is about 450 nm, resulting in white light with a CCT of 3000 K. The BSDF for the phosphor plate was characterized with the setup described in [7], consisting of a goniometer with a fixed position light source and a mobile detector, with a position and inclination adjustable sample holder in between the light source and the detector. For every incident polar angle $(\theta_i = 5^\circ, 45^\circ, 56^\circ)$ the scattered spectral flux $\Phi_{e,\lambda,s}$ was measured for the scattered polar angles $0^\circ \leq \theta_s \leq 90^\circ$ in the incident plane in increments of 5° for both the reflection (backwards) and transmission (forwards) hemispheres. Two incident spectra have been applied: “blue light” within the excitation spectrum (Figure 1-right) of the fluorescent material mimicking the pump-LED and “yellow light”. The BSDF measurement when “yellow light” impinges is required in order to characterize the interaction between the phosphor plate and the emission spectrum of the phosphor after being reflected in the mixing cavity.

In total three different BSDFs are defined, corresponding to the elastic and inelastic scattering in response to the blue incident light, and to the elastic scattering in response to the yellow incident light. These functions are converted into tables that define the scattering simulation model in the ray tracing program. Each of this functions are assigned as a surface property to the geometrical representation of the phosphor plate. The mixing chamber consists of a cylindrical cavity with radius 35 mm and height 43 mm, whose inner surface has the BRDF characteristic of an MPET material. The light

source is represented by a ray-file of four blue LEDs located at the base of the mixing chamber and equidistantly distributed along a radius of 18 mm (Figure 1 -left). The ray-file was measured by a near-field goniometer equipped with a luminance camera (TechnoTeam Rigo 801).

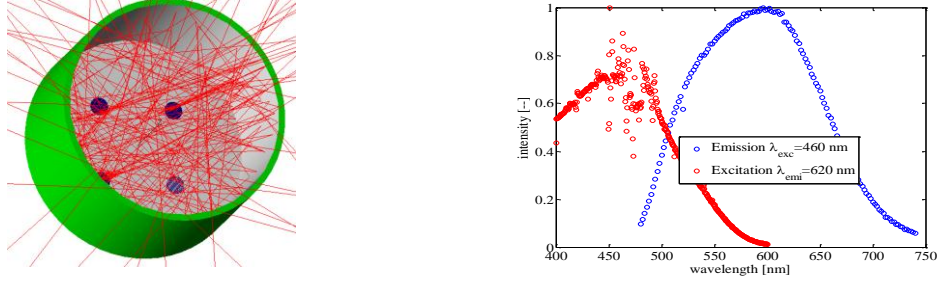


Figure 1 Whole module simulation in ray tracing (left); Excitation and emission spectrum for the phosphor plate (right)

4. Results and Discussion

From the phosphor characterization one incident angle is chosen ($\theta_i = 45^\circ$) to illustrate the response of the phosphor plate to the blue and yellow light.

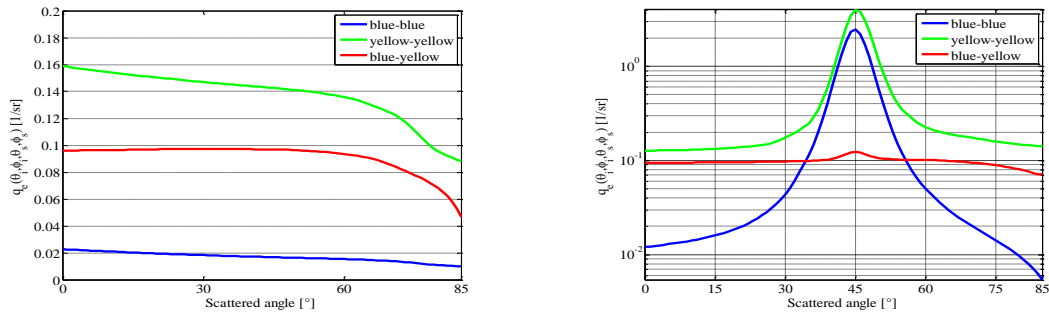


Figure 2 Responses of the phosphor plate to excitation at an incident angle of 45° . Bi-directional transmittance distribution function (Left); Bi-directional reflectance distribution function (Right)

From Figure 2 the transmittance distribution function presents a rather lambertian behaviour for the three responses due to the effect of the diffuse (polycarbonate) plate along with the phosphor coating. On the other hand, the reflectance distribution functions present higher values around the specular angle for the elastic scattering, and lambertian for the inelastic scattering.

To validate the simulation model of the whole module it has been compared: (1) the spatial distribution of the exitance at the outer surface of the phosphor plate, and (2) the intensity distribution in the far-field region. The spatial distribution of the exitance was calculated for each concentric ring equally distributed over the phosphor plate.

A good agreement exists between the experimental and simulation results as showed in Figure 3. From the simulation it is possible to determine the increment in light extraction due to the light recycled by the mixing chamber. Simulations performed when attributing a reflectance of zero to the mixing chamber are compared to the simulation results when the MPET characteristics have been used. The light extraction with the mixing chamber is 1.7 times the amount of light extracted when the mixing chamber is totally absorbing. These results are confirmed with integrating sphere spectral radiant flux measurements of the whole module, equipped with reflecting and absorbing walls of the mixing chamber respectively.

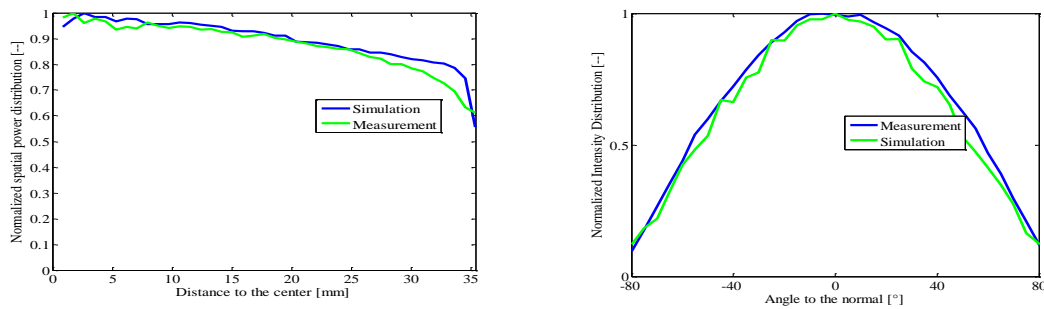


Figure 3 Validation of the simulation model for the whole module. The exitance over concentric rings characterized by the distance to the centre (left) and the normalized intensity distribution (right).

5. Conclusions

The simulation model of a cylindrical mixing chamber covered by a remote phosphor plate (a phosphor coating in combination with a diffuse polycarbonate plate) has been developed. This model allows to predict the response of the phosphor plate to different mixing chamber designs. Future work will be focused towards the use of the model in optimizing the geometry and form factor of the mixing chamber.

Acknowledgments

The authors appreciate the financial support of: the Hercules Foundation – project AKUL035 “Near-Field Imaging Luminance Goniometer”, Colciencias (Administrative Department of Science, Technology and Innovation - Colombia) (Paula Acuña), and the Agency for Innovation by Science and Technology in Flanders (IWT) (SB-091442, Jan Audenaert). The authors wish to thank Professor. Philippe Smet for his help in conducting the fluorescence measurements of the phosphor plate.

References

- [1] K. Yamada, Y. Imai, and K. Ishii, "Optical Simulation of Light Source Devices Composed of Blue LEDs and YAG Phosphor," *Journal of Light & Visual Environment*, vol. 27, p. 70, 2003.
- [2] Y. Zhu and N. Narendran, "Investigation of Remote-Phosphor White Light-Emitting Diodes with Multi-Phosphor Layers," *Japanese Journal of Applied Physics*, vol. 49, no. 10, p. 100203, Oct 2010.
- [3] Christian Sommer, Paul Hartmann, Peter Pachler, Hans Hoschopf, and Franz P. Wenzl, "
- [4] Chien-Hsiang Hung and Chung-Hao Tien, "Phosphor-converted LED modeling by bidirectional photometric data," *Opt. Express*, vol. 18, no. S3, pp. A261--A271, Sep 2010. [Online]. <http://www.opticsexpress.org/abstract.cfm?URI=oe-18-103-A261>
- [5] F. E. Nicodemus, *Geometrical considerations and nomenclature for reflectance*, U.S. Government Printing, Ed.: U.S. Dept. of Commerce, National Bureau of Standards : for sale by the Supt. of Docs., U.S. Govt. Print. Off. (Washington), October 1977.
- [6] Matthias B. Hullin et al., "Acquisition and analysis of bispectral bidirectional reflectance and reradiation distribution functions," *ACM Trans. Graph.*, vol. 29, no. 4, pp. 97:1--97:7, #jul# 2010. [Online]. <http://doi.acm.org/10.1145/1778765.1778834>
- [7] Frederic B. Leloup, Stefaan Forment, Philip Dutré, Michael R. Pointer, and Peter Hanselaer, "Design of an instrument for measuring the spectral bidirectional scatter distribution function," *Appl. Opt.*, vol. 47, no. 29, pp. 5454-5467, Oct 2008. [Online]. <http://ao.osa.org/abstract.cfm?URI=ao-47-29-5454>
- [8] ASTM Standard E1392, 1996(2002), Standard Practice for Angle Resolved Optical Scatter Measurements on Specular or Diffuse Surfaces, 2002.

Microwave Modeling and Analysis of an InP based Phase Shifter from a Generic Foundry Process

W. Yao,¹ G. Gilardi,¹ M. Smit,¹ and M. J. Wale^{1,2}

¹ COBRA Research Institute, Photonic Integration Group, Department of Electrical Engineering, University of Technology Eindhoven, The Netherlands

² Oclaro Technology Ltd., Caswell, Towcester, Northamptonshire, NN12 8EQ, United Kingdom

Theoretical analysis and numerical simulations on the microwave properties of a III-V integrated phase shifter are presented and compared with experimental results. A 3D-electro-magnetic model of the phase shifter is used to study the effect of geometrical and material parameter changes on the modulator's transmission line parameters including its bias voltage dependency. The model predictions match well with measurements on phase shifter structures fabricated in a generic integration process and can be used to analyze electrical crosstalk between modulators in high-capacity WDM transmitter chips.

Introduction

Monolithically integrated high capacity multichannel transmitters are becoming more and more attractive, e.g. in optical interconnect or access network applications. Fabrication of such transmitters through a generic foundry approach stands to reason due to reduced development time and cost [1]. A steady demand for higher capacity, channel count and smaller chip size gives rise to many design and fabrication challenges. One such challenge lies in the design of electro-optical phase shifters for high speed modulation and in the electrical crosstalk between them due to small separation distances on chip. High frequency losses and reflections in phase shifters affect the electrical signal propagation and degrade their performance whereas crosstalk introduces noise and distortions. Therefore, careful analysis of their microwave characteristics is required. This paper studies those based on a 3D solver approach, similar to [2], and extends the model to account for crosstalk effects.

Phase Shifter Model and Simulation

The phase shifter structure is shown in figure 1(a) and consists of a shallow optical waveguide with a top metal electrode and trenches on each side with dielectric filling for passivation. Propagation of the microwave signal along the top electrode is described by transmission line theory and defined through the propagation constant $\gamma = \alpha + j\beta$, where α is the attenuation and β the phase constant, and the characteristic impedance Z_C [2]. The full-wave solver CST MWS is used here to model the phase shifter cross section and determine the microwave parameters. Its electric field solution is shown in figure 1(b) and corresponds to a microstrip mode with a quasi-TEM behaviour, centered around the depletion area between the intrinsic layer and the p-doped cladding. Bias dependency is incorporated through variation of the depletion thickness.

Electrical scattering parameters have been calculated for three different phase shifter lengths and are presented in figure 1(c). The 1500 μm long phase shifter shows an elec-

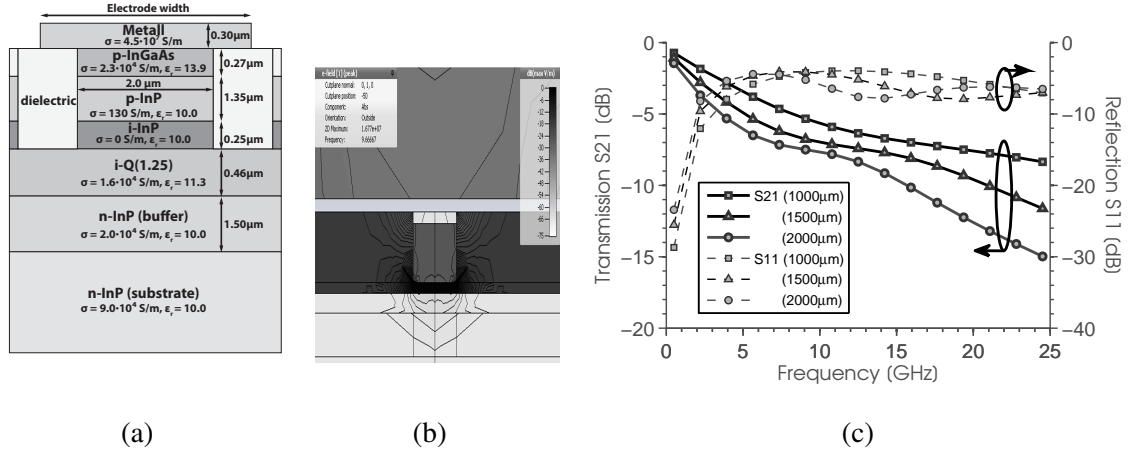


Figure 1: (a) Phase shifter cross section; (b) its quasi-TEM field solution; (c) simulated scattering parameters for three different lengths (20 μm width).

trical -6dB bandwidth of 7GHz allowing for 10Gbit/s operation. The bandwidth can be improved by decreasing the length in exchange for less phase shift per applied voltage.

Microwave Properties and Crosstalk

In this section, the dependence of the phase shifter's properties on the electrode width, the substrate conductivity and applied reverse bias are analyzed. Figure 2(a) and 2(b) show the influence of changing electrode width on its characteristic impedance, attenuation and scattering parameters at 10 GHz. The attenuation is lowest for 20 μm and increases towards smaller and higher widths. For small widths, the electric field is located more at the lossy p-doped cladding area and the metal cross section is smaller, increasing the dielectric and conductor losses. For high width values, the metal extends over the trench area and lies on a thin dielectric on top of the p-i-n layers, increasing the conductor loss again. Best transmission is obtained for widths between 10 μm and 20 μm .

Depending on the substrate conductivity, different kinds of mode propagation (skin-effect, slow-wave and dielectric) can occur in a microstrip line [3]. This can be observed in figure 2(c) and 2(d), where the influence of substrate conductivity on the microwave properties are shown. At high conductivities, the substrate behaves like a lossy conductor resulting in higher attenuation and impedance (skin-effect mode) and at very low conductivities, the substrate acts as a dielectric with very low losses. Inbetween lies the slow-wave region. Transitions between those three propagation regions typically show attenuation peaks [3] which are observed also here. For the n-doped substrate used in the COBRA generic integration process ($\sigma \sim 10^5$), propagation occurs in the transition region between slow-wave mode and skin-effect mode. The transmission is low because of low impedance and high attenuation in the slow-wave region. Therefore, a highly conductive or a semi-insulating substrate would result in better microwave performance.

The effect of applied reverse bias on the phase shifter is shown in figure 2(e) and 2(f). As the reverse bias increases, the depletion area gets thicker, increasing the effective thickness of the microstrip and therefore Z_C , and allowing for more field to penetrate dielectric instead of conductive material, reducing the attenuation. However, large bias voltages are not preferred in general as the optical waveguide loss and electrical power consumption is also increased.

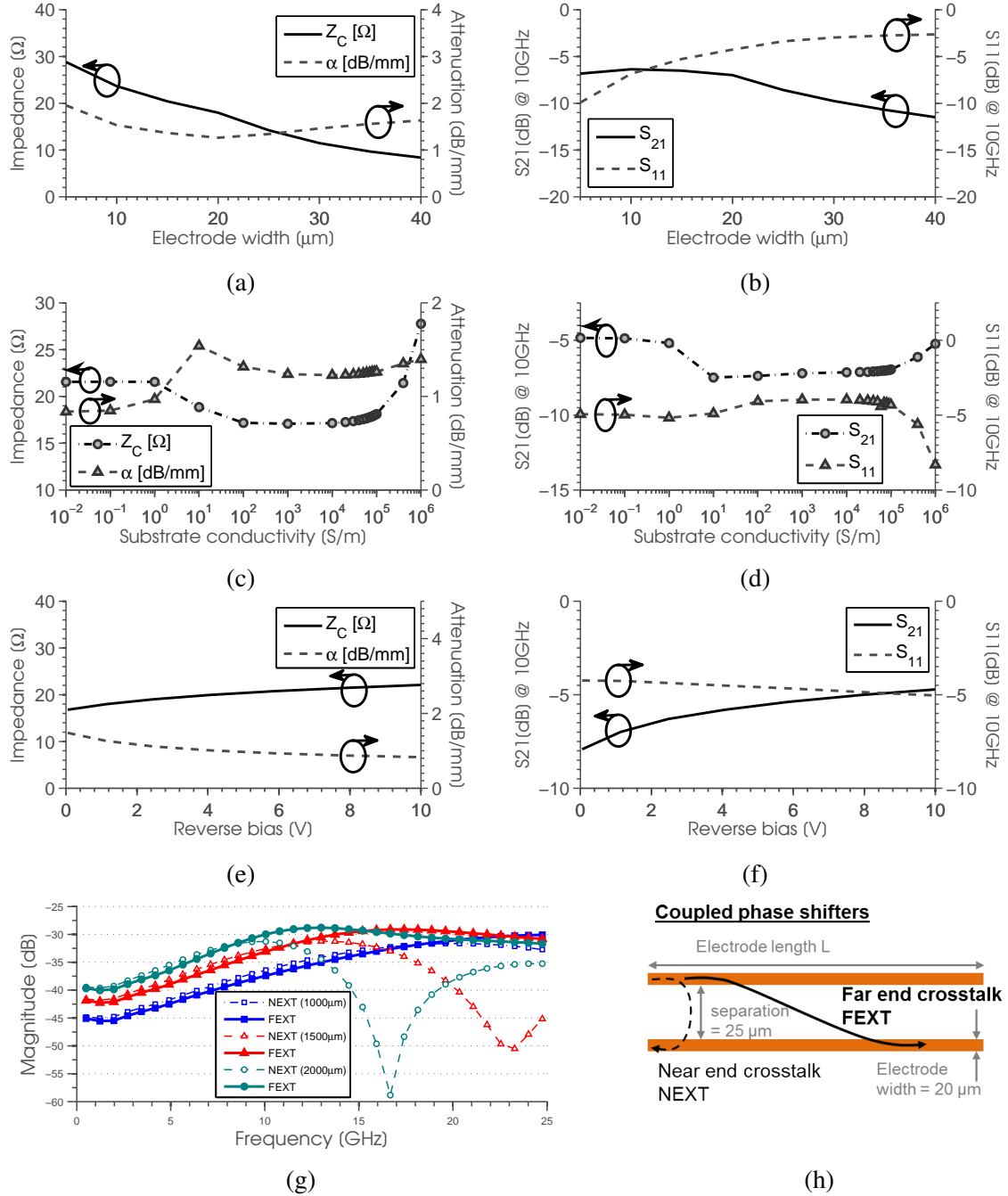


Figure 2: Influence of electrode width (a), substrate conductivity (c) and reverse bias (e) on the characteristic Impedance Z_C , microwave attenuation α , and their influence on scattering parameters (b), (d), (f) of a 1500 μm long phase shifter (values are from simulations at 10 GHz). (h) Configuration of two coupled phase shifters; (g) their NEXT and FEXT for different coupling lengths.

Near end and far end crosstalk from two coupled phase shifters (see figure 2(h)) at a distance of 25 μm have been analyzed for three coupling lengths by extending the simulation approach to the coupled structure and are shown in figure 2(g). Crosstalk is higher for longer coupling lengths and reaches -30 dB at 10 GHz for the 2000 μm structure. FEXT is more dominant at higher frequencies but starts to roll off due to high

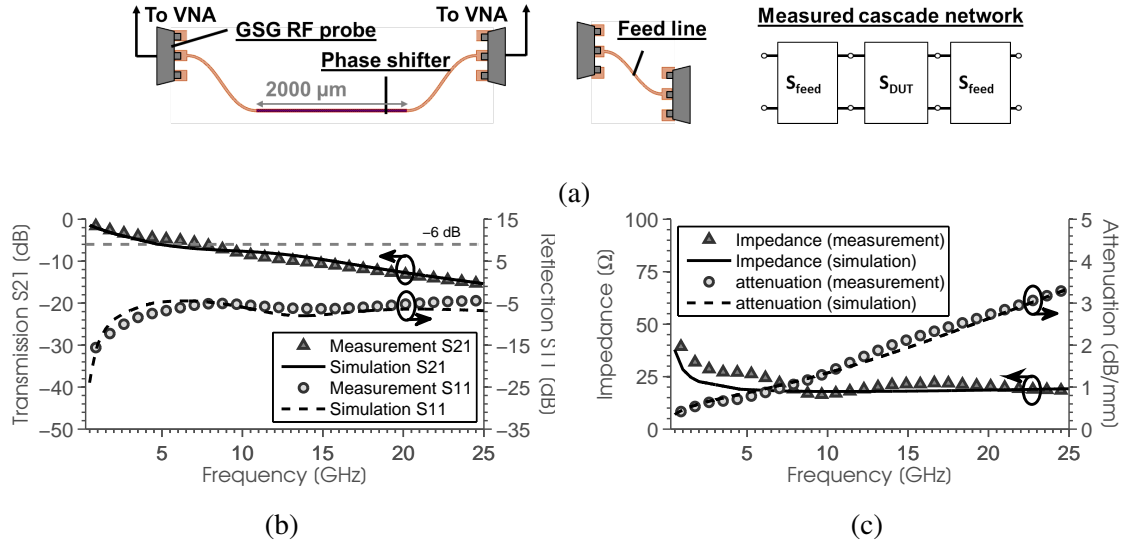


Figure 3: (a) Illustration of phase shifter with de-embedding configuration. S-parameters (b) and transmission line characteristics (c) of a 2000 μm long, 20 μm wide phase shifter.

frequency attenuation whereas NEXT shows periodic minima at resonance frequencies.

Experimental Results

Phase shifter test structures have been fabricated in the generic process and characterized using a 2-port vector network analyzer for model verification. De-embedding of the probe pad and feeding lines from the RF measurements has been performed using a cascade network approach as indicated in figure 3(a). The characteristics of the phase shifter section S_{DUT} can be extracted from the measurement when the feed line network S_{feed} is known. The measured scattering parameters of a 2000 μm long phase shifter are shown in figure 3(b) and match well with the simulated values. Extracted microwave parameters in figure 3(c) show an impedance around 25 Ω and attenuation of 1.5 dB/mm at 10GHz.

Conclusion

Microwave characteristics of an optical phase shifter have been analyzed for different electrode widths, substrate conductivities and reverse bias voltages and the model predictions have been verified by measurements on fabricated phase shifters. The 3D-EM model has been used to analyze crosstalk between two coupled phase shifters. Suitable testing structures need to be designed and measured in future work for further comparison with the crosstalk results.

References

- [1] M. Smit, X. Leijtens, E. Bente, J. v. d. Tol, H. Ambrosius, D. Robbins, M. Wale, N. Grote, and M. Schell. Generic foundry model for InP-based photonics. *IET Optoelectronics*, 5(5):187–194, 2011.
- [2] R. Lewen, S. Irmscher, and U. Eriksson. Microwave CAD circuit modeling of a traveling-wave electroabsorption modulator. *IEEE Transactions on Microwave Theory and Techniques*, 51(4):1117 – 1128, April 2003.
- [3] H. Hasegawa, M. Furukawa, and H. Yanai. Properties of microstrip line on si-SiO₂ system. *IEEE Transactions on Microwave Theory and Techniques*, 19(11):869–881, 1971.

Thermal Crosstalk reduction in InP based Photonic Integrated Circuits

G. Gilardi^{1,*}, W. Yao¹, X. Leijtens¹, M. Smit¹ and M. Wale^{1,2}

¹COBRA Research Institute, Photonic Integration Group, Department of Electrical Engineering,
University of Technology Eindhoven, The Netherlands

²OCLARO Technology Ltd., Caswell, Towcester, Northamptonshire, NN12 8EQ, United Kingdom
Corresponding author - *g.gilardi@tue.nl

Abstract: In this paper we numerically investigate the thermal crosstalk reduction that can be obtained by etching deep trenches in Indium Phosphide based photonic integrated circuits. We show how deep trenches between adjacent components modify the heat transfer path. The current injected in active components and the geometry of the trenches are the parameters considered in our analysis. We demonstrate how the geometry of the trenches play a role in the reduction of the thermal crosstalk. The numerical results show a reduction of the distance between components up to 50%.

Introduction

Since the introduction of the Arrayed Waveguide Grating (AWG) in 1988 [1] the complexity of Indium Phosphide (InP) based Photonic Integrated Circuits (PIC) has increased exponentially from a few to a few hundreds components. Significant progress in the development of PICs were reported with the introduction of WDM receivers [2] and transmitters [3]. The most severe limitations to further chip complexity development are: *i*) the unavoidable losses in passive components that restrict the total number of components that can be cascaded, *ii*) in active PICs the number of Semiconductor Optical Amplifier (SOA) is typically restricted up to a maximum of a few hundreds, because of heat sinking limitations and *iii*) the optical, electrical and thermal interaction between components, commonly identified with the term *crosstalk*. The most problematic crosstalk contributions in PICs are: the radiofrequency crosstalk, mostly related to the inductive and capacitive coupling; the optical crosstalk, related to unwanted phenomena as scattering, coupling and reflection of light; and the thermal crosstalk, due to the heat transfer from active components, i.e. SOA to passive components i.e. waveguides, phase modulators, AWG.

This paper focuses on the thermal crosstalk between components. Here we investigate how the thermal crosstalk affects the performance of a generic PIC and moreover we investigate the thermal crosstalk reduction that can be obtained by defining rectangular-shaped deep trenches between active and passive components.

Electro - Thermal model

By using a 3D finite elements method, we model the electro-thermal interaction in active components and the heat transfer from them to the rest of the PIC. Our model works as follows: *a*) A current I is injected in the active components, such as SOAs, and the Joule's heating is calculated, *b*) The heat transfer from the SOAs to the rest of the PIC is evaluated by solving the heat transfer equation, *c*) The local temperature in every interesting point of the PIC is evaluated. We simplify the heat transfer equation by considering the steady state regime, so that the equation governing the pure conductive heat transfer in a solid become:

$$C_p \rho \frac{\partial T}{\partial t} + \nabla \cdot (-k \nabla T) = Q \quad (1)$$

where k [W/(m·K)] is the thermal conductivity, ρ [kg/m³] is the material density, C_p [J/(kg·K)] is the specific heat capacity at constant pressure, T [°K] is the absolute temperature. Q [W/m³] contains the heat sources and it is related to the Joule's effect.

Thermal crosstalk simulations

In Figure 1 (left), we consider a simple photonic circuit based on one SOA and one Mach-Zehnder (MZ) modulator. The SOA is part of a more complex section of the PIC but it is not related to the MZ.

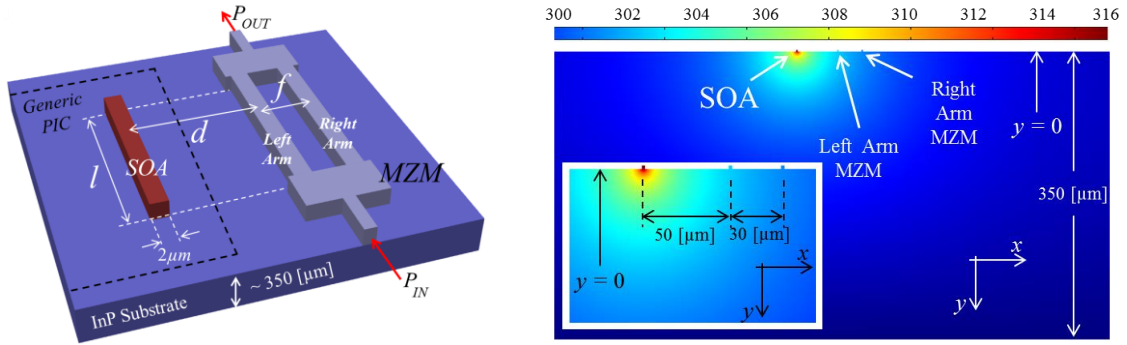


Figure 1: (left) Photonic integrated circuit considered in our model and (right) Temperature distribution when a current density of 10000 [A/cm²] is injected in the SOA (200 mA for a SOA length of 1 mm).

To reduce the number of geometrical variables we consider the same length, l , for the SOA and for MZ arms. Moreover we consider the distance between the arms of the modulator fixed: $f = 30 \mu\text{m}$. The thickness of the InP substrate is $t = 350 \mu\text{m}$. d is a variable in our analysis. The temperature of 300 [°K] is imposed at the bottom side of the chip by a copper heat sink (not shown in Figures 1) whose thermal conductivity is high enough to ensure a fixed temperature. Figure 2 (left) shows the SOA peak temperature, versus the injected current density. The quadratic behavior is due to the Joule's effect. Figure 2 (Right) shows the temperature distribution along the x -coordinate (with $y = 0$) as a function of the current density injected in the SOA. The left and right arms of the MZ are, respectively, at distance d and $d+f$, from the SOA and then, from Figure 2 (Right), the arms of the MZ are at different temperature. The mismatch in temperature, and then the mismatch in the refractive index, leads to a variation of the output optical power, with respect to the ground state (i.e. $J = 0$). The optical output power P_{out} , can be expressed as:

$$P_{out} = E_0 \cdot E_0^* \quad \text{where} \quad E_0 = \frac{E_{in}}{2} \left[e^{-j \frac{2\pi}{\lambda} n_L L} + e^{+j \frac{2\pi}{\lambda} n_R L} \right] \cdot e^{-\alpha L} \quad (2)$$

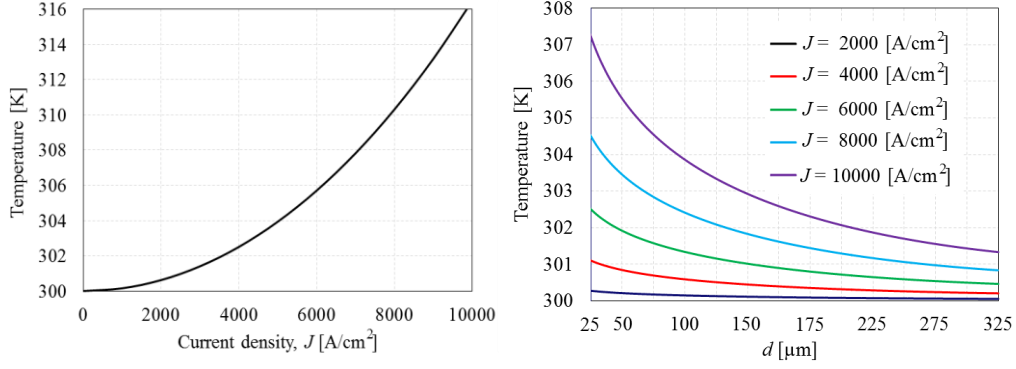


Figure 2: (Left) Peak temperature in a single SOA vs injected current density and (Right) Temperature distribution along the x-coordinate of the InP chip, with $y = 0$.

For the arms of the MZ we assume as optical loss $\alpha = 2$ [dB/cm] and we neglect its dependence with the temperature, because it does not change significantly for small temperature variations. E_{in} in equation (3) is the unitary field considered as MZ optical input, while n_L and n_R are, respectively, the effective refractive index for the left and right arm of the MZ modulator. Both n_L and n_R depend on the temperature: $n_{R(L)} = n_0 + \eta \Delta T$. $n_0 = 3.25$ is the effective refractive index considered for each arm of the MZ at $T = 300$ [°K], while $\Delta T_{L(R)}$ is the temperature variation in the arm. The coefficient $\eta = 2.5 \cdot 10^{-4}$ [1/°K] is the thermo-optical coefficient considered for InP.

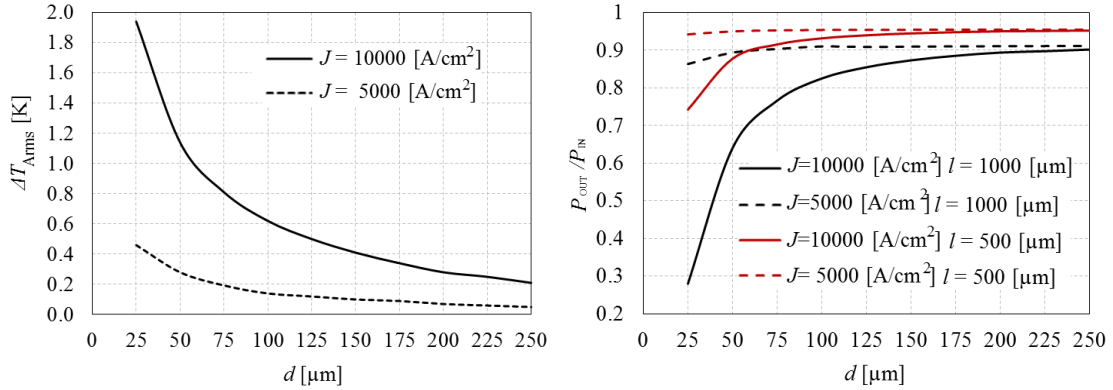


Figure 3: (Left) temperature difference between the left and right arm of the MZ and (Right) P_{out} vs position of the MZ for two length and two values of injected current.

Figure 3 (left) reports the difference in temperature between the two arms of the modulator as a function of the distance between modulator and SOA for two values of current density injected in the SOA. Figure 3 (Right) shows the effect of the thermal crosstalk to the optical output power for two different MZ lengths and for two values of injected current. For high values of d , P_{out} is only limited by the waveguide losses. Up to $l = 1$ mm, we consider the SOA and the MZ “isolated”, when $P_{out} > 0.9P_{in}$ for a current density value up to 10000 A/cm². For instance, the minimum values of d (d_{MIN}) to avoid the crosstalk effects for $J = 10000$ [A/cm²] and $l = 1000$ μm, is $d_{MIN} \sim 240$ μm.

Trench effects

The trenches are intended as deep apertures between components with the purpose to modify the heat transfer path. They do not modify the optical properties of the waveguides because they are far from the guiding structures. We consider the trench positioned in the middle between the SOA and the MZ. To evaluate the performances of the trenches we consider the case of $J = 10000 \text{ [A/cm}^2\text{]}$ for a length $l = 1000 \text{ }\mu\text{m}$. In this case d_{MIN} is $240 \text{ }\mu\text{m}$ if no trenches are considered between the SOA and MZ.

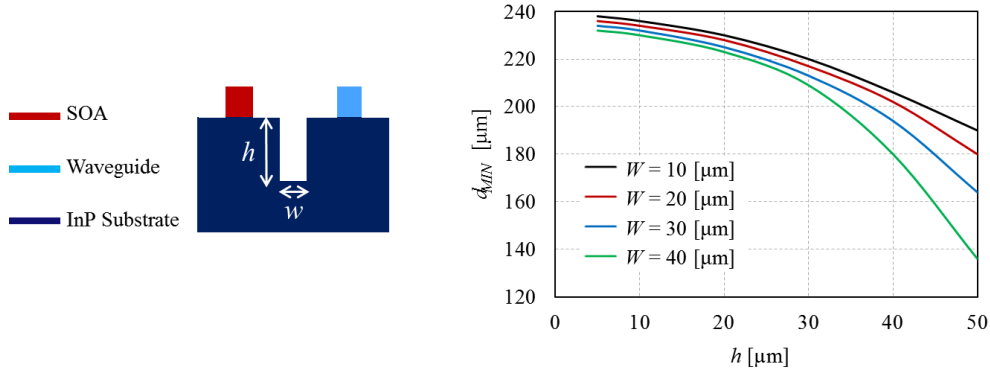


Figure 4: (left) Trench geometrical definition and (right) Reduction of the minimum distance between components due to the trenches.

Figure 4 (Right) shows the effect of the trench in relation to its geometry. Both parameters w and h play a role in the modification of the heat transfer path. The depth of the trenches is not critical for the mechanical integrity of the InP wafer since it is, in the most severe case reported in our simulation, less than 20% of the total thickness of the wafer. Moreover the trenches are localized around the active components and they do not cover the whole chip. From our simulation the trench with $w = 40 \text{ }\mu\text{m}$ and $h = 50 \text{ }\mu\text{m}$ allows the reduction of the distance between SOA and MZ up to $135 \text{ }\mu\text{m}$: more than 40% if compared with the case without trenches, where d_{MIN} is $240 \text{ }\mu\text{m}$.

Conclusions

We have developed a model to investigate the thermal crosstalk effect in photonic integrated circuits including both active and passive components. The model is applied to investigate the thermal crosstalk reduction that can be obtained by etching deep trenches between active and passive components. We demonstrate how the geometries of the trenches play a role in the reduction of the thermal crosstalk. The numerical results show that the distance between components can be reduced up to about 50%.

References

- [1] M. K. Smit "New focusing and dispersive planar component based on an optical phased array," Electron. Lett. 24(7), 385-386 (1988).
- [2] M. R. Amersfoort, C. R. de Boer, Y. S. Oei, B. H. Verbeek, P. Demeester, F.H. Groen, and J.W. Pedersen, in: Proceedings of the 19th European Conference on Optical Communication (ECOC'93), Montreux, Switzerland, 1993, Vol. 3, pp. 49-52.
- [3] M. Zirngibl and C. H. Joyner "12 frequency WDM laser-based on a transmissive waveguide grating router," Electron. Lett. 30(9), 701, 702 (1994).

Design of a MEMS tunable mid-infrared VCSEL integrated on the SOI platform

Ruijun Wang^{1,2}, Dorian Sanchez^{1,2}, Sulakshna Kumari^{1,2}, Roel Baets^{1,2}, Gunther Roelkens^{1,2}

¹ Photonics Research Group, INTEC Department, Ghent University-IMEC, Belgium

² Center for Nano- and Biophotonics (NB-Photonics), Ghent University, Belgium

A widely-tunable mid-infrared vertical-cavity surface-emitting laser (VCSEL) structure based on Si-electronics-compatible processes and adhesive wafer bonding technology is suggested and numerically investigated. This hybrid laser consists of a silicon-on-insulator high-index contrast grating (HCG), a III-V active region and a distributed Bragg reflector (DBR). The HCG works as a highly-reflective mirror to replace the conventional bottom DBR. In this paper, an overview of the HCG design, VCSEL cavity design and the simulated device tunability is presented. In this context, the angle dependence of the reflectivity of the HCG is analyzed and a tuning range of about 100 nm and a wavelength tuning efficiency of 0.205 $\mu\text{m}/\mu\text{m}$ are predicted for the device.

Introduction

Laser sources emitting in the near- and mid-infrared region has been attracting a lot of attention recently for security and environmental applications, since several important gases, like CO, CH₄, N₂O, etc. can be detected using this wavelength range [1]. For example, the wavelength range around 2.3 μm offers the first water absorption free spectral window for CO detection. Vertical-cavity surface-emitting laser (VCSELs) are good candidates for sources in this wavelength range, since it can provide valuable characteristics such as low power consumption, small beam divergence, wide tunability and cost-effective packaging. Among the III-V material systems, GaSb-based heterostructures are a perfectly suited semiconductor material for covering the 2 – 3 μm range. Recently, GaSb-VCSELs emitting at wavelengths around 2.3 μm have been demonstrated based on a monolithic [2] or hybrid [3] configuration, both containing thick and lossy semiconductor distributed Bragg reflectors (DBRs) which could be replaced by high-index contrast grating (HCG) reflectors. GaAs and InP-based VCSELs have been reported at respectively 0.85 and 1.55 μm using one or two HCGs as mirrors [4-6], however such a configuration has not yet been demonstrated in the GaSb system [7].

In this paper, we propose a widely-tunable mid-infrared electrically-pumped VCSEL structure based on a CMOS-compatible HCG mirror and adhesive wafer bonding technology. The silicon-on-insulator (SOI)-based HCG is analyzed by the rigorous coupled-wave analysis (RCWA) method. Furthermore, a two-dimensional finite-difference time-domain (FDTD) method is used to study the lasing properties.

VCSEL Integration Design

The suggested GaSb HCG VCSEL structure is shown in Figure 1, it consists of a III-V die bonded on a SOI-HCG. In this design the III-V contains an active region as well as a semiconductor DBR. The resonant cavity is formed between the DBR and the free-

standing HCG. The fabrication of the designed SOI-HCG structures is based on a CMOS compatible process: 193 nm deep UV lithography is used to pattern SOI with a 220 nm thick silicon layer. Then the SOI die is etched in buffered HF solution to fabricate freestanding HCG. The integration of the III-V die on the freestanding HCG is realized by adhesive bonding using an ultra-thin Benzocyclobutene (DVS-BCB) layer as an adhesive bonding agent. After bonding, the GaSb substrate is removed and the VCSEL is processed. Specifically, good electro-optical confinement is achieved by selectively etching the 20 nm-thin InAsSb layer of the tunnel junction [8]. The VCSEL is then electrically contacted and the HCG can be electro-statically actuated using the intra-cavity contacts.

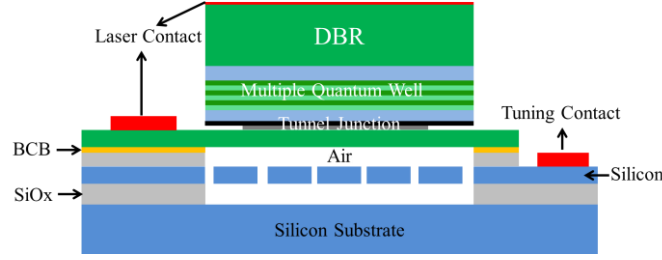


Figure 1: Schematic drawing of the tunable GaSb VCSEL integrated on SOI.

HCG Design

The SOI-HCG mirror structure is composed of a 220 nm thick sub-wavelength grating mirror on top of a silicon substrate as shown in Figure 2(a). Because some parameters such as the silicon layer thickness (220nm) and buried oxide thickness (2 μm) are fixed by the standard SOI technology, by playing with the grating period and duty cycle we can change the optical properties of the grating [9]. Figure 2(b) shows the reflectivity spectra simulated by the RCWA method of a SOI-HCG and typical 20-pair semiconductor DBR made of GaSb/AlAsSb. The HCG parameters used in this simulation are: period = 1.5 μm , duty cycle = 50%, the refractive index of the silicon is 3.48, air is 1 and the incident angle α is zero degree. No losses are considered in this simulation. Both the HCG and DBR exhibit high reflection in the range around 2.3 μm . For the HCG, a very broadband mirror with reflectivity >99% is obtained over the range 2.25 μm -2.38 μm as shown in the inset image of Figure 2(b). From this simulation it is clear that the HCG has a strong polarization dependence.

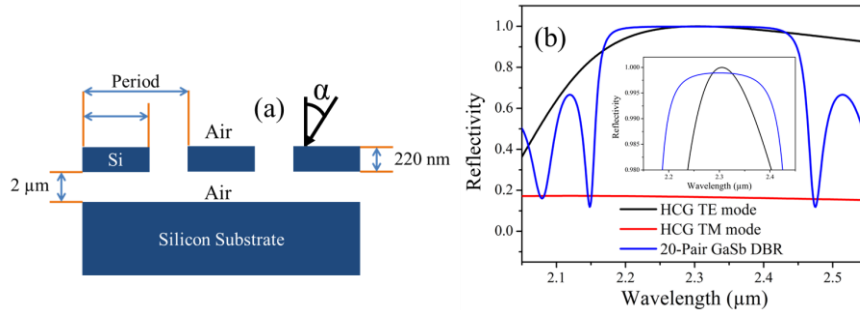


Figure 2: (a) Schematic drawing of the SOI-HCG structure, (b) reflectivity spectra of the SOI-HCG and the 20-pair GaSb-AlAsSb DBR.

Numerical simulations based on RCWA method were carried out to study the fabrication tolerance of different parameters in the HCG structure. The contour plot in Figure 3(a) shows the reflectivity of the HCG as a function of the period and duty-cycle

for a fixed wavelength of $2.3\ \mu\text{m}$. We can see the duty cycle has around 30% fabrication tolerance while still keeping 99% reflectivity. Because the beam profile in VCSELs usually carries high incident angle components that are defined by the optical aperture, the design of the HCG dimensions should also consider the angle dependence of the reflectivity. As shown in Figure 3(b), the reflectivity and its incident angle dependence are plotted for varying duty cycles at a fixed HCG-period of $1.5\ \mu\text{m}$. The regions between $\text{DC}=25\text{-}30\%$ and $50\text{-}55\%$ shows a better angular dependence and a higher reflectivity ($>99.9\%$) than the region around $\text{DC}=40\%$. Since the high-order modes in a VCSEL have an angle divergence larger than 10° , HCGs are particularly interesting to enhance single-mode emission of VCSELs [4].

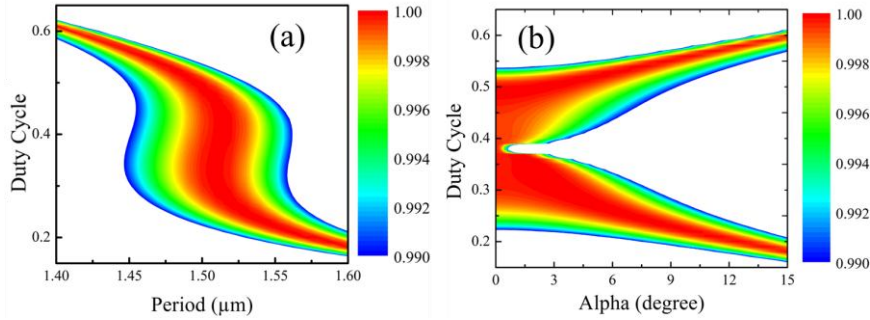


Figure 3: (a) RCWA simulated SOI-HCG reflectivity as a function of grating period and duty cycle for fixed $\lambda = 2.3\ \mu\text{m}$, (b) contour plot of reflectivity versus duty cycle and incident angle.

Simulated Lasing Properties

The quality factor and the field distribution of the laser mode were investigated using the FDTD method. In this simulation, a Gaussian pulse is used to excite the cavity mode. The FDTD simulated resonant spectra shown in Figure 4(a) indicate a cavity resonance at $2.31\ \mu\text{m}$, and the estimated quality factor of this cavity mode is about 1600. The mode profile of this laser structure, shown in Figure 4(b), clearly shows that a strong vertical resonance occurs between the bottom HCG and top DBR.

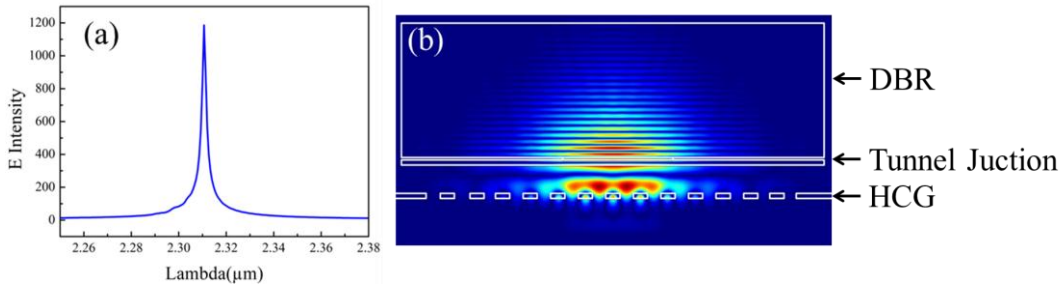


Figure 4: (a) FDTD simulated resonant spectra of the HCG GaSb VCSEL, (b) field profile of the resonant mode of the structure.

The vertical displacement of the HCG can change the optical cavity length, thus results in a change in the lasing wavelength [6]. So we can electro-statically actuate the HCG to tune the VCSEL emission wavelength. In order to increase the tuning efficiency, we can deposit a $200\ \text{nm}$ SiNx antireflection (AR) layer on the n-GaSb layer. Figure 5 shows the resonant spectra and quality factor of the tunable VCSEL with AR layer as a function of the displacement of the HCG: by displacing the HCG 500nm , a wavelength

tuning from 2.31 μm to 2.41 μm can be obtained. Therefore this structure has great potential for the realization of a widely tunable VCSEL. Over the whole wavelength range, the Q-factor of the cavity is calculated to be above 1300.

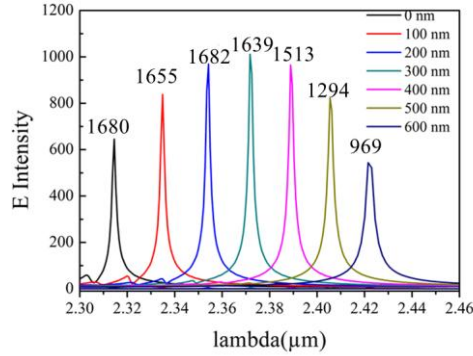


Figure 5: Resonant spectra of the tunable VCSEL versus movement of HCG.

Conclusion

In conclusion, we have suggested a hybrid laser structure for mid-infrared silicon photonics by integrating a GaSb VCSEL on an SOI grating. RCWA and FDTD simulation results show that the SOI-HCG can work as a highly-reflective mirror to replace conventional GaSb-based DBRs. This hybrid structure exhibits promising tunability and Q-factor characteristics suitable for a widely tunable VCSEL.

Acknowledgments

This work was carried out in the framework of the FP-7 ERC project MIRACLE.

References

- [1] A. Vicet, D. A. Yarekha, A. Perona, Y. Rouillard, S. Gaillard, and A. N. Baranov, "Trace gas detection with antimonide-based quantum-well diode lasers," *Spectrochim. Acta, A*, vol. 58, 2405–2412, 2002.
- [2] A. Bachmann, K. Kashani-Shirazi, S. Arafin, and M.-C. Amann, "GaSb-Based VCSEL with buried tunnel junction for emission around 2.3 μm ," *IEEE Select. Top. in Quant. Electron.*, vol. 15, 933–940, 2009.
- [3] D. Sanchez, L. Cerutti, E. Tournié, "Single-mode monolithic GaSb vertical-cavity surface-emitting laser," *Optics Express*, vol. 20, 15540–1554, 2012.
- [4] M. C. Y. Huang, Y. Zhou, and C. J. Chang-Hasnain, "A surface-emitting laser incorporating a high index-contrast subwavelength grating," *Nat. Photonics*, vol. 1, 119–122, 2007.
- [5] C. Sciancalepore, B. Bakir, X. Letartre, J. Harduin, N. Olivier, C. Seassal, J. M. Fedeli, and P. Viktorovitch, "CMOS-compatible ultra-compact 1.55- μm emitting VCSELs using double photonic crystal mirrors," *IEEE Photon. Technol. Lett.*, vol. 24, 455–457, 2012.
- [6] M. C. Y. Huang, Y. Zhou, and C. J. Chang-Hasnain, "A nanoelectromechanical tunable laser," *Nat. Photonics*, vol. 2, 180–184, 2008.
- [7] Y. Laaroussi, C. Chevallier, F. Genty, N. Fressengeas, L. Cerutti, T. Taliercio, O. Gauthier-Lafaye, P.-F. Calmon, B. Reig, J. Jacquet, and G. Almuneau, "Oxide confinement and high contrast grating mirrors for Mid-infrared VCSELs," *Opt. Mater. Express*, vol. 3, 1576, 2013.
- [8] D. Sanchez, L. Cerutti, and E. Tournié, "Selective lateral etching of InAs/GaSb tunnel junctions for mid-infrared photonics," *Semicond. Sci. Technol.*, vol. 27, 085011–085015, 2012.
- [9] R. Wang, D. Sanchez, and G. Roelkens, "Design of a High Contrast Grating GaSb-based VCSEL integrated on Silicon-On-Insulator," in *IEEE PHOTONICS CONFERENCE*, vol. 3, 91–92, 2013.

Investigation of Carbon Doped Amorphous Silicon, an Alternative Material for All-Optical Signal Processing for On-Chip SOI PICs

P. K. Pal, G. Morthier

Ghent University, Department of Information Technology, Sint-Pietersnieuwstraat 41, Ghent, Belgium

We investigate the properties of carbon-doped hydrogenated amorphous silicon ($a\text{-Si}_x\text{C}_{1-x}\text{H}$) thin-films produced by radio frequency plasma enhanced chemical vapour deposition (rf-PECVD) under low temperature condition, and compare them with those of non-carbon-doped amorphous silicon. Spectroscopic ellipsometry (SE) analysis has been used to characterise the deposited thin-films. During deposition argon gas has been used for passivation with different dilution ratio. The deposition temperature, dilution ratio and rf-power are important parameters that influence both the hydrogen content and the optical band gap. Optical multimode waveguides have been fabricated with this material on an SOI wafer and have been characterised.

Introduction

Silicon based photonic devices have great potential for applications in optical communications. They are small in dimensions, need low power consumption and are compatible with present CMOS technology. Many optical signal-processing applications like optical signal regeneration, wavelength conversion [1, 2], multiplexing and optical logic use non-linear effects. In the communication wavelength range, silicon on insulator (SOI) photonic integrated circuits (PICs) are ideal for those operations having low loss, high power confinement and high power density. Amorphous silicon (a-Si) on SOI has many advantages over crystalline silicon (c-Si) such as high Kerr-effect and low non-linear absorption. Non-linear effects [1, 3] based on the Kerr effect such as Self-Phase Modulation (SPM) and Cross-Phase Modulation (XPM) are useful for all optical signal regeneration, multiplexing, wavelength conversion [4, 5].

In spite of many advantages though, hydrogenated amorphous silicon (a-Si:H) exhibits a degradation when exposed to high intensity of light for a long time. This effect is called the Staebler-Wronski effect. By slightly increasing the band gap value by doping carbon in a-Si:H, it could be possible to reduce this effect to a large extent.

Experimental

We prepared various carbon doped a-Si:H and non-doped a-Si:H thin-layers on glass and silicon wafer by a high frequency rf plasma-enhanced chemical vapour deposition (PECVD) using different rf powers and different substrate temperatures. The substrate temperature was kept between 180°C and 200°C. The rf power was varied from 20 to 150W. Silane (SiH_4) and methane (CH_4) flow-ratio control the percentage of carbon-doping during deposition. Argon gas was used for passivation. Both the carbon doped a-Si:H and a-Si:H thin-films were characterized by ultraviolet-visible-infrared (UV-VIS-IR) spectroscopic ellipsometry (SE). The SE data are analyzed to obtain structural and

optical properties of the carbon doped a-Si:H and a-Si:H thin-films. In order to calculate the desired values (e.g. films thickness, optical constants) from the measured data, a suitable optical model has been applied.

First, 220 nm of a-Si:H was deposited using PECVD process on top of 2000 nm buried oxide. Waveguides of varying width (2 μ m to 8 μ m) were fabricated using optical lithography and dry etching [6]. The waveguides were cleaved at both facets with different lengths and interfaced to optical lensed fibers for input and output coupling of light.

Carbon doped a-Si:H and a-Si:H thin-films were exposed to high power radiation (15mW cw laser at 1550nm) for 30 and 50 hours to estimate the degradation.

Results

The deposition rate increases with increasing r.f. power (Fig.1 (a)). From SE data analysis of optical constants, it is evaluated that the band gap value decreases with increasing r.f. power (Fig.1 (b)). It is observed that the Ar gas flow has strong influence on the deposition rate. It is found that the deposition rate varies from 38nm/min to 50nm/min for a substrate temperature at 180^oC. Also the band gap value decreases with increasing dilution ratio for Ar gas (Fig.2).

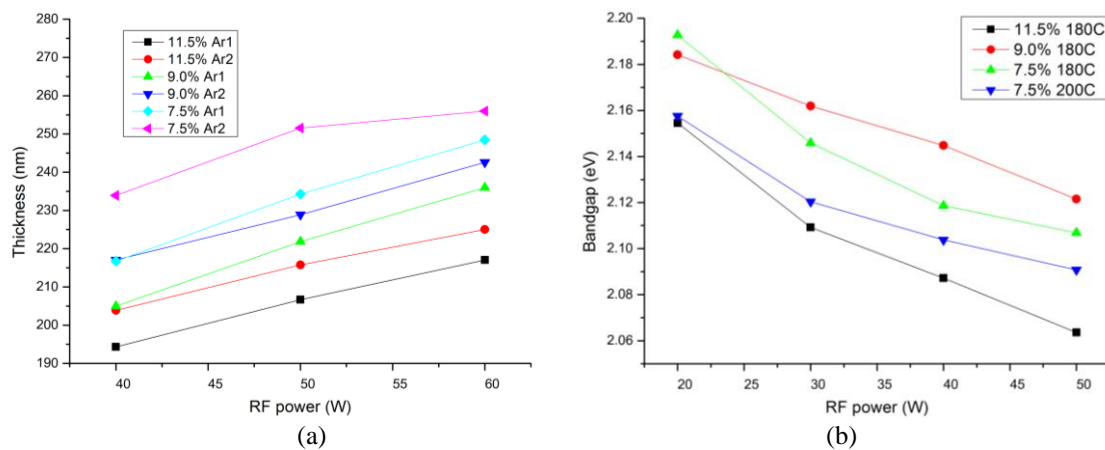


Fig.1: (a) Variation of deposition thickness and (b) band gap value with the r.f. power for different SiH₄-CH₄ mixtures and different temperatures.

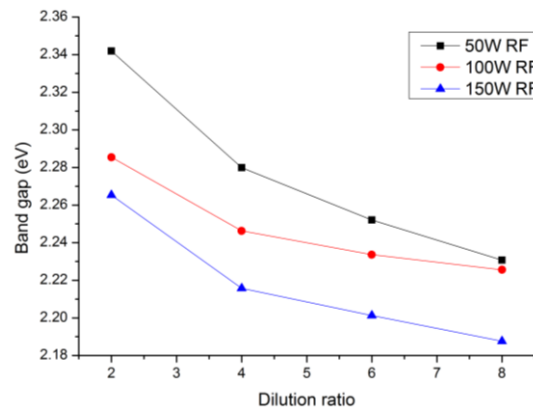


Fig.2: Variation of band gap value with dilution ratio of Ar gas with different rf power.

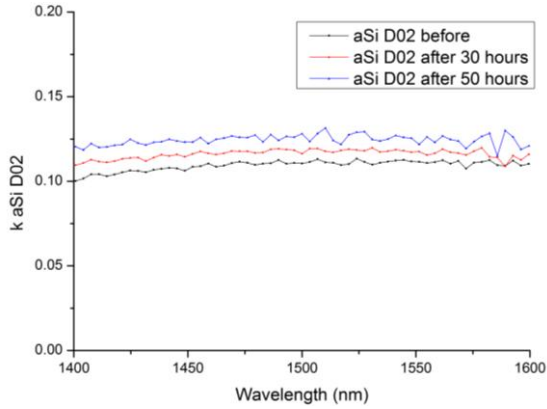


Fig.3: Increase in k -value of a-Si:H due to degradation with exposure of high intensity light for 30 and 50 hours.

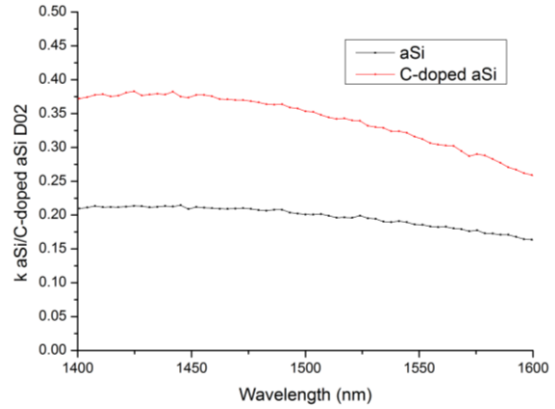


Fig.4: Relative comparison for k -values between aSi:H and carbon-doped aSi:H.

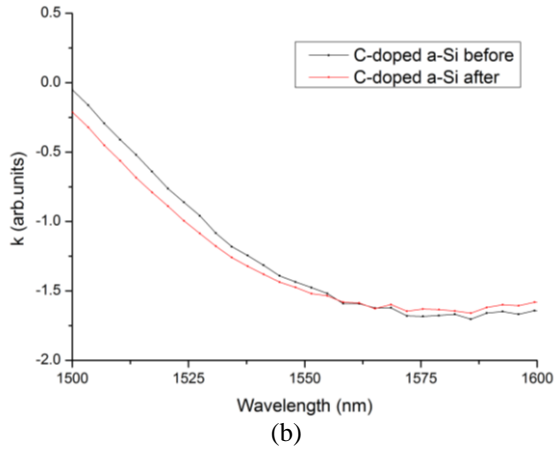
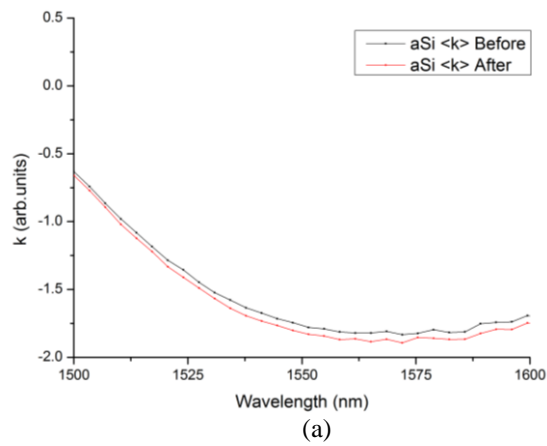


Fig.5: (a) Change in k -value of a-Si:H and (b) carbon doped a-Si:H thin-films deposited on SOI with exposure of high intensity light for 30 hours.

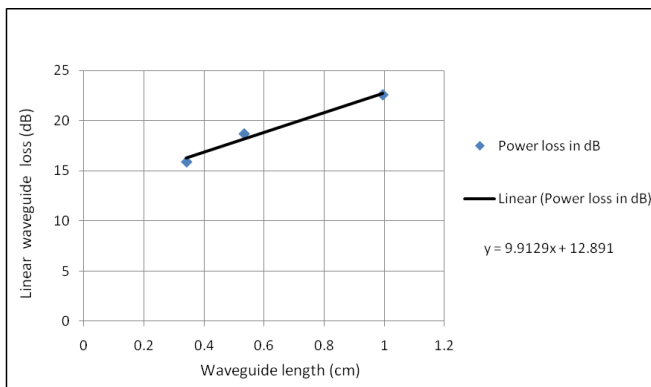


Fig.6: Linear loss of carbon-doped a-Si:H waveguide with dimensions $6\mu\text{m} \times 0.220\mu\text{m}$

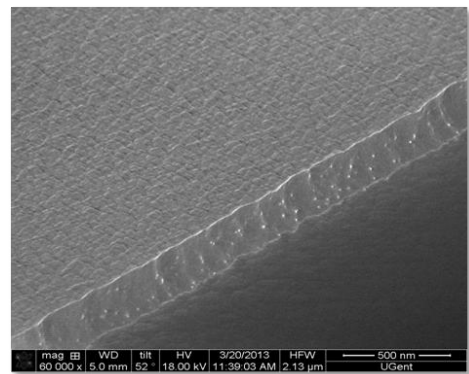


Fig.7: SEM image of $6\mu\text{m}$ wide carbon-doped a-Si:H waveguide.

Fig.3 shows the degradation of a-Si:H due to exposure with high intensity of light for 30 and 50 hours. Syntune tuneable cw laser has been used for exposure at 12dBm output power and with central wavelength tuned at 1550nm. It is found from the figure that we have around 10% and 20% increased in k -value for the exposed duration of 30 and 50 hours respectively. Fig.4 shows a relative comparison for k -values between aSi:H and

carbon-doped aSi:H. Fig.5.(a) and Fig.5.(b) represents the change in k-values for a-Si:H and carbon-doped a-Si:H thin-films deposited on SOI with exposure of high intensity of light for 30 hours. It is found that the carbon-doped a-Si:H thin-film has less degradation for the central wavelength around 1550nm.

Fig.6 represents the measured linear loss of carbon-doped a-Si:H waveguides with cross-sectional dimensions as $6\mu\text{m} \times 0.220\mu\text{m}$. The linear loss for the multimode waveguides have been calculated as 9.9dB/cm. Fig.7 shows the sidewall roughness of such multimode waveguides.

Conclusions

Thin film thickness, structural and optical properties of carbon doped a-Si:H and a-Si:H thin films deposited using PECVD system have been measured by UV–VIS-IR SE. It has been found that carbon doped a-Si:H material has low degradation compared to a-Si:H in the wavelength regime around 1550nm. Carbon-doped a-Si:H waveguides have been successfully fabricated and measured for linear loss. The sidewall roughness of those waveguides needs to be minimized by optimizing the etching process to have low linear loss waveguides.

Acknowledgement

The authors acknowledge the financial support from the Belgian IAP network Photonics@be.

References

- [1] H K Tsang and Y Liu, "Nonlinear optical properties of silicon waveguides," *Semicond. Sci. Technol.* Vol.23, 064007, 2008.
- [2] Guo-Wei Lu; Tipsuwannakul E.; Miyazaki T.; Lundstrom C.; Karlsson M.; Andrekson P.A., "Format Conversion of Optical Multilevel Signals Using FWM-Based Optical Phase Erasure," *Journal of Lightwave Technology*, Volume: 29 Issue:16, pp.2460 – 2466, 2011.
- [3] B. Kuyken, H. Ji, S. Clemmen, S. Selvaraja, J. Safiouui, H. Hu, M. Pu, M. Galili, P. Jeppesen, G. Morthier, S. Massar, L.K. Oxenlowe, G. Roelkens, R. Baets, Nonlinear properties of and nonlinear processing in hydrogenated amorphous silicon waveguides, *Optics Express*, 19(26), p.B146-B153, 2011.
- [4] Amy C. Turner-Foster, Mark A. Foster, Jacob S. Levy, Carl B. Poitras, Reza Salem, Alexander L. Gaeta, and Michal Lipson, "Ultrashort free-carrier lifetime in low-loss silicon nanowaveguides ," *Optics Express*, Vol. 18, Issue 4, pp. 3582-3591, 2010.
- [5] Shoji, Yuya; Nakanishi, Koichi; Sakakibara, Youichi; Kintaka, Kenji; Kawashima, Hitoshi; Mori, Masahiko; Kamei, Toshihiro, "Hydrogenated Amorphous Silicon Carbide Optical Waveguide for Telecommunication Wavelength Applications", *Applied Physics Express*, Volume 3, Issue 12, pp. 122201-122201-3, 2010.
- [6] S. K. Selvaraja, *et al.*, "Low-loss amorphous silicon-on-insulator technology for photonic integrated circuitry," *Optics Communications*, vol. 282, pp. 1767-1770, 2009.

C₆₀-assisted electron-beam lithography for loss reduction in InP membrane waveguides

Y. Jiao, J. Pello, E. Smalbrugge, E.J. Geluk, M.K. Smit, and J.J.G.M. van der Tol

COBRA, Eindhoven University of Technology, The Netherlands

In this contribution we present a method to prepare a mixed material composed of a positive electron-beam resist (ZEP520A) and C₆₀ fullerene. The addition of C₆₀ to the ZEP resist changes the material properties under electron beam exposure significantly. This mixed material has shown an increased clearance dose as well as an increased reflow temperature. An improvement of the mixed material on the thermal resistance has been demonstrated by fabricating multimode interference couplers and coupling regions of micro-ring resonators. This shows improvement with respect to the same structures fabricated with normal ZEP resist. An improvement on the propagation loss of the InP membrane waveguides from 6 to 3 dB/cm using this mixed material is shown.

Introduction

The ever-growing demand for high-speed chip-scale data transport in computers has inspired the development of on-chip optical interconnects [1], among which the InP membrane on Si (IMOS) technology [2] is a novel concept for realizing such a photonic interconnect layer on top of a conventional complementary metal oxide semiconductor (CMOS) circuit. Compared to other concepts such as III-V bonded on silicon-on-insulator (SOI) or Si/Ge, the major advantage of the IMOS technology is the potential to realize monolithic III-V active-passive integration with both compact passive photonic devices and high-performance active devices.

The IMOS passive waveguides and devices can be fabricated using electron-beam lithography (EBL) with ZEP520A resist. During the characterization of those devices we have observed a relatively high propagation loss of the InP membrane waveguides. The average propagation loss is around 10-15 dB/cm with a best result of 6 dB/cm. It is suspected to be mostly caused by the sidewall roughness on the ZEP resist pattern after exposure and development. Furthermore the erosion on the resist pattern when using it as plasma etching mask increases the roughness. Such high propagation loss will significantly limit the performance of both active and passive InP membrane devices. Therefore it is crucial to develop an improved electron-beam resist with reduced roughness.

One of the practical approaches to loss reduction is to use the so-called fullerene-assisted resist system [3]. The incorporation of fullerene in a resist system can improve the material strength during physical etching (e.g., reactive ion etching (RIE)) as well as wet chemical etching (e.g., developer solution) [3]. As a result a reduced sidewall roughness of the resist pattern can be obtained. The reduction of waveguide propagation loss has been experimentally demonstrated for Si wire waveguides [4] and InGaAsP wire waveguides [5] by incorporating C₆₀ (one of the fullerene types) into ZEP resist.

In this contribution we will present the preparation of such C₆₀-assisted ZEP resist and use it in the EBL process for realizing InP waveguides. We will show the change of the resist properties due to the C₆₀ material. Finally we will demonstrate the reduction of waveguide propagation loss using this mixed resist.

Resist preparation

The preparation procedure of the C₆₀/ZEP mixed resist is similar to what has been described in [3]. The C₆₀ powder is first dissolved in anisole (solubility is about 5.6 g per liter [6]) and then mixed with ZEP520A resist solution by magnetic stirring. The mass ratio between C₆₀ and ZEP material is 1:9. The final mixed solution will appear black due to the presence of C₆₀, instead of transparent as for normal ZEP resist.

Since additional amount of anisole is added as solvent into the mixed resist solution, the concentration of ZEP material will decrease. As a result the thickness of the mixed resist after spin-coating will be less than that of the normal ZEP resist. For instance, the thickness of the mixed resist at a spin speed of 2000 rpm is about 100 nm, while the thickness of the normal ZEP resist at 4000 rpm is 300 nm.

Resist properties

The addition of C₆₀ material in the ZEP resist changes significantly the properties of the resist system regarding the clearance dose during EBL and the thermal behaviour. It is found that in the Raith 150-2 EBL system with 20 kV voltage and 10 μm aperture settings, the clearance dose of the mixed resist has increased to 48 $\mu\text{C}/\text{cm}^2$ while the normal ZEP resist has a clearance dose of 38 $\mu\text{C}/\text{cm}^2$.

A post-exposure bake is crucial for obtaining a smooth resist sidewall. The bake temperature is chosen close to the reflow temperature, so that the roughness on the sidewalls can be smoothened during controlled reflow. After mixing with C₆₀, the reflow temperature of the mixed resist has increased from 154 $^{\circ}\text{C}$ for normal ZEP to 170 $^{\circ}\text{C}$. This is due to the increased thermal strength provided by the C₆₀ material. Furthermore, the mixed resist also shows much less deformation after 170 $^{\circ}\text{C}$ baking compared to the normal ZEP resist after 154 $^{\circ}\text{C}$ baking. As can be seen from Fig. 1(a), the corners in the MMI coupler structure are all rounded due to the reflow of the normal ZEP resist at 154 $^{\circ}\text{C}$. This might increase fabrication errors of the devices. On the other hand after 170 $^{\circ}\text{C}$ baking, the mixed resist still shows relatively sharp, as designed corners (see Fig.1(b)).

The improved thermal resistance of the mixed resist also helps to realize structures with

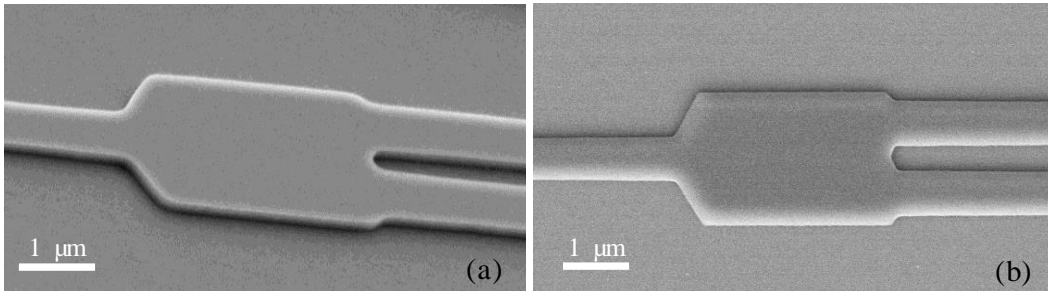


Fig. 1 (a) The MMI coupler structure fabricated by using normal ZEP resist. (b) The MMI coupler structure fabricated by using the mixed resist.

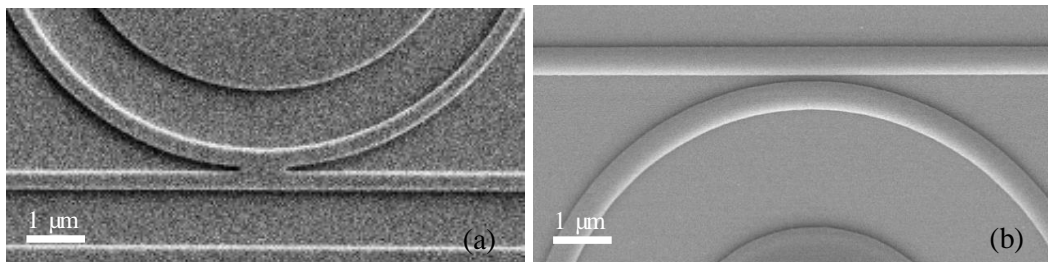


Fig. 2 (a) The coupling region of MRRs fabricated by using normal ZEP resist. (b) The coupling region of MRRs fabricated by using the mixed resist.

narrow gaps. For instance the coupling regions of micro-ring resonators (MRRs) are fabricated using both mixed resist and normal ZEP, and baked at 170 °C and 154 °C, respectively. It can be clearly seen from Fig. 2(a) and (b) that the gap in the coupling region fabricated with normal ZEP resist has already closed due to the deformation of the material. On the other hand, the gap fabricated with the mixed resist survives after baking. Thus it is obvious that the IMOS photonic devices can benefit more fabrication accuracy from this enhancement of the thermal resistance in the mixed resist.

Loss reduction

Straight IMOS passive waveguides of different lengths are fabricated using the mixed resist for loss measurement. The fabrication starts by depositing a 1850 nm thick SiO₂ layer on top of a Si wafer and a 50 nm SiO₂ layer on top of an InP wafer by using plasma enhanced chemical vapor deposition (PECVD). The InP wafer contains a 250 nm-thick InP membrane layer as the future waveguiding layer and a 300 nm-thick InGaAs sacrificial layer between the membrane layer and the substrate. The Si wafer and the InP wafer are adhesively bonded using 50 nm-thick DVS-BCB (divinylsiloxane-bisbenzocyclobutene) material [7]. After wet-chemically removing the InP substrate and the InGaAs sacrificial layer, the 250 nm-thick InP membrane is tightly bonded on top of the SiO₂/Si carrier wafer. The fabrication requires two steps of EBL. Both steps utilize a 50 nm-thick PECVD-deposited SiN_x layer on top of the InP membrane as the hard mask. The 100 nm-thick mixed resist material is spin-coated on top of this SiN_x layer, and the designed patterns are written on the resist layer by EBL with 20 kV voltage and 10 µm aperture settings. After development, the patterns on the resist layer are transferred to the SiN_x layer by means of CHF₃/O₂ RIE. Finally the patterns are formed in the InP membrane layer using CH₄/H₂ InP RIE. The first EBL step prints all the waveguide designs as well as the local markers for alignment of the next EBL. The final InP waveguide will have a width of 400 nm and an etch depth of 220 nm. The second EBL step prints the grating couplers for coupling light between optical fibers and the waveguides. The gratings will have a etch depth of 100 nm. The processing procedure is the same as for the standard IMOS passive processing [2], [8], except for the change of the resist material from normal ZEP to the mixed resist. The fabricated membrane waveguides have five different lengths from 140 µm to 940 µm, with 200 µm increment.

The measurement of the waveguide loss is performed by using a commercial laser with the wavelength of 1550 nm with an output power in fiber of 12 dBm. The laser light is coupled to the input grating coupler by means of a single-mode fiber with a cleaved facet. The transmitted light from the output grating coupler is collected by another fiber. Both fibers are placed at 10 degrees from surface normal of the chip. The output optical

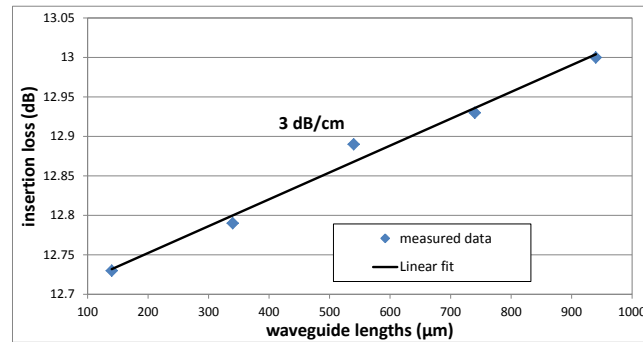


Fig. 3 The measured insertion loss of the IMOS passive waveguides as a function of waveguide length.

power is measured with a power meter. The measurement result of the insertion loss (including both propagation loss and grating coupling loss) of the five waveguides, as a function of the waveguide length, is shown in Fig. 3. The measured data is fitted with a linear function from which a propagation loss of 3 dB/cm and a fiber-grating coupling loss of 6.4 dB/coupling are extracted. Compared to the propagation loss of more than 10 dB/cm in average by using the normal ZEP resist, the measured 3 dB/cm propagation loss by using the mixed resist proves that a significant loss improvement is achieved by the assistance of C₆₀ material.

Conclusion

In this contribution we have presented a method to prepare a mixed material composed of ZEP520A resist and C₆₀ fullerene. Compared to the normal ZEP resist, the mixed resist has shown an increased clearance dose and an enhanced thermal resistance. The IMOS MMI couplers and the coupling regions of MRRs are fabricated using both mixed resist and normal ZEP. The comparison between two resists has indicated an improvement on the fabrication accuracy by using the mixed resist. Loss measurement on the IMOS passive waveguides also demonstrated a significantly reduced propagation loss (3 dB/cm) with the mixed resist.

Acknowledgements

This work is supported by the ERC NOLIMITS grant. Thanks to the Nanolab@TU/e for the cleanroom facilities.

References

- [1] M. Haurylau, G. Chen, H. Chen, J. Zhang, N. A. Nelson, D. H. Albonese, E. G. Friedman, and P. M. Fauchet, "On-Chip Optical Interconnect Roadmap: Challenges and Critical Directions," *Selected Topics in Quantum Electronics, IEEE Journal of*, vol. 12, pp. 1699-1705, 2006.
- [2] J. van der Tol, R. Zhang, J. Pello, F. Bordas, G. Roelkens, H. Ambrosius, P. Thijs, F. Karouta, and M. Smit, "Photonic integration in indium-phosphide membranes on silicon," *Optoelectronics, IET*, vol. 5, pp. 218-225, 2011.
- [3] T. Ishii and K. Shigehara, "Fullerene Nanocomposite Resists for Nanolithography," in *Hybrid Nanocomposites for Nanotechnology*, L. Merhari, Springer, 2009.
- [4] K. Inoue, D. Plumwongrot, N. Nishiyama, S. Sakamoto, H. Enomoto, S. Tamura, T. Maruyama, and S. Arai, "Loss Reduction of Si Wire Waveguide Fabricated by Edge-Enhancement Writing for Electron Beam Lithography and Reactive Ion Etching Using Double Layered Resist Mask with C₆₀," *Japanese Journal of Applied Physics*, vol. 48, p. 030208, 2009.
- [5] J. Lee, Y. Maeda, Y. Atsumi, Y. Takino, N. Nishiyama, and S. Arai, "Low-Loss GaInAsP Wire Waveguide on Si Substrate with Benzocyclobutene Adhesive Wafer Bonding for Membrane Photonic Circuits," *Japanese Journal of Applied Physics*, vol. 51, p. 042201, 2012.
- [6] R. S. Ruoff, D. S. Tse, R. Malhotra, and D. C. Lorents, "Solubility of fullerene (C₆₀) in a variety of solvents," *The Journal of Physical Chemistry*, vol. 97, pp. 3379-3383, 1993/04/01 1993.
- [7] S. Keyvaninia, M. Muneeb, S. Stankovi, P. J. Van Veldhoven, D. Van Thourhout, and G. Roelkens, "Ultra-thin DVS-BCB adhesive bonding of III-V wafers, dies and multiple dies to a patterned silicon-on-insulator substrate," *Opt. Mater. Express*, vol. 3, pp. 35-46, 01/01 2013.
- [8] J. Pello, M. Muneeb, S. Keyvaninia, J. J. G. M. van der Tol, G. Roelkens, and M. K. Smit, "Planar Concave Grating Demultiplexers on an InP-Membrane-on-Silicon Photonic Platform," *Photonics Technology Letters, IEEE*, vol. 25, pp. 1969-1972, 2013.

Reflective AWG with flattened response

E. Kleijn, M. K. Smit and X. J. M. Leijtens

COBRA Research Institute, Technische Universiteit Eindhoven, Postbus 513,
5600 MB Eindhoven, The Netherlands. Email: e.kleijn@tue.nl

A new principle for flattening AWG responses is demonstrated. The approach works in reflection, where the spectrum of the reflected light shows a box like shape, with only a small passband ripple. The method is in principle lossless. The main part of the device is formed by a general multimode interference reflector. This MIR works as a retro-reflector that not only preserves the field shape, but also the position of the field. A pure propagation direction reversal is obtained in this way. The theory behind the principle is explained, and we present simulation results and initial measurement results.

Introduction

Various methods for flattening the response of Arrayed Waveguide Gratings (AWGs) have been proposed. The most prominent are using multimode output waveguide [1], parabolic input tapers [2], dual focal point arrays [3], and synchronized designs [4]. The first three methods increase the insertion loss of the AWG. The last method is in principle lossless, but is quite complex to realize. We propose to use a special multimode interference reflector (MIR) [5], which is inserted in the output free propagation region (FPR) of an AWG. Light within the MIR aperture is reflected back while light outside the aperture is not. This leads to a flat reflection band. When using a platform suitable for active-passive integration, the reflector itself can be made active. This would enable the reflected light to be modulated by a data signal. An application for such a device would be as an optical network unit (ONU) in a passive optical network [6]. Such an ONU should be wavelength-independent and cost-competitive [6]. The device presented here could fulfill both requirements.

Theory

MIRs are on-chip reflectors that are based on MMIs [5]. Such a reflector consists of two 45° mirrors and a multimode section, as shown in Fig. 1a. By choosing the length of the reflector equal to $L_{\text{MIR}} = 1.5 \cdot L_\pi$, a so called general interference 1-port reflector is obtained [5]. Here L_π is the familiar beat length from MMI theory, between the fundamental and first order mode in the multimode section of the device [7]. Though this device is markedly longer than a 1-port reflector based on symmetric interference, it offers some interesting properties. The most significant of which is its ability to reflect an arbitrary shaped input field. What this means is that the location of the input waveguide is not restricted to a single position. In other words, the value of x' in Fig. 1a can be chosen freely along the MIR input aperture.

The field at the input of the MIR does not have to be guided there by a waveguide. It can also be imaged through a free propagation region, like the one found in an AWG. Due to the dispersive properties of AWGs, the spot at the output side moves as a function of

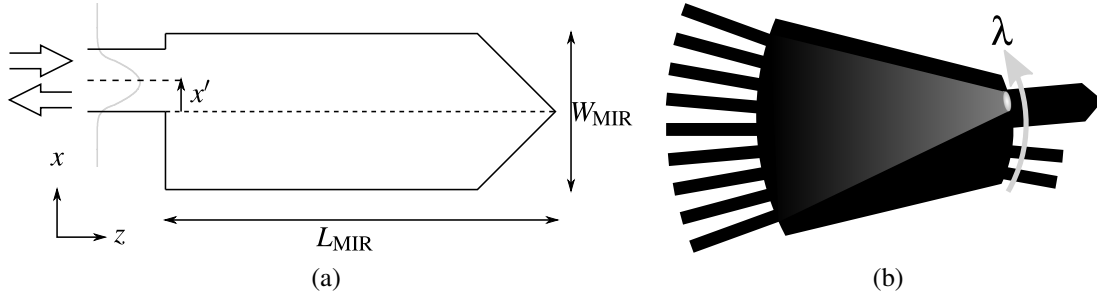


Fig. 1: (a) Generic MIR layout. An input field is launched from position $x = x'$, and is imaged back to the same position. This accomplishes a pure propagation reversal which has only a small dependence on the position x' . (b) Schematic representation of the output FPR. The array waveguides are shown on the left, and the regular output waveguides on the right. Light is focused onto a position that depends on the wavelength λ of the input signal, as indicated by the arrow.

wavelength. This is shown schematically in Fig. 1b. The spot will be reflected back as long as it is within the aperture of the MIR.

Simulation

The fundamental mode of a $2\ \mu\text{m}$ wide waveguide is launched at the input side of an AWG. The coupling through the AWG to the modes of order v in a multimode waveguide was calculated using an analytical model [8]. This model calculates the coupling T_v by taking the overlap between the AWG output field and each of the modes. The multiple modes are then propagated by multiplying them by a phase factor $\exp(-j[2\beta_v L_{\text{MIR}} + \pi v])$, where β_v is the mode dependent propagation constant. The factor πv causes all odd modes to be flipped, which models the effect of the 45° mirrors. Finally, all modes are propagated through the same AWG again, and the overlap with the input mode is taken. The total reflection is thus modeled as

$$R = \sum_v T_v \exp(-j[2\beta_v L_{\text{MIR}} + \pi v]) T_v \quad (1)$$

Fig. 2 shows the simulated reflection using (1) for an AWG designed for the COBRA InP layer stack. An $8\ \mu\text{m}$ wide MIR is connected to the output FPR. The central wavelength of the AWG is $1550\ \text{nm}$, the dispersion is $50\ \text{GHz}/\mu\text{m}$, and the free spectral range is $1800\ \text{GHz}$. The input waveguide is $2\ \mu\text{m}$ wide. The simulation results clearly show a flattened response. A difference in passband ripple can be seen between TE and TM. This is caused by the birefringence of the layer stack, and a resulting different optimal wavelength for TM. The passband is slightly slanted with the short wavelength side being $0.6\ \text{dB}$ lower than the long wavelength side, because the MIR is connected to the FPR with an angle of -4.0° . The $3\ \text{dB}$ bandwidth is $2.59\ \text{nm}$ ($332\ \text{GHz}$). This is much larger than the non-flattened bandwidth of $0.72\ \text{nm}$ ($90\ \text{GHz}$).

Measurement

After fabrication at NanoLab@TU/e the chips were anti-reflection coated and characterized. Light from a tunable laser source was coupled into the chip by using a microscope

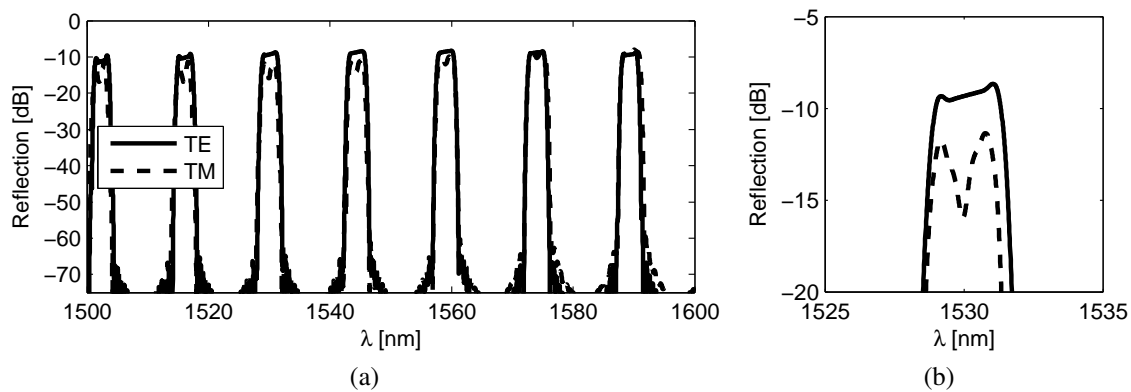


Fig. 2: Simulation of the reflective bandpass filter response for TE and TM. (a) Three FSRs of the flattened AWG response. (b) Close-up of the passband closest to the central wavelength. The ripple in the TM polarized passband signal is due to a different optimal wavelength for this polarization.

objective, which focused a collimated beam from a fiber launch stage onto the chip facet. A circulator allowed the back reflected signal to be recorded. A polarizing beam splitter was inserted in the collimated beam, and set to pass TE polarized light.

Figure 3 shows the measured back-reflected signal. The residual reflection of the coating, estimated to be between -20 dB and -30 dB, together with the strong reflection of the MIR, gave rise to significant fringes within the passband. Outside the passband the fringes are caused by interference between the residual facet reflection and the crosstalk of the circulator. The difference in reflectivity in-band and out-of-band was measured to be 14 dB. By improving the anti-reflection coating and the circulator isolation, this difference can be increased to 24 dB, which is the measured AWG crosstalk level. There is a strong dip in the middle of the passband. At this point it is unclear what causes this, but it is known that a deviation of the design width of the MIR causes ripples in the passband. Another possibility is a distortion of the phase front along the aperture of the MIR because of a slight oblique incidence. Also polarization rotation effects inside the AWG could play a role. When we ignore the dip, the 3 dB passband width is 2.6 nm. This is extremely close to the design width of 2.59 nm.

Conclusion

A new method of flattening the passband of an AWG was introduced, which works in reflection mode. Devices using this new principle were fabricated and characterized. Measurements showed that a strong dip is present in the passband. The 3 dB passband width is 2.6 nm in the measured device, which is extremely close to the design width of 2.59 nm. More measurements and modeling are necessary to understand the cause of the dip. If this effect can be mitigated, the presented device could be used, for example, as a reflective optical network unit in passive optical networks.

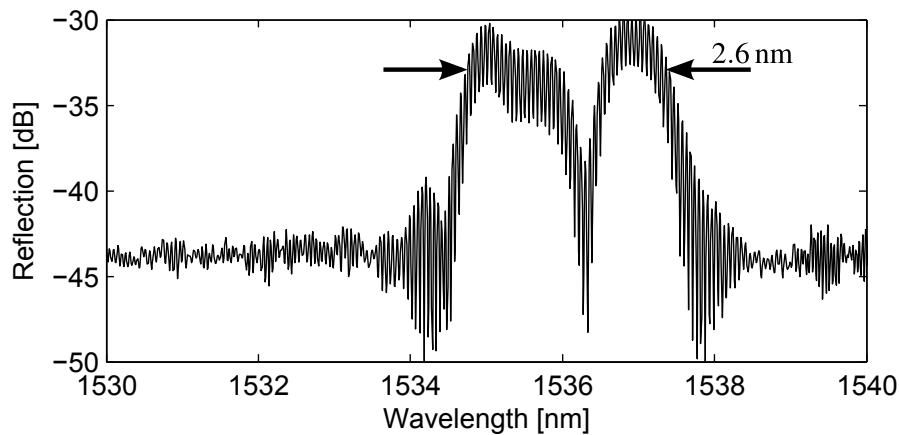


Fig. 3: Measured response of passband flattened AWG. The passband shows an unexpected dip in the center. Ignoring this dip, the 3 dB passband width is 2.6 nm. The reflection level was normalized to the maximum in the passband.

Acknowledgments

The research leading to these results has received funding from the European Community's Seventh Framework Programme FP7/2007-2013 under grant agreement ICT 257210 PARADIGM. The authors wish to thank D. D'Agostino for coating the chips with a silicon nitride anti-reflection coating.

References

- [1] M.R. Amersfoort, C.R. de Boer, F.P.G.M. van Ham, M.K. Smit, P. Demeester, J.J.G.M. van der Tol, and A. Kuntze. Phased-array wavelength demultiplexer with flattened wavelength response. *Electron. Lett.*, 30(4):300–302, February 1994.
- [2] K. Okamoto and H. Yamada. Flat spectral response arrayed waveguide grating multiplexer with parabolic waveguide horns. *Electron. Lett.*, 32(18):1661–1662, August 1996.
- [3] D. Trouchet, A. Beguin, H. Boek, C. Prel, C. Lermieux, and R.O. Maschmeyer. Passband flattening of phasar wdm using input and output star couplers designed with two focal points. In *Optical Fiber Communication. OFC 97., Conference on*, pages 302–303, 1997.
- [4] C.R. Doerr, L.W. Stulz, and R. Pafchek. Compact and low-loss integrated box-like passband multiplexer. *IEEE Photon. Technol. Lett.*, 15(7):918–920, July 2003.
- [5] Emil Kleijn, Meint Smit, and Xaveer Leijtens. Multimode interference reflectors: a new class of components for photonic integrated circuits. *J. Lightwave Technol.*, 2013. doi:10.1364/AO.51.000789.
- [6] Wooram Lee, Mahn Yong Park, Seung Hyun Cho, Jihyun Lee, Chulyoung Kim, Geon Jeong, and Byoung Whi Kim. Bidirectional WDM-PON based on gain saturated reflective semiconductor optical amplifiers. *IEEE Photon. Technol. Lett.*, 17(11):2460–2462, November 2005.
- [7] L.B. Soldano and E.C.M. Pennings. Optical multi-mode interference devices based on self-imaging: Principles and applications. *J. Lightwave Technol.*, 13(4):615–627, April 1995.
- [8] Emil Kleijn, Meint K. Smit, and Xaveer J.M. Leijtens. New analytical arrayed waveguide grating model. *J. Lightwave Technol.*, 2013.

Colloidal Quantum Dot Silicon Nitride Platform

Yunpeng Zhu¹, Weiqiang Xie¹, Steven Verstuyft¹, Tangi Aubert², Zeger Hens² and Dries Van Thourhout¹

¹ Photonics Research Group, Ghent University, 9000 Gent, Belgium

² Physics and Chemistry of Nanostructures, Ghent University, Krijgslaan 281-S3, 9000 Gent, Belgium

The tunability of semiconductor quantum dots offers many opportunities for development of on-chip integrated light sources. Therefore we want to develop a high index contrast waveguide platform compatible with colloidal quantum dots (CQDs) integration. Silicon nitride (Si_3N_4) is promising because of its high index contrast with air and compatibility with the emitting wavelengths of CQDs. We have developed recipes for low temperature Si_3N_4 deposition (helps us to retain the quantum yield of CQDs) and etching. With these optimized recipes, we demonstrated waveguide loss at 900 nm of 0.95dB/cm @ 2 μm width (without CQDs and 4dB/cm @ 2 μm width (with CdSe/CdS CQDs having a band gap transition at 610 nm embedded), while the CQDs keep quite good quantum efficiency and couple efficiently into the waveguide.

Introduction

A full integrated photonics platform requires an efficient light emitter. On the silicon integrated photonics platform, researchers have managed to use bonding techniques to combine III-V materials (which exhibit excellent light properties as light emitters) with the silicon photonics platform. Using these bonding techniques efficient on chip integrated light sources were demonstrated. However, it is difficult to scale up this technology to full wafer scale and alternatives are still being searched for.

Colloidal quantum dots (CQDs) are nanometer-sized semiconductor particles synthesized and suspended in the solution phase using chemical methods. In the past several decades, they have attracted considerable attention as an important new class of materials because their high quantum yield and wide-ranging spectral tunability afforded by the quantum size effect make them perfect candidates for realizing an on chip light source. Since CQDs are synthesized using wet chemistry, they are mostly investigated while still in solution or as stand alone films. For further intergration, there is a need of developing methods to embed CQDs in a solid matrix, guaranteeing both stability and functionality. [1]

A high index contrast waveguide platform is particular interesting for integrated photonics as it allows small bending radii and hence compact devices. The traditional silica waveguide platform provides a very large transparent window, ranging from the visible to the infrared. However, its low index contrast results in large devices. The silicon waveguide platform provides a very high index contrast but it can not support shorter wavelengths. Si_3N_4 , which is also widely used in the CMOS industry as a dielectric, has proven to be a very good optical waveguide material and has a transparent window covering both the visible and the infrared wavelength ranges. Moreover, its relatively high index (~ 2) offers a small bending radius and a high mode confinement. All these features make this material very suitable for integration with CQDs.

In this work, we developed a Si_3N_4 waveguide platform for integration of CQDs. First, we demonstrated low loss Si_3N_4 waveguides consisting of just a single layer of Si_3N_4

and double layers of different types of Si_3N_4 films. Next we demonstrated low loss Si_3N_4 waveguides with a monolayer of CdSe/CdS CQDs in the middle. We pumped this waveguide and observed the luminescence from the CQDs. However, due to the thin layer of CQDs and re-absorption from the layer, the output power is not yet very high. [2]

Si_3N_4 Waveguide Platform

Our aim is to develop a Si_3N_4 platform with integrated CQDs, maintaining CQDs luminescence while having a low waveguide loss at the same time. We would like to position the CQDs layer in the area where they have high overlap with the electromagnetic field inside the waveguide. Previous experiments show that a high temperature PECVD environment damages the CQDs and lower their photoluminescence. So we proposed a sandwich waveguide structure as shown in Figure 1, consisting of a standard Si_3N_4 layer (deposited using PECVD at 270°C), the CQD layer and then a second Si_3N_4 layer deposited at low temperature (120°C). The CQD layer can be deposited using the Langmuir-Blodgett (L-B) method or using spin coating. Reducing the temperature of the second Si_3N_4 to 120°C reduces its optical quality somewhat but helps preserving the luminescence of the CQD-layer. [3] [4] A single etch step then determines the waveguide structure.

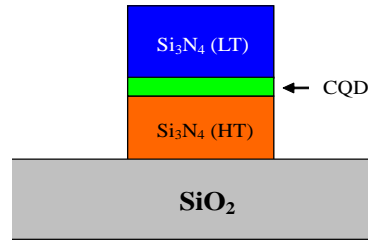


Figure 1. CQD integrated sandwich waveguide structure

We have fabricated spiral waveguides with different length and widths and measured the waveguide transmission for different wavelengths. From these we determined the waveguide loss at 900, 1310 and 1550 nm. The spiral waveguide lengths are 1, 2, 4 and 8 cm, and the spiral waveguide widths are 0.8, 0.9, 1, 1.1, 1.2, 1.5, and 2 μm , respectively. Figure 2 shows the waveguide loss at 900 nm with just one layer of 200 nm high temperature Si_3N_4 . As we can see the waveguide loss goes down as the waveguide width is increased. This indicates that for the narrow waveguide, the loss mainly comes from the sidewall roughness. As the waveguide becomes wider, overlap of the sidewall with the modal field decreases, thereby resulting in a reduced scattering loss. Also from Figure 2 we notice a dramatic increase of loss for waveguides narrower than $1\mu\text{m}$. This indicates our lithography system cannot guarantee a good pattern transfer when the feature size gets below $1\mu\text{m}$ and the defects introduced result in additional loss.

We also fabricated double layer stack Si_3N_4 waveguides, initially without CQDs layer. As shown in Figure 1, these waveguides have one layer of high temperature Si_3N_4 on the bottom and one layer of low temperature Si_3N_4 on the top, both layers' thickness is 200nm. Figure 3 shows the result of the waveguide loss measurement. Compared to the waveguide loss of

just one layer of high temperature nitride, the loss of the double layer waveguide

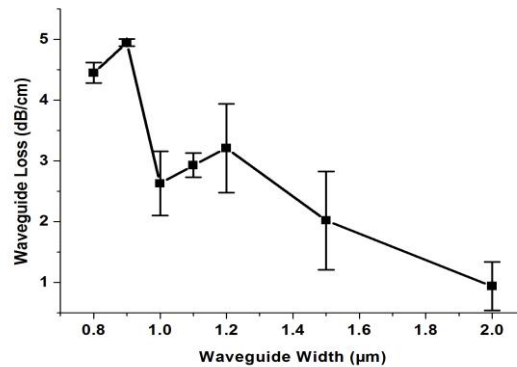


Figure 2. Si₃N₄ waveguide loss at 900nm. Waveguide has one 200nm layer of high temperature Si₃N₄.

increases considerably. The extra loss mainly comes from the additional sidewall scattering. Because here two different layers are used, the etching process reduces in quality and additional sidewall roughness is introduced. There is also some loss caused by the low quality of low temperature Si₃N₄ and the defects from the interface. However, as above, the waveguide loss decreases for wider waveguides. The waveguide loss measured at 1550 nm is very large and originates from the OH⁻ absorption peak around 1520 nm. This loss can be reduced by high temperature annealing, but this will damage the CQDs if we want to have CQDs embedded in the waveguide.

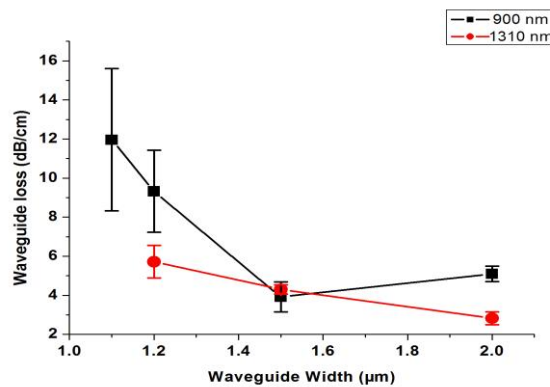
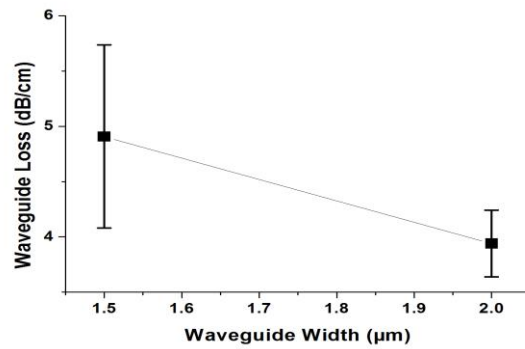


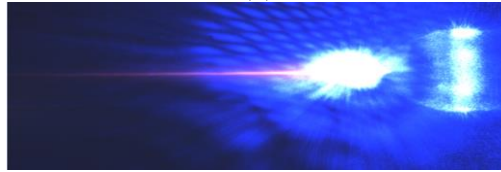
Figure 3. Si₃N₄ waveguide loss at 900nm and 1310nm. The waveguide consists of a 200nm layer of high temperature Si₃N₄ and a 200nm layer of low temperature Si₃N₄.

We also fabricated CQDs embedded Si₃N₄ waveguides and measured the waveguide transmission. The embedded CQDs have an emission peak at 610 nm when they are in the solution phase. The peak will slightly shift when embedded in the solid matrix. [3] The embedded CQDs layer is deposited using the Langmuir-Blodgett method, guaranteeing a perfect monolayer of CQDs.

From Figure 4(a), we can see that with one monolayer of CQDs embedded in the waveguide, the waveguide loss did not dramatically increase. With transmitted 900 nm light having a lower photon energy than the CdSe/CdS CQDs' bandgap, the CQDs layer shows very low absorption and scattering.



(a)



(b)

Figure 4 (a) Si_3N_4 waveguide loss at 900nm with monolayer of CQDs inside
 (b) Camera picture of Si_3N_4 waveguide with monolayer of CQDs inside pumped with side coupled blue light

transmitted 900nm light. We also tried to pump the waveguide with a 445 nm laser, as shown in Figure 4(b). We can clearly see the luminescent red light being scattered along the waveguide and decaying as the light propagates along the waveguide. Thus far we have not yet successfully collected the luminescence because the signal is very weak when reaching the end of the waveguide. We assume this is because of CQDs' re-absorption, which we will verify by further experiments.

Conclusion

We have experimentally demonstrated a colloidal quantum dot silicon nitride platform. By improving the deposition and etching processes, we have developed the technique to retain the photoluminescence from CQDs and obtain low waveguide loss at the same time. We demonstrated the emission from CQDs couples very well into the waveguide.

References

- [1] Jin Young Kim, Oleksandr Voznyy, David Zhitomirsky, and Edward H. Sargent, "25th Anniversary Article: Colloidal Quantum Dot Materials and Devices: A Quarter-Century of Advances," *Advanced Materials*, vol. 25, issue 36, 4986-5010, Sep. 25, 2013.
- [2] A. Omari, P. Geiregat, D. Van Thourhout, Z. Hens, "Light absorption in hybrid silicon-on-insulator/quantum dot waveguides," *Optics Express*, vol. 21, issue 20, p.23272-23285, Sep. 2013.
- [3] B. De Geyter, K. Komorowska, E. Brainis, P. Emplit, P. Geiregat, A. Hassinen, Z. Hens, D. Van Thourhout, "From fabrication to mode mapping in silicon nitride microdisk with embedded colloidal quantum dots," *Applied Physics Letters*, vol.101, issue 16 p.161101~4, Oct. 2012.
- [4] Lambert, K.; Capek, R. K.; Bodnarchuk, M. I.; Kovalenko, M. V.; Van Thourhout, D.; Heiss, W.; Hens, Z., *Langmuir* "Schaefer Deposition of Quantum Dot Multilayers. *Langmuir*, vol 26, p. 7732-7736, 2010.

Fabrication and characterization of a wet-etched InP-based vertical coupling mirror

R. Santos¹, D. D'Agostino¹, F.M. Soares², H. Rabbani Haghighi¹,
M.K. Smit¹, X.J.M. Leijtens¹

¹ COBRA Institute, Photonic Integration Group, Eindhoven University of Technology, P.O. Box 513,
5600MB Eindhoven, the Netherlands

² Fraunhofer-Institut für Nachrichtentechnik Heinrich-Hertz-Institut Bereich Photonische Komponenten
Einsteinufer 37, 10587 Berlin, Germany

In this work we describe the fabrication and characterization of couplers realized with a wet etching process that is compatible with the standard COBRA active-passive process. The implementation of this broadband structure allows for wafer-scale waveguide-loss and absolute-wavelength measurements.

Introduction

Recent developments in large-scale production of photonic integrated circuits (PICs) require the use of process control modules (PCMs) that allow the foundries to monitor and guarantee the quality of their fabrication process and increase the production yield [1]. One particularly interesting component is a vertical input/output coupler for optical signals. The realization of this type of structure would allow on-wafer characterization of the properties of individual building blocks, before cleaving and separating each individual PIC from the wafer. In particular it would allow the study of the spectral performance of the devices. One approach to achieve vertical coupling is through grating couplers which are widely used in Si membrane technologies [2]. However, in standard InP technology, this approach cannot be used because the transversal index contrast is not large enough for making efficient couplers. In previous works, efficient vertical couplers have been successfully realized by us in a standard InP layer stack using a Focused Ion Beam milling technique. However, this method has the drawback of not being well-suited for large-scale wafer processing [3].

In this work we report on the fabrication and characterization of a new type of vertical coupler. To realize this coupler, a wet-etching process alongside with etched-facet waveguides was developed. This process is compatible with the full-wafer standard active-passive integration that is used by COBRA. However, fabrication of the structures may be compatible with other processes, such as the ones of Oclaro and the Heinrich-Hertz institute.

Device fabrication

Typically, waveguide endings in InP technology are at the cleaved facets of a chip. Here we take a different approach, where the end of the waveguides is etched with a vertical etch. This has a number of advantages. Firstly it is now possible to end the waveguide at an angle to reduce the backreflections, while at the same time this ending can be designed such that the light exits the chip perpendicular to the edge of the chip, thus enabling coupling, for example, to a fiber array. The second advantage is that the waveguide end is on the wafer and thus accessible for characterization before cleaving or dicing out the individual chips. To improve the (vertical) in and out-coupling, these

waveguides were fabricated in a spot-size converter layer-stack for achieving larger alignment tolerance and better mode profile matching between the waveguide and the optical fiber. The fundamental mode in such a waveguide has a diameter around $3\mu\text{m}$. InP has a crystallographic plane at an angle of 55° with respect to the (001) surface [4]. By anisotropic etching the InP in this plane a mirror will be formed that allows the light coming from a waveguide to be reflected into the vertical direction. This mirror should be positioned in front of the waveguide. The reflectivity of this mirror is calculated to be around 32% for TE and 21 % for TM polarization. That is sufficient for accurate on-wafer measurements. A high-reflection coating can be applied to the angled mirror, should a higher reflectivity be required.

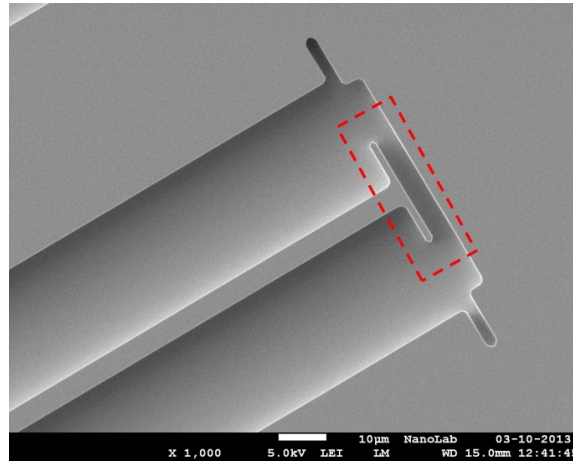


Fig. 1 – SEM picture showing the etched facet indicating the special structure for preventing diffraction rounding.

The fabrication process has two main steps, the first one is the etching of both the waveguides and the waveguide endings (“etched facets”) and second, the processing of the angled mirrors for vertical out-coupling. It is important to have a very high quality of the etched facet, to prevent scattering and to ensure a proper beam shape. For this reason the end of the waveguide was widened over a short distance, in order to avoid rounding of the waveguide due to diffraction effects during the lithography of the waveguides. The widened waveguide end consists of a $2\mu\text{m}$ long, $25\mu\text{m}$ wide bar is included at the end of the waveguide so that possible rounding of the corners of this structure do not affect the central part of the waveguide where the light exits (Fig. 1). These waveguides and facets were processed using a chlorine-based ICP etching.

A resume of the process flow for the fabrication of the angled mirrors is schematized in Fig. 2. First, SiN_x is deposited using PECVD over the SSC waveguides with etched facets (Fig 2 (a)). The thin SiN_x is used as hard mask for the wet-etching process (Fig 2 (b)). Then, after the lithography using AZ-4533 photoresist due to the profile of the device, the SiN_x hard-mask is opened. Once the hard mask is opened, the realization of the mirrors was done by wet-etching using Br_2 :methanol (Fig 2 (c)). This wet-etching process forms a V-groove shape at the edge of the facet. When the chips are cleaved out of the wafer, these V-grooves will also allow for precision cleaving of the PIC devices, leaving the etched facets as the normal out-coupling waveguides.

After fabrication of the waveguides and the angled mirrors, a scanning electron microscopy inspection was made of the coupler structure (Fig. 3).

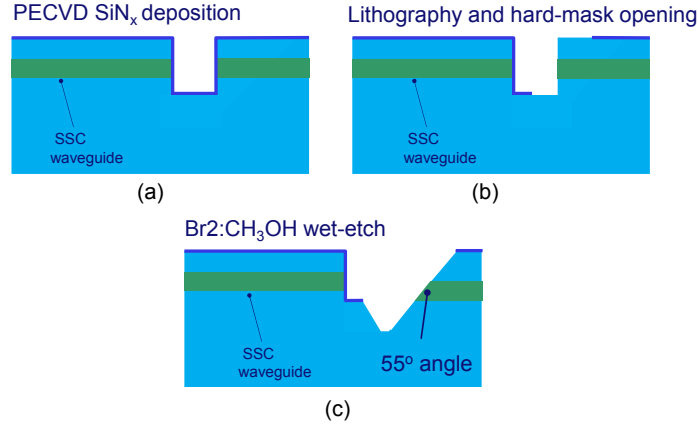


Fig. 2 Schematic of the process flow used to fabricate the vertical couplers: (a) PECVD depositions of SiN_x; (b) Lithography and hard-mask opening and (c) wet-etch for the mirror processing.

As can be seen in this figure, the surface of the mirror is smooth. For this particular device, the waveguides have a separation pitch of 25 μm and the mirror is separated 10 μm from the etched facets.

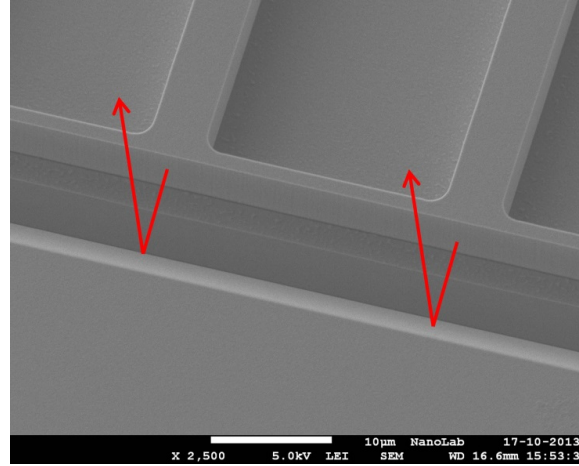


Fig. 3 – SEM picture of the vertical out coupling mirrors. The arrows indicate the light path out of the device.

Experimental characterization

To characterize the performance of vertical coupler, first we measured the propagation losses of the waveguides. For that we used the Fabry-Perot method which has the advantage to be independent from the input and output coupling to the waveguide [4]. The losses can be determined with the following expression:

$$\alpha = -\frac{1}{L} \ln \left[\frac{1}{\sqrt{R_1 R_2}} \frac{\sqrt{C_R} - 1}{\sqrt{C_R} + 1} \right] \quad (1)$$

Where L is the length of the waveguides, R_1 and R_2 are the reflectivities for each one of the facets and C_R is the amplitude of the measured fringes. The facet reflectivity for this waveguide geometry is calculated to be 0.25. From the measurement over a set of 1.1 cm long waveguides, the losses were found to be 2.0 dB/cm.

To measure the coupling loss between the fiber and the vertical structure, the setup scheme described in figure 4 was used. The input light enters thru the etched facet and the output is collected by a fiber positioned vertically. As shown in Fig. 4 (a), the angle

at which the fiber is positioned has not been optimized yet, due to experimental setup constraints, and could deviate by as much as 20° . Under these conditions, the coupling efficiency was measured to be approximately -20 dB. However, this non-optimized coupling, still allowed us to determine the reflectivity of the etched facets. By using the same method as described by equation (1) and using the measured propagation loss of the waveguides, the reflectivity of the etched facet was measured to be 0.25, equal to the calculated value for a perfect mirror. This indicates that the etched facets were smooth and vertical.

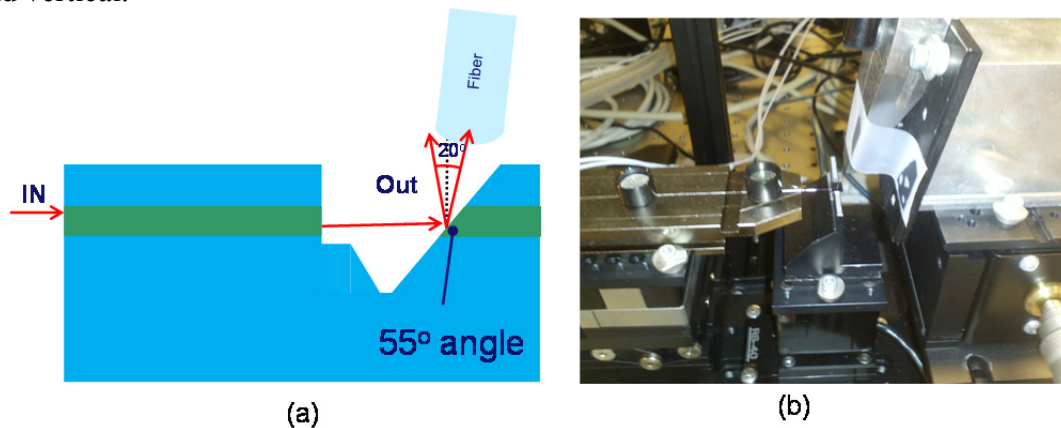


Fig. 4 – (a) Schematic of the measurement setup used to characterize the vertical coupler and (b) photograph of the setup.

Conclusions

In this work, we report on the successful fabrication and characterization of a vertical outcoupling structure. The structure was realized by wet-etching an angled mirror in front of an expanded-beam waveguide with etched facets. From the measurements we were able to determine the reflectivity of the etched facets using the vertical coupler structure.

Acknowledgments

This research is carried out in the ProCon Project 11369, supported by the Dutch Technology Foundation STW, which is part of the Netherlands Organization for Scientific Research (NWO), and which is partly funded by the Dutch Ministry of Economic Affairs.

References

- [1] M. Smit, X. Leijtens, E. Bente, J. van der Tol, H. Ambrosius, D. Robbins, M. Wale, N. Grote, M. Schell, "Generic foundry model for InP-based photonics", *IET Optoelectron.*, Vol. 5, Iss. 5, pp. 187–194, 2011.
- [2] [2] - D. Taillaert, F. Van Laere, M. Ayre, W. Bogaerts, D. Van Thourhout, P. Bienstman, and R. Baets, "Grating Couplers for Coupling between Optical Fibers and Nanophotonic Waveguides," *Jpn. J. Appl. Phys.* 45, 6071–6077, 2006.
- [3] R. Santos, B. Barcones Campo, M. Smit, and X. Leijtens, "Vertical coupling mirror for on-wafer optical probing of photonic integrated circuits", paper JT3A.15, *Integrated Photonics Research, Silicon and Nanophotonics 2013*.
- [4] Sadao Adachi and Hitoshi Kawaguchi, "Chemical Etching Characteristics of (001) InP", *J. Electrochem. Soc.* volume 128, issue 6, 1342-1349, 1981.
- [5] D. F. Clark and M. S. Iqbal, "Simple extension to the Fabry–Perot technique for accurate measurement of losses in semiconductor waveguides," *Opt. Lett.* 15, 1291-1293, 1990.

Ferrule-top optical fibre sensor for the measurement of magnetic fields

M. Aerssens,^{1,2} G. Gruca,³ A. Gusarov,² V. Massaut,² P. Mégret,¹ D. Iannuzzi,³ and M. Wuilpart¹

¹ UMONS, Dept of Electromagnetism and Telecommunications, Blvd Dolez 31, 7000 Mons, BE.

² Belgian Nuclear Research Center SCK-CEN, Boeretang 200, 2400 Mol, BE.

³ VU University, Dept of Physics and Astronomy, de Boelelaan 1081 Amsterdam, NL.

We present a magnetic field sensor based on a micromachined cantilever (with a N45 Neodymium magnet fixed on the upper end) carved on top of a ferruled fiber by means of a cost-effective picosecond-laser ablation. The interferometric readout of the ferrule-top (FT) sensor is based on a 1544 nm laser diode and an infrared photodetector. The FT calibration was obtained by moving the sensor along the principal axis of a stack of permanent toroidal magnets with a maximum magnetic field of 0.24T. The developed sensor has no hysteresis and presents a proportional relationship between the magnetic field and the interferometric cavity size.

Introduction

Ferrule-top cantilevers are a new generation of monolithic micromechanical sensors obtained by carving microstructures on the top of ferrule fibers. The movement of the structure can be monitored by means of laser light coupled into the fiber from the opposite end. They offer all the advantages of fiber optic sensors (e.g. small dimensions, remote sensing, insensitivity to electromagnetic noise, harsh environments resistance). Ferrule-top sensors can work in two modes. The static mode is based on recording elastic deflection of the cantilever and the dynamic mode relies on tracking changes in its mechanical properties (resonance frequency, quality factor). In this paper we present experimental results of the magnetic field measurement using a FT monitored in static mode.

Fabrication of ferrule-top sensors

The main idea is to use ferruled fibers as the building block of the ferrule-top device. The outer diameter of the ferrule is typically 1.8 mm. A standard single-mode optical fiber is inserted and glued into a pierced cylindrical ferrule made out of glass. The diameter of the piercing hole that passes through the ferrule along the axis of the cylinder is 127 μm . The single-mode fiber is glued into the ferrule so robustly that it is possible to carve a micromachined cantilever on top of the ferruled fiber by means of a cost-effective technique, namely picosecond-laser ablation. The different manufacturing steps are exhaustively described in [1] and illustrated in figure 1. The geometry of the sensor can be changed depending on the application. Nevertheless, in most of the cases the micromechanical element is a simple beam clamped on one side. To create from ferrule-top devices transducers to measure changes in the magnetic field, we have adhered to the upper end of the ferrule a thin slice of 200 μm of a N45 Neodymium magnet (alloy of neodymium, iron, and boron $\text{Nd}_2\text{Fe}_{14}\text{B}$) cut with a diamond wire-cutter according to the magnetic north-south

axis. The pico second laser from Optec makes it possible through a graphical interface to control a linear translation table and define the regions subjected to laser ablation (Fig.2).

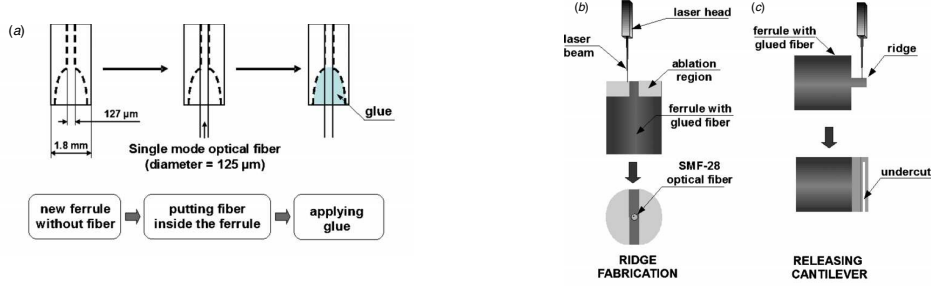


Figure 1: (a) Schematic view of a ferruled optical fiber; (b) and (c) milling steps in the fabrication of a ferrule-top cantilever [1]

Interferometric readout

The interferometric readout for the ferrule-top cantilever is based on a 1.544 μm laser diode and an infrared photodetector. The light of the laser beam, coupled to the cantilever through an optical circulator, is partially reflected at the fiber-to-air, air-to-cantilever and cantilever-to-air interfaces. The three backward propagating components interfere with each other, creating an interference pattern. The interference signal is then coupled to the photodiode through the circulator (Fig.3). As outlined by Iannuzzi et al. [2] and by Gruca et al. [1], the interference signal depends on the distance d between the fiber-to-air interface and the bottom surface of the cantilever. If multiple reflections from the cantilever are neglected, the output of the readout system may be described according to the following equation [2]:

$$W(d) = \left[1 + V \cdot \cos \left(\frac{4\pi d}{\lambda} + \phi_0 \right) \right] \quad (1)$$

where ϕ_0 is a constant phase shift that only depends on the geometry of the cantilever, λ the wavelength of the laser (1.544 μm) and V the fringe visibility. The midpoint interference signal W_0 and V are related to the output signals corresponding to maximum (W_-) and minimum (W_+) interference according to:

$$W_0 = \frac{W_+ + W_-}{2} \quad V = \frac{W_+ - W_-}{W_+ + W_-} \quad (2)$$

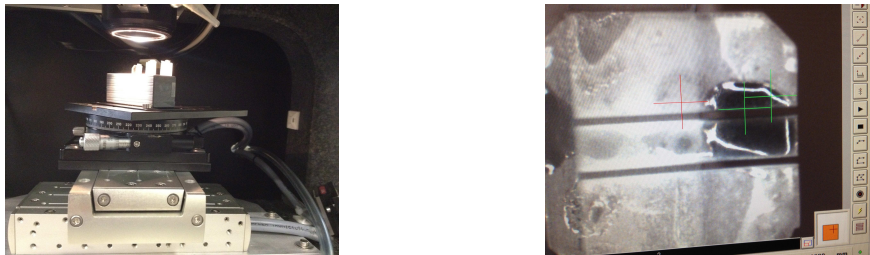


Figure 2: (left) XY linear translation and Z Axis rotation stage controlled by the ps-ablation laser. (right) Top of the ferrule during the ablation process.

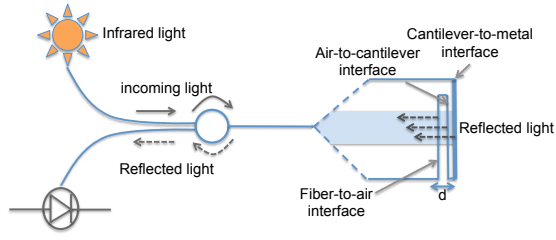


Figure 3: Schematic view of the readout setup. Dashed arrows represent the light reflected at the fiber-to-air, air-to-cantilever, and cantilever-to-metal interfaces.

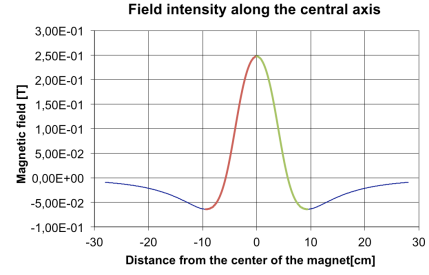


Figure 4: Magnetic field simulated along the axis of a stack of permanent toroidal magnets.

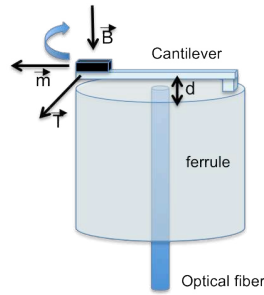


Figure 5: Magnet with a magnetic moment \vec{m} on top of a cantilever submitted to a magnetic field \vec{B} . The magnet and the beam undergo a torque that changes the size of the cavity between the end of the optical fiber and the bottom of the cantilever.

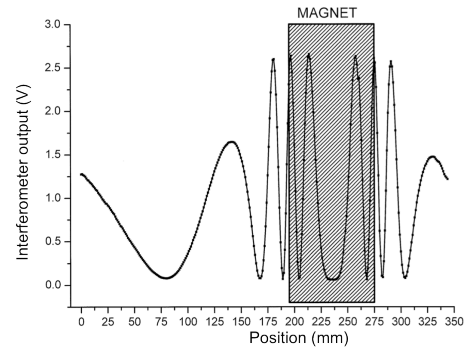


Figure 6: Output voltage measured by the interferometric readout when the sensor moved along the axis of a stack of permanent toroidal magnets.

Measurements and sensor calibration

The set-up consists in a ferrule-top sensor mounted on the end of a non-metallic arm that can move inside a stack of permanent toroidal magnets with a maximum magnetic field of $0.24T$ with a position measured to the hundredth of a millimeter (Fig.4). When the sensor is moved along the axis of the magnet, the interaction between the magnetic moment \vec{m} and the magnetic field \vec{B} gives rise to a torque that changes the size of the cavity between the end of the optical fiber and the bottom of the cantilever (Fig.5). Based on Eq.1, we deduce that the interferometric output changes from minimum to maximum and vice versa when d undergoes a change of $\lambda/4 = 387.5\text{nm}$. The evolution of the interferometer readout (Fig.6) gives approximately a modification of the cavity size d of 2712nm for a magnetic field $B \in [-0.06T \ 0.24T]$.

If we represent the interferometer output according to the magnetic field (combination of Fig.4 and Fig.6) for the areas where the magnetic field is respectively monotonically increasing (red curve on Fig.4) and decreasing (green curve on Fig.4), we obtained two similar calibration curves for $[-0.06T \ 0.24T]$ (Fig.7) showing that our sensor is not subjected to any hysteresis. Assuming that the magnetic field applied to the sensor is low

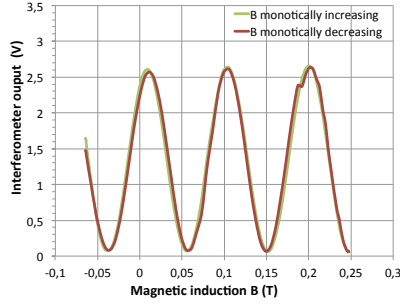


Figure 7: Evolution of the interferometer output for the monotonically increasing (red curve) and the monotonically decreasing (green curve) area of the magnetic field.

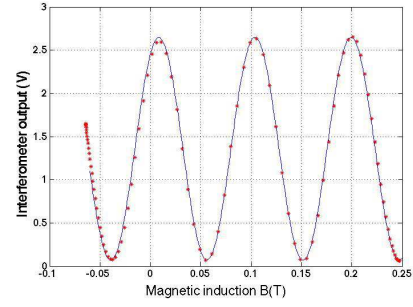


Figure 8: Fitting with a sine function of the monotonically increasing area of the magnetic field.

enough to generate a linear deformation of the cantilever, Eq.1 shows that the evolution of the interferometer as a function of the magnetic field should follow a sinusoid. The assumption of proportionality between the magnetic field and the length of the sensor cavity is verified for $B \in [-0.06\text{T } 0.24\text{T}]$ since we observe a good matching between the output of the interferometer and the sine function that best fits in the least-squares sense (Fig.8).

$$y = 1.36 + 1.29 * \sin\left(\frac{B - 0.08}{0.048}\right) \quad (3)$$

Conclusion

In this paper we use a ferrule top sensor with a small neodymium magnet glued on top of the ferrule in conjunction with an interferometer system to measure the magnetic field. To prevent the overheating of the sensor inherent with an electromagnet, we use a stack of toroidal permanent magnets to generate a stable magnetic field. The sensor was moved along the principal axis of the magnet and we recorded via the output of the interferometer the static bending of the cantilever. Experimental results demonstrate on one hand that the sensor has no hysteresis in the range $[-0.06\text{T } 0.24\text{T}]$. On the other hand, the size modification of the interferometric cavity d is proportional to the amplitude of the magnetic field, meaning that the evolution of the interferometric output as a function of magnetic field is sinusoidal.

Acknowledgements

This work was supported by the European Research Council under the European Community's Seventh Framework Programme (FP7/2007-2013)/ERC grant agreement number 201739 and the COST TD1001 action OFSeSa.

References

- [1] G. Gruca, S.D. Man, M. Slaman et al., "Ferrule-top micromachined devices: design, fabrication, performance", *Measurement science Technology*, vol. 21, No. 9, pp. 094033, 2010.
- [2] D. Iannuzzi, S. Deladi, V.J. Gadgil et al., "Monolithic fiber-top sensor for critical environments and standard applications", *Applied Physics letters*, vol. 88, No. 5, pp. 053501, 2006.
- [3] G. Gruca, D. Chavan, A. Cipullo, et al., "Development of fiber optic ferrule-top cantilevers for sensing and beam-steering applications", in *Proceedings of the Conference SPIE*, vol. 8439, pp. 84390E, 2012.

Test structures for SOA gain and absorption measurement

D. I. Pustakhod, M. K. Smit, and X. J. M. Leijtens

Eindhoven University of Technology, Dept. of Electrical Engineering
Den Dolech 2, 5600 MB, Eindhoven, The Netherlands

Semiconductor optical amplifiers are essential building blocks in photonic integration technology. Assessment of their properties is indicative of the quality of fabrication process and detailed knowledge is important for designing complex active circuits and devices. We investigate methods and test-structures for measuring gain and absorption of active materials that are suitable for integrated electrical on-wafer testing. We report measurement results for the Oclaro InP integration platform.

Introduction

In recent years progress was made in the development of an InP generic integration platform [1]. This platform provides the possibility to design complex circuits and manufacture them using a standard fabrication process. Designs of different users may be combined in so-called multi-project wafer runs (MPW). With such an approach designers can benefit from a well-developed semiconductor technology without having to go into the details of the production. The foundry is responsible to guarantee the performance of the basic building blocks (BBB) which are used by the designers. For the purpose of qualification of the production process, test cells containing specific test circuits are used. These circuits are designed to measure one or a few BBB parameters, such as waveguide loss for passive waveguides, phase modulation efficiency for phase modulators, gain for active material, etc. The main requirements to the test circuits and measurement methods are simplicity, speed and footprint on the cell. There is progress in development of electrical testing methods [2], making use of integrated light sources and detectors. They reduce the testing to measuring electrical performance of test circuits and deriving optical characteristics from the values obtained. Another methodology is to couple light into and/or out of test circuits and subsequently analyse it with external equipment. The latter method benefits from the functionality present in external equipment which is at the moment not available in integrated circuits. Using this method for on-wafer testing requires access to on-chip circuits through vertical couplers, which are currently being developed [3].

In the present work we concentrate on the development of test structures with optical outputs meant for measuring gain and absorption spectra of semiconductor optical amplifiers (SOA), which are of particular importance for building on-chip lasers and amplifiers.

Structures for gain measurements

Methods for measuring gain have been intensively studied. There is family of methods which derives the gain spectrum from the modulation of amplified spontaneous emission spectrum by the Fabry–Pérot modes of an on-chip laser cavity [4, 5]. These methods

require a high spectrometer resolution and are applicable below threshold current density only. A method based on the measurement of the amplified spontaneous emission (ASE) spectrum as a function of the SOA length was proposed by Oster [6]. It makes use of the relation between output intensity I_{out} and the length SOA length L

$$I_{\text{out}}(\lambda) = \frac{I_{\text{sp}}(\lambda)}{G(\lambda)} (e^{G(\lambda)L} - 1), \quad (1)$$

where I_{sp} is the intensity of the spontaneous emission per unit length, and G is modal gain. The difficulty for this method is to ensure the same collection efficiency for all waveguides. As a modification of this method Thomson [7] proposed to use a multisectional SOA. The design of this type of test structure should guarantee absence of any reflections so that light passes through the amplifier only once. Several measurements are taken at the same current density.

ASE measurements using a multisectional SOA

In our measurements we used a multisection SOA test structure (fig. 1). The structure consists of several SOA sections of various length with separate electrical contacts. Sections are separated with short $L_{\text{isol}} \sim 30 \mu\text{m}$ isolation sections. In order to prevent reflections from the facet, angled output waveguides which approach the facet at a 7° angle and/or an antireflection coating on the facet can be used. Active-passive butt-joints are angled for the same purpose.

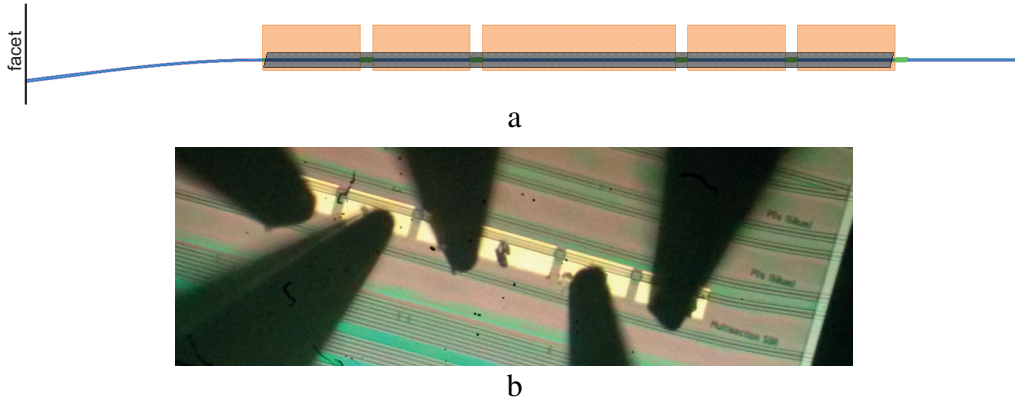


Figure 1: Example of a 5-section SOA test structure. (a) Mask design. Angled outputs are visible on the left side. (b) The fabricated chip (COBRA platform). The lengths of the sections are 200, 200, 400, 200, 200 μm .

Pumping and reverse biasing for spectra recording

The ASE spectra from SOAs of various length can be obtained by pumping different combinations of SOA sections with the same current density J_{pump} . Thus, by pumping first sections we obtain the spectrum for a SOA of length L_1 , pumping first two sections gives the ASE for a SOA of length $L_1 + L_2$, etc. The resulting measured output spectra are shown in fig. 2a. The location of the peak for all three curves is at the same wavelength, which confirms that the current density for all devices is the same. In order to calculate SOA absorption spectrum (SOA is reverse biased), we apply reverse biases to the first

closest to the output SOA and continue pumping one or few following SOA sections. Spectra measured in this way are displayed on the fig. 2b.

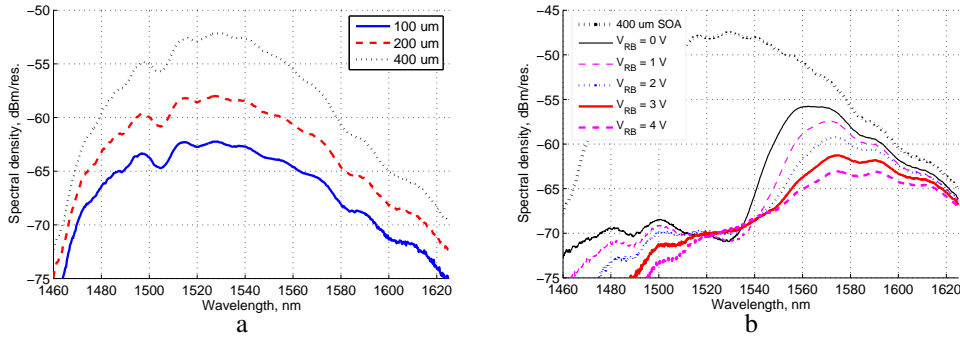


Figure 2: ASE from a multisection SOA on the Oclaro platform for gain and absorption measurements. (a) ASE from SOA of various length. Current density $J_{\text{pump}} = 3.2 \text{ kA/cm}^2$. (b) Emission spectra from 300 μm SOA after passing through a reverse-biased absorber. For comparison, the ASE spectrum of a 400 μm SOA (top curve) is shown.

Gain calculation

A specific selection of the lengths of the SOA sections (i.e. $L_2 = 2L_1 \equiv 2L$, and $L_3 = 2L_2 \equiv 4L$) leads to straightforward way of calculating the gain using [7]:

$$G(\lambda) = \frac{1}{L} \left[\ln \left(\frac{I_L(\lambda)}{I_{2L}(\lambda)} \right) - 1 \right], \quad (2)$$

where I_L and I_{2L} are the ASE intensities at particular wavelengths for SOAs of length L and $2L$, respectively. Therefore the measured values of the emission intensities I_L , I_{2L} , and I_{4L} at each wavelength are used to calculate modal gain in three different ways:

1. using (2) for a pair I_L , I_{2L} ;
2. using (2) for a pair I_{2L} , I_{4L} ;
3. using non-linear least square fit with (1) for all three intensities.

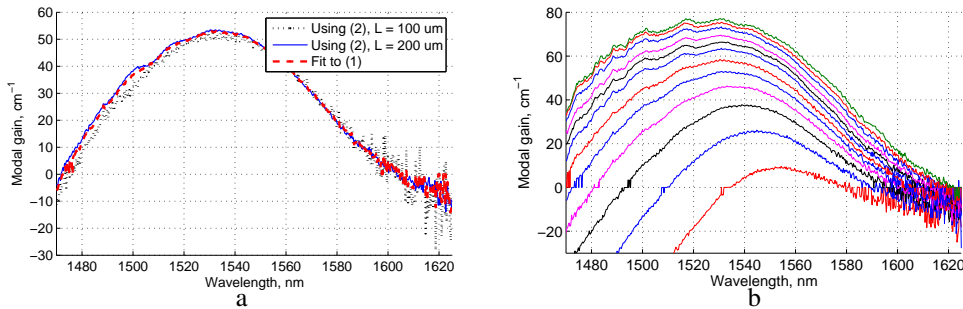


Figure 3: Modal gain for the Oclaro platform. (a) Modal gain calculated with various methods. Current density $J_{\text{pump}} = 3.2 \text{ kA/cm}^2$. (b) Modal gain calculated by fit to (1). Current densities: $J_{\text{pump}} = 1.1; 1.6; 2.1; 2.6; 3.2; 3.7; 4.2; 4.7; 5.3; 6.3; 7.4; 8.4 \text{ kA/cm}^2$

The comparison of the results is shown in fig. 3a. The values from the three methods agree with each other. The advantage of the fitting method is that it provides means to recognize measurement faults such as the bias during the intensity measurements, which becomes clear in fitting quality. The results for the shortest pair, $L = 100 \mu\text{m}$, are more sensitive to the intensity variations and noise, which are larger for the relatively weak emission from the short SOA.

The fitted modal gain spectra in the range of pump current densities is displayed in fig. 3b.

Absorption calculation

In order to calculate the absorption we assume it complies to the Beer-Lambert law

$$I_{\text{out}}(\lambda) = I_{\text{in}}(\lambda)e^{-\alpha(\lambda, V_{\text{RB}})L_{\text{SOA}}}, \quad (3)$$

where $\alpha(\lambda, V_{\text{RB}})$ is the absorption coefficient which is dependent on the applied reverse voltage, and L_{SOA} is the length of reverse biased SOA. Measuring the output spectrum $I_{\text{out}}(\lambda)$ (fig. 2b) and calculating the incoming power $I_{\text{in}}(\lambda)$ from (1) with the previously obtained gain G and spontaneous emission spectrum I_{Sp} , we can evaluate the absorption (fig. 4).

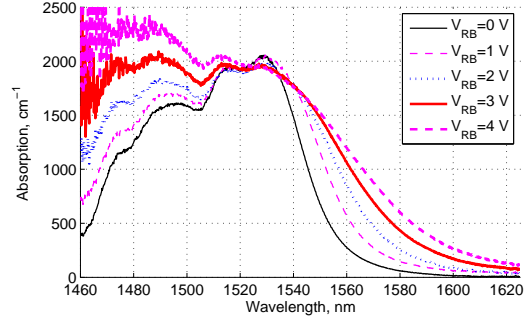


Figure 4: Calculated SOA absorption spectra for Oclaro platform for different reverse voltages. Current density is $J_{\text{pump}} = 2.6 \text{ kA/cm}^2$

Conclusions

We discussed various types of test structures for measurement of gain and absorption of SOAs. Experimental results on the Oclaro platform show that multisection SOAs can be successfully used for these measurements. Further quantitative analysis of the measurement accuracy is to be done.

Acknowledgement

This research is carried out in the ProCon Project 11369, supported by the Dutch Technology Foundation STW, which is part of the Netherlands Organization for Scientific Research (NWO), and which is partly funded by the Dutch Ministry of Economic Affairs.

References

- [1] M. Smit, X. Leijtens, E. Bente, J. van der Tol, H. Ambrosius, D. Robbins, M. Wale, N. Grote, and M. Schell, "Generic foundry model for InP-based photonics," *IET Optoelectronics*, vol. 5, pp. 187–194, 2011.
- [2] E. Bitincka and M. K. Smit, "On-wafer testing of basic building blocks in Photonic Integrated Circuits (PICs)," in *Proceedings of the 2012 Annual Symposium of the IEEE Photonics Benelux Chapter*, 29–30 November 2012, Mons, Belgium, pp. 147–150, 2012.
- [3] R. Santos, B. Barcones Campo, M. K. Smit, and X. Leijtens, "Vertical coupling mirror for on-wafer optical probing of photonic integrated circuits." Paper JT3A.15, *Integrated Photonics Research, Silicon and Nanophotonics*, 2013.
- [4] B. W. Hakki and T. L. Paoli, "Gain spectra in GaAs double-heterostructure injection lasers," *J. Appl. Phys.*, vol. 56, no. 3, pp. 1299–1305, 1975.
- [5] H. Wang and D. T. Cassidy, "Gain measurements of Fabry–Pérot semiconductor laser using a nonlinear least-squares fitting method," *IEEE J. Quantum Electron.*, vol. 41, pp. 532–540, 2005.
- [6] A. Oster, G. Erbert, and H. Wenzel, "Gain spectra measurements by a variable stripe length method with current injection," *Electronics Letters*, vol. 3, pp. 864–866, 5 1997.
- [7] J. D. Thomson, H. D. Summers, P. J. Hulyer, P. M. Smowton, and P. Blood, "Determination of single-pass optical gain and internal loss using a multisection device," *Appl. Phys. J.*, vol. 75, no. 17, pp. 2527–2529, 1999.

Manipulating optical qubits in the frequency domain

L. Olislager,^{1,*} E. Woodhead,² K. Phan Huy,³ J.-M. Merolla,³ P. Emplit,¹ and S. Massar²

¹ Service OPERA-Photonique, Université libre de Bruxelles, Brussels, Belgium

² Laboratoire d'Information Quantique, Université libre de Bruxelles, Brussels, Belgium

³ Département d'Optique P. M. Duffieux, Université de Franche-Comté, Besançon, France

* lolislag@ulb.ac.be

During the past years, we have shown that radio-frequency phase modulation of frequency entangled photons leads to a high-dimensional two-photon interference pattern in the frequency domain. By using periodic frequency filters, photons can be grouped into "even" and "odd" frequencies, thereby reducing the high-dimensional photon state to a two-dimensional photon state. We show that a new interference pattern arises when these qubits are made to interfere in the frequency domain, and that this interference pattern exhibits a high visibility and violates the standard two-dimensional Bell inequality, the CHSH inequality. This is realized with components adapted to fiber quantum communication at telecommunication wavelengths.

Introduction

Entangled photon pairs are an essential resource to achieve quantum communication protocols, such as quantum key distribution or quantum teleportation. [1] Photons entangled in energy and time have been extensively studied because they are conveniently produced – possibly at telecommunication wavelengths – by pumping a nonlinear crystal or waveguide. They can also be efficiently manipulated in various ways, for example as *time bins* [2] or as *frequency bins* [3, 4]. Hereafter, we focus on this last method.

As shown in [3, 4], radio-frequency phase modulation of photons belonging to a high-dimensional frequency entangled state leads to a high-dimensional two-photon interference pattern in the frequency domain. While this high dimensionality could be beneficially used, it is sometimes desirable to work with well-known two-dimensional quantum states – qubits – for which most standard quantum information protocols are designed.

Here we first recall the principles behind frequency-bin two-photon experiments, and we show how we can manipulate frequency bins as effective qubits. We then briefly present the experimental setup allowing such a manipulation, and some of our results, including two-dimensional two-photon interference and Bell inequality violation.

Method

An illustrative scheme of frequency-bin two-photon experiments is depicted in figure 1. A continuous laser at frequency ω_P pumping a nonlinear waveguide generates the frequency entangled state

$$|\Psi\rangle = \int d\omega f(\omega) |\omega_0 + \omega\rangle_A |\omega_0 - \omega\rangle_B, \quad (1)$$

with $\omega_0 = \omega_P/2$ for parametric down-conversion in a $\chi^{(2)}$ material, and $\omega_0 = \omega_P$ for four-wave mixing in a $\chi^{(3)}$ material. The function $f(\omega)$ characterizes the source bandwidth.

Manipulating optical qubits in the frequency domain

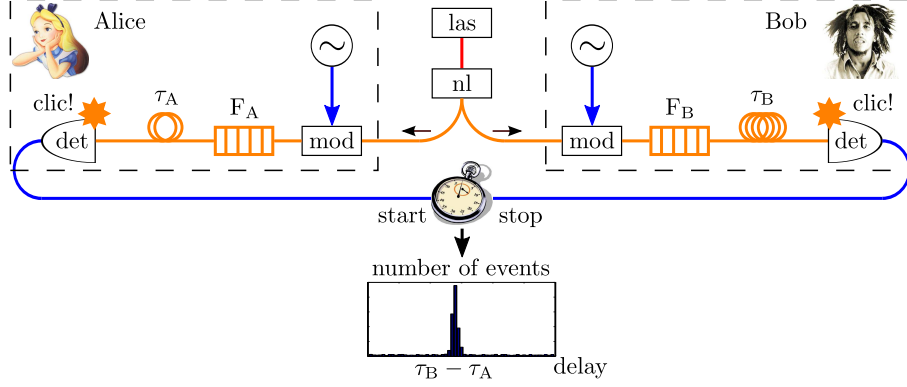


Figure 1: Principle of frequency-bin two-photon experiments. A laser (las) pumps a nonlinear medium (nl), generating frequency entangled photons. Each photon is sent to a different protagonist. It is subject to radio-frequency phase modulation (mod) and passes through a frequency filter ($F_{A,B}$) before detection by a single-photon detector (det). Correlations between detections are analyzed with a histogram of coincident events: when photons are generated simultaneously, a coincidence peak can emerge at a delay $\tau_B - \tau_A$ fixed by the experimenter. When filters are transparent to only a specific frequency $\omega_{A,B}$ and modulation is inactive, a coincidence peak appears only when $\omega_A + \omega_B = 2\omega_0$.

The photons are entangled in frequency: the sum of their frequencies is well defined, while their individual frequency is not.

Signal and idler photons are separated, one being sent to Alice (A) and the other to Bob (B). If A and B measure the frequency of their photon, their results are random, the probability of each result being governed by the function $f(\omega)$. On the other hand, the results are perfectly correlated: if A obtains $\omega_0 + \omega$, B obtains $\omega_0 - \omega$ with certainty.

In order to obtain non-trivial correlations, A and B can manipulate their photon before measuring its frequency. This is realized by modulating the phase of each photon with a radio-frequency signal of the form $V(t) = V_{\text{RF}} \sin(\Omega_{\text{RF}}t - \phi_{\text{RF}})$. Subject to such a signal, a photon state is transformed according to

$$|\omega\rangle \rightarrow \sum_{p \in \mathbb{Z}} U_p |\omega + p\Omega_{\text{RF}}\rangle, \quad \text{with } U_p = J_p(\pi V_{\text{RF}}/V_\pi) \exp(ip\phi_{\text{RF}}), \quad (2)$$

where J_p is the p th-order Bessel function of the first kind and V_π characterizes the response of the electro-optic phase modulator. The photon therefore ends up in a high-dimensional coherent superposition of different frequencies. Applying transformation (2) to state (1), with $V_A(t) = V_A \sin(\Omega_{\text{RF}}t - \phi_A)$ and $V_B(t) = V_B \sin(\Omega_{\text{RF}}t - \phi_B)$, we obtain

$$|\Psi\rangle \rightarrow \int d\omega' \sum_{\delta \in \mathbb{Z}} |\omega_0 + \omega'\rangle_A |\omega_0 - \omega' + \delta\Omega_{\text{RF}}\rangle_B C_\delta(V_A, \phi_A, V_B, \phi_B), \quad (3)$$

so that the probability $P(\omega_A + \omega_B = 2\omega_0 + \delta\Omega_{\text{RF}}) = |C_\delta(V_A, \phi_A, V_B, \phi_B)|^2$ is non-zero for different values of δ : a two-photon interference pattern emerges in the frequency domain, and it can be precisely controlled with the parameters V_A, ϕ_A, V_B, ϕ_B . [3, 4]

In practice, in order to detect such an interference pattern, A and B must measure the frequency of their photon with a precision better than Ω_{RF} . This is realized by using

filters transparent to only a frequency range $[\omega_{A,B} - \Omega_F/2, \omega_{A,B} + \Omega_F/2]$, with $\Omega_F < \Omega_{RF}$. Photons selected by a filter of bandwidth Ω_F with center frequency $\omega_0 + n\Omega_{RF}$ are said to belong to the *frequency bin* n .

This way to proceed causes, however, a practical problem: the simultaneous measurement of all possible results n_A and n_B would require a large number of cascaded frequency filters, causing high cost and losses. In [3, 4], only two detectors were used, such that the different results could not be measured simultaneously. This has negative consequences for applications. For example, one has to make additional assumptions to demonstrate experimentally Bell inequality violation. [5]

Here, we introduce another way to measure frequency correlations of frequency-bin entangled photons: by using *frequency interleavers*. These periodic filters give access to two outputs corresponding to orthogonal *sets* of frequencies, which we call *even* (E) and *odd* (O) frequencies. We therefore reduce the high-dimensional frequency entangled state to an effective two-dimensional frequency entangled state, see figure 2.

The advantage of such a procedure is that all measurement results are accessible with only four detectors – two for each protagonist. Manipulating effective qubits, we can apply standard procedures for two-dimensional states. For example, simultaneous measurement of all results allows violation – with no further assumption – of the standard two-dimensional Bell inequality, the CHSH inequality. [6]

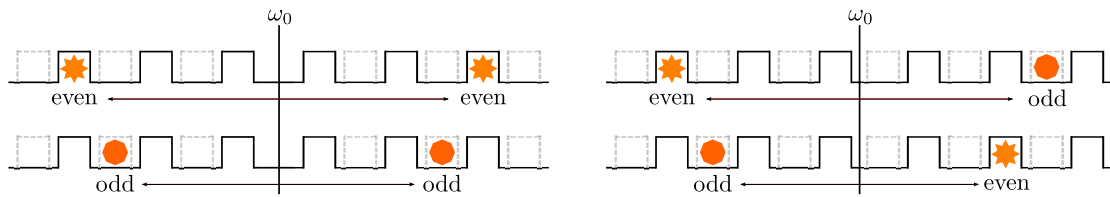


Figure 2: Frequency correlations between signal and idler photons when modulation is inactive. Depicted are the idealized orthogonal outputs of a frequency interleaver: photons with even (continuous dark line) and odd (dotted grey line) frequencies end up in different outputs of the filter. Depending on the position of the degeneracy frequency ω_0 , one will observe only EE and OO (left) or EO and OE (right) coincidences.

Experiment

Our experimental setup follows the scheme of figure 1. A continuous laser with power $P \approx 0.7$ mW and stabilized wavelength $\lambda_p = 776.1617$ nm pumps a periodically poled lithium niobate waveguide, generating entangled photons with $\omega_0/2\pi = 193.125$ THz located on the International Telecommunication Union DWDM grid in the C-band.

The photons then pass through a 12.5–25 GHz frequency interleaver from which only one output is collected; this ensures a good orthogonality between E and O subspaces. The photons are separated with a programmable filter which also limits the bandwidth to only a few frequency bins; this guarantees that dispersion is negligible.

The polarization of each photon is controlled with a fiber polarization controller followed by a polarizer, before modulation by a 25-GHz radio-frequency sinusoidal signal with adjustable amplitude and phase. Finally, on each side, a 25–50 GHz interleaver allows collection of E and O results by two avalanche photodiodes. A data acquisition system acquires simultaneously all possible results, i.e. EE, EO, OE and OO coincidences.

Results

Some of our results are presented in figure 3. When modulation is inactive, we obtain, as expected, only EE and OO (for the case shown) coincidences, at a rate $\approx 1.5\text{Hz}$ and with a coincidence-to-accidental ratio ≈ 2 . These low values are due to high losses and to detector inefficiency. When modulation is active, we observe two-photon interference. The experimental measurements, plotted with statistical error bars and noise subtracted, are in good agreement with the theoretical predictions, which we do not demonstrate here. The interference visibility is about 90%. Collecting coincidences for some specific settings, we have demonstrated the violation of CHSH inequality by more than 40 standard deviations, therefore demonstrating the presence of frequency entanglement.

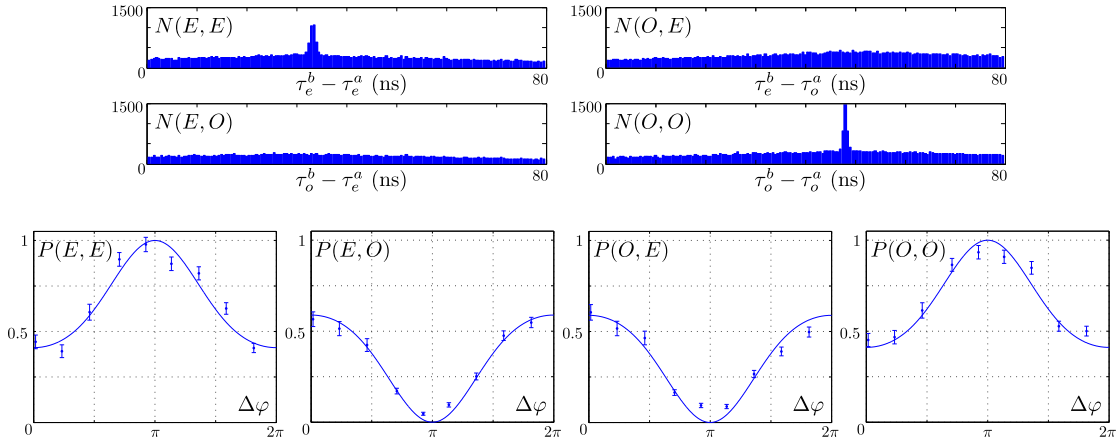


Figure 3: Experimental results. Top: coincidences when modulation is inactive. Bottom: probability of coincidence versus radio-frequency phase shift $\varphi_A - \varphi_B$.

Conclusion

In summary, we have demonstrated the manipulation of effective optical qubits in the frequency domain by using frequency interleavers.

This research was supported by the Interuniversity Attraction Poles program of the Belgian Science Policy Office, under grant IAP P7-35 photonics@be.

References

- [1] M. A. Nielsen and I. L. Chuang, "Quantum Computation and Quantum Information", Cambridge University Press, Cambridge, 2000.
- [2] J. Brendel, N. Gisin, W. Tittel, and H. Zbinden, "Pulsed Energy-Time Entangled Twin-Photon Source for Quantum Communication", *Physical Review Letters* **82**, 2594 (1999).
- [3] L. Olislager, J. Cussey, A. T. Nguyen, P. Emplit, S. Massar, J.-M. Merolla, and K. Phan Huy, "Frequency-bin entangled photons", *Physical Review A* **82**, 013804 (2010).
- [4] L. Olislager, I. Mbodji, E. Woodhead, J. Cussey, L. Furfaro, P. Emplit, S. Massar, K. Phan Huy, and J.-M. Merolla, "Implementing two-photon interference in the frequency domain with electro-optic phase modulators", *New Journal of Physics* **14**, 043015 (2012).
- [5] J. F. Clauser and M. A. Horne, "Experimental consequences of objective local theories", *Physical Review D* **10**, 526 (1974).
- [6] J. F. Clauser, M. A. Horne, A. Shimony, and R. A. Holt, "Proposed Experiment to Test Local Hidden-Variable Theories", *Physical Review Letters* **23**, 880 (1969).

Design and simulation of a high bandwidth optical modulator for IMOS technology based on slot-waveguide with electro-optical polymer

A.J. Millán-Mejía,¹ J.J.G.M. van der Tol,¹ and M.K. Smit,¹

¹ Photonic Integration Group (PhI), Dept. of Electrical Engineering, Technische Universiteit Eindhoven, Den Dolech 2, 5612 AZ Eindhoven, The Netherlands

Electro-optical modulators are considered to be a key devices for optical interconnects. In order to implement this device in the new InP membrane On Silicon platform (IMOS), a slot-waveguide configuration with a high nonlinear polymer is studied. Simulations and electrical calculations show good performance and fabrication tolerance using n-doped InP as the slot-waveguide material. The small dimensions of the structure and the high electro-optical coefficient of the polymer allow devices with a small footprint (hundreds of μ^2), high bandwidth ($> 100\text{GHz}$) and low $V_\pi \times L$ value ($\sim 0.7\text{Vmm}$). This solution is suitable for integration with passive devices already developed for this platform, and with active devices that are under development.

Introduction

It has become clear in the last years that optical interconnects are replacing more and more electrical wires in shorter distance links. Some of the reasons for this technological migration are the demand for faster speed communications and lower energy consumption inside computer chips [1]. These requirements cannot be supported by electronics interconnects alone, therefore, a new technology has to emerge. One of the proposed solution is the use of a thin optical layer bonded with BCB on top of the electronic chips (InP Membranes On Silicon (IMOS)) [2]. This configuration allows the total integration of electronics chips with photonic counterparts. The signal processing is done in the electric layer (Si), while most of the communications is done optically in the InP layer.

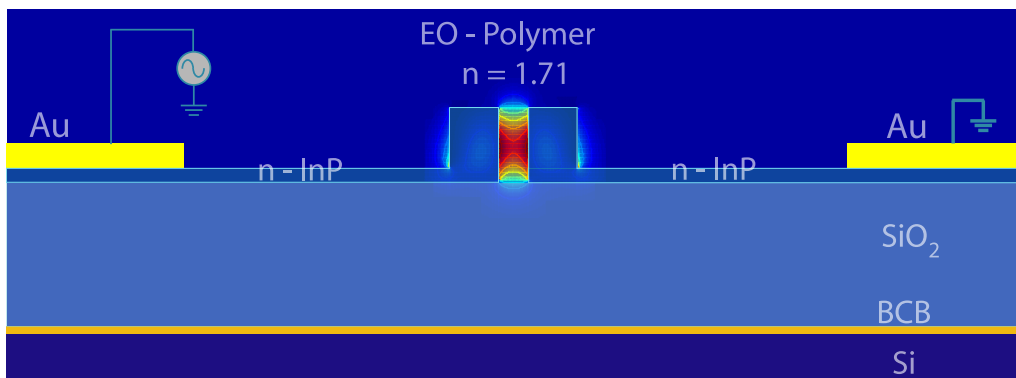


Figure 1: Cross section of the InP slot waveguide with the field strength of the TE mode indicated in the slot.

In order to create a working platform, several devices are needed. From the optical elements that need to be developed, an optical modulator has a key importance for communications applications. The configuration we select has to deal with two main problems: it has to be small to be attractive for on-chip/on-board interconnects, and it needs to be able to integrate with other devices (e.g. laser and detectors). Considering the aspects presented above, a Mach-Zehnder (MZ) interferometer structure as a phase modulator based on a slot waveguide and an electro-optical polymer could fulfill the two main requirements. Moreover, this configuration is able to show high performance in terms of bandwidth, extinction ratio, half wave voltage and energy consumption.

The slot waveguide enhances and confines the TE mode in the low index refractive material due to the boundary conditions for a large discontinuity of the electric field at high index-contrast interfaces. These conditions force the mode to be confined in the slot obtaining a high overlap with the electro-optical polymer. Figure 1 shows a cross section of the slot waveguide with the field of the TE mode in a structure based on n-doped InP material. The waveguide is placed on an insulator layer of SiO_2 and the two layers are bonded on a Silicon wafer. The insulator layer, due to its high refractive index contrast interface with InP, and lower refractive index than the electro-optical polymer ($n = 1.71$), will maintain the optical mode inside the slot in the vertical direction. The n-doped InP-layer next to the slot waveguide is necessary to apply a voltage to the slot. Due to this electrical connection, the applied electric field inside the slot is strong, besides it is highly coupled to the optical mode, allowing an efficient phase modulation effect on the optical mode.

Optimization of the Slot Waveguide

In order to optimize the structure, we set the thickness of the membrane to be $H = 300nm$. One reason for this decision is that previous passive IMOS devices were already optimized for this thickness [3]. In terms of slot waveguide properties, the confinement factor of the optical mode in the slot increases if the thickness of the membrane increases, however, if the thickness is too large, higher order modes can propagate as well. Taking these elements into account, $H = 300nm$ presents a good trade-off. Another consideration is to use a thickness of $t = 50nm$ for the connection layer next to the slot waveguide. This value is a trade-off between the resistance of this layer (which increases when we shrink its thickness) and the confinement factor of the TE mode in the slot (which is maximum when the thickness is zero). Furthermore, this layer works as a protector layer of the insulator layer (SiO_2) during processing.

To determine the width of the ridges (W) and the size of the slot (W_g), a study was carried out with an eigenmode solver (LumericalTM MODE solver). Figure 2 (a) displays how the confinement factor (Γ) changes for these two parameters. The maximum of the confinement (30%) is found for a ridge width of $W = 240nm$. One issue consists that in the lower left part of the plot, the parameters are close to the cut-off condition of the TE mode. In order to have fabrication tolerance, we consider that a gap from $W_g = 120nm$ to $W_g = 150nm$ provides a stable optical mode with a good confinement factor and fabrication tolerances.

In the fabrication process, the waveguides are made with not perfectly vertical sidewalls. In the slot-waveguide, the optical field is strongly confined at the interface of the InP material and the EO polymer. This condition lets small angles have a huge effect on the optical mode. In figure 2 (b) we analyze the behavior of the confinement factor with variation in

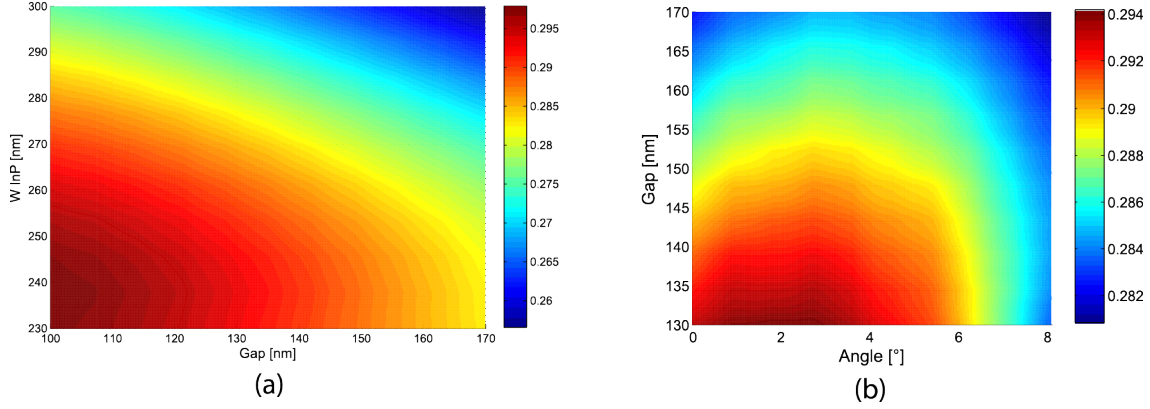


Figure 2: (a) Confinement factor Γ versus the width of the ridges (W) and the gap of the slot (W_g), with $H = 300nm$ and $t = 50nm$; (a) Γ versus the gap of the slot (W_g) and the sidewalls angle, with $H = 300nm$ and $t = 50nm$ and $W = 240nm$.

the sidewall angle and the gap width (W_g) of the slot. According to previous experience, a sidewall angle between 2 and 5 [°] can be obtained. In the plot 2 (b), considering the range $120nm < W_g < 150nm$, the slot gap of $W_g = 130nm$ presents the maximum confinement factor, nevertheless, we select a gap of $W_g = 140nm$ to gain some tolerance for fabrication process moving far from the cut-off conditions.

Performance analysis

For the slot waveguide modulator we contemplate to use an electro-optical (EO) polymer material from SoluxraTM. The electro-optical coefficient is up to $110pm/V$ if a good poling technique is developed. We can determine the half wave voltage by the equation 1.

$$V = \frac{\lambda d}{2n_0^3 r_{33} L \Gamma} \quad (1)$$

with wavelength $\lambda = 1.55\mu m$, refractive index of the EO polymer $n_0 = 1.71$, and desire length of $L = 300\mu m$. Due to the high EO coefficient and a strong electric effect originated by the slot waveguide, we obtain a half wave voltage $V_\pi = 2.34V$. The $V \times L$ product is around $\sim 0.7Vmm$, much lower than typical values in $LiNbO_3$ modulators ($\approx 10Vmm$) [4]. The MZ modulator we consider is a push-pull configuration. This scheme allows to halve the length of the MZ since the same voltage is applied to both MZ arms with opposite polarity.

For bandwidth analysis, with the help of a semiconductor device simulator (SilvacoTM), the resistance of the structure as a function of the doping level is found (figure 3). At low levels of doping, the resistance increases dramatically, so high doped material has to be use. In order to limit the losses, a value of $1e18cm^{-1}$ was selected which correspond to losses in the InP material of $L \approx 13db/cm$ [5]. This value allows some tolerance for the doping levels without sacrificing so much the resistance properties of the material. A resistance $< 10\Omega$ is predicted for our device with a connection layer of $2\mu m$ length.

In the case of capacitance, we calculate it to be $C = 15fF$. The theoretical bandwidth based on the RC time constant is around $1.3THz$. The limitation in the bandwidth will be

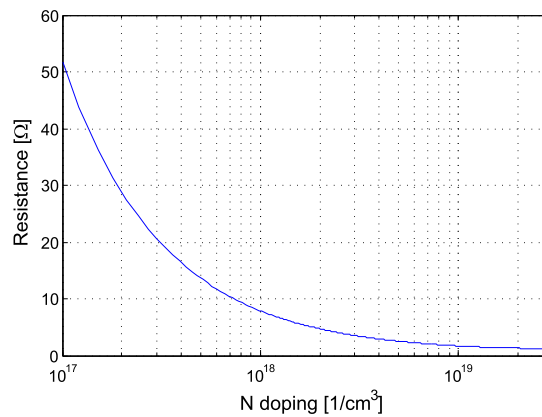


Figure 3: Resistance of the slot waveguide versus the doping concentration.

mostly due to the walk-off effect between the microwave signal in the electrodes and the optical mode. If we consider the effective refractive index of the slot waveguide ≈ 2 and a typical effective microwave refractive index of ≈ 4.6 [6]. The bandwidth for a $300\mu\text{m}$ long modulator is $f_0 = 170\text{GHz}$.

Conclusions

The design of using a slot waveguide phase modulator based on electro-optical polymer has been presented. Optimization of the slot waveguide structure leads to for a high optical confinement (30%) and good fabrication tolerances. A Mach-Zehnder modulator using this configuration can be achieved with 0.7Vmm , and a theoretical bandwidth limit around 170GHz . These parameters will allow the use of simplified electrode configurations for our devices.

Acknowledgments

This work was supported by the ERC project NOLIMITS

References

- [1] David a B Miller. Optical interconnects to electronic chips. *Applied optics*, 49(25):F59–70, September 2010.
- [2] J. van der Tol, R. Zhang, J. Pello, F. Bordas, G. Roelkens, H. Ambrosius, P. Thijs, F. Karouta, and M. Smit. Photonic integration in indium-phosphide membranes on silicon. *IET Optoelectronics*, 5(5):218, 2011.
- [3] J Pello, P Saboya, S. Keyvaninia, J. J. G. M. van der Tol, G. Roelkens, H. P. M. M. Ambrosius, and M. K. Smit. Post-bonding fabrication of photonic devices in an Indium phosphide membrane bonded on glass. ... *the IEEE Photonics* ..., pages 213–216, 2011.
- [4] K. Noguchi, O. Mitomi, and H. Miyazawa. Millimeter-wave Ti: LiNbO₃ optical modulators. *Journal of Lightwave* ..., 16(4):615–619, April 1998.
- [5] RG Broeke. A wavelength converter integrated with a discretely tunable laser for wavelength division multiplexing networks. (September), 2003.
- [6] A. Chen and E. Murphy. *Broadband Optical Modulators: Science, Technology, and Applications*. Taylor & Francis, 2011.

A new zero-level package approach for receiver modules

P.duan,¹ O.Raz,¹ B. E. Smalbrugge,¹ and H.J.S Dorren¹

¹ COBRA research school, Eindhoven University of Technology, Den Dolech 2, 5600MB, Eindhoven,
The Netherlands

Compact integrated receiver modules are key building blocks for high bandwidth density interconnection links. Previously, a 3D stacked receiver module was fabricated by utilizing an ultra-thick photoresist ramp to form a wafer level package strategy. In this paper, we will demonstrate another integrated approach based on the same technology. Instead of stacking the photodiode array on the TIA/LA chip, we placed them side-by-side on a silicon carrier in very close proximity. The metallic connections between the photodiode pads and TIA/LA pads were realized using electrical plating after a photoresist bridge is created between the two components. Visual inspection using a SEM show that connecting metal stripes are uniform and of good quality.

Introduction

The performance of today's computer systems is limited by signal transport (data communication), rather than by the logic operation speed or memory capacity [1-4]. Although, traditional copper wires are improving their performance by exploiting advanced techniques, such as active copper cables [5], these advances will not satisfy future interconnect requirements of bandwidth density and bandwidth distance product, due to the inherent limitation of the electrical wires [2].

Optics has improved bandwidth distance product and bandwidth density and if implemented in a cost effective-manner, optics may bring substantial system performance improvements [2]. Parallel optical links are already widely used in today's supercomputers for chassis-to-chassis and rack-to-rack communications [4]. These optical interconnects continue support higher speed, smaller package size, lower energy per bit and lower cost. Especially for cost-sensitive data center application, one of the critical figure of merits has decreased from \$100/Gbps in 2004 (VCSEL is around \$10 per each die) [3] to today's \$1/Gbps [2], and it needs to go below 10's of cents/Gbps [4] to support further penetration of this technology. In this paper, we will demonstrate a new zero-level package approach. This approach can allow for placing devices close to each other, without the need to accommodate requirements which normally exists in wire bonding technology [6]. It also processed at modest temperature, which is not the case for the flip chip [7]. Finally we show that with the same technology steps we can also improve coupling to fibers by making micro lenses on top of the O/E and E/O dies.

Fabrication

Previously, we have proposed a novel 3D stacking solution [8]. It can be used as an efficient way to connect any fix paths of two quite different height surfaces on a wafer scale process, such as integration of VCSEL array, photodiode array with its counterpart CMOS IC to form a 3D stacked transmitter and receiver array[9]. Recently, we explored a new package approach, which offers an effective way to connect devices on the same

carrier. The key step is to use the good topology cover ability and reflow character of ultra-thick photoresist, to form the photoresist bridge for plating process. This PR bridge can be deposited on all the metal connections between all the pads at once.

In the experiment, a 2-inch silicon quarter is utilized as a carrier since silicon has high thermal conductivity, which matches the thermal expansion of the CMOS IC chip and it is cheap. A 12-channel PD array and TIA/LA chip will be placed side by side on the carrier to form the receiver module. To speed up the pick and place process, 50nm silicon nitride are firstly deposited on silicon quarters, then using lithography and dry etching the placement spots of photodiode array and TIA array are defined. In this way, automatic pick and place machine can be used to put devices on the carrier through image recognition software. The photodiode array and TIA/LA array are successively placed on a dummy silicon quarter. After removing the redundant PR bonding layer, the sample is shown in Figure 1, the photodiode array is juxtaposed to a TIA/LA chip.

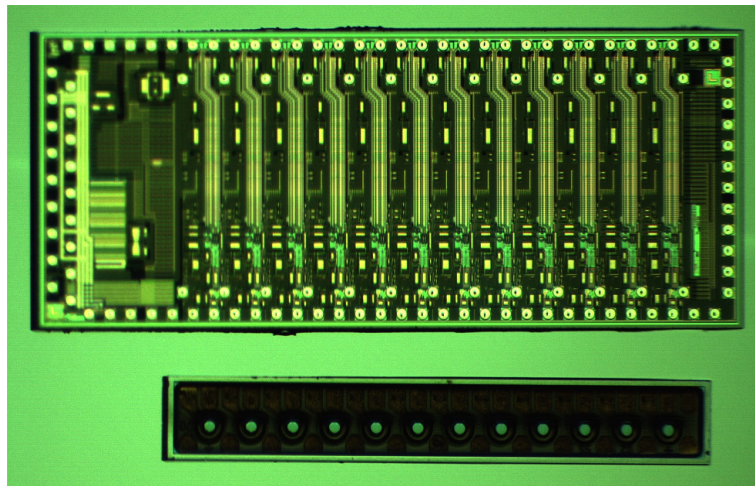


Fig. 1: 3D stacking model demonstration after placement

The photoresist pattern is obtained in the similar way as reported in [8]. After lithography, the chip is shown in Figure 2(a). You can see, the PR pattern covered the edge of TIA/LA chip as well as the edge of the photodiode array very well. In this process, we also introduced a cylinder pattern which fulfills two purposes. Firstly it provides protection to the sensitive area on the aperture of the photodiode array, shown in the Figure 2(b). Secondly it can be used as micro-lenses to help improve the coupling efficiency [9].

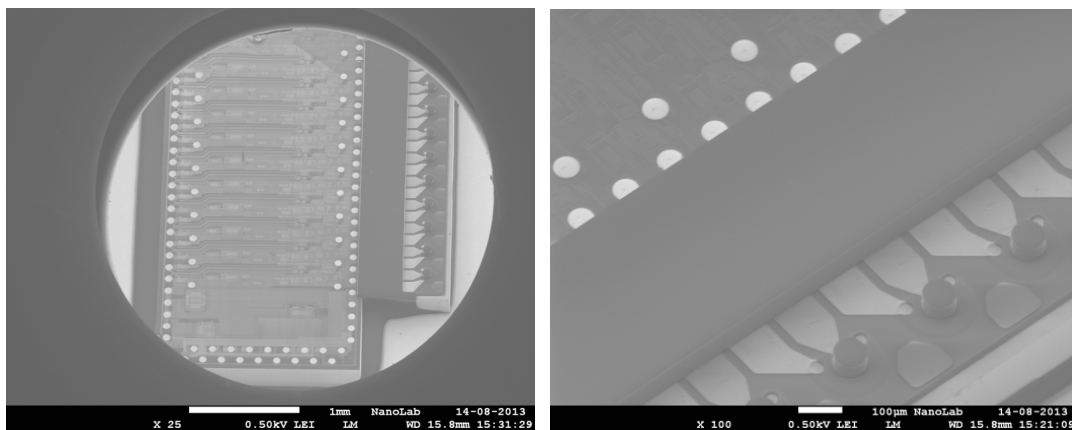


Fig. 2: (a) the sample outlook after lithography; (b) the zoom-in picture to show the photoresist cylinder pattern on the active area of photodiode array

The next step is to reflow the PR. As shown in the Figure 3, the photoresist ramp is smoothly formed between CMOS IC and photodiode array after the reflow step. The cylinder photoresist patterns turn under these conditions into semi-spheres due to the surface tension.

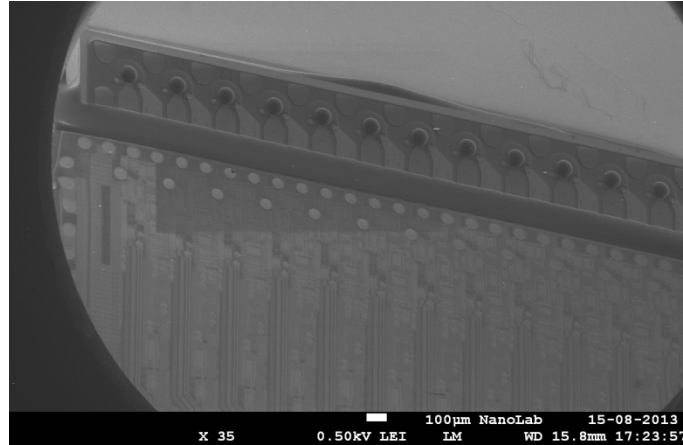


Fig. 3: the sample after reflow

After sputtering of a seed layer, we use lithography to define the plating area. Since the PD and the TIA/LA chip are placed side by side, the height between photodiode array surface and TIA/LA surface is decreased, so less overdevelop is needed in the process compared with previous approach [8], and much denser pitch can be realized in this way. As shown in the Figure 4, the opening rectangular pattern is formed on the seed layer, which will be plated with gold in the next step.

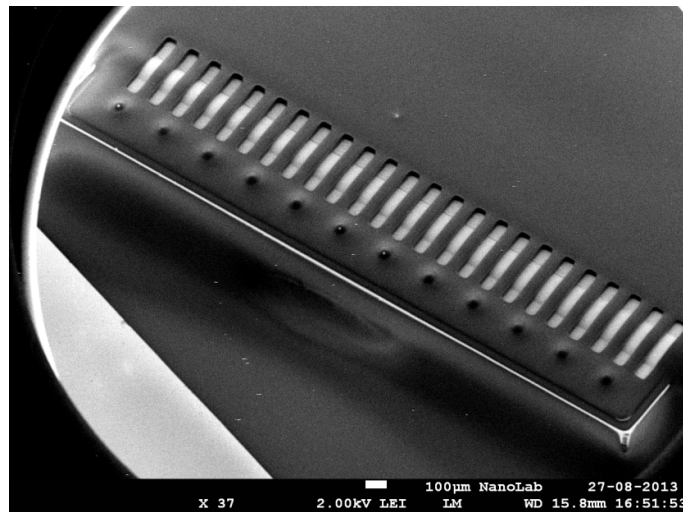


Fig. 4: the sample after lithography to define the plating area

The plating process determines the thickness of the metal paths. After plating, the photoresist and the seed layer are removed one by one. The chip looks like in Figure 5(a) after the process is complete. All 24 plated gold paths show good connections between photodiode pads and TIA/LA pads, and all the lenses are strongly attached onto the aperture of the photodiode array, as shown in the Figure 5(b). The resistance of each metal trace is negligible, the dark current and I-V curve of each photodiode remains the same as those for the original dies, and the photocurrent of each photodiode channels is double the number of the original photocurrent per each die at the same intensity flood light testing environment, thanks to the focusing of the lenses. In addition, you can also

see the metal paths are quite short, less than 200 μm when we pushed the photodiode array to almost touch the TIA/LA chip. Together with possibility to design the metal stripes to be impedance matched, this technique is very promising for higher data rate transmitter and receiver modules. Furthermore, the process itself is simpler due to the small height difference between each device on the carrier.

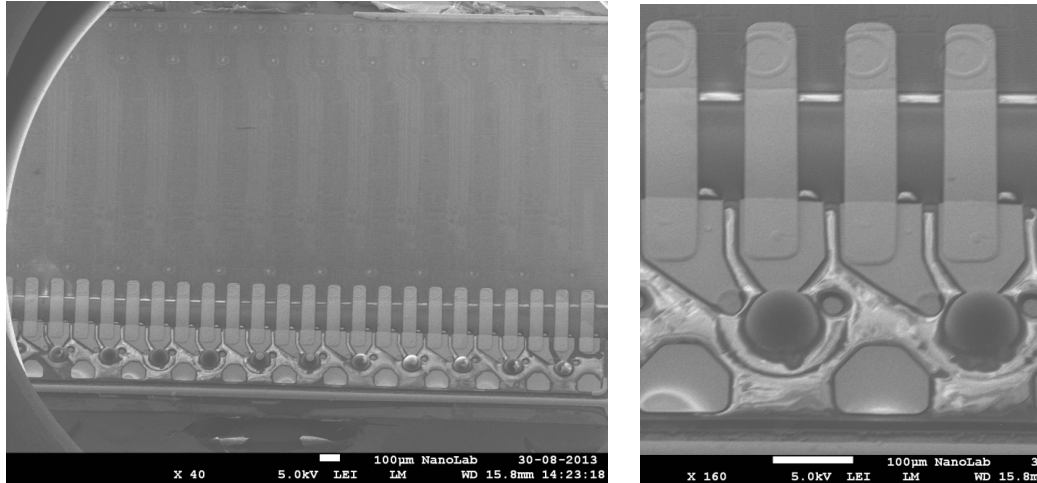


Fig. 5: (a) final shape of the side-by-side placed receiver chip, (b) the picture of micro-lenses and the plating metal paths

Conclusions

In this paper, a new integrated approach is demonstrated. Instead of stacking the photodiode array on the TIA/LA chip, we placed them side-by-side on a silicon carrier in close proximity. The primary test results show robust performance is achieved together and that the micro-lenses included in the fabrication process improve coupling. This new method can also be used for other high-speed, pressure-sensitive and temperature-sensitive devices interconnections and packaging challenges.

Acknowledgements

Work on this project is supported by Vici grant and the smartmix-MEMPHIS project.

References

- [1] <http://spectrum.ieee.org/semiconductors/optoelectronics/get-on-the-optical-bus>.
- [2] A.Benner, "Cost-effective optics: enabling the exascale roadmaps," Hot Interconnects 17, Aug. 2009.
- [3] D.V. Plant and A.G.Kirk, "Optical interconnects at the chip and board level challenges and solutions," <http://asia.stanford.edu/events/Spring03/slides/plantSlides.pdf>.
- [4] M.A.Taubenblatt, "Optical Interconnects for High-Performance Computing", Journal of Lightwave Technology, pp. 448-458, 2012.
- [5] J.Mitchell, G. ogranessyan, "Introduction to active infiniband interconnects", http://www.hpcadvisorycouncil.com/pdf/IB_Active_Interconnects.pdf, Oct. 2010.
- [6] J. Pan, and P. Fraud, "Wire Bonding Challenges in Optoelectronics Packaging", Society of Manufacturing Engineers, TP04PUB284, 2004.
- [7] H. Tong, Y. Lai, and C. wong, "Advanced Flip Chip Packaging", Springer New York Heidelberg Dordrencht London, 2013.
- [8] P.duan, O. Raz, B. E. Smalbrugge, J. Duis, and H.J.S Dorren, "A Novel 3D Stacking Method for Opto-Electronic Dies on CMOS ICs", in the proceedings of ECOC 2012, Tu.3.E.2.
- [9] P.duan, O. Raz, B. E. Smalbrugge, and H.J.S Dorren, "Demonstration of Wafer Scale Fabrication of 3D Stacked Transmitter and Receiver Modules for Optical Interconnects", Accepted in Journal of Lightwave Technology.

Towards densely integrated lasers for optical data communication

Aura Higuera-Rodriguez¹, Dominik Heiss¹, Andrea Fiore², Meint Smit¹

Eindhoven University of Technology, Den Dolech 2, 5612AZ, Eindhoven, The Netherlands

¹ Photonic Integration, Department of Electrical Engineering

² Photonics and Semiconductor Nanophysics, Department of Applied Physics

Optical data links are employed at ever shorter distances, most recently with a few meters length in between cabinets in warehouse sized computer systems. A continuation of this trend to optical chip-to-chip and on-chip communication will require highly efficient and densely integrated optical devices. We will discuss general requirements to achieve such targets in nano- and micro- scale lasers integrated with a photonic membrane platform, where we focus on the optical cavity design and the electrical properties. Additionally, we will compare the advantages of laser concepts based on metallic-dielectric confinement, photonic crystal cavities and distributed feedback using sidewall gratings.

Introduction

Optically active devices on the micro and nano scale have been of great interest in recent years. The ultimate objective is on-chip communication using densely integrated directly modulated lasers at room temperature. Such devices have been demonstrated [1]; however, output powers in the hundred micro watt regime remain challenging as efficient cooling is needed. Currently, high density deployment in an on-chip scheme is not limited by the device footprint but rather by the high serial resistance of nano lasers and the associated heat generation. As an example, in a nano laser with an output power of 100 μ W, a wall plug efficiency of 0.1, and a high performance water cooling mechanism, the device density is limited 1000/mm² [4]. High wall plug efficiency, low threshold currents and low serial resistance are, therefore, mandatory for densely integrated devices. Moreover, methods to couple the light source to a waveguide with a high efficiency have been proposed [1, 2], but not demonstrated to our knowledge.

In the first part of this paper, we discuss the requirements for an efficient electrically pumped micrometer laser in general terms of optical and electrical properties independently of a specific implementation.

In the second part, we describe three design approaches and compare their suitability to the requirements derived in the first part: sidewall grating, metallic-dielectric optical confinement [3] and 1D photonic crystal (PC). We also consider the fabrication complexity for each concept, and assess the potential to integrate it with a photonic membrane platform, InP Membrane On Silicon (IMOS), that would allow integration of photonic circuits with electronics.

Requirements for micro-nano scale lasers design

Miniaturization is essential for lasers in high density integrated photonic circuits (PICs). While it brings advantages as low device footprint and threshold current, it raises challenges due to the shortening of the gain section, which in turn, requires very efficient mirrors. This can be illustrated by considering a Fabry Perot cavity with mirror reflectivity R_{mirror} , length l and a modal gain g_{modal} . For a better understanding, we plot $1-R_{\text{mirror}}$ on a logarithmic scale of such a cavity as a function of length for a range of modal gains between 10/cm and 500/cm. Values up to 1800/cm and 3000/cm are typically reached for QWs and bulk gain media respectively. As the length of a laser is reduced more perfect mirrors are required, for example $R_{\text{mirror}}=0.98$ is needed for lasers shorter than a micron (at g_{modal} 500/cm) which is very challenging to achieve. In the following we consider a five micrometer length laser and a modal gain of 500/cm. As shown in Figure 1a) a facet reflection of 90% is needed in this case.

To get an estimate of the threshold current as a function of device length we calculate the carrier recombination current in a 200 nm thick InGaAs active region. Here, we consider the Auger, radiative recombination and surface recombination (velocity) at threshold charge carrier density ρ_{th} . We can deduce the threshold carrier density from the differential gain using a logarithmic gain model for bulk InGaAs ($g_0=3000$, $N_{\text{tr}}=1.1$, $N_s=5$ [5]). In Figure 1b) the threshold current is plotted as a function of device length for different mirror reflectivities. At higher reflectivities the minimal threshold current is found for shorter cavity lengths. However, a minimum threshold current does not guarantee efficient laser operation, since one of the mirrors need to allow out-coupling of the laser light. A better figure of merit is the wall plug efficiency as discussed in the following.

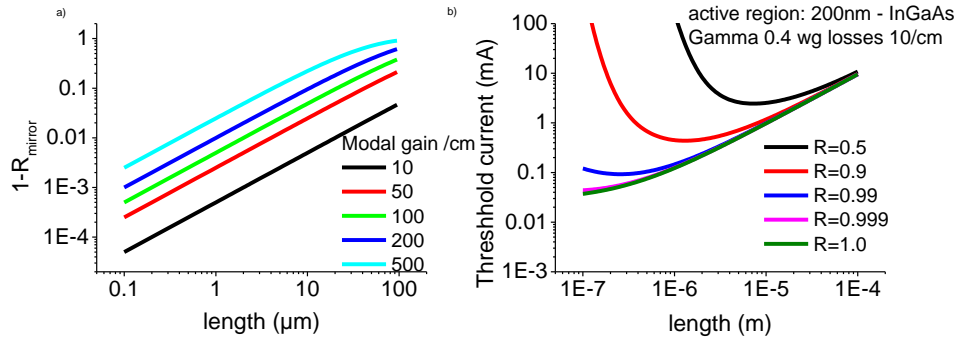


Figure: a) threshold current in mA versus device length in m b) facet reflectivity versus device length in μm .

The wall plug efficiency is the ratio of the optical output power over the total electrical power used by the device. A high WPE reduces the power consumption and reduces the amount of heat generated by the device leading to higher integration densities. In a simple model the WPE depends on the series resistance R_{ser} , differential efficiency η_d , threshold current I_{th} , current-independent series voltage V_s , and the ideal diode voltage V_d .

$$WPE = \frac{P_o}{P_{in}} = \frac{\eta_d \frac{h\nu}{q} (I - I_{th}) \cdot (I > I_{th})}{I^2 R_{ser} + IV_d + IV_s}$$

Figure 2 illustrates the dependence of the WPE on these parameters. In Figure 2a) the parameters are set to typical values for nano lasers ($\eta=0.5$, $I_{th}=100\ \mu\text{A}$ and $R_{ser}=1\text{K}\Omega$), and the WPE is plotted as a function of the output power (black line). The WPE is maximal with a value of 0.2 at an output power of $100\ \mu\text{W}$. For lower powers the WPE is limited by the threshold current as illustrated by the green line, where the series resistance is set to 0. For higher output power the threshold current is negligible compared to the current feeding the stimulated emission, and the WPE is limited by the series resistance of the device (red line). The maximum WPE is limited by the differential efficiency, as illustrated by the blue line in fig 2a), where both I_{th} and R_{ser} are equal to zero. An improvement of the WPE can be achieved by increasing the differential efficiency (i.e. $\eta=0.7$ in figure 2b), reducing the threshold current ($I_{th}=5\mu\text{A}$ in 2c) or reducing the series resistance ($R_{ser}=100\ \Omega$ in 2d). Note that the maximum efficiency shifts when changing these parameters, making the ideal optimization dependent on the desired power output range. In each case a high differential efficiency is desired.

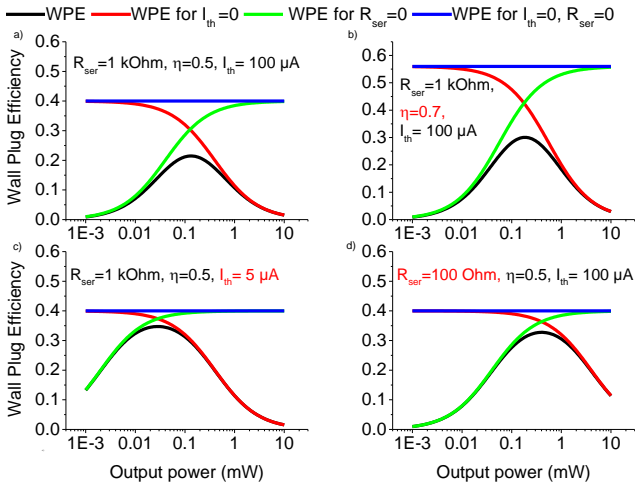
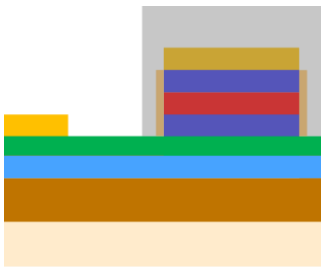


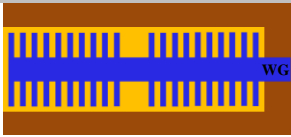

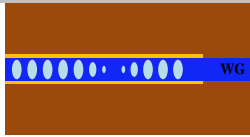
Figure: WPE vs. Output power in mW for a) $R_{ser}=1\text{K}\Omega$, $\eta=0.5$ and $I_{th}=100\ \mu\text{A}$ b) $R_{ser}=1\text{K}\Omega$, $\eta=0.7$ and $I_{th}=100\ \mu\text{A}$ c) $R_{ser}=1\text{K}\Omega$, $\eta=0.5$ and $I_{th}=5\ \mu\text{A}$ and d) $R_{ser}=100\ \Omega$, $\eta=0.5$ and $I_{th}=100\ \mu\text{A}$.

Conclusion: laser concepts summary

Table 1 summarizes the results obtained by 3D FDTD simulations. It shows the general layer stack in a cross sectional cut and the longitudinal view of each design. Some of the critical parameters that define advantages and drawbacks for each schematic are also shown.

Table 1. Summary of the main required parameters for different laser concepts

Layer stack cross section		
		<div>SiNx</div> <div>p-InP</div> <div>n-InP</div> <div>p-contact</div> <div>n-contact</div> <div>InGaAs</div> <div>Q 1.25</div> <div>BCB</div> <div>Si</div> <div>Ag</div>

Laser concept	DFB	Metal wrapped	PhC-x
Longitudinal Cross section			
Differential efficiency	9%	20 %	Up to 40%
Facets reflectivity	70% at 20 periods	99 %	83% at 5 periods
Q factor	~240	~750	~650
Length	~15 μm	5 μm	5 μm

The first concept considered in Table 1 is the side wall grating laser. At least 20 grating periods are needed to reach reflections compatible with achievable material gains. This results in a large device length exceeding 15 μm . Furthermore, the η_d is around 9%, which severely limits the achievable WPE of the device. However, a DFB laser has the advantage of an accurate wavelength control, and is less complex to fabricate than the other schemes.

The main advantage of the metal wrapped cavity presented in column two is a high Q factor of 700 due to the 99% of reflection on a silver/silicon nitride (Ag/SiNx) facet. Furthermore, the length of the cavity can be squeezed to a 5 μm length. Due to the metal mirrors, this design cannot be butt coupled to an output waveguide. Symmetric evanescent coupling to a parallel output waveguide results in a η_d up to 20%. Additionally, the design relies critically on low material losses achieved with high quality silver. Although the fabrication is at some extent challenging, there are currently techniques that tackle the critical fabrication steps of metallic-dielectric cavities [1, 6]. Finally, our most promising design is a photonic crystal nano-beam with a cavity length as short as 5 μm and a Q factor of 650. Five periods are sufficient to achieve more than 83% of reflection. This concept shows good wavelength control and low threshold currents. Moreover, in this design it is possible to reduce the losses in the cavity by placing the ohmic contact to the side of the structure, leading to high η_d from 40% up to 60%, which would allow high WPE. This concept is challenging to fabricate. Due to the large surface to volume ratio it is critical to reduce surface recombination and avoid erosion of the conducting layers.

References

- [1] K. Ding, M. Hill, Z.C. Liu, L. J. Yin, P.J van Veldhoven, and C.Z. Ning, "Record performance of electrical injection sub-wavelength metallic-cavity semiconductor lasers at room temperature," *Optics Express*, vol. 21, No. 4, 4728-4733, 2013.
- [2] M. Kim, A. M. Lakhani, and M. C. Wu, "Efficient waveguide-coupling of metal-clad nanolaser cavities," *Optics Express*, Vol.19, No.23, 23504-23512, 2011.
- [3] V. Dolores-Calzadilla, D. Heiss, A. Fiore, and M. Smit, "Waveguide-coupled nanolasers in III-V membranes on silicon," proceedings at ICTON IEEE, 978-1-4799-0683-3, 2013.
- [4] D. Heiss, V. Dolores-Calzadilla, A. Fiore, and M. Smit, "Design of a waveguide-coupled nanolaser for photonic integration," in proceedings of the conference OSA IPR, Puerto Rico, 2013.
- [5] L. A. Coldren, "Gain and current relations 4.6," in *Diode lasers and photonic integrated circuits*, John Wiley & Sons, New Jersey, pp.224-225, 2012.
- [6] M. T. Hill, and M. Marell, "Novel plasmon nanolasers," 15th OptoElectronics and Communications Conference (OECC2010) Technical Digest, Sapporo Convention Center, Japan, 218-219, 2010.

Spatial polarization domain-wall in colloidal semiconductor nanocrystals

M. Swaelens,¹ S.-P. Gorza,¹ P. Kockaert,¹ S. Coen,² and M. Haelterman¹

¹ Service OPERA Photonique, Université libre de Bruxelles (U.L.B.), 50 Av. F. D. Roosevelt, CP 194/5, B-1050 Bruxelles, Belgium

² Department of Physics, University of Auckland, Private Bag 92019, Auckland, New Zealand

Optical domain-walls can be formed at the boundary separating two distinguishable adjacent laser beams. They constitute the fundamental soliton associated with Berkhoer and Zakharov modulational instability. These solitons exist in defocusing Kerr-type materials providing that cross-phase modulation is higher than self-phase modulation. To date, these solitons have only been experimentally observed in the temporal domain. In this work, we investigate the formation of spatial domain-walls in colloidal semiconductor nanocrystals by numerical simulations.

Introduction

In anomalous nonlinear Kerr media, it is well known that bright solitons are related to modulational instability. In the same way, Haelterman *et al.* predicted the existence of a new kind of soliton related to the Berkhoer and Zakharov modulational instability that occurs in the normal dispersion regime of propagation [1]. Such structures can be formed when cross-phase modulation is higher than self-phase modulation. They consist in the transition between two domains of opposite circular polarizations, and were therefore named “polarisation domain wall solitons” (PDW) [2]. The existence of PDW has experimentally been demonstrated in the temporal domain in 1999 [3].

Up to now, the domain-wall soliton has not yet been observed in the spatial domain, probably because its observation requires the propagation of light beam in a medium exhibiting a strong negative instantaneous nonlinear refractive index (n_2). In this work, we propose to make use of colloidal semiconductor quantum dots (CSQD), as they can present the required strong negative n_2 [4]. Although the crystalline structure of semiconductors is not isotropic, the use of CSQD ensures isotropy on a macroscopic scale, which in turns implies that cross-phase modulation effects are two times higher than self-phase modulation.

The geometry of our system is as follows: two orthogonally polarized beams are copropagating side by side so that the soliton is formed at their boundary. Below we report on the numerical simulations that were performed in order to determine the experimental conditions enabling the observation of the spatial PDW soliton.

Propagation Equations

The propagation of two orthogonal circularly polarized optical beams in an isotropic medium with nonresonant electronic instantaneous defocusing Kerr nonlinearity can be described by the normalized coupled nonlinear schrödinger equations:

$$\begin{aligned} i\partial_z A_+ + \frac{1}{2}\Delta_\perp A_+ - (|A_+|^2 + 2|A_-|^2)A_+ &= 0, \\ i\partial_z A_- + \frac{1}{2}\Delta_\perp A_- - (|A_-|^2 + 2|A_+|^2)A_- &= 0, \end{aligned}$$

where A_+ (A_-) is the slowly varying beam envelope of the right (left) handed circularly polarized electric field, normalized with respect to $\sqrt{3\gamma L_D}$, with $\gamma = \frac{2\omega n_2}{9c} < 0$, the non-linear coefficient and $L_D = ka^2$ with k the wave number in the material; $\Delta_\perp = \partial_{xx}^2 + \partial_{yy}^2$ denotes the transverse Laplacian where x and y are normalized with respect to a ; and z is the longitudinal coordinate normalized with respect to L_D .

Numerical results

The two beams were propagated using the well-known split-step Fourier method. Since PDW corresponds to the transition between two beams of constant amplitude, we have first analyzed how the PDW formation is affected by the finite size and the shape of the beam profile modulating the PDW. The initial condition consists of two half-supergaussian beams, right- and left-handed polarized, while the transition is an hyperbolic tangent of variable width w_0 :

$$\begin{aligned} A_+ &= \left(\frac{1 + \tanh\left(\frac{y}{w_0}\right)}{2} \right) e^{-\left(\frac{x}{x_0}\right)^{2g}} e^{-\left(\frac{y}{y_0}\right)^{2g}}, \\ A_- &= \left(\frac{1 + \tanh\left(-\frac{y}{w_0}\right)}{2} \right) e^{-\left(\frac{x}{x_0}\right)^{2g}} e^{-\left(\frac{y}{y_0}\right)^{2g}}, \end{aligned}$$

where g is the order of the supergaussian.

Figure 1a shows clearly that using a PDW inscribed onto a broader square-shaped ($g > 1$) beam, the carrier beam broadens as a result of diffraction, while the domain-wall propagates without distortion as a result of the interaction between diffraction and nonlinearity [5].

In a practical experiment, it would be desirable to simplify the beam shaping as much as possible. Therefore, we investigate the case where the carrier beam is Gaussian ($g = 1$). Figure 1b shows that with Gaussian beams, since the domains are not pseudo-infinite, the diffraction of the Gaussian beam induces a change of peak power that in turn alters the domain-wall, *i.e.* the change in peak power lowers the magnitude of the nonlinear effect, which results in the broadening of the domain-wall.

As the broadening of the PDW inscribed on a Gaussian beam prevents us to identify the PDW as a structure that propagates undistorted, we will define a parameter V , called “visibility”, allowing for the comparison between the linear and the nonlinear propagation regimes. This parameter is defined as the ratio $\frac{w_L}{w_{NL}}$ between the width of the domain wall (at an intensity value of $I = 0.5$) after propagation in the linear (L) and the nonlinear (NL) regime:

$$V = \frac{w_L}{w_{NL}}.$$

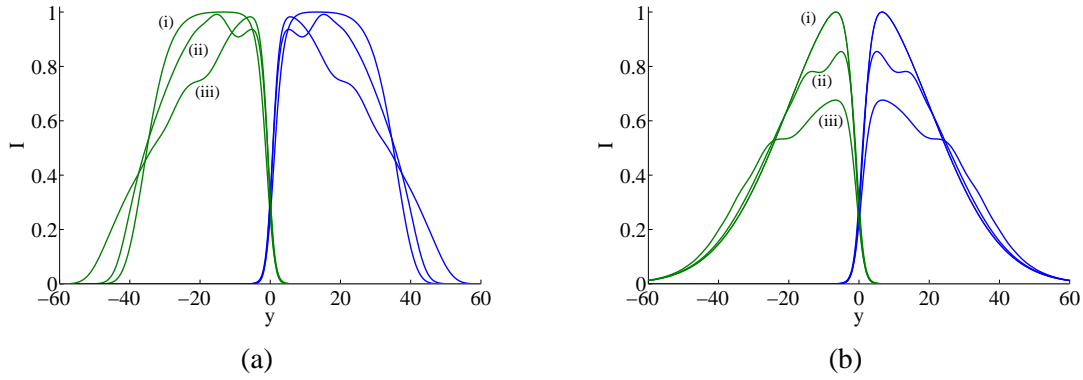


Figure 1: Evolution of the beam component intensities along the propagation: (i) $z = 0$, (ii) $z = 16$, (iii) $z = 32$, with two different input beams: (a) supergaussian ($g = 4$); and (b) Gaussian ($g = 1$), with $w_0 = 3$ and $x_0 = 40$.

In Figure 2a, the visibility V is plotted as a function of the PDW width w_0 , at $z = 10$ and for $x_0 = 30$ and $y_0 = 40$. We observe a maximum around $w_0 = 3$, which is the optimum value when the domains are not pseudo-infinite. Moreover, these results suggest that the formation of a PDW should be observed even for step-like profiles ($w_0 \rightarrow 0$). As can be seen in Figure 2b for $w_0 = 3$, the visibility monotonically increases with the input Gaussian beam width $x_0 = y_0$. However, at a value of $x_0 = y_0 \approx 30$ we already have a good visibility. By taking into account the Kerr coefficient of PbS Qdots ($n_2 \approx 10^{-11} \text{ cm}^2/\text{W}$) a power of 80 kW is needed to form the spatial DW. Given this rather high value despite the large nonlinear coefficient n_2 , we are considering the propagation in planar waveguide to decrease the spatial width of the beam in the x direction. We expect the formation of a PDW providing that the beating length between TE and TM modes is sufficiently long in comparison with the propagation length.

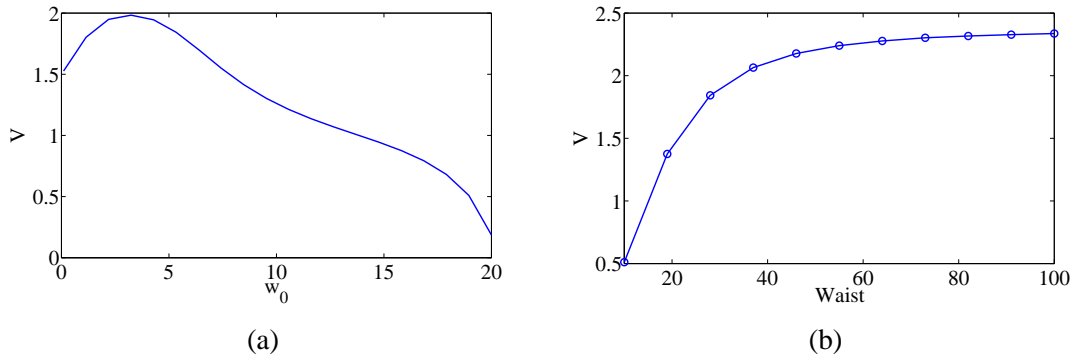


Figure 2: Visibility as a function of the parameters of the input beams : (a) visibility with respect to PDW width w_0 ; (b) visibility with respect to $x_0 = y_0$.

Experimental set-up

The experimental setup currently built for the observation of the spatial PDW is depicted in Fig. 3. The beam at the output of a pulsed laser source is first split in two linearly polarized components E_x and E_y . The vertically polarized beam passes through a π -phase-step plate in such a way that after the recombination of the two beams, we end up with opposite circularly polarized adjacent components $E_{\pm} = \frac{E_x \pm iE_y}{\sqrt{2}}$. The recombined beam is then focused on the colloidal nanocrystals cell and at the output the profile of both polarized components are recorded.

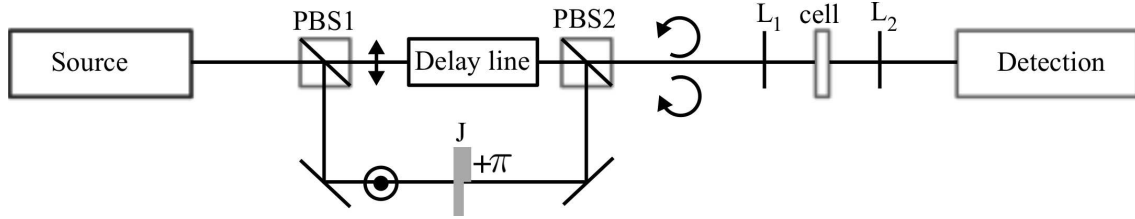


Figure 3: Experimental principle set-up

Conclusion

PDW solitons have been predicted two decades ago but are still only experimentally demonstrated in the temporal domain. In this work, we have shown that the formation of spatial PDW is possible even with initial condition far from ideal, i.e. with a sharp initial transition between the two polarization components and Gaussian shape for the beam the domain wall is inscribed on. Since PDWs are transitions between pseudo-infinite domains, the overall extent of the beam should be sufficiently large with respect to the width of the DW. This result in required beam peak powers of the order of 80 kW to observe spatial PDW in CSQD, despite their large nonlinear Kerr coefficient in comparison with other conventional nonlinear defocusing Kerr media. A possible solution to decrease the required power is to resort to planar waveguide made up of CSQD.

References

- [1] M. Haelterman and A. P. Sheppard. Extended modulational instability and new type of solitary wave in coupled nonlinear Schrödinger equations. *Physics Letters A*, 185(3):265–272, 1994.
- [2] M. Haelterman and A. P. Sheppard. Bifurcations of the dark soliton and polarization domain walls in nonlinear dispersive media. *Physical Review E*, 49(5):4512–4518, 1994.
- [3] S. Pitois, G. Millot, P. Grelu, and M. Haelterman. Generation of optical domain-wall structures from modulational instability in a bimodal fiber. *Physical Review E - Statistical Physics, Plasmas, Fluids, and Related Interdisciplinary Topics*, 60(1):994–1000, 1999.
- [4] A. Omari, I. Moreels, F. Masia, W. Langbein, P. Borri, D. Van Thourhout, P. Kockaert, and Z. Hens. Role of interband and photoinduced absorption in the nonlinear refraction and absorption of resonantly excited pbs quantum dots around 1550 nm. *Physical Review B - Condensed Matter and Materials Physics*, 85(11), 2012.
- [5] M. Haelterman and A. P. Sheppard. Polarization domain walls in diffractive or dispersive kerr media. *Optics Letters*, 19(2):96–98, 1994.

Design of a Uni-Traveling-Carrier (UTC) photodetector in InP Membrane on Silicon (IMOS)

L. Shen,¹ J.J.G.M. van der Tol,¹ G. Roelkens,^{1,2} and M.K. Smit¹

¹ Eindhoven University of Technology, COBRA, Den Dolech 2, 5612AZ Eindhoven, The Netherlands

² Ghent University - IMEC, INTEC, Sint-Pietersnieuwstraat 41, 9000 Gent, Belgium

InP Membrane on Silicon (IMOS) technology provides a new platform for integrating a full set of photonic components on top of CMOS chips. In this paper, a design of a uni-traveling-carrier photodetector in this platform is presented. Optical simulations have been performed to determine both the coupling loss and the metal loss. Electrical simulations have also been performed to optimize the RC constant and the transit time. The simulation shows that a bandwidth beyond 100 GHz with a responsivity of 0.8 A/W can be achieved. This provides promising integrated solutions for ultrafast optical interconnects and microwave applications.

Introduction

InP Membrane on Silicon (IMOS) technology promises the integration of ultra-small active and passive photonic devices in a single layer. This photonic membrane layer is bonded on a silicon wafer with polymer benzocyclobutene (BCB). By combining the best features of InP related material and Si based chips, IMOS opens up a wide range of applications with potential improvements in speed, integration density and energy consumption. Recently, a variety of passive components have been realized in this platform [1] and an electrically pumped membrane laser at 1.55 μm is being developed [2]. In this paper, a design of a photodetector (PD) in the IMOS platform is reported.

The uni-traveling-carrier (UTC) structure is chosen due to its superiority in bandwidth and power handling capability. The carrier transport in UTC-PDs is dominated by electrons due to the utilization of a p-type doped absorption layer [3]. The higher velocity of electrons than that of holes results in a higher bandwidth compared to conventional PIN-PDs. Furthermore, the space charge effect is also reduced, leading to a higher saturation current. These features of UTC-PDs provide new integration solutions for applications in coherent photonics and microwave photonics [4].

Structure design

The structure of our UTC-PD is shown in Fig. 1. The width of the mesa is designed as 3 μm . A 300 nm thick undoped InP layer is used both as the passive waveguide and as the electron collector (depleted) in the UTC region. A 150 nm thick p-type (Zn) doped InGaAs layer is used both as the absorber and the p-contact. In this way the photodetector can achieve a high responsivity while maintaining a simple layer stack which is desired for active/passive integration in the membrane platform. The doping concentration in the InGaAs layer is graded from 10^{18} cm^{-3} at the collector-absorber interface to 10^{19} cm^{-3} at the contact surface. A quasi-field formed by this graded doping profile defines the diffusion direction of electrons (toward the collector) and reduces their transit time in this absorber [3]. Hence, the graded doping design is crucial for high collection efficiency and high bandwidth. To further enhance the performance a novel double-side processing technology will be developed: p-metals (Ti/Pt/Au) are firstly

evaporated on one side; after bonding this InP sample onto a silicon substrate, the remaining processing steps are performed from the other side.

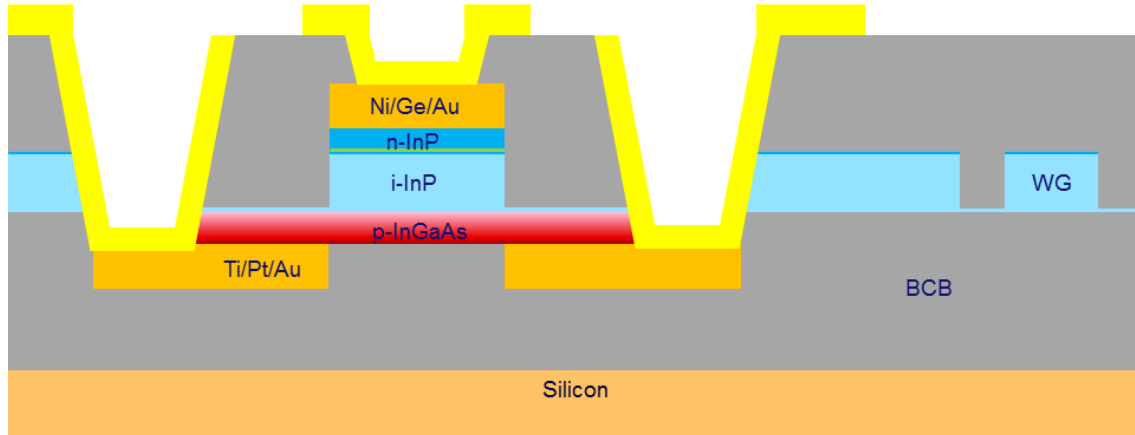


Fig. 1. Cross-section of the UTC-PD (not to scale)

Responsivity

In order to determine the responsivity of the UTC-PD, optical simulations are performed by using a fully vectorial mode solver and a 3D optical propagation tool based on eigenmode expansion (Fig. 2) [5]. The modal absorption coefficient is calculated to be 3600 cm^{-1} at $1.55 \text{ }\mu\text{m}$, which implies that over 97% of the input light will be absorbed within a length of $10 \text{ }\mu\text{m}$. The metal loss is estimated by setting the absorption coefficient of InGaAs to be zero and only taking into account the absorption in the metal contacts. This approximation gives a number of 340 cm^{-1} , indicating that the loss due to the metal contacts is limited. The coupling of the input signal from the waveguide to the photodetector region is also simulated. The coupling coefficient from the fundamental mode in the waveguide to the one in the photodetector is 75% from this simulation; the rest are coupled to higher order modes which suffer more from the metal loss. Other factors that may influence the efficiency are also taken into account. The free carrier absorption is negligible compared to the material absorption of InGaAs. The minority diffusion length in the Zn doped InGaAs with a doping concentration between 10^{18} cm^{-3} to 10^{19} cm^{-3} is one order of magnitude larger than the InGaAs layer thickness [6], implying that the collection efficiency will not be affected by the doping level. Overall, the coupling is the limiting factor of the device efficiency and a responsivity of 0.8 A/W is predicted for a $10 \text{ }\mu\text{m}$ long photodetector.

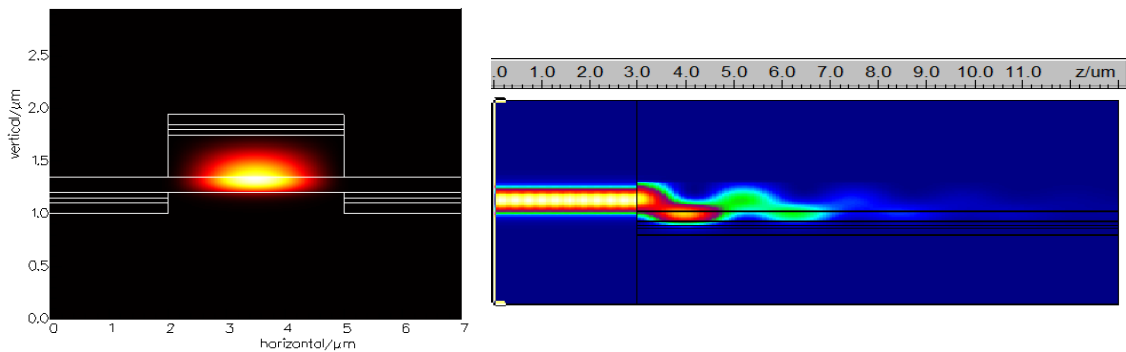


Fig. 2. Optical simulation results showing the fundamental mode profile (left) and the coupling from the waveguide to the photodetector (right)

Bandwidth

The bandwidth of a photodetector is limited by the RC time constant and the carrier transit time. The junction capacitance of a UTC-PD with 10 μm length, 3 μm width and a 0.3 μm thick depletion layer is as low as 10 fF. The parasitic capacitance can be neglected by planarizing thick BCB as isolation from the silicon substrate. The relatively high sheet resistance of a thin membrane device is the major limiting factor for the bandwidth. In this structure, however, the series resistance can be reduced dramatically by putting the p-metals close to the mesa, which is the major advantage of the double-side processing technology. The contact resistance on both p and n sides are currently being optimized to the target value of $3 \times 10^{-6} \Omega\text{cm}^2$. A stationary electrical simulation is performed with COMSOL to determine the total resistance (Fig. 3). It is assumed that the illumination results in a uniform carrier distribution in the depletion region. A resistance below 50 Ω is obtained from the simulation with the dimensions and the contact resistivity mentioned above. By using the equation

$$f_{3db,RC} = \frac{1}{2\pi \cdot R \cdot C}$$

The bandwidth limited by the RC constant is calculated to be as high as 150 GHz in a 50 Ω load environment.

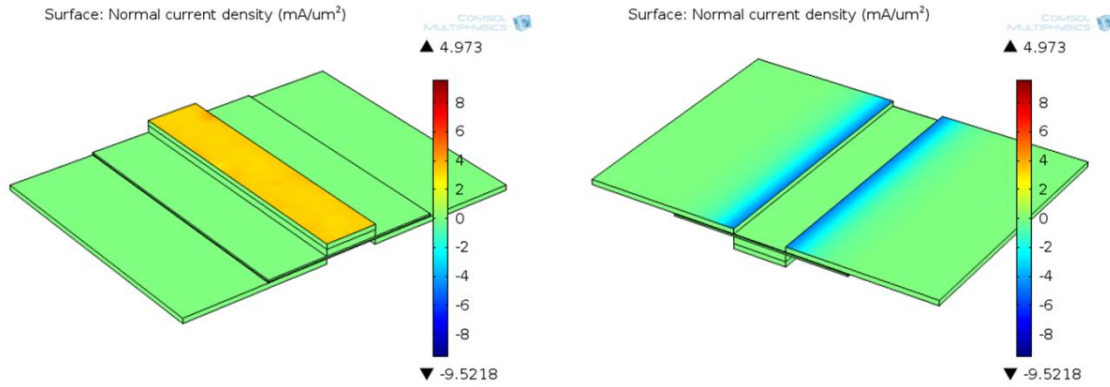


Fig. 3. Electrical simulation results showing the surface normal current density at -5 V bias

The transit time of UTC-PDs consists of two terms: the electron diffusion time in the undepleted InGaAs absorber, and the electron drift time in the depleted InP collector. The first term is studied in detail in [3] by considering the electron diffusion transport, thermionic emission process and the effect of the quasi-field. Based on this study, the diffusion time is estimated to be below 1 ps for a 150 nm thick InGaAs absorber with a graded doping from 10^{18} cm^{-3} to 10^{19} cm^{-3} . In terms of the electron drift time, UTC-PDs are usually set with an optimal bias voltage so that electrons travel at the velocity overshoot (above $2 \times 10^7 \text{ cm/s}$, 5 times higher than the velocity of holes). At this optimal bias, the electron drift time through the 300 nm collector is only 1.5 ps. The bandwidth limited by a total transit time of 2.5 ps is calculated to be 150 GHz by the following equation:

$$f_{3db,tr} = \frac{2.4}{2\pi \cdot \tau_{tr}}$$

Taking into account the RC constant limited bandwidth of 150 GHz, the final bandwidth of such a UTC-PD is expected to be beyond 100 GHz according to the equation:

$$\frac{1}{f_{3db,total}^2} = \frac{1}{f_{3db,RC}^2} + \frac{1}{f_{3db,tr}^2}$$

Other considerations

The power handling capability of a photodetector is very important particularly in coherent photonics and microwave applications. The saturation output of a photodetector is mainly limited by space charge effects and thermal failure. UTC-PDs show much reduced space charge effects due to the high electron velocity in the depletion layer. In terms of thermal effects, it becomes more severe in a membrane device with materials of low thermal conductivity (SiO₂ and BCB) blocking the heat dissipation to the substrate. In this design with double-side processing, the metals on both sides of the UTC-PD are expected to help to dissipate the heat to large-area metal pads on top. Followed by top cooling approaches, the thermal management of this design can be very effective.

The IMOS platform aims at providing a technology for photonic integrated circuits (PICs). By developing the double-side processing technology, we expect to integrate this UTC-PD with other components like lasers, by just adding layer stacks and a few processing steps from one of the two sides. In addition, the relatively simple layer stack allows selective-area regrowth as an alternative approach for the integration.

Conclusions

A high performance UTC photodetector in InP membrane on Silicon is designed. A bandwidth beyond 100 GHz and a responsivity of 0.8 A/W are shown by simulations. Moreover, it has the potential for fully integrated, high power applications.

References

- [1] J.J.G.M. van der Tol, *et. al.*, "Photonic integration in indium-phosphide membranes on silicon," IET Optoelectronics, vol. 5, 218-225, 2011.
- [2] S.P. Bhat, *et. al.*, "Design of InP Membrane Laser in a Photonic Integrated Circuit," in Proceedings of the 17th Annual Symposium of the IEEE Photonics Society Benelux Chapter, 2012.
- [3] T. Ishibashi, *et. al.*, "InP/InGaAs Uni-Traveling-Carrier Photodiodes," IEICE Transactions on Electronics, Vol.E83-C, 938-949, 2000.
- [4] C.C. Renaud, "Ultra-high-speed uni-traveling carrier photodiodes and their applications," in Proceedings of the Conference OFC/NFOEC, 2013.
- [5] Photon Design, FIMMPROP, <http://www.photond.com>.
- [6] D. Cui, *et. al.*, "Impact of doping and MOCVD conditions on minority carrier lifetime of zinc-and carbon-doped InGaAs and its applications to zinc-and carbon-doped InP/InGaAs heterostructure bipolar transistors." Semiconductor science and technology, vol. 17, 503-509, 2002.

Optimization of fiber Bragg grating physical parameters for polarization-assisted transverse strain measurements

F. Descamps¹, S. Bette¹ and C. Caucheteur¹

¹ Université de Mons - Faculté Polytechnique, Service d'Electromagnétisme et de Télécommunications, 31, Boulevard Dolez, 7000 Mons, Belgium.

In fiber Bragg grating (FBG) sensors, the evolution of the wavelength maximum polarization dependent loss (PDL) amplitude is used to determine the birefringence of the fiber. For low birefringence value, the relation between the wavelength maximum PDL amplitude and the birefringence is nearly linear and so it can be approximated by a straight line with a slope that depends on the physical parameters of the FBG. An analytical formula for this slope is derived. The comparison of the analytical approximation with simulations values for weak gratings gives errors below 0.05 dB for a birefringence up to $1.5 \cdot 10^{-5}$.

Introduction

Fiber Bragg grating sensors have become very common and recently new sensors that take advantage of the polarization properties of the fiber Bragg grating response have been developed [1, 2]. The polarization-assisted sensors use the value of the maximum polarization dependent loss (PDL) to determine the birefringence created in the fiber by the physical parameter (load, magnetic field) to be determined. The relationship between the maximum value of the PDL and the birefringence is nearly linear for small values of the birefringence. The sensor will be used in this range. The value of the slope of the maximum PDL versus birefringence depends on the parameters of the FBG and it determines the accuracy and the operating range of the sensor. The value of the slope is therefore crucial in the design of polarization-assisted sensors. In this work, we determine an approximate analytical formula for this slope that helps designing such sensors.

Birefringence and polarization dependent loss (PDL)

The response of a uniform FBG in transmission was analyzed in details in [3]. The grating parameters δn , L , Λ and the coefficients α , κ , $\hat{\sigma}$ used in the following come from [3]. When the fiber is not perfectly symmetric due to intrinsic dissymmetry or external factors such as strain, it exhibits birefringence and the response of the FBG then depends on the state of polarization of light that is launched into

the fiber Bragg grating (FBG). The response of the FBG can be determined by separating all polarizations at the entrance in the basis of the two FBG eigenstates (labelled x and y). The eigenstates x and y have respectively an effective refractive index of the core given by n_{eff} and $n_{\text{eff}} + \Delta n$ with Δn the birefringence of the fiber. The PDL is given by [4]:

$$PDL = \left| 10 \log_{10} \frac{T_x}{T_y} \right| \quad (1)$$

where T_x and T_y are the transmission intensities spectrum for the 2 eigenstates.

Determination of an approximate analytical formula for the slope between the PDL maximum and the birefringence

To find an approximate formula for the slope, we proceed in 3 steps. First, we define an approximate wavelength position for the maximum of the PDL when the birefringence is small. Then, we compute the slope for each wavelength by calculating $\frac{d(PDL)}{d(\Delta n)}$ evaluated for $\Delta n = 0$. Finally, we combine the two former points and simplify the formula obtained. In general, to find a maximum we equal the derivative to 0 but in the case of the PDL the equation to be solved contains hyperbolic functions and the analytical solution cannot be found easily. Instead of finding an exact solution, we approximate the wavelength of the maximum to be such that $\alpha L = i\pi/2$. This hypothesis is justified by the following considerations:

1. The PDL maximum is between 2 well defined points. The first one is the band edge characterized by $\alpha L = 0$ and the second one is the first zero of the reflection that corresponds to $\alpha L = i\pi$. The point such that $\alpha L = i\pi/2$ is then a good estimation of the wavelength of PDL maximum. The band edge and the first zero of reflection of an FBG are shown in Figure 1a.
2. We see on Figure 1a that the value of the PDL varies smoothly near its maximum value so a small error in the position of the PDL maximum does not strongly affect the slope. This is not the case for strong gratings (reflectivity $\geq 98\%$) in which a small error in the wavelength position of the PDL maximum will result in a strong error in the slope.
3. For usefulness, the expression of the slope is reduced by taking $\alpha L = i\pi/2$ so as to suppress the hyperbolic function.

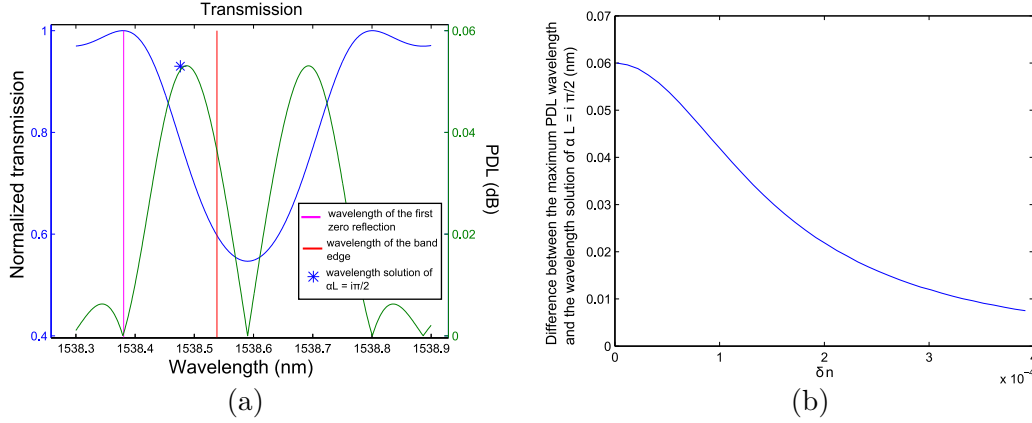


Figure 1: (a) Transmission spectrum versus wavelength and PDL versus wavelength with the band edge and the first zero also plotted (b) Wavelength difference between the max PDL wavelength and the $\alpha L = i\pi/2$ wavelength

For FBGS, the mean modulation index is small compared to the effective refractive index of the core $\delta n \ll n_{\text{eff}}$ and also the period of the grating is small compared to the FBG length $\Lambda \ll L$. When determining the wavelength (λ_{app}) such that $\alpha L = i\pi/2$, we only keep the first order terms in δn and Λ . We obtain for λ_{app} :

$$\lambda_{\text{app}} = \frac{4L\Lambda n_{\text{eff}}(2\delta n + n_{\text{eff}})}{2L(n_{\text{eff}} + \delta n) + (L^2\delta n^2\nu^2 + 4\Lambda^2 n_{\text{eff}}^2)^{1/2}} \quad (2)$$

Inserting equation (2) in $\left. \frac{d(PDL)}{d(\Delta n)} \right|_{\Delta n=0}$ yields the slope S :

$$S = \frac{-10}{\ln(10)} \frac{4\pi(\hat{\sigma}^2 + \alpha^2)}{\alpha^2 \lambda_{\text{app}} \hat{\sigma}} = \frac{10}{\ln(10)} \frac{16L^2 \kappa^2}{\pi \lambda_{\text{app}} \hat{\sigma}} \quad (3)$$

with $\alpha^2 = -\pi^2/4L^2$.

Equation (3) can be further simplified by developing κ and replacing λ by $2\Lambda n_{\text{eff}}$ everywhere except in $\hat{\sigma}$ (because $\hat{\sigma} = 0$ if we replace λ by $2\Lambda n_{\text{eff}}$):

$$S = \frac{10}{\ln(10)} \frac{16L^2 \pi \nu^2 \delta n^2}{(2\Lambda n_{\text{eff}})^3 \hat{\sigma}} \quad (4)$$

Developing and comparing the remaining terms allow additional simplifications:

$$S = \frac{40}{\ln(10)} \frac{L^3 \delta n^2 \nu^2}{\Lambda^2 n_{\text{eff}}^2 (L^2 \delta n^2 \nu^2 + \Lambda^2 n_{\text{eff}}^2)^{1/2}} \quad (5)$$

Results

In this section, we compare the maximum value of the PDL with the value given by the linear approximation. The absolute errors between the linear approximation

and the real value are shown in Figure 2b and stay below 0.05 dB for a birefringence up to $1.5 \cdot 10^{-5}$.

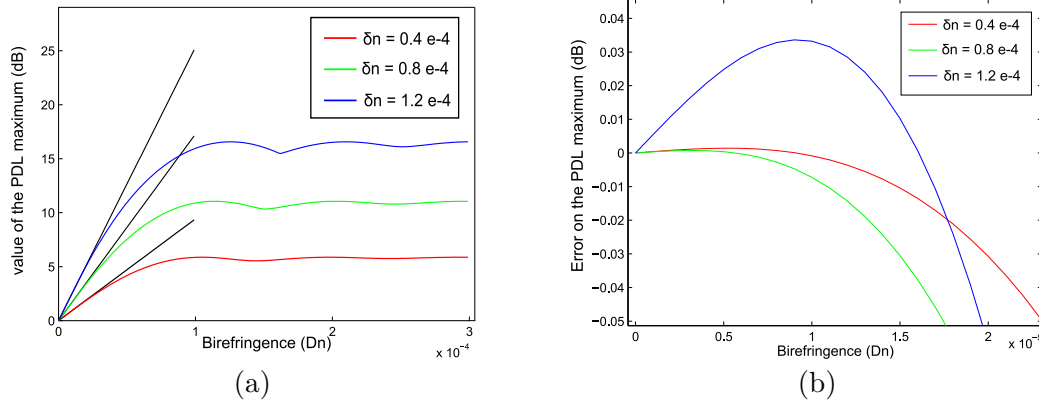


Figure 2: (a) Evolution of the maximum PDL with birefringence for 3 different values of δn
 (b) Absolute error for different values of δn

Conclusion

We presented an analytical formula that links the parameters of an FBG with the value of the slope between the birefringence and the maximum value of the PDL. The difference between the linear approximation and simulation value gives errors below 0.05 dB for a birefringence up to $1.5 \cdot 10^{-5}$. The formula is simple enough to be helpful for designing polarization-assisted FBG sensors.

Acknowledgments

This research has been conducted in the frame of the ERC (European Research Council) Starting Independent Researcher Grant PROSPER (grant agreement N° 280161 - <http://www.umons.ac.be/erc-prosper>). C. Caucheteur is supported by the F.R.S.-FNRS.

References

- [1] C. Caucheteur et al., "Transverse Strain Measurements Using the Birefringence Effect in Fiber Bragg Gratings", *IEEE Photonics Technology Letters*, vol. 19, pp. 966-968, 2007.
- [2] Y. Su et. al., "Use of the polarization properties of magneto-optic fiber Bragg gratings for magnetic field sensing purposes", *Optical Fiber Technology*, vol. 17, pp. 196-200, 2011.
- [3] T. Erdogan, "Fiber Grating Spectra", *Journal of Lightwave Technology*, vol. 15, pp. 1277-1294, 1997.
- [4] C. Caucheteur et al., "Influence of the Grating Parameters on the Polarization Properties of Fiber Bragg Gratings", *Journal of Lightwave Technology*, vol. 27, pp. 1000-1010, 2009.

Uniform planarization technique for the realization of a twin-guide membrane laser

S. P. Bhat¹, L. Fernandez², J.J.G.M. van der Tol¹, G. Roelkens^{1,3}, H.P.M.M. Ambrosius¹, and M.K. Smit¹

¹ Photonic Integration Group (PhI), Dept. of Electrical Engineering, Technische Universiteit Eindhoven, Den Dolech 2, 5612 AZ Eindhoven, The Netherlands

² Engineering school, ENSICAEN, 6 Boulevard Maréchal Juin, CS 45053, 14050 Cedex 04, France

³ Photonics Research Group (INTEC), Dept. of Information Technology, Universiteit Gent, Sint-Pietersnieuwstraat 41, 9000 Gent, Belgium

Abstract: The InP Membrane on Silicon (IMOS) generic technology promises high index contrast photonic integrated circuits. To make this a reality fabrication of an electrically pumped twin-guide laser is pursued. In this paper, one of the bottle-necks for the processing is discussed, the planarization step and subsequent etch-back. Benzocyclobutene (BCB) is used to planarize SOA structures before contacting. Complete curing of BCB at 280°C creates uniformity issues during etch-back. To mitigate this, a partial cure at 180°C before the etch-back and a complete cure afterwards is performed. Experiments show repeatability and reproducibility. Good uniformity after etch-back is found.

Introduction

InP Membrane on Silicon (IMOS) is a novel technology to realize high index contrast photonic integrated circuits. Passive components such as single mode waveguides, 1x2 MMI couplers, ring resonators and polarization converters have already been fabricated and characterized [1]. The next step in the development of this technology is to make active components such as electrically pumped lasers. Feasibility studies of such lasers on the IMOS platform have been reported in [2]. Furthermore, different configurations for such a laser integrated with other components have been designed [3].

As part of the process flow, one of the fabrication steps involves planarization of the SOA structures for p-metal definition. The schematic for this is shown in Fig.1. Divinylsiloxane-bis-benzocyclobutene (DVS-BCB, in short BCB) is the obvious candidate of choice for this purpose, based on its physical properties, such as the high degree of planarization, low moisture absorption, low curing temperature, excellent chemical resistance, low dielectric constant, rapid curing, low viscosity and

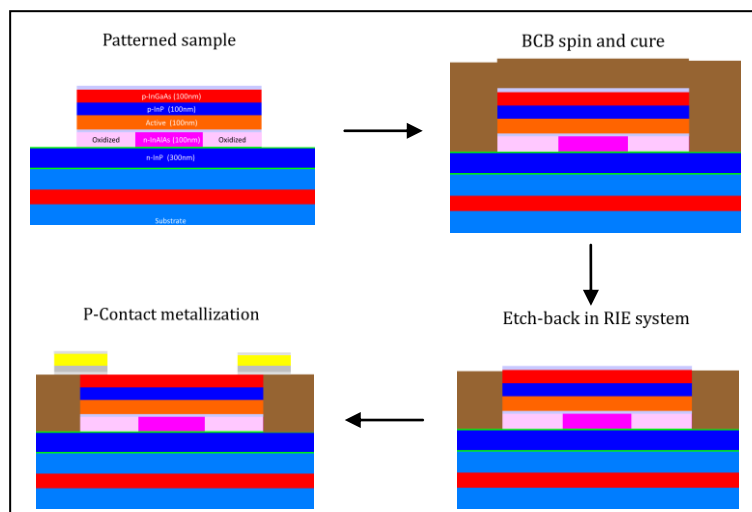


Fig.1: Schematic of the planarization and metallization process.

dry-etch compatibility [4].

The procedure involves spinning BCB on top of the patterned sample, curing, and etching back the cured BCB in a reactive-ion etching (RIE) system to expose the semiconductor surface for contacting. However, complete curing at 280°C followed by etch-back in the RIE system creates non-uniformities in the etch-depth at different positions on the sample. Possible cause could be solidification of BCB after complete curing at 280°C (see Fig.2) leading to larger thermal non-uniformities affecting the reaction rates at different positions. With the step height on the patterned sample being only 400 nm, a non-uniformity of 300 nm is not tolerable. This could result in the p-contact metal reaching the n-doped side of the diode, giving a short circuit. To alleviate this problem and to have better uniformity over the entire sample, a new recipe is developed. This involves a partial cure at 180°C, followed by etch back in a RIE system. Because of the partial preservation of fluidity, a reflow and a better thermal conductivity is obtained, creating a better uniformity. Finally, a complete cure at 280°C is performed. The detailed procedure is described in the next section.

Planarization technique

As described in the previous section, a new recipe is developed to mitigate uniformity issues during etch-back. A thin layer (70-80 nm) of PECVD SiO_x is deposited on the patterned sample to improve the adhesion of BCB to the surface. BCB is spin-coated at 3000 rpm and the sample is placed inside a baking oven for curing. Partial curing at 180°C is performed for one hour. For these conditions, as is evident from Fig.2, the extent of cross-linking in the polymer is around 50%.

After the spin coating and the partial cure, the step-height in the patterned substrate is reduced from 400 nm to ~ 40 nm clearly showing the planarization property of BCB. The total thickness of the BCB layer itself is ~ 1.3 μm . This has to be reduced to 400 nm or a little less, to expose the semiconductor surface for further processing. For this, an

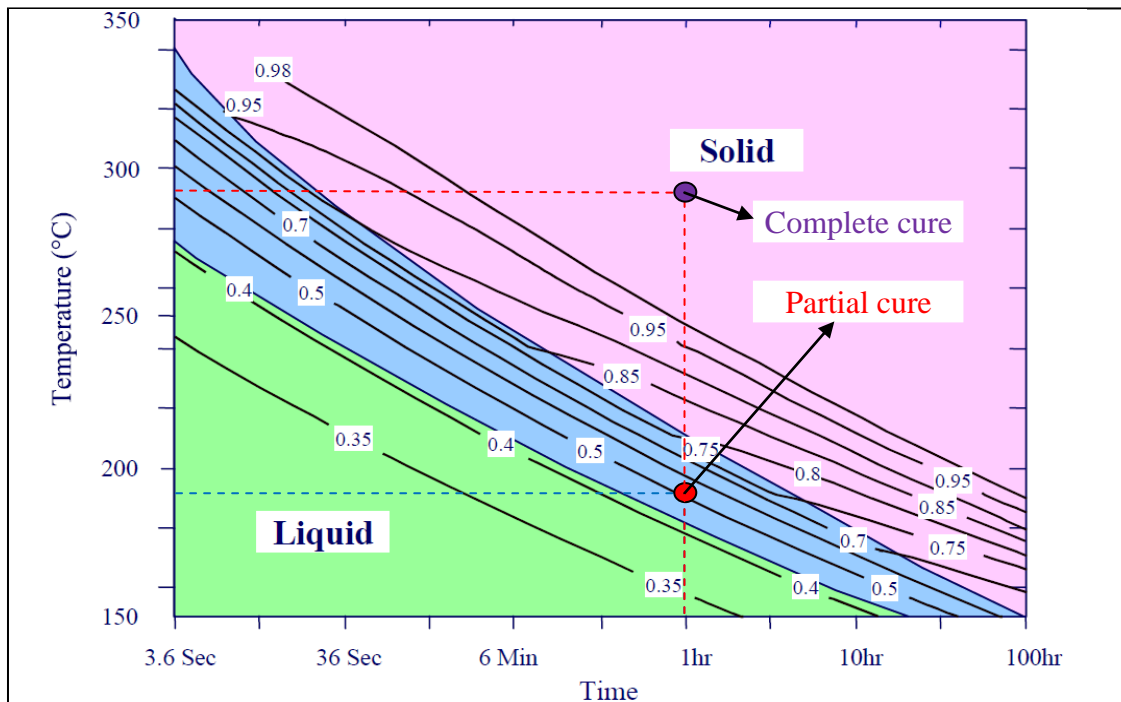


Fig.2: Extent of BCB cure (cross-linking fraction) as a function of temperature and time

etch-back is performed in a RIE system for polymers with a combination of $\text{CHF}_3 - \text{O}_2$ gases. The RF power, the chamber pressure and the flow rates of both these gases are optimized for BCB etching. The reaction is dependent on the temperature and the chemical reaction itself is exothermic. These factors, combined with the low thermal conductivity of BCB, could result in localized points with higher etch rates. To avoid non-uniformities from such effects, the etch-back is done in short cycles (1 minute), allowing a cooling down phase in-between. After every step, height variations are measured at nine different positions on the sample.

After sufficient etch-back, SiO_x layer on the semiconductor surface is exposed. The sample is subjected to another curing step at 280°C for one hour. In this step, BCB is almost completely cured and solidifies into a harder, uniform layer (Fig.2). As a final step, the SiO_x is etched in a RIE system. This exposes the semiconductor surface for further processing: p-contact definition and metallization. A uniformity of within 50 nm between the nine different measurement positions is obtained. The test is repeated several times to check for reproducibility.

During the test runs, FIB cuts are performed at all the intermediate steps to check the BCB and SiO_x layers (Fig.3). Platinum is evaporated locally before the cut to avoid deformation of the top surface during the cut. While planarity and uniformity are apparent from these images, sometimes as seen in Fig. 3 (a) and (b), voids are observed at the edges of the SOA structures. An explanation could be that during the curing steps there is shrinkage in the BCB, and the adhesive force of the SiO_x on the semiconductor surface is not large enough to resist this.

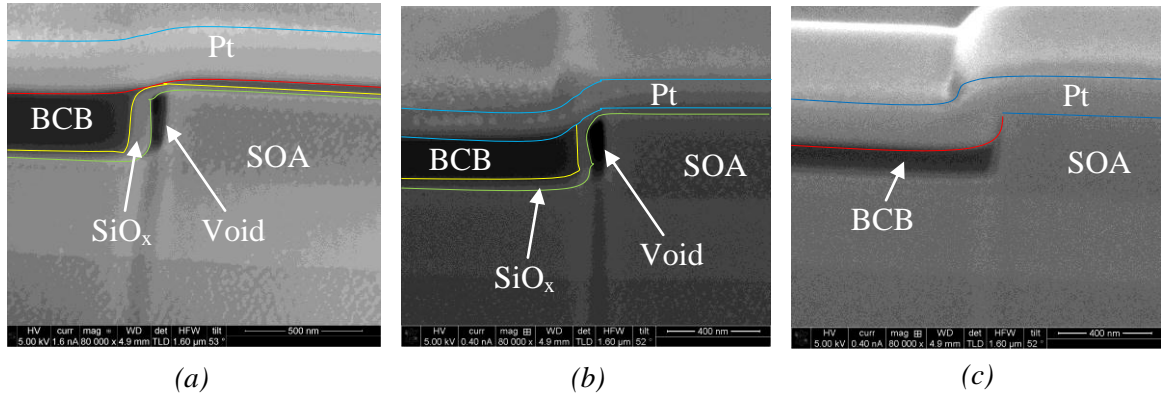


Fig.3: FIB images of the etch-back process after (a) Partial BCB etch, (b) Complete BCB etch, and (c) Complete SiO_x etch.

Conclusions

BCB is used to planarize SOA structures before contacting. To mitigate uniformity issues with complete curing at 280°C , a new recipe involving partial cure at 180°C , followed by etch-back and complete cure, is developed. After every process step, step-height measurements at nine different positions all over the sample are performed. A uniformity of within 50 nm between different positions is obtained by this technique. The process is found to be reproducible.

Acknowledgements

The authors thank STW-IMOS project for financial support. S.P. Bhat thanks J. Bolk for help with RIE systems, B. Barcones Campo for help with FIB imaging, and S. Keyvaninia and M. Muneeb for useful discussions.

References

- [1] J.J.G.M. van der Tol, R. Zhang, J. Pello, F. Bordas, G. Roelkens, H. Ambrosius, P. Thijs, F. Karouta and M.K. Smit, "Photonic Integration in Indium-Phosphide Membranes on Silicon", IET optoelectronics, Volume 5, Issue 5, pp. 218-225, October, 2011.
- [2] S.P. Bhat, J.J.G.M. van der Tol, G. Roelkens and M.K. Smit, "Feasibility study of an InP Membrane On Silicon (IMOS) laser," in Proceedings of the 16th European Conference on Integrated Optics (ECIO2012), Sitges, Spain, April 18-20, 2012.
- [3] S.P. Bhat, G. Roelkens, J.J.G.M. van der Tol and M.K. Smit, "Design of InP Membrane Laser in a Photonic Integrated Circuit," in Proceedings of the 17th Annual Symposium of the IEEE Photonics Benelux Chapter, Mons, Belgium, pp-203-206, November 29-30, 2012.
- [4] Y. H. So, P. Garrou, J. H. Im, D. M. Scheck, "Benzocyclobutene-based polymers for microelectronics" in Chemical innovation, ACS publication, Volume 31, No.12, pp. 40-47, December, 2001.

SOI Lattice Filters Design Framework: from Functional Parameters to Layout

A. Ruocco,¹ D. Van Thourhout,¹ and W. Bogaerts¹

¹ Photonic Research Group (INTEC), Ghent University - imec
Sint-Pieternieuwstraat 41, B-9000 Ghent, Belgium

In this paper we demonstrate a lattice filter based WDM framework on SOI platform. Finite Impulse Response filter synthesis routines are used to calculate the design specifications. The inputs are functional parameters: normalized cut-off frequency, free spectral range, filter order and windowing function. The obtained specifications are passed to the Caphe circuit simulator. Then we convert the design parameters to physical parameters in IPKISS for layout and mask design. The measured results prove the validity, but also the limitations of the framework. The latter, more pronounced in high order filters, are mainly attributed to errors in the weak coupling sections.

Introduction

SOI (Silicon on Insulator) photonics offers a way to reduce the footprint of passive photonic devices. Moreover the SOI processing is compatible with CMOS technology, potentially enabling mass production. Networking applications based on wavelength division multiplexing require wavelength filters for the routing and multiplexing operations: these can be based on ring resonators, AWG (Arrayed Waveguide Grating), Echelle, MZI (Mach-Zehnder Interferometers) based filters, or a combination of them [1], [2]. We will discuss cascaded MZI filters, as shown in Figure 1. Cascaded MZIs are optical FIR (Finite Impulse Response) filters. A FIR filter is composed of n 2×2 power splitting devices and $n - 1$ delay stages. Increasing the order of such device, better performance in terms of extinction ratio and roll-off can be achieved. On the other hands, increasing the order the contribution of every single stage nonidealities arise. These two requirements are the main element in the designing trade-off condition.

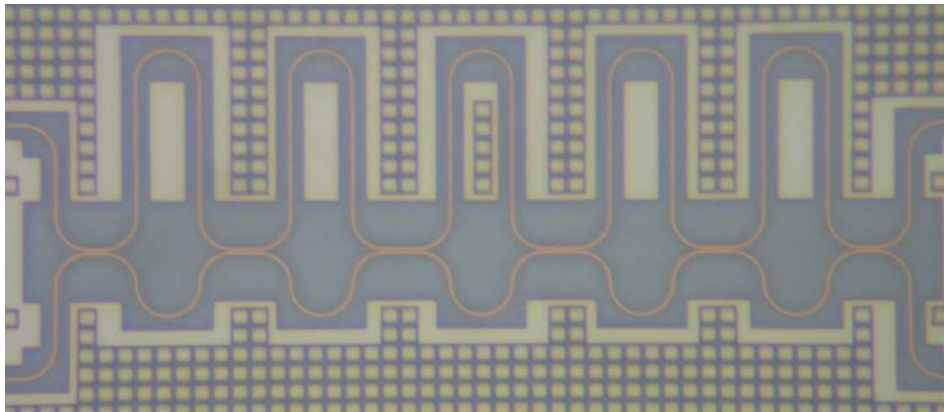


Figure 1: A Mach-Zehnder based lattice filter

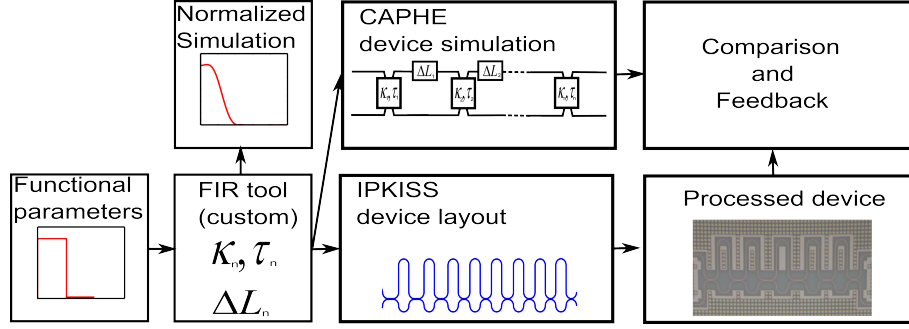


Figure 2: description of the framework

Theoretical Background

The multi-stage lattice filter can be modeled as a cascade of blocks. Neglecting any reflections back into the input ports, the initial 4×4 T-matrix can be reduced to a 2×2 transmission matrix for each elementary block. With these conditions, representative matrix are the (1) and (2) respectively for directional coupler section and delay lines section.

$$S_{cou}^i = \begin{bmatrix} \tau_i & -j\kappa_i \\ -j\kappa_i & \tau_i \end{bmatrix} \quad (1)$$

$$S_{del}^i = \begin{bmatrix} e^{-j\beta\Delta L} & 0 \\ 0 & 1 \end{bmatrix} \quad (2)$$

In the eq.(1) the relation in between the variables is $\tau = \sqrt{1 - \kappa^2}$. In the eq.(2) the variable β is the propagation constant of the waveguides and ΔL is the physical length difference between the two arms. We assume the same type of waveguides in both arms, but the formulas can be extended for different waveguide cross sections. The final analysis formula of a n^{th} order lattice filters is represented in (3). It the product of the T-matrix of the cascaded building blocks. The (4) gives the relation to be used for the calculation of the delay length between the arms.

$$S = S_c^{n+1} \prod_{i=1}^n S_{del}^i S_{cou}^i \quad (3)$$

$$\Delta L = \frac{c}{g_i FSR} \quad (4)$$

Framework description

The developed framework is described in the Figure 2. The input consists of the spectral filter requirements such as central wavelength, FSR. After these basic parameters, we can set additional design specifications such as the main filter windowing function and its associated variables. We typically use a Chebyshev window, where we specify the normalized cut-off frequency and the stop band attenuation. The design values are fed in to the FIR filter design routines which calculate the required coupling ratios. The delay in the arms is calculated using analytical formulas. The FIR design tool then converts the functional specifics to design parameters. Once all the design specifics are obtained,

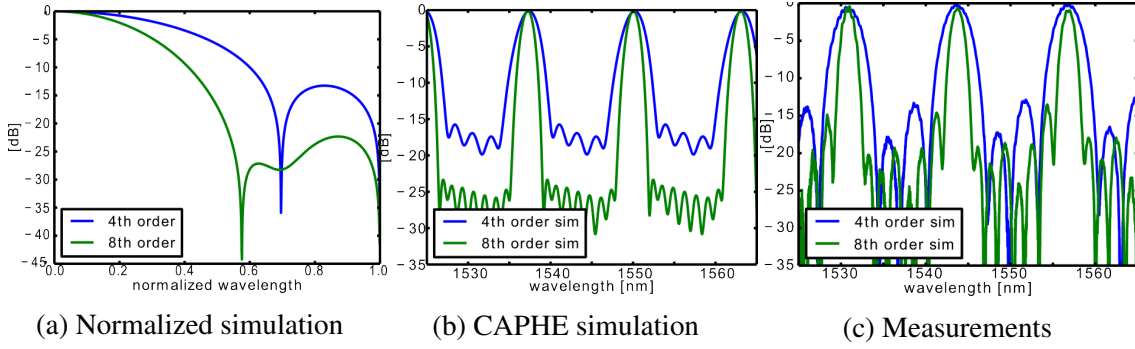


Figure 3: Simulation and measurements

they are passed in parallel to the CAPHE photonic circuit simulations and IPKISS layout designer. CAPHE simulates the entire PIC (Photonic Integrated Circuit) as an optical circuit, linking the elementary building blocks together: waveguides combined together to obtain 2×2 delay sections and directional couplers. The IPKISS mask design is then used to convert functional specifications into layout specifications with physical dimensions for the directional couplers and the waveguides.

Filter Synthesis

The unknown quantities in eq.(1) and eq.(2) are τ and ΔL . The value κ in the directional couplers is related to τ . The ΔL path difference of the arms determines the FSR of the transfer function associated to the filter. The delay time between the arms is obtained from both physical path difference and group index of the waveguide used. The other parameter required is the power coupling ratios in each of the coupling sections. To calculate those, we use the FIR (Finite Impulse Response) filter synthesis tools available in scientific python. The inputs for such tools are the type of filtering window and its parameters: for the purpose of this work we mainly used Chebyshev windowing, which require at least three parameters: the order of the filter (the number of stages), the cut-off frequency and the attenuation in the stop band. Figure 3a shows the response of lattice filter in the case of 0.250 cut-off normalized frequency.

Filter Simulation

The PIC software used is CAPHE [3]. Basic n-port blocks are connected together to obtain complex photonic circuits. Each elementary block is represented by its T-matrix. Directional couplers are photonic integrated devices with a rather strong wavelength dependence. We define n directional couplers with power splitting ratios obtained by the FIR design tool. The directional couplers are chained together with the $n - 1$ delay sections. The relative delay of the arms is defined according to the (4). The output of such a simulation is a replica of the Figure 3a, but shifted to the center wavelength, and with wavelength periodicity equal to the FSR. Figure 3b show the simulation of the devices chosen for testing of the framework. The FSR, at 1600GHz , is the same for both. The simulated devices act as single channel drop filters. The same design approach can be extended to a full WDM mux/demux. By choosing the order of the filter, the response can be tailored: the plot Figure 3b correspond to a 4th order and an 8th design, respectively.

		IL [dB]	ER [dB]	1 dB/10dB BW	area[μm^2]
4 th order	4X400GHz	-0.66	15.7	0.33	4280
	8X200GHz	-1.08	14.6	0.33	4200
8 th order	4X400GHz	-0.40	17.9	0.33	7744
	8X200GHz	-0.55	12.1	0.32	7808
12 th order	4X400GHz	-0.77	5.8	0.57	11172
	8X200GHz	-2.72	8.9	0.38	11336

Table 1: Measurement results

Layout and experimental results

The parameters obtained by the FIR tool are handed over to IPKISS [4] for the layout generation. This step includes the translation of the functional parameters to physical parameters. This conversion requires good knowledge of the elementary building block characteristics. First of all the n_{eff} and the n_g of the guiding structures has to be known. The n_{eff} is used for the designing of the proper ΔL associated to the required delay. The coupling coefficients of the directional couplers can be split up in two parts: the first is the κ associated to the straight section, and proportional to the length of the coupler, and the κ_0 associated to the bent section. In general, the former dominates the latter, but when weak coupling is required (i.e. rings, lattice filters) the coupling associated to the bent section assumes a predominant rule. The coupling strengths can be extracted from physical simulations or measurements. Figure 3c shows the measurements relative to the simulated devices. The table 1 tabulates the measurement results for the different fabricated filters, in particular: IL (Insertion Loss), ER (Extinction Ratio), 1dB/10dB bandwidth ration and dimensions.

Conclusion

We present a design procedure for MZI lattice filters starting from filter synthesis techniques down to the physical circuit layout, and we show the correspondence between measured and simulated devices.

References

- [1] W. Bogaerts, P. Dumon, D. Van Thourhout, D. Taillaert, P. Jaenen, J. Wouters, S. Beckx, and R. Baets. Compact wavelength-selective functions in silicon-on-insulator photonic wires. *Journal Selected Topics in Quantum Electronics*, Vol. 12 no. 6:1394–1401, December 2006.
- [2] Shoji T. Tsuchizawa T. Watanabe T. Takahashi J. Yamada, K. and S Itabashi. Silicon-wire-based ultrasmall lattice filters with wide free spectral ranges. *Optics letters*, vol.28:Issue 18 pp 1663–1664, 2003.
- [3] M. Fiers, T. Van Vaerenbergh, K. Caluwaerts, J. Dambre, and P. Bienstman. Caphe: Time-domain and frequency-domain modeling of nonlinear optical components. *Advanced Photonics Congress*, IM2B.3, June 2012.
- [4] W. Bogaerts, P. Dumon, E. Lambert, M. Fiers, S. Pathak, and A. Ribeiro. Ipkiss: A parametric design and simulation framework for silicon photonics. *9th International Conference on Group IV Photonics*, vol.:p.30–32, August 2012.

Improving organic photovoltaic cell efficiency with enhanced charge-transfer recovery by incorporating local field enhancement of sub-bandgap infrared light

T.A. Hendriks,¹ M.A. Sefunc,¹ L.J.A. Koster,² S.M. Garcia-Blanco,¹ *Member IEEE*

¹ University of Twente, Optical Sciences group, MESA+ Institute for Nanotechnology, P.O. Box 217, 7500 AE Enschede, The Netherlands, e-mail: t.a.hendriks@student.utwente.nl

² Zernike Institute for Advanced Materials, University of Groningen
Nijenborgh 4, 9747 AG Groningen, The Netherlands, e-mail: l.j.a.koster@rug.nl

Illuminating organic solar cell active materials with infrared light, ranging from 0.3 to 1.25 eV, has shown to be a potential way of enhancing solar cell efficiency due to enhanced charge-transfer state recovery. This paper focuses on the fabrication and application of plasmonic nanostructures in organic solar cells to give local field enhancement within these wavelengths.

Aluminum gratings and nanorods are investigated to give local field enhancement at 0.58 eV to enhance charge-transfer state recovery and improve photovoltaic cell performance. This work encompasses a first practical application combining plasmonics and sub-bandgap light to enhance charge-transfer state recovery.

Introduction

In view of the global need for clean energy, using solar energy to generate electricity is one of the more promising solutions [1]. However, the efficiency of photovoltaic devices is low in general and even lower for the less expensive ones such as organic photovoltaic devices (OPVs). Furthermore, not all wavelengths are equally absorbed and parts of the solar spectrum (mainly the lower energies) are not even utilized. Different strategies to trap light within the cell to improve its absorption have been proposed, such as stacking multiple active layers absorbing at different spectral bands [2], placing concentrators or lenses in front of the devices [2] and introducing small particles which either produce local field enhancement or increase scattering within the active layer of the device [3]. Such strategies benefit most the intrinsically thin photovoltaic cells such as OPVs [4].

Organic solar cells have an active layer wherein two different materials (the donor and the acceptor) form an interface where excitons (electron-hole pairs generated by a photon with energy above the bandgap of the donor material) can dissociate into weakly interacting charge-transfer states (CT-states). After dissociation of the CT-state the electron and hole (charge separated (CS) states) travel towards their respective electrode to generate current. The selection of materials together with the interface morphology has huge impact on the performance of OPVs. The efficiency of these devices is still low. The highest reported efficiency for a tandem organic solar cell is 12% [11] whereas the highest reported efficiency for an inorganic solar cell (triple junction of InGaP/GaAs/InGaAs) is $44.4 \pm 2.6\%$ [5].

The lower efficiency of OPVs can be mainly attributed to trapped states. At the interface of donor and acceptor, CT-states occur, increasing the recombination rate. Sufficient

energy is needed to overcome the trap and let charges diffuse towards their respective electrode.

Enhanced dissociation of CT-states into separate charges has been investigated by using “pump-probe” mechanics [6]. Typically, the lowest unoccupied molecular orbit (LUMO) levels of the donor and acceptor should be chosen such that sufficient excess energy permits dissociation of the CT-states [7]. This choice in LUMO levels limits the open-circuit output voltage of the OPV with the subsequent loss of efficiency.

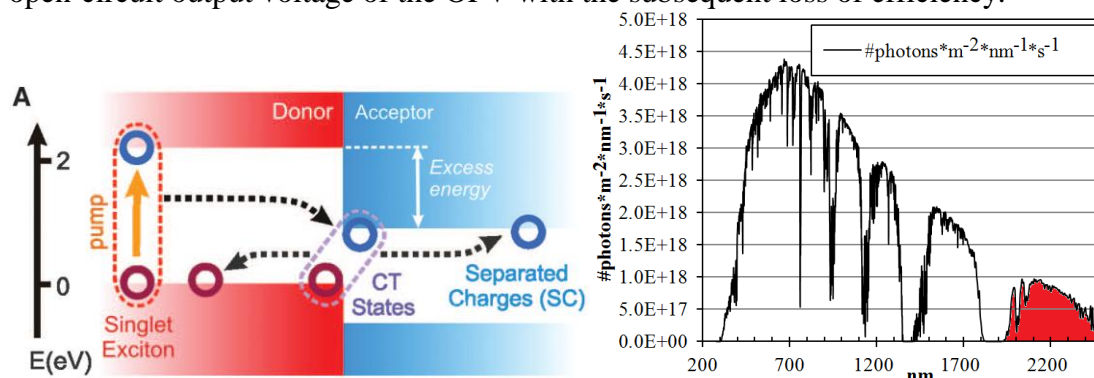


Figure 1. a) Band diagram showing the trapped states and how excess energy is used for separation of the charges. Taken from [6]. b) ASTM G173-03 reference spectra showing the amount of photons per nm per second per square meter. The red marked area shows the range of solar radiation targeted by this work to enhance dissociation of the CT-states.

In [6] an infrared laser (3 μm) is used as probe to push electrons or holes from their trapped state and help them diffuse from the interface. Infrared excitation between 0.3 – 1 eV has been claimed to repopulate “hot” CT-states, increasing the chance to evolve to separated charges (SC-states) [6].

In this work we propose to utilize plasmonic nanostructures to enhance the absorption of infrared photons with energies in the 0.3 – 1 eV range [present in the solar spectrum as shown in Fig. 1 (b)] to help the dissociation of CT-states into CS-states, increasing current output and allowing for smaller LUMO-offset choices, thereby increasing open-circuit output voltage [8], [9]. This paper will focus on the design, fabrication and preliminary results of fabrication of such plasmonic structures.

Finite difference time domain (FDTD) simulations

Given the wavelength range targeted in this work (2.0 – 2.4 μm), aluminium exhibits a good performance. Since aluminium is relatively low cost and it is already sometimes present as back electrode in the fabrication of OPVs [10], it was selected in this study as the material for the nanostructures.

Figure 2(a) shows the layer structure of the device considered in this work. It consists of a 180 nm thick layer of indium tin oxide (ITO), a 60 nm thick layer of PEDOT:PSS, a 200 nm layer of P3HT:PCBM and a 360 nm aluminium layer that acts as back electrode.

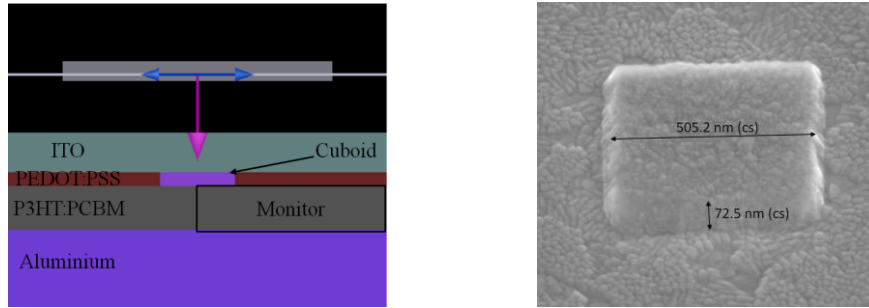


Figure 2. (a) Layout as seen in Lumerical FDTD Solutions. The different layers and the area where the electric field is monitored are shown. (b) SEM picture of fabricated Al nanoparticle on ITO. SEM settings: magnification: 100 000x, 5.00 kV, 45° tilt. Particle size is estimated to be 505.2 nm wide with a height of 72.5 nm.

Square aluminium particles were placed in contact below the ITO. Both the dimensions and periodicity of the particles were investigated to obtain maximum enhancement at the wavelength of 2135 nm (0.58 eV).

In the simulations, a plane wave source was placed 260 nm above the ITO and periodic symmetric and anti-symmetric boundary conditions were utilised to reduce computation time. Non-uniform mesh setting with additional mesh regions in the ITO layer (20 nm), the P3HT:PCBM layer (20 nm) and around the aluminium particle (10 nm) were implemented. Sweeps of the particle parameters: height (10 – 80 nm), width (50 – 600 nm), length (400 – 800 nm) and periodicity (both in x and y direction (1.5 – 2.5 μm) were performed.

Enhancement was calculated as the power [measured with the monitor shown in Fig. 2 (a)] inside the active material on a device with aluminium particle divided by the power on a structure without particle. This ratio is shown in Fig. 3. It was found that a square particle of 560 nm wide and 60 nm high performed best in an array of 2x2 μm . Enhancement up to a factor of 2.82 in the infrared region (peak at 2135 nm) is found. A decrease in the amount of light absorbed in the visible range (an average decrease of 0.926) is also observed. This is undesirable but can be expected due to the shadowing effect of the aluminium particles.

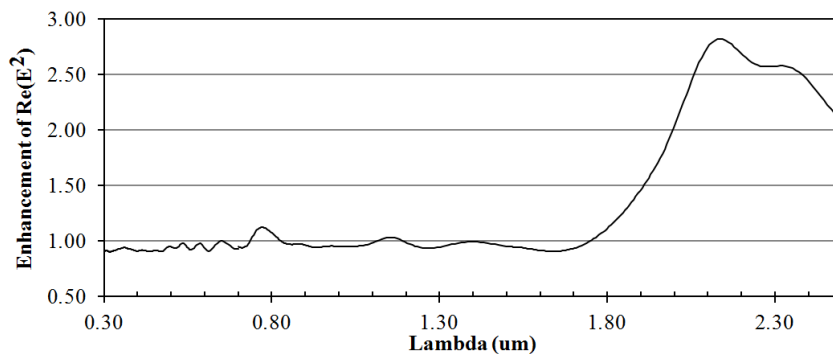


Figure 3. Simulated enhancement of the electric field intensity versus wavelength.

Fabrication

The fabrication process based on electron-beam lithography followed by lift-off is currently being developed to experimentally realize the designed nanostructures. Figure 2 (b) shows a scanning electron microscope (SEM) picture of a fabricated structure. As it can be clearly seen, further optimization is needed to produce nanostructures with the targeted dimensions.

Conclusion

Preliminary simulation results show modest enhancement of the amount of light coupled into the active material at around 2135 nm. It was shown that fabrication is possible. However, optimization is needed to reach the right particle size. Other lower-cost fabrication methods are also being evaluated, such as direct-laser writing and nano-imprint lithography.

Acknowledgements

L.J.A.K. acknowledges support by a grant from STW/NWO (VENI 11166).

References

- [1] H. A. Atwater and A. Polman, "Plasmonics for improved photovoltaic devices.," *Nat. Mater.*, vol. 9, no. 3, pp. 205–13, 2010.
- [2] A. Polman and H. A. Atwater, "Photonic design principles for ultrahigh-efficiency photovoltaics.," *Nat. Mater.*, vol. 11, no. 3, pp. 174–7, 2012.
- [3] K. R. Catchpole and A. Polman, "Plasmonic solar cells," *Opt. Express*, vol. 16, no. 26, 2008.
- [4] H. Shen, P. Bienstman, and B. Maes, "Plasmonic absorption enhancement in organic solar cells with thin active layers," *J. Appl. Phys.*, vol. 106, no. 7, 2009.
- [5] M. A. Green, K. Emery, Y. Hishikawa, W. Warta, and E. D. Dunlop, "Solar cell efficiency tables (version 42)," *Prog. Photovoltaics Res. Appl.*, vol. 21, pp. 827–837, 2013.
- [6] A. A. Bakulin, A. Rao, V. G. Pavelyev, P. H. M. van Loosdrecht, M. S. Pshenichnikov, D. Niedzialek, J. Cornil, D. Beljonne, and R. H. Friend, "The role of driving energy and delocalized States for charge separation in organic semiconductors.," *Science*, vol. 335, pp. 1340–4, 2012.
- [7] N. C. Greenham, "Polymer solar cells," *Philos. Trans. R. Soc. A*, vol. 371, 2013.
- [8] N. Yeh and P. Yeh, "Organic solar cells: Their developments and potentials," *Renew. Sustain. Energy Rev.*, vol. 21, pp. 421–431, 2013.
- [9] H. Zhou, L. Yang, and W. You, "Rational Design of High Performance Conjugated Polymers for Organic Solar Cells," *Macromolecules*, vol. 45, no. 2, pp. 607–632, 2012.
- [10] D. Di Nuzzo, G. A. H. Wetzelaer, R. K. M. Bouwer, V. S. Gevaerts, S. C. J. Meskers, J. C. Hummelen, P. W. M. Blom, and R. A. J. Janssen, "Simultaneous Open-Circuit Voltage Enhancement and Short-Circuit Current Loss in Polymer: Fullerene Solar Cells Correlated by Reduced Quantum Efficiency for Photoinduced Electron Transfer," *Adv. Energy Mater.*, vol. 3, no. 1, pp. 85–94, 2013.
- [11] Press release (2013) Heliatek GmbH. January 16, 2013
http://www.novaled.com/uploads/media/130116_PR_Heliatek_achieves_record_cell_efficiency_for_OPV.pdf

Silicon Nitride based high contrast grating for heterogeneously integrated tunable VCSELs.

S. Kumari^{1,2}, R. Wang^{1,2}, D. Sanchez^{1,2}, J. Gustavsson³, R. Safaisini³, A. Haglund³, J. Bengtsson³, A. Larsson³, G. Roelkens^{1,2}, R. Baets^{1,2}

¹ Photonics Research Group, Ghent University/IMEC, Sint Pietersnieuwstraat 41, 9000 Ghent, Belgium

² Center for Nano and Biophotonics (NB Photonics), Ghent, Belgium

³ Department of Microelectronics and Nanoscience, Photonics Laboratory, Chalmers University of Technology, Göteborg SE-412 96, Sweden

We propose a novel design for a dielectric subwavelength grating for the integration of a GaAs Vertical Cavity Surface Emitting Laser (VCSEL) operating in the near-infrared ($\lambda=700-1000\text{nm}$). The design uses a Si₃N₄/Air high-contrast grating (HCG), that can be fabricated using standard CMOS technology to replace the conventional DBR as bottom mirror. The optimized mirror reflects strongly ($>99\%$) over a fractional optical bandwidth $\Delta\lambda/\lambda$ of about 9% with a strong polarization selectivity and reasonable tolerance on the grating dimensions. A continuous wavelength tuning can be achieved by implementing these single-layer free standing HCGs as the VCSEL bottom mirror when it is electrostatically actuated.

Introduction

Silicon nitride (SiN) is a promising platform for integrated photonics applications in the visible and near IR spectrum due to its transparency in the near-infrared and visible spectrum and full compatibility with the standard complementary metal-oxide semiconductor (CMOS) technology, which can significantly lower costs of the devices in high volume manufacturing [1]. The realization of CMOS compatible light sources is considered to be the biggest challenge of silicon photonics. Hybrid integration approaches, which can keep the advantages of III-V devices grown in a homoepitaxial process before the film is transferred on silicon, is considered to be an attractive route in the development of silicon lasers because of its potential for high efficiency [2]. Such sources integrated on the silicon platform have important applications in datalinks and in spectroscopy. GaAs-based VCSELs are close to being the “perfect” laser: they are very compact, have very low power consumption, single mode behaviour, are very cheap and are realized with very mature production technology. These lasers are the perfect choice for laser emission in the visible-Near IR (covering 0.65–1.3 μm) range [3]. Recently a high-reflectivity broadband mirror using a high-index-contrast subwavelength grating (HCG) has been proposed to replace the traditional DBR structure in VCSELs [4,5]. These HCG mirrors can provide several advantages over DBRs such as a reflectivity equivalent to many pairs of DBR resulting in substantial thickness reduction of the device, high polarization sensitivity, large fabrication tolerance and the suppression of higher order transverse modes [4,5]. Here, we propose a CMOS-compatible SiN HCG mirror which can be integrated with a half GaAs VCSEL using adhesive wafer bonding technology.

HCG design

The HCG design has been optimized by the Rigorous Coupled-Wave Analysis (RCWA) software RODIS for the Air/SiN grating as shown in figure 1 (a). Parameters for

optimization of this structure are the period of the grating (Λ), the duty cycle (DC) and the thickness of the nitride layer. We optimize these parameters of the grating to get a broadband high reflection with high fabrication tolerance. Our optimized grating structure consists of 300nm thick Silicon nitride on Silicon substrate using Silicon dioxide as sacrificial layer in order to achieve a free standing HCG. With a grating period of 800nm and a duty cycle of 40% the HCG shows a reflection bandwidth of 75 nm with reflection coefficient >0.99 centered at 850nm, hence giving a fractional optical bandwidth $\Delta\lambda/\lambda$ of about 9%. The high reflection band arising in our grating design is supported by the presence of two leaky modes shown as two transmission dips inside the high reflection band in figure 1(b). These transmission dips correspond to a guided mode resonance at which transmittance approaches zero [6].

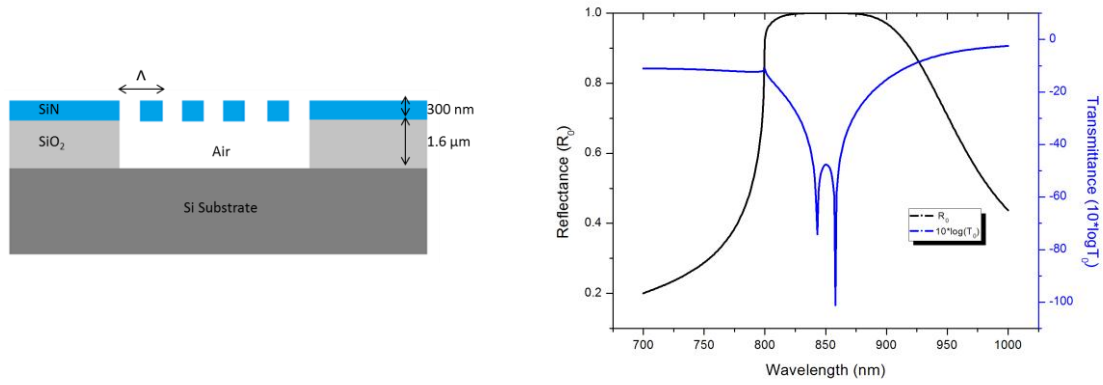


Figure 1: (a) Schematic drawing of the SiN HCG structure, (b) Reflectivity (black curve) and transmission on a logarithmic (blue curve) scale as a function of wavelength for the following grating parameters: Period 800nm, DC=40%, SiN thickness 300nm

The fabrication tolerance for this grating parameter also has been calculated using the RCWA method by varying two parameters at a time while fixing other parameters.

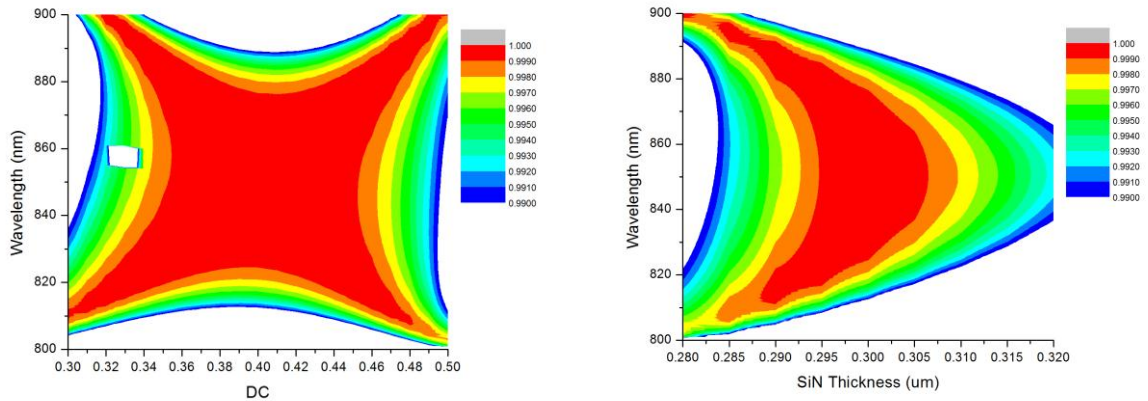


Fig 1(a) Reflectivity as function of DC and wavelength when the Silicon Nitride thickness and period of grating is 300 nm and 800 nm respectively. (b) Reflectivity as function of Silicon Nitride thickness and wavelength when the DC and period of grating is 40% nm and 800 nm respectively.

The contour plot in Figure 2(a) shows the reflectivity of the HCG as a function of the wavelength and duty cycle for a fixed grating thickness of 300nm. It shows that this grating has $\pm 9\%$ fabrication tolerance while keeping $> 99\%$ reflectivity. Other parameters like the thickness of the SiN layer also gives a tolerance of $\pm 15\text{nm}$ for $> 99\%$ reflectivity as shown in the contour plot in figure 2(b).

Integrated VCSEL design and fabrication

We can also take advantage of the SiN HCG as a highly reflecting broadband movable mirror. This mirror can be easily deflected by electrostatic actuation. By applying a voltage, between the grating and the VCSEL, the mirror will be displaced leading to a change in the cavity length resulting in a change in the emission wavelength. Hence continuous tuning can be achieved by electromechanical movement of these mirrors. Fig 3 shows the schematic of a GaAs VCSEL integrated with a SiN HCG mirror.

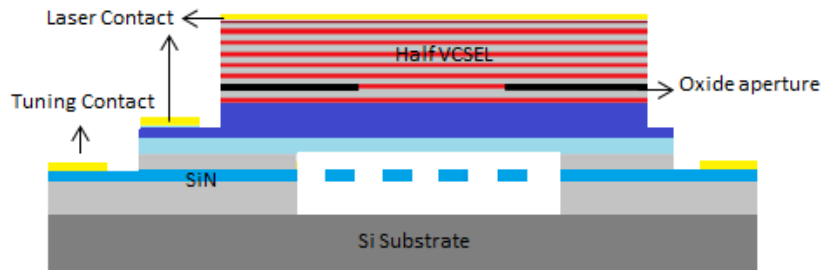


Figure 3: Schematic drawing of the integrated tunable GaAs VCSEL.

The free standing SiN HCG mirrors can be fabricated by selective wet etching by under etching the sacrificial oxide layer below the grating in a Buffered Hydrofluoric (BHF) solution. The half GaAs VCSEL die consist of a GaAs substrate, an AlAs etch stop layer, top DBRs, a multiple Quantum Well active region and a current spreading layer. The half VCSEL die can then be bonded to the free standing grating using ultra-thin adhesive polymer BCB (CycloteneTM) bonding. The GaAs substrate is then completely removed by mechanical grinding followed by a selective wet etching process. In this way we get a thin film of epitaxial III-V structure on the Si wafer. The oxide aperture can then be fabricated by lateral oxidation of the AlGaAs layer to achieve transverse optical and current confinement.

Conclusion

In conclusion, we propose a design for a broadband SiN HCG mirror to replace conventional DBRs. These mirrors can be integrated with GaAs half VCSELs to achieve a tunable laser structure in the near-IR.

References

- [1] Sebastian Romero-García et al., "Silicon nitride CMOS-compatible platform for integrated photonics applications at visible wavelengths", *Optics Express*, Vol. 21, Issue 12, pp. 14036-14046 (2013)
- [2] S. Keyvaninia, et al., "Ultra-thin DVS-BCB adhesive bonding of III-V wafers, dies and multiple dies to a patterned silicon-on-insulator substrate", *Optical Materials Express*, Vol. 3, No. 1, 2013
- [3] Anders Larsson, "Advances in VCSELs for Communication and Sensing", *IEEE Journal of Selected Topics in Quantum Electronics*, Vol. 17, No. 6, 2011.
- [4] Carlos FR. Mateus, Michael CY. Huang, Lu Chen, Yuri Suzuki, and Connie J. Chang-Hasnain, "Ultra broadband mirror using sub-wavelength grating", *IEEE PHOTONICS TECHNOLOGY LETTERS*, VOL. 16, NO. 2, FEBRUARY 2004.
- [5] M. C. Y. Huang, Y. Zhou, and C. J. Chang-Hasnain, "A nanoelectromechanical tunable laser," *Nat. Photonics*, vol. 2, 180–184, 2008.
- [6] Michael C. Y. Huang, Ye Zhou & Connie J. Chang-Hasnain, "A nanoelectromechanical tunable laser", *Nature Photonics* 2, 180 - 184 ,2008.
- [7] Robert Magnusson and Mehrdad Shokooh-Saremi, "Physical basis for wideband resonant reflectors", *Optics Express*, Vol. 16, No. 5, 2008

Optical radiative cross-talk in photonic integrated circuits

D. Melati¹, F. Morichetti¹, G.G. Gentili¹, M. Achouche², D. Lanteri², H. Debregeas²,
F.M. Soares³, N. Grote³, and A. Melloni¹

¹ Politecnico di Milano, Dip. di Elettronica, Informazione e Bioingegneria, 20133 Milano, Italy

² III-V Lab, Route de Nozay, 91460 Marcoussis, France

³ Fraunhofer Heinrich Hertz Institute, 10587 Berlin, Germany

The mitigation of cross-talk effects between photonic devices integrated onto the same chip is of primary importance in order to respond to the pressing demand of high component density and circuit area reduction. In this work, we present an extensive experimental investigation on the radiative optical cross-talk in InP integrated circuits. Results demonstrate that waveguide sidewall roughness generates an interference signal between passive devices that decreases quadratically with the distance. The phase coherence between exciting and coupled modes is investigated as well, revealing a gradual decorrelation for increasing gap between the waveguides.

Introduction

In the last decades integrated photonics observed an increasing demand of circuit complexity with a trend that is destined to continue in the near future [1]. Larger scale of integration implies device footprint reduction and more relevant issues related to cross-talk interaction. Investigation and characterization of these phenomena is then of primary importance for a proper development and design of highly integrated photonic circuits.

A significant fraction of the waveguide propagation loss is generated by imperfections of the guiding structure, and in particular by sidewall roughness [2]. Radiation mode excited in one waveguide can partially reach another device placed nearby and be coupled back to a guided mode of the second structure, thereby acting as an optical cross-talk vehicle. Models and experimental investigation have been proposed in literature for radiation mediated coupling in both waveguides [3] and integrated components as directional couplers [4]. However, to the best of our knowledge, information is still missing on the dependence of optical cross-talk power on the waveguides distance as well as on the phase properties of the coupled light.

In this work an experimental investigation of the radiative cross-talk between adjacent passive waveguides is presented. The dependence of the coupled power on the distance between the waveguides is studied and compared to the results obtained with electromagnetic simulations to confirm the absence of any effect related to the evanescent field. The phase correlation characteristics of the coupled modes is investigated as well.

Cross-talk power dependence on the waveguide gap

Experimental analyses were carried out on the test structure of Fig. 1, which was realized with the weakly-etched InP-based rib waveguide described in [5] and reported in the inset of the figure, with a width of $2\ \mu\text{m}$. This waveguide is particularly adapted for this analysis, because the lateral slab provides a vertical confinement to radiation modes,

emphasizing cross-talk effects between neighbour structures. The device is composed by two waveguides. The first one (‘‘direct waveguide’’, beginning at port A) is a s-bend with three straight sections and two bent waveguides and a very smooth aspect ratio of $6 \text{ mm} \times 100 \text{ }\mu\text{m}$. The second waveguide (‘‘coupled waveguide’’) begins few hundreds of microns after the beginning of the long central straight section of the first one to avoid coupling due to field radiated at the first bend. The distance between the two waveguide varies on different devices from $g = 2 \text{ }\mu\text{m}$ to $g = 30 \text{ }\mu\text{m}$ while the straight coupling section is kept fixed at 3 mm . The distance between the output ports (ports B and C) is $30 \text{ }\mu\text{m}$ for all the devices. The shape of the device reduces the straight-light coupling between the input fibre (at port A) and the coupled waveguide.

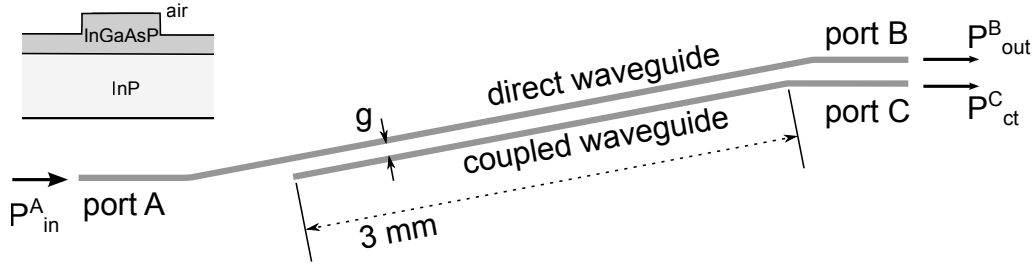


Figure 1: Test structure designed for the cross-talk characterization. The waveguide structure is reported in the inset.

In the experimental characterization, the input light is coupled at port A and the output power at ports B and C is measured, for different gap distances, by an Optical Spectrum Analyser. The measurements of P_{out}^B and P_{ct}^C are shown in Fig. 2 for the TE mode when $P_{in}^A = 0 \text{ dBm}$. Similar results were obtained for TM state of polarization. Blue marks represents P_{out}^B , namely the power that remains in the direct waveguide. The power level is substantially constant around -12 dBm at any gaps, indicating that the light coupled in the other waveguide is a small fraction of the total. Since the coupled power P_{ct}^C (red circles) falls from a values of about -15 dBm at $g = 2 \text{ }\mu\text{m}$ to less than -50 dBm at $g = 30 \text{ }\mu\text{m}$, the ratio between P_{out}^B and P_{ct}^C drops from 0 dB to -35 dB . The experimental data suggests a dependence on the gap in the form g^{-x} with $1 < x < 2$ (red dashed line, for $x = 2$) if the point at $g = 2 \text{ }\mu\text{m}$ (where evanescent coupling is dominant) is excluded from the fitting.

To correctly interpret these results, the pure evanescent coupling contribution to the total coupled power was simulated. Evanescent coupling (blue and black lines in Fig. 2 for port B and C, respectively) is the dominant mechanism for $g < 2 \text{ }\mu\text{m}$, where a strong power exchange oscillation between the two waveguide can be observed. For $g = 3 \text{ }\mu\text{m}$ and $g = 5 \text{ }\mu\text{m}$ the device works in an intermediate situation, where there is a residual contribution of the evanescent coupling but the radiative cross-talk becomes a significant fraction of the total power exchange. This can be argued from the difference between the predicted power at port C from pure evanescent coupling and the higher power actually measured. Finally for $g \geq 10 \text{ }\mu\text{m}$ only the coupling via radiative modes exists.

The major limit to the dynamic range of the measurement is represented by the presence of light in the thin slab region around the rib waveguide structure. This feature can be seen in Fig. 2 where the gray marks represent the power measured moving the output fibre by about $100 \text{ }\mu\text{m}$ far from port B (P_{sub}). Reasonably, this power does not depend on the value of the gap since is related directly to the input fibre excitation. It is clear how

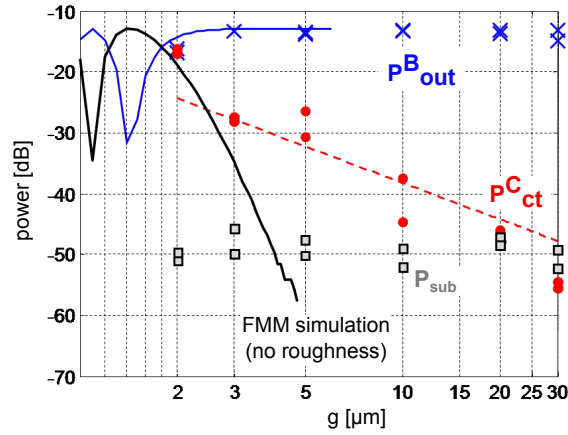


Figure 2: Output power at the direct (P_{out}^B , blue mark) and coupled (P_{ct}^C , red marks) waveguides and in the slab/substrate region (gray dots) as function of the gap. Simulation of the evanescent coupling regime are superposed for comparison (blue and black solid lines).

the power level in the slab results to be a real limit to the measurements of the cross-talk efficiency, that between $20 \mu\text{m}$ and $30 \mu\text{m}$ can be hardly distinguished from this noise floor.

Phase decorrelation of coupled modes

In order to characterize the properties of the phase of the mode excited by radiated power, the test structures used in the previous section have been reversed in order to injected light at port C. In this way it is possible to exploit the two strong reflection generated by the abrupt termination of both waveguides (in the middle of the chip and at chip facet) as phase measurement points. The experiment was conducted with an Optical Frequency Domain Reflectometry (OFDR) technique [6], which allows an interferometric analysis of the light reflected along a waveguide. An example of the measured space-domain trace is reported in Fig. 3 (a), which represents the reflected power as function of the optical distance with respect to the input facet. The first highlighted peak refers to the reflection generated by the termination of the input waveguide. The second is due to the light that crosses the coupler, is reflected by the chip facet and crosses the coupling region a second time, reaching again port C.

The phase spectra of this reflections can be measured and the relative difference computed at each wavelength. Figure 3(b) represents this quantity, compensated for the phase contribution related to propagation, for the devices with $g = 2, 5, 10 \mu\text{m}$. In Fig. 3(c) the probability density functions (PDFs) of the previous data are reported. In the evanescent coupling regime (black solid line) this difference is substantially zero for the entire considered bandwidth, consistently with this type coupling which is coherent and preserve the phase relation between exciting and coupled mode. The PDF is a narrow peak around zero (black squares), confirming that the phase difference is almost zero at each wavelength. For $g = 5 \mu\text{m}$ (blue solid line) some noise appears in the spectral data and the PDF radically changes its shape, spreading around zero (blue squares), and indicating that the light is affected by radiation mode coupling. This is confirmed by the device with $g = 10 \mu\text{m}$ (red solid curve) where the coupling is due exclusively to radiative modes and strong spectral oscillations appears and the PDF.

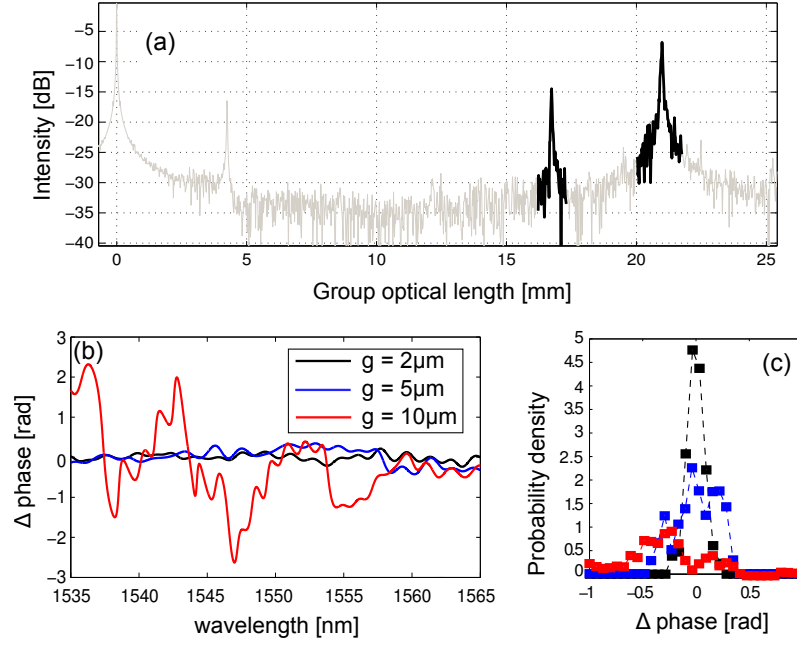


Figure 3: (a) Example of space-domain trace measured for the reversed devices (light input from port C). Two strong reflections are recognisable. (b) Spectra of the phase difference between the reference and the coupled signal for different gaps and (c) corresponding PDF.

We can then conclude that the coupling mediated by radiative modes (unlike evanescent coupling) is an incoherent mechanism, which does not preserve the phase relation between the coupled modes in the adjacent waveguides and hence causes a decorrelation of the coupled power from the modes of the original waveguides that excite the radiation modes. This decorrelation becomes stronger when the waveguide distance increases.

Acknowledgement

The research leading to these results has received funding from the European Community's Seventh Framework Program FP7/2007-2013 under grant agreement ICT 257210 PARADIGM.

References

- [1] P. Lo Guo-Qiang S. Danziger D. Prather M. Hochberg T. Baehr-Jones, T. Pinguet. Myths and rumours of silicon photonics. *Nature Photonics*, 6, 2012.
- [2] F.P. Payne and J.P.R. Lacey. A theoretical analysis of scattering loss from planar optical waveguides. *Optical and Quantum Electronics*, 26(10):977–986, 1994.
- [3] D. Marcuse. Crosstalk Caused by Scattering in Slab Waveguides. *Bell System Technical Journal*, 50(6):1817–1831, 1971.
- [4] J.C. Powelson, Wei Feng, Sihan Lin, Robert J. Feuerstein, and D. Tomic. Crosstalk of passive directional couplers. *Lightwave Technology, Journal of*, 16(11):2020–2027, 1998.
- [5] D. Melati, F. Morichetti, A. Canciamilla, D. Roncelli, F.M. Soares, A. Bakker, and A. Melloni. Validation of the Building-Block-Based Approach for the Design of Photonic Integrated Circuits. *Lightwave Technology, Journal of*, 30(23):3610–3616, 2012.
- [6] F. Morichetti, A. Canciamilla, C. Ferrari, M. Torregiani, A. Melloni, and M. Martinelli. Roughness Induced Backscattering in Optical Silicon Waveguides. *Phys. Rev. Lett.*, 104:033902, Jan 2010.

Guided waves in hyperbolic media

N. J. Schilder,^{1,2} and H. P. Urbach¹

¹ Optics Research Group, Faculty of Applied Sciences, Delft University of Technology,
Lorentzweg 1, 2628 CJ Delft, The Netherlands.

² Laboratoire Charles Fabry, Institut d'Optique, CNRS, Univ. Paris-Sud, 2 Avenue Augustin
Fresnel, 91127 Palaiseau Cedex, France.

Nowadays there is a lot of scientific interest in optical hyperbolic media. This class of media supports propagating waves which are not restricted in spatial frequency by the diffraction limit. Furthermore, in waveguides consisting of hyperbolic media there can be infinitely many guided modes. This is interesting for both optical communication and optical sensing. In this research we discuss the properties of the guided waves in hyperbolic media and explain transmission properties of hyperbolic media in terms of the guided modes.

Introduction

The propagation of electromagnetic waves through matter is a topic that is very important to understand. In normal media, whether isotropic or anisotropic, the diffraction spot size is limited by the diffraction limit. Surpassing this diffraction limit is a very hot topic. The diffraction limited resolution is proportional to the wavelength and inversely proportional to the Numerical Aperture of the optical system ($\frac{\lambda}{NA}$), which in turn depends linearly on the index of refraction of the medium in which the spot is focussed. An example from industry where the diffraction limit is extremely important is in optical lithography for fabricating chips. To be able to make small chips, they keep trying to reduce the smallest feature size of the structures. For this, the wavelength is reduced and/or the numerical aperture is enhanced. A prototype lithographic machine which uses light of wavelength 13.5 nm has been realized recently. Another way to get a better resolution is by changing the index of refraction, hence the effective wavelength in a medium ($\lambda = \lambda_0/n$, with λ_0 being the vacuum wavelength). By increasing the (effective) index of refraction of the medium, we could also improve the resolution. This is the principle behind hyperbolic media. We will show in this Letter that the effective index of refraction of a hyperbolic medium is higher than the index of refraction of the individual layers it consists of.

Not only imaging is a nice application of hyperbolic media, but optical waveguiding is as well. Optical waveguiding is getting more and more important. One field of interest is in Photonic Integrated Circuits (PIC). In order to be able to continue Moore's law [3], which states that every year the optical components density on a chip gets doubled, we need to switch from electronics to optics, as there is less heat produced and dimensions can be reduced. For optical communication, we need to guide the light by optical waveguides. Optical waveguides are known to guide a discrete and finite number of modes. This limits the amount of information which can be transported. It turns out that waveguides made of lossless hyperbolic media are able to support an **infinite amount of discrete modes**.

In this Letter we will propose an explanation of transmission properties of hyperbolic

media in terms of guided modes and some guiding properties of hyperbolic media are reviewed.

Hyperbolic Media

A hyperbolic medium is a relatively new class of medium [6] which is by definition uniaxial anisotropic, hence the material has a unique optical axis. To illustrate what hyperbolic means in this case, we will assume to have a lossless uniaxial crystal (i.e. $\text{Im } \epsilon = 0$). The reference frame is chosen such that the z -axis corresponds to the optical axis. Then, the permittivity tensor can be written as:

$$\bar{\bar{\epsilon}} = \begin{bmatrix} \epsilon_{\perp} & 0 & 0 \\ 0 & \epsilon_{\perp} & 0 \\ 0 & 0 & \epsilon_{\parallel} \end{bmatrix}. \quad (1)$$

In anisotropic media, both ϵ_{\perp} and ϵ_{\parallel} are positive, hence the tensor is positive definite. However, the key property of hyperbolic media is that the permittivity tensor is not positive definite, i.e. $\epsilon_{\perp} \cdot \epsilon_{\parallel} < 0$. The consequence of this is that the isofrequency surface for TM-polarized light in reciprocal k -space is hyperbolic instead of elliptic. We define this as hyperbolic spatial dispersion in this Letter¹. Consider a plane wave with wavevector $\vec{k} = \vec{k}_{\perp} + k_z \hat{z}$, then the Fresnel's equation of wave normals is:

$$\left(\frac{k_{\perp}^2 + k_z^2}{\epsilon_{\perp}} - k_0^2 \right) \cdot \left(\frac{k_{\perp}^2}{\epsilon_{\parallel}} + \frac{k_z^2}{\epsilon_{\perp}} - k_0^2 \right) = 0. \quad (2)$$

The first factor corresponds to TE-polarization and clearly refracts ordinarily at an interface between an isotropic medium and the hyperbolic medium of which the normal is parallel to the optical (z -) axis. The second factor corresponds to TM-polarization and describes an ellipse when both ϵ_{\perp} and ϵ_{\parallel} are positive. However, for hyperbolic media the signs are opposite, which means that the isofrequency surface is a hyperboloid. This is the origin of the name hyperbolic media. A TM-polarized wave then exhibits negative refraction at the mentioned interface.

What is important to mention, is that for hyperbolic media with $\epsilon_{\perp} > 0$ and $\epsilon_{\parallel} < 0$, there do not exist evanescent waves for TM-polarized light, when the interface lies in the (x, y) -plane, i.e. whatever the spatial frequency k_{\perp} , the corresponding k_z is always real and hence the wave is always propagating:

$$k_z = \pm \sqrt{\epsilon_{\perp} k_0^2 + \frac{\epsilon_{\perp}}{|\epsilon_{\parallel}|} k_{\perp}^2}. \quad (3)$$

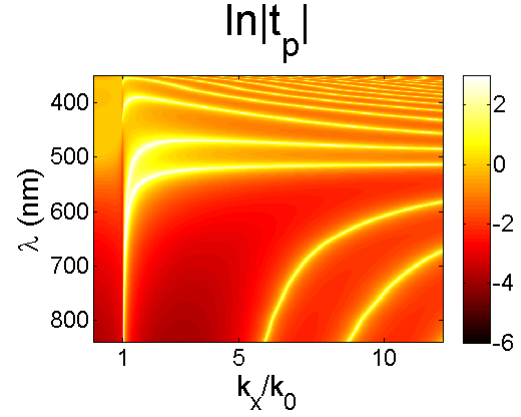
Transmission properties

In the fields of for example imaging or sensing, we are often limited by the diffraction limit. This imposes a lowerbound on the smallest dimension which can be imaged or sensed. However, in hyperbolic media we do not have this constraint and ideally we can have a high transmission for all TM-polarized spatial modes. This can be seen in Figure 1.

¹Normally the term spatial dispersion is differently used, namely for waves in non-local media.

The Fresnel transmission coefficient of TM-polarized light through a 150nm thick layer of hyperbolic medium has been plotted. The input and output media are both air and k_0 is the wavenumber in air. Both angle of incidence and wavelength have been changed. For a more thorough discussion on this figure and a nice review paper on hyperbolic media, please refer to [7].

A question which arises is about the origin of so many transmission peaks for each wavelength? According to a review paper [7] the occurrence of the transmission peaks for the long wavelength part of the visible spectrum can be understood as excitations of coupled surface plasmon polariton waves. In this Letter, we propose a different explanation for the origin of the transmission peaks, namely guided waves.



Origin of transmission peaks

In the visible part of the electromagnetic spectrum, no hyperbolic media have been found so far. This means that we need to mimic spatial dispersion. As an example, this can be done by making a multilayer stack of a dielectric ($\text{Re } \epsilon > 0$, in our simulations titaniumdioxide) and a metal ($\text{Re } \epsilon < 0$, in our simulations silver). Each layer is about 15 nm thick. Effective Medium Theory can be applied when the thicknesses of the layers are subwavelength and it can be shown that the effective permittivity tensor is of a hyperbolic medium, i.e. $\epsilon_{\perp} \cdot \epsilon_{\parallel} < 0$. We calculated rigorously the transmission and reflection coefficients t_{\downarrow} , t_{\uparrow} , r_{\downarrow} , r_{\uparrow} , where the arrows indicate the direction of the incident beam [8]. We searched for a guided mode inside the multilayer stack, i.e. a field distribution, which does not need to have any input field. This corresponds to finding the poles of $t_{\uparrow}t_{\downarrow} - r_{\uparrow}r_{\downarrow}$.

Figure 1: The natural logarithm of the transmission through a 150nm thick slab of hyperbolic medium. Dispersion has been taken into account and the angle has been changed (k_x/k_0). Losses have been neglected.

For our assertion, both figures in Figure 2 look very similar, which is the reason that the excitation of guided modes makes a large field around the edges of the multilayer stack.

Properties of guided modes

A hyperbolic medium has some peculiar guiding properties. Some differences compared to common waveguides are:

- There are infinitely many guided modes.
- The mode with the smallest propagation constant has the fewest oscillations in the direction of confinement. Because k_z increases with increasing propagation constant, the number of oscillations in the confinement direction keeps increasing.

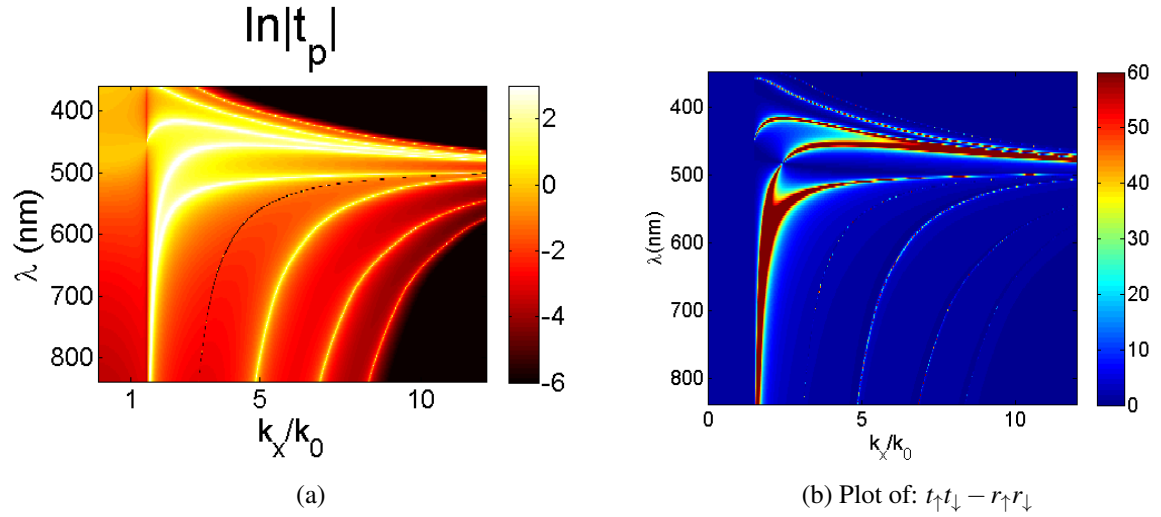


Figure 2: Comparison between the transmission plot and $t_{\uparrow}t_{\downarrow} - r_{\uparrow}r_{\downarrow}$. Material dispersion has been included, but we neglected losses in order to show the guided modes clearly.

Conclusion

In hyperbolic media, the wavevector behaves differently we are used to. When we consider a slab waveguide, consisting of a hyperbolic material, then for TM-polarized guided waves, the wavevector component in the confinement direction increases, while the propagation constant increases. This only occurs in hyperbolic media. Hyperbolic dispersion can be mimicked by a multilayer stack made of a metal and a dielectric with layer thicknesses (much) smaller than the wavelength. The high transmission of plane waves with high spatial frequencies which is obtained can be explained by the excitation of guided modes. In lossless, homogeneous hyperbolic media, there are infinitely many guided modes possible. This is in contrast with normal waveguides, where a cut-off propagation constant exists.

References

- [1] J.B. Pendry, "Negative refraction makes a perfect lens", *Phys Rev Lett*, vol. 85, pp. 3966-9, 2000.
- [2] A.C. Assafrao, "On super resolved spots in the near-field regime", *PhD-thesis, Delft University of Technology*, 2013, pp. 123-125.
- [3] G.E. Moore, "Cramming More Components onto Integrated Circuits", *Electronics*, vol. 38, pp. 114-117, 1965.
- [4] W.D. Newman, C.L. Cortes and Z. Jacob, "Enhanced and directional single-photon emission in hyperbolic metamaterials", *Journal of the Optical Society of America B-Optical Physics*, vol. 30, 2013.
- [5] C. Guclu, S. Campione and F. Capolino, "Hyperbolic metamaterial as super absorber for scattered fields generated at its surface", *Physical Review B*, vol. 86, 2012.
- [6] D.R. Smith, P. Kolinko and D. Schurig, "Negative refraction in indefinite media", *Journal of the Optical Society of America B-Optical Physics*, vol. 21, 2004, pp. 1032-1043.
- [7] C. L. Cortes, W. Newman, S. Molesky and Z. Jacob, "Quantum nanophotonics using hyperbolic metamaterials", *Journal of Optics*, vol. 14, 2012.
- [8] O. El Gawhary, M.C. Dheur, S.F. Pereira and J.J.M. Braat, "Extension of the classical Fabry-Perot formula to 1D multilayered structures", *Applied Physics B-Lasers and Optics*, vol. 111, 2013, pp. 637-645.

Fabrication technology of metal-cavity nanolasers in III-V membranes on silicon

V. Dolores-Calzadilla,¹ E. J. Geluk,¹ T. de Vries,¹ B. Smalbrugge,¹ P. J. van Veldhoven,² H. Ambrosius,¹ D. Heiss,¹ A. Fiore,² and M. Smit¹

COBRA Research Institute, Eindhoven University of Technology,
Postbus 513, 5600 MB Eindhoven, The Netherlands.

¹ Photonic Integration, Department of Electrical Engineering

² Photonics and Semiconductor Nanophysics, Department of Applied Physics

Electrically pumped metal-cavity nanolasers in III-V semiconductors are promising for their application in optical interconnects, where high integration density and low optical powers are required. They offer a low threshold current and excellent cooling properties due to the metal encapsulation. In this contribution, an overview about the technology required for the fabrication of a nanolaser coupled to an InP-membrane waveguide on silicon is presented. A variety of techniques are used including electron-beam lithography, dry and wet etching, as well as deposition of dielectrics and metals. The technological challenges to fabricate such a complex nanostructure are also discussed.

Introduction

Metal-cavity semiconductor nanolasers were recently demonstrated experimentally. This new type of lasers are interesting in view of their potential characteristics, which include high integration density, excellent cooling properties, ultra-fast modulation, etc, which make them attractive for low power applications such as optical interconnects. First devices showed lasing at cryogenic temperatures [1], and lasing at room temperature was achieved later [2]. These devices radiated into the far field. For their integration in photonic circuits waveguide coupling is mandatory, which increases their fabrication process complexity.

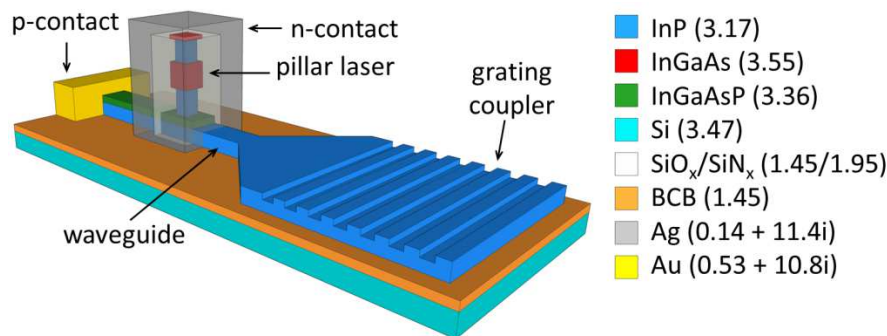


Figure 1. Schematic of a metal-cavity nanolaser coupled to an InP-membrane waveguide connected to a grating coupler. The refractive index of each material at 1.55 μm is shown in parenthesis.

We propose a metal-cavity nanopillar structure coupled by evanescent field to an InP-membrane waveguide as shown in Fig. 1 [3]. Both the laser and waveguide are fabricated in a III-V layer stack bonded to a silicon substrate with Benzocyclobutene (BCB) [4]. The pillar has an undercut above and below the active region (InGaAs) to increase the cavity quality factor. It is covered by a dielectric layer and then encapsulated with silver to form the metal-cavity that provides a strong feedback to the

TE mode supported by the cavity. The metal cladding makes electric contact on the top of the pillar, whereas a lateral p-contact is deployed over a large area to minimize its contact resistance. For characterization purposes, we include a grating coupler to couple the light out of the chip.

The present contribution gives an overview of the fabrication technology of this nanolaser, that we are presently developing. The most relevant and critical fabrication steps are discussed, as well as the challenges that have to be met.

Electron-beam lithography and etching processes

The definition of the nanostructure is carried out by electron-beam lithography (EBL) due to the high resolution required. This is done in three EBL steps. During the first lithography, the nanopillar is defined. Later, an overlay exposure is needed to define the waveguide and, finally, the grating coupler is defined with another overlay exposure. Three different lithographic masking schemes are used during these EBL steps, which are depicted in Fig. 2(left) and discussed in the following.

The first EBL exposure is done using HSQ resist, which is a negative resist well known for its usage in high resolution lithography [5]. Since it can be thinner than 100 nm, the influence of the electron scattering inside the resist is limited. Nevertheless, its thickness is not enough to etch a hardmask able to withstand the etching of the pillar (about one micrometer high), and therefore it has to be used in combination with another resist in a bilayer resist scheme in order to be able to etch high aspect ratio structures [6]. The pattern in HSQ is transferred to an underlying HPR504 resist by means of a reactive-ion-etching (RIE) process using oxygen, which in turn is used to transfer the pattern into a SiO_x layer with a CHF_3 -based RIE. Finally, the SiO_x is used as a hardmask to etch the semiconductor pillar using inductively coupled plasma RIE (ICP-RIE) using a methane-hydrogen chemistry ($\text{CH}_4:\text{H}_2$).

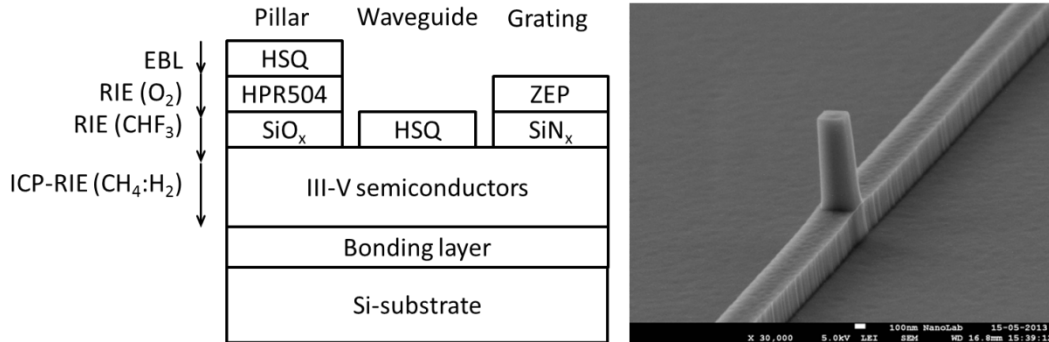


Figure 2. Left: Processing schemes to fabricate the nanostructures. The top layer of each lithographic scheme is always defined by EBL and development. Right: Pillar after waveguide etching and removal of hardmasks.

In a second EBL exposure, the waveguide is defined at the bottom of the pillar structure. During this step, a mask protection for the pillar is mandatory, otherwise the pillar will be eroded during the waveguides etching. For this purpose, the hardmask to etch the pillar is not removed after the first lithography.

An overlay EBL normally demands a prior planarization of the surface to keep the resist thickness uniform as well as the hardmask layer. We avoid such planarization by using the HSQ resist directly as the hardmask. This technique requires enhancing the resistance of HSQ to the semiconductor etching chemistry used in the RIE, what can be

done either by hardly curing HSQ [7] or by treating it with an oxygen plasma [8]. In this way, after the pillars have been etched, HSQ is spun, e-beam exposed, developed, and treated with an O_2 -plasma. Later, this HSQ is used as the hardmask to etch the waveguide using methane hydrogen in a RIE process. The result of these two lithography steps is shown in Fig. 2(right).

A final e-beam lithography is required to fabricate the grating coupler. In this case, ZEP resist in combination with a SiN_x mask is used. This is preferred because it is a positive resist, which means that any non-exposed region (i.e. the pillar and waveguide) will be protected by the SiN_x hardmask during the grating etching. The undercut to enhance the quality factor of the cavity, as described in our laser design [3], can be fabricated right after the pillar etching by a selective wet etching of InP as it is shown in Fig. 3.

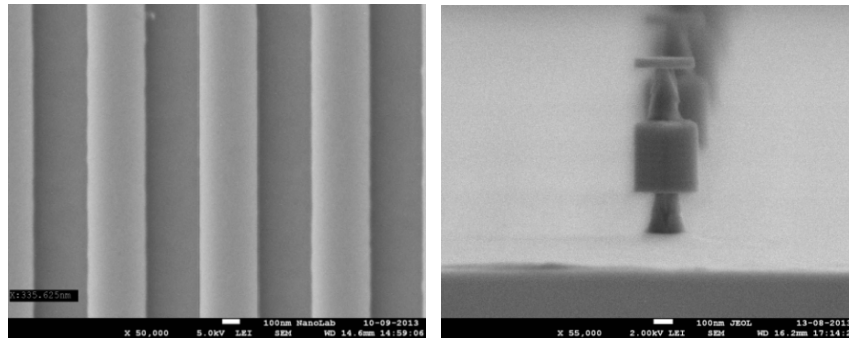


Figure 3. Left: Top view of a typical grating coupler. Right: Pillar with undercut fabricated using the solution $H_2O:H_3PO_4:HCl$.

Deposition of dielectrics and metals

The metal cladding of the cavity would create a short circuit unless a dielectric layer is deposited before silver, which also helps to reduce the metal loss according to the design [3]. For this purpose, either SiN_x or SiO_x can be deposited by plasma-enhanced chemical vapor deposition (PECVD), however it has been found that a SiO_x cladding would result in a higher quality factor due to its lower refractive index. Before the actual deposition of the chosen dielectric, a thin passivation layer of SiN_x of a few nanometers can be deposited at low temperatures to reduce the surface recombination [9]. Since the resonant wavelength is mainly given by the cavity size (thickness of the dielectric cladding plus the semiconductor pillar width), it is important to consider that the PECVD deposition rate on sidewalls is about two thirds of the deposition rate on a flat surface.

After the pillar has been covered with a dielectric layer, silver can be thermally evaporated to form the metal-cavity. However, since silver does not stick on SiO_x/SiN_x , an adhesion layer must be previously deposited by lift-off, for example Ti/Au [1], chromium [10] or germanium. In order to properly cover the sidewalls of the pillar, the silver evaporation should be done at different angles. Moreover, since the evaporation leads to the formation of silver grains, rapid thermal annealing (RTA) is applied after the evaporation to increase the metal grain size resulting in a more uniform metal with reduced scattering loss. Figure 4 shows a pillar covered with silver before and after RTA.

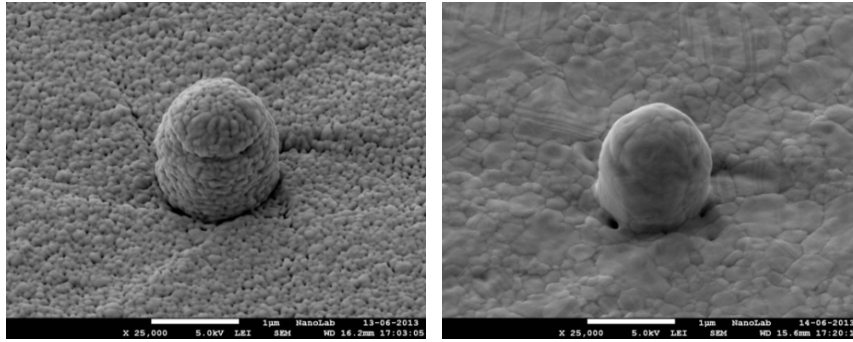


Figure 4. Left: Pillar after silver evaporation. Silver grains of about 30 nm are formed. Right: Silver-covered pillar after RTA.

Conclusions

A general overview of the processing technology to fabricate waveguide-coupled metal-cavity nanolasers in InP-membranes bonded to silicon has been presented. The most critical fabrication steps have been presented, which can also be used for other metal-based nanophotonic circuits.

References

- [1] M. T. Hill, *et al.*, “Lasing in metallic-coated nanocavities”, *Nature Photonics*, 1(10), pp. 589–594, 2007.
- [2] M. P. Nezhad, *et al.*, “Room-temperature subwavelength metallo-dielectric lasers”, *Nature Photonics* 4(4), pp. 395–399, 2010.
- [3] V. Dolores-Calzadilla, *et al.*, “Metallo-dielectric nanolaser coupled to an InP-membrane waveguide”, 17th Annual Symposium of the IEEE Photonics Benelux Chapter, 2012.
- [4] J. van der Tol, *et al.*, “Photonic integration in Indium-Phosphide Membranes on Silicon (IMOS)”, *IET Optoelectronics*, 5(5), pp. 218–225, 2011.
- [5] A. E. Grigorescu and C. W. Hagen, “Resists for sub-20-nm electron beam lithography with focus on HSQ: state of the art”, *Nanotechnology*, 20(29), pp. 1-30, 2009.
- [6] F. van Delft, *et al.*, “Hydrogen silsesquioxane/novolac bilayer resist for high aspect ratio nanoscale electron-beam lithography”, *J. Vac. Sci. Technol. B* 18(6), pp. 3419-3423, 2000.
- [7] L. O’Faolain, *et al.*, “Fabrication of photonic crystals using a spin-coated hydrogen silsesquioxane hard mask”, *J. Vac. Sci. Technol. B* 24(1), pp. 336-339, 2006.
- [8] M. Carette, “Simple technological process for the fabrication of optical InP nanowires integrated into a benzocyclobutene matrix”, *Journées Nationales sur les Technologies Emergentes en Micronanofabrication*, 2008.
- [9] J. Kim, *et al.*, “RPCVD Silicon Nitride Passivation on InGaAsP with Temperature Ramping during Deposition”, 207th Electrochemical Society Meeting, pp. 361-366, 2005.
- [10] J. Hyoungh Lee, “Electrically pumped sub-wavelength metallo-dielectric pedestal pillar lasers”, *Optics Express* 19(22), pp. 21524-21531, 2011

Towards High-Density Space Division Multiplexed Transmission Systems

C.M. Okonkwo*, R.G.H. van Uden, H. Chen, H. de Waardt, and A.M.J Koonen

COBRA Research Institute, Eindhoven University of Technology, The Netherlands

* cokonkwo@tue.nl

Spatial division multiplexing (SDM) is increasingly become the next logical step in extending the capacity within a single fiber through the transmission of multiple spatial channels either in a multi-core or multi-mode fiber. Further enabled by multiple-input multiple-output (MIMO) digital signal processing (DSP), emerging low-loss (de)multiplexers are discussed for providing high-density SDM transmission of >1TB/s per channel over a single fiber.

Introduction

The recent interest in mode-division multiplexed transmission over multi-mode/core fibers is due to the dramatic increase in the capacity of a single optical fiber by exploiting the spatial dimension. To this end, ongoing developments have been focused on achieving low, or compensated, differential group delay (DGD) few mode fibers (FMF) [1], multi-mode amplifiers [2] and integrated mode couplers [3]. The latter is of primary importance, as low-loss and effective coupling into and out of the FMFs can be achieved. In earlier subsystems focused on 3 mode transmission, phase plates were proposed and exhibited losses in the order of 8-10dB at the multiplexer (MUX) and demultiplexer (DEMUX) [4]. In state-of-the-art FMFs where losses are 0.19dB/km [1], losses of 20dB at both the MUX and DEMUX side could equate to about 100km less transmission capability. In addition to low loss launching, to support the scalability to higher number of mode channels, appropriate technologies are being considered which are capable of exciting all spatial modes of the FMF. Several technologies have been investigated within the ongoing European FP7 project MODEGAP based on spot-based mode couplers [5], waveguides [6], and silicon on insulator multiplexers [3] and photonic lanterns. These have been realized and demonstrated to realize MUX and DEMUX features in transmission systems [5,7]. In this work, the principle of the MUX/DEMUX techniques are discussed with their design optimised currently for 3-mode operation. These technologies are evaluated in transmission systems. Finally we provide an overview of the emerging techniques likely to allow the expansion to higher number of modes channel transmitted over a single fiber.

Spot Launching Techniques

According to [8], various spot arrangements can be constructed by adding a spot for each non-degenerate mode and two spots of degenerate modes. The 3-mode coupler is the simplest for investigation. In this work, the excitation of linearly polarized (LP) modes, LP_{01} , LP_{11a} and LP_{11b} are of primary focus, where the latter two are degenerate modes. Hence to generate the three modes, three spots carrying the light beams are arranged in a triangular shape in order to achieve the optimum performance. Based on the free-space setup, a single 3-surface prism is used to combine the collimated beams. Two vertical surfaces of the prism are perpendicular and the top surface is 45 degrees with respect to the horizon.

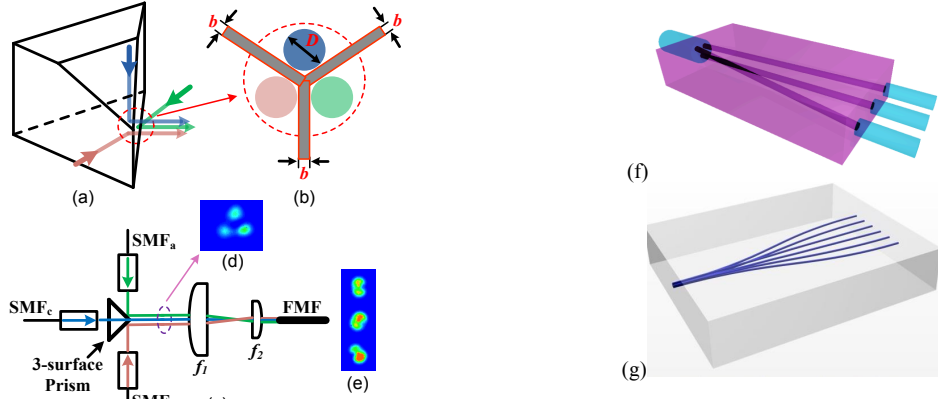


Fig 1: (a) 3-surface prism for combining 3 light beams; (b) prism bevels; (c) the setup of the 3-surface prism based 3-spot mode coupler; (d) The 3 combined light beams and (e) FMF output fields (f) 3D waveguide design for a 3-mode spot launcher, (g) A design allowing scalability to 6 modes

As shown in Fig. 1(b), to influence the spacing between the spots, the widths of the bevels on the prism are less than $10\mu\text{m}$ which is 50 times smaller than the collimated light beam with a diameter of $500\mu\text{m}$. Therefore, the influence from the bevels becomes negligible. A telecentric setup composed of two lenses with focal length of $f_1=150\text{mm}$ and $f_2=2.7\text{mm}$ are utilized to image the 3 spots into the FMF, as shown in Fig. 1(c). Fig. 1(d) shows the captured light beams. The tested coupler inserted loss (CIL) of the 3-spot mode coupler as a mode MUX and DEMUX is 3.9dB and 2.8dB, respectively, for a step-index FMF with a core diameter of $19.4\mu\text{m}$. Fig. 1(e) shows the output fields excited for each spot. For a graded-index FMF with a core diameter of $11\mu\text{m}$, the best CIL at the mode MUX and DEMUX achievable is 3.7dB and 3.5dB, respectively [5]. As the proof of principle is based on 3-mode propagation using free-space techniques, the scalability to higher number of modes as suggested in [9], is not investigated with free-space spot arrangement. To scale to a higher number of modes, the spots from the free space launcher can be further optimized and placed closer by using 3D silica waveguides inscribed by femto-second pulsed lasers [6,8]. Each input excites a different orthogonal set of modes, which are fully mixed when propagated along a few-mode fiber. The key consideration for the design of such waveguides is the placement of the spots such that the supermodes approximate the modes of the few-mode fiber with minimum CIL and mode dependent loss (MDL). As shown in Fig 1(f) and (g) it becomes relatively easy to scale to higher number of spots.

An Silicon on Insulator Integrated Multiplexer

In contrast to bulky free space components discussed, photonic integration provides the possibility for the (de)multiplexer to be placed with local oscillator lasers, modulators and photodetectors. This is key if these are to be combined and realised cost effectively in a transponder. To this end, a photonic integrated mode coupler based on Silicon-on-insulator device was designed and fabricated. The device utilizes push-pull and center launch to excite LP_{11} and LP_{01} mode. Supporting 6 channels (both polarizations of 3 modes), the device creates two Gaussian-like spots with a phase difference $\Delta\phi$ of π , since LP_{11} mode has a bipolar field distribution. As shown in Fig. 2(a), to create such bipolar field for LP_{11} mode coupling, two 2D grating couplers, push-pull driven with opposite phase are employed. To further illustrate this concept Fig. 2(b) shows full 6-channel integrated mode coupler where the center 2D grating coupler is for launching or channeling the LP_{01} mode for reception. The mode coupler connects 6 individual SMFs

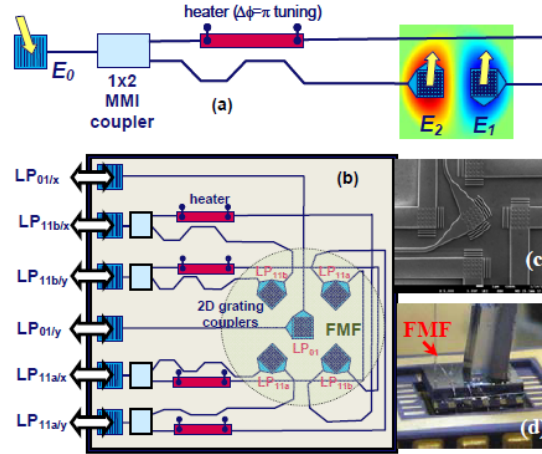


Fig 2: Push-pull scheme realized by a pair of grating couplers for LP11 mode excitation; (b) circuit for multiplexing LP01 and LP11 modes; (c) Scanning electron microscope image of the five vertical grating couplers and (d) The packaged integrated mode coupler

through one-dimensional grating couplers to the five 2D grating couplers for coupling into the few-mode fiber. The five small 2D vertical grating couplers, as shown in Fig. 2(c), excite 6 channels: the x- and y polarization of LP₀₁ and two orthogonal LP₁₁ modes (LP_{11a} and LP_{11b}). Fig. 2(d) shows the picture of the packaged mode coupler.

Experimental Validation – Spot Launcher and SOI Multiplexer

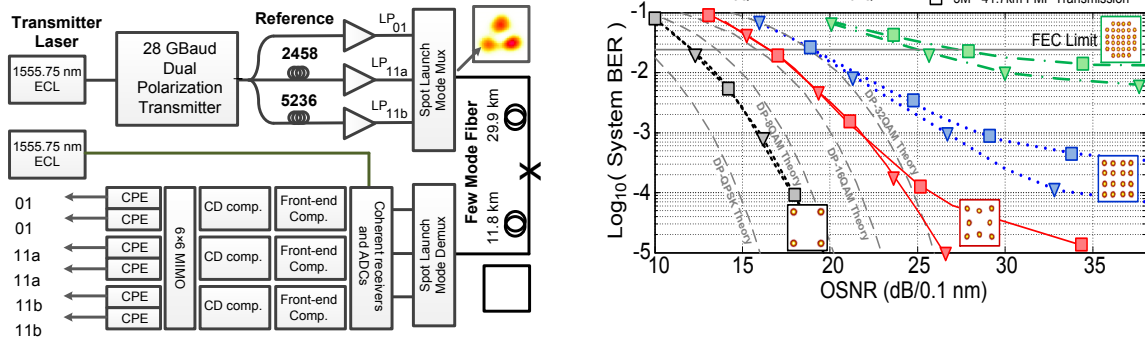


Fig 3(a): The experimental setup verifies the performance of the spot Launch Mux/Demux (inset: measured spot alignment). (b) Results

Firstly the performance of the free-space spot launcher is experimentally verified using the setup depicted in Fig. 3a. At the transmitter, the IQ-modulator is modulated at 28GBaud and driven by two digital-to-analog converters (DACs) for the in-phase and quadrature component of the transmitted constellation. The gray coded QPSK, 8, 16 and 32QAM constellations were used. By employing a number of gray coded, fully uncorrelated pseudo random bit sequences (PRBS) for the transmitted sequence in the digital domain each of length 2^{15} . The output of the IQ-modulator is split, and one arm is delayed by 1233 symbols for the emulation of polarization multiplexing. After recombining the two arms, the DP signal is noise loaded to characterize the optical signal to noise ratio (OSNR) system performance. To achieve 3 DP multiplexed transmission channels, the noise-loaded signal is split into three equal tributaries. Two arms are delayed for mode decorrelation by 2458 and 5236 symbols, respectively. As the single prism mode MUX is used, equal excitation of the three LP modes is expected to guarantee full mixing. For all inputs, the losses are approximately 3.7dB. The transmission link consists of two spans of graded index few-mode fiber with length of

41.7 km and a DMD of +3.82ns. A similar setup to the MUX is used for the DEMUX operation where the loss is 4.5 dB for each output.

In the digital domain, the optical front-end impairments are compensated. Then, the chromatic dispersion (CD) is removed. To invert the channel mixing effects, a 6×6 MIMO time-domain equalizer (TDE) with adaptive step size is used [12]. The weight matrix of the TDE is heuristically updated using the least mean squares (LMS) algorithm during convergence and decision-directed least mean squares (DD-LMS) during data transmission. One carrier phase estimation (CPE) block per output channel in the form of a digital phase locked loop is used to compensate for phase offset[11]. As shown in Fig 3b, at the FEC limit, the penalty is quite low for QPSK, 8/16 QAM.

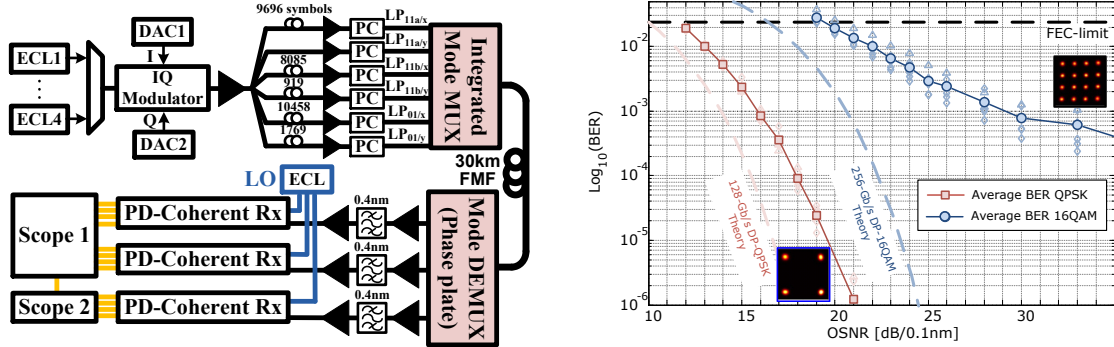


Fig 4(a): The experimental setup verifies the performance of the spot Launch Mux/Demux (inset: measured spot alignment).(b) Results

To validate the integrated multiplexer, the setup in Fig 4a is used. The 3dB wavelength bandwidth of the integrated MUX is larger than 40nm, which is sufficient for C-band [3]. Hence, 4 ECLs operated with 1THz frequency spacing are combined and modulated. In this particular test, the DACs are operated for QPSK or 16QAM symbols. Unlike the conventional method for polarization diversity (PD) through a polarization beam combiner with a delay line, the 2D grating coupler combines the two polarizations, the signal is directly split into six tributaries, which are amplified and input to the six ports of the integrated mode coupler. Polarization controller (PC) is used to maximum the diffraction efficiency of the grating couplers. The delays with respect to the $LP_{11a/b}$ port are decorrelated as in Fig 4a. After the DEMUX, the signals are sent into PD coherent receivers for capture and processing. Fig 4b. shows that with respect to theory, a penalty of 2dB and 3dB are observed for QPSK and 16QAM respectively

Conclusions

Within the MODEGAP project, various technologies have been shown to potentially offer a path to scalable mode multiplexing and coupling into emerging low-loss FMMFs. Through integration and low-loss waveguides, a higher number of modes can enable 1Tb/s per wavelength channel transmission over single fibers.

We acknowledge the EU FP7-ICT MODE-GAP project (grant agreement 258033), the IT R&D Program of MKE/KIAT (2010-TD-200408-001) of the Republic of Korea, We want to thank Lars Grüner-Nielsen and Yi Sun from OFS Denmark and OFS USA, respectively, for the few-mode fibers

References

- [1] L. Grüner-Nielsen et al., IEEE JLT. **30**(23)(2012).
- [2] Y. Jung et al., Opt. Exp. **19**, B952 (2011)
- [3] A. M. J. Koonen et al., IEEE PTL, **24** (2012)
- [4] R. Ryf et al., JLT **30**, 4 (2012)
- [5] H. Chen et al., Proc. OECC, PD3-6 (2013)
- [6] V.A.J.M. Sleiffer, proc. IPC, PD6 (2013)
- [7] H. Chen et al., Proc. OECC, PD2-5 (2013)
- [8] R. Ryf et al., IEEE PTL **24**(21) 1973-1976 (2012)
- [9] R. Ryf et al., proc. OFC, PDP5A.1 (2013)
- [10] R.G.H. van Uden et al., Proc. Sum. TopWC4.2 (2013).
- [11] R.G.H. van Uden et al., IEEE PTL **25**(14), (2013).
- [12] R.G.H. van Uden et al., proc. ECOC, Th.2.C.2 (2013)
- [13] R.G.H. van Uden et al., proc OFC 2014 submitted

Dynamic Routing in a Resonant Switch Matrix

P. DasMahapatra, R. Stabile, A. Rohit, and K.A. Williams

Eindhoven University of Technology, COBRA Research Institute, Eindhoven, The Netherlands.

Higher order ring resonators offer a possible avenue for broadband routing of optical signals. Recently we have reported broad bandwidth and high signal extinction in a 4×4 monolithically integrated optical switch matrix using fifth order resonators. In this paper we study the first dynamic multi-path routing experiments across a range of paths in the resonant switch matrix connecting two inputs to one output at a time. Further, we report the routing across a higher number of switching elements with modest losses, connecting combinations of ports for up to eight inputs and two outputs in the same monolithic optical switch matrix.

Introduction

High fabrication tolerance CMOS process combined with high confinement, low loss, Silicon on Insulator (SOI) waveguides has led to considerable and renewed research into micro-ring resonator technology. Optical switch architectures have been studied in some detail, primarily by placing single-order micro-rings switch elements at the intersections of multiple meandering waveguides to create modest connectivity 'optical router' elements [1,2]. The single order micro-ring is conceptually attractive but the inherent trade-off between the spectral-passband-width and the pass-band-to-stop-band signal extinction [3] compromises the switch scalability. Additionally, nanoscale fluctuations in waveguide dimensions lead to resonant wavelength fluctuations in the order of 1nm in nominally-identical ring resonators across a wafer [4,5] which is significant when compared to the narrow operating bandwidth. Simultaneous optimization of the passband width and switch extinction has been demonstrated in higher-order ring resonant elements though [6]. We have recently demonstrated 40Gbps routing across representative paths in a 4×4 switch matrix of higher order resonators [7]. In this work, we use this scalable crosspoint switch matrix to demonstrate dynamic multi-path routing for the first time in a large optical switch matrix with paths with up to eight elements in one row.

Circuit Fabrication

The optical switch matrix was fabricated on a $12\times 12\text{mm}^2$ SOI chip diced from an ePIXfab multi-project wafer. Low-cross-sectional area $500\times 220\text{nm}^2$, high-confinement silicon waveguides are used along with $1.2\mu\text{m}$ and $2\mu\text{m}$ upper and lower SiO_2 cladding layers. The input and output buses required for the optical crosspoint matrix run vertically and horizontally across the chip respectively and fifth order resonant switch elements are located at each intersection. Waveguide crossings are implemented with $32\times 3\mu\text{m}^2$ MMI couplers to complete the formation of the matrix. Grating couplers optimised for TE polarisation are used in combination with horizontal tapers to couple light into each input and output. These are located at the bottom edge of photograph which is shown in Fig. 1.

On-off switching is realized by tuning the transfer function of each ring by means of a thermo-optically induced refractive index change. Micro-heaters are fabricated on top of the foundry-supplied SOI circuits. A metallisation comprising 100nm Ti, 20nm Pt and 300nm Au is evaporated and patterned to create the on-chip wiring and microheaters. The on-chip wiring is implemented with 18.5 μ m-wide tracks and the heater elements are constricted in width to 3 μ m. A selective Au etch is carried out for the micro-heater elements to increase their resistance to around 400 Ω . A polyimide layer is spun over the photonic circuit and the microheaters to provide protection against thermally-induced degradation. The bondpads and the grating couplers are re-opened at the end of the process for electrical and optical connections.

The microheater at each switch element is individually addressed. A common ground is used for the entire circuit and hence the fabricated $m \times n$ matrix has $(m \times n) + 1$ electrodes. Wire bonds leading off from the chip as shown in Fig.1, enable external electrical connectivity to each switch element. The chip is fixed to a water-cooled mount in order to maintain the chip at a constant temperature of 22 $^{\circ}$ C.



Fig. 1. Photograph of assembled circuit. Wire bonds leading to the left and right of the image are control lines. Wire bonds leading to the bottom edge are the common ground lines.

Results

A 10Gbps, $2^{31}-1$ PRBS, on-off keyed optical signal is generated with a tunable laser tuned at 1551.35nm and a Mach-Zehnder modulator. The signal is split into two and input into two ports of the switch matrix. The output from the switch matrix is initially amplified by a low noise amplifier with an output optical signal to noise ratio (OSNR) of 30dB/0.1nm. A 0.9nm full-width at half maximum band pass filter (BPF) is used for noise rejection. The amplified output is fed into an optical receiver and viewed on a sampling oscilloscope as shown in Fig. 2.

Three fibers are used perform multi-path analysis: Two fibers are used as the input into the chip and with polarisation controllers put in place to optimise the input polarisation. The third connects the output to test equipment. All three fibres are separately aligned to minimise the fibre-chip coupling loss to 6dB per fiber.

Initial assessment of the switch elements is carried out by characterizing the error rates for the full range of paths. A selection of the paths tested are summarised in Table I. A

path independent power penalty is noted with the highest penalty being 0.7dB for the path from input 5 to output 2.

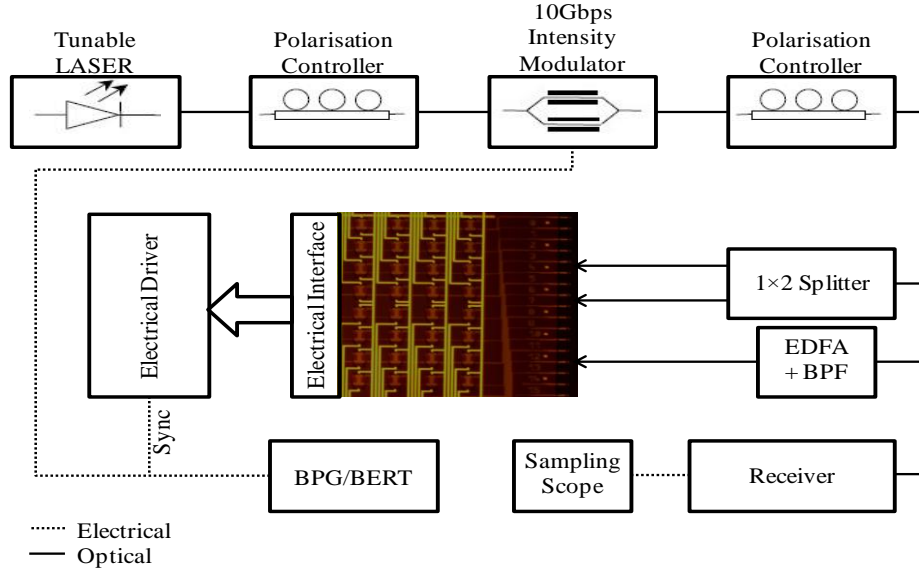


Fig. 2. Experimental arrangement for the study of dynamic multi-path routing.

Table I: Power penalty and bias voltage levels for selected paths through the optical switch matrix

Ring Element	“On” state bias (V)	“Off” state bias (V)	Power penalty in the “On” state (in dB)
8×2	3.14	7.44	0.3
7×2	3.47	6.93	0.5
6×2	2.84	7.21	0.6
5×2	5.22	8.71	0.7
8×1	0.00	6.71	0.3
6×1	2.22	7.15	0.5

Bias conditions are optimised individually and example values are included in Table I. Each micro-heater is actuated with one control voltage and this tunes all five resonators together for the fifth order switch element. The absolute values for the on and off state biases do vary between the switch elements and this highlights the requirement compensate for the nanometer scale fabrication variations and resonant wavelength registration errors across the optical switch matrix.

Dynamic routing is subsequently demonstrated by applying 750μs period square wave signals to two of the optical switch elements. Routing is performed from inputs 6 and 8 to output 2 and also from inputs 5 and 7 to output 2.

The time traces shown in Fig 3a and b show the output signals toggling from input 6 to 8 and input 5 to 7 to output 2 respectively. The vertical axis is fixed for each of the measurements to show modest levels of path dependant loss. Fig 3c and d show routing to output 1. Fig. 3a, b and c show a distinct difference in signal levels which correspond to the path dependant losses across the chip. The power levels in the guard bands is nearly zero which is consistent with the measured off state signal leakage of below 20dB.

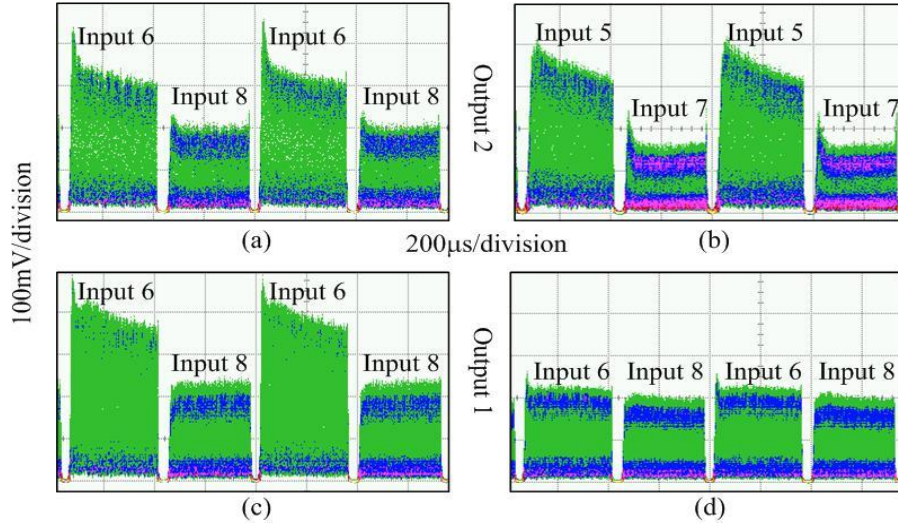


Fig. 3. Dynamic routing for 10Gb/s data for three combinations of inputs to outputs with (a-c) power equalized at the input to the optical switch matrix, and (d) power equalized at the output of the optical switch matrix through additional optimised losses on the input side.

There is a time-dependent power drop visible in Fig. 3a, b and c but this can be removed when the input power levels are adjusted to give equalized output levels as shown in Fig. 3d. The power excursions in Fig. 3a to 3c may be attributable to the carrier lifetime in the fibre amplifier.

Conclusions

We have successfully demonstrated signal routing at 10Gbps across multiple paths of a switch matrix with static power penalties below 0.7dB. The first demonstration of dynamic connection of multiple inputs to a single output is also carried out. This facilitates routing across a span of up to eight inputs and two columns, and the prospect of further scaling in microresonant switch matrices.

References

- [1] A. Biberman, B.G. Lee, N. Sherwood-Droz, M. Lipson and K. Bergman, "Broadband Operation of Nanophotonic Router for Silicon Photonic Networks-on-Chip," *IEEE Photon. Technol. Lett.*, vol. 22, no. 12, pp. 926-928, Jun. 2010.
- [2] R. Ji, L. Yang, L. Zhang, Y. Tian, J. Ding, H. Chen, Y. Lu, P. Zhou, and W. Zhu, "Five-port optical router for photonic networks-on-chip," *Opt. Express*, vol. 19, no. 21, pp. 20258-20268, Oct. 2011.
- [3] K.A. Williams, A. Rohit, M. Glick, "Resilience in optical ring-resonator switches," *Opt. Express*, vol. 19, no. 18, pp. 17232-17243, Aug. 2011.
- [4] T. Barwicz et al., "Silicon photonics for compact, energy-efficient interconnects [Invited]," *J. Opt. Netw.*, vol. 6, no. 1, pp. 63-73, Jan. 2007.
- [5] S.K. Selvaraja, W. Bogaerts, P. Dumon, D.V. Thourhout and R. Baets, "Subnanometer Linewidth Uniformity in Silicon Nanophotonic Waveguide Devices Using CMOS Fabrication Technology," *IEEE J. Select Topics Quantum Electron.*, vol. 16, no. 1, pp. 316-324, Jan. 2010.
- [6] Y. Vlasov, M.J. Green and F. Xia, "High-throughput silicon nanophotonic wavelength-insensitive switch for on-chip optical networks," *Nature Photon.*, vol. 2, no. 4, pp. 242-246, Apr. 2008.
- [7] P. DasMahapatra, R. Stabile, A. Rohit and K.A. Williams, "40Gb/s data routing through a scalable 2D matrix of higher order ring resonator switches", *IEEE Electronics Letters* (Accepted).

WDM Modulator Circuit for High Energy Physics Applications

D. Gajanana,^{1,2} M.G. van Beuzekom,¹ M.K. Smit² and X.J.M. Leijtens²

¹ Nikhef, National Inst. for Subatomic Physics, Science Park 105, 1098 XG Amsterdam, The Netherlands.

² TU Eindhoven, Photonic Integration, Den Dolech 2, 5612 AZ Eindhoven, The Netherlands.

Particle detectors in High Energy Physics experiments provide huge amounts of data which needs to be transported to the data center. Fiber-optic links provide a high-capacity low-mass solution. However, the performance of semiconductor lasers used in such links is shown to degrade by the amount of radiation that is generated when particles with high energy collide. We investigate a wavelength-division multiplexing (WDM) scheme in which only the semiconductor modulators are in the high radiation environment, and test the modulators for radiation hardness. The InP-based WDM modulator circuits are designed for fabrication on generic integration platforms. The samples will be irradiated with a 23 MeV proton beam at Karlsruhe Institute of Technology (KIT) up to various doses. Here we discuss the system concept and preliminary measurements of non-irradiated samples that will later be compared with the irradiated samples.

Introduction

The large hadron collider (LHC) at CERN in Geneva collides two highly energetic particle beams against each other 40 million times per second, producing billions of interactions. The subatomic particles that are created in such interactions are detected by so called particle detectors. Particle detectors are made of sensors elements and electronic chips are attached to the sensors to read out the data. Particle detectors produce enormous amounts of data and are read out on high speed links to a computer farm, located hundred meters away. As experiments progress to higher luminosities, future detectors will be designed to read all data to the computer farm, unlike the present selective readout. Each read out chip needs serial data rates of multiple Gbps making it several Tbps for the whole detector. Presently, the data rate is low enough to be transmitted electrically for the first couple of meters and then perform electro-optic conversion by direct modulation of a laser. Electrical read out of data using copper cables at data rates of 10 Gbps for a couple of meters of cable is already very challenging. With higher data rates, the electro-optic conversion is preferred as close to the detector as possible.

Particle beams colliding against each other produce high amounts of radiation close to the interaction point. The detector circuits have to withstand high radiation levels [1]. High energy subatomic particles created in the collisions fly through the circuits, causing damage to the crystal structure and giving rise to trapping of charges at interfaces etc. These phenomena affect the performance of the circuits. Direct modulation of lasers in such a harsh environment is challenging as literature suggest that the lasers degrade significantly already at less severe radiation environments [2]. Modulation of a continuous wave laser using external modulators is another interesting option. However, relatively little is known about the performance of such modulators under radiation and more research is needed on the subject. Consider the following configuration: The laser is placed in a low radiation environment and the Continuous

Wave (CW) laser beam is brought inside the particle detector area on an optical fiber. This CW is then modulated by the read out chip using an optical modulator circuit. The modulated light is sent back to the data acquisition and processing part at the computer farm on a return optical fiber (Fig. 1).

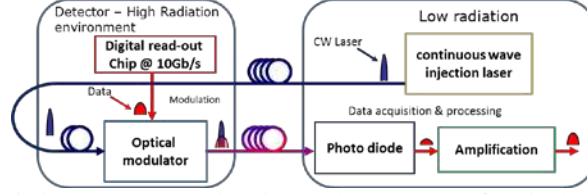


Fig. 1: Block diagram depicting external modulation and placement of optical devices in radiation zones.

The steps taken in the direction of indirect modulation technique include:

- To investigate and understand how existing modulators behave in the radiation environment.
- To design Wavelength Division Multiplexed (WDM) modulators for irradiation tests.

Design of ASPIC and sub-mount

The Application Specific Photonic Integrated Circuit (ASPIC) shown in Fig. 2 was designed in the COBRA generic integration platform [3]. It includes two WDM modulator circuits with a possibility of pre-amplification or post-amplification. In addition, there are a number of test structures to test the individual components. The circuits are built using standard building blocks like modulators, Semiconductor Optical Amplifiers (SOAs) and Arrayed Waveguide Gratings (AWG). Phase modulator sections of ~2 mm length are designed in Mach-Zehnder (MZ) interferometer configuration. Alternatively, small SOA sections can be used as modulators. Larger SOA sections provide optical gain. The AWGs have 2 inputs and 5 outputs, with a channel spacing of 400 GHz and Free Spectral Range (FSR) of 2400 GHz. A SOA is included in one of the inputs of the AWG giving the circuit the capability of pre or post amplification of signals. The 3 wavelengths are modulated using MZ interferometers and the remaining 2 are modulated using the smaller SOAs. The building blocks are also separately placed as test structures.

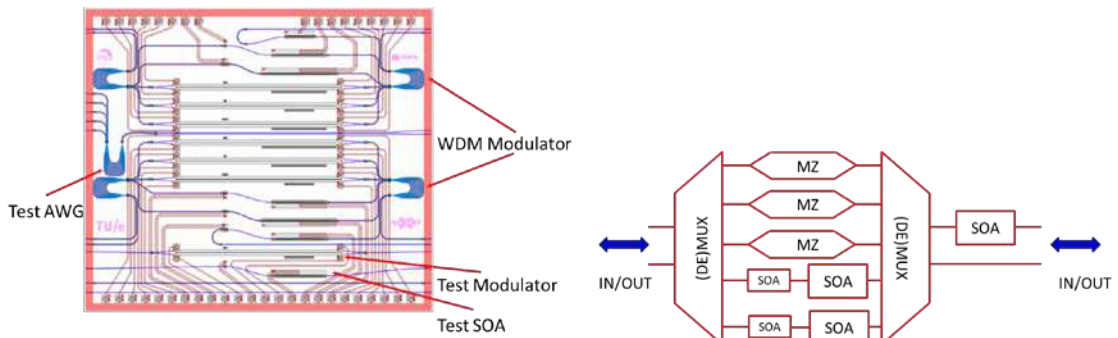


Fig. 2: (L) ASPIC designed in the TU/e COBRA generic integration platform. (R) Circuit schematic.

Little is known about radiation hardness of InP based passive devices compared to LiNbO₃ devices [4]. Literature [5]-[8] suggests that Multiple Quantum Well (MQW) based devices perform better than bulk devices under irradiation. All passive circuits in

the COBRA platform are bulk devices and the active circuits are devices with multiple quantum wells. The modulators supplied by Oclaro in bar form consist of 22 MZ modulators per bar and are based on multiple quantum wells. Four samples from COBRA and four modulator bars from Oclaro will be exposed to 10^{12} , 10^{13} , 10^{14} and 10^{15} protons/cm² fluence (1 MeV neutron equivalent), respectively. These devices are compared in performance for different exposure levels and between technologies. During irradiation, the circuits need to be electrically biased to imitate actual operating conditions. Therefore a PCB sub-mount was designed for electrical and optical access to the sample as shown in Fig.3.



Fig. 3: (L to R) ASPIC glued and bonded on the sub-mount measuring 5×5 cm². Sub-mount mounted on the motherboard for measurements.

Measurement results for non-irradiated samples

All measurement results reported here are on the non-irradiated test structures in the COBRA circuit. A simple schematic sketch of a MZ modulator is shown in Fig. 4. Light from a 1550 nm laser is coupled through a fiber-based polarization controller to a lensed fiber on the left facet of the chip. After transmission through the chip, the light is collected with a second lensed fiber on the right facet of the chip and coupled to an external power meter. Typical measurements on the modulator included: phase versus voltage characteristics and determining the extinction ratio. The non-irradiated sample had a V_{π} of 6.5 V and an extinction ratio of 14 dB as shown in Fig. 4. The SOA was tested using a current source and recording the light output power by an optical power meter. The light output power and the Amplified Spontaneous Emission (ASE) spectrum measurements are in agreement with expected values. Further, light from a tunable laser source with an output power of 0.7 dBm at 1550 nm was injected into an SOA and the output spectrum was recorded. The peak output power is +4 dBm. From this we estimate a SOA gain around 13.4 dB, as the SOA has compensated the coupling loss (2×4.5 dB) and waveguide propagation loss (1.1 dB). The AWG response was measured using an Erbium-Doped Fiber Amplifier (EDFA) source with a broad optical spectrum. The output spectrum was recorded using an Optical Spectrum Analyser (OSA). Measurements of the AWG show a channel spacing of 400 GHz, FSR of 2400 GHz and a crosstalk of 16 dB.

Conclusions and Future

The individual building blocks of the WDM modulator circuit have been characterized and show proper functionality. Detailed optical measurements on the ASPIC are being carried out now. Irradiation tests of the WDM circuits and the Oclaro modulators [9] in the 23 MeV proton beam at KIT are planned. The irradiated samples will be measured

and the performance will be compared with non-irradiated samples. Thorough investigation is needed to analyse the results of characterisation and understand the radiation hardness performance of the modulator.

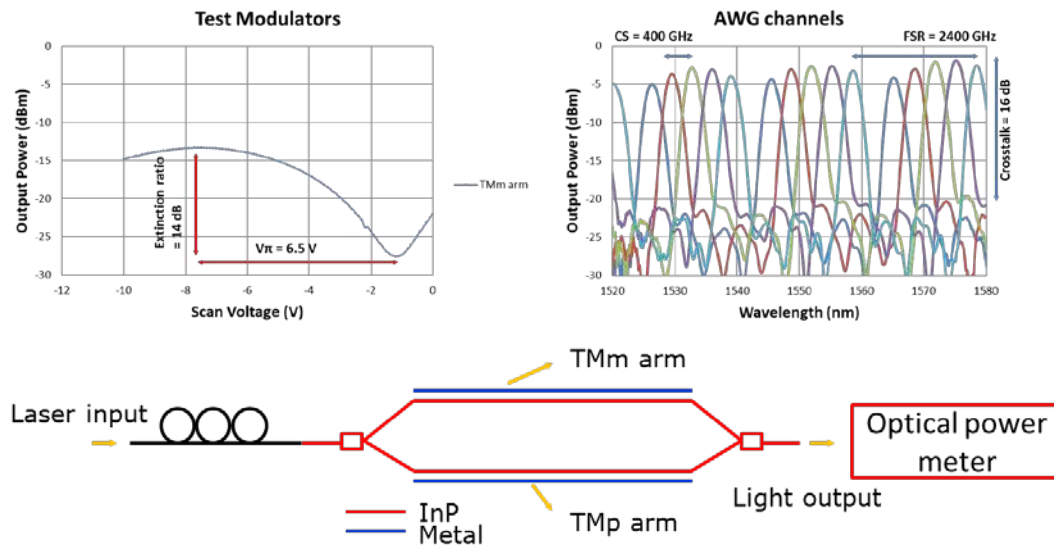


Fig. 4: (Clockwise) Measurements on the non-irradiated test MZ modulator; Measurements on the AWG; Schematic of the MZ measurements.

Acknowledgements

This work is part of the research program of the "Stichting voor Fundamenteel Onderzoek der Materie (FOM)", which is financially supported by the "Nederlandse organisatie voor Wetenschappelijke Onderzoek (NWO)".

References

- [1] F. Faccio, "COTS for the LHC radiation environment: the rules of the game", in Proceedings of LHC Electronics Workshop, 2000.
- [2] P. Le Metayer et al., "Proton damage effects on GaAs/GaAlAs vertical cavity surface emitting lasers", Journal of Applied Physics, vol. 94, pp. 7757-7763, 2003.
- [3] M. Smit, X. Leijtens, E. Bente, J. Van der Tol, H. Ambrosius, D. Robbins, M. Wale, N. Grote, M. Schell, "Generic foundry model for InP-based photonics", IET Optoelectronics, Vol. 5, Iss. 5, pp. 187-194, 2011.
- [4] C. D'hose et al., "Electrical and Optical Response of a Mach-Zehnder Electrooptical Modulator to Pulsed Irradiation", IEEE Trans. on Nuc. Sci., Vol. 45, pp 1524-1530, 1998.
- [5] R. Leon et al., "Effects of Proton Irradiation on Luminescence Emission and Carrier Dynamics of Self- Assembled III-V Quantum Dots", IEEE Trans. on Nuc. Sci., Vol. 49, pp 2844-2851, 2002.
- [6] F. Guffarth et al., "Radiation hardness of InGaAs/GaAs quantum dots", Applied Physics Letters, vol. 82, pp. 1941-1943, 2003.
- [7] M. Boutillier et al., "First Evaluation of Proton Irradiation Effects on InAs/InP Quantum Dash Laser Diodes Emitting at 1.55 μm ", IEEE Trans. on Nuc. Sci., Vol. 55, pp 2243-2247, 2008.
- [8] S. F. Tang et al., "Investigations for InAs/GaAs multilayered quantum-dot structure treated by high energy proton irradiation", Journal of Thin Solid Films, vol. 518, pp. 7425-7428, 2010.
- [9] D. Gajanana, M.G. van Beuzekom, M.K. Smit, X. J. M. Leijtens, "Irradiation studies on InP- based Mach Zehnder modulator", Proceedings of the 2012 Annual Symposium of the IEEE Photonics Benelux Chapter, pp 291 – 294, 2012.

An InP based generic integration platform for Photonic Integrated Circuits operating up to 2 μm wavelength

D. D'Agostino, S. Latkowski, H. Rabbani, E. Kleijn, E.A.J.M. Bente, H.P.M.M. Ambrosius and M.K. Smit

Technical University of Eindhoven (TU/e), Dept. of Electrical Engineering, Photonic Integration group, COBRA, PO Box 513 - 5600 MB, Eindhoven, the Netherlands

We are developing a generic integration platform for Photonic Integrated Circuits with a target wavelength of 2 μm . The platform is based on the platform process for 1.55 μm which supports monolithic integration of a wide range of passive and active components as amplifiers, modulators and detectors. In this paper we discuss the extension to longer wavelengths and its impact on the performance of the passive components, supported by initial characterization results of the waveguide loss and an Arrayed Waveguide Grating in a wavelength window from 1.88 to 2 μm .

Introduction

Generic integration platforms offer a set of standardized components, which can be integrated monolithically to obtain the functionality for a broad range of applications. With this approach, which is conceptually similar to the CMOS process in electronics, a variety of integrated circuits have been demonstrated [1,2].

Driven by the needs of telecommunication applications, a platform with a range of capabilities has been established in the wavelength region of 1550 nm. An extension of the supported wavelength range will allow for new applications. Wavelengths around 2000 nm are especially interesting for medical and sensing applications. These comparatively long wavelengths, allow for efficient evanescent field sensors, gas sensors or low-cost OCT systems [3].

Technologically the extension of the platform requires only a few modifications. Our active-passive integration scheme used for the 1550 nm window [1,2], can easily be adapted for the desired wavelength region [4]. By keeping the passive waveguide section the same, the necessary platform adaptations are restricted to redesign and characterization on the basic component level. The fabrication processes can be maintained and we obtain a low-cost platform, allowing a wide range of applications.

In this paper we will evaluate the performance of the passive waveguide section, for wavelengths up to 2000 nm. We discuss the wavelength dependent propagation loss and compare the results to measurements obtained with the Fabry-Perot Method from 1880 nm to 2000 nm. Furthermore we demonstrate first experimental results from an Arrayed Waveguide Grating operating at 2000 nm.

Wavelength dependent absorption

A generic process is based on a common layer stack, shared among all users of the platform. For maximum compatibility with the existing process, it is convenient to change the stack as little as possible. One of the most important properties of the layer stack is the propagation loss, which is sensitive to the materials and the doping levels employed. For InP based platforms, the waveguides are based on an InGaAsP layer between two partially doped InP cladding layers. The doping is chosen to form a pin

diode around the waveguide core, with a gradually increasing concentration of p-dopant towards the top. This is done to make the layer stack also suitable for use in electro-optic modulators and amplifiers while minimizing propagation loss.

The decreasing confinement in the waveguide core with increasing wavelength, gives rise to an increase of the confinement in the highly doped regions. The absorption in the p-doped cladding is dominant. In the highly doped regions, the absorption can become higher than 100 dB/cm. Therefore even a small increase of the field in the p-doped region will lead to a substantial increase of the propagation loss.

In order to get a quantitative estimate of the increase of loss due to absorption we have performed simulations with the commercially available Finite Difference complex mode solver in Field Designer, offered by Phoenix BV. These calculations, which are based on the models mentioned below, are compared to waveguide loss measurements in the following section. The reference layer stack with detailed material parameters can be found in [5].

For our simulations we used the following assumptions. The real part of the refractive index is obtained by using the model provided by Fiedler and Schlachetzki [6]. The change in refractive index due to the presence of dopant is derived from the plasma effect. By distinguishing between different effective masses, we take into account the polarity of the dopant [7]. The absorption due to presence of dopant has been based on two different models. For n-type absorption, we assume that most of the loss is a result of scattering introduced through electron-optical phonon, electron-acoustical phonon, and electron-ionized impurity interaction [8]. For p-type dopant the loss can be reduced to intervalence band absorption, which has an exponential dependence on the wavelength [9].

Waveguide loss measurement

To verify the assumptions described above, we characterized waveguides using the Fabry-Perot Method. A proper estimation of the wavelength dependent reflection coefficients has been obtained with MIRE, a software tool developed by ETH Zürich. Two different types of waveguides have been considered. The first type is in agreement with the standard layer stack used in the 1550 nm platform [5]. The other has a core thickness of 600 nm and does not contain any p dopant. Both sets of waveguides are about 11 mm long and contain shallowly etched waveguides to reduce the influence of surface roughness. As source we used an external cavity laser in Littman configuration based on the tuneable laser kit, Thorlabs TLK-1950R. Prior to a wavelength scan, the SMSR of the laser has been checked over the tuning range using a YOKOGAWA AQ6375 optical spectrum analyser (OSA). By maximizing the power through the waveguide using a manual polarization controller, we assume that the best measurements will result in a TE polarization.

Typical measurement results are displayed in Figure 1. The plot contains the photodiode signal against the relative displacement of the external grating over time. The black circles represent a typical result obtained from the undoped waveguides. Compared to the doped waveguides plotted in dark gray, we measure a significant difference in contrast ratio at a wavelength of 1922 nm. The contrast ratio decreases further at 1990 nm, as waveguide absorption increases. This effect is further enhanced by decrease of the laser power when it is detuned from its central wavelength. This hampers the extraction of accurate loss values when approaching a wavelength of 2000 nm.

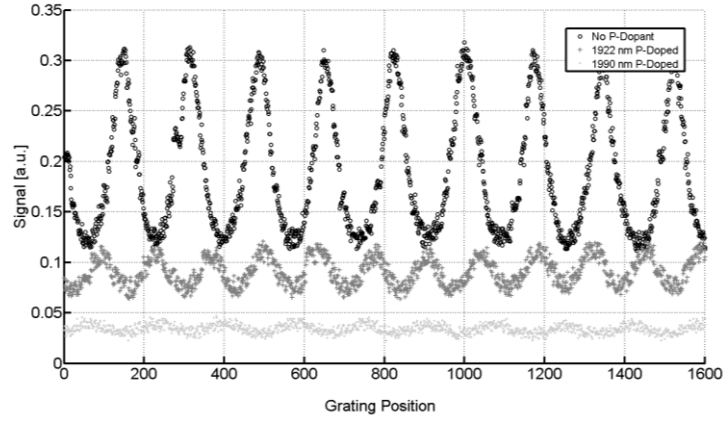


Figure 1: Typical Fabry-Perot measurements

The summarized loss dependence between 1880 nm and 2000 nm is shown in Figure 1. We see good agreement between the simulation and the measurement results. The samples containing no p-dopant have a low loss with negligible wavelength dependence. The measured value is slightly higher, as we did not take into account effects of surface roughness. As expected, the p-doped set of waveguides show a higher loss with a steady increase. The overall trend coincides with the prediction, which indicates that the p-dopant introduces strong exponential wavelength dependence.

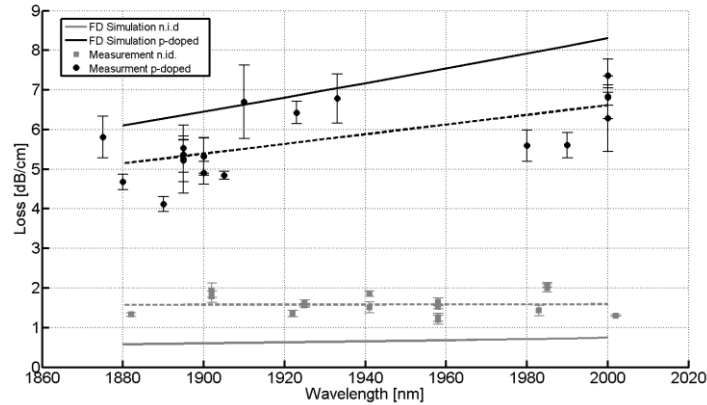


Figure 2: Wavelength dependent loss for n.i.d. (gray) and doped (black) waveguides between 1880 nm and 2000 nm (TE)

An Arrayed Waveguide Grating

Based on the measurements of undoped waveguide samples, we extracted the necessary parameters for our standard AWG module. In this way, we obtain a compact AWG with a deeply etched waveguide array section. The minimum bending radius has been set to 150 μm . This reduces the insertion loss of the device for longer wavelengths. The shallow to deep transitions have been adjusted and angled waveguide terminations were used to avoid back reflections at the coupling interface. Using the Thorlabs TLK-1950R, we display 2 channels of a 4x4 AWG with a target FSR of 1600 GHz and a channel spacing of 400 GHz in Figure 3. For wavelength reference, we measured the wavelength at the beginning and end of the laser sweep with the OSA and interpolated the points in between. From our measurement data we estimate an insertion loss of about 2.5 dB for the central channel, by comparing to a straight waveguide. This is a promising result for the long wavelength platform.

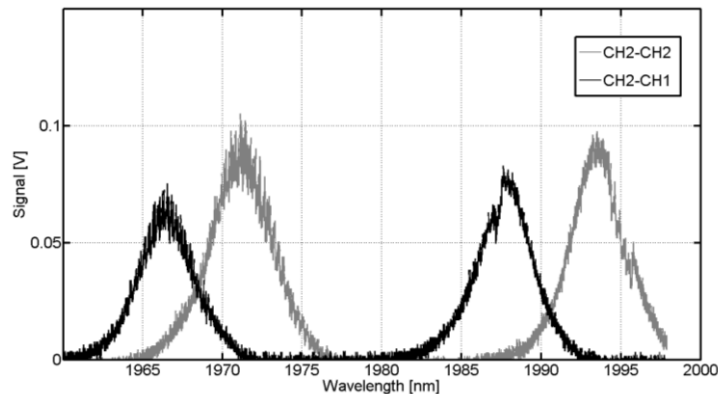


Figure 3: First demonstration of an AWG operating at 2 μm

Conclusion

We have modelled and measured waveguide loss, for InP ridge waveguides in the wavelength window between 1880 nm and 2000 nm. Measurement results obtained via the Fabry Perot Method show a loss of about 7 dB/cm for non-optimized InP waveguides at a wavelength of 2000 nm. We have verified that the main contribution for the high loss is the presence of p-dopant, as samples containing no p-dopant showed loss below 2 dB/cm with negligible wavelength dependence. We demonstrated an AWG with good performance on the long-wavelength platform.

Acknowledgments

The research leading to these results has received funding from the European Community's Seventh Framework Programme FP7/2007-2013 under grant agreement ICT 257210 PARADIGM, the Dutch IOP Photonic Devices under the project TULGAS and the Technology Foundation STW under the project LWAVE-TECH.

References

- [1] Leijtens, X., "JePPIX: the platform for Indium Phosphide-based photonics," *Optoelectronics, IET*, vol.5, no.5, pp.202,206, October A.B. Author, Title of Book, New York: IEEE Press, ch. 6, pp. 23-35, 1995.
- [2] M. Smit, et.al, "Generic foundry model for InP-based photonics", *IET Optoelectron.*, 2011, Vol. 5, Iss. 5, pp. 187-194
- [3] Tilma, B.W., et. al.. Integrated tunable quantum-dot laser for optical coherence tomography in the 1.7 μm wavelength region. *IEEE Journal of Quantum Electronics*, 48(2), 87-98
- [4] S. Latkowski et. al., "Small signal modal gain measurement of ridge waveguide semiconductor optical amplifiers operating at 2 μm suitable for active-passive integration" in *2012 IEEE Photonics Conference (IPC), 2013(in press)*
- [5] R. G. Broeke, A Wavelength Converter Integrated with a Discretely Tunable Laser for Wavelength Division Multiplexing Networks, 2002, TU Delft
- [6] F. Fiedler, "Optical parameters of InP-based waveguides", *Solid state electronics*, vol. 30, no. I, pp. 73-83, 1987
- [7] B. Reid, et. al., "Absorption and index of refraction for the modeling of InGaAsP/InP photonic devices," *Canadian Journal of Physics*, vol.71, no. 9-10. NRC Research Press, pp. 410-416,
- [8] Walukiewicz, W., et. al., "Electron mobility and free carrier absorption in InP; determination of the compensation ratio," *Journal of Applied Physics*, vol.51, no.5, pp.2659,2668, May 1980
- [9] J. Weber, "Optimization of the Carrier Induced Effective Index Change in InGaAsP Tunable Bragg Filters," *Quantum*, vol. 30, no. 8, pp. 1801-1816, 1994

Robust Optimization of 2x2 Multimode Interference Coupler Affected by Parametric Uncertainties

Samee ur Rehman, Matthijs Langelaar, Fred van Keulen

Precision and Microsystems Engineering, Delft University of Technology, Delft, the Netherlands

Robust optimization of an integrated photonic device affected by parametric uncertainties is exhibited. The optimization is performed on an approximate, cheap model of the expensive integrated photonic device simulation. This model is constructed using an interpolation technique known as Kriging. To illustrate the method, we robustly minimize the imbalance of an MMI coupler affected by an etching uncertainty that causes dilation or shrinkage of the fabricated device geometry. The robust optimum is found by minimizing the maximum realizable value of the imbalance with respect to the uncertainty set. The method can be applied to other photonic devices affected by uncertainties.

Introduction

The feature size of integrated photonic devices is steadily becoming smaller. With this reduction in size, sensitivity to fabrication variations becomes acute. If the designer does not take the limitations of the fabrication process into account, the designed devices either can't be fabricated or have low yield.

These uncertainties may arise due to variations in the material properties, fabricated design geometry, temperature variations, *etc.* Uncertainties can be categorized into two types. Parametric uncertainties affect the problem data or parameters, while implementation error affects the design variables of a problem. The design variables are variables that are controlled by the designer to direct the optimization process.

It is assumed in this work that only the bounds within which each uncertainty varies are known while the probability distribution of the uncertainty set is not available. In this situation, the robust optimization of a device is performed by finding the best worst-case solution for the objective with respect to the uncertainty set. We apply the optimization on a cheap model of the computationally expensive integrated photonics simulation. The metamodel, based on Kriging [1], is constructed by sampling the expensive integrated photonics simulation using a space-filling technique known as Latin hypercube sampling (LHS) [2]. We showcase the application of robust optimization on an integrated photonic device by minimizing the imbalance of a 2x2 multimode interference coupler affected by variations in its fabricated design geometry.

This paper is related to the work by Rehman *et al* [3], in that metamodeling is used to apply robust optimization on an MMI coupler in both works. The research by Rehman *et al.* [3], however, was focused on applying robust optimization on an integrated photonic device affected by implementation error. In this work, we apply robust optimization on an integrated photonic device under the more general supposition that the device is affected by parametric uncertainty.

Robust optimization of problems affected by parametric uncertainties

A deterministic unconstrained optimization problem is an optimization problem that

does not involve uncertainties. Such a problem is defined as

$$\min_{\mathbf{x}} f(\mathbf{x}) \quad (1)$$

where, $f(\mathbf{x})$ is the objective and \mathbf{x} is the set of design variables. We now assume that our problem is affected by a parametric uncertainty. Parametric uncertainties reside in a dimension that is separate from the design domain. Let us denote the set of parametric uncertainties as $\Delta\mathbf{p}$, where $\Delta\mathbf{p}$ belongs to the uncertainty set \mathcal{U} . In order to find the robust optimum we must minimize the maximum possible realization of the objective $f(\mathbf{x}, \Delta\mathbf{p})$ with respect to the uncertainty set \mathcal{U} . This can be defined as

$$\min_{\mathbf{x}} g(\mathbf{x}, \Delta\mathbf{p}) \quad (2)$$

where

$$g(\mathbf{x}, \Delta\mathbf{p}) = \max_{\Delta\mathbf{p} \in \mathcal{U}} f(\mathbf{x}, \Delta\mathbf{p}). \quad (3)$$

$g(\mathbf{x}, \Delta\mathbf{p})$ represents the worst-case cost of the objective with respect to \mathcal{U} . We seek to find the best worst-case cost, which means that we must minimize $g(\mathbf{x}, \Delta\mathbf{p})$.

Numerical Modelling

Robust optimization is applied on an approximate Kriging [1] model of the expensive integrated photonic device simulation. We construct the cheap model by sampling the expensive simulation using design of experiments. We use a space-filling technique known as Latin hypercube sampling to provide these sampling locations.

Kriging is an interpolation technique that uses a parameterized Gaussian basis function. The values for the unknown parameters are chosen by the Kriging fitting process such that the likelihood of the observed data is maximized. Based on these parameters, the Kriging interpolation is performed by maximizing the combined likelihood of the observed data and the Kriging prediction.

Robust optimization of integrated photonic devices: MMI coupler

A multimode interference coupler is a well-known integrated photonic device which is used to split, combine or couple light [4]. In this work, the focus is on designing an MMI coupler that performs 3dB splitting of the input light. The device is simulated in Phoenix software [5]. The coupler is designed in Silicon-on-Insulator (SOI) and operates at a wavelength of $1.55\mu\text{m}$. A mode solver is used to compute the length at which we should ideally observe 3dB splitting, given a nominal width of $W = 1.5\mu\text{m}$.

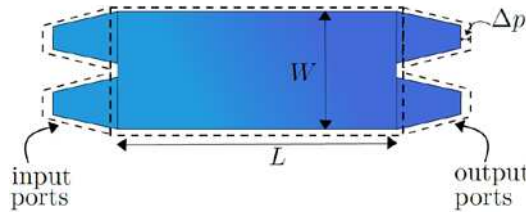


Fig. 1: 2x2 MMI coupler top view. The dashed line shows the dilation due to etching uncertainty Δp

The corresponding length for 3dB splitting was $L = 8.23\mu\text{m}$. Ideally, this should be the length for 3dB splitting when no uncertainty is involved. Bidirectional eigenmode propagation (BEP) is used as the propagation simulation. The propagation simulation is needed to analyze the performance of the MMI coupler in the presence of uncertainties.

Optimization problem definition

It is assumed that during fabrication, the etch step is only accurate up to a range of $\mathcal{U} = [-30nm, 30nm]$. This etching uncertainty Δp causes a dilation or shrinkage of the whole geometry, meaning the principal MMI waveguide as well as the input/output ports. The length and width of the MMI coupler are used as design variables.

Since our focus is on achieving 3dB splitting, the imbalance between the two output ports, in the presence of the etching uncertainty Δp , needs to be minimized. The imbalance is defined as

$$\text{Imb} = 10 \log_{10}(P_1/P_2) \quad (4)$$

where P_1 and P_2 are the powers at the upper and lower output port respectively. The robust optimization problem, in the presence of the uncertainty Δp , can be written as:

$$\min_{L,W} g(L,W,\Delta p) \quad (5)$$

where

$$g(L,W,\Delta p) = \max_{\Delta \in \mathcal{U}} \{(\text{Imb}(L,W,\Delta p))^2\} \quad (6)$$

The design domain is limited to a $\pm 4\%$ variation around the nominal values for L and W . We take the square of the imbalance so that the response remains positive and differentiable.

Results

In this work, we compare the relative effectiveness of two sampling strategies to find the robust optimum on the MMI coupler. The first strategy is a 1-stage approach where the design space is sampled across the three design variables, using LHS, at $N = 40$ locations and the response is computed on the expensive MMI simulation. A Kriging metamodel is constructed based on the samples and robust optimization is applied on the resulting design landscape.

Tab. 1: Robust optimization of imbalance of a 2x2 MMI coupler under parametric uncertainty using 1-stage and 2-stage approach

	1-stage approach	2-stage approach
$W (\mu m)$	1.507	1.506
$L (\mu m)$	8.281	7.905
$\Delta p (\mu m)$	0.006	0.006
Kriging worst-case Imb(dB)	0.432	1.440
True worst-case Imb(dB)	2.179	1.755

The second strategy is a 2-stage approach where, at the first stage, the design space is sampled at $n_1 = 25$ locations using LHS and the robust optimum is found based on the Kriging metamodel of the response at these locations. We then sample the design space again at $n_2 = 15$ locations in a local region centered around the robust optimum found at the first stage. A Kriging metamodel is built based on the n_2 samples and robust optimization is performed in this local region.

The robust optima found using the two approaches are compared. Tab. 1 shows the results. The respective robust width and length values found through the two methods are shown in Tab. 1. The table also shows both the true best worst-case imbalance found on the expensive simulation of the MMI, for the respective length and width values, as well as the values for Δp at which this best worst-case result is found.

Comparing the worst-case imbalance on the expensive MMI simulation for the two methods, we note that the 2-stage approach provides a result that is 0.4 dB better, i.e. lower, than the 1-stage approach. In both cases, this worst-case result is not found at the boundaries of the uncertainty set Δp . This shows that the response is multimodal even within the uncertainty set and an approximate design landscape is difficult to model with a small number of samples. Interestingly, the worst-case imbalance predicted on Kriging by the 2-stage approach much better matches the corresponding result on the expensive simulation than the 1-stage approach. This indicates that in the local area around the robust optimum, the 2-stage approach predicts the true behavior of the MMI more accurately. The results exhibit that an adaptive sampling strategy such as *expected improvement* [1] may be better suited to applying robust optimization on a metamodel of an MMI coupler than a space-filling technique such as Latin hypercube sampling.

We observe that the width found for the robust optimum for both approaches is almost the same and this value is also quite similar to the nominal value of $W = 1.5\mu\text{m}$. However, the length at which the robust optimum is found for the 2-stage approach is significantly lower than the length found for the 1-stage approach as well as the nominal value of $L = 8.23\mu\text{m}$. This suggests that the coupler is much more sensitive to changes in length as opposed to the width.

Conclusion

In this work, we have applied robust optimization on the imbalance of a 2x2 MMI coupler in the presence of an etching uncertainty that causes a dilation or shrinkage of the fabricated device geometry. It was shown that the fabrication variation can be treated as a parametric uncertainty. Under this framework, robust optimization was applied on a cheap approximate model of the device using two different sampling strategies. We observed that robust optimization based on a 2-stage adaptive sampling strategy provided better results on the MMI coupler than a 1-stage space-filling sampling strategy. This indicates that an adaptive sampling strategy such as *expected improvement* may be better suited for this application. The method shown in this work is generic and can easily be applied to other photonic devices affected by parametric uncertainties.

References

- [1] Jones *et al.*, “Efficient Global Optimization of Expensive Black-Box Functions”, Journal of Global Optimization, 13, 455-492 (1998)
- [2] Morris, M *et al.*, “Exploratory designs for computational experiments”, Journal of Statistical Planning and Inference, 43(3), 381–402 (February 1995).
- [3] ur Rehman, S *et al.*, “Robust optimization of 2x2 multimode interference couplers with fabrication uncertainties”, Proc. SPIE 8627, (March 2013)
- [4] Bachmann, M *et al.*, “General self-imaging properties in NxN multimode interference couplers including phase relations”, Appl. Opt. **33**, 3905-3911 (June 1994)
- [5] PhoeniX Software, [version 4.0.6], Enschede, the Netherlands

Optical memory operation of two semiconductor ring lasers coupled by a single waveguide

G. Van der Sande¹, W. Coomans¹, and L. Gelens¹

¹ Applied Physics Research Group (APHY), Vrije Universiteit Brussel, Pleinlaan 2,
B-1050 Brussels, Belgium

We present a numerical analysis of the dynamical behavior of semiconductor ring lasers coupled by a single bus waveguide. Both a weak and strong coupling are considered. Specifically, we show that this coupled system is multistable and can promote instabilities. We relate the internal dynamics in the individual lasers to the field effectively measured at the output of the waveguide. We suggest design constraints leading to coupling phases that avoid instabilities. Finally, we focus on the advantages and disadvantages for optical memory operation of coupled semiconductor ring lasers versus solitary ones.

Introduction

Semiconductor ring lasers (SRLs) are semiconductor lasers where the laser cavity consists of a ring-shaped waveguide. SRLs can generate light in two counterpropagating directions referred to as the clockwise (CW) and the counterclockwise (CCW) mode. Bistability between both directional modes has been demonstrated, allowing to encode digital information in the direction of emission of SRLs [1]. This bistable operation allows SRLs to be used in systems for all-optical switching and as all-optical memories, both in solitary [2, 3, 4] and coupled [1, 5, 6, 7, 8] configurations. Moreover, SRLs are highly integrable and scalable [9], making them ideal candidates for key components in photonic integrated circuits.

One of the seminal works reporting on the potential of SRLs as optical memories is the letter by Hill *et al.* [1]. To demonstrate fast optical flip-flop operation, the authors fabricated two SRLs coupled by a single waveguide, rather than a solitary SRL. Nevertheless, the literature shows that a single SRL can also function perfectly as an all optical memory [4]. This raises the question whether coupling two SRLs to realize a single optical memory has any advantage over using a solitary SRL, taking into account the obvious disadvantage of a doubled footprint and power consumption. In a recent experimental investigation of coupled SRLs, we have demonstrated that coupling between SRLs can destabilize the system by exciting relaxation oscillations, similar to an optically injected laser system [8]. In Ref. [10], we have pursued a more in-depth theoretical investigation of dynamics induced by the coupling. Similar as in [8], we consider the single waveguide coupling configuration as shown in Fig. 1. The coupling provides the system with two extra degrees of freedom, the coupling strength and the physical distance between the SRLs. The latter is taken into account by defining a coupling phase equal to the optical phase difference accumulated when traveling from one SRL to another. However, explicit time delay effects in the coupling (because of the finite traveling time between the

lasers) are neglected. More details concerning this modelling and the numerical results can be found in Ref. [10].

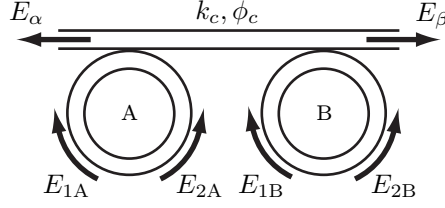


Figure 1: The counterpropagating fields in SRL A (B) are referred to as E_{1A} and E_{2A} (E_{1B} and E_{2B}). The total field at the left (right) output is referred to as E_α (E_β). The coupling amplitude is referred to as k_c , and the coupling phase as ϕ_c .

Model

To model the single waveguide coupled SRLs, we use the rate equation model for a solitary SRL (see e.g. [11, 3]) and modify it to comply with our coupling configuration, as illustrated in Fig. 1. For each SRL X ($X = \{A, B\}$), the model consists of two slowly varying complex envelopes of the counterpropagating waves E_{1X} (CW) and E_{2X} (CCW) and a third equation for the carrier population inversion N_X :

$$\dot{E}_{1A} = \kappa(1 + i\alpha)[g_{1A}N_A - 1]E_{1A} - ke^{i\phi_k}E_{2A} \quad (1a)$$

$$\dot{E}_{2A} = \kappa(1 + i\alpha)[g_{2A}N_A - 1]E_{2A} - ke^{i\phi_k}E_{1A} - k_ce^{i\phi_c}E_{2B} \quad (1b)$$

$$\dot{E}_{1B} = \kappa(1 + i\alpha)[g_{1B}N_B - 1]E_{1B} - ke^{i\phi_k}E_{2B} - k_ce^{i\phi_c}E_{1A} \quad (1c)$$

$$\dot{E}_{2B} = \kappa(1 + i\alpha)[g_{2B}N_B - 1]E_{2B} - ke^{i\phi_k}E_{1B} \quad (1d)$$

$$\dot{N}_A = \gamma[\mu - N_A - g_{1A}N_A|E_{1A}|^2 - g_{2A}N_A|E_{2A}|^2] \quad (1e)$$

$$\dot{N}_B = \gamma[\mu - N_B - g_{1B}N_B|E_{1B}|^2 - g_{2B}N_B|E_{2B}|^2] \quad (1f)$$

where $g_{1X} = 1 - s|E_{1X}|^2 - c|E_{2X}|^2$ and $g_{2X} = 1 - s|E_{2X}|^2 - c|E_{1X}|^2$. The coupling between the SRLs is modeled by a coupling amplitude k_c and a coupling phase ϕ_c . We assume that the travel time between the SRLs is of the same order as the cavity round trip time, so that we can neglect any effects of a delay time. The two coupling sections to couple the light in and out of each SRL introduce an additional $\pi/2$ phase shift [12]. The light that is coupled from one SRL to the other passes through two such couplers. These two phase-shifts add up to π , which explains the minus sign in front of the coupling term. For simplicity, we use identical parameter values for SRL A and B (for the parameter values see Ref. [10]).

Results

We focus on the asymmetric modes of the system, where both SRLs are either both dominantly lasing in the CW direction (A_{cw}) or in the CCW direction (A_{ccw}). When comparing these states, we noticed that the power levels at the β (α) port are comparable, but that the power levels at the α (β) port are higher for the $\phi_c = \pi/2$ than for the $\phi_c = 0$ case. The underlying reason for this is that the inter-SRL phase

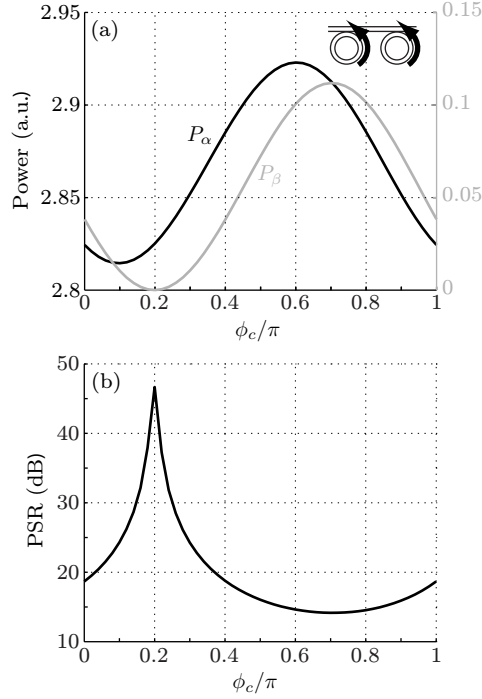


Figure 2: Numerical simulations of Eqs. (1). (a) Steady state power levels at the α -port (left axis, black) and β -port (right axis, red) of the A_{ccw} state as a function of the coupling phase ϕ_c . The minimum value of P_β is 6×10^{-5} . (b) Power suppression ratio (PSR) of the A_{ccw} state as a function of the coupling phase ϕ_c . Parameters values: $k_c = 0.3k$, $\mu = 3$.

difference between the high-power modes remains constant when changing ϕ_c , while the phase difference between the low-power modes changes.

As a result, the relative amount of variation of the power level as a function of ϕ_c is very different at the output ports P_α and P_β . This is illustrated in Fig. 2(a). In this Figure, we have chosen $\mu = 3$. It is clear that while P_α only varies a few percent, P_β ranges from 0.11 to practically zero (6×10^{-5}). This minimum occurs at the point where the phase difference between the low-power modes at the output port, $\chi_1 - \phi_c$, is equal to π , yielding destructive interference (this happens when $\phi_c = 0.2\pi$). Naturally, this causes a sharp peak of 47dB in the power suppression ratio P_α/P_β , as shown in Fig. 2(b). The solitary SRL has a PSR of 18dB at $\mu = 3$ (at the same parameter values). So using two coupled SRLs seems to be advantageous from the viewpoint of PSR. However, since we need to bias two SRLs at $\mu = 3$ to achieve the PSR of 47dB, it is better to compare it with a solitary SRL biased at twice the current $\mu = 6$, which has a PSR of 26dB. This comparison still shows an improved PSR for the coupled case. Nevertheless, the practical advantage of the higher PSR of single waveguide coupled SRLs (as also reported in Ref. [6]) can be argued since it arises rather due to a decrease of the low-power level, than to an increase in the high power level.

Discussion

In Ref. [10], we have shown that weak coupling can have a stabilizing influence on the SRL operating regimes. If the coupling phase ϕ_c is near zero, oscillatory regimes are completely suppressed in the weakly coupled SRLs, even at parameter ranges where solitary SRLs exhibit alternate oscillations. The power level of the high-power port in the asymmetric states is independent of ϕ_c , but the power level of the low-power port is not. The reason for this is that the high-power modes of each SRL impose a fixed inter-SRL phase relationship very close to $-\pi/2$, whatever the value of ϕ_c . The inter-SRL phase difference between the low power modes is therefore slaved and spans the whole $[0, 2\pi]$ interval for ϕ_c going from 0 to π . The interference of the low-power modes of each SRL will hence be destructive or constructive depending on the value of ϕ_c , yielding different power suppression ratios. More insight into these results concerning a system of coupled SRLs can be found in Ref. [10].

References

- [1] M. T. Hill, H. J. S. Dorren, T. de Vries, X. J. M. Leijtens, J. H. den Besten, B. Smalbrugge, Y. S. Oei, H. Binsma, G. D. Khoe, and M. K. Smit. A fast low-power optical memory based on coupled micro-ring lasers. *Nature*, 432(7014):206–209, 2004.
- [2] M. Sorel, P.J.R. Laybourn, G. Giuliani, and S. Donati. Unidirectional bistability in semiconductor waveguide ring lasers. *Appl. Phys. Lett.*, 80(17):3051–3053, 2002.
- [3] L. Gelens, S. Beri, G. Van der Sande, G. Mezosi, M. Sorel, J. Danckaert, and G. Verschaffelt. Exploring multistability in semiconductor ring lasers: Theory and experiment. *Phys. Rev. Lett.*, 102:193904, 2009.
- [4] L. Liu, R. Kumar, K. Huybreghts, T. Spuesens, G. Roelkens, E. Geluk, T. de Vries, P. Regreny, D. Van Thourhout, R. Baets, and G. Morthier. An ultra-small, low-power, all-optical flip-flop memory on a silicon chip. *Nature Photon.*, 4(3):182–187, 2010.
- [5] S. Ishii, A. Nakagawa, and T. Baba. Modal characteristics and bistability in twin microdisk photonic molecule lasers. *IEEE J. Sel. Top. Quant.*, 12(1):71–77, 2006.
- [6] Y. De Koninck, K. Huybrechts, G. Van der Sande, J. Danckaert, R. Baets, and G. Morthier. Nonlinear dynamics of asymmetrically coupled microdisk lasers. In *2009 IEEE LEOS Annual Meeting Conference Proceedings*, volume 1 and 2, pages 503–504, Belek-Antalya, Turkey, 4-8 October 2009.
- [7] J. D. Lin, Y. Z. Huang, Y. D. Yang, Q. F. Yao, X. M. Lv, J. L. Xiao, and Y. Du. Optical bistability in GaInAsP/InP coupled-circular resonator microlasers. *Opt. Lett.*, 36(17):3515–3517, 2011.
- [8] W. Coomans, L. Gelens, G. Van der Sande, G. Mezosi, M. Sorel, J. Danckaert, and G. Verschaffelt. Semiconductor ring lasers coupled by a single waveguide. *Appl. Phys. Lett.*, 100:251114, 2012.
- [9] T. Krauss, P. J. R. Laybourn, and J. Roberts. Cw operation of semiconductor ring lasers. *Electron. Lett.*, 26(25):2095–2097, 1990.
- [10] W. Coomans, G. Van der Sande, and L. Gelens. Oscillations and multistability in two semiconductor ring lasers coupled by a single waveguide. *Phys. Rev. A*, 88:1033813, 2013.
- [11] L. Gelens, G. Van der Sande, S. Beri, and J. Danckaert. Phase-space approach to directional switching in semiconductor ring lasers. *Phys. Rev. E*, 79:016213, 2009.
- [12] D. Marcuse. The coupling of degenerate modes in two parallel dielectric waveguides. *Bell Syst. Tech. J.*, 50(6):1791–1816, 1971.

Nonmagnetic transformation optics for two-dimensional photonic devices

Sophie Viaene,¹ Vincent Ginis,¹ Philippe Tassin,² and Jan Danckaert¹

¹ Applied Physics Research Group, Vrije Universiteit Brussel, B-1050 Brussel, Belgium

² Department of Applied Physics, Chalmers University, SE-412 96 Göteborg, Sweden

In the past decade, some extraordinary devices, e.g., invisibility cloaks, perfect lenses and beam manipulators, have been realized thanks to a new design tool called transformation optics. This technique leads to unprecedented control of optical fields through complex material structures designed according to a predefined coordinate transformation. In order to achieve the intended flow of light without unwanted side-effects, transformation-optical devices must be impedance-matched. Often this leads to designs of sophisticated materials with inhomogeneous and anisotropic permeability and permittivity. In this contribution, we investigate how it is possible to relax the impedance-matching condition in realistic 2D transformation-optical systems.

Transformation optics

The control of macroscopic material parameters, such as the permittivity ϵ and the permeability μ , is of utmost importance in the manipulation of the propagation of light. This is illustrated by Fermat's principle. Observable light trajectories extremize a new measure of length, the optical path length, which is determined by the refractive index profile of the medium through which light is propagating. Therefore, complex materials affect the propagation of light by imposing a new geometry within which light follows an extremal path.

Transformation Optics (TO) extends Fermat's principle to describe the effect of inhomogeneous and anisotropic material parameters on wave propagation [1]. Transformation-optical devices explicitly introduce a nontrivial geometry starting from a metric tensor G , which transforms the perceived distances for light. Light propagates along trajectories of extremal length, called geodesics, which are completely determined by this metric. Thus, a device whose electromagnetic interactions are described by macroscopic Maxwell equations, manipulates light in the same way as an empty space, called physical space, with a geometry G .

To design a metric G and its corresponding device, an auxiliary electromagnetic space is introduced. The electromagnetic space is equipped with its own metric G' and material parameters $\tilde{\epsilon}$ and $\tilde{\mu}$. A coordinate transformation between both spaces links geometries G and G' and maps the fundamental behaviour of light in electromagnetic space to physical space. If electromagnetic space is simply vacuum, the coordinate transformation ensures light will also propagate throughout physical space as if it were in vacuum. This approach is used in cylindrical cloak design [2] to avoid reflections from an object hidden within the device. Even more impressively, if both electromagnetic and physical space contain

a metal sheet, which is flat in electromagnetic space and irregularly curved in physical space, light reflects off this irregular sheet in physical space as if it really encounters a planar metal sheet. In this way a ground plane cloak is constructed, capable of hiding bumps and irregularities in a metal surface [3]. Next to determining fundamental behaviour of light within physical space, form invariance of the macroscopic Maxwell equations under coordinate transformations also predicts the material parameters ϵ and μ of the device

$$\epsilon = \frac{\sqrt{\det G'} \Lambda^T G' \tilde{\epsilon} \Lambda}{\sqrt{\det \Gamma} \det \Lambda}, \quad (1)$$

$$\mu = \frac{\sqrt{\det G'} \Lambda^T G' \tilde{\mu} \Lambda}{\sqrt{\det \Gamma} \det \Lambda}, \quad (2)$$

where the Jacobian of the transformation Λ , the metric G' and electromagnetic space material parameters $\tilde{\epsilon}$ and $\tilde{\mu}$ clearly influence the design.¹ The remainder of this contribution considers two-dimensional transformation-optical devices. These devices have one normal coordinate that does not mix with the remaining planar coordinates during the transformation, as for beam bends, beam splitters and the cylindrical cloak.

Two-dimensional transformation-optical devices

The field of photonic circuitry [4] has led to innovative two-dimensional waveguiding schemes and surface plasmon optical devices. Two-dimensional circuits require structures capable of sustaining surface waves, such as metal-dielectric interfaces or graphene sheets. Transformation optics (TO) is a valuable tool to guide and optimize component designs. In particular, TO might reduce decoupling losses of conventional beam benders and beam splitters inherent to confined waveguides. To our knowledge, two interesting developments ([5] and [6]) extend TO to two-dimensional systems.

Huidobro *et al.* [5] applied the TO framework to a metal-dielectric interface to investigate the relative importance of metals and dielectrics on material parameters. Because TO predicts bulk, three-dimensional permittivity and permeability distributions, an ideal design includes metamaterials both in the dielectric and the metal side of the interface. These regions include several decay lengths of the evanescent surface wave in order to capture all electromagnetic energy. Since form-invariance of macroscopic Maxwell equations is required for TO to be applicable, the dimensions of metamaterial structures in the metal need to be much smaller than its skin depth. To simplify fabrication, the authors limit manipulation of material parameters to the dielectric side of the interface (Figure 1) and compare the resulting wave propagation with full TO simulations.

Both the geometry and the decay length in the dielectric affect the efficiency of the device. Long decay lengths yield very good results since the energy mostly resides within the dielectric and the metal's contribution is negligible. Functionalities are excellently conserved in the telecommunication window ($\lambda \approx 1.5 \mu\text{m}$), but not very good at optical wavelengths ($\lambda \approx 600 \text{ nm}$). Some geometries that naturally require a metal interface in order to function, e.g. the ground plane cloak, do not suffer from the restricted implementation while others, such as the cylindrical cloak, suffer greatly from the discontinuous

¹ Additionally, the metric Γ is introduced to correct for coordinates used to describe the device in physical space.

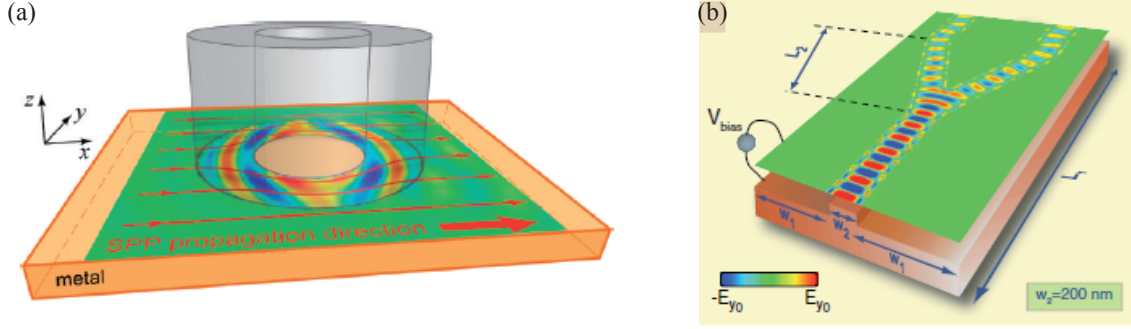


Figure 1: (a) A two-dimensional cylindrical cloak for surface plasmon polaritons on a metal-dielectric interface. Figure reproduced from reference [5]. (b) A two-dimensional beam splitter on graphene. Figure reproduced from reference [6].

metal interface.

A second interesting contribution concerns propagation manipulation of TE or TM on a graphene sheet [6]. The conductivity $\sigma = \sigma_r + i\sigma_i$ of graphene is spatially modulated by an externally applied field through changes in the chemical potential. A spatially varying external voltage or a constant voltage applied to a substrate with inhomogeneous permittivity distribution, induces a designed conductivity distribution to manipulate light propagation with high accuracy (Figure 1). More specifically, the imaginary part σ_i might be positive, acting as a dielectric sustaining a TM mode, or negative, acting as a metal and prohibiting a TM mode on the sheet. The conductivity pattern selects those regions where TM waves are allowed to propagate, leading to many applications such as TM beam splitters, perfect TM mirrors or subwavelength lenses. Next to the design of macroscopic devices, conductivity distributions are also useful to construct two-dimensional IR metamaterials. Instead of conventional resonating circuits or nanoparticle equivalents of lumped circuits [7], local fields are tuned by conductivity variations. Patches of negative σ_i might, for example, act as scatterers, similar to metallic nanoparticles.

Nonmagnetic two-dimensional systems

The fundamental trade-off between confinement and propagation length of surface waves implies that not every material is capable of sustaining long-range surface waves. Despite desirable properties, such as conductivity tunability and confinement of graphene, its propagation length at terahertz frequencies is too small for propagating applications [8]. Those applications require metal-dielectric or purely dielectric devices with long decay constants. In addition, equation (2) shows that TO devices inherently need magnetic response to satisfy material parameters linked to a coordinate transformation. Since materials are mostly nonmagnetic at high frequencies, metamaterials need to have resonating structures [9], such as Split Ring Resonators or Fishnet Structures, to obtain the desired magnetic response. The dispersion associated to these resonators leads to significant losses and limits operating frequencies.

Omitting magnetic responses has serious consequences. For a cylindrical cloak, impedance-matched parameters ensure waves propagate throughout the device without reflections

despite inhomogeneous permittivity and permeability variations. Without magnetic response, impedance-matching is violated and reflections would indicate the presence of an object hidden inside. Still, there are several approaches to relax relations (1) and (2).

Coordinate transformations are often optimized to decrease material parameter anisotropy. If optimization results in (quasi)conformal coordinate transformations, a single refractive index distribution describes all responses of the device. This approach is frequently used at optical frequencies, e.g., for a planar cloak [10], because magnetic responses of resonators saturate at optical frequencies. However, two-dimensional devices are inherently anisotropic because of the distinction between normal and planar coordinates. Another way to simplify material parameters, consists of choosing a polarization, TE or TM, for which the device is optimized. In the case of a cylindrical cloak [2], all electric field components different from the normal coordinate are set to zero. Six independent material parameters reduce to three, namely one permittivity component and two magnetic susceptibility components. Finally, the ray approximation regime uses slow variations in material parameters with respect to the wavelength to simplify the TO device in two ways. From a theoretical point of view, matching dispersion relations between the simplified device and the TO device is sufficient to match ray trajectories of both devices. From a practical point of view, slow material variations enable stacked homogeneous slices to approximate the continuous distribution inducing minor reflections and maintaining functionalities.

Acknowledgments

Work at VUB was supported by the Belgian Science Policy Office (IAP-Photonics@be, grant IAP P7-35) and by the FWO-Vlaanderen. V.G. is a Ph.D. Fellow of the Research Foundation-Flanders (FWO-Vlaanderen).

References

- [1] U. Leonhardt and T.G. Philbin, "Transformation Optics and the Geometry of Light", *Progress in Optics*, vol. 53, pp. 69-152, 2009.
- [2] D. Schurig *et al.*, "Metamaterial Electromagnetic Cloak at Microwave Frequencies", *Science*, vol. 314, pp.977-980, 2006.
- [3] J. Li and J.B. Pendry, "Hiding under the Carpet: A New Strategy for Cloaking", *Physics Review Letters*, vol. 101, 203901, 2008.
- [4] T.W. Ebbesen, C. Genet and S.I. Bozhevolnyi, "Surface-plasmon circuitry", *Physics Today*, vol. 61, pp. 44-50, 2008.
- [5] P.A. Huidobro *et al.*, "Transformation Optics for Plasmonics", *Nano Letters*, vol. 10, pp. 1985-1990, 2010.
- [6] A. Vakil and N. Engheta, "Transformation Optics Using Graphene", *Science*, vol. 332, pp. 1291-1294, 2011.
- [7] N. Engheta, "Circuits with Light at Nanoscales: Optical Nanocircuits Inspired by Metamaterials", *Science*, vol. 317, pp. 1698-1702, 2007.
- [8] P. Tassin, T. Koschny and C.M. Soukoulis, "Graphene for Terahertz Applications", *Science*, vol. 341, pp. 620-621, 2013.
- [9] T. Koschny, L. Zhang and C. Soukoulis, "Isotropic three-dimensional left-handed metamaterials", *Physical Review B*, vol. 71, 121103(R), 2005.
- [10] T. Ergin *et al.*, "Three-dimensional Invisibility Cloak at Optical Wavelengths", *Science*, vol. 328, pp. 337-339, 2010.

Single contact double-waveguide SOAs in AWG-based lasers fabricated on InP generic photonic integration platform

K. Ławniczuk,^{1,2} M. J. Wale,^{1,3} P. Szczepański,^{2,4} R. Piramidowicz,²
M. K. Smit,¹ and X. J. M. Leijtens¹

¹ Photonic Integration Group, Eindhoven University of Technology, P.O. Box 513,
5600 MB Eindhoven, the Netherlands; k.lawniczuk@tue.nl

² Institute of Microelectronics and Optoelectronics, Warsaw University of Technology,
Koszykowa 75 Str. 00-662 Warsaw, Poland

³ Oclaro Technology Ltd., Caswell, Towcester, Northamptonshire, NN12 8EQ, United Kingdom

⁴ National Institute of Telecommunications, Szachowa 1, 04-894 Warsaw, Poland

By implementing SOAs that guide two waveguides through a single contact active section, we can reduce dimensions of photonic integrated circuits (PICs) and decrease the number of electrical contacts of current injection. In this paper we demonstrate linear 4-channel and 8-channel AWG-based lasers that take advantage of such SOAs. This resulted in a reduction of the required number of active regions and contacts by a factor two. Measurements showed that these sources operate with an output power of 1 mW per AWG-channel and side-mode suppression ratio better than 40 dB. The lasers were fabricated in a multi-project wafer run on an indium phosphide (InP)-based generic photonic integration platform.

AWG-based lasers

Multiwavelength sources that emit light simultaneously at different wavelengths can be successfully realized using arrayed waveguide gratings (AWGs) [1-2]. While AWG-based lasers (AWGLs) can be realized in many configurations, the most common is the linear configuration. In this configuration a separate semiconductor optical amplifier (SOA) is dedicated to each generated wavelength and thus for each AWG passband [3]. Biasing more than one SOA at the same time will result in simultaneous lasing at several channels. The AWG acts as an intra-cavity filter in the lasers and might be used as a multiplexer of the generated optical signals. In these devices the number of SOAs in the laser array scales linearly with the number of required operational channels.

One of the methods to reduce the number of SOAs in the array by a factor two and reduce the size of PICs is by implementing single contact double-waveguide SOAs. These components guide two waveguides, corresponding to two AWG passbands, through a single active section. The operation principle of the sources remains unchanged. In this configuration we obtain compact multiwavelength sources with

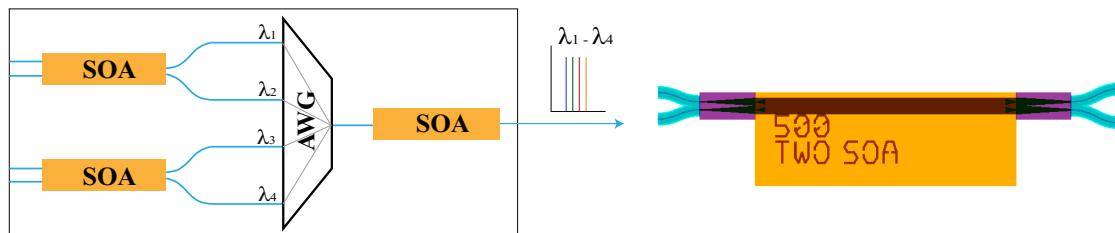


Fig. 1. Schematic of an AWG-based laser (left) and mask layout of the double-waveguide SOA (right).

easier driving mechanism, due to the reduction of the number of contacts requiring current injection.

In this paper we present linear 4-channel and 8-channel AWGLs that take advantage of a novel design with single contact double-waveguide SOAs. The devices were processed on an InP-based platform that allows for monolithic integration of active and passive components. The sources were realized following the generic integration concept [4] and fabricated in cooperation with an industrial foundry partner [5] in a multi-project wafer (MPW) run [6].

Design and fabrication of AWG-based lasers

Generic integration on InP-based photonics platforms enables designing and fabricating of functionally advanced photonic integrated circuits (PICs), yet utilizing only a limited set of components called building blocks (BBs) [4], [6]. We developed our AWGLs using three elementary BBs: (1) deeply etched passive waveguide structures, (2) shallowly etched SOAs and (3) low-loss deep-shallow transition elements that were inserted between the SOA and each waveguide. The SOAs with double-waveguide geometry were offered by the foundry [5] as parameterized BBs. The schematic of such AWGL and the mask layout of the single contact double-waveguide SOA are presented in Figure 1. As can be seen, two lasing channels operating in two AWG-passbands can be activated using only a single contact on the double-waveguide amplifier.

The fab that carries out the MPW runs, such as the one in which the AWGLs were fabricated, uses integration processes that were developed over many years and that are used commercially for the fabrication of devices such as tunable laser-Mach-Zehnder PICs employed in tunable XFP-format transceivers [5]. The technological process utilizes six MOVPE epitaxial growth stages for: source wafer growth with InGaAsP multi-quantum well (MQW); bulk quaternary Q1.42 tuning section infill; strong waveguide infill; spot-size converter (SSC) and upper confinement layer overgrowth. Gain regions are defined by dielectric patterning and subsequent etch processes. Infill stages use a selective growth approach, where a dielectric mask is used as a non-growth barrier. The waveguide ridge for the amplifier is formed by dry and wet etching following the overgrowth stage. The etch depth is controlled by the material structure and is limited by an etch-stop layer. Strong ridge formation is done by dry etching. Following deposition and definition of a dielectric isolation layer, the p-contact metal is sputtered and annealed in order to provide low contact resistance. Gold bond pads are deposited onto the p-metal to enable efficient current injection and heat dissipation.

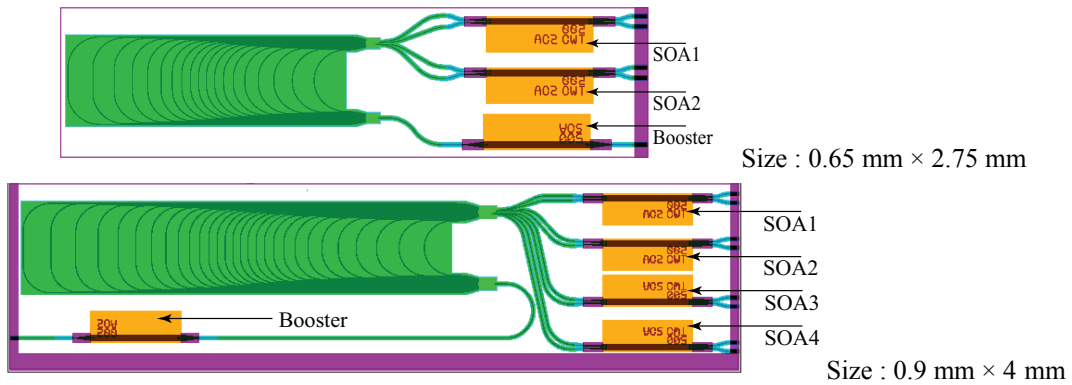


Fig. 2. Mask layout of 4-channel (*top*) and 8-channel (*bottom*) AWG-based lasers.

The layouts of the 4-channel and 8-channel AWGLs are presented in Figure 2, with indicated SOAs and boosters. Both AWGs were designed for a central wavelength $\lambda_c = 1550$ nm with a channel spacing $\Delta\lambda = 200$ GHz (1.6 nm) in case of the 4-channel device and $\Delta\lambda = 100$ GHz (0.8 nm) in case of the 8-channel device. The free spectral ranges (FSRs) of the 4-channel and 8-channel sources are 800 GHz and 900 GHz respectively. The length of each SOA is 500 μm . The AWG laser dimensions are 0.65 mm \times 2.75 mm (4-channel device) and 0.9 mm \times 4 mm (8-channel device).



Fig. 3. Wire-bonded 4-channel AWGL on measurement setup. The device was placed in a 2 mm \times 4 mm cell.

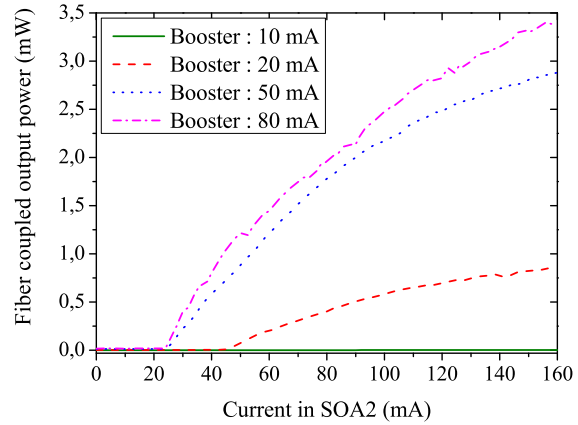


Fig. 4. *LI* characteristics of 4-channel AWGL, for SOA2, and for different currents in the booster.

Measurement results

The devices were mounted on a ceramic submount and wire bonded to external DC pads to ease access to the SOA contacts. A lensed fiber was used to couple the light out from the chip. A high resolution (0.16 pm) Optical Spectrum Analyzer, APEX P2041A, was used to record the spectra. The devices were measured at room temperature. A photograph of the 4-channel AWGL on a measurement setup is presented in Figure 3. The threshold currents of the AWGLs depend on the current applied to the booster amplifier. This is because the booster was implemented within the laser cavity and at the output waveguide coupler. The results of experiment performed on SOA2 of 4-channel AWGL are shown in Figure 4. The threshold current is less than 25 mA while biasing the booster with 50 mA. The threshold currents measured for each SOA of the 8-channel AWG laser are less than 35 mA, while biasing the booster with 50 mA.

The spectral characteristics of 8-channel AWGL measured while biasing the booster with 80 mA are demonstrated in Figure 5. During our first experiments we obtained a single-mode operation for AWG passbands in the case of 3 out of 4 double-waveguide SOAs. By biasing one double-

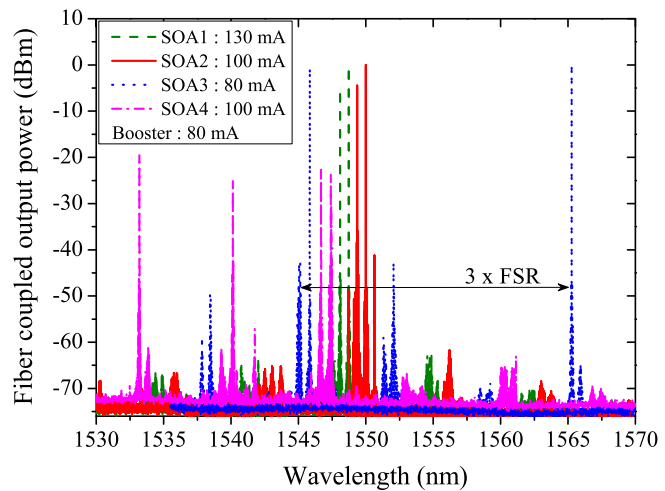


Fig. 5. Spectral characteristics of the 8-channel AWGL. By activating one double-waveguide SOA we obtain laser operation on two AWG passbands.

waveguide SOA we achieved double AWG channel operation of the lasers. The detected output power in the fiber was in the range of 1 mW per AWG passband with a side mode suppression ratio (SMSR) better than 40 dB. The channel spacing between adjacent signals ranged from 0.64 nm to 0.85 nm. The variation is caused by the relatively long cavity resulting in closely spaced longitudinal modes. The presented source also reveals operation on FSR orders different than the central FSR, which can be suppressed for example by introducing wavelength selective mirrors, such as distributed Bragg reflector (DBR)-based gratings.

Summary and further work

We demonstrated novel AWG-based lasers that use single-contact double-waveguide SOAs. The devices were fabricated on a generic InP-based platform. The obtained size of the array of the SOAs is twice smaller when compared to other linear configurations of AWG sources, which makes these components and devices promising for further utilization. The first characterization results show a good performance of the multiwavelength sources. The detected output power is in the range of 1 mW per activated AWG passband with a SMSR better than 40 dB. Operation in a single order of the AWG can be ensured in a next design, by using wavelength-selective mirrors or by chirping the waveguide grating.

Future work concerns a detailed spectral characterization of the sources and focuses on a theoretical analysis of single contact double-waveguide SOAs in lasers.

Acknowledgement

The authors would like to thank Christophe Kazmierski from Alcatel-Thales III-V labs (Marcoussis, France) for mounting and wire-bonding of the AWG-based lasers.

The research leading to these results has received funding from EU FP7/2007-2013 grant agreement no 228839: EuroPIC [7] and from the Dutch Ministry of Economic Affairs through the Smartmix project Memphis [8].

References

- [1] M. Zirngibl and C. Joyner, "12 frequency WDM laser based on a transmissive waveguide grating router," *Electron. Lett.*, vol. 30, no. 9, pp. 701–702, 1994.
- [2] K. Ławniczuk, R. Piramidowicz, P. Szczepański, P.J. Williams, M.J. Wale, M.K. Smit and X.J.M. Leijtens, "8-channel AWG-based multiwavelength laser fabricated in a multi-project wafer run," *Proc. 23rd Int. Conf. Indium Phosphide and Related Materials*, Berlin, Germany, 22-26 May (2011).
- [3] C. Doerr, C. Joyner, and L. Stulz, "40-wavelength rapidly digitally tunable laser," *IEEE Photon. Technol. Lett.*, vol. 11, no. 11, pp. 1348–1350, Nov. 1999.
- [4] M. Smit, X. Leijtens, E. Bente, J. van der Tol, H. Ambrosius, D. Robbins, M. Wale, N. Grote, M. Schell, "Generic foundry model for InP-based photonics," *IET Optoelectron.*, vol. 5, no. 5, pp. 187–194, 2011.
- [5] Oclaro Technologi Ltd., <http://www.oclaro.com/>.
- [6] X. Leijtens, "Jeppix: the platform for indium phosphide-based photonics," *IET Optoelectronics*, vol. 5, no. 5, pp. 202–206, 2011.
- [7] EuroPIC, European Manufacturing Platform for Photonic Integrated Circuits, <http://europic.jepix.eu>.
- [8] Memphis, Merging Electronics and Micro & Nano-Photonics in Integrated Systems, <http://www.smartmix-memphis.nl>.

Wavelength-driven positioning of a trapped particle on a photonic crystal waveguide

M.M. van Leest and J. Caro

Kavli Institute of Nanoscience Delft and Department of Imaging Science and Technology
Delft University of Technology, Delft, The Netherlands

We demonstrate novel discrete positioning of a microparticle optically trapped on a tapered Si photonic crystal waveguide. Upon sweeping the wavelength in a range beyond pinch-off for transmission, we observe trapping at specific positions. When the wavelength is swept up, it hops towards the wider side of the waveguide. When it is swept down, it hops in the reverse direction, the stable trapping positions being the same. The spacing between the positions equals the lattice constant of the crystal. FDTD simulations and force calculations allow interpretation of the phenomenon, which arises from the special slow-light mode of the waveguide.

Introduction

In the field of biophotonic sensing optical manipulation of micro- and nanoparticles with on-chip photonic structures receives increasing attention [1], to overcome disadvantages of optical tweezers [2] such as big size and high costs. In this integrated photonics approach optical trapping and propulsion of particles are basic functionalities. Important examples of trapping devices giving static trapping sites are dual-waveguide traps [3], plasmonic evanescent field traps [4] and photonic crystal cavities [5,1]. Trapping and subsequent particle propulsion can be accomplished using the evanescent field of ridge waveguides [6] and slot waveguides [7]. In these structures the evanescent field gives rise to trapping via the gradient force, while propulsion is induced by the scattering force arising from scattering of the propagating waveguide mode at the trapped particle. A new playground in this context are photonic crystal waveguides in a photonic crystal slab. Such a waveguide is a line defect in the crystal. Its characteristics can be engineered to give special properties of the waveguide mode, such as slow light [8] and light localization [9]. These effects can be used for manipulation of a particle trapped on the waveguide. In this contribution we demonstrate and interpret novel wavelength-driven discrete positioning of a particle optically trapped on a tapered W1 waveguide in a Si photonic crystal slab.

Tapered photonic crystal waveguide

The device is fabricated in the 200 nm thick Si layer of silicon-on-insulator material, using e-beam lithography and dry etching. We use a triangular hole-type photonic crystal of lattice constant $a=430$ nm and $r/a=0.3$ (r =hole radius). The waveguide in the crystal is very similar to a W1 waveguide, the difference being that its width is accurately tapered down with 2 nm per 430 nm, giving a tapering angle of 0.26 degree. A 50 μ m wide and 30 μ m deep fluidic channel is built on the chip using a dry resist technique. Water with dispersed 1 μ m diameter polystyrene beads can be flown perpendicularly and with a controlled velocity across the waveguide, so that a trapping situation is created. In Fig. 1 a scanning electron microscope (SEM) picture of the device is shown, limited to the central device region.

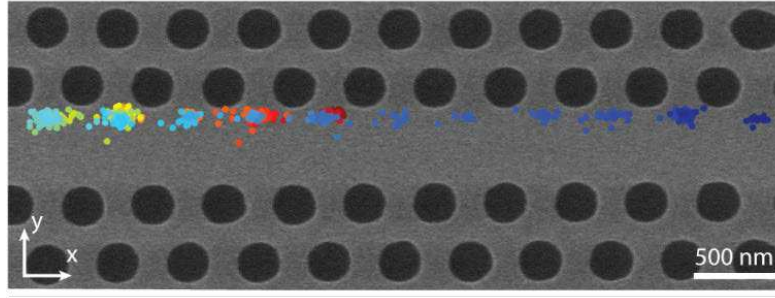


Fig. 1. SEM picture of the tapered W1 photonic crystal waveguide. Picture taken after underetching of the crystal. The waveguide tapers down in width from left to right with 2 nm per lattice constant ($a=430$ nm). The dots superimposed on the picture represent a 2D scatter plot of tracked positions of a trapped polystyrene bead, derived from the frames of a movie recorded while sweeping the wavelength down and up. The color of the dots indicates the time order in which they were taken (blue to red is initial to final).

From in-plane transmission measurements in water with TE-polarized laser light we find that the waveguide supports a range of wavelengths in the photonic band gap, with on the long wavelength side a pinch-off wavelength $\lambda_{p,0}$ of about 1560 nm. In the experiments we couple light of wavelengths just above $\lambda_{p,0}$ (1564-1604 nm) and with a power on the order of one mW into the broad waveguide entrance, so that it propagates into the taper.

Trapping and wavelength-driven positioning of particles

In a trapping experiment a steady water flow (≈ 5 $\mu\text{m/s}$) with beads is passed over the waveguide, while recording the top-view microscope observation. We can clearly observe optical trapping of an individual bead on the waveguide for wavelengths above $\lambda_{p,0}$ when it enters the evanescent field. Being trapped, the bead hovers at the trapping site with small excursions, indicating confined Brownian motion. When the laser is switched off, the bead is immediately released into the flow, confirming that we observe optical trapping and not adhesion to the surface.

We observe a very special sequence of trapping events upon sweeping the excitation wavelength, *viz.* an already trapped bead repeatedly hops to an adjacent stable trapping position for every 1.6 nm wavelength change. Hopping is towards the wide side of the waveguide with increasing wavelength and the narrow side with decreasing wavelength. When changing direction of the repositioning of the bead (*i.e.* sweep direction), the effect shows hysteresis in wavelength. Snapshots of a movie of a trapping sequence are given in Fig. 2. On the movie we perform a tracking analysis of the

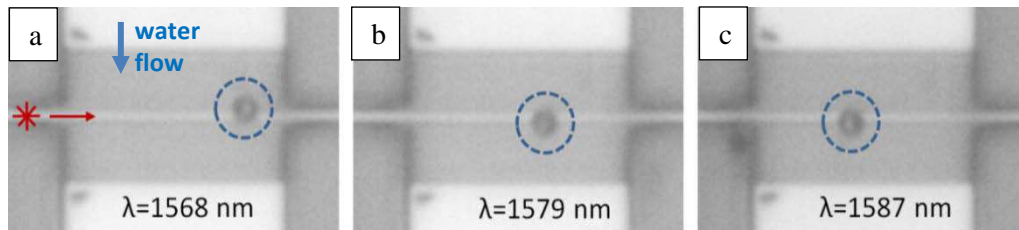


Fig. 2. Snapshots (a-c) of a movie of a trapping sequence of a polystyrene bead (encircled, $d=1$ μm) on the tapered waveguide, showing the systematic shift of the stable trapping position to the left (*i.e.* wider waveguide side) with increasing wavelength. For wavelengths in between the stated values the bead visited several intermediate sites. Water-flow direction is as indicated. In a) the trapping position is slightly offset with respect to the waveguide axis in the positive y -direction, in b) and c) in the negative y -direction.

particle position. A typical scatter-plot result is shown in Fig. 1, superimposed on the waveguide. The positions of the bead show up as small and clearly separated clouds of tracked positions. The clouds reflect confined Brownian motion of the bead in a trapping potential. To emphasize the discrete positioning, the data have been reduced in Fig. 3 to a plot of the particle's trapping position versus the frame number of the movie. The plateaus in Fig. 3 are equidistant, with a spacing to a high degree of accuracy (1%) equal to the lattice constant of 430 nm. We conclude that we measure wavelength-driven lattice-quantized positioning of the bead. In connection to Fig. 2, we further note that the trapping positions are displaced with respect to the centerline of the waveguide. This effect is not biased by the flow of the water as is apparent from the figure, where it can be seen that the stable trapping position can be on either side of the centerline.

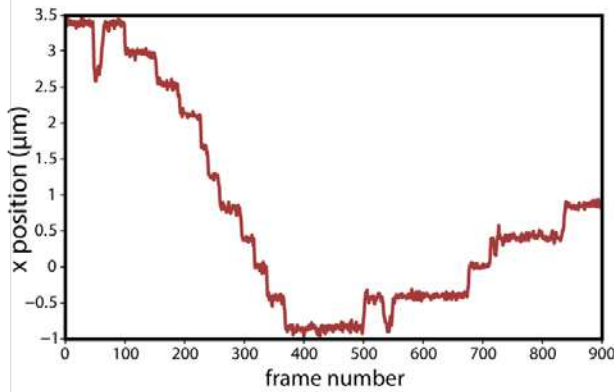


Fig. 3. Traced position of the trapped bead on the waveguide in the x -direction versus frame number of the movie (frame rate 30 fps, total time span 30 s), showing quantized positioning with a stepsize of 430 nm. In time, the wavelength was first swept up and then down, so that the bead moves to larger x -positions after a minimum.

Interpretation and discussion

To interpret these results, we perform finite-difference time domain (FDTD) simulations of the light in the waveguide, in dependence of the excitation wavelength. An example of a resulting mode in the waveguide for $\lambda=1578$ nm, represented by the electric field energy, is given in Fig. 4. It is seen that the light penetrates into the waveguide up to a stop point, where a local resonance occurs with properties similar to a resonance of a photonic crystal cavity. From calculations of the photonic band structure of the waveguide, which we model by a concatenation of constant width sections, we derive that the resonance arises as a result of operation of the waveguide in the slow-light regime. For each waveguide width a specific photonic band comes into play, in particular a mode of that band close to the Brillouin zone boundary, where $d\omega/dk \rightarrow 0$ (group velocity becomes very low). This mode can only penetrate into the waveguide up to a distance determined by the width-dependent band index of the mode. As a result of spatial compression of the slow light and reflection of the mode at the stop point, a resonance due to interference builds up. Via the width dependence of the bands, the resonance position depends continuously on wavelength. For the resonance we find from simulations a field (ϵE^2) enhancement factor of about 45 with respect to the value at the entrance of the waveguide. This property of field enhancement suggests a strong gradient force exerted on a particle, making it likely that trapping occurs at the position of the resonance, as we observe.

To understand the quantized positioning, we use the the Maxwell stress-tensor method to calculate the trapping force exerted on the bead. We simulate the force for 20 bead positions in the xy -plane 4 nm above the surface, near the symmetry axis ($x,y=0$) and for various wavelengths. We find a calculated stable trapping position or a potential

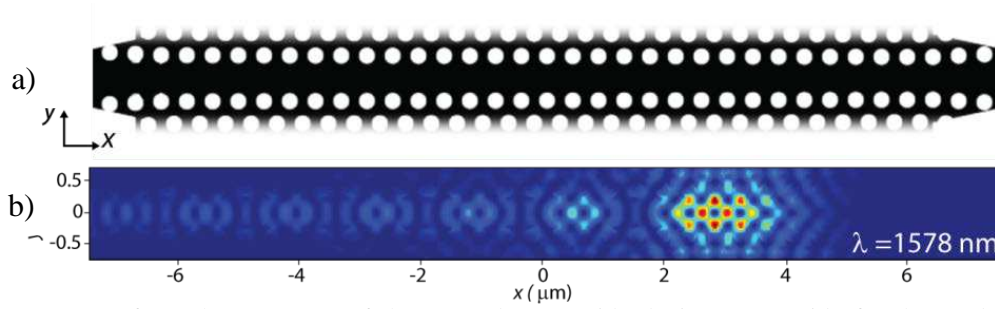


Fig. 4. (a) Cut from the geometry of the tapered waveguide device, as a guide for the mode profile below. (b) Mode profile ϵE^2 for $\lambda = 1578$ nm, showing the prominent resonance at the stop point. The sub-resonances occurring left from the main resonance are part of the total mode interference pattern

well near $(x, y) = (0 \text{ nm}, 110 \text{ nm})$, slightly shifted in the positive y -direction with respect to $y=0$. During a wavelength downsweep of 1.5 nm, the initial well is gradually weakened and a second well is created (double-well potential), finally giving a shift of the resonance region over one lattice constant. Upon completion of this shift, the gradient force pulls the particle in the newly created well at $(x, y) = (430 \text{ nm}, 110 \text{ nm})$. This result closely agrees with the observed quantized positioning.

Conclusion

In conclusion, we demonstrate wavelength-driven lattice-quantized positioning of a polystyrene bead trapped on a tapered photonic crystal waveguide. For every 1.6 nm wavelength change, the trapped bead is controllably moved over a distance of the lattice constant. This effect arises from a local resonance, built up from interference of an incoming and spatially compressed slow-light mode and its reflection. By calculating the wavelength-dependent optical force on the bead, we find that its interaction with the shifting resonance leads to stable trapping positions one lattice constant apart, as measured.

References

- [1] D. Erickson *et al.*, “Nanomanipulation using near field photonics”. *Lab Chip* **11**, 995-1009, 2011.
- [2] K.C. Neuman and S.M Block, “Optical Trapping”, *Rev. Sci. Instrum.* **75**, 2787-2809, 2004.
- [3] M.M. van Leest, F. Bernal Arango and J. Caro, “Optical forces and trapping potentials of a dual-waveguide trap based on multimode solid-core waveguides”, *JEOS Rap. Public.* **6**, 11022, 2011.
- [4] M.L. Juan *et al.* “Plasmon nano-optical tweezers”, *Nature Photon.* **5**, 349-356, 2011.
- [5] T. van Leest and J. Caro, “Cavity-enhanced optical trapping of bacteria using a silicon photonic crystal cavity”, *Lab Chip* **13**, 4359-4365, 2013.
- [6] S. Gaugiran *et al.*, “Optical manipulation of microparticles and cells on silicon nitride waveguides”, *Optics Express* **13**, 6956-6963, 2005.
- [7] A.H.J. Yang *et al.*, “Optical manipulation of nanoparticles and biomolecules in sub-wavelength slot waveguides”, *Nature* **457**, 71-75, 2009.
- [8] T.F. Krauss, “Slow light in photonic crystal waveguides”, *J. Phys. D: Appl. Phys.* **40**, 2666-2670, 2007.
- [9] T. Baba *et al.* “Light localizations in photonic crystal line defect waveguides”, *IEEE J. Quant. Electron.* **10**, 484-491, 2004.

On-chip Raman spectroscopy with a Triplex dual-waveguide trap

M. Boerkamp,¹ J. T. Heldens,¹ T. van Leest,¹ A. Leinse,² M. Hoekman,²
R. Heideman,² and J. Caro¹

¹ Kavli Institute of Nanoscience Delft, Department of Imaging Science and Technology of TU Delft and Wetsus, The Netherlands

² LioniX B.V., Enschede 7522, The Netherlands

We present a new approach to on-chip Raman spectroscopy based on the dual-waveguide trap geometry. In the device counter-propagating interfering beams emanate from opposing TripleX waveguides to produce a confined optical field in a fluidic channel. The field is used to induce optical trapping of microparticles supplied by a flow. The transparency window of TripleX allows application of the standard Raman wavelength of 785 nm, thereby making an additional laser path for Raman excitation redundant. With the device we generate Raman spectra of trapped polystyrene beads and bacterial spores. This approach is promising for on-chip fingerprinting of bacteria and other cells.

Introduction

There is a strong interest in lab-on-a-chip devices capable of identifying biological samples, including devices that make use of Raman spectroscopy. This technique already has many off-chip applications to identify biological samples. With Raman spectroscopy one measures the chemical composition of the sample by obtaining information on its molecular vibrations which can therefore yield a spectroscopic fingerprint [1]. Samples need to be kept stationary during a Raman measurement and for small samples, such as single cells, this can be achieved by using laser light in a technique called optical trapping. Off-chip this is often performed by creating a tightly focussed laser beam [2] or by opposing two laser beams [2, 3], whilst on-chip waveguides [4] or photonic crystal cavities [5, 6] are used. Using the trapping light for Raman generation is a method called Laser Tweezers Raman Spectroscopy (LTRS) [7]. On-chip trapping and Raman generation could be performed by using two opposing waveguides as a dual-beam optical trap as first proposed by van Leest *et al.* [8] where simulations were shown of the trapping potential of such a device. So far, one device has been reported on that uses an integrated dual-beam optical trap consisting of opposing waveguides [4, 9]. The reported devices are very well capable of optical trapping [4, 9], however, the waveguide material Ta₂O₅ is not transparent for the Raman wavelength 785 nm and cannot use the trapping light for Raman excitation and requires an additional off-chip Raman laser. Furthermore, Ta₂O₅ is a research material in photonics and therefore not suitable for mass-production.

We now report on a dual-waveguide device capable of optical trapping and Raman generation. The dual-waveguide device is fabricated in TripleX waveguide technology [10, 11]. TripleX waveguides are highly transparent in the visible and NIR range (405-2350 nm), contrary to other waveguide materials, such as SOI, InP and Ta₂O₅. As a result, the standard Raman wavelength of 785 nm can be used for the trapping light, in

contrast with [9]. TripleX is an established waveguiding platform [11] and is suited for mass-production and compatible with CMOS technology.

Methodology

The dual-waveguide device consists of a fluidic channel, an entry waveguide and a Y-junction splitting the waveguides into two semi-circles which terminate oppositely in the walls of the integrated fluidic channel (see Figure 1a). The waveguide has a base and top width of 1.1 and 1.0 μm , respectively, and height of 1.0 μm (see Figure 1c) and consists of 50 nm thick Si_3N_4 and an inner region of SiO_2 . The fluidic channel is 5 μm wide and 15 μm long, which tapers up to 1 mm wide in two steps (see Figure 1b) and is created by dry etching successively through the upper cladding (12 μm SiO_2), the waveguide and the lower cladding (8 μm SiO_2). Finally, the fluidic channel is sealed by bonding onto the structure a glass wafer with pre-etched holes for access to the fluidic channel.

Laser light of 785 nm is coupled via a single mode polarization maintaining fibre, butt coupled to the TripleX input waveguide, exciting the lowest TE mode. An immersion objective placed above the optical trap collects the Raman photons. Polystyrene beads of 1 μm diameter or bacterial spores (*Bacillus Subtilis*) dispersed in water are made to flow through the channel with a syringe pump. Flow velocities for the experiments, in the range 7 - 90 $\mu\text{m}/\text{s}$, are obtained by stabilizing the flow without pump activity.

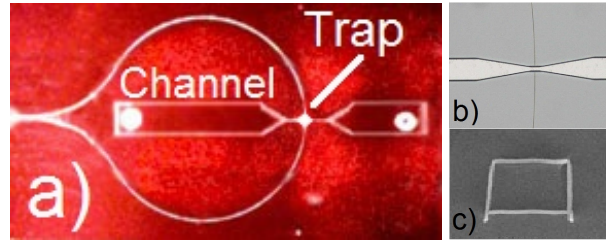


Figure 1: a) the integrated Raman trapping device fabricated in TripleX waveguide technology. A Y-junction splits the entry waveguide into half-circular arms (diameter = 7mm) that terminate in the walls of the fluidic channel. b) The middle tapered section of the fluidic channel with opposing waveguides (top and bottom). c) Cross-section of a TriPLeX waveguide.

Dual-waveguide optical trapping and Raman spectroscopy

Using the light from the opposing waveguides, we have demonstrated optical trapping of polystyrene beads that are transported through the fluidic channel. Stable trapping can be performed for at least 10 minutes, provided that there is no collision with another bead transported through the fluidic channel. One or more beads can be trapped at one given time. These multiple beads are usually trapped in a necklace perpendicular to the flow direction. Images of one or more beads trapped are shown in Figure 2.

The light in the trap can be used to generate Raman photons off the trapped particles. Therefore, we have studied the capability of using our device for on-chip Raman Spectroscopy by measuring photons inelastically scattered from trapped single polystyrene (PS) beads or bacterial spores (*Bacillus Subtilis*) with a spectrometer. This is first demonstrated by the measured spectra of PS shown in Figure 3a, taken for five different integration times in the range of 0.25 - 15 s. We observe that with increasing integration time

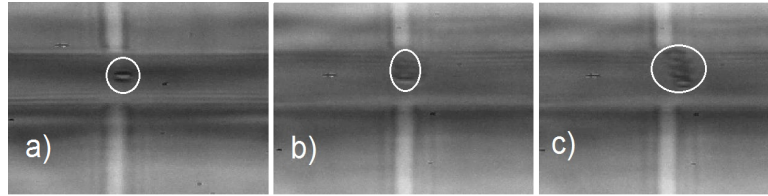


Figure 2: Trapped beads inside the fluidic channel (left to right) between the waveguides (top and bottom).

distinctive peaks develop in the spectra. The labeled peaks in Figure 3a agree with the literature values. The peaks at 1003 and 1033 cm^{-1} are clearly discernible for an integration time as short as 0.25 s . This is useful for experiments concerning fingerprinting of bio-objects such as single cells, that have a relatively weak Raman signal and therefore will unavoidably lead to longer integration times. In addition, we have trapped and measured bacteria spores, the spectrum is shown in Figure 3b. Bacteria spores are more difficult to trap due to their lower refractive index and higher transparency. This unavoidably leads to longer integration times, which in this case is 10 minutes. However, the obtained spectrum is a first of its kind in on-chip trapping and Raman generation and could lead to a multitude of applications, including on-chip biological Raman identification.

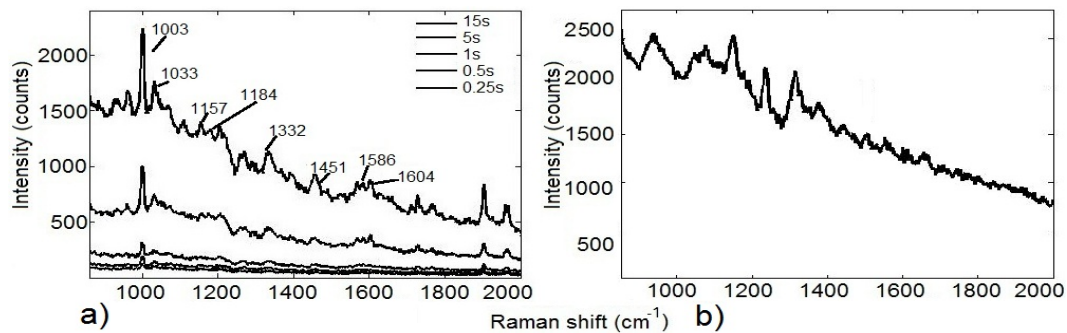


Figure 3: a) Raman spectra of an optically trapped PS bead, for integration times as indicated. Typical PS peaks are indicated with the 15 s spectrum. b) Raman spectrum of optically trapped bacteria spore *Bacillus Subtilis* for integration time 10 min . Measurements were performed using an estimated optical power between the 7 and 10 mW .

To further characterize the device, we performed finite-difference time domain (FDTD) simulations of the optical fields, using commercial software (FDTD solutions 8.5.3, Lumerical Solutions Inc., Canada). Simulated intensity profiles between the waveguides are shown in Figure 4a, both for the xz -plane and the yz -plane (x is along the flow direction, y is the height and z is the gap axis). The simulated profiles show an interference pattern that is well confined between the waveguides, hereby creating a strong field for optical trapping resulting in strong optical forces. The forces that act on these trapped particles have been calculated for the x -, y - and z -axis using the Maxwell stress tensor. In Figure 4b we give the resulting forces (in one direction for x and z due to symmetry, however, in two directions for y due to lack in symmetry, y_1 is towards to top of the waveguide).

The graph in Figure 4b shows the optical forces for x and y that pull the particle back to the centre point when it is moved away. The F_z shows a sinusoidal dependence on the bead position, which is in agreement with stable trapping points being located at the interference maxima (shown in Figure 4a). This explains why multiple beads can be trapped along the z -axis (see Figure 2). The calculated forces shown in Figure 4b are high and comparable to [4]. Therefore our trap can be characterized as a strong trap.

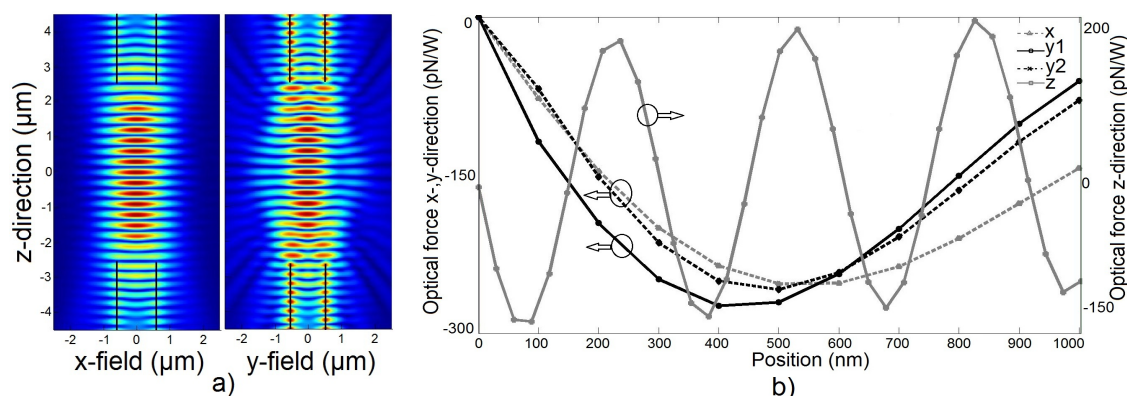


Figure 4: On left: Simulated intensity patterns in the xz - and the yz -plane. On right: Calculated forces of the trap as a function of bead position on the x -, y -, and z -axis.

Conclusion

We have presented a TriPleX dual-waveguide device capable of generating Raman spectra from on-chip optically trapped polystyrene beads or bacteria spores that are supplied through an integrated fluidic channel. We successfully and reproducibly trapped particles and obtained Raman spectra from them. The results presented are the first of its kind. The dual-waveguide device could lead to, amongst others, on-chip biological identification.

References

- [1] Richard L. McCreery. "Raman Spectroscopy for Chemical Analysis", volume 157. John Wiley & Sons, Inc., 2000.
- [2] A. Ashkin. History of Optical Trapping and Manipulation of Small-Neutral Particle, Atoms, and Molecules. *IEEE Journal On Selected Topics In Quantum Electronics*, vol.6:pp. 841–856, 2000.
- [3] A. Constable, J. Kim, J. Mervis, F. Zarinetchi, and M. Prentiss. Demonstration of a fiber-optical light-force trap. *Optics Letters*, vol.18:pp. 1867–1869, 1993.
- [4] Olav Gaute Hellesø, Pål Løvhaugen, Ananth Z. Subramanian, James S. Wilkinson, and Balpreet Singh Ahluwalia. Surface transport and stable trapping of particles and cells by an optical waveguide loop. *Lab on a Chip*, vol.12:pp. 3436–3440, 2012.
- [5] Yih-Fan Chen, Xavier Serey, Rupa Sarkar, and David Erickson. Controlled Photonic Manipulation of Proteins and Other Nanomaterials. *Nano Letters*, vol.12:pp. 1633–1637, 2012.
- [6] Thijs van Leest and Jacob Caro. Cavity-enhanced optical trapping of bacteria using a silicon photonic crystal. *Lab on a Chip*, vol.13(22):pp. 4358–4365, 2013.
- [7] Changan Xie, Mumtaz A. Dinno, and Yong-qing Li. "near-infrared raman spectroscopy of single optically trapped biological cells". *Optics Letters*, vol.27(4):pp. 249–251, 2002.
- [8] T. van Leest, F. Bernal Arango, and Jaap Caro. Optical forces and trapping potentials of a dual-waveguide trap based on multimode solid-core waveguides. *Journal of the European Optical Society - Rapid Publications*, vol.6:pp. 11022–1–11022–6, 2011.
- [9] Pål Løvhaugen, Balpreet Singh Ahluwalia, Thomas R. Huser, and Olav Gaute Hellesø. Serial Raman spectroscopy of particles trapped on a waveguide. *Optics Express*, vol.21(3):pp. 2964–2970, 2013.
- [10] TriPleX is a registered trademark from LioniX BV (www.lionixbv.nl).
- [11] A Leinse, R.G Heideman, M. Hoekman, C.M. Bruinink, C.G.H. Roeloffzen, Leimeng Zhuang, D.A.I. Marpaung, and M. Burla. TriPleXTM platform technology: Low-loss waveguide platform for applications from UV to IR. *16th European Conference on Integrated Optics, ECIO 2012*, pages 1–2, 18-20 April 2012 2012.

Design and Performance of a Packaged InP Wavelength Meter

R. G. Broeke,¹ D. Melati,² F. Morichetti²

¹ Bright Photonics BV, Netherlands, ronald.broeke@brightphotonics.eu, www.brightphotonics.eu

² Politecnico di Milano, Dipartimento di Elettronica, Informazione e Bioingegneria, via Ponzio 34/5, 20133 Milano, Italy

Over the past years many users of multi-project wafer (MPW) runs successfully demonstrated their Photonic ICs in the lab. However, for this generic technology to be successful outside a university environment it is pivotal to fully package PICs. This paper demonstrates a fully-packaged wavelength-meter prototype fabricated in an InP MPW run, as well as a design tolerance analysis. The device measures wavelength shifts across a 3 nm band with the potential to go below femtometer accuracy, centered anywhere in the 1465 to 1600 nm wavelength range. Additionally, we report on a novel integrated on-chip temperature sensor.

Introduction

Photonics has been identified by the European Union and industry alike as a key-enabling technology of the future, i.e. it is one of the drivers for innovation, high-tech start-ups, high added value and job creation in small and medium sized companies. One of the most interesting developments over the last few years is the rise of the generic foundry model for Photonic Integrated Circuits (PICs) in Europe [1]. The model provides cost sharing for PIC users at fabrication level, process level and wafer level and it established a software design environment with Photonic Design Kits (PDK). It reduces the financial and technological threshold for access to PIC prototypes by several orders of magnitude. This model is the vehicle by which PICs find their way to a multitude of diverse new applications. One of the first fields that benefits of this development is Sensing. This paper presents a wavelength sensor fabricated on an InP multi-project wafer (MPW) run [2], fiber pigtailed and fully packaged. It is the first report of a device from the InP MPW runs that demonstrates the full chain from photonic building blocks (BB) to a characterized prototype, including a tolerance analysis at circuit level.

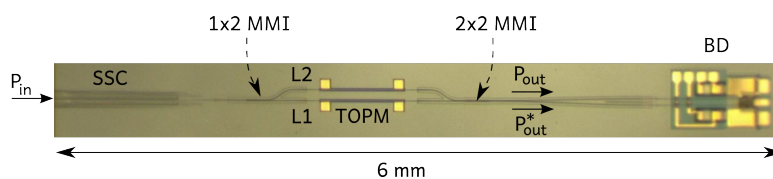


Figure 1: Photograph of the fabricated 6 mm long device.



Figure 2: The packaged device.

Device description

The wavelength meter is based on the well established interferometric effect: An optical component splits a light beam in two. Each beam travels along a path of optical length $n_{\text{eff}} \cdot L_1$ and $n_{\text{eff}} \cdot L_2$, respectively, where L_1 and L_2 are the geometrical path lengths and n_{eff} the effective refractive index of the paths. After traversing the paths a second component interferometrically recombines the beams. The phase relation at recombination depends on the optical path length difference $\Delta L = L_2 - L_1$ as $\Delta\theta = n_{\text{eff}} \cdot \Delta L / \lambda$. The output field, in complex numbers and omitting the time dependence of the electromagnetic wave, becomes $E_{\text{out}} = E_{\text{in}} \exp(i\Delta\theta)$. Here E_{in} denotes the amplitude of the input field, λ the wavelength and we omit loss. For $\Delta L \neq 0$ the output field amplitude E_{out} , and its intensity $P_{\text{out}} = [\text{Re}(E_{\text{out}})]^2$, become a nearly sinusoidal function of λ with a period or Free Spectral Range (FSR) of $\lambda_{\text{FSR}} = \lambda^2 / (n_g \Delta L)$, where $n_g = n_{\text{eff}} - \lambda \cdot \frac{\delta n_{\text{eff}}}{\delta \lambda}$ represents the group index.

The wavelength meter exploits precisely this wavelength dependency of P_{out} . However, a fluctuation of input power $P_{\text{in}} = |E_{\text{in}}|^2$ also modulates P_{out} , hence balanced detection (BD) is used to distinct between power fluctuations in the input and a wavelength shift. BD combines P_{out} and its inverted companion $P_{\text{out}}^* = [\text{Im}(E_{\text{out}})]^2$, also generated at interference, into balanced parameter $B = (P_{\text{out}} - P_{\text{out}}^*) / (P_{\text{out}} + P_{\text{out}}^*)$ independent of P_{in} .

The wavelength meter has been realized (Fig. 1) as a PIC on the FhG-HHI InP foundry in the form of a 1x2 Mach-Zehnder Interferometer (MZI) consisting of a 1x2 multi-mode interference (MMI) coupler in combination with a 2x2 MMI. The signals in the two outputs of the 2x2 MMI are inverted with respect to each other, i.e. two sinus-like functions 180 degrees out of phase, and fed into the balanced detector (BD) on the right side. The optical input on the left has an integrated spot-size converter (SSC) matching the circular 10 μm mode diameter of standard fiber. The arm-lengths in the MZI were optimized for a FSR = 10 nm at $\lambda = 1550$ nm. Both MZI arms contain a Thermo-Optical Phase Modulator (TOPM), which can tune the position of the MZI transfer function across a full λ_{FSR} period. The MMIs, BD, SSC, TOPMs and interconnecting waveguides were available as foundry-compatible GDS building blocks in the mask-layout design environment. Figure 2 shows the package of the anti-reflection coated device.

Tolerance analysis

The MZI performance is sensitive to random variations of the optical and geometrical design parameters, for example as caused by fabrication. A tolerance analysis with an optical circuit simulator in the design flow is able to perform a statistical analysis of the MZI. Figure 3(a) shows the wavelength meter's circuit model in AspicTM[3], assembled with BBs from the FhG-HHI library. The library describes each BB by a realistic model containing information of its statistical behavior. Figure 3(b) shows the effects of tolerances on the MZI transmission through a number of random device realizations; It considered the variability of loss and splitting ratio's of the 1x2 MMI (α_{12} , K_{12}) and of the 2x2 MMI (α_{22} , K_{22}), together with a variability of waveguide loss (α_{wg}) and n_{eff} . The circuit simulator processes these data through numerical approaches or analytical models [4]. This provides information on several statistical quantities such as the expected value and the variance of the circuit response, and a yield estimation and sensitivity analysis.

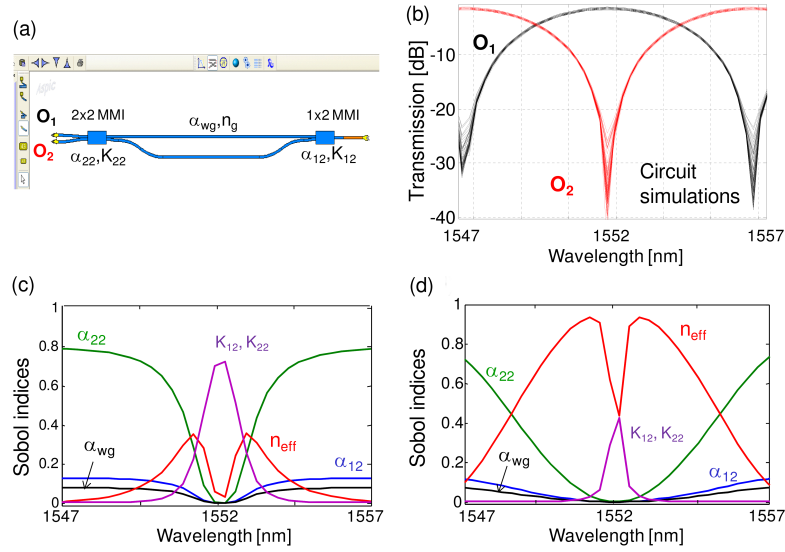


Figure 3: (a) Schematic of the MZI wavelength meter designed in AspicTM; (b) Effects of tolerances of the BB optical parameters on the MZI transmission at output ports O_1 (black curves) and O_2 (red curves). (c) and (d) show the sensitivity analysis (Sobol indices) of the MZI considering a thermal stabilization of 0.1°C (c) and 0.5°C (d).

A sensitivity analysis for finding the most critical parameters of the circuit can be done effectively by Sobol indices [5], which express the contribution of each parameter to the total variance of the process: The higher the Sobol index (between 0 and 1) is for a parameter, the more critical the parameter is to device performance. For instance, Fig. 3(c) shows that MZI extinction at port O_2 at $\lambda = 1552\text{ nm}$ is strongly sensitive to the MMI splitting ratios (K_{12} and K_{22} , purple curves); conversely, at the MZI transmission maxima (1547 nm and 1557 nm), excess loss (α_{22} , green curve) of the 2x2 MMI becomes dominant. These results assumed thermal stabilization within $\pm 0.1^\circ\text{C}$, corresponding to a n_{eff} fluctuation of about $\pm 2e-5$. For a coarser thermal stability (e.g. $\pm 0.5^\circ\text{C}$, $\pm 1e-4 n_{eff}$ fluctuations) n_{eff} is the most critical parameter at most wavelengths, as shown in Fig. 3(d).

Measurement results

For characterization of the packaged device a tunable laser served as the optical source. An optical attenuator followed by a polarization controller fixed the optical input power to the package. Two Keithly source meters simultaneously read the currents from the balanced photo-diodes while the laser scanned the wavelength of the input light. A TEC controller stabilized the temperature of the device at 20°C . Figure 4 presents the periodic diode response versus λ for TE and TM polarization, normalized at maximum current. The response is displayed in dB scale to better show the symmetrical response of the device, though this is not critical in this sensing application. The extinction ratio is around 25 dB, but due to the resolution of the data this is not always clear from the plot. The efficiency from fiber power to diode current was measured at $R_{fd} = 0.29\text{ A/W}$ for $\lambda = 1520$ to 1575 nm . For λ down to 1465 nm this was still 0.21 A/W . We expect the device to operate well above 1600 nm based on other data, resulting in a large 150 nm operational span. The FSR = 10 nm at $\lambda = 1550\text{ nm}$, as designed. TE and TM curves are

displaced with respect to each other, because the waveguides are not polarization independent. Figure 3 shows the excellent balanced-detection response B . Wavelength sensing operates in the bandwidth of about $\lambda_{bw} = 3$ nm on any steep section of the curves, as indicated by the dotted rectangle on the TM curve. The sensitivity of the wavelength meter follows from $\lambda_s = \lambda_{bw} \cdot NEP \cdot f / (R_{fd} \cdot P_{in})$, where NEP is the noise equivalent power of the diodes and f the sampling rate frequency. At $f = 10$ kHz, $P_{in} = -10$ dBm, and $NEP \approx 0.2$ pW/ $\sqrt{\text{Hz}}$ we find $\lambda_s \approx 2$ fm. With higher input power and/or lower f a sensitivity of attometers seems within reach.

The above sensitivity is an ideal case without temperature fluctuations, among others. However, the MZI has a novel feature: an integrated temperature sensor. Its sensitivity is 10 mV/ $^{\circ}\text{C}$ and multiple of these sensors can be integrated on a single chip. Therefore, accurate real time calibration for local temperature changes in the MZI is feasible.

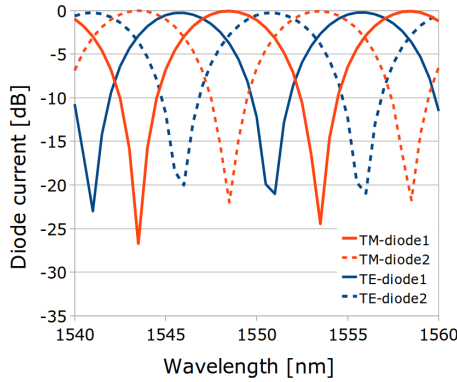


Figure 4: Measured balanced-detector photocurrents across two MZI periods.

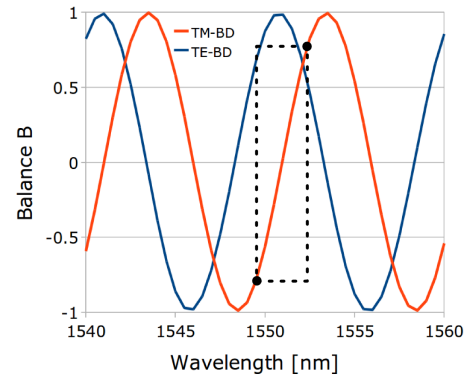


Figure 5: Measured balance B in the wavelength meter.

Acknowledgements

The authors wish to thank Warsaw University of Technology and Krzysztof Anders for characterization support, Andrea Melloni and Davide Cassano from Politecnico de Milano, and Arjen Bakker and Remco Stoffer from Phoenix Software for software support, FhG-HHI for their excellent foundry services, Detlef Pech for packaging, and Francisco Soares for the valuable discussions. The research leading to these results has received funding from EU FP7/2007-2013 under grant agreement ICT 257210 PARADIGM.

References

- [1] M. Smit, X. Leijtens, E. Bente, J. van der Tol, H. Ambrosius, D. Robbins, M. Wale, N. Grote, and M. Schell. Generic foundry model for InP-based photonics. *IET Optoelectronics*, 5(5):187–194, 2011.
- [2] Francisco M. Soares, Klemens Janiak, Jochen Kreissl, Martin Moehrle, and Norbert Grote. Semi-insulating substrate based generic inp photonic integration platform. In *Proc. SPIE 8767, Integrated Photonics: Materials, Devices, and Applications II*, page 10.1117/12.2017431, May. 22 2013.
- [3] AspicTM Filarete srl, Italy, www.aspicdesign.com; Phoenix BV, Netherlands, www.phoenixbv.com.
- [4] F. Morichetti D. Cassano and A. Melloni. Statistical analysis of photonic integrated circuits via polynomial-chaos expansion. In *Proceed. of Advanced Photonics*, page JT3A.8. Optical Society of America, Jul. 17–Jul. 19 2013.
- [5] I.M. Sobol. Global sensitivity indices for nonlinear mathematical models and their monte carlo estimates. *Mathematics and Computers in Simulation*, 55(1–3), 2001.

Scalable Optical Switch System with Optical Flow Control for Flat Datacenter Architecture

Wang Miao, Stefano Di Lucente, Jun Luo, Harm Dorren, and Nicola Calabretta

COBRA Research Institute, Eindhoven University of Technology, PO Box 512, 5600MB Eindhoven, the Netherlands

An optical flat datacenter network based on scalable optical switch system with optical flow control has been proposed and studied in this paper. The validation of 4x4 switch system shows error free operation at 40 Gb/s with 1dB penalty. The minimum end-to-end latency (including 25m transmission link) is less 300ns and $<10^{-5}$ packet loss for 0.5 load with buffer size of 16 packets is reported.

Introduction

Emerging services such as cloud computing and social networks are steadily boosting the Internet traffic. For every byte transmitted over Internet to or from a data center (DC), 1 GB of data is moved through the DC network (DCN) [1], putting a tremendous pressure on DCN. In large DCs with 10,000's of servers, merchant silicon top-of-the rack (TOR) switches are used to interconnect servers in a group of 40 per rack with 1 Gb/s link (10 Gb/s expected soon). To interconnect the 100's of TORs, with 10/40 Gb/s aggregated traffic (100Gb/s is expected soon) per TOR, current DCN is built up on multiple switches, each with limited port count and speed, organized in fat-tree topology [2]. This multi-layer topology has intrinsic scalability issues in terms of bandwidth, latency, costs and power consumption (larger number of high speed links).

To improve the performance and costs, flattened DCN is currently being widely investigated. Optical technologies have the potential of exploiting the space, time, and wavelength domain for scaling the port count while switching high speed data at nanoseconds time scale with low power and small footprint photonic integrated devices. Despite the several optical switch architectures presented so far [3], no one has been proved a large number of ports while providing a port-count independent reconfiguration time for low latency operation. Moreover, the lack of a practical optical buffer demands complicated and unfeasible system control for store-and-forward operation and contention resolution.

In this work, we propose and experimentally investigate a novel flat DCN architecture for TOR interconnect based on a scalable optical switch system with hardware flow control. Experimental evaluation of a 4x4 optical switch system shows dynamic operation including multicasting and only 1dB power penalty at 40Gb/s data rate. A buffer size of 16 packets sufficiently guarantees $<10^{-5}$ packet loss for 0.5 input load and less than 300ns minimum end-to-end latency could be achieved within 25m distance. Scalability investigation also indicates that the optical switch can potentially scale up to more than 64x64 ports with less than 1.5dB penalty while the same latency is retained.

System operation

The proposed flat DCN architecture based on NxN highly distributed control OPS architecture is shown in Fig. 1. Traffic load is balanced and configured by aggregation controller at the transmitter side. Each cluster groups N TORs, which transmit with

different wavelength $\lambda_1, \lambda_2 \dots \lambda_M$. Switching is performed based on per packet attached label information. At OPS node, the highly distributed control of the OPS [4] allows processing the M channels of each cluster in parallel, minimizing the reconfiguration time of the switch and thus the latency. Label extractor separates the optical label from the optical payload by using a fiber Bragg grating (FBG). The optical payload is then fed into the SOA based broadcast & select $1 \times N$ switch while the extracted label is split into two parts. One of them is detected and processed by the switch controller after optical-to-electrical conversion (O/E). The switch controller checks possible contentions, and configures the $1 \times N$ switch to block the contended packets with low priority and to forward packets with high priority [5]. Moreover, the switch controller generates the ACK signals used to acknowledge the aggregation controller on the reception or re-transmission of the packets. The other part of label power is re-modulated in an RSOA driven with the base band ACK signal generated by the switch controller and sent back to cluster side. This fulfills the efficient optical flow control in hardware which minimizing the latency and buffer size. Baseband ACK contributes to easy process by using a low pass filter and no interference with label information.

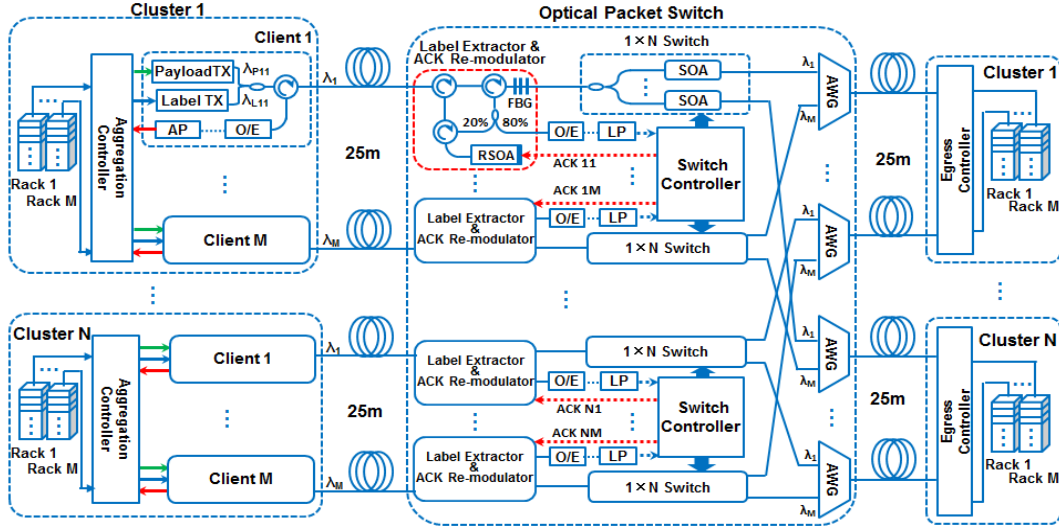


Fig. 1. WDM OPS architecture with highly distributed control.

Experimental set-up and results

For the validation of the DCN, we experimentally investigate the full dynamic operation including flow control of a 4×4 system. Packetized 40Gb/s NRZ-OOK payloads are generated with 540ns duration and 60ns guard time. An FPGA acts as aggregation controller that generates for each packet the label according to the port destination, and simultaneously provides a gate signal to enable the transmission of the payload with a certain load. Buffer manager inside FPGA stores the label information in a FIFO queue with a size of 16 packets and removes the label from the queue in response to a positive ACK. Otherwise the label and payload are retransmitted after re-signaling the input optical gates, implementing the packets retransmission.

RF tone labeling technique and bi-directional optical system are deployed to efficiently transmit the labels and ACK in a single fiber. Such labeling technique allows the parallel processing of the label bits which will greatly reduce the OPS processing time [4]. Here we use two RF tones ($f_1=284.2\text{MHz}$, $f_2=647.1\text{MHz}$) for coding the 2-bit label

information. Payload wavelengths are placed at $\lambda_{P11}=\lambda_{P21}=1544.9\text{nm}$ and $\lambda_{P12}=\lambda_{P22}=1548.0\text{nm}$. The label wavelengths, each carrying two RF tones, are centered at $\lambda_{L1}=1545.1\text{nm}$ and $\lambda_{L2}=1548.2\text{nm}$. The average optical power of the payload and the label at the OPS input is 2.5dBm and -2dBm, respectively. FBG is centered at label wavelength and has a -3dB bandwidth of 6 GHz which avoid spectral distortion of the payload. Optical spectra of the packets before and after label extractor for Cluster1 are shown in Fig. 2a and Fig. 2b.

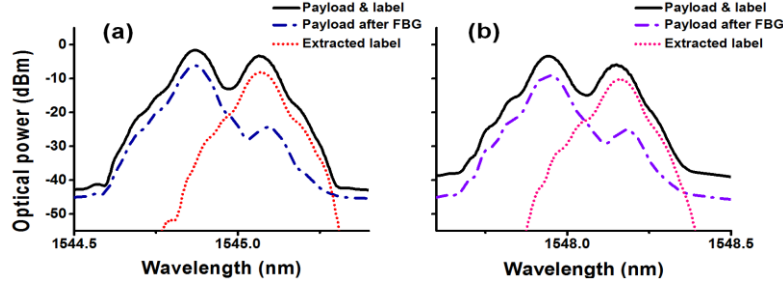


Fig. 2. Optical spectrum before and after label extractor for (a) Client1 (b) Client2.

Fig. 3 shows the dynamic operation of label and payload from both clusters. The time traces of the label detected by switch controller and the ACK feed-back detected by the aggregation controller at transmitter side are reported at the top. 2-bit label brings up 3 possibilities of switching since “00” represents no packet. “01” stands for output1, “10” for output2 and “11” for multicasting the payload to both ports. To clearly show the contention and switching mechanism, fixed priority has been adopted in the contention resolution algorithm. If two packets from different clients have the same destination, Client 1’s packet will be forwarded at the output while the packet from Client 2 will be blocked and a negative ACK will be sent back requesting packet retransmission. If Client1 is multicast, any data in Client2 will be blocked. Client2’s multicasting will only be approved if Client1 has no data.

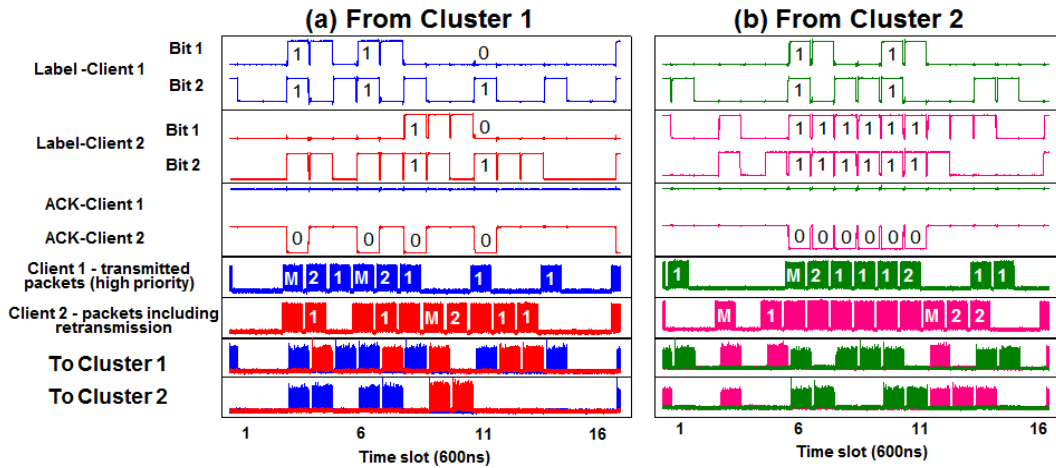


Fig. 3. Dynamic operation of labels and payloads from (a) Cluster1; (b) Cluster2

One or both of the SOA will be switched on to forward the packets to right destination. The waveforms of the transmitted packets (including retransmitted packets for Client 2) and the switch outputs are shown at bottom. “M” packet stands for multicast packet, which should be forwarded to both output ports. If Client 2 contends with Client 1 the packets will be blocked which are shown with unmarked packets in Fig. 3. In this case, a negative ACK is generated to inform buffer manager that the packets have to be

retransmitted. Fig. 3 clearly shows the successful optical flow control and multicasting operation. The minimum end-to-end latency (no retransmission) is 300ns including 250ns propagation delay introduced by 25m link.

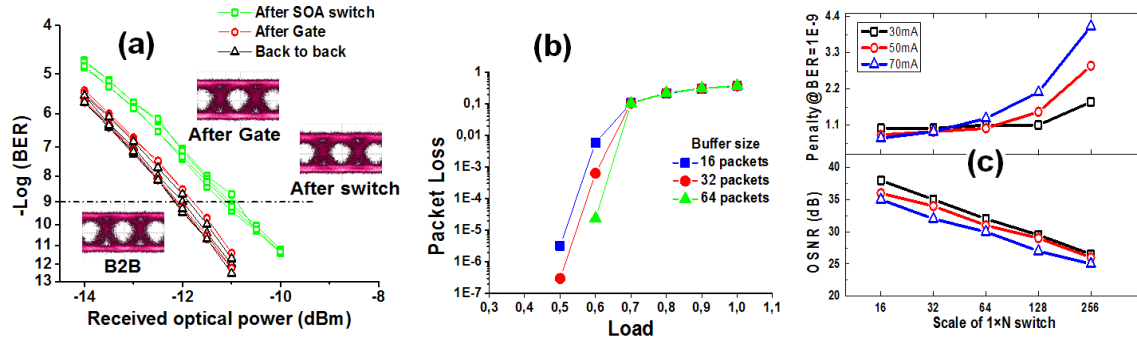


Fig. 4. (a) 40Gb/s payload BER curves and eye diagrams; (b) Packet loss vs. load with different buffer size (c) Penalty and OSNR vs. scale of 1xN switch.

Fig. 4a shows the measured BER performance for the system. Error free operation with only 1dB power penalty after the switch was measured. Less than 10^{-5} packet loss has been measured at 0.5 load and 16-packet buffer size as shown in Fig. 4b. Larger buffer size would improve the packet loss performance for the load smaller than 0.7. We further investigate the 1xN switch scalability of the proposed system by using an attenuator before the 1xN switch to emulate the coupling loss of the broadcast and select. Fig. 4c shows the penalty (measured at 1E-9) and OSNR of switch output as a function of N within different SOA bias current. It clearly shows that at N=64, less than 1.5 dB penalty is obtained which indicates that the OPS can be scaled to a large number of ports at the expense of limited extra penalty.

Conclusions

We experimentally demonstrate a 4x4 DCN architecture for 40 Gb/s packets. Exploiting the highly distributed control architecture, the efficient optical flow control, and the fast SOA switches, we report 300 ns minimum end-to-end latency (including 250 ns offset provided by the 25m transmission link) and packet loss of 10^{-5} for 0.5 input load and limited buffer size. Investigation on the switch scalability indicates that scaling up to 64x64 ports is possible at cost of 1.5dB extra power penalty.

Acknowledgements

This work has been supported by the FP7 European Project LIGHTNESS (FP7-318606).

References

- [1] G. Astfalk, "Why optical data communications and why now?," *Applied Physics A*, vol. 95, 933-940, 2009.
- [2] L. A. Barroso and U. Hölze, "The datacenter as a computer: an introduction to the design of warehouse-scale machines," Morgan and Claypool Publishers, Los Angeles, 2009.
- [3] C. Kachris and I. Tomkos, "A survey on optical interconnects for data Centers," *IEEE Communication Surveys & Tutorials*, vol. 14, 1021-1036, 2012.
- [4] J. Luo et al., "Optical Packet Switch with Distributed Control Based on InP Wavelength-Space Switch Modules," *IEEE Photon. Technol. Lett.*, vol. 24, 2151-2154, 2012.
- [5] S. Di Lucente et al., "Numerical and experimental study of a high port-density WDM optical packet switch architecture for data centers," *Optical Express*, vol. 21, 263-269, 2013.

Author Index

- Abbasi, A., 139
Abdulla, S.M.C., 69
Achouche, M., 235
Acuña, P., 147
Aerssens, M., 183
Ambrosius, H.P.M.M., 81, 219, 243, 259
Aubert, T., 175
Audenaert, J., 147
Augustin, L., 97

Baets, R., 49, 131, 159, 231
Barry, L.P., 11
Bengtsson, J., 231
Bente, E.A.J.M., 89, 97, 127, 259
Bette, S., 215
Beuzekom, M.G. van, 255
Bhat, S.P., 219
Bienstman, P., 113
Bitincka, E., 61
Boer, B.M. de, 69
Boerkamp, M.J., 283
Bogaerts, W., 223
Bolk, J., 93
Boom, H.P.A. van den, 135
Bosman, E., 65
Broeke, R.G., 287

Calabretta, N., 291
Cao, Z., 135
Caro, J., 279, 283
Carpintero, G., 127
Caucheteur, C., 117, 215
Cen, M., 73
Chen, H., 29
Chen, J., 73
Cheng, W.-H., 13
Coen, S., 207
Coomans, W., 267
Corradi, A., 127

D'Agostino, D., 81, 179, 259
Danckaert, J., 93, 271
DasMahapatra, P., 251
De Vries, T., 97
Debliquy, M., 117
Debregeas, H., 235
Deconinck, G., 147
Dekoster, J., 57
Descamps, F., 215
Dhakar, A., 49, 131
Di Lucente, S., 291
Dijkstra, M., 77
Dolores-Calzadilla, V., 243
Dorren, H.J.S., 199, 291
Duan, P., 199
Duport, F., 109

Ellis, A.D., 11
Elmogi, A., 65
Emplit, P., 191
Evenblij, R., 15

Fagan, A., 11
Fernandez, L., 219
Fiore, A., 203, 243

Gajanana, D., 255
García-Blanco, S.M., 77, 227
Gassenq, A., 41
Gelens, L., 267
Geluk, E.J., 167, 243
Gentili, G.G., 235
Gilardi, G., 151, 155
Ginis, V., 271
Golling, M., 3
Gorza, S.-P., 207
Grote, N., 85, 235
Gruca, G., 183
Guindi, R., 65
Guo, W., 57

Author Index

- Gusarov, A., 183
Gustavsson, J., 231
- Haelterman, M., 207
Haglund, A., 231
Hanselaer, P., 147
Harmsma, P.J., 69
Heideman, R., 283
Heiss, D., 203, 243
Heldens, J.T., 283
Hendriks, T.A., 227
Hens, Z., 41, 175
Higuera-Rodriguez, A., 203
Hoekman, M., 283
Hoste, J.-W., 113
Hu, C., 41
Hu, X., 117
Huynh, T., 11
Håkansson, J., 105
- Iannuzzi, D., 183
- Jiao, Y., 167
Justo, Y., 41
- Kalathimekkad, S., 65
Kat, P., 15
Keller, U., 3
Keulen, F. van, 263
Keyvaninia, S., 139
Khoder, M., 93
Kinet, D., 117
Kleijn, E., 171, 259
Klenner, A., 3
Kockaert, P., 207
Koelemeij, J.C.J., 25
Koonen, A.M.J., 29, 101, 121, 135, 247
Koster, L.J.A., 227
Kumari, S., 159, 231
- Langelaar, M., 263
Lanteri, D., 235
Larsson, A., 231
Latkowski, S., 97, 259
Ławniczuk, K., 275
Le Thomas, N., 49, 131
Leest, M.M. van, 279
Leest, T. van, 283
- Leijtens, X.J.M., 93, 155, 171, 179, 187, 255, 275
Leinders, S.M., 37
Leinse, A., 283
Lenstra, D., 53
Leyre, S., 147
Link, S.M., 3
Lo Cascio, D.M.R., 69
Loo, R., 21
Luo, J., 291
- Maes, B., 33, 143
Malik, A., 21
Mangold, M., 3
Massar, S., 109, 191
Massaut, V., 183
Mehta, N., 101
Melati, D., 85, 235, 287
Melloni, A., 85, 235
Merckling, C., 57
Merolla, J.-M., 191
Meuret, Y., 147
Miao, W., 291
Millán-Mejía, A., 195
Missinne, J., 65
Moeyart, V., 73
Morichetti, F., 85, 235, 287
Morthier, G., 139, 163
Moskalenko, V., 89
Mountjoy, J., 11
Muneeb, M., 21
Mégret, P., 73, 117, 183
- Nguimdo, R.M., 93
Nuijts, R., 25
- Oh, C.W., 121
Okonkwo, C.M., 25, 29, 247
Olislager, L., 109, 191
- Pace, A., 77
Pal, P.K., 163
Paladugu, M., 57
Pantouvaki, M., 57
Pathak, S., 21
Patra, M.K., 109
Pello, J., 167
Peyskens, F., 49, 131

- Phan Huy, K., 191
 Piramidowicz, R., 275
 Pironio, S., 109
 Pozo, J.M., 37, 69
 Pustakhod, D., 187

 Rabbani Haghighi, H., 81, 179, 259
 Raz, O., 199
 Rehman, S.U., 263
 Rivolta, N., 143
 Roelkens, G., 21, 41, 139, 159, 211, 219, 231
 Rohit, A., 45, 251
 Rosolen, G., 33
 Ruocco, A., 223
 Ryckeboer, E.M.P., 41

 Safaisini, R., 231
 Safioui, J., 109
 Sanchez, D., 159, 231
 Santos, R., 179
 Schilder, N.J., 239
 Sefünc, M.A., 77, 227
 Sengo, G., 77
 Shen, L., 211
 Shi, K., 11
 Shimura, Y., 21
 Smalbrugge, E., 167, 199, 243
 Smit, M.K., 61, 81, 89, 97, 127, 151, 155, 167, 171, 179, 187, 195, 203, 211, 219, 243, 255, 259, 275
 Soares, F.M., 85, 179, 235
 Sotiropoulos, N., 25
 Stabile, R., 45, 251
 Subramanian, A.Z., 49, 131
 Swaelens, M., 207
 Szczepański, P., 275

 Tangdiongga, E., 101, 121, 135
 Tassin, P., 271
 Teigell Beneitez, N., 65
 Thijs, P., 81
 Tian, B., 57
 Tilma, B.W., 3
 Tol, J.J.G.M. van der, 167, 195, 211, 219

 Uden, R.G.H. van, 29, 247
 Urbach, H.P., 37, 239

 Van Campenhout, J., 21, 57
 Van der Sande, G., 267
 Van Steenberge, G., 65
 Van Thourhout, D., 57, 105, 175, 223
 Veldhoven, P.J. van, 81, 243
 Verschaffelt, G., 93
 Verstuyft, S., 175
 Viaene, S., 271
 Vries, T. de, 243

 Waardt, H. de, 25, 29, 247
 Wale, M.J., 151, 155, 275
 Walsh, A.J., 11
 Wang, R., 159, 231
 Wang, Z., 57
 Werquin, S., 113
 Westerveld, W.J., 37
 Williams, K.A., 45, 251
 Woodhead, E., 191
 Wuilpart, M., 73, 183
 Wuytens, P., 49

 Xie, W., 175

 Yao, W., 151, 155
 Yousefi, M., 37, 53

 Zaugg, C.A., 3
 Zhang, Chao, 117
 Zhu, Y., 175